CORRALLING ELECTRONS IN METASTABLE VANADIUM OXIDES: IMPLICATIONS FOR NEUROMORPHIC COMPUTING, ELECTROCHEMICAL ENERGY STORAGE AND PHOTOCATALYSIS

A Dissertation

by

JUSTIN L. ANDREWS

Submitted to the Office of Graduate and Professional Studies of
Texas A&M University
in partial fulfillment of the requirements for the degree of

DOCTOR OF PHILOSOPHY

Chair of Committee,	Sarbajit Banerjee
Committee Members,	Timothy Hughbanks
	Matthew Sheldon
	Donald Naugle
Head of Department,	Simon North

May 2021

Major Subject: Chemistry

ABSTRACT

Charge ordering resulting from the localization of electrons in periodic potential wells is a characteristic manifestation of strong electron correlation in periodic solids. Synthetic approaches that allow for independent control over composition and crystal structure provide a means to independently modulate the strength of electron correlation across different polymorphs of the same compound as a result of the strong coupling of spin, charge, orbital, lattice, and atomic degrees of freedom. Binary, and ternary vanadium oxides represent a promising system to systematically tune electron correlation because of the availability of multiple, easily accessible redox states ($V^{5+}/V^{4+}/V^{3+}$); a wide range of structural and bonding motifs accessed through connecting tetrahedral, square pyramidal, and octahedral units VO_x units; and the ability of extended V_2O_5 frameworks to intercalate ions spanning the periodic table to yield a diverse palette of ternary phases with the composition $M_xV_2O_5$. Navigating “rugged” energy landscapes across this system to identify local minima, each representing a metastable polymorph, holds much promise for accessing a greatly expanded set of bonding motifs and functional properties and for exploring the interplay between spin, charge, orbital, lattice, and atomic degrees of freedom.

In this dissertation, an extensive toolset of topochemical transformations has been developed, yielding metastable binary V_2O_5 phases. Furthermore, efforts to independently tune the composition (*i.e.*, the identity of M and its

stoichiometry, *x*) and structure (*i.e.*, the connectivity of the V—O framework) across binary and ternary (and even quaternary) vanadium oxides have been detailed. These approaches have served to elucidate structure—property relationships in these systems and further facilitated control over electron correlation, electronic structure, and ion diffusion pathways, enabling the design of candidate materials for neuromorphic computing, insertion cathodes of lithium and “beyond lithium” batteries, and photocatalysis. Some salient functional properties accessed within this palette of materials include the first high voltage, high capacity, and high cyclability insertion host for Mg ions, ζ-V_2O_5; a metastable β-$Sn_xV_2O_5$ compound that resolves the longstanding challenge of photocorrosion of light-harvesting quantum dots; and layered materials that afford control over electron correlation as a function of layer thickness and degree of hydration of inserted cations.

DEDICATION

This dissertation is dedicated to my parents. We often joke that even when I was a child, my mother never let me beat her at anything unless I had well and truly won; she instilled in me a sense of competition and a drive to succeed. Growing up, my father never shielded me from the realities of life by blunting the consequences of my failures; he taught me to take failure in stride, learn from my mistakes, and to never be sated by successes. Not only was this sound parenting, but, in retrospect, it was fitting preparation for the rigors of academic research. For each success you read about in this dissertation there were many more failures. Thank you, Mom and Dad, for setting me up for success. In reality there is no such thing as an individual accomplishment. I don't know that I could have gotten to this point without you.

ACKNOWLEDGEMENTS

I would like to thank my advisor and mentor, Dr. Banerjee, for tirelessly advocating for his students within and without the Texas A&M Department of Chemistry. Despite being a first-generation college student uninitiated in the culture of higher education, he recognized in me an ability that I still struggle to acknowledge myself. He is an exemplar of successful mentoring and continuously tailors his mentoring style to maximize the potential of each and every student in his group. I am grateful that he has pushed me to succeed while at all times teaching me the tools to achieve that success.

I would like to thank my committee members, Dr. Hughbanks, Dr. Sheldon, and Dr. Naugle for their guidance and support throughout the various milestones of the chemistry Ph.D. program. I would like to thank Dr. Meyya Meyyappan, my advisor during the course of my NASA Space Technology Research Fellowship, for his guidance and support during this research and for his words of wisdom.

I would like to thank the many outstanding collaborators that I have had the good fortune of working with in the labs of Dr. Bai-Xiang Xu, Dr. Stan Williams, Dr. Alex Moewes, Dr. David Prendergast, Dr. Ganapathy Sambandamurthy, Dr. Louis Piper, Dr. Dave Watson, Dr. Robert Klie, Dr. Jordi Cabana, Dr. Peihong Zhang, Dr. Patrick Shamberger, and Dr. James Batteas. I would also like to thank all of the hard-working beamline scientists that I have worked with at the Canadian Light Source and in particular Dr. Jian Wang, Dr. Lucia Zuin, and Dr. Teak Boyko.

I would like to thank the many members of the Banerjee Research Group that I have had the pleasure of working with during my time in graduate school. All have been kind and collaborative colleagues and some have become life-long friends. Special thanks to Dr. Luis De Jesus for showing me ropes of synchrotron science. Many thanks to Dr. Rachel Davidson and Erick Braham for weekly coffee breaks and for solidarity throughout the graduate school experience. I would also like to acknowledge Dr. Peter Marley whose pioneering work in the Banerjee Research Group laid a strong foundation upon which my work has built and who invested the time to train me when I first joined the group.

Finally, a thousand thanks to my wife, Allie. Without you, my time in graduate school would have had far fewer laughs, far fewer smiles, far fewer (and often much-needed) breaks, and far more frustration. Your hard work and dedication to your own career have been a constant inspiration to me and I will always remember how you challenged me to do my best and encouraged me in the most stressful of times.

CONTRIBUTORS AND FUNDING SOURCES

Contributors

This work was supported by a dissertation committee consisting of Professor Sarbajit Banerjee, Professor Timothy Hughbanks of the Department of Chemistry, Professor Matthew Sheldon of the Department of Chemistry, and Prof. Donald G. Naugle of the Department of Physics.

Dr. Thomas Tolhurst, under the advisement of Dr. Alex Moewes, collected and analyzed resonant inelastic X-ray scattering data and performed the DFT calculations shown in Chapter 2. Dr. Luis De Jesus, under the advisement of Dr. Sarbajit Banerjee, helped collect and analyze the STXM data shown in Chapter 2. Dr. Peter Marley, under the advisement of Dr. Sarbajit Banerjee, collected Raman data shown in Appendix A and assisted with the collection of diffraction data shown in Chapter 2. Dr. Sujay Singh and Dr. Colin Kilcoyne, under the advisement of Dr. Ganapathy Sambandamurthy, collected and analyzed the electrical transport data shown in Chapter 3 and in Appendix B. Dr. Peter Stein, under the advisement of Dr. Bai-Xiang Xu, created compositional and strain maps and performed finite element simulations shown in Chapter 5 and in Appendix C. David Santos and Dr. Cody Chalker, under the advisement of Dr. Sarbajit Banerjee and Dr. James Batteas, prepared the V_2O_5 inverse opal structures shown in Chapter 5 and in Appendix C. David Santos, under the advisement of Dr. Sarbajit Banerjee, collected the Raman spectra shown in Appendix C. Dr.

Rachel Davidson, under the advisement of Dr. Sarbajit Banerjee, helped collect the scanning transmission X-ray microscopy images shown in Chapter 5 and Appendix C. Dr. Arijita Mukherjee, under the advisement of Dr. Robert Klie, collected scanning transmission electron microscopy (STEM) images, collected electron energy-loss spectra, and collected single nanowire energy-dispersive X-ray spectra shown in Chapter 6. Dr. Hyun Deog Yoo, under the advisement of Dr. Jordi Cabana, performed electrochemical measurements shown in Chapter 6 and in Appendix D. Dr. Abhishek Parija, under the advisement of Dr. Sarbajit Banerjee and Dr. David Prendergast, performed density functional theory (DFT) calculations shown in Chapter 6. Dr. Abhishek Parija, under the advisement of Dr. Sirine Fakra, collected vanadium K-edge spectra shown in Chapter 6. Dr. Junsang Cho and Kelly Nieto assembled the $M_xV_2O_5$/CdX heterostructures shown in Chapter 7 under the advisement of Dr. Sarbajit Banerjee. Dr. Junsang Cho collected and analyzed transient absorption data shown in Chapter 7 under the advisement of Dr. Sarbajit Banerjee and Dr. Matthew Sfeir. Dr. Junsang Cho, under the advisement of Dr. Sarbajit Banerjee, collected TEM images shown in Chapter 7. Dr. Linda Wangoh collected hard X-ray photoelectron spectroscopy and X-ray photoelectron spectroscopy under the advisement of Dr. Louis Piper. Dr. Nuwanthi Suwandaratne performed catalytic hydrogen evolution reactions shown in Chapter 7 under the advisement of Dr. Dave Watson. Dr. Karthika Kadassery performed the gas chromatography shown in Appendix E under the advisement of Dr. David C. Lacy. Dr. Peihong Zhang performed DFT

measurements shown in Figure 7 and in Appendix E. Alec Mohr and Michelle Gross performed experiments for Chapter 7 and Chapter 5, respectively, as part of their undergraduate research experiences. All other work conducted for the dissertation was completed by the student independently.

Funding Sources

Graduate study and dissertation research were supported by a Space Technology Research Fellowship (NSTRF) from the National Aeronautical and Space Administration under grant number 80NSSC17K0182. This work was also made possible in part by the NSF under DMR 1504702 and DMR 1809866. Its contents are solely the responsibility of the authors and do not necessarily represent the official views of the NSF. Use of the Advanced Photon Source at Argonne National Laboratory was supported by the U.S. Department of Energy, Office of Science, Office of Basic Energy Sciences, under Contract No. DE-AC02-06CH11357. Scanning transmission X-ray microscopy (STXM) and resonant inelastic X-ray spectroscopy (RIXS) were performed at the Canadian Light Source, which is supported by the Natural Sciences and Engineering Research Council of Canada, the National Research Council Canada, the Canadian Institutes of Health Research, the Province of Saskatchewan, Western Economic Diversification Canada, and the University of Saskatchewan. Use of the TAMU Materials Characterization Facility is acknowledged. Use of the Texas A&M Microscopy and Imaging Center is acknowledged.

TABLE OF CONTENTS

Page

LIST OF FIGURES

Page

as the background spectrum (I_0, labeled with a square region) and used to convert the obtained transmission data to absorption data. (B) Region-of-interest (ROI) analysis is performed by selecting specific regions of the sample and averaging the spectrum across the user-defined pixels. (C) In order to better understand the spatial distribution of spectrally similar regions of the sample, principal component analysis (PCA) coupled to cluster analysis is employed. PCA defines mutually-orthogonal eigenspectra (see Figure C.7, Figure C.12D, and Figure C.15D) that provide the best separation of the spectra obtained at each pixel in the STXM image by maximizing variance and covariance within the hyperspectral data. (D) Thickness maps can be generated from the raw STXM data as required for generating composition maps. (E) The pixels (i.e., spectrum at each pixel) are scored along each eigenspectrum and then clustered together based on the similarity of their scores. The maps in Figure 5.2D, Figure C.14, and Figure C.18 thus reveal the spatial distribution of spectrally similar pixels. Each pixel is assigned a single color despite receiving contribution from multiple eigenspectra and for this reason PCA-clustering is referred to as a "winner-takes-all" approach to image processing. The resulting PCA-clustering spectra are obtained by integrating the spectra across all clustered pixels (i.e., the "Cluster 3" spectrum in Figure 5.2A is obtained by integrating the spectra at each red pixel in Figure 5.2D). (F) Singular value decomposition (SVD) can be performed to map each of these eigenspectra and their weights across each pixel of the image, which provides a means of developing a composition map. (G) Compositional values are assigned to each of the spectra obtained by PCA-clustering by comparison to previously published theoretical and experimental studies of lithiated V_2O_5 materials [Maganas, D.; et al. First Principles Calculations of the Structure and V L-Edge X-Ray Absorption Spectra of V_2O_5 Using Local Pair Natural Orbital Coupled Cluster Theory and Spin-Orbit Coupled Configuration Interaction Approaches. *Phys. Chem. Chem. Phys.* 2013, *15* (19), 7260–7276.; Scanlon, D. O.; et al. An Ab Initio Study of Reduction of V_2O_5 through the Formation of Oxygen Vacancies and Li Intercalation. *J. Phys. Chem. C* 2008, *112* (26), 9903–9911.; De Jesus, L. R.; et al. Striping Modulations and Strain Gradients within Individual Particles of a Cathode Material upon Lithiation. *Mater. Horizons* 2018, *5*, 486–498.].(H) The SVD maps in (F) and the spectra/composition values assigned in (G) can be used to generate compositional and stress maps for individual nanoparticles [De Jesus, L. R.; et al. Striping Modulations and

LIST OF TABLES

Page

1. INTRODUCTION*

1.1. Overview: Corralling Electrons in Metastable Vanadium Oxides

Charge ordering resulting from the localization of electrons in periodic potential wells is often observed in strongly correlated systems. Synthetic approaches that allow for precise control over the periodicity, pattern, and strength of electron localization are greatly desired; however, modulating periodic electron localization predictably and with measurable tunability represents a significant challenge. In principle, such a synthetic approach would involve varying the electronic coupling between adjacent metal sites either through modulation of bonding or composition, but such attempts commonly effect phase transitions to entirely different crystal structures. Given the strong coupling between spin, charge, orbital, lattice, and atomic degrees of freedom in transition metal oxides, which is a direct result of the narrow bands derived from d-orbitals, it is imperative to devise synthetic approaches that would afford wholly independent control over composition and crystal structure. As such, there is great interest in the design of synthetic methods that allow for free energy landscapes of extended solids to be

* Part of this chapter is reprinted (adapted) with permission from Andrews, J. L.; Santos, D. A.; Meyyappan, M.; Williams, R. S.; Banerjee, S. Building Brain-Inspired Logic Circuits from Dynamically Switchable Transition-Metal Oxides. *Trends in Chemistry*, **2019**, *1* (8), 711-726.
Part of this chapter is reprinted (adapted) with permission from Andrews, J. L.; Banerjee, S. It's Not Over Until the Big Ion Dances: Potassium Gets Its Groove On. *Joule*, **2018**, 2 (11), 2194-2197.

efficiently navigated in a manner that allows for shallow local minima, corresponding to metastable polymorphs, to be accessed.

Owing of the complexity of the problem, the choice of chemical system within which to investigate synthetic methods for tuning electron correlation is of critical importance. At a minimum, members of the system ought to exhibit a wide range of electronic behavior intermediate to and spanning the two extremes between itinerant and highly localized electron behavior. The wider energy dispersion of bands when directly compared to discrete molecular orbitals in single molecules typically favors far greater delocalization of electrons and the multiplicity of sites implies that dimensional confinement of carriers can be established only for specific (low-dimensional) crystallographic motifs. Consequently, the d-bands of the materials must not be so wide as to render charge localization not feasible due to a high degree of electron delocalization but also not so narrow as to inhibit band transport. The framework must also exhibit a large number of charge degrees of freedom so as to be robust towards oxidation/reduction while maintaining framework connectivity. Vanadium oxides represent such a system due to the availability of multiple, easily accessible redox states (V^{5+}/ V^{4+}/ V^{3+}), relatively narrow 3d bands with energy dispersion tunable as a function of ionicity/covalency of vanadium—oxygen bonds, and the accessibility of a variety of low-dimensional structural motifs amenable to dimensional confinement of carriers.[1] As an added benefit, oxides of vanadium tend to crystalize in open-framework structures that can further intercalate ionic

species spanning the breadth of periodic table from (i.e., from alkali to main group elements and lanthanides as well as some organic cations) to create a diverse set of ternary compounds with the stoichiometry of $M_xV_2O_5$.[2–10]

These ternary vanadium oxide compounds ($M_xV_2O_5$) tend to exhibit varying degree of charge localization. Upon intercalation, the inserted ion, M, donates its valence electrons to the vanadium oxide framework and the empty V 3d orbitals (d^0) of V_2O_5 framework become partially filled (d^1/d^0) with the extent of electron delocalization and charge ordering varying sensitively as a function of the V_2O_5 framework and the identity of the cation. In some instances, V—O hybrid states further hybridize with specific states (e.g., lone-pair states of p-block cations or d-states of late transition metals) of the intercalated M ions, dramatically, modulating the electronic structure of the $M_xV_2O_5$ materials. Depending on the identity of the intercalated ion, M, its stoichiometry, *x*, and thereby the extent of hybridization with the vanadium oxide framework, $M_xV_2O_5$ materials can exhibit insulating, semiconducting (exhibiting a broad range of bandgaps), or even metallic behavior. Furthermore, a wide range of structural and bonding motifs are observed through a number of permitted edge- and/or corner-sharing connections between tetrahedral, square pyramidal, and octahedral VO_n units. This high degree of compositional, structural, and functional tunability renders the $V_2O_5/M_xV_2O_5$ systems highly desirable as a sandbox for precisely altering the degree of charge localization.

Surprisingly, these ternary compounds have the ability to avoid collapse upon topochemical transformations (e.g., deintercalation of the ‘M’ cation). This ability is owed, at least in part, to the strong bonding between vanadium and oxygen and the ability of vanadium to robustly undergo oxidation/reduction ($V^{5+}/V^{4+}/V^{3+}$) upon deintercalation of the M-site cations. Following deintercalation of the M-site cation the V—O framework is left largely unaltered, enabling the stabilization of several metastable binary oxides that differ in structure and bonding but not composition, enabling fundamental studies that elucidate structure—property relationships in these systems and provide insight into the role of V—O atomic connectivity on electron correlation and ion diffusion pathways. The plethora of experimentally accessed and theoretically predicted V_2O_5 polymorphs delineate the "rugged” energy landscape of the V—O binary system, which is characterized by a multiple closely spaced local minima.

Finally, these metastable empty polymorphs can be intercalated with various M-site cations to yield metastable ternary phases to prepare a number of isostructural $M_xV_2O_5$ materials that differ in composition but not in structure, enabling bandgap engineering and elucidating the role of the M cation in tuning correlation. Taken together, these topochemical approaches provide a means of navigating what represents very “rugged” energy landscapes. These approaches and the ability to stabilize metastable binary and ternary phases holds much promise for accessing a greatly expanded set of bonding motifs and functional

properties and for exploring the interplay of spin, charge, orbital, lattice, and atomic degrees of freedom.

In this dissertation, an extensive toolset of topochemical transformations in the V_2O_5—$M_xV_2O_5$ system are described. Efforts to independently tune the composition and structure of binary (V_2O_5) and ternary ($M_xV_2O_5$) vanadium oxides with a goal of further facilitating control over electron correlation, electronic structure, and ion diffusion pathways are detailed. These approaches have been applied to the rational design of candidate materials for neuromorphic computing (Chapters 2-4), insertion cathodes (Chapters 5 and 6), and photocatalysis (Chapter 7). In Chapter 2, a method for modulating the band gap and the extent of electron correlation in layered $M_xV_2O_5$ materials through chemical exfoliation is discussed. In Chapter 3, the nonlinear transport characteristics of a layered class of hydrated ternary vanadium oxide compounds is discussed as a potential neuromorphic circuit element. In Chapter 4, a new type of metal—insulator transition mechanism that relies on coupled electronic and ionic diffusion is detailed. In Chapters 5 and 6, polaron localization in vanadium oxide cathode materials is explored and mitigated through incorporation of mesoscale curvature (Chapter 5) and by modulation of atomistic structure to fundamentally alter diffusion pathways and polaron localization (Chapter 6). In Chapter 7, a metastable vanadium oxide is intercalated with divalent tin to design a hole extraction and transport layer that enables sub-ps hole transfer from photoexcited

quantum dots. A brief overview of the background material for each field and the resulting motivation for designing specific materials is provided below.

1.2. Overview: Implications for Neuromorphic Computing

Processing, storing, and transmitting information accounts for ~10% of global energy use; projections suggest that computational energy demands will be 10× higher than the projected global energy supply by 2040. Realizing solid-state analogs of neural circuitry, using 'neuromorphic' materials, holds promise for enabling a new energy-efficient computing paradigm. The metal-insulator transitions of electron-correlated transition-metal oxides provide an attractive vector for achieving large conductance switching with minimal energy dissipation. Here, we review current understanding of the mechanisms underpinning electronic instabilities, discuss methods for modulation of spiking behavior through tuning of atomistic and electronic structure, and highlight the need for establishing deterministic and independent control of transformation characteristics such as switching magnitude, energy thresholds, heat dissipation, hysteresis, and dynamics of relaxation.

1.2.1. Brain-Like Computing with Transition-Metal Oxides

The primary driver of the electronics revolution of the past 40 years, the exponential improvement in Si integrated circuits with time (known as Moore's scaling), has saturated. This has occurred just as the era of 'big data' has arrived. We are now collecting more data than we can transmit, store, and analyze. Projections suggest that the demand for computation would be 10× higher than

the projected global energy supply can support by 2040.[11] Without exponential increases in computing power and efficiency, transformative visions such as the Internet of Things, autonomous transportation, and personalized medicine will be throttled by the inability of current computing technologies to handle the magnitude and complexity of human- and machine-generated data. The energy inefficiency of existing computing architectures derives from the fundamental constraints imposed by the physics of thermionic excitation of charge carriers across semiconductor conduction channels (Figure 1.1A).[12–14] This translates to power demand and accompanying heat dissipation that no longer decrease with reduction in size of active elements; in the modern 'age of dark silicon', a significant fraction of the chip must be left inoperative as a result of insurmountable power constraints.[13]

The human brain processes complex information at least 10^4 times more efficiently than digital computing on silicon.[16,18] Neurons combine information received across synaptic connections with many other dendrites and encode output information through specifically timed trans-synaptic pulses, called 'action potentials.' Figure 1.1B shows the famous measurement by Hodgkin and Huxley across a giant squid axon.[15] Specific spike timings further enable the retention of multiple internal states (constituting memory), imbuing the ability to 'learn' through evolution of internal neuronal weights.[19] Thus, unlike currently utilized von Neumann architectures, computing and memory functions are co-located in the

human brain, enabling improved energy efficiency and reducing the need to shuttle data.

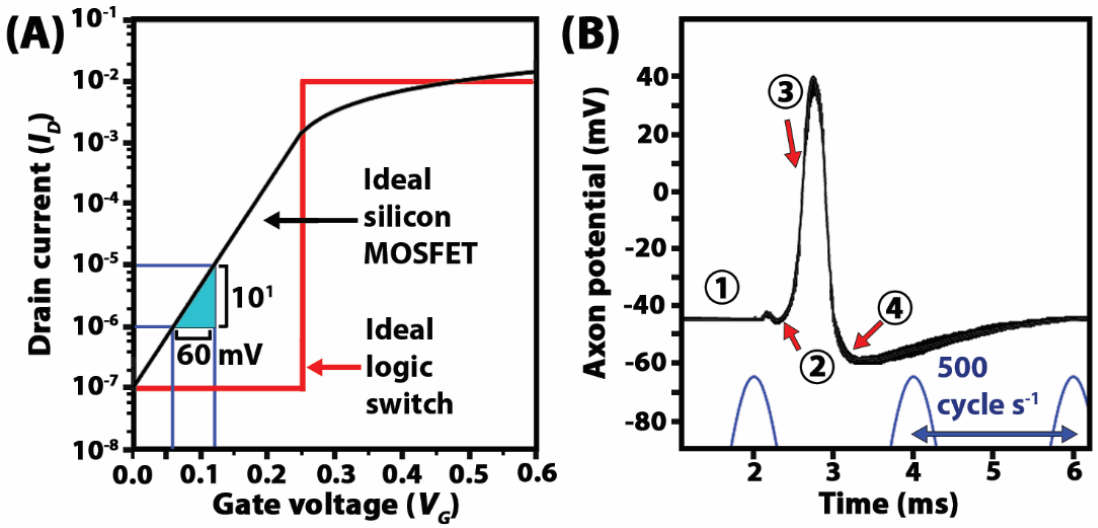

Figure 1.1. (A) Switching characteristics of workhorse Si-based metal-oxide semiconductor field-effect transistors (MOSFET) are shown in black; the Fermi-Dirac electron distribution of electron energies at room temperature limits the steepness of switching characteristics to 60 mV (V_G) per decade increase in current (I_D) across the transistor channel. Such characteristics embody the inefficiencies of digital computing.[14] An ideal logic switch with a much sharper slope is shown in red. (B) Action potential of a giant squid axon as originally recorded by Huxley and Hodgkin ('digitally-remastered' using graph digitizer software). Four distinct regions of the action potential are highlighted, including: (1) resting potential; (2) sodium-channel-driven hyperpolarization; (3) potassium-channel-driven depolarization; and (4) a refractory recovery period. (C) Neuromorphic action potential generated using a VO_2 memristor maps to the biological action potential in (B) with high fidelity. This neuromorphic function is underpinned by the metal-insulator transition (MIT) of VO_2 and derives from the negative differential resistance (NDR) of the device. (D) Demonstration of NDR in an NbO_2 device. (B), (C), and (D) are adapted from references: [15], [16], and [17], respectively.

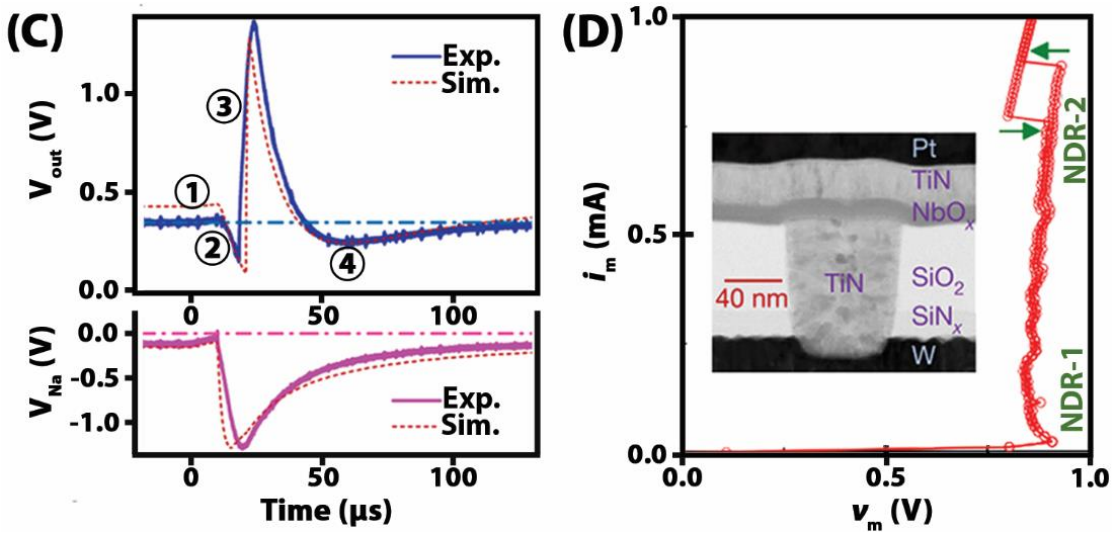

Figure 1.1. Continued.

1.2.1.1. Emulating Neural Circuitry Using Physical Devices

Neuromorphic computing aims to design logic circuity that emulates neuronal logic and memory function. The possibility of emulating neuronal function using theorized circuit elements named ‘neuristors’ was first proposed in 1962 – yet full realization of such a notion necessitates switching of the electrical conductance of solid-state compounds across orders of magnitude in an energy-efficient manner.[20] Initial approaches to neuromorphic computing utilized standard digital processors but were wasteful in terms of silicon area and power dissipation. Consequently, the next advance was to design new silicon-based chip architectures such as complementary metal-oxide semiconductors (CMOS) explicitly for neural network applications,[21,22] seeking to mimic the leaky integrate-and-fire (LIF) behavior of neurons.[23,24] Nevertheless, these attempts have failed to approach the energy efficiency of the human brain and are constrained by the

thermodynamic limitations of free-carrier generation mechanisms in electrostatically modulated semiconductors (Figure 1.1A). Another key limitation of neuronal architectures emulated on conventional chips is their inability to mimic the chaotic current dynamics observed in biological counterparts, which are key to the success of the latter in pattern recognition.[16,17,25]

1.2.1.2. A Better Way to Emulate Neurons in the Solid-State

For the abovementioned reasons, there is a clear need to design solid-state compounds that exhibit sharp spiking behavior characteristic of neurons; however, the palette of functional materials that exhibit intrinsic switchability of conductance to perform 'brain-like' computing tasks is sparse.[2] Emulating the complexity and diversity of neuronal characteristics requires independent control of multiple functional attributes of electronic phase transformations, including: magnitude and energy threshold of conductance switching, heat dissipation, hysteresis, dynamics of relaxation between states, and the number of accessible internal states.[3,7,16,26–32] Recent demonstrations illustrate that electronic transitions within strongly correlated materials can be leveraged to emulate biological neurons (Figure 1.1C).[16,17,29] These neuro-emulative capabilities are underpinned by the tendency of such materials to manifest solid—solid metal-insulator transitions (MIT) in response to specific external stimuli such as temperature (T_C) or applied electric field. As exemplified in Figure 1.1D for NbO_2, MITs represent an energy-efficient class of 'memristive' behavior, where the

resistance value at a given point in time captures both the present state of the system and its history, reflecting the capacity to evolve and learn.[16,31,33]

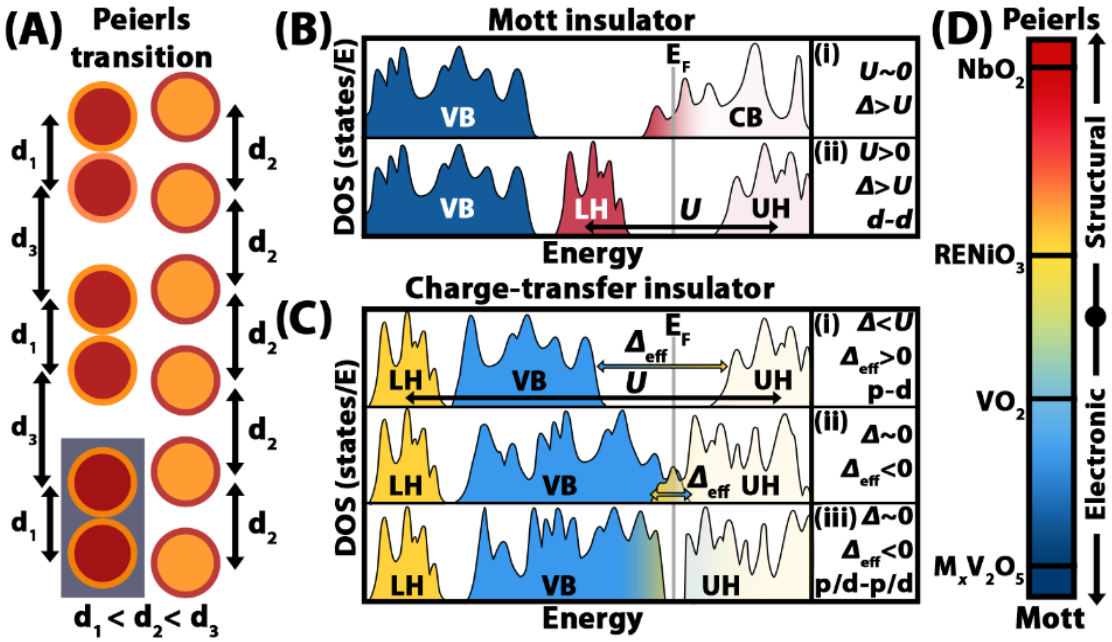

Figure 1.2. Metal-insulator transitions (MIT) can be conceptualized to arise from a weighted coupling of structural (i.e., Peierls) distortions and electron (i.e., Mott) correlation. (A) Schematic representation of a Peierls' transition driven by dimerization of adjacent of metal centers. (B) An example of a Mott-type transition where electron correlation (*U*) gives rise to upper and lower Hubbard bands. (C) An example of an electronic transition wherein increased transition metal 3d—O 2p hybridization at high temperature results in closing of a p/d—p/d quasi-gap, as reported for rare-earth nickelates.[37] (D) Representation of the Mott-to-Peierls spectrum that describes the mechanistic origin of MITs in the materials discussed here. (E) Graphical representation of the MIT behavior of several correlated oxide materials; the horizontal axis shows MIT temperatures (T_C) and the vertical axes show reported changes in resistivity and conductivity. The height of each floating bar corresponds to the change in resistivity/conductivity between the metallic (bottom) and insulating (top) phases. Note that the change in resistivity for $RENiO_3$ materials to the right of $SmNiO_3$ is held constant since, in the absence of high-quality crystals, the achievable magnitudes of conductance switching remains to be determined.[38] Vertical lines at room temperature (298K) and at the typical operating temperature of a computing unit (~400K) are shown. A break in the *x* axis (650—1050K) is further included in light of the sparse few examples in this range. Data shown in (E) were collated from references: [3,7,8,30,32,39–48].

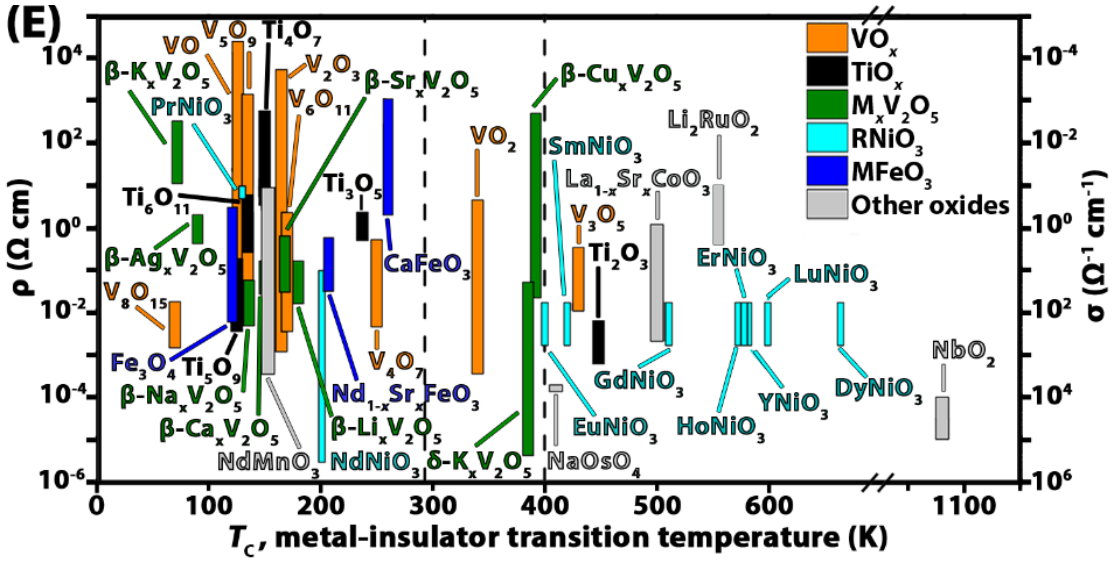

Figure 1.2. Continued.

Despite these recent successes,[16,17,29] independent control of transformation characteristics remains to be established.[26,34] For instance, NbO_2 has too high a transition temperature (~1080 K) and thus consumes too much power,[17,25,33] whereas VO_2 has a transition temperature that is too low (~340 K) given the ~400 K operating temperatures of modern computing architectures.[16] Here, four classes of MIT materials are discussed: vanadium dioxide (VO_2); niobium dioxide (NbO_2); rare-earth nickelates ($RENiO_3$); and ternary vanadium oxides ($M_XV_2O_5$).[2,16,17,29] In particular, we focus on exploring means of *a priori* design of free-energy landscapes (such as the landscape depicted in Figure 1.3D) to enable switching function depicted for materials included in Figure 1.2D.[35,36]

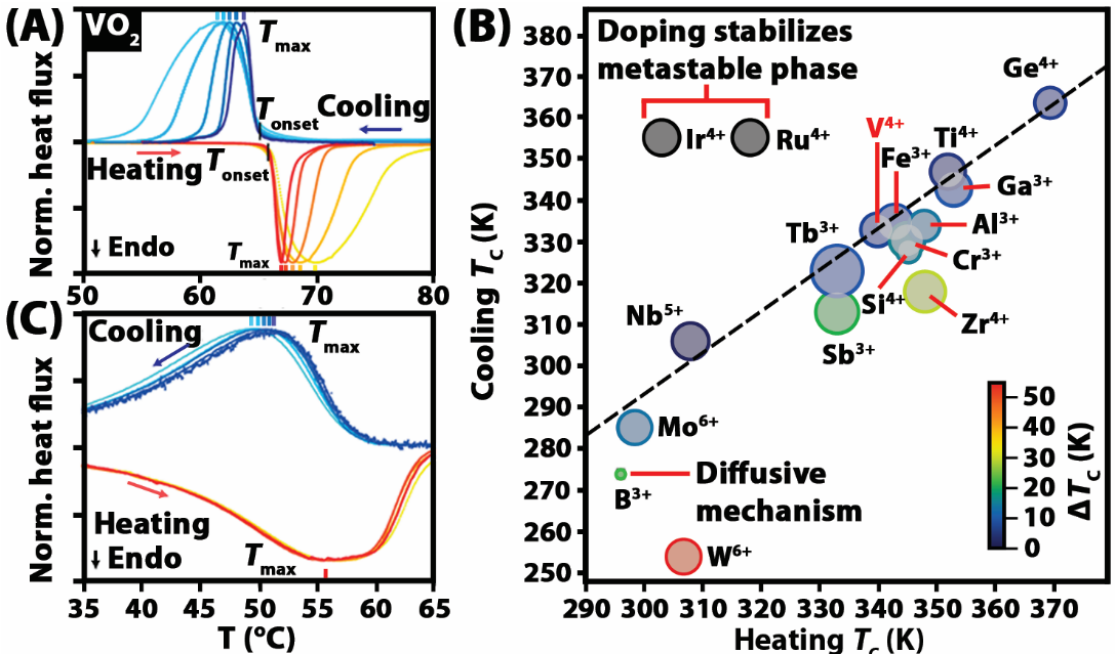

Figure 1.3. (A) Thermally-induced MIT of VO_2 nanowires as measured by differential scanning calorimetry (DSC). The hysteresis becomes more pronounced with increasing ramp rate. (B) VO_2 can be doped with homovalent (e.g., Ti^{4+}) or aliovalent (e.g., W^{6+}) cations to alter the heating and cooling critical temperature (T_C) of the MIT. Reports of T_C modulation upon incorporation of various dopants is summarized.[28,65,67–74] Effort was made to obtain data only from differential scanning calorimetry (powders) or electrical resistivity measurements (thin films) and were limited to studies providing diffraction data verifying retention of the M_1/M_2 (insulating) to R (metallic) transition. The dashed line acts as a reference indicating symmetric change in the heating/cooling hysteresis (ΔT_C) relative to undoped VO_2. The size and color of individual data points correspond to the crystal radius and magnitude of hysteresis for each dopant, respectively. T_C values have been selected based on the maximum solubility reported for a given dopant. Several dopants (H^+, Ir^{4+}, Ru^{4+}) stabilize insulating metastable polymorphs that do not transition to the metallic rutile phase.[75] (C) The intrinsic MIT properties of VO_2 can be modulated through dopant incorporation, which alters the relative thermodynamic stabilities and electronic structure of the insulating M_1 and metallic R phases. Tungsten-doping has been shown to significantly lower the T_C of VO_2 and alter the hysteresis width. (D) Structural relationships between the various reported polymorphs of VO_2 are shown. (A) and (C) were adapted from.[76] Data in (B) were collated from.[70,75–83] Structures in (D) were collated from references: [65,84,85].

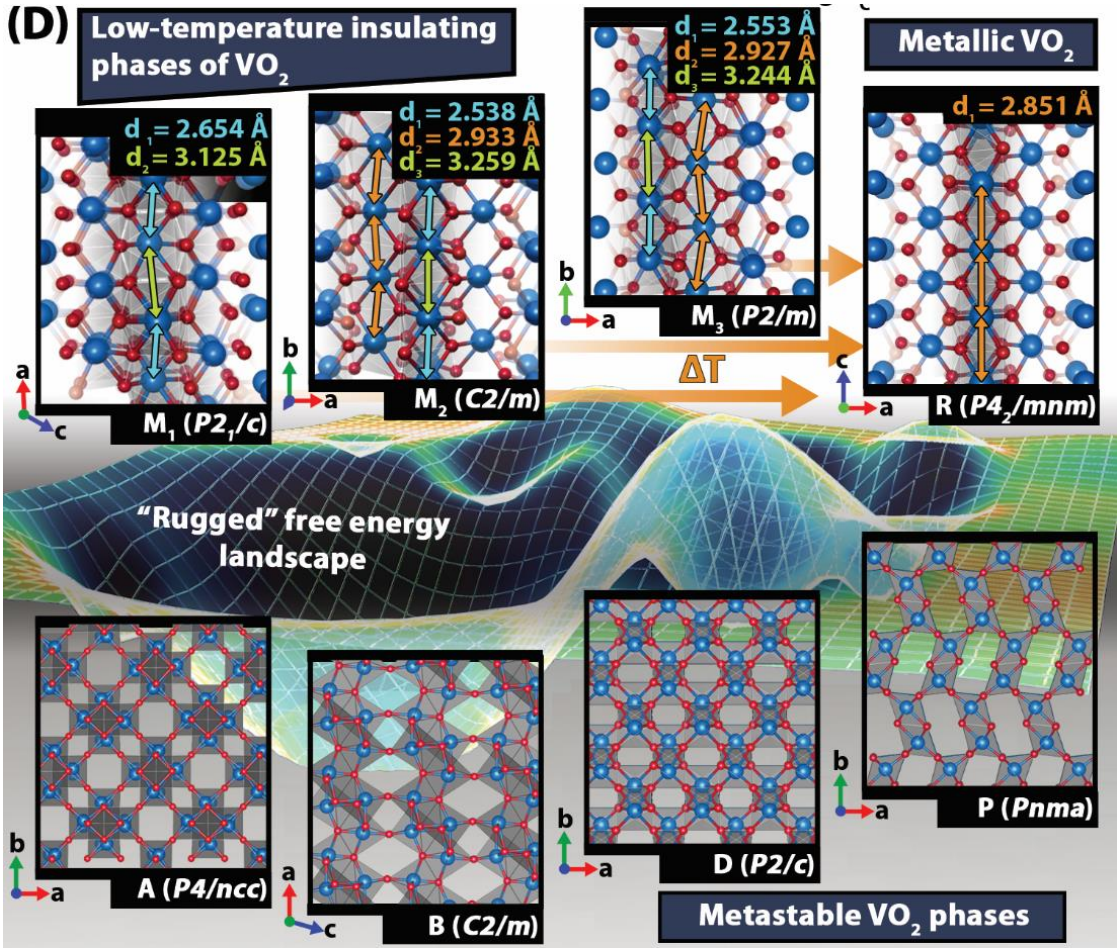

Figure 1.3. Continued.

1.2.1.3. Unstable by Design: Electronic Transitions in Correlated Oxides

In strongly electron-correlated materials, electrons can no longer be considered as non-interacting, giving rise to complex many-body phenomena manifested as close coupling of structural, electronic, and spin degrees of freedom.[2,49–55] This often gives rise to materials that have localized charge carriers in the ground state but are at the cusp of transitioning to an itinerant state following: (a) structural transformations that alter the chemical bonding and

degree of hybridization, or (b) an increase in charge carrier density (e.g., through application of an electric field or through thermal broadening of occupied Hubbard bands) such that electron—electron repulsions are screened. In contrast to systems wherein long-range ion diffusion or filament formation/dissolution underpins neuromorphic function,[26,56] correlated oxides can exhibit relatively subtle structural transformations, resulting in intrinsically lower entropy production and thereby greater energy efficiency. The relative contributions of lattice distortions and electron correlation within such systems determine the energetic costs of transformations and governs the accessible dynamics. Electronic transitions within such compounds can be considered to derive from a convolution of structural (Peierls) and electronic (Mott) origins (Figure 1.2). In the Peierls case (Figure 1.2A), the equivalent of a dimerization gives rise to the improved overlap of electronic-states across adjacent metal centers.[57,58] In the case of Mott-insulators (Figure 1.2B), Coulombic repulsion between electrons causes splitting of a half- or partially-filled band into an upper and lower Hubbard band separated by the Hubbard '*U*', defining an energy gap proportional to the on-site electrostatic repulsion and thereby lowering the overall energy of the system.[2] For Mott—Hubbard insulators, when the width of the Hubbard bands is less than *U* (as is the case in the ground state), insulating behavior is observed. Alternatively, when the width is greater than *U*, metallic behavior is observed. In purely electronic transitions, broadening of Hubbard bands can be effected through thermal broadening of the bandwidth[3,7] or introduction of additional charge carriers that

screen repulsive interactions.[59] Mott insulators are distinguished from charge-transfer insulators by the nature of their bandgap. In charge-transfer insulators, the lower Hubbard band is situated below the ligand p-band ($U>\Delta$, the crystal field splitting) and the effective bandgap (charge-transfer energy, Δ_{eff}) is between the upper edge of the ligand p- and lower edge of the unoccupied metal d-band (for $\Delta_{eff}>0$) or between correlation-split p/d hybridized states (for $\Delta_{eff}<0$) (Figure 1.2C).[41,60] Closing of the p-d or p/d—p/d gaps induced through alteration of bandwidths or filling of the bands and concomitant shifting of the Fermi level provides a means of inducing a MIT.

Although MITs have been evaluated in transition metal chalcogenides, these materials tend to rely on electric field pulses and show degradation under field stress.[23,61,62] Their quasi-2D electronic structure nevertheless holds potential for establishing deterministic control of conduction pathways through surface functionalization. In this article, we focus on transition-metal oxides, which offer improved robustness and better compatibility with foundry processes, in addition to an extensive phase space where the extent of hybridization (bandwidths, overlap integrals) can be readily tuned.[2,3,7,8,30,32,39–41,43–48] The four materials classes discussed here have been approximately positioned along a 'Mott-Peierls spectrum' in Figure 1.2D, albeit their specific positioning along this spectrum is not without controversy. This illustration highlights increasing realization of the importance of coupling between ionics, subtle structural distortions, and electron correlation in driving MITs. The massive phase space occupied by strongly

correlated oxide materials is reflected in Figure 1.2E, which relays the critical transition temperatures (T_C) and the change in resistivity of representative oxide materials. Many materials exhibit a T_C<200 K, sparse few near room temperature, and still fewer above the 400K threshold imperative for computing. The lack of materials with T_C>400 K underscores the need for mechanistic understanding and design of correlated systems. The four classes discussed here (Figure 1.2D) have been selected from among those shown in Figure 1.2E for the diversity of their metal-insulator transition mechanisms, recent demonstrations of their use as memory elements for brain-like computing, and for exhibiting compositional tunability of switching characteristics.

1.2.2. The Binary Oxides of Vanadium and Niobium

VO_2 and NbO_2 represent model MIT materials well-separated along the Mott-Peierls spectrum with respect to the MIT mechanism (Figure 1.2D) and furthermore exhibit vastly different transition temperatures (Figure 1.2E).[63] The structural instability underpinning the MIT in VO_2 spans a complex phase space (Figure 1.3D).[28,35,64,65] Around T_C = 340 K, VO_2 undergoes a first-order diffusionless phase transformation from a high-symmetry rutile-type phase (>340 K) to one of several stable (M_1) or metastable (M_2/M_3) low-symmetry phases (<340 K), as shown in Figure 1.3A. The high-temperature rutile phase exhibits a singular V—V bond distance (2.851Å), which is distinguished from the low-temperature phase that is characterized by V—V dimers, with alternating long

(3.125 Å) – short (2.654Å) bonds (M_1) or alternating dimerized/undimerized V-V chains (M_2/M_3), as shown in Figure 1.3D.[66]

The degree of coupling between the electronic Mott transition and the structural transition (*i.e.,* positioning on the 'Mott-Peierls spectrum') has been the subject of much controversy. Density functional theory incorporating dynamical mean-field theory (DFT+DMFT) calculations show that the MIT is impacted by correlation-driven effects that dictate intradimer exchange.[58,86] A recent neutron scattering study provides a more quantitative accounting and suggests that phonons account for ~2/3 of the total increase in entropy at the MIT.[87]

1.2.2.1. Approaches to Modifying the Metal—Insulator Transition Threshold in VO_2

Two aspects of VO_2 are particularly relevant to its use as a memristor in neuromorphic computing applications: the transition temperature, T_C, and the thermal hysteresis width ($\Delta T_C = T_{Cooling} - T_{Heating}$). Deterministic control over ΔT_C is particularly important since a smaller hysteresis is required to minimize energy dissipation and achieve fast dynamics, whereas a large hysteresis could enable nonvolatile on/off states.[28,88] Importantly, ΔT_C in VO_2 is critically dependent on both intrinsic (doping, point defect concentration, and grain size; Figure 1.3B)[28,65,67–73] and extrinsic (strain) considerations.[89,90]

The influence of incorporating a range of dopants in VO_2 at vanadium sites, oxygen sites, or within tetrahedral holes has been investigated (Figure 1.3B).[28,65,67–74] The inclusion of dopant atoms modifies the "rugged" free energy

landscape of VO_2 (Figure 1.3D) in terms of relative phase stabilities and transformation barriers thereby non-trivially altering the coupling of lattice/electronic/spin degrees of freedom. As an example, tungsten strongly depresses the MIT and broadens the hysteresis.[28,73,91] In undoped VO_2, the thermal hysteresis is rate-dependent and symmetric for both monoclinic→rutile and rutile→monoclinic transitions since the transitions appear to be nucleated at point defects (Figure 1.3A). Upon tungsten-doping, VO_2 exhibits an asymmetric modulation of transition temperatures and dynamics (Figure 1.3C).[28,91] Doping with tungsten[92] induces anisotropic lattice expansion and a local increase in symmetry around the dopant site,[93] stabilizing M_2 domains (Figure 1.3D). The insulator→metal transition in W-doped VO_2 is therefore facile, being nucleated at twin planes and M_1/M_2 stacking faults (wherein transformation dislocations can readily be stabilized),[36] whereas the reverse metal→insulator transition originates at point defects such as oxygen vacancies that are suppressed upon aliovalent tungsten-doping. Tungsten-doping thus functions similarly to tensile strain by enabling facile nucleation of rutile domains during the monoclinic→rutile transformation but renders the reverse rutile→monoclinic transformation more difficult, thereby engendering anisotropic hysteresis.[92]

Alternatively, homovalent titanium-doping raises the transition temperature and diminishes hysteresis width,[94] which has been ascribed to the role of the dopant atoms in modifying the local lattice symmetry to mitigate lattice mismatch between the monoclinic and tetragonal polymorphs.[69] Germanium-doping

strongly increases the transition temperature, almost to 400 K (Figure 1.3B), which has been rationalized based on chemical pressure arguments, albeit the local structure around the dopant Ge atom and its impact on the electronic structure of VO_2 remains to be elucidated.[67] Doping at the oxygen sites with fluorine or sulfur atoms is less explored and while modestly altering the T_C, appears to degrade the magnitude of the transition.[95] An intriguing report illustrates nearly complete elimination of hysteresis upon simultaneous incorporation of Cr^{3+} and Nb^{5+} in VO_2.[70] In still other examples, dopants (*e.g.*, H^+, Ir^{4+}, and Ru^{4+})[65,70,96] stabilize altogether different polymorphs (Figure 1.3D). Finally, interstitial doping of elemental boron into tetrahedral holes of the M_1-phase of VO_2 has recently been demonstrated, providing a notable post-synthetic approach to tuning T_C and hysteresis of VO_2.[72] Clear-cut design principles relating dopants to the transition temperature and hysteresis of VO_2 remain to be gleaned and will be pivotal to the utilization of VO_2 in neuromorphic computing.

1.2.2.2. NbO_2, an Unusual High-Temperature MIT Material

NbO_2 (Figure 1.4A, panel i) also exhibits a pronounced MIT, albeit at a much higher temperature in the range of 1000—1100 K.[25,97] Despite striking similarities to VO_2, a mechanistic understanding of the underlying MIT has emerged only recently.[63,98,99] Upon heating, NbO_2 transitions from a distorted rutile structure with dimerized Nb—Nb pairs (2.685Å and 3.304Å, Figure 1.4A panel I and ii) to a high-symmetry rutile structure with uniform Nb—Nb distances

(3.032 Å, Figure 1.4A panels iii and iv).[97,99] Thus, the low-temperature Nb—Nb dimers are decoupled across this phase transition (Figure 1.4A), resulting in quasi-linear Nb chains and manifesting an order-of-magnitude spike in conductivity.[25,63,99,100] Electron correlation is expected to play a less-significant role in NbO_2 as compared to VO_2 owing to the greater energy dispersion of 4d-bands; Demkov has noted the emergence of soft phonon modes in the Brillouin zone, a hallmark of the Peierls instability.[99] Even so, a comparative DFT+DMFT investigation has demonstrated that electronic correlations, though less prominent, are non-negligible.[63] This is supported by observations of a strong renormalization of the t_{2g} levels, concurrent with the emergence of Hubbard subbands in the metallic phases of both VO_2 and NbO_2.[63]

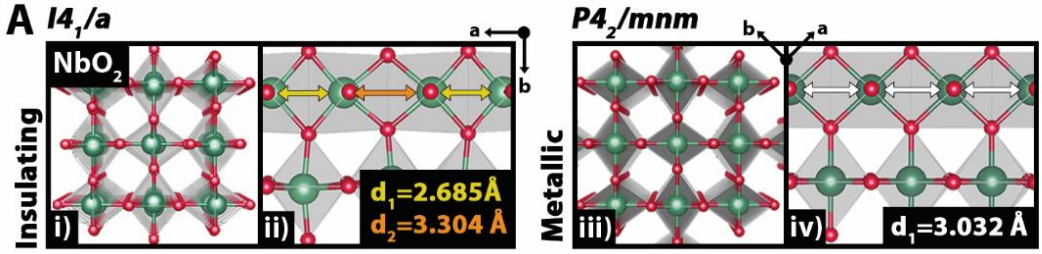

Figure 1.4. (A) The MIT of NbO_2 is underpinned by a phase transition between low- and high-symmetry tetragonal distortions. The low-temperature ($I4_1/a$) phase of NbO_2 exhibits distinct Nb—Nb dimers (alternating 2.685 and 3.304 Å distances), whereas the high-temperature phase ($P4_2/mnm$) exhibits a singular Nb—Nb distance (3.032 Å). As discussed in the text, the structural transition plays a considerably greater role in the MIT of NbO_2 as compared to VO_2. (B) A simplified representation of structural perturbations observed in $SmNiO_3$ across its metal-insulator transition, showing only an exaggerated change in the <O-Ni-O> bond angle across the MIT. Breathing distortions comprising alternating NiO_6 octahedra are omitted. (C) As an exemplar of electronic instabilities of $M_xV_2O_5$ phases, the metal-insulator transition in β/β′-$Cu_xV_2O_5$ is observed to occur with retention of the 1D tunnel framework [7,101]. (C) was adapted from reference [7].

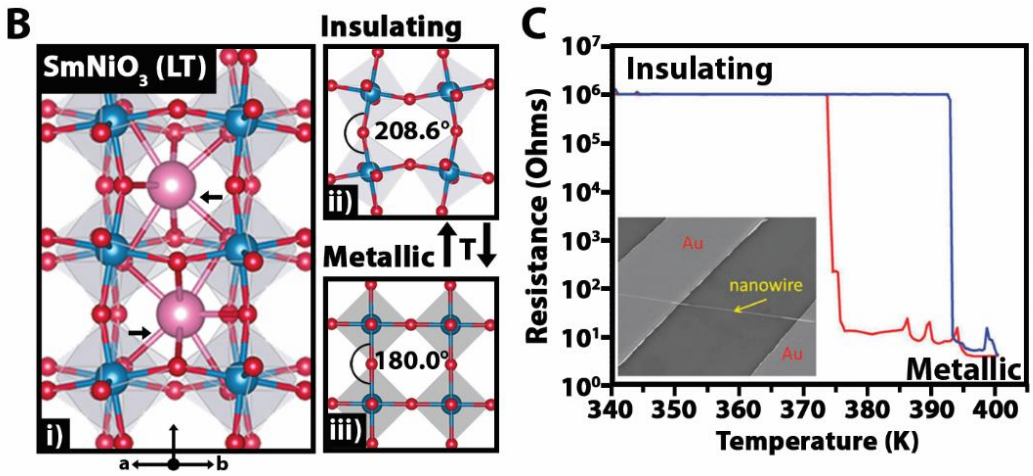

Figure 1.4. Continued.

Given the strong parallels between NbO_2 and VO_2, attempts to alloy VO_2 and NbO_2 to achieve a T_C intermediate between the two seems a straightforward solution. Indeed, doping NbO_2 with 5 at.% V results in an ~100K decrease in T_C. However, the lattice incongruence, coupled with the large discrepancy in ionic radii, leads to the stabilization of a semiconducting phase (for $0.95>x>0.05$ in $Nb_{1-x}V_xO_2$), which does not undergo an MIT.[97]

1.2.2.3. Leveraging the MIT in NbO_2 to Realize Brain-Like Computing

Recent results for NbO_2 have highlighted its viability as a neuromorphic material,[17,25,99,102] emphasizing the importance of "negative differential resistance" (NDR, defined as $dV/dI<0$) behavior as a hallmark of memristive properties (Figure 1.1D).[31,33,103] Unlike traditional circuit elements, voltage-driven memristors are nonlinear dynamical elements for which current (I) evolves with time (t) as per:

$$I(t) = G(\Theta,V)V(t) \quad \textbf{1.1}$$

$$d\Theta/dt = f(\Theta,V) \quad \textbf{1.2}$$

where V is the time-dependent input voltage and G is the conductance, which is a function of V and an internal state variable, Θ (in this case temperature). The rate of change of the state variable depends upon the value of the state variable (thus incorporating memory) and V.[16,17,104]

Two distinct NDR regimes are observed in NbO_2 (Figure 1.1D) and are driven by nonlinear thermally activated conduction and the MIT, potentially allowing for decoupling of the non-linear conductance response from the atomic rearrangement. This, combined with demonstration of 'edge of chaos' dynamics reminiscent of neuronal function,[17] have generated much interest in NbO_2 as a neuromorphic computing material; yet, the high transition temperature of NbO_2 (1050—1100 K)[25,97,100] and the dominance of the Peierls-type transition results in excessive energy consumption. By comparison, VO_2 consumes just 16% of the energy per switch and can be switched 100× times faster as compared to NbO_2.[16,17] This is succinctly reflected in their respective volumetric free energy cost to trigger an MIT (<1 $fJ \cdot spike^{-1}$ for VO_2 and ~6 $fJ \cdot spike^{-1}$ for NbO_2).[16,105] Despite promising results for VO_2, its T_C (~340 K) is low, reinforcing the importance of understanding mechanisms by which Ti-, Ga-, and Ge-doping increase T_C and the identification of methods that allow for amplification of this effect.[67,69,94] In light of energy efficiency considerations, subsequent sections emphasize the design and stabilization of materials with greater electronic (rather than lattice) contributions.

1.2.3. Towards an Expanded Palette: Rare-Earth Nickelates and Mixed-Valence Vanadium Oxides as Neuromorphic Materials

1.2.3.1. Perovskites Take the Stage with Rare-Earth Nickelates

Rare-earth nickelates and ternary vanadium oxides provide a vastly expanded design space enabled by ternary and quaternary compositions, thereby expanding the scope for tuning electronic instabilities and thus transition temperatures.[2,49,106,107] Rare-earth nickelates ($RENiO_3$) belong to a family of oxide perovskites that adopt distortions from a nominally cubic ($Pm\bar{3}m$) structure.[32,40,108] With the exception of $LaNiO_3$ which is always metallic,[108] $RENiO_3$ (RE = Pr, Nd, Sm, Eu, Gd, Dy, Ho, Er, Lu) compounds exhibit a sharp MIT that can be tuned across a wide range (T_C = 130-599 K; Figure 1.2E).[32,49,109,110] Strain in cubic perovskite structures can be applied 'chemically' by varying the size of the rare-earth cation[40,111,112] or extrinsically by epitaxial mismatch.[32,113–115] Analogous to VO_2 and NbO_2, the MIT of $RENiO_3$ is concomitant with a structural transition distinguished by a loss of symmetry from orthorhombic (*Pbnm*) in the metallic state to monoclinic ($P2_1/n$) in the insulating state.[40,111,116–119] Locally, the MIT is observed to coincide with a slight 'breathing' distortion that involves the concerted motion of nickel-centered octahedra, inevitably altering Ni 3d-O 2p hybridization[120] stabilizing chains of alternating inequivalent Ni polyhedra with long and short Ni-O bonds.[60,121,122] An early proposed mechanism for the resistance-switching phenomenon invoked a charge disproportionation mechanism, wherein the 'breathing' lattice distortion was accompanied by disproportionation to a mixed

Ni valence state (i.e., $2(d^7) \rightarrow d^{7+\delta} + d^{7-\delta}$).[112,118,121] However, a definitive mechanism for the MIT in $RENiO_3$ has been difficult to ascertain.

Recent consensus delineates $RENiO_3$ materials as 'negative charge-transfer' insulators (Figure 1.2C) whereby hybridization between occupied O 2p and unoccupied Ni 3d states give rise to a p/d-p/d quasi-gap.[41,49,60,123] Indeed, resonant inelastic X-ray scattering (RIXS) supported by many-body cluster and single-impurity Anderson model (SIAM) calculations point to a 'negative charge-transfer' scenario as the underlying electronic structure origin of the observed conductance modulation (Figure 1.2C).[41,60,123] Interestingly, Bisogni et al. have proposed the emergence of an O 2p-O 2p quasi-gap owing to an increased number of holes in the O 2p band, which deviates somewhat from the explicit hybridization of overlapping O 2p-Ni 3d states invoked in other studies.[49,124,125] In the insulating state, the migration of a Ni hole to hybridized oxygen 2p states is observed.[60] Another model suggests that a pair of ligand holes (L^2) strongly couples with the breathing-type lattice distortion by occupying alternating NiO_6 octahedra (bipolaron condensation).[122] In this mechanism, Ni 3d electrons on one sublattice ($3d^8$) are decoupled from nearby octahedra undergoing the observed stretching motion ($3d^8L^2$).[126] Each adjacent sublattice then distorts along specific phonon modes to maximize delocalization of the holes between the O 2p and Ni 3d states. The so-called "site-selective Mott transition" mechanism has gained recent experimental support.[60,123] While the precise underlying mechanisms remain to be elucidated, these compounds illustrate a distinctive mode of

coupling of electronic structure (negative charge-transfer, charge disproportionation, site-selective Mott transitions) with lattice distortions (breathing distortions and octahedral rotations) corroborating the idea of a mechanistic spectrum spanning structural and electronic considerations coupled to different degrees.[113,121–123]

The extent of perturbation of bond angles required to close the negative charge-transfer gap is in essence correlated to the Goldschmidt tolerance factors[40] of the perovskite structure and thus smoothly varies across the lanthanide series. As such, T_C can be varied systematically either through chemical substitution at the rare-earth site or through epitaxial strain.[110,113,114] Despite the smooth variation of the MIT temperature across the lanthanide series and the generally high miscibility of lanthanides, the formation of solid solutions remains underexplored. Huang and coworkers have demonstrated the use of Sm and Nd miscibility to bridge the gap between the MITs of $SmNiO_3$ and $NdNiO_3$.[112] Superlattices and random alloying on both rare-earth and nickel lattices warrant further exploration to establish independent control of transformation characteristics.[112]

Alternatively, lattice mismatch by epitaxial growth of $RENiO_3$ thin films on different substrates provides a tool for tuning T_C, and has been extensively explored for $SmNiO_3$ (Figure 1.4B). At relatively modest strains, a large diminution of T_C is observed from 380 K to 140 K. Inducing a strain of ε = -2.3% by epitaxial growth on a $YAlO_3$ substrate completely suppresses the insulating phase within

the measured temperature range (T > 4 K).[32,114] While evidently powerful, modulation of the conductance response by epitaxial strain renders T_C static and the use of epitaxial strain to increase T_C has not been demonstrated. In contrast, ionic liquid gating provides a means of dynamically modulating T_C.[29,115,127] Nickelates can reversibly accommodate large concentrations of oxygen vacancies.[109,112] Ramanathan has demonstrated that creation of oxygen vacancies through ionic-liquid-induced gating affords deterministic control of the conductivity of $SmNiO_3$ transistors upon application of a gate voltage, thereby yielding a means of mimicking synaptic function with time-correlated spikes.[29] Despite much work devoted to tuning T_C in $RENiO_3$, scarce little attention has been devoted to tuning hysteresis.

1.2.3.2. Ternary Vanadium Oxides as a Promising Design Space

Ternary vanadium oxides ($M_xV_2O_5$) crystallize in a variety of low-dimensional motifs including quasi-1D tunnel (Figure 1.5) and quasi-2D layered structures with varying stacking sequences and extents of condensation (single/double-layered).[2,3,7,31,128] $M_xV_2O_5$ are nominally mixed valence in the ground state; they are formed by the reductive intercalation of various cations that span the breadth of the periodic table (s-block, transition metal, p-block; Figure 1.5) as well as organic cations within different frameworks of V_2O_5.[3,7,30,42,128–131] The “rugged” energy landscape of V_2O_5 is characterized by scores of possible metastable structures; upwards of 6 have been experimentally stabilized.[35,107,130,132]

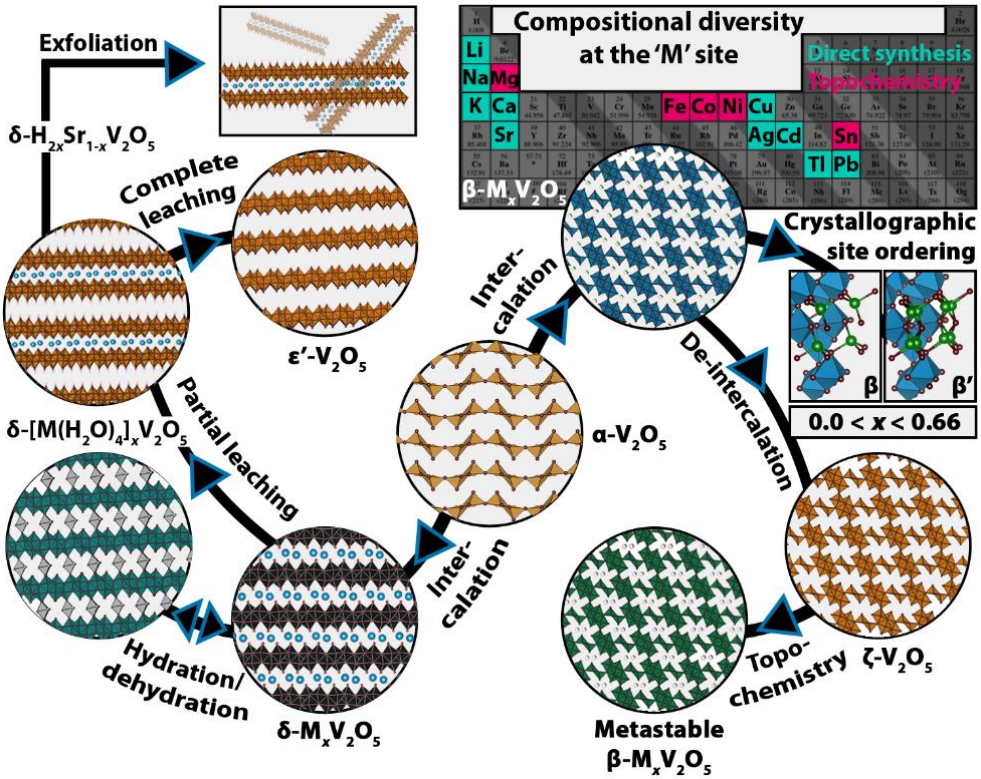

Figure 1.5. Intercalation-induced transformations in the $M_xV_2O_5$ phase space. Thermodynamically-stable single-layered α-V_2O_5 (center) can be intercalated with alkali metals (Li, Na, K), alkaline metals (Mg, Ca, Sr), transition metals (Co, Ni, Cu, Zn, Ag), and p-block elements (Sn, Pb, Tl) to form ternary vanadium oxides ($M_xV_2O_5$) with substantially altered vanadium-oxygen frameworks. Depending on the size of the intercalating ion, M, and its stoichiometry, *x*, the framework rearranges to form "double-layered" (left) or tunnel-structured (right) phases. Soft chemistry can be utilized to induce transformations that allow control over the extent of electronic coupling between adjacent vanadium metal centers. The layered δ-$M_xV_2O_5$ structures can be reversibly hydrated to form hydrated materials δ-[M $(H_2O)_4]_xV_2O_5$ that have been shown to exhibit pinched *I*/*V* hysteresis loops characteristic of memristors. These materials can be partially leached and exfoliated to alter the extent of electronic coupling between adjacent V_4O_{10} double-layers or fully leached to form a metastable V_2O_5 polymorph.[107,131,132] Alternatively, tunnel-structured β-$M_xV_2O_5$ phases can be stabilized (right) for several intercalants (light blue, periodic table).[3,128] Topochemical modification enables control over stoichiometry, *x*, and crystallographic site (β/β') occupied by the metal cation and therefore the extent of charge ordering. The intercalated ions can be completely leached to stabilize a new metastable polymorph, ζ-V_2O_5, that exhibits significantly different V-O hybridization as compared to the thermodynamically stable α-V_2O_5 phase.[130] This empty polymorph can finally be re-intercalated with additional metals to form metastable ternary vanadium oxides (pink, periodic table), representing a method for installing specific electronic states.[129,130] Structures in (E) are based on original data reported in references: [7,31,129–132].

Upon intercalation, the V_2O_5 lattice is partially reduced, resulting in a mixture of V^{4+}/V^{5+} oxidation states. Given the strong degree of electron correlation in V 3d-bands, electrons tend to localize on vanadium sites adjacent to intercalating cations, forming charge-ordered patterns characterized by the formation of Mott-Hubbard bands rather than delocalized metals (Figure 1.1B).[133] Many of these materials undergo a Mott metal-insulator transition with only a slight structural contribution derived from ionic rearrangement of the intercalated cations or pinching of the V_2O_5 framework.[3,7,30,128] With increasing temperature, select bond distances are decreased, leading to increased electronic coupling between adjacent metal centers (Figure 1.2B). As such, the MIT is critically dependent on V—V distances within the structure, the carrier density, and the positioning of intercalated-ion-derived "midgap" states.[5,106,128,129] This is evidenced in the $M_xV_2O_5$ series for (M = alkali metals) wherein transition temperature monotonically increases with decreasing ionic radius (for similar values of *x*), which is correlated with the V—V bond distance along the *b*-axis.[42] Indeed, the wealth of electronic phase transitions in $M_xV_2O_5$ systems has been widely demonstrated in the form of metal-insulator,[5,7,8,30,42,101,128] and semiconductor-semiconductor[3] transitions facilitated by Mott instabilities.

In contrast to the previous systems, the spin, orbital, and electronic degrees of freedom in $M_xV_2O_5$ compounds are to a greater extent independently tunable through selection of the intercalated cation (M),[3,7,8,30,128] its stoichiometry (*x*), and the vanadium-oxygen connectivity of the polymorph (single/double-layered,

quasi-1D, etc.). The frameworks are furthermore characterized by distinctive interstitial sites that can accommodate specific cations, enabling stabilization of quaternary compositions with ordered arrays of different intercalated cations. Topochemical methods have been developed to extract “native” cations, stabilize metastable V_2O_5 polymorphs,[35,107] and insert altogether different ions to access compounds inaccessible from direct synthesis (Figure 1.5). β-$M_xV_2O_5$ (M = Mg, Sn, Co, Ni)[129,130] have been prepared by this route; p-block cations with stereoactive lone-pair electrons introduce a midgap state within the bandgap rendering these compounds amenable to voltage-induced MITs.[5,128] Recently, massive MITs have been observed for individual single-crystalline nanowires (Figure 1.4C);[3,8,30] albeit, the sensitivity to stoichiometry *x* makes it difficult to fully unravel the coupling of electronic structure and lattice distortions. One proposed mechanism suggests band-width broadening owing to anharmonic copper oscillations.[7,101] In the case of δ-$Ag_xV_2O_5$, high-resolution X-ray diffraction has been used to evaluate the structure above and below the metal-insulator transition. Subtle changes in the V—V distance indicate increased V d_{xy} overlap, consistent with an increase in the bandwith of the lower Hubbard band bridging the Mott gap.[3] Exfoliation of these layered quasi-2D $M_xV_2O_5$ materials has been explored and provides an additional knob for tuning electron correlation and bandgap by alteration of local symmetry.[131,132] The intercalated ions within such 2D systems can further be solvated to form materials with the composition δ-$[M(H_2O)_4]_xV_2O_5$ (M = Co, Ni, Zn), which have furthermore been shown to exhibit

memristive behavior ascribed tentatively to proton diffusion.[31] The insertion of solvated ions further suggests that the discipline of coordination chemistry has much to contribute to controlling electron delocalization on the V_2O_5 framework.

1.2.4. Concluding Remarks on Materials for Neuromorphic Computing

Recently, using only two VO_2 memristors, Yi and colleagues were able to simulate 23 distinct biological neuron spiking behaviors. In contrast, a CMOS artificial neuron made from 1300 logic gates was able to simulate only 11 neuronal behaviors.[16] The realization of the full promise of neuromorphic computing requires the design of new dynamical materials and systems that directly emulate the functionality of neurons and synapses to weave memory, computation, and communication into one fabric. Rather than build ‘better transistors’, we need to develop novel dynamical materials with nonlinear conductance switching that directly emulate neuronal elements and to build entirely new circuit elements from such materials that can perform tasks that presently require hundreds to thousands of transistors. Such an advance will increase the energy efficiency of computing by orders of magnitude; this is furthermore required since most computation will need to be performed at ‘the edge of the internet’, in close proximity to where data is collected and where power availability will likely be low and intermittent. Such high-fidelity neuronal emulation at ‘the edge’ will enable immediate system updating (learning) in response to external events, thereby enabling realization of the full promise of artificial intelligence (AI) to learn and respond in real-time.

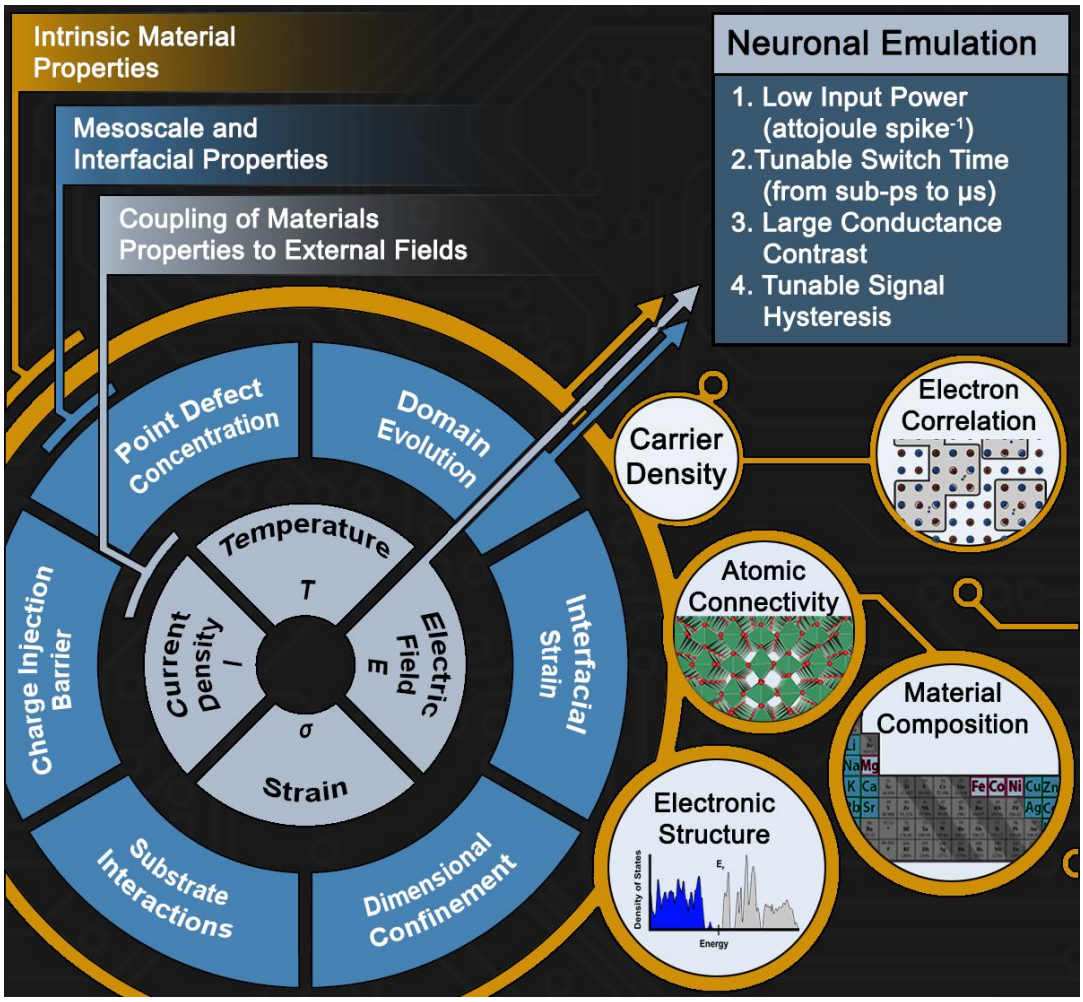

Figure 1.6. The coupling of intrinsic chemical properties and extrinsic characteristics in determining neuromorphic function. Schematic delineating desired device characteristics (grey inner circle), tunable intrinsic material properties derived from composition and structure (blue circle), and tunable extrinsic device/materials characteristics (orange circle, exterior circles). Images within the maroon "extrinsic device characteristics" circles were adapted in part from references: [16,28,31,32].

While considerable recent attention has focused on the use of AI to accelerate the design of novel materials and syntheses, novel compounds and syntheses are urgently needed to allow realization of the promise of AI in full measure. The design of materials that 'turn on a dime' requires the elucidation of

design principles underpinning electronic instabilities as well as independent control of transformation characteristics such as the transition temperature, hysteresis width, magnitude of conductance switching, dynamics of relaxation between states, and the number of accessible internal states (Figure 1.6). Deterministic control of conduction pathways is further an urgent imperative. The interplay between device properties, intrinsic chemical descriptors, and extrinsic tunable properties is illustrated in Figure 1.6. The challenges described here span the discovery of new compounds, synthetic approaches to stabilizing metastable compounds to obtain independent control of transformation characteristics, and understanding of dynamical processes away from equilibrium, which represents a rich new frontier at the intersection of chemistry and information science.

1.3. Overview: Implications for Electrochemical Energy Storage

Li-ion batteries have played a pivotal role in underpinning a revolution in consumer electronics, which has had far-reaching consequences for our everyday lives by democratizing access to information and allowing for global interconnectedness at a scale unprecedented in human history. This technology is now being pushed to its limits by the needs of electric vehicles, and on a much larger scale, by the requirements of grid-level storage as power grids seek to adapt to a greater reliance on renewable energy sources and to better offset daily and seasonal fluctuations in demand. The fabrication and operation of Li-ion batteries in large-area formats comes with its own set of complex constraints with safety, materials criticality, and operational lifetime being of foremost importance.

The intrinsic propensity of metallic Li to form dendrites, which has led to numerous highly publicized catastrophic failures, as well as severe bottlenecks in the supply of critical battery materials have sparked concerns and arguably slowed the momentum of electrochemical energy storage at a critical juncture.[134,135] Notably, over 50% of the world's cobalt, critical to lithium cobalt oxide cathode materials, is mined in the Democratic Republic of the Congo and ca. 54% of world Li reserves are narrowly located in the so-called Li triangle.[135] Lessons from over a century of singular over-reliance on fossil-fuels suggest that an undiversified strategy is unwise for the energy future of the planet. Technological and materials diversity is arguably the key to mitigating the costs of price volatility and fluctuations in materials availability.

Battery research stands poised at an interesting juncture today with some researchers seeking to design fundamentally distinct alternatives to Li-ion batteries, whereas others remain convinced that some of the fundamental challenges in Li-ion systems can be resolved through approaches that facilitate the adaption of metallic Li anodes and by precisely orchestrating the transport of Li-ions from the level of individual particles to that of complete systems. Continued progress in electrochemical energy storage necessitates both streams of research but urgently requires an expanded portfolio of energy storage vectors for evaluation with respect to the trade-offs in materials consumption, cost, and performance. Several pretenders to the reigning Li-ion technology have emerged in recent years but Li-ion batteries continue to reign supreme. Multivalent batteries

utilizing Mg^{2+}, Ca^{2+}, Zn^{2+} and Al^{3+} are of interest for their potential to facilitate a several-fold increase in energy density (Figure 1.7A) both by virtue of shuttling multiple electrons per ion and by allowing for the use of energy-dense supposedly "dendrite-free" metal anodes.[136–138] Figure 1.7 contrasts the ionic potential, crystal radii, reduction potentials, metal electrode capacities, and earth abundance for these alternative insertion technologies.

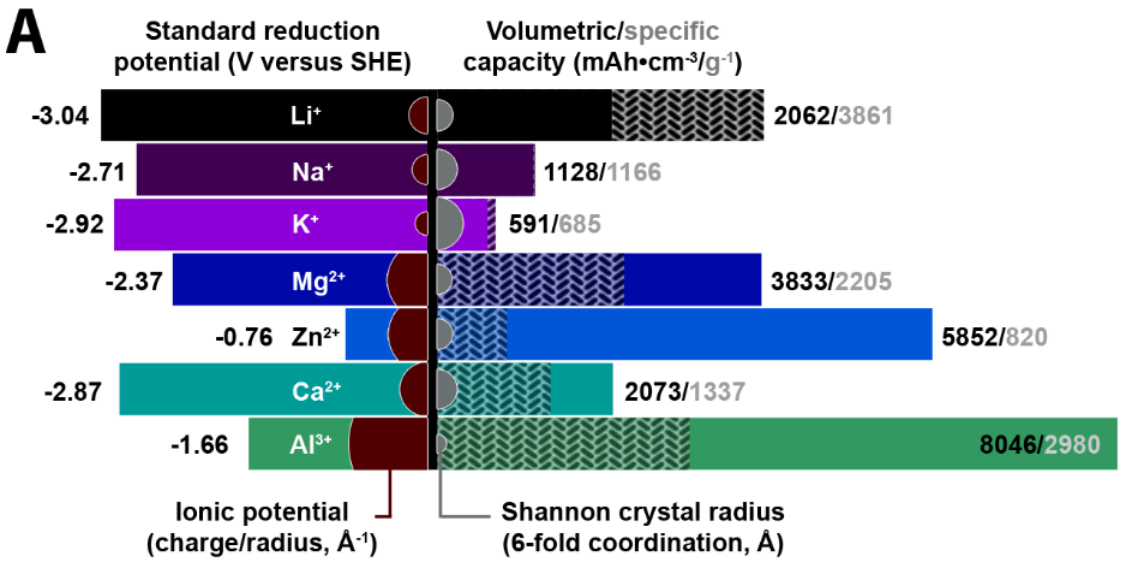

Figure 1.7. (A) Comparison of standard reduction potentials, volumetric (solid) and specific (shaded) storage capacities, crystal radii (grey semicircles), and ionic potential (maroon semicircles) for mono- and multivalent metal batteries. (B) Comparison of crustal distribution of abundant elements (red pie chart, 25.7% earth's crust) and trace elements (blue circle, 0.1269%) of relevance to battery technology. Referenced abundance values are taken from the Handbook of Chemistry and Physics, which aggregates abundance estimates from several prominent sources as shown in reference [136].

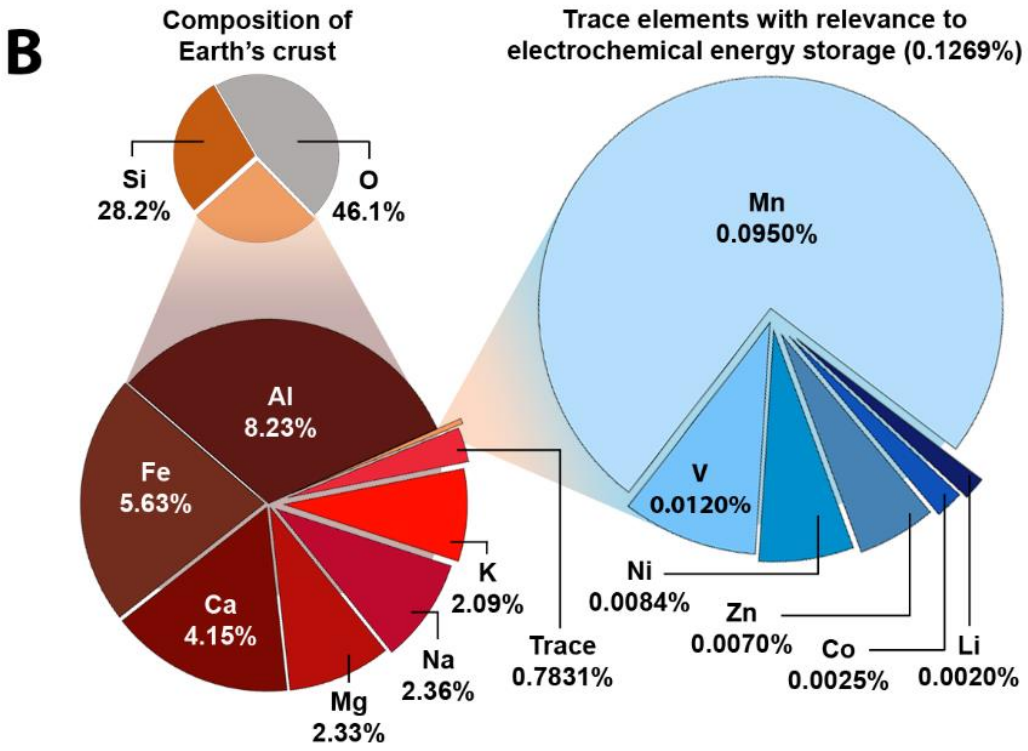

Figure 1.7. Continued.

1.3.1. The Demand for Beyond Lithium Batteries

The impetus for the design of Mg batteries (as compared to Li-ion batteries) derives from promises of improved volumetric and specific capacities (leading to smaller and lighter batteries, respectively) as well as from the prospect of inherently safer batteries. The four-fold increased weight of Mg *vs* Li would predictably lead to undesirable increases weight of the electrolyte and consequently the battery cell; however, this increase in weight would be mitigated in part the ability to use ultra-thin metallic Mg as the anode, reducing the weight of the battery as a whole by eliminating the need for C, Sn, Si, or other anode materials used in Li-ion batteries. While it has recently been shown that, like Li,

Mg forms dendrites under certain extreme cycling conditions.[139] Mg is much safer in that it has a higher melting point (thereby reducing the risk of thermal runaway) and is still much less prone to uneven plating.

In addition to issues related to the design of electrolytes that both reversibly plate metallic Mg without forming dendrites,[139] multivalent battery chemistries continue to be plagued by a dearth of available cathodes that can allow for facile diffusion and desolvation of polarizing divalent and trivalent cations. At the center of “the cathode problem” of Mg-ion batteries lies the highly polarizing nature of Mg^{2+} which presents challenges during diffusion through a crystalline lattice not engendered by the significantly softer Li^{+}.

1.3.2. The Challenge of Designing Mg-Ion Batteries

Regardless of the promise of Mg batteries, suitable cathode materials for Mg-ion batteries have remained elusive. The dearth of suitable materials has been the primary hindrance in moving towards worthwhile device integration. Only a handful of materials have successfully been shown to intercalate magnesium: α-V_2O_5,[140–143] MnO_2,[144,145] and the cluster-based Chevrel phases of Mo_6S_8.[146–148] The difficulty in designing Mg-ion cathode materials stems from the nature of divalent-ion diffusion through a solid-state material. In extended solid structures, diffusion of a charged species creates two distinct structural perturbations. First, the additional electron reduces the framework and depending on the electronic structure of the material and availability of sites, the resulting electrons are localized at specific sites or delocalized across multiple sites. In the case of α-

V_2O_5, DFT calculations show[149] that the electrons localize in specific d-orbitals (d_{xy}). When extrapolated to an extended solid, these d-orbitals form split-off d-bands.[137] Second, the cation experiences a strong electrostatic interaction with the surrounding framework and induces a strong perturbation of the atoms from their equilibrium position, manifesting in the polarization of the anionic sublattice (in the case of V_2O_5, O^{2-}) and the cationic framework (In the case of V_2O_5, V^{4+}/V^{5+}) towards and away from the intercalating species, respectively. The polarization of the framework resulting from the presence of the charged species (e^-, M^{n+}) is represented by the change in average atomic positions, but should be understood as the polarization of the structure towards the intercalating species (for the purposes of this proposal, Li^+) due to an induced change of the magnitude and direction of the vectors of the phonon modes of the V-O bonds with respect to the pristine structure. Classically, the coupling of the electron and its diffusion to a specific phonon mode is known as a polaron.[149–151] There is a strong coupling between the phonon and the cation as described in the latter case and as observed in vanadium oxides[149,152,153] and other cathode materials.[154–156] Importantly, these two quasi-particles are intrinsically coupled, as the diffusion of Li^+ and the e^- (and by extension Mg^{2+} and $2e^-$) is concomitant. Understanding how to mitigate this problem is important, because this phenomenon is common to most large bandgap cathode materials–not just V_2O_5.[149,154–156] What varies between cathode materials is the depth of polaronic confinement which depends on the strength of the phonon-charged particle coupling and thus on the dispersion

of bands, the relative energetic stability of the diffusing species in its equilibrium crystallographic position, the character of the M-L bonds in the cathode material, and the identity/polarizability of the inserted species. Restated, the ease with which this pair diffuses depends (i) on the degree to which the framework is polarized and thus the 'depth' of the polaron well and (ii) the ease with which the electron can move between adjacent metal-centered orbitals. As such, diffusing Mg-ions through the lattice requires mitigation of impediments to polaron diffusion as well as cation migration. First, mitigation of the [electron—phonon] polaron must be addressed by electronic structure engineering to improve d-band overlap to facilitate electron diffusion. Simultaneously, V-O bonding motifs and covalency must be modified to facilitate diffusion of [cation—phonon] polaron. The only realistic approach is to either altogether change the chemistry of the cathode material or alternatively to vary the bonds within the existing material. The latter approach, which we have shown to be effective,[157–159] requires the use of metastable structures to diminish the strength of the polaron confinement. This is accomplished by the use of the metastability of the structure to introduce frustrated coordination environments (to mitigate the [cation—phonon] polaron) and to modify the splitting and overlap of d-bands (to mitigate the [electron—phonon] pair). Polaronic confinement of this type can thus be considered a sort of 'charge localization' which must be mitigated or circumvented in the design of successful cathode materials.

1.4. Overview: Implications for Photocatalysis

Structural diversity in the $M_xV_2O_5$ system (Figure 1.8) enables the topochemical stabilization of metastable polymorphs of binary V_2O_5 via oxidation and extraction of the inserted species, M, as discussed above. This method has been employed to stabilize several metastable polymorphs of V_2O_5 with distinctive structure and bonding motifs. A portion of this dissertation research has focused on using these empty metastable vanadium oxides as hosts for intercalating ions in an effort to install specific electronic states. The motivation behind this approach to bandgap engineering is the design of band-aligned photocatalytic heterostructures, which rely on hole transport from photoexcited quantum dots to support structures.[160–163] These efforts have led to the discovery of a new metastable material, β-$Sn_xV_2O_5$ which is able to achieve sub-picosecond hole transfer when combined with CdSe. quantum dots.

More broadly, this approach, whereby metastable vanadium oxides can be used as solid-state “synthons” for synthesizing metastable ternary phases, represents a truly modular approach to materials design in that it enables independent synthetic control over M, its stoichiometry, *x*, and the V—O bonding of the structural framework.

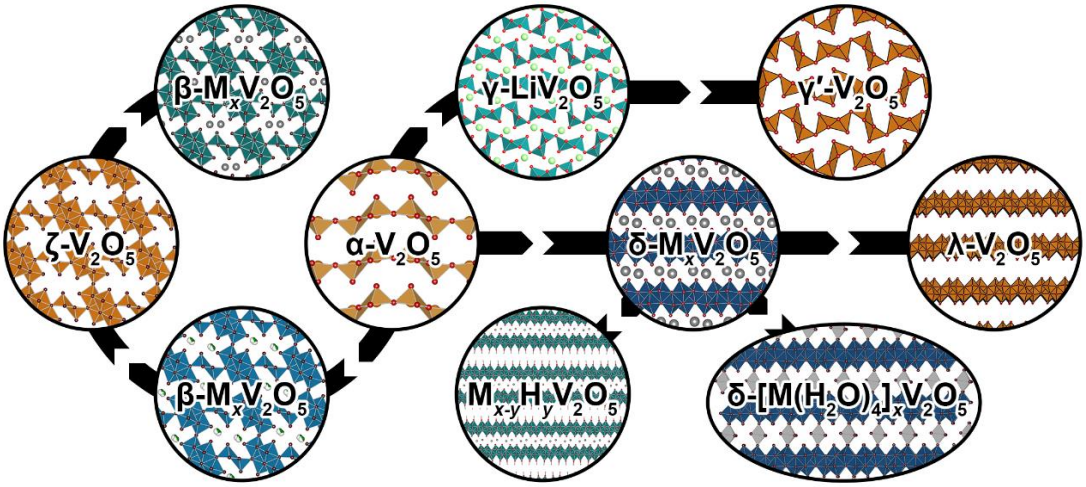

Figure 1.8. Schematic illustrating topochemical synthetic route to the stabilization of four distinct polymorphs of V_2O_5 (α-, ζ-, γ′-, and λ-V_2O_5).

1.5. References

(1) Zavalij, P. Y.; Whittingham, M. S. Structural Chemistry of Vanadium Oxides with Open Frameworks. *Acta Crystallogr. B* **1999**, *55* (5), 627–663.

(2) Marley, P. M.; Horrocks, G. A.; Pelcher, K. E.; Banerjee, S. Transformers: The Changing Phases of Low-Dimensional Vanadium Oxide Bronzes. *Chem. Commun.* **2015**, *51* (25), 5181–5198.

(3) Marley, P. M.; Singh, S.; Abtew, T. A.; Jaye, C.; Fischer, D. A.; Zhang, P.; Sambandamurthy, G.; Banerjee, S. Electronic Phase Transitions of δ-$Ag_xV_2O_5$ Nanowires: Interplay between Geometric and Electronic Structures. *J. Phys. Chem. C* **2014**, *118* (36), 21235–21243.

(4) Marley, P. M.; Banerjee, S. Reversible Interconversion of a Divalent Vanadium Bronze between δ and β Quasi-1D Structures. *Inorg. Chem.* **2012**, *51* (9), 5264–5269.

(5) Wangoh, L.; Marley, P. M.; Quackenbush, N. F.; Sallis, S.; Fischer, D. A.; Woicik, J. C.; Banerjee, S.; Piper, L. F. J. Electron Lone Pair Distortion Facilitated Metal-Insulator Transition in β-$Pb_{0.33}V_2O_5$ Nanowires. *Appl. Phys. Lett.* **2014**, *104* (18), 182108.

(6) Andrews, J. L.; De Jesus, L. R.; Tolhurst, T. M.; Marley, P. M.; Moewes, A.; Banerjee, S. Intercalation-Induced Exfoliation and Thickness-Modulated Electronic Structure of a Layered Ternary Vanadium Oxide. *Chem. Mater.* **2017**, *29* (7), 3285–3294.

(7) Patridge, C. J.; Wu, T.-L.; Sambandamurthy, G.; Banerjee, S. Colossal Above-Room-Temperature Metal-Insulator Switching of a Wadsley-Type Tunnel Bronze. *Chem. Commun.* **2011**, *47* (15), 4484–4486.

(8) Wu, T.-L.; Stabile, A. A.; Patridge, C. J.; Banerjee, S.; Sambandamurthy, G. Electrically Driven Metal-Insulator Switching in Δ−$K_xV_2O_5$ Nanowires. *Appl. Phys. Lett.* **2012**, *101* (16), 163502.

(9) Oka, Y.; Yao, T.; Yamamoto, N. Crystal Structures of Hydrated Vanadium Oxides with δ-Type V_2O_5 Layers: δ -$M_{0.25}V_2O_5 \cdot H_2O$ M=Ca , Ni. *J. Solid State Chem.* **1997**, *329* (132), 323–329.

(10) Horrocks, G. A.; De Jesus, L. R.; Andrews, J. L.; Banerjee, S. X-Ray Spectroscopy and Imaging as Multiscale Probes of Intercalation Phenomena in Cathode Materials. *JOM* **2017**, *69* (9), 1469–1477.

(11) Schuller, I. K.; Stevens, R. *Neuromorphic Computing: From Materials to Systems Architecture - Report of a Roundtable Convened to Consider*

Neuromorphic Computing Basic Research Needs; Gaithersburg, Maryland, 2015. https://www.osti.gov/biblio/1283147-neuromorphic-computing-from-materials-research-systems-architecture-roundtable (accessed Dec 2, 2020)

(12) Salahuddin, S.; Ni, K.; Datta, S. The Era of Hyper-Scaling in Electronics. *Nat. Electron.* **2018**, *1* (8), 442–450.

(13) Taylor, M. B. A Landscape of the New Dark Silicon Design Regime. *IEEE Micro* **2013**, *33* (5), 8–19.

(14) Ionescu, A. M.; Riel, H. Tunnel Field-Effect Transistors as Energy-Efficient Electronic Switches. *Nature* **2011**, *479* (7373), 329–337.

(15) Hodgkin, A. L.; Huxley, A. F. Action Potentials Recorded from inside a Nerve Fibre. *Nature* **1939**, *144*, 710–711.

(16) Yi, W.; Tsang, K. K.; Lam, S. K.; Bai, X.; Crowell, J. A.; Flores, E. A. Biological Plausibility and Stochasticity in Scalable VO_2 Active Memristor Neurons. *Nat. Commun.* **2018**, *9* (1), 4661.

(17) Kumar, S.; Strachan, J. P.; Williams, R. S. Chaotic Dynamics in Nanoscale NbO_2 Mott Memristors for Analogue Computing. *Nature* **2017**, *548* (7667), 318–321.

(18) Yang, C. S.; Shang, D. S.; Liu, N.; Shi, G.; Shen, X.; Yu, R. C.; Li, Y. Q.; Sun, Y. A Synaptic Transistor Based on Quasi-2D Molybdenum Oxide. *Adv. Mater.* **2017**, *29* (27), 1700906.

(19) Torrejon, J.; Riou, M.; Araujo, F. A.; Tsunegi, S.; Khalsa, G.; Querlioz, D.;

Bortolotti, P.; Cros, V.; Yakushiji, K.; Fukushima, A.; Kubota, H.; Yuasa, S.; Stiles, M. D.; Grollier, J. Neuromorphic Computing with Nanoscale Spintronic Oscillators. *Nature* **2017**, *547* (7664), 428–431.

(20) Crane, H. Neuristor-a Novel Device and System Concept. *Proc. IRE* **1962**, *50* (10), 2048–2060.

(21) Jouppi, N. P.; Borchers, A.; Boyle, R.; Cantin, P.; Chao, C.; Clark, C.; Coriell, J.; Daley, M.; Dau, M.; Dean, J.; Gelb, B.; Ghaemmaghami, T. V.; Gottipati, R.; Gulland, W.; Hagmann, R.; Ho, C. R.; Hogberg, D.; Hu, J.; Hundt, R.; Hurt, D.; Ibarz, J.; Jaffey, A.; Jaworski, A.; Kaplan, A.; Khaitan, H.; Killebrew, D.; Koch, A.; Kumar, N.; Lacy, S.; Laudon, J.; Maggiore, A.; Mahony, M.: Miller, K.; Nagarajan, R.; Narayanaswami, R.; Ni, R.; Nix, K.; Norrie, T.; Omernick, M.; Penukonda, N.; Phelps, A.; Ross, J.; Ross, M.; Salek, A.; Samadiani, E.; Severn, C.; Sizikov, G.; Snelham, M.; Souter, J.; Steniberg, D.; Swing, A.; Tan, M.; Thorson, G.; Tian, B.; Toma, H.; Tuttle, E.; Vasudevan, V.; Walter, R.; Wang, W.; Wilcox, E.; Yoon, D. H.; In-Datacenter Performance Analysis of a Tensor Processing Unit. *Proc. 44th Annu. Int. Symp. comuter Archit.* **2017**, *45* (2), 1–12.

(22) Merolla, P. A.; Arthur, J. V.; Alvarez-Icaza, R.; Cassidy, A. S.; Sawada, J.; Akopyan, F.; Jackson, B. L.; Imam, N.; Guo, C.; Nakamura, Y.; Brezzo, B.; Vo, I.; Esser, S. E.; Appuswamy, R.; Taba, B.; Amir, A.; Flickner, M. D.; Risk, W. P.; Manohar, R.; Modha, D. S. A Million Spiking-Neuron Integrated Circuit with a Scalable Communication Network and Interface. *Science*

2014, *345* (6197), 668–673.

(23) Stoliar, P.; Tranchant, J.; Corraze, B.; Janod, E.; Besland, M.-P.; Tesler, F.; Rozenberg, M.; Cario, L. A Leaky-Integrate-and-Fire Neuron Analog Realized with a Mott Insulator. *Adv. Funct. Mater.* **2017**, *27* (11), 1604740:1-7.

(24) Han, J. W.; Meyyappan, M. Leaky Integrate-and-Fire Biristor Neuron. *IEEE Electron Device Lett.* **2018**, *39* (9), 1457–1460.

(25) Kumar, S.; Wang, Z.; Davila, N.; Kumari, N.; Norris, K. J.; Huang, X.; Strachan, J. P.; Vine, D.; Kilcoyne, A. L. D.; Nishi, Y.; Williams, R. S. Physical Origins of Current and Temperature Controlled Negative Differential Resistances in NbO_2. *Nat. Commun.* **2017**, *8* (1), 658.

(26) Wang, Z.; Joshi, S.; Savel'ev, S. E.; Jiang, H.; Midya, R.; Lin, P.; Hu, M.; Ge, N.; Strachan, J. P.; Li, Z.; Wu, Q.; Barnell, M.; Li, G.-L.; Xin, H. L.' Williams, R. S.; Xia, Q.; Yang, J. J. Memristors with Diffusive Dynamics as Synaptic Emulators for Neuromorphic Computing. *Nat. Mater.* **2017**, *16* (1), 101–108.

(27) Wang, Z.; Rao, M.; Han, J.; Zhang, J.; Lin, P.; Li, Y.; Li, C.; Song, W.; Asapu, S.; Midya, R.; Zhuo, Y.; Jiang, H.; Yoon, J. H.; Upadhyay, N. K.; Joshi, S.; Hu, M.; Strachan, J. P.; Barnell, M.; Wu, Q.; Wu, H.; Qiu, Q.; Williams, R. S.; Xia, Q.; Yang, J. J. Capacitive Neural Network with Neuro-Transistors. *Nat. Commun.* **2018**, *9* (1), 3208.

(28) Braham, E. J.; Sellers, D.; Emmons, E.; Villarreal, R.; Asayesh-Ardakani,

H.; Fleer, N. A.; Farley, K. E.; Shahbazian-Yassar, R.; Arròyave, R.; Shamberger, P. J.; Banerjee, S. Modulating the Hysteresis of an Electronic Transition: Launching Alternative Transformation Pathways in the Metal–Insulator Transition of Vanadium(IV) Oxide. *Chem. Mater.* **2018**, *30* (1), 214–224.

(29) Shi, J.; Ha, S. D.; Zhou, Y.; Schoofs, F.; Ramanathan, S. A Correlated Nickelate Synaptic Transistor. *Nat. Commun.* **2013**, *4*, 3676.

(30) Patridge, C. J.; Wu, T. L.; Jaye, C.; Ravel, B.; Takeuchi, E. S.; Fischer, D. A.; Sambandamurthy, G.; Banerjee, S. Synthesis, Spectroscopic Characterization, and Observation of Massive Metal-Insulator Transitions in Nanowires of a Nonstoichiometric Vanadium Oxide Bronze. *Nano Lett.* **2010**, *10* (7), 2448–2453.

(31) Andrews, J. L.; Singh, S.; Kilcoyne, C.; Shamberger, P. J.; Sambandamurthy, G.; Banerjee, S. Memristive Response of a New Class of Hydrated Vanadium Oxide Intercalation Compounds. *MRS Commun.* **2017**, *7* (3), 634–641.

(32) Catalano, S.; Gibert, M.; Bisogni, V.; Peil, O. E.; He, F.; Sutarto, R.; Viret, M.; Zubko, P.; Scherwitzl, R.; Georges, A.; Sawatzky, G. A.; Schmitt, T.; Triscone, J.-M. Electronic Transitions in Strained SmNiO3 Thin Films. *APL Mater.* **2014**, *2* (11), 116110:1-7.

(33) Pickett, M. D.; Medeiros-Ribeiro, G.; Williams, R. S. A Scalable Neuristor Built with Mott Memristors. *Nat. Mater.* **2012**, *12* (2), 114–117.

(34) Li, S.; Liu, X.; Nandi, S. K.; Elliman, R. G. Anatomy of Filamentary Threshold Switching in Amorphous Niobium Oxide. *Nanotechnology* **2018**, *29* (37), 375705.

(35) Parija, A.; Waetzig, G. R.; Andrews, J. L.; Banerjee, S. Traversing Energy Landscapes Away from Equilibrium: Strategies for Accessing and Utilizing Metastable Phase Space. *J. Phys. Chem. C* **2018**, *122* (45), 25709–25728.

(36) Hudak, B. M.; Depner, S. W.; Waetzig, G. R.; Talapatra, A.; Arroyave, R.; Banerjee, S.; Guiton, B. S. Real-Time Atomistic Observation of Structural Phase Transformations in Individual Hafnia Nanorods. *Nat. Commun.* **2017**, *8* (May), 15316.

(37) Bisogni, V.; Catalano, S.; Green, R. J.; Gibert, M.; Scherwitzl, R.; Huang, Y.; Strocov, V. N.; Zubko, P.; Balandeh, S.; Triscone, J.-M.; Sawatzky, G.; Schmitt, T. Ground-State Oxygen Holes and the Metal–Insulator Transition in the Negative Charge-Transfer Rare-Earth Nickelates. *Nat. Commun.* **2016**, *7* (1), 13017.

(38) Middey, S.; Chakhalian, J.; Mahadevan, P.; Freeland, J. W.; Millis, A. J.; Sarma, D. D. Physics of Ultrathin Films and Heterostructures of Rare-Earth Nickelates. *Annu. Rev. Mater. Res.* **2016**, *46* (1), 305–334.

(39) Bartholomew, R. F.; Frankel, D. R. Electrical Properties of Some Titanium Oxides. *Phys. Rev.* **1969**, *187* (3), 828–833.

(40) Torrance, J.; Lacorre, P.; Nazzal, A.; Ansaldo, E.; Niedermayer, C. Systematic Study of Insulator-Metal Transitions in Perovskites $RNiO_3$

(R=Pr,Nd,Sm,Eu) Due to Closing of Charge-Transfer Gap. *Phys. Rev. B* **1992**, *45* (14), 8209–8212.

(41) Rogge, P. C.; Chandrasena, R. U.; Cammarata, A.; Green, R. J.; Shafer, P.; Lefler, B. M.; Huon, A.; Arab, A.; Arenholz, E.; Lee, H. N.; Lee, T.-L.; Nemsak, S.; Rondinelli, J. R.; Gray, A. X.; May, S. J. Electronic Structure of Negative Charge Transfer $CaFeO_3$ across the Metal-Insulator Transition. *Phys. Rev. Mater.* **2018**, *2* (1), 015002.

(42) Yamauchi, T.; Isobe, M.; Ueda, Y. Charge Order and Superconductivity in Vanadium Oxides. *Solid State Sci.* **2005**, *7* (7), 874–881.

(43) Kachi, S.; Kosuge, K.; Okinaka, H. Metal-Insulator Transition in V_nO_{2n-1}. *J. Solid State Chem.* **1973**, *6*, 258–270.

(44) Catalano, S.; Gibert, M.; Fowlie, J.; Iniguez, J.; Triscone, J.-M.; Kreisel, J. Rare-Earth Nickelates $RNiO_3$: Thin Films and Heterostructures. *Reports Prog. Phys.* **2018**, *81*, 046501.

(45) Zhang, X.; Yan, W.; Xie, Y. Synthetic Beta-$K_{0.33}V_2O_5$ Nanorods: A Metal-Insulator Transition in Vanadium Oxide Bronze. *Chem. - An Asian J.* **2011**, *6* (12), 3230–3235.

(46) Tanaka, K.; Nasu, T.; Miyamoto, Y.; Ozaki, N.; Tanaka, S.; Nagata, T.; Hakoe, F.; Yoshikiyo, M.; Nakagawa, K.; Umeta, Y.; Imoto, K.; Tokoro, H.; Namai, A.; Ohkoshi, S.-I. Structural Phase Transition between γ-Ti_3O_5 and δ-Ti_3O_5 by Breaking of a One-Dimensionally Conducting Pathway. *Cryst. Growth Des.* **2015**, *15* (2), 653–657.

(47) Chang, C. F.; Koethe, T. C.; Hu, Z.; Weinen, J.; Agrestini, S.; Zhao, L.; Gegner, J.; Ott, H.; Panaccione, G.; Wu, H.; Haverkort, M, W.; Roth, H.; Komarek, A. C.; Offi, F.; Monaco, G.; Liao, Y.-F.; Tsuei, K.-D.; Lin, H.-J.; Chen, C. T.; Tanaka, A.; Tjeng, L. H. *C*-Axis Dimer and Its Electronic Breakup: The Insulator-to-Metal Transition in Ti_2O_3. *Phys. Rev. X* **2018**, *8* (2), 021004.

(48) Greenberg, E.; Leonov, I.; Layek, S.; Konopkova, Z.; Pasternak, M. P.; Dubrovinsky, L.; Jeanloz, R.; Abrikosov, I. A.; Rozenberg, G. K. Pressure-Induced Site-Selective Mott Insulator-Metal Transition in Fe_2O_3. *Phys. Rev. X* **2018**, *8* (3), 031059.

(49) Middey, S.; Chakhalian, J.; Mahadevan, P.; Freeland, J. W.; Millis, A. J.; Sarma, D. D. Physics of Ultrathin Films and Heterostructures of Rare-Earth Nickelates. *Annu. Rev. Mater. Res.* **2016**, *46* (1), 305–334.

(50) Goodenough, J. B. Metallic Oxides. *Prog. Solid State Chem.* **1971**, *5*, 145–399.

(51) Fulde, P.; Thalmeier, P.; Zwicknagly, G. Strongly Correlated Electrons. *Solid State Physics* **2006**, *60*, 1–180.

(52) Elbio, D. Complexity in Strongly Correlated Electronic Systems. *Science* **2005**, *309* (July), 257–262.

(53) Basov, D. N.; Averitt, R. D.; Van Der Marel, D.; Dressel, M.; Haule, K. Electrodynamics of Correlated Electron Materials. *Rev. Mod. Phys.* **2011**, *83* (2), 471–541.

(54) Imada, M.; Fujimori, A.; Tokura, Y. Metal-Insulator Transitions. *Rev. Mod. Phys.* **1998**, *70* (4), 1039–1263.

(55) Monceau, P. Electronic Crystals: An Experimental Overview. *Adv. Phys.* **2012**, *61* (4), 325–581.

(56) Wang, Z.; Rao, M.; Midya, R.; Joshi, S.; Jiang, H.; Lin, P.; Song, W.; Asapu, S.; Zhuo, Y.; Li, C.; Wu, H.; Xia, Q.; Yang, J. J. Threshold Switching of Ag or Cu in Dielectrics: Materials, Mechanism, and Applications. *Adv. Funct. Mater.* **2018**, *28* (6), 1704862.

(57) Yang, D.-S.; Baum, P.; Zewail, A. H. Ultrafast Electron Crystallography of the Cooperative Reaction Path in Vanadium Dioxide. *Struct. Dyn.* **2016**, *3* (3), 034304.

(58) Brito, W. H.; Aguiar, M. C. O.; Haule, K.; Kotliar, G. Metal-Insulator Transition in VO_2: A DFT + DMFT Perspective. *Phys. Rev. Lett.* **2016**, *117* (5), 056402.

(59) Jeong, J.; Aetukuri, N.; Graf, T.; Schladt, T. D.; Samant, M. G.; Parkin, S. S. P. Suppression of Metal-Insulator Transition in VO_2 by Electric Field-Induced Oxygen Vacancy Formation. *Science (80-.).* **2013**, *339* (6126), 1402–1405.

(60) Bisogni, V.; Catalano, S.; Green, R. J.; Gibert, M.; Scherwitzl, R.; Huang, Y.; Strocov, V. N.; Zubko, P.; Balandeh, S.; Triscone, J. M.; ; Sawatzky, G.; Schmitt, T. Ground-State Oxygen Holes and the Metal-Insulator Transition in the Negative Charge-Transfer Rare-Earth Nickelates. *Nat. Commun.*

2016, *7*, 13017.

(61) Sun, K.; Sun, S.; Zhu, C.; Tian, H.; Yang, H.; Li, J. Hidden CDW States and Insulator-to-Metal Transition after a Pulsed Femtosecond Laser Excitation in Layered Chalcogenide 1T-$TaS_{2-x}Se_x$. *Sci. Adv.* **2018**, *4*, 9660.

(62) Zhang, S.; Luo, S.; Xu, N.; Zou, Q.; Song, M.; Yun, J.; Luo, Q.; Guo, Z.; Li, R.; Tian, W.; Li, X.; Zhou, H.; Chen, H.; Zhang, Y.; Yang, X.; Jiang, W.; Shen, K.; Hong, J.; Yuan, Z.; Xi, L.; Xia, K.; Salahuddin, S.; Dieny, B.; You, L. A Spin–Orbit-Torque Memristive Device. *Adv. Electron. Mater.* **2019**, *5*, 1800782.

(63) Brito, W. H.; Aguiar, M. C. O. O.; Haule, K.; Kotliar, G. Dynamic Electronic Correlation Effects in NbO_2 as Compared to VO_2. *Phys. Rev. B* **2017**, *96* (19), 195102.

(64) Kumar, S.; Strachan, J. P.; Pickett, M. D.; Bratkovsky, A.; Nishi, Y.; Williams, R. S. Sequential Electronic and Structural Transitions in VO_2 Observed Using X-Ray Absorption Spectromicroscopy. *Adv. Mater.* **2014**, *26*, 7505–7509.

(65) Braham, E. J.; Andrews, J. L.; Alivio, T. E. G.; Fleer, N. A.; Banerjee, S. Stabilization of a Metastable Tunnel-Structured Orthorhombic Phase of VO_2 upon Iridium Doping. *Phys. Status Solidi Appl. Mater. Sci.* **2018**, *215* (16), 1700884.

(66) Whittaker, L.; Patridge, C. J.; Banerjee, S. Microscopic and Nanoscale Perspective of the Metal-Insulator Phase Transitions of VO_2: Some New

Twists to an Old Tale. *J. Phys. Chem. Lett.* **2011**, *2* (7), 745–758.

(67) Krammer, A.; Magrez, A.; Vitale, W. A.; Mocny, P.; Jeanneret, P.; Guibert, E.; Whitlow, H. J.; Ionescu, A. M.; Schüler, A. Elevated Transition Temperature in Ge Doped VO_2 Thin Films. *J. Appl. Phys.* **2017**, *122* (4), 045304.

(68) Krammer, A.; Bouvard, O.; Schüler, A. Study of Si Doped VO_2 Thin Films for Solar Thermal Applications. *Energy Procedia* **2017**, *122*, 745–750.

(69) Wu, Y.; Fan, L.; Liu, Q.; Chen, S.; Huang, W.; Chen, F.; Liao, G.; Zou, C.; Wu, Z. Decoupling the Lattice Distortion and Charge Doping Effects on the Phase Transition Behavior of VO_2 by Titanium (Ti^{4+}) Doping. *Sci. Rep.* **2015**, *5* (1), 9328.

(70) Miyazaki, K.; Shibuya, K.; Suzuki, M.; Sakai, K.; Fujita, J. I.; Sawa, A. Chromium-Niobium Co-Doped Vanadium Dioxide Films: Large Temperature Coefficient of Resistance and Practically No Thermal Hysteresis of the Metal-Insulator Transition. *AIP Adv.* **2016**, *6* (5), 055012.

(71) Wang, N.; Duchamp, M.; Dunin-Borkowski, R. E.; Liu, S.; Zeng, X.; Cao, X.; Long, Y. Terbium-Doped VO_2 Thin Films: Reduced Phase Transition Temperature and Largely Enhanced Luminous Transmittance. *Langmuir* **2016**, *32* (3), 759–764.

(72) Alivio, T. E. G. G.; Sellers, D. G.; Asayesh-Ardakani, H.; Braham, E. J.; Horrocks, G. A.; Pelcher, K. E.; Villareal, R.; Zuin, L.; Shamberger, P. J.; Arróyave, R.; Shahbazian-Yassar, R.; Banerjee, S. Postsynthetic Route for

Modifying the Metal—Insulator Transition of VO_2 by Interstitial Dopant Incorporation. *Chem. Mater.* **2017**, *29* (12), 5401–5412.

(73) Patridge, C. J.; Whittaker, L.; Ravel, B.; Banerjee, S. Elucidating the Influence of Local Structure Perturbations on the Metal–Insulator Transitions of $V_{1-x}Mo_xO_2$ Nanowires: Mechanistic Insights from an X-Ray Absorption Spectroscopy Study. *J. Phys. Chem. C* **2012**, *116* (5), 3728–3736.

(74) Wu, Y.; Fan, L.; Chen, S.; Chen, S.; Chen, F.; Zou, C.; Wu, Z. A Novel Route to Realize Controllable Phases in an Aluminum (Al^{3+})-Doped VO_2 System and the Metal-Insulator Transition Modulation. *Mater. Lett.* **2014**, *127*, 44–47.

(75) Braham, E. J.; Andrews, J. L.; Alivio, T. E. G.; Fleer, N. A.; Banerjee, S. Stabilization of a Metastable Tunnel-Structured Orthorhombic Phase of VO 2 upon Iridium Doping. *Phys. status solidi* **2018**, *215* (16), 1700884.

(76) Braham, E. J.; Sellers, D.; Emmons, E.; Villarreal, R.; Asayesh-Ardakani, H.; Fleer, N. A.; Farley, K. E.; Shahbazian-Yassar, R.; Arròyave, R.; Shamberger, P. J.; Banerjee, S. Modulating the Hysteresis of an Electronic Transition: Launching Alternative Transformation Pathways in the Metal–Insulator Transition of Vanadium(IV) Oxide. *Chem. Mater.* **2018**, *30* (1), 214–224.

(77) Krammer, A.; Bouvard, O.; Schüler, A. Study of Si Doped VO2thin Films for Solar Thermal Applications. *Energy Procedia* **2017**, *122*, 745–750.

(78) Krammer, A.; Magrez, A.; Vitale, W. A.; Mocny, P.; Jeanneret, P.; Guibert, E.; Whitlow, H. J.; Ionescu, A. M.; Schüler, A. Elevated Transition Temperature in Ge Doped VO2thin Films. *J. Appl. Phys.* **2017**, *122* (4), 045304.

(79) Wu, Y.; Fan, L.; Liu, Q.; Chen, S.; Huang, W.; Chen, F.; Liao, G.; Zou, C.; Wu, Z. Decoupling the Lattice Distortion and Charge Doping Effects on the Phase Transition Behavior of VO2 by Titanium (Ti4+) Doping. *Sci. Rep.* **2015**, *5* (1), 9328.

(80) Wang, N.; Duchamp, M.; Dunin-Borkowski, R. E.; Liu, S.; Zeng, X.; Cao, X.; Long, Y. Terbium-Doped VO2Thin Films: Reduced Phase Transition Temperature and Largely Enhanced Luminous Transmittance. *Langmuir* **2016**, *32* (3), 759–764.

(81) Alivio, T. E. G. G.; Sellers, D. G.; Asayesh-Ardakani, H.; Braham, E. J.; Horrocks, G. A.; Pelcher, K. E.; Villareal, R.; Zuin, L.; Shamberger, P. J.; Arróyave, R.; Shahbazian-Yassar, R.; Banerjee, S. Postsynthetic Route for Modifying the Metal—Insulator Transition of VO 2 by Interstitial Dopant Incorporation. *Chem. Mater.* **2017**, *29* (12), 5401–5412.

(82) Patridge, C. J.; Whittaker, L.; Ravel, B.; Banerjee, S. Elucidating the Influence of Local Structure Perturbations on the Metal-Insulator Transitions of V1-XMoxO2nanowires: Mechanistic Insights from an X-Ray Absorption Spectroscopy Study. *J. Phys. Chem. C* **2012**, *116* (5), 3728–3736.

(83) Wu, Y.; Fan, L.; Chen, S.; Chen, S.; Chen, F.; Zou, C.; Wu, Z. A Novel Route

to Realize Controllable Phases in an Aluminum (Al3+)-Doped VO2system and the Metal-Insulator Transition Modulation. *Mater. Lett.* **2014**, *127*, 44–47.

(84) Liu, L.; Cao, F.; Yao, T.; Xu, Y.; Zhou, M.; Qu, B.; Pan, B.; Wu, C.; Wei, S.; Xie, Y. New-Phase VO_2 Micro/Nanostructures: Investigation of Phase Transformation and Magnetic Property. *New J. Chem.* **2012**, *36* (3), 619–625.

(85) Yao, T.; Oka, Y.; Yamamoto, N. A Structural Study of the High-Temperature Phase of VO_2(A). *J. Solid State Chem.* **1994**, *112* (1), 196–198.

(86) Nájera, O.; Civelli, M.; Dobrosavljević, V.; Rozenberg, M. J. Resolving the VO_2 Controversy: Mott Mechanism Dominates the Insulator-to-Metal Transition. *Phys. Rev. B* **2017**, *95* (3), 035113.

(87) Budai, J. D.; Hong, J.; Manley, M. E.; Specht, E. D.; Li, C. W.; Tischler, J. Z.; Abernathy, D. L.; Said, A. H.; Leu, B. M.; Boatner, L. A.; McQueeney, R. J.; Delaire, O. Metallization of Vanadium Dioxide Driven by Large Phonon Entropy. *Nature* **2014**, *515* (7528), 535–539.

(88) Shank, J. C.; Tellekamp, M. B.; Wahila, M. J.; Howard, S.; Weidenbach, A. S.; Zivasatienraj, B.; Piper, L. F. J.; Doolittle, W. A. Scalable Memdiodes Exhibiting Rectification and Hysteresis for Neuromorphic Computing. *Sci. Rep.* **2018**, *8* (1), 12935.

(89) Park, J. H.; Coy, J. M.; Kasirga, T. S.; Huang, C.; Fei, Z.; Hunter, S.; Cobden, D. H. Measurement of a Solid-State Triple Point at the Metal-

Insulator Transition in VO_2. *Nature* **2013**, *500* (7463), 431–434.

(90) Fan, W.; Cao, J.; Seidel, J.; Gu, Y.; Yim, J. W.; Barrett, C.; Yu, K. M.; Ji, J.; Ramesh, R.; Chen, L. Q.; Wu, J. Large Kinetic Asymmetry in the Metal-Insulator Transition Nucleated at Localized and Extended Defects. *Phys. Rev. B - Condens. Matter Mater. Phys.* **2011**, *83* (23).

(91) Whittaker, L.; Wu, T.-L.; Patridge, C. J.; Sambandamurthy, G.; Banerjee, S. Distinctive Finite Size Effects on the Phase Diagram and Metal–Insulator Transitions of Tungsten-Doped Vanadium(IV) Oxide. *J. Mater. Chem.* **2011**, *21* (15), 5580–5592.

(92) Yang, M.; Yang, Y.; Bin Hong; Wang, L.; Hu, K.; Dong, Y.; Xu, H.; Huang, H.; Zhao, J.; Chen, H.; Song, L.; Ju, H.; Zhu, J.; Bao, JH.; Li, X.; Gu, Y.; Yang, T.; Gao, X.; Luo, Z.; Gao, C. Suppression of Structural Phase Transition in VO_2 by Epitaxial Strain in Vicinity of Metal-Insulator Transition. *Sci. Rep.* **2016**, *6* (1), 23119.

(93) Asayesh-Ardakani, H.; Nie, A.; Marley, P. M.; Zhu, Y.; Phillips, P. J.; Singh, S.; Mashayek, F.; Sambandamurthy, G.; Low, K. Bin; Klie, R. F.; Banerjee, S.; Odegard, Shahbazian-Yassar, R. Atomic Origins of Monoclinic-Tetragonal (Rutile) Phase Transition in Doped VO_2 Nanowires. *Nano Lett.* **2015**, *15* (11), 7179–7188.

(94) Chen, S.; Liu, J.; Wang, L.; Luo, H.; Gao, Y. Unraveling Mechanism on Reducing Thermal Hysteresis Width of VO_2 by Ti Doping: A Joint Experimental and Theoretical Study. *J. Phys. Chem. C* **2014**, *118* (33),

18938–18944.

(95) Riapanitra, A.; Asakura, Y.; Cao, W.; Noda, Y.; Yin, S. Supercritical Temperature Synthesis of Fluorine-Doped VO_2(M) Nanoparticle with Improved Thermochromic Property. *Nanotechnology* **2018**, *29* (24), 244005.

(96) Filinchuk, Y.; Tumanov, N. A.; Ban, V.; Ji, H.; Wei, J.; Swift, M. W.; Nevidomskyy, A. H.; Natelson, D. In Situ Diffraction Study of Catalytic Hydrogenation of VO_2: Stable Phases and Origins of Metallicity. *J. Am. Chem. Soc.* **2014**, *136* (22), 8100–8109.

(97) Rao, C. N. R.; Rao, G. R.; Rao, G. V. S. Semiconductor-Metal Transitions in NbO_2 and NbMetal-Insulator Transition in $V_{1-x}O_{2n-1}$VMetal-Insulator Transition in $V_nO_{2x-1}O_2$. *J. Solid State Chem.* **1973**, *6* (3), 340–343.

(98) Rana, R.; Klopf, J. M.; Grenzer, J.; Schneider, H.; Helm, M.; Pashkin, A. Nonthermal Nature of Photoinduced Insulator-to-Metal Transition in NbO_2. *Phys. Rev. B* **2019**, *99* (4), 041102.

(99) O'Hara, A.; Demkov, A. A. Nature of the Metal-Insulator Transition in NbO_2. *Phys. Rev. B - Condens. Matter Mater. Phys.* **2015**, *91* (9), 094305.

(100) Slesazeck, S.; Mähne, H.; Wylezich, H.; Wachowiak, A.; Radhakrishnan, J.; Ascoli, A.; Tetzlaff, R.; Mikolajick, T. Physical Model of Threshold Switching in NbO_2 Based Memristors. *RSC Adv.* **2015**, *5* (124), 102318–102322.

(101) Onoda, M.; Sato, T. Polaronic Nonmetal–Correlated Metal Crossover System B′-$Cu_xV_2O_5$ with Anharmonic Copper Oscillation and

Thermoelectric Conversion Performance. *J. Phys. Soc. Japan* **2017**, *86* (12), 124801.

(102) Funck, C.; Menzel, S.; Aslam, N.; Zhang, H.; Hardtdegen, A.; Waser, R.; Hoffmann-Eifert, S. Multidimensional Simulation of Threshold Switching in NbO_2 Based on an Electric Field Triggered Thermal Runaway Model. *Adv. Electron. Mater.* **2016**, *2* (7), 1600169.

(103) Gibson, G. A.; Musunuru, S.; Zhang, J.; Vandenberghe, K.; Lee, J.; Hsieh, C. C.; Jackson, W.; Jeon, Y.; Henze, D.; Li, Z.; Williams, R. S. An Accurate Locally Active Memristor Model for S-Type Negative Differential Resistance in NbO_X. *Appl. Phys. Lett.* **2016**, *108* (2), 023505.

(104) Pershin, Y. V.; Di Ventra, M. Memory Effects in Complex Materials and Nanoscale Systems. *Adv. Phys.* **2011**, *60* (2), 145–227.

(105) Pickett, M. D.; Stanley Williams, R. Sub-100 FJ and Sub-Nanosecond Thermally Driven Threshold Switching in Niobium Oxide Crosspoint Nanodevices. *Nanotechnology* **2012**, *23* (21), 215202.

(106) Cho, J.; Sheng, A.; Suwandaratne, N.; Wangoh, L.; Andrews, J. L.; Zhang, P.; Piper, L. F. J.; Watson, D. F.; Banerjee, S. The Middle Road Less Taken: Electronic-Structure-Inspired Design of Hybrid Photocatalytic Platforms for Solar Fuel Generation. *Acc. Chem. Res.* **2019**, *52* (3), 645–655.

(107) Parija, A.; Liang, Y.; Andrews, J. L.; De Jesus, L. R.; Prendergast, D.; Banerjee, S.; Jesus, L. R. De; Prendergast, D.; Banerjee, S. Topochemically De-Intercalated Phases of V_2O_5 as Cathode Materials for

Multivalent Intercalation Batteries: A First-Principles Evaluation. *Chem. Mater.* **2016**, *28* (16), 5611–5620.

(108) Guo, H.; Li, Z. W.; Zhao, L.; Hu, Z.; Chang, C. F.; Kuo, C.-Y.; Schmidt, W.; Piovano, A.; Pi, T. W.; Sobolev, O.; Khomskii, D. I.; Tjeng, L. H.; Komarek, A. C. Antiferromagnetic Correlations in the Metallic Strongly Correlated Transition Metal Oxide $LaNiO_3$. *Nat. Commun.* **2018**, *9* (1), 43.

(109) Nikulin, I. V.; Novojilov, M. A.; Kaul, A. R.; Mudretsova, S. N.; Kondrashov, S. V. Oxygen Nonstoichiometry of $NdNiO_{3-\delta}$ and $SmNiO_{3-\delta}$. *Mater. Res. Bull.* **2004**, *39* (6), 775–791.

(110) Xuan, X. F.; Gao, G. Y.; Chen, F.; Wang, L. F.; Wu, W. B.; Tan, X. L.; Lian, X. K.; Jin, S. W. Controlling the Sharpness of Room-Temperature Metal-Insulator Transition in Epitaxial $Sm_{0.5}Nd_{0.5}NiO_3$ Films. *AIP Adv.* **2013**, *3* (6), 062133.

(111) Alonso, J. A.; García-Muñoz, J. L.; Fernández-Díaz, M. T.; Aranda, M. A. G. G.; Martínez-Lope, M. J.; Casais, M. T. Charge Disproportionation in $RNiO_3$ Perovskites: Simultaneous Metal-Insulator and Structural Transition in $YNiO_3$. *Phys. Rev. Lett.* **1999**, *82* (19), 3871–3874.

(112) Huang, H.; Luo, Z.; Yang, Y.; Yang, M.; Wang, H.; Pan, G.; Lu, Y.; Gao, C. The Effect of Growth Oxygen Pressure on the Metal-Insulator Transition of Ultrathin $Sm_{0.6}Nd_{0.4}NiO_{3-\delta}$ Epitaxial Films. *RSC Adv.* **2014**, *4* (98), 55082–55086.

(113) Liao, Z.; Gauquelin, N.; Green, R. J.; Muller-Caspary, K.; Lobato, I.; Li, L.;

Van Aert, S.; Verbeeck, J.; Huijben, M.; Grisolia, M. N.; Rouco, V.; Hage, R. E.; Villegas, J. E.; Mercy, A.; Bibes, M.; Ghosez, P.; Sawatzky, G. A.; Rijinders, G.; Koster, G. Metal–Insulator-Transition Engineering by Modulation Tilt-Control in Perovskite Nickelates for Room Temperature Optical Switching. *Proc. Natl. Acad. Sci.* **2018**, *115* (38), 9515–9520.

(114) Liu, J.; Kargarian, M.; Kareev, M.; Gray, B.; Ryan, P. J.; Cruz, A.; Tahir, N.; Chuang, Y.-D. De; Guo, J.; Rondinelli, J. M.; Freeland, J. W.; Fiete, G. A.; Chakhalian, J. Heterointerface Engineered Electronic and Magnetic Phases of $NdNiO_3$ Thin Films. *Nat. Commun.* **2013**, *4* (1), 2714.

(115) Heo, S.; Oh, C.; Eom, M. J.; Kim, J. S.; Ryu, J.; Son, J.; Jang, H. M. Modulation of Metal-Insulator Transitions by Field-Controlled Strain in $NdNiO_3$/$SrTiO_3$/PMN-PT (001) Heterostructures. *Sci. Rep.* **2016**, *6*, 22228.

(116) Alonso, J. A.; Martínez-Lope, M. J.; Casais, M. T.; Aranda, M. A. G.; Fernández-Díaz, M. T. Metal-Insulator Transitions, Structural and Microstructural Evolution of RNiO3 (R = Sm, Eu, Gd, Dy, Ho, Y) Perovskites: Evidence for Room-Temperature Charge Disproportionation in Monoclinic $HoNiO_3$ and $YNiO_3$. *J. Am. Chem. Soc.* **1999**, *121* (20), 4754–4762.

(117) Medarde, M.; Fernández-Díaz, M. T.; Lacorre, P. Long-Range Charge Order in the Low-Temperature Insulating Phase of $PrNiO_3$. *Phys. Rev. B - Condens. Matter Mater. Phys.* **2008**, *78* (21), 212101.

(118) Medarde, M.; Dallera, C.; Grioni, M.; Delley, B.; Vernay, F.; Mesot, J.;

Sikora, M.; Alonso, J. A.; Martínez-Lope, M. J. Charge Disproportionation in $RNiO_3$ Perovskites (R=rare Earth) from High-Resolution x-Ray Absorption Spectroscopy. *Phys. Rev. B* **2009**, *80* (24), 245105.

(119) Staub, U.; Meijer, G. I.; Fauth, F.; Allenspach, R.; Bednorz, J. G.; Karpinski, J.; Kazakov, S. M.; Paolasini, L.; D'Acapito, F. Direct Observation of Charge Order in an Epitaxial $NdNiO_3$ Film. *Phys. Rev. Lett.* **2002**, *88* (12), 126402.

(120) Mercy, A.; Bieder, J.; Íñiguez, J.; Ghosez, P. Structurally Triggered Metal-Insulator Transition in Rare-Earth Nickelates. *Nat. Commun.* **2017**, *8* (1), 1677.

(121) Balachandran, P. V.; Rondinelli, J. M. Interplay of Octahedral Rotations and Breathing Distortions in Charge-Ordering Perovskite Oxides. *Phys. Rev. B* **2013**, *88* (5), 054101.

(122) Shamblin, J.; Heres, M.; Zhou, H.; Sangoro, J.; Lang, M.; Neuefeind, J.; Alonso, J. A.; Johnston, S. Experimental Evidence for Bipolaron Condensation as a Mechanism for the Metal-Insulator Transition in Rare-Earth Nickelates. *Nat. Commun.* **2018**, *9* (1), 86.

(123) Green, R. J.; Haverkort, M. W.; Sawatzky, G. A. Bond Disproportionation and Dynamical Charge Fluctuations in the Perovskite Rare-Earth Nickelates. *Phys. Rev. B* **2016**, *94* (19), 195127.

(124) Khomskii, D. Unusual Valence, Negative Charge-Transfer Gaps and Self-Doping in Transition-Metal Compounds. *Lith. J. Phys.* **1997**, *65*.

(125) Mizokawa, T.; Namatame, H.; Fujimori, A.; Akeyama, K.; Kondoh, H.;

Kuroda, H.; Kosugi, N. Origin of the Band Gap in the Negative Charge-Transfer-Energy Compound $NaCuO_2$. *Phys. Rev. Lett.* **1991**, *67* (12), 1638–1641.

(126) Park, H.; Millis, A. J.; Marianetti, C. A. Site-Selective Mott Transition in Rare-Earth-Element Nickelates. *Phys. Rev. Lett.* **2012**, *156402* (October), 156402.

(127) Bubel, S.; Hauser, A. J.; Glaudell, A. M.; Mates, T. E.; Stemmer, S.; Chabinyc, M. L. The Electrochemical Impact on Electrostatic Modulation of the Metal-Insulator Transition in Nickelates. *Appl. Phys. Lett.* **2015**, *106* (12), 122102.

(128) Marley, P. M.; Stabile, A. A.; Kwan, C. P.; Singh, S.; Zhang, P.; Sambandamurthy, G.; Banerjee, S. Charge Disproportionation and Voltage-Induced Metal-Insulator Transitions Evidenced in β-$Pb_xV_2O_5$ Nanowires. *Adv. Funct. Mater.* **2013**, *23* (2), 153–160.

(129) Andrews, J. L.; Cho, J.; Wangoh, L.; Suwandaratne, N.; Sheng, A.; Chauhan, S.; Nieto, K.; Mohr, A.; Kadassery, K. J.; Popeil, M. R.; Thakur, T. K.; Sfeir, M.; Lacy, D. C.; Lee, T.-L.; Zhang, P.; Watson, D. F.; Piper, F. F. J.; Banerjee, S. Hole Extraction by Design in Photocatalytic Architectures Interfacing CdSe Quantum Dots with Topochemically Stabilized Tin Vanadium Oxide. *J. Am. Chem. Soc.* **2018**, *140* (49), 17163–17174.

(130) Andrews, J. L.; Mukherjee, A.; Yoo, H. D.; Parija, A.; Marley, P. M.; Fakra, S.; Prendergast, D.; Cabana, J.; Klie, R. F.; Banerjee, S. Reversible Mg-Ion

Insertion in a Metastable One-Dimensional Polymorph of V_2O_5. *Chem* **2018**, *4* (3), 564–585.

(131) Andrews, J. L.; De Jesus, L. R.; Tolhurst, T. M.; Marley, P. M.; Moewes, A.; Banerjee, S. Intercalation-Induced Exfoliation and Thickness-Modulated Electronic Structure of a Layered Ternary Vanadium Oxide. *Chem. Mater.* **2017**, *29* (7), 3285–3294.

(132) Tolhurst, T.; Leedahl, B.; Andrews, J.; Banerjee, S.; Moewes, A. Electronic Structure of ε'-V_2O_5: An Expanded Band Gap in a Double-Layered Polymorph with Increased Interlayer Separation. *J. Mater. Chem. A* **2017**, *5*, 23694–23703.

(133) De Jesus, L. R.; Horrocks, G. A.; Liang, Y.; Parija, A.; Jaye, C.; Wangoh, L.; Wang, J.; Fischer, D. A.; Piper, L. F. J.; Prendergast, D.; Banerjee, S. Mapping Polaronic States and Lithiation Gradients in Individual V_2O_5 Nanowires. *Nat. Commun.* **2016**, *7*, 12022.

(134) Vaalma, C.; Buchholz, D.; Weil, M.; Passerini, S. A Cost and Resource Analysis of Sodium-Ion Batteries. *Nat. Rev. Mater.* **2018**, *3* (4), 18013.

(135) Olivetti, E. A.; Ceder, G.; Gaustad, G. G.; Fu, X. Lithium-Ion Battery Supply Chain Considerations: Analysis of Potential Bottlenecks in Critical Metals. *Joule* **2017**, *1* (2), 229–243.

(136) Abundance of Elements in the Earth's Crust and in the Sea. In *CRC Handbook of Chemistry and Physics*; Rumble, J. R., Lide, D. R., Bruno, T. J., Martinsen, D., Eds.; CRC Pres/Taylor & Francis, Boca Raton, FL., 2018;

pp 1–1532.

(137) De Jesus, L. R.; Andrews, J. L.; Parija, A.; Banerjee, S. Defining Diffusion Pathways in Intercalation Cathode Materials: Some Lessons from V_2O_5 on Directing Cation Traffic. *ACS Energy Lett.* **2018**, *3* (4), 915–931.

(138) Andrews, J. L.; Mukherjee, A.; Yoo, H. D.; Parija, A.; Marley, P. M.; Fakra, S.; Prendergast, D.; Cabana, J.; Klie, R. F.; Banerjee, S. Reversible Mg-Ion Insertion in a Metastable One-Dimensional Polymorph of V_2O_5. *Chem* **2018**, *4* (3), 564–585.

(139) Davidson, R.; Verma, A.; Santos, D.; Hao, F.; Fincher, C.; Xiang, S.; Van Buskirk, J.; Xie, K.; Pharr, M.; Mukherjee, P. P.; Banerjee, S. Formation of Magnesium Dendrites during Electrodeposition. *ACS Energy Lett.* **2019**, *4* (2), 375–376.

(140) Sa, N.; Wang, H.; Proffit, D. L.; Lipson, A. L.; Key, B.; Liu, M.; Feng, Z.; Fister, T. T.; Ren, Y.; Sun, C. J.; Vaughey, J. T.; Fenter, P. A.; Persson, K. A.; Burrell, A. K. Is Alpha-V_2O_5 a Cathode Material for Mg Insertion Batteries? *J. Power Sources* **2016**, *323*, 44–50.

(141) Gershinsky, G.; Yoo, H. D.; Gofer, Y.; Aurbach, D. Electrochemical and Spectroscopic Analysis of Mg2+ Intercalation into Thin Film Electrodes of Layered Oxides: V2O5 and MoO3. *Langmuir* **2013**, *29* (34), 10964–10972.

(142) Brezesinski, T.; Wang, J.; Tolbert, S. H.; Dunn, B. Ordered Mesoporous Alpha-MoO3 with Iso-Oriented Nanocrystalline Walls for Thin-Film Pseudocapacitors. *Nat. Mater.* **2010**, *9* (2), 146–151.

(143) Yoo, H. D.; Jokisaari, J. R.; Yu, Y. S.; Kwon, B. J.; Hu, L.; Kim, S.; Han, S. D.; Lopez, M.; Lapidus, S. H.; Nolis, G. M.; Ingram, B, J.; Bolotin, I.; Ahmed, S.; Klie, R. F.; Vaughey, J. T.; Fister, T. T.; Cabana, J. Intercalation of Magnesium into a Layered Vanadium Oxide with High Capacity. *ACS Energy Lett.* **2019**, *4*, 1528–1534.

(144) Sun, X.; Bonnick, P.; Duffort, V.; Liu, M.; Rong, Z.; Persson, K. A.; Ceder, G.; Nazar, L. F. A High Capacity Thiospinel Cathode for Mg Batteries. *Energy Environ. Sci.* **2016**, *9* (7), 2273–2277.

(145) Sun, X.; Duffort, V.; Mehdi, B. L.; Browning, N. D.; Nazar, L. F. Investigation of the Mechanism of Mg Insertion in Birnessite in Nonaqueous and Aqueous Rechargeable Mg-Ion Batteries. *Chem. Mater.* **2016**, *28* (2), 534–542.

(146) Levi, E.; Gershinsky, G.; Aurbach, D.; Isnard, O. Crystallography of Chevrel Phases, MMo_6T_8 (M = Cd, Na, Mn, and Zn, T = S, Se) and Their Cation Mobility. *Inorg. Chem.* **2009**, *48* (18), 8751–8758.

(147) Wan, L. F.; Perdue, B. R.; Apblett, C. A.; Prendergast, D. Mg Desolvation and Intercalation Mechanism at the Mo_6S_8 Chevrel Phase Surface. *Chem. Mater.* **2015**, *27* (17), 5932–5940.

(148) Yoo, H. D.; Shterenberg, I.; Gofer, Y.; Gershinsky, G.; Pour, N.; Aurbach, D. Mg Rechargeable Batteries: An on-Going Challenge. *Energy Environ. Sci.* **2013**, *6* (8), 2265–2279.

(149) De Jesus, L. R.; Horrocks, G. A.; Liang, Y.; Parija, A.; Jaye, C.; Wangoh, L.; Wang, J.; Fischer, D. A.; Piper, L. F. J.; Prendergast, D.; Banerjee, S.

Mapping Polaronic States and Lithiation Gradients in Individual V_2O_5 Nanowires. *Nat. Commun.* **2016**, *7*, 12022:1-9.

(150) Devreese, J. T. Polarons. *Encylcopedia Appl. Phys.* **1996**, *14*, 383–409.

(151) Stoneham, A. M.; Gavartin, J.; Shluger, A. L.; Kimmel, A. V; Ramo, D. M.; Rønnow, H. M.; Aeppli, G.; Renner, C. Trapping, Self-Trapping and the Polaron Family. *J. Phys. Condens. Matter* **2007**, *19* (25), 255208.

(152) Nagasawa, H.; Onoda, M.; Kanai, Y.; Kagoshima, S. Polarons and Bipolarons in Quasi-1-D Conductor Vanadium Bronzes. *Synth. Met.* **1987**, *19* (1–3), 971–976.

(153) Parija, A.; Liang, Y.; Andrews, J. L.; De Jesus, L. R.; Prendergast, D.; Banerjee, S. Topochemically De-Intercalated Phases of V_2O_5 as Cathode Materials for Multivalent Intercalation Batteries: A First-Principles Evaluation. *Chem. Mater.* **2016**, *28* (16), 5611–5620.

(154) Ellis, B.; Perry, L. K.; Ryan, D. H.; Nazar, L. F. Small Polaron Hopping in $Li_x FePO_4$ Solid Solutions: Coupled Lithium-Ion and Electron Mobility. *J. Am. Chem. Soc.* **2006**, *128* (35), 11416–11422.

(155) Yu, J.; Sushko, M. L.; Kerisit, S.; Rosso, K. M.; Liu, J. Kinetic Monte Carlo Study of Ambipolar Lithium Ion and Electron − Polaron Diffusion into Nanostructured TiO_2. *J. Phys. Chem. Lett.* **2012**, *3*, 2076–2081.

(156) Luntz, A. C.; Viswanathan, V.; Voss, J.; Varley, J. B.; Nørskov, J. K.; Scheffler, R.; Speidel, A. Tunneling and Polaron Charge Transport through Li_2O_2in Li–O_2 Batteries. *J. Phys. Chem. Lett.* **2013**, *4* (20), 3494–3499.

(157) Parija, A.; Prendergast, D.; Banerjee, S. Evaluation of Multivalent Cation Insertion in Single- and Double- Layered Polymorphs of V_2O_5. *ACS Appl. Mater. Interfaces* **2017**, *9* (28), 23756–23765.

(158) Marley, P. M.; Abtew, T. A.; Farley, K. E.; Horrocks, G. A.; Dennis, R. V.; Zhang, P.; Banerjee, S. Emptying and Filling a Tunnel Bronze. *Chem. Sci.* **2015**, *6* (3), 1712–1718.

(159) Tolhurst, T. M.; Leedahl, B.; Andrews, J. L.; Marley, P. M.; Banerjee, S.; Moewes, A. Contrasting 1D Tunnel-Structured and 2D Layered Polymorphs of V_2O_5 : Relating Crystal Structure and Bonding to Band Gaps and Electronic Structure. *Phys. Chem. Chem. Phys.* **2016**, *18* (23), 15798–15806.

(160) Razek, S. A.; Popeil, M. R.; Wangoh, L.; Rana, J.; Suwandaratne, N.; Andrews, J. L.; Watson, D. F.; Banerjee, S.; Piper, L. F. J. Designing Catalysts for Water Splitting Based on Electronic Structure Considerations. *Electron. Struct.* **2020**, *2* (2), 023001.

(161) Milleville, C. C.; Pelcher, K. E.; Sfeir, M. Y.; Banerjee, S.; Watson, D. F. Directional Charge Transfer Mediated by Mid-Gap States: A Transient Absorption Spectroscopy Study of CdSe Quantum Dot/β-$Pb_{0.33}V_2O_5$ Heterostructures. *J. Phys. Chem. C* **2016**, *120* (9), 5221–5232.

(162) Pelcher, K. E.; Milleville, C. C.; Wangoh, L.; Chauhan, S.; Crawley, M. R.; Marley, P. M.; Piper, L. F. J.; Watson, D. F.; Banerjee, S. Integrating β-$Pb_{0.33}V_2O_5$ Nanowires with Cdse Quantum Dots: Toward Nanoscale

Heterostructures with Tunable Interfacial Energetic Offsets for Charge Transfer. *Chem. Mater.* **2015**, *27* (7), 2468–2479.

(163) Pelcher, K. E.; Milleville, C. C.; Wangoh, L.; Cho, J.; Sheng, A.; Chauhan, S.; Sfeir, M. Y.; Piper, L. F. J.; Watson, D. F.; Banerjee, S. Programming Interfacial Energetic Offsets and Charge Transfer in β-$Pb_{0.33}V_2O_5$/Quantum-Dot Heterostructures: Tuning Valence-Band Edges to Overlap with Midgap States. *J. Phys. Chem. C* **2016**, *120* (51), 28992–29001.

2. INTERCALATION-INDUCED EXFOLIATION AND THICKNESS-MODULATED ELECTRONIC STRUCTURE OF A LAYERED TERNARY VANADIUM OXIDE*

2.1. Overview

Solid-state compounds wherein electrons cannot be described as non-interacting particles and instead show strongly correlated behavior are of interest both as systems manifesting novel quantum chemical phenomena as well as for electronic device applications. In the absence of predictive theoretical descriptors, modulation of the properties of these compounds tends to challenging and generalizable strategies for modulating closely coupled lattice, orbital, and spin degrees of freedom are exceedingly sparse. Here, it is shown that exfoliation mediated by cation intercalation can serve as a powerful means of modulating the electronic structure of layered correlated materials. Using a strongly correlated and charge-ordered layered compound, δ-$Sr_{0.50}V_2O_5$ as a model system, it is shown that the band gap can be drastically altered from ca. 1.07 to 2.32 eV and the electron correlation strength can be greatly modified by intercalation-driven exfoliation to 2D nanosheets upon elimination of structural coherence along one

* Reprinted (adapted) with permission from Andrews, J. L.; De Jesus, L. R.; Tolhurst, T. M.; Marley, P. M.; Moewes, A.; and Banerjee, S. Intercalation-induced dimensional reduction and thickness-modulated electronic structure of a layered ternary vanadium oxide, Chem. Mater. *29* (7), 3285-3294. Copyright 2017 American Chemical Society.

dimension. These findings suggest that intercalation chemistry and solution-phase exfoliation provide a versatile strategy for modulating the electronic structure of quantum materials with potential for realizing Mott and neuromorphic circuitry.

2.2. Introduction

Since the advent of graphene[1,2] many techniques aimed at effectively reducing framework connectivity, including dimensional reduction in the case of materials with inherently 3D structures[3,4] and exfoliation for those with inherently 2D structures, have emerged as powerful design tools for tuning material properties.[5,6] In the latter case, the stabilization of nanosheets spanning only a few unit cells in thickness enables the manifestation of emergent properties, which arise from the distinctive characteristics of atomically thin materials such as topologically protected states, loss of inversion symmetry, elimination of interlayer phonon scattering, stabilization of metastable polymorphs exhibiting unusual coordination environments, and the modulation of band structure.[7,8] Two-dimensional materials exhibit a broad range of properties including carrier mobilities that are inaccessible in the bulk, highly anisotropic thermal conductivity, potential for spin-filtered transport, ion conduction pathways that facilitate rapid cation diffusion, remarkable capacitive and pseudo-capacitive properties, and high catalytic activity.[6,9–15] Disparate 2D nanosheets can further be stacked to form van der Waals' heterostructures that enable unprecedented functionality inaccessible within layered compounds.[16,17] Graphene with its distinctive

electronic structure characterized by a linear dispersion of bands near the Fermi level represents the most thoroughly studied example of dimensionally modulated electronic structure, but several classes of materials such as transition metal dichalcogenides and carbide phases have also attracted substantial recent attention.[9,15,18–20] Famously, in the case of MoS_2, the monolayer hexagonal phase is a direct bandgap semiconductor, whereas few-layered and bulk MoS_2 are indirect bandgap semiconductors with red-shifted bandgaps characterized by substantially lower luminescence efficiencies.[20] Two broad streams of research can be distinguished in terms of the development of dimensionally reduced materials. The mechanical exfoliation or direct epitaxial growth of the so-called van der Waals' solids is predicated on the weak interlayer interactions along the crystallographic *c* direction. The weak interlayer bonds permit cleavage of individual layers or allow for highly anisotropic 2D crystal growth.[21,22] Alternatively, in the case of several main group compounds, transition metal oxides, layered double hydroxides, and transition metal carbides, ion exchange and deintercalation have been used to facilitate exfoliation.[12,21,23–26] Upon the removal of cations that play a pillaring role, layered compounds can oftentimes be exfoliated to stabilize few-layered nanosheets in solution. While the thickness-dependent modulation of electronic structure in the former set of van der Waals' compounds has been extensively examined by both theory and experiment, the use of intercalation chemistry as a means of modulating electronic structure remains much less explored. Transition-metal oxides exhibit tremendous

structural and compositional diversity and include compounds that exhibit a wide range of distinctive electronic phenomena, including charge density waves,[27] metal-insulator transitions,[28,29] superconductivity,[30,31] and spin-orbit coupling effects.[32] Several transition metal oxides have layered structures amenable to exfoliation. However, much of the focus in exfoliating transition metal oxides has been directed at the development of synthetic methods and the stabilization of colloids, for example, in layered niobates, manganates, and tungstates.[21,23] Scarce little effort has focused on examining the influence of interlayer separation on the electronic structure of these layered compounds.

Vanadium oxides are a particularly rich subclass of transition-metal oxides with an incredibly rich structural chemistry including many layered quasi-two-dimensional structures.[33] Ternary vanadium oxide bronzes ($M_xV_2O_5$), specifically the double-layered *d*-type structures, exhibit a variety of remarkable properties including charge-ordering, metal-insulator transitions, and even superconductivity[30,34] all derived from the unique charge-ordered network that is stabilized upon intercalation of metal cations.

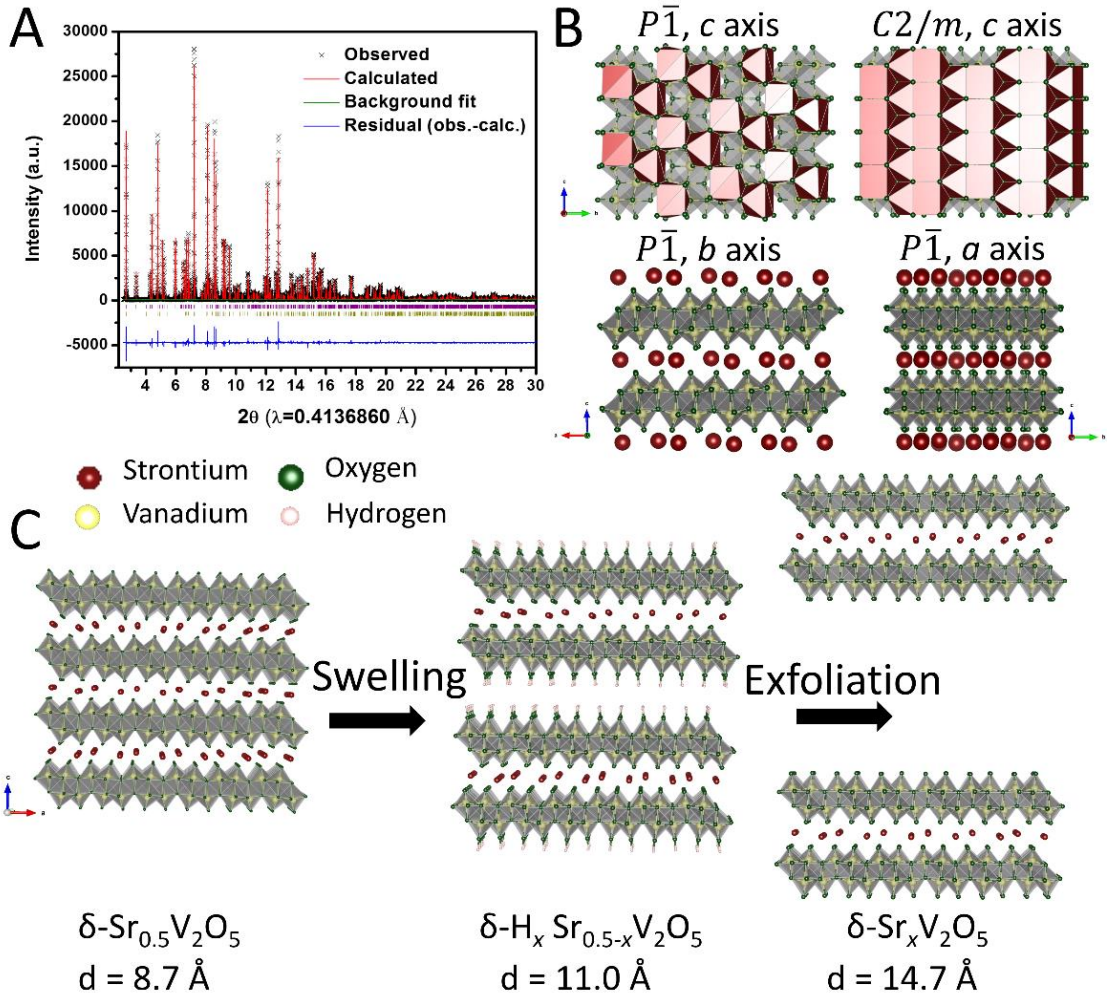

Figure 2.1. (A) Rietveld refinement of high-resolution synchrotron powder XRD pattern (λ = 0.413746 Å) of δ-$Sr_xV_2O_5$ micro-sheet powder acquired at 295 K in transmission mode (See Table A.1 and Table A.2 for details). Red ticks indicate the position of reflections corresponding to the *C2/m* monoclinic space group without Sr ordering whereas gold tick marks indicate reflections resulting from the distorted pseudo-monoclinic (α, β ~ 90) resulting from the ordering of interstitial strontium cations, P$\bar{1}$ (*a* = 6.16969(1), *b* = 7.39947(1), *c* = 8.79509(1), α = 89.9701, β = 91.6452, γ = 107.4916); (B) Structure obtained by Rietveld refinement yields a composition of δ-$Sr_{0.503}V_2O_5$ (Local coordination polyhedral depicted in Figure A.2). Strontium ordering (b) can be observed by comparing the arrangement of Sr atoms in the monoclinic *C2/m* and triclinic P$\bar{1}$ superstructure. The general synthetic approach (C) to exfoliation of this layered structure by successive protonation, swelling, and subsequent surfactant intercalation. The experimentally measured interlayer spacing is noted in each case, describing a monotonic increase in average spacing between the [V_4O_{10}] layers with swelling and exfoliation.

These structures form infinite 2D $[V_4O_{10}]_n$ sheets separated by intercalated cations (Figure 2.1); partial reduction of the 2D $[V_4O_{10}]$ layers by the cations leads to an array of half-filled d^1 V^{4+} sites and is the underlying origin of electron correlation in this system. In other words, the role of the intercalated cations in Figure 2.1 is to primarily induce periodic ordered arrays of localized charge along the 2D sheets. In recent work, we have observed temperature and electric field induced electronic transitions in single nanowires of δ-$K_xV_2O_5$ and δ-$Ag_xV_2O_5$, indicating that the properties of these $M_xV_2O_5$ materials are both stoichiometry-(*x*) and cation- (M) dependent.[35,36] Despite numerous reports of the remarkable correlation-induced electronic and magnetic peculiarities of these bronzes and their tendency to crystalize in structures with reduced dimensionality,[33] to the best of our knowledge, no reports related to exfoliating these materials are available in the literature. Consequently, scarce little is known about the influence of 2D confinement on their electronic structure. The single-layered wide-band-gap d^0 compound V_2O_5 is the only related structure to have been exfoliated.[37] Given the urgent imperative to find electron correlated materials that can be implemented in Mott field-effect transistors and similar energy efficient computing vectors, which could potentially be electrostatically gated, the investigation of thickness-dependent electronic structure modulation of ultra-thin transition metal oxides assumes special significance.[38–40] In this work, we report the exfoliation of the layered electron-correlated material δ-$Sr_xV_2O_5$[41,42] to several unit cell thickness spans and describe the exfoliation-induced stepwise evolution of its electronic

structure using X-ray absorption and emission spectroscopies. The pronounced intrinsic anisotropy of the crystal structure, low barrier to ion diffusivity,[34] and the relatively facile modulation of interlayer spacing in this system makes it particularly attractive as a target for exfoliation.[43] The electronic structure and thickness of the exfoliated phases has been simultaneously and directly mapped using scanning transmission X-ray microscopy and indicates a pronounced opening of the bandgap with decreasing thickness. The band gap increases with increasing degree of exfoliation in the order: bulk δ-$Sr_{0.50}V_2O_5$ < expanded δ-$H_xSr_{0.50-x}V_2O_5$ < surfactant-intercalated lamellar δ-$Sr_xV_2O_5$. Topochemical deintercalation and exfoliation thus provide a remarkable means of greatly modulating electronic structure while preserving the intrinsic planar structural motifs of these layered structures.

2.3. Results and Discussion

2.3.1. Mapping Structure across Loss of 3D Structural Coherence

δ-$Sr_xV_2O_5$ is a double-layered ternary vanadium oxide ($M_xV_2O_5$) and is part of a broader family of layered vanadium oxide compounds wherein a range of alkali, alkaline-earth, or transition metal cations occupy interstitial sites and separate condensed double layers of [V_4O_{10}], which in turn are constructed from edge- and corner-shared [VO_6] octahedra.[33,44] Such compounds are stable over a broad range of cation stoichiometries, *x*, yielding substantial control over charge ordering in these compounds. Figure 2.1A depicts a synchrotron powder X-ray diffraction pattern (λ = 0.413686 Å) acquired for extended crystals of δ-$Sr_{0.50}V_2O_5$

prepared from the hydrothermal reaction of V_2O_5 and $Sr(CH_3COO)_2$ in acidic media. The high-resolution diffraction pattern is refined to the structure depicted in Figure 2.1B, which indicates that the structure adopts a pseudo-monoclinic *C2/m* structure wherein infinite V_4O_{10} double-layered slabs are constituted from edge- and corner-sharing octahedra and are separated by intercalated Sr cations that are coordinated by apical oxygens from the vanadium-centered octahedra. A Sr occupancy of 0.5003 yields the best fit to the structure, which can be assumed to be 0.500 within a margin of error and has been independently verified by energy dispersive X-ray spectroscopy (Figure A.1) and is the stoichiometric limit for larger alkaline earth cations. The local coordination environments for the vanadium and strontium atoms are shown in Figure A.2, and can be described as distorted octahedral and trigonal prismatic, respectively. A similar seven-coordinate environment of the intercalating M in δ-type structures has been previously reported for δ-$Ag_{0.85}V_2O_5$.[35] The appearance of superlattice reflections that can be indexed to the $P\bar{1}$ space group suggests the precise 2D ordering of Sr cations between the double layers, which further indicates a high degree of charge ordering in these compounds.[41] As a result of the ordering of the interstitial Sr cations, a pseudo-monoclinic cell ($\alpha/\gamma \approx 90$) with unit cell parameters doubled along the *a* and *b* axes yields the best fit to the data. Table A.1 depicts the lattice parameters, atom positions, bond distances, occupancies, and thermal displacement parameters obtained from the refinement. Figure 2.1B indicates the

highly anisotropic 2D layered structure that is amenable to exfoliation upon topochemical removal of alternate layers of cations.

Lustrous black crystals of δ-$Sr_{0.50}V_2O_5$ (Figure A.1) that crystallize with a rectangular ribbon-like cross-section have been exfoliated by first protonating the galleries between the layers by reaction with a dilute solution of HCl, which replaces a fraction of the Sr atoms with protons, resulting in a swelling of the structure due to increased interlayer repulsions (Figure 2.1).[23] The swelling of the layers after protonation is reflected by a shift of the basal plane (00*l*) reflections to lower *2θ* values (all other reflections are greatly diminished in intensity as a result of the loss of 3D structural coherence); the lattice spacing along the *c* direction is expanded from 8.795 Å for δ-$Sr_{0.50}V_2O_5$ crystals to 11.042 Å for δ-$H_xSr_{0.50-x}V_2O_5$, as illustrated by Figure 2.2, panels A and D. The swelling results from the larger size of intercalated hydronium ions and the further hydration of the galleries. The ion-exchange and deintercalation of Sr^{2+} ions is likely to proceed *via* a staging phenomenon, as commonly observed upon intercalation in layered materials and schematically illustrated by Figure 2.1C.[45–47] As such, ion exchange is more likely to occur in non-adjacent layers, resulting in a retention of roughly half of the alternating [V_2O_5/Sr/V_2O_5] character of the starting material. The layered morphology of the expanded structure is clearly discernible in the scanning electron microscopy (SEM) and transmission electron microscopy (TEM) images shown in Figure 2.2E and Figure 2.2F, respectively.

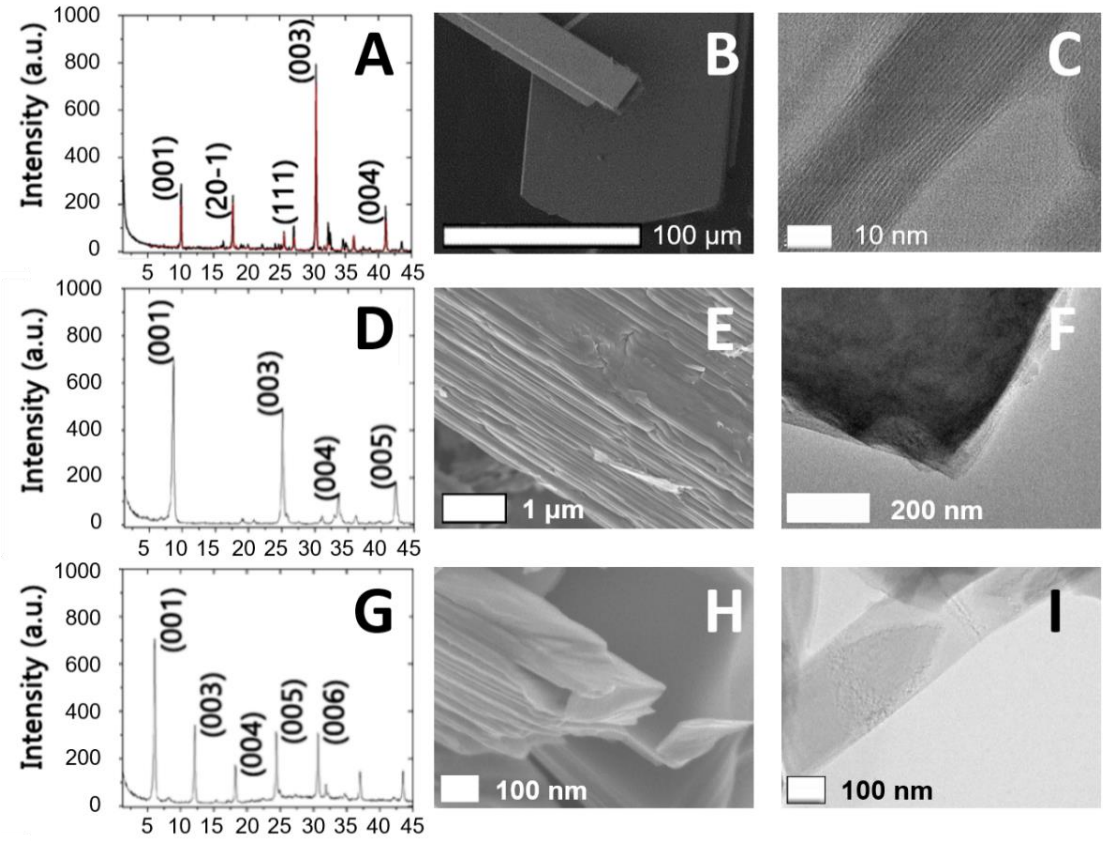

Figure 2.2. Indexed powder X-ray diffraction patterns, SEM images, and TEM images of (A-C) as-prepared δ-$Sr_xV_2O_5$ crystals, with a calculated pattern to the *C2/m* space group given in red and $\boldsymbol{C2/m}$ reflections labeled in black; (D-F) acid-treated δ-$H_xSr_{0.5-x}V_2O_5$ after protonation, where the loss of 3D coherence upon swelling due to partial protonation of the oxide framework in already apparent. Solely basal (00*l*) reflections are observed in the diffraction patterns; (G-I) a partially-exfoliated lamellar compound after intercalation with surfactant. Fully exfoliated sheets, when dried, also flocculate and exhibit the same diffraction pattern depicted for lamellae here. (J) A powder XRD pattern for exfoliated nanosheets exhibiting a halo pattern arising from diffuse scattering, with only the first order (00*l*) reflection still visible at 2θ = 6°; (K) a SEM image of δ-$Sr_xV_2O_5$ nanosheets drop-cast onto a Si/SiO_2 (300 nm) substrate, and (L) TEM image of nanosheets depicting very thin layers near the edges. See Figure A.1 for analysis of composition at each stage of exfoliation and Figure A.3 for evidence of retention of precursor structural units.

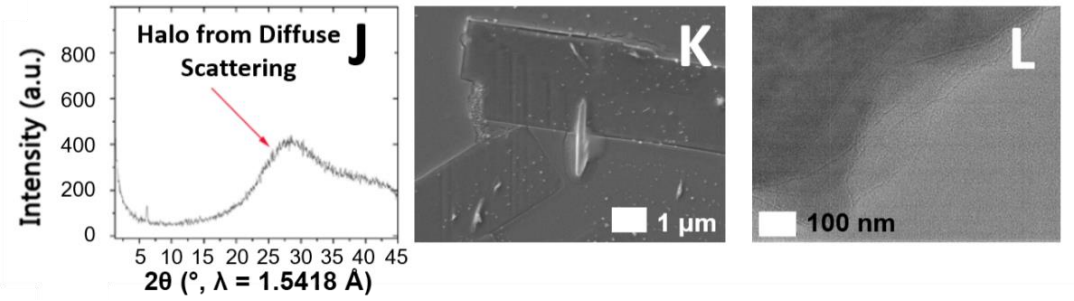

Figure 2.2. Continued.

The obtained materials are dark green in color and EDX analysis suggests removal of approximately half of the initial Sr cations (Figure A.1). Next, the protonated and expanded material is treated with tetrabutylammonium hydroxide (TBAOH), which has a large steric footprint and facilitates further layer expansion. This quaternary ammonium cation can substitute the protons (which are bound less strongly, having diffused into expanded layers as compared to the divalent Sr cations within unmodified layers) preferentially expanding and subsequently exfoliating the layers upon stirring or application of shear. Centrifugation of the resulting suspension yields a green paste, which exhibits a broad halo feature (Figure 2.2, panel J) indicative of diffuse scattering of X-rays by the suspended sheets and a loss of long-range order associated with the partially expanded precursor. Figure 2.2, panel G depicts diffraction collected for flocculated powders suggests a further increased interlayer separation of 14.718Å. The SEM images in Figure 2.2H as well as Figure A.1 illustrate the stacked lamellar ordering of the flocculated solid. Very thin sections of the material are observed to splay apart at the edges of the lamellar structures (Figure 2.2I). Figure 2.2, panels K and L depict

SEM and TEM images acquired for exfoliated nanosheets spun cast onto a Si/SiO_2 substrate (for SEM image). The thin layers at the edges of the exfoliated sheets are clearly visible in Figure 2.2L. The elimination of 3D structural coherence but retention of short-range order is further corroborated by Raman spectroscopy analysis, which provides a perspective of the local structure (Figure A.4). In analogy with V_2O_5, the Raman modes are assigned to local V=O stretches, V-O-V stretches along the plane, and in-plane $[VO_6]$—$[VO_6]$ modes as depicted in Figure A.4.[48] With increasing interlayer separation from the as-prepared to acid-treated to fully exfoliated materials, the in-plane and localized Raman modes are preserved, albeit with some broadening that likely derives from phonon confinement. The preservation of the Raman modes despite the increase in interlayer spacing and partial removal of Sr^{2+} cations, suggests retention of the local symmetry and structure of the individual layers.

2.3.2. Electronic Structure Consequences of Exfoliation

In order to examine the influence of interlayer separation and loss of three-dimensional charge-ordering on electronic structure, X-ray emission and absorption spectroscopy measurements have been performed to directly probe the occupied and unoccupied partial density of electronic states (Figure 2.3), in order to measure the bandgap of the materials. This method is much more precise as compared to optical absorption spectroscopy measurements, which provide values for optical band-gaps, because the materials studied here are indirect band-gap semiconductors. The electronic band-gaps provided by combined

XAS/XES measurements are of directly relevant to the design of gated transistor devices.

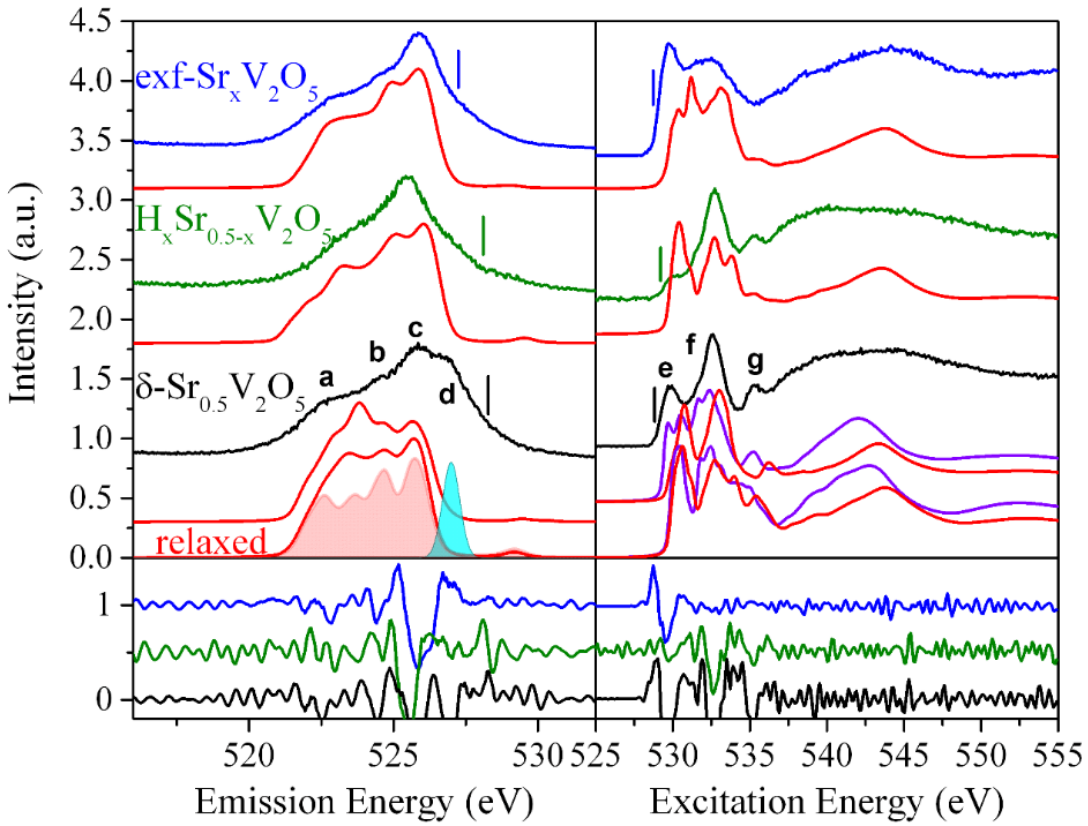

Figure 2.3. Measured emission and absorption spectra for all samples are shown in the left and right frames, respectively. The emission spectra are all non-resonant (NXES) spectra collected with an excitation energy of 557.8 ± 0.1 eV, well above the onset of the absorption edge. Data from δ-$Sr_{0.5}V_2O_5$, the expanded (δ-$H_xSr_{0.5}$-xV_2O_5) and exfoliated (exf-$Sr_xV_2O_5$) samples are given in black, green and blue, respectively. Calculated ground state spectra are given in red, while core hole calculations are shown in violet. The shaded red curve shows the calculated spectrum from the relaxed structure, corrected for absorption by the matrix. Prominent features are labeled with lower case Latin letters. The shaded cyan curve indicates the location of the lower Hubbard band (region d). The lower frames show color-coded second derivatives of the measured spectra, which are used to determine the bandgap. The peak energies taken as band onsets from the second derivatives are indicated by vertical dashes above the X-ray spectra (Table A.3).

For unexfoliated δ-$Sr_{0.50}V_2O_5$, four distinctive features are clearly resolved in X-ray emission spectra and are labeled as a-d, whereas three distinct spectral features are discernible in O K-edge X-ray absorption spectra, labeled e-g. As with other vanadium oxide bronzes and as further borne out by calculations shown in Figure 2.4, the valence band is predominantly O 2p in nature,[49–51] whereas the bottom of the conduction band comprises V 3d—O 2p hybrid states. Regions a and b are attributed to V—O σ and π bonding states, respectively, whereas the pronounced c region corresponds to the non-bonding oxygen 2p states.[50,51] Interestingly, the top part of the valence band denoted as Region d is not accurately reproduced by density functional theory calculations in the generalized gradient approximation although these calculations are very effective in describing all other features of the relaxed structure as indicated by the red shaded region of Figure 2.3. This feature is thus attributed to a lower Hubbard band arising from electron correlation effects induced by charge ordering (Figure 2.1B), which indeed render this material a small-gap insulator despite the half-filled d-orbitals.[42] Based on the DFT calculations presented in Figure 2.4 (and in analogy with assignments for V_2O_5), features E and F are attributed to V—O π and σ hybrid states, respectively, corresponding to hybridization of O 2p states with the t_{2g} ($3d_{xy}$, $3d_{xz}$, and $3d_{yz}$) states for E and with the e_g ($3d_{x2-y2}$, $3d_{z2}$) states for F.[49,51,52] Region g is unusual for vanadium oxide bronzes and is indicative of Sr—O coordination.

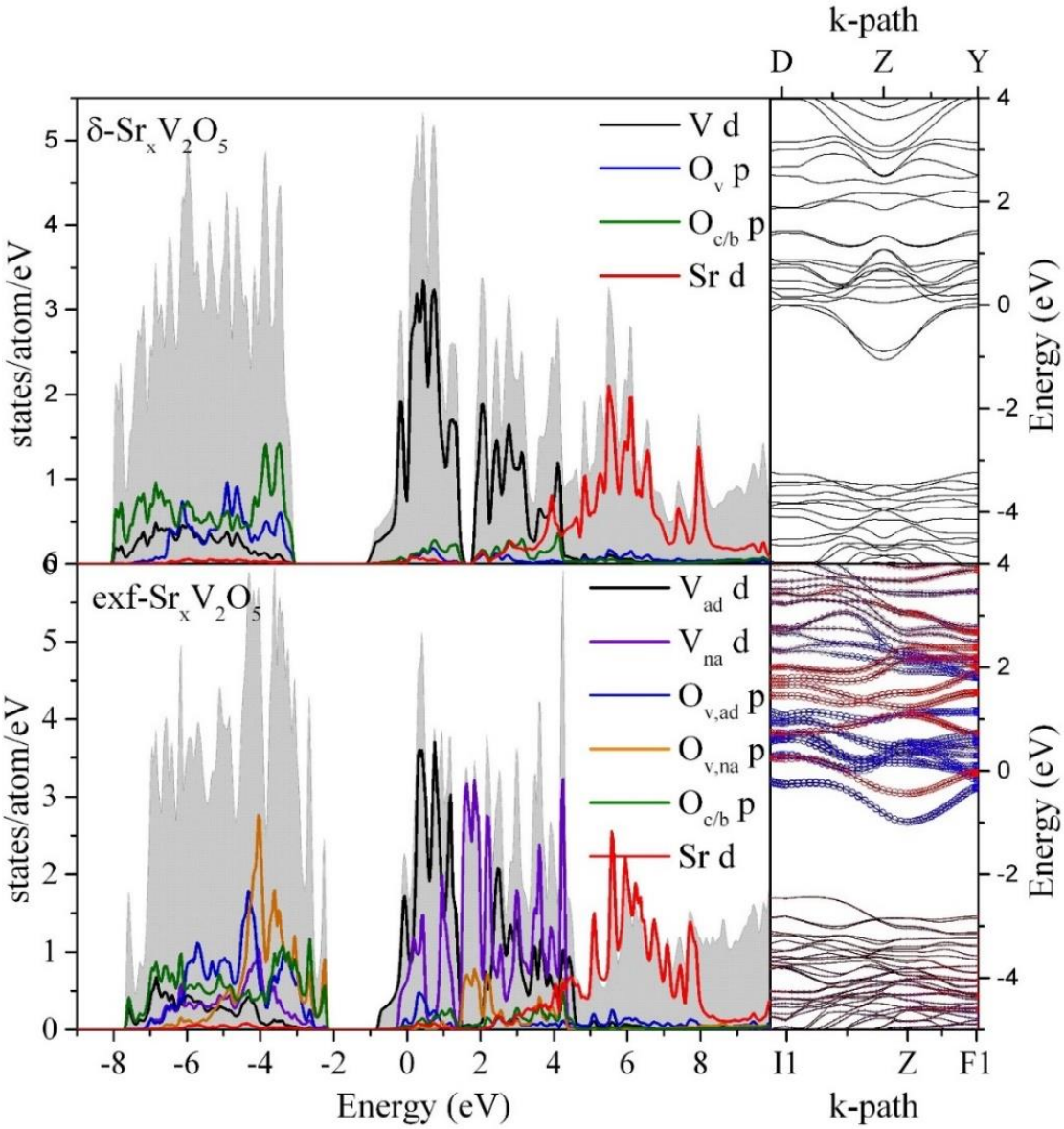

Figure 2.4. The results of calculations performed using the relaxed δ-$Sr_xV_2O_5$ and exfoliated sample structures are given in the upper and lower panels, respectively. The rightmost frames show the band structures corresponding to the adjacent DOS. Band characters for the adjacent (blue circles) and non-adjacent (red circles) V atoms are shown for the exfoliated system, where the size of the circle is proportional to the relative contribution of an atom to the states. Characters are not shown for δ-$Sr_xV_2O_5$ due to the roughly equal contributions of the nonequivalent V sites to the states of the lower conduction band. The k-path and labelling of the Brillouin zone are described in previous work.[53]

As a result of electron correlation and the appearance of the lower Hubbard band, the bandgap of δ-$Sr_{0.5}V_2O_5$ is only ca. 1.07±0.20 eV (Figure 2.3), which is significantly decreased from the 1.90±0.20 eV measured for α-V_2O_5.[51] The bandgap has been determined using the second derivative method, which is relatively unaffected by the choice of linear background. Table A.3 compares the values obtained from the second derivative method with values obtained from the leading-edge method. Appendix A further includes a comparison of these two approaches. Upon expansion and subsequent exfoliation, the electronic structure and bandgap are substantially modified. Region d is diminished in intensity upon protonation and almost completely eliminated after exfoliation suggesting considerably reduced electron correlation. The reduced electron—electron repulsion can be attributed to a greater degree of covalency in the exfoliated systems. For the bilayered structure depicted in Figure 2.1C, the elimination of Sr—O bonds above and below the V_4O_{10} slabs results in stronger V—O hybridization and thus relatively less electron localization along the V—V chains. The XAS spectra also show pronounced changes in the relative intensities of the spectral features. E is strongly suppressed with respect to F upon protonation of the vanadyl sites, which reflects the reduction of the π bond strength, as also observed upon Li-ion intercalation in V_2O_5.[52]

The bandgap of the expanded phase increased to ca. 1.96±0.20 eV as a result of the loss of the lower Hubbard band. Elimination of the protons and exfoliation substantially restores the intensity of region e and again the absence

of Sr—O bonds on either side of V_4O_{10} slabs results in stronger V—O π hybridization. The exfoliated phase is rendered substantially more insulating with a bandgap of 2.32±0.20 eV (Table A.3). In stark contrast to graphene and the transition metal dichalcogenides, exfoliation increases the bandgap by strengthening the V—O π interactions. It is important to note that the large increase in band gap on expansion and exfoliation arise primarily from changes in interlayer spacing, as the fundamental in-plane bonding motifs of the parent structure are retained during exfoliation (Figure A.4). Unlike graphene and other van der Waals' compounds, materials such as δ-$Sr_xV_2O_5$ cannot be exfoliated as-prepared due to strong bonding interactions between the intercalating Sr and V—O framework. Some degree of chemical modification is required, in this case removal of some Sr-ions followed by surfactant intercalation, in order to exfoliate the material. For this reason, some changes in the band-gap arise from anticipated chemical modification of the material; however, given that the bandgap is derived primarily from O 2p and V 3d states, the primary origin of the modulation of electronic structure is observed to be the loss of translational symmetry and crystallographic inequivalence induced by exfoliation.

2.3.3. Mapping Electronic Structure

Given the distinctive XAS signatures of the pristine, expanded, and exfoliated phases (Figure 2.3), scanning transmission X-ray microscopy (STXM) has been used to map the electronic structure of the exfoliated nanosheets. By finely raster scanning an incident beam of monochromated soft X-rays across the

sample, STXM provides a spatially resolved map of local variations in electronic structure. STXM has been widely used to investigate inhomogeneities in polymers and biomaterials,[54–56] and more recently as a probe of intercalation gradients in V_2O_5[52] and particle-to-particle lithiation of $LiFePO_4$.[57,58] The energy calibration, corrections for detector linearity, and beam point spread function are addressed in the Methods section. Figure 2.5 depicts a STXM image of a lamellar sheet with ca. 60 nm thickness as well as the integrated V L- and O K-edge spectra acquired for this sample. The V L-edge is characterized by V L_{III} and V L_{II} spectral features corresponding to transitions from V $2p_{3/2} \rightarrow$ V 3d (ca. 518 eV) and V $2p_{1/2} \rightarrow$ V 3d (ca. 525 eV) states, respectively, which are split by the spin-orbit coupling of the V 2p atomic orbitals of ca. 7 eV in α-V_2O_5. A distinct sharp low-energy feature at the V L_{III} edge of α-V_2O_5 is attributed to transitions to final states that are predominantly of V $3d_{xy}$ symmetry.[49,59] This state is considerably diminished in intensity for the δ-$Sr_xV_2O_5$ nanosheets as a result of the partial reduction (and thus electron occupation) of vanadium sites,[52] (Figure 2.5B) as a result of Pauli blocking. A redshift of the L_{II} peak, giving rise to a spin-orbit coupling splitting of ca. 6.2 eV, is furthermore a result of the partial reduction of V atoms.[60] The O K-edge features corresponds to transitions from O 1s states to states with O 2p character and are labeled e-g as in Figure 2.3 that can be assigned based on the density of states plotted in Figure 2.4. The two distinct sets of resonances observed for V_2O_5 correspond to hybridization of the O 2p states with V 3d orbitals of t_{2g} and e_g symmetry (e and f in Figure 2.3 and Figure 2.5), reflecting the crystal

field splitting of the V 3d orbitals. The additional higher energy feature G at ca. 532 eV observed for the δ-$Sr_xV_2O_5$ nanosheets is attributed to hybridization of O 2p states with Sr d states (Figure 2.4). The height profile in , panel c indicates that the lamellar sheet is c. 60 nm thick, but along its edges thinner nanosheets with a ca. 6 nm thickness, corresponding to a thickness spanning only 4 unit cells, are apparent.

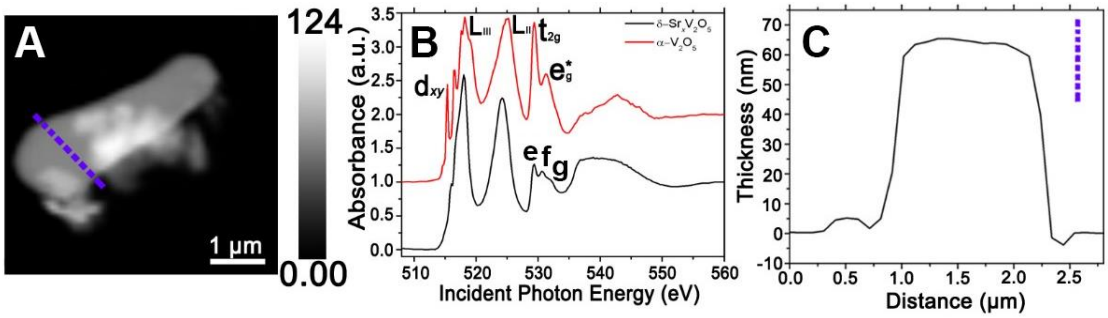

Figure 2.5. (A) STXM image of a ca. 60 nm thick exfoliated □-$Sr_xV_2O_5$ lamellar structure. The image was collected in transmission mode and converted to absorption using a reference spectrum; brighter regions are more absorbing as compared to darker regions. The dashed line indicates the directional line scan used to create the thickness profile in panel C. (B) Integrated X-ray absorption spectrum of the lamellar structure; an integrated spectrum acquired for an α-V_2O_5 nanowire is shown for comparison. (C) Thickness profile acquired across the width of the sheet. The thickness profile is calculated using the relative optical density of the sample as discussed in the 2.5 Experimental Section.

STXM maps in Figure 2.6, panel a indicate that the O K-edge spectra for most of the sample corresponds well to the XAS signature of the exfoliated sheets noted in Figure 2.4 with a pronounced spectral weight for feature E as a result of the strong V—O π bonding that results from elimination of Sr—O hybridization on

the two surfaces of exfoliated $Sr_xV_2O_5$ bilayers. Figure 2.6B shows a spectral component at the edges, likely corresponding to thinner exfoliated sheets where the spectral intensity of feature E appears to be somewhat stronger. We posit that lamellar interlayer interactions slightly reduce the π-bonding strength in Figure 2.6A.

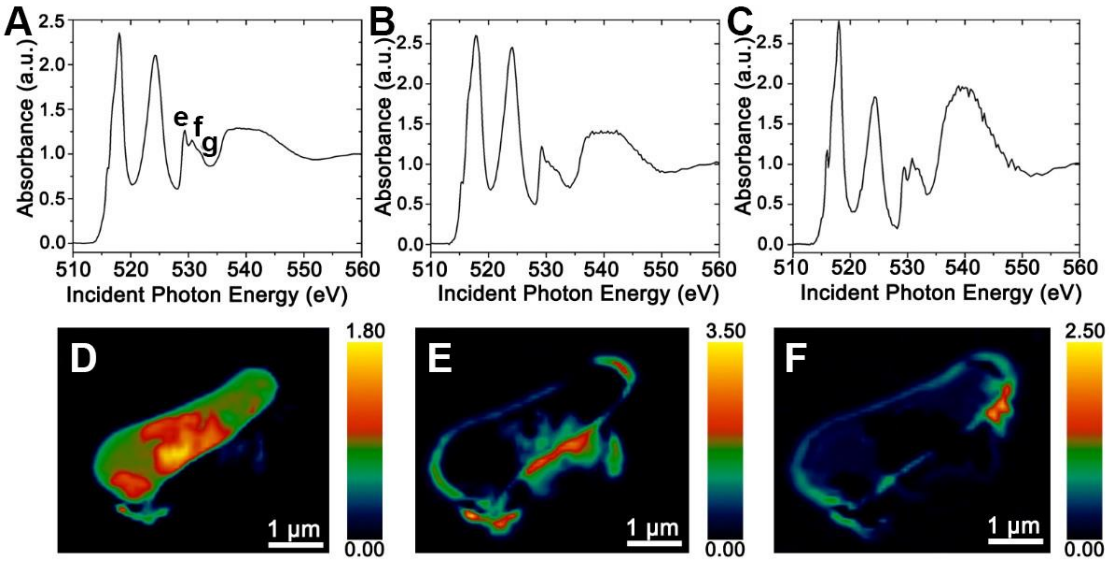

Figure 2.6. (A-C) Three spectral components that contribute to the overall integrated spectrum obtained from region of interest analysis of the nanosheet; (D-F) the intensity maps for each component are depicted below each spectrum. The scale bar is 1 μm for all of these images. All spectra have been pre- and post-edge normalized to facilitate meaningful comparison. The colored scale bars represent the optical density of the respective spectral feature.

A smaller localized contribution is mapped in Figure 2.6C and shows characteristic signatures of the protonated and hydrated phase suggesting incomplete exfoliation of the flake. The STXM maps corroborate the idea of a

strongly modified electronic structure for the exfoliated nanosheets and are consistent with the greater bandgap predicted by DFT calculations (Figure 2.4) and observed by XAS/XES measurements for such structures. Subtle differences between the spectra in panel A and B in Figure 2.6 suggest that the interlayer coupling allows for modulation of π-bonding strength.

2.4. Conclusion

The exfoliation of layered double hydroxides, primarily Mg/Ca/Al hydroxides to obtain ultra-thin nanosheets has been explored for several decades and indeed such exfoliated structures have found use in various composite materials.[61,62] Transition metal compounds crystallized with a layered motif present a much richer range of properties, particularly optical and electronic properties, as a result of crystal field splitting, spin—orbit coupling, and electron correlation effects.[33,39] Given the close coupling of spin, lattice, and orbital degrees of freedom in these compounds, exfoliation represents an attractive route for modulating electronic structure. In this work, we examine the exfoliation of a strongly electron correlated system δ-$Sr_{0.50}V_2O_5$, which is characterized by 2D charge ordering and distinctive Mott—Hubbard states. Expansion of the interlayer spacing by topochemical insertion of hydronium ions followed by surfactant intercalation and exfoliation yields 2D nanosheets spanning one to a few bilayers in thickness. The loss of translational symmetry along the *c* direction and the change in the local bonding at the surfaces brings about a pronounced modulation of electronic structure, particularly stronger V—O π bonding as a result of reduced

Sr—O hybridization. The increased π bonding substantially decreases the electron correlation and results in a ca. 1.25 eV increase of the indirect bandgap. The observed modulation of Mott-Hubbard states will be the focus of future work. This pronounced modulation of the bandgap and relative strengths of π and σ bonding suggests that exfoliation could play a critical role in interrupting 3D charge ordering and in modifying the electronic structure of ultra-thin transition metal oxides with implications for applications such as Mott field-effect transistors, neuromorphic circuitry, and frequency agile electronics wherein precisely tunable electron correlation strengths and electronic phase transitions are desirable.

2.5. Experimental Section

2.5.1. Materials Synthesis

Layered crystals of δ-$Sr_{0.50}V_2O_5$ spanning microns in dimension were prepared as follows: stoichiometric amounts of V_2O_5 (Sigma Aldrich) and $Sr(CH_3COO)_2$ powders (Sigma Aldrich) in a 2:1 ratio were mixed in 14 mL of deionized water (ρ = 18 MΩ/cm) and 1 mL of glacial acetic acid (Sigma) and placed within a 23 mL polytetrafluoroethylene (PTFE) vessel, which in turn was placed within a sealed stainless steel autoclave (Parr Instruments) and heated to 250°C for 72 h. The obtained powder comprised large lustrous crystals that were purple/black in color.

Exfoliation of the layered crystals was achieved by modification of a method originally developed for exfoliation of single crystals of $K_{0.8}Ti_{1.73}Li_{0.27}O_4$.[23] δ-$Sr_{0.50}V_2O_5$ was first reacted with stoichiometric amounts of 0.02 M HCl (aq.) for 48

h to protonate the oxide ions and swell the lattice. The powder was then dispersed in a stoichiometric solution of tetrabutylammonium hydroxide (TBAOH, Aldrich) or cetylmethylammonium bromide (CTAB, Aldrich) and gently stirred for 7 days in order to promote mechanical exfoliation. The resulting suspension of exfoliated nanosheets was drop-cast onto a TEM grid and 300 nm SiO_2/Si chip for further characterization. Centrifugation of the suspension at 12,000 RPM yielded a paste-like product that was used for powder X-ray diffraction (PXRD) analysis.

2.5.2. High-Resolution X-Ray Powder Diffraction

High-resolution XRD data for the as-prepared δ-$Sr_{0.50}V_2O_5$ crystals were collected in a poly-oxydiphenylene-pyromellitimide capillary in transmission geometry at 295 K at beamline 11-BM of the Advanced Photon Source at Argonne National Laboratory (λ = 0.4136860). Rietveld refinement of the collected data was performed using the GSAS/EXPGUI software suite.[63] Unit cell parameters, atom positions, thermal parameters, and site occupancies were refined and are listed in Table A.1. XRD data for the expanded, lamellar, and exfoliated samples were collected in Bragg—Brentano geometry on a short-arm Bruker D8-Focus diffractometer (Cu Kα(λ = 1.5418 Å source, 40 kV voltage, 25 mA current) equipped with a Lynxeye detector.

2.5.3. Electron Microscopy

The morphology of the material during layer expansion and exfoliation was examined by TEM, SEM, and EDS in order to evaluate the extent of exfoliation and the thickness of the obtained nanosheets. TEM was performed on a JEOL

JEM-2010 instrument at an accelerating voltage of 200 kV. SEM was performed on a JOEL JSM-7500F FE-SEM equipped with an Oxford EDS spectrometer for elemental characterization.

2.5.4. Soft X-Ray Absorption Spectroscopy

X-ray absorption spectroscopy (XAS) measurements were conducted at the Spherical Grating Monochromator (SGM) Beamline at the Canadian Light Source in Saskatoon, Saskatchewan, Canada. The measurements were conducted under a high vacuum of ~10^{-8} Torr. The absorption measurements were collected using total electron yield (TEY) and partial fluorescence yield (PFY). The TEY is determined by monitoring the current required to neutralize the sample during measurements. The PFY was determined using energy dispersive silicon drift detectors, which have a FWHM of ~100 eV. The PFY intensity at each step in the absorption scans was determined by fitting Gaussian peaks to the O K-edge and V L-edge emissions, as shown in previous works.[51] The x-ray Emission spectroscopy (XES) measurements were conducted in a high vacuum of ~10^{-9} Torr at Beamline 8.0.1.1 at the Advanced Light Source in Berkeley, California, USA. The spectra were recorded using a Rowland Circle spectrometer with p-polarized incident radiation with an excitation energy of 557.8±0.1 eV, well above the onset of the absorption edge. In all cases the samples were adhered to standard sample plates under ambient conditions before being transferred to the vacuum chambers.

2.5.5. XES and XAS Band Onset Determination

The onset of the valence and conduction bands was determined from the measured XES/XAS spectra by taking the second derivative and assigning the onset to the maxima of the second derivative near the onset. This method allows the choice of onset to be uncompromised by choice of linear background fit. The leading-edge method specifies the band edge as the intersection of a line fit to the leading edge of the XES or XAS spectrum, and a line fit to the background of the same spectrum, that is to say the line of zero intensity. Whereas the choice of fitting range for the linear background will not affect the results of the second derivative method, the leading-edge method gives a result that is highly dependent on the exact form of the linear background. Here the leading-edge method results are based on a linear background fit to data points within a few eV of the high-energy edge of the spectrum, where it is essentially flat. The second derivative method is comparatively unambiguous, where its first peak above the noise level will correspond to the first maximum in the slope of the spectrum and thus the onset of the density of states. As a comparison, the band-gaps were determined by the leading-edge method to be very similar, and the results are compared in Table A.3.

2.5.6. Scanning Transmission X-Ray Microscopy

STXM measurements were performed at the SM (10-ID1) beamline of the Canadian Light Source (CLS), a 2.9 GeV third-generation synchrotron facility. Right circularly polarized light X-rays, generated by an elliptically polarized

undulator (EPU), were used in the experiments. A 25 nm outermost-zone zone plate was used to obtain a diffraction-limited spatial resolution better than 30 nm. A 500 line mm^{-1} plane grating monochromator (PGM) was used to acquire the V L-edge and O K-edge spectral stacks. The incident photon flux (I_o) count rate was optimized to ca. 17 MHz as read by the STXM detector within a hole located in proximity of the sample of interest and measured at 560 eV by adjusting the exit slits to 20/20 µm (dispersive/non-dispersive). The V L- and the O K-edge stacks were acquired in the energy range from 508—560 eV with energy steps of 0.2 eV in the region of interest and with energy steps 1 eV in the continuum region beyond the specific elemental edges with a dwell time of 1 ms for each spectral section. All STXM data were analyzed and processed using aXis2000 (http://unicorn.mcmaster.ca/aXis2000.html). STXM maps were derived based on singular value decomposition of the image stack in aXis2000 and by using as a reference the region of interest (ROI) spectra identified within different regions of the same image sequence. This operation produces a set of composition maps where intensities represent the signal strength of each of the spectral components (Figure 2.6A—C) at each specific pixel of that highlighted area.

Nonlinearity in the STXM detector was corrected by the method previously described by Collins and Ade[64] and as detailed in the authors‘ most recent work.[52] The thickness maps were created by fitting the V L- and O K-edge stack to a linearly scaled spectrum of δ-$Sr_xV_2O_5$ (spectrum scaled to the δ-$Sr_xV_2O_5$ X-ray

elemental profile of a 1 mm thick material, assuming the density to be 3.891 g cm^{-3}, as calculated by aXis2000).

2.5.7. Raman Characterization

Raman spectra for powders of as-prepared, expanded and exfoliated/flocculated samples were collected on a Jobin-Yvon Horiba Labram HR instrument equipped with an Olympus BX41 microscope (using the 514.5 nm line from an Ar-laser as the excitation source). Spectral resolution better than 2 cm^{-1} was achieved during collection using an 1800 lines per mm grating. Any observed background signal was subtracted.

2.5.8. DFT Calculations

The density functional theory (DFT) calculations were performed with the WIEN2k software package.[65] The calculations use linearly augmented plane waves and augmented plane waves with local orbitals (LAPW and APW+lo) to solve the Kohn-Sham equations for each system.[65] The generalized gradient approximation of Perdew, Burke and Ernzerhof (GGA-PBE) was used to approximate the exchange correlation energies.[66] A 12x5x12 k-mesh was used for δ-$Sr_xV_2O_5$, and a 19x3x19 mesh was used for the other structures. Supercell calculations were performed with a δ-$Sr_xV_2O_5$ cell doubled along the b-axis, and an appropriately scaled k-mesh. Structural relaxations were performed by iteratively displacing the atoms within the unit cell until the forces on each atom fell below 2 mRY/Bohr.[65] The k-path and labelling of the Brillouin zone for the two

structures, depicted in Figure 2.2, is as shown in previous work for the monoclinic system.[53]

2.6. References

(1) Novoselov, K. S.; Geim, A. K.; Morozov, S. V; Jiang, D.; Katsnelson, M. I.; Grigorieva, I. V; Dubonos, S. V; Firsov, A. A. Two-Dimensional Gas of Massless Dirac Fermions in Graphene. *Nature* **2005**, *438* (7065), 197–200.

(2) Novoselov, K. S. Electric Field Effect in Atomically Thin Carbon Films. *Science* **2004**, *306* (5696), 666–669.

(3) Tulsky, E. G.; Long, J. R. Dimensional Reduction: A Practical Formalism for Manipulating Solid Structures. *Chem. Mater.* **2001**, *13* (4), 1149–1166.

(4) Li, T.; Goldberger, J. E. Atomic-Scale Derivatives of Solid-State Materials. *Chem. Mater.* **2015**, *27* (10), 3549–3559.

(5) Ma, R.; Sasaki, T. Nanosheets of Oxides and Hydroxides: Ultimate 2D Charge-Bearing Functional Crystallites. *Adv. Mater.* **2010**, *22* (45), 5082–5104.

(6) Butler, S. Z.; Hollen, S. M.; Cao, L.; Cui, Y.; Gupta, J. A.; Gutiérrez, H. R.; Heinz, T. F.; Hong, S. S.; Huang, J.; Ismach, A. F.; Johnston-Halperin, E.; Kuno, M.; Plashnitsa, V. V. Robinson, R. D.; Ruoff, R. S.; Salauddin, S.; Shan, J.; Shi, L.; Spencer, M. G.; Terrones, M.; Windl, W.; Goldberger, J. E. Progress, Challenges, and Opportunities in Two-Dimensional Materials beyond Graphene. *ACS Nano* **2013**, *7* (4), 2898–2926.

(7) Lukowski, M. A.; Daniel, A. S.; Meng, F.; Forticaux, A.; Li, L.; Jin, S.

Enhanced Hydrogen Evolution Catalysis from Chemically Exfoliated Metallic MoS_2 Nanosheets. *J. Am. Chem. Soc.* **2013**, *135* (28), 10274–10277.

(8) Ambrosi, A.; Sofer, Z.; Pumera, M. 2H → 1T Phase Transition and Hydrogen Evolution Activity of MoS_2, $MoSe_2$, WS_2 and WSe_2 Strongly Depends on the MX_2 Composition. *Chem. Commun.* **2015**, *51* (40), 8450–8453.

(9) Castro Neto, A. H.; Guinea, F.; Peres, N. M. R.; Novoselov, K. S.; Geim, A. K. The Electronic Properties of Graphene. *Rev. Mod. Phys.* **2009**, *81* (1), 109–162.

(10) Kara, A.; Enriquez, H.; Seitsonen, A. P.; Lew Yan Voon, L. C.; Vizzini, S.; Aufray, B.; Oughaddou, H. A Review on Silicene - New Candidate for Electronics. *Surf. Sci. Rep.* **2012**, *67* (1), 1–18.

(11) Fleurence, A.; Friedlein, R.; Ozaki, T.; Kawai, H.; Wang, Y.; Yamada-Takamura, Y. Experimental Evidence for Epitaxial Silicene on Diboride Thin Films. *Phys. Rev. Lett.* **2012**, *108* (24), 245501:1-5.

(12) Bianco, E.; Butler, S.; Jiang, S.; Restrepo, O. D.; Windl, W.; Goldberger, J. E. Stability and Exfoliation of Germanane: A Germanium Graphane Analogue. *ACS Nano* **2013**, *7* (5), 4414–4421.

(13) Liu, D.; Zhang, W.; Mou, D.; He, J.; Ou, Y.-B.; Wang, Q.-Y.; Li, Z.; Wang, L.; Zhao, L.; He, S.; Peng, Y.; Liu, X.; Chen, C.; Yu, L.; Liu, G.; Dong, X.; Zyhang, J.; Chen, C.; Xu, Z.; Hu, J.; Chen, X.; Ma X.; Xue, Q.; Zhou, X. J.

Electronic Origin of High-Temperature Superconductivity in Single-Layer FeSe Superconductor. *Nat. Commun.* **2012**, *3*, 931:1-6.

(14) Johnson, N. W.; Vogt, P.; Resta, A.; De Padova, P.; Perez, I.; Muir, D.; Kurmaev, E. Z.; Le Lay, G.; Moewes, A. The Metallic Nature of Epitaxial Silicene Monolayers on Ag(111). *Adv. Funct. Mater.* **2014**, *24* (33), 5253–5259.

(15) Lukatskaya, M. R.; Mashtalir, O.; Ren, C. E.; Dall'Agnese, Y.; Rozier, P.; Taberna, P. L.; Naguib, M.; Simon, P.; Barsoum, M. W.; Gogotsi, Y. Cation Intercalation and High Volumetric Capacitance of Two-Dimensional Titanium Carbide. *Science* **2013**, *341* (6153), 1502–1505.

(16) Gao, G.; Gao, W.; Cannuccia, E.; Taha-Tijerina, J.; Balicas, L.; Mathkar, A.; Narayanan, T. N.; Liu, Z.; Gupta, B. K.; Peng, J.; Yin, Y.; Rubio, A.; Ajayan, P.M. Artificially Stacked Atomic Layers: Toward New van Der Waals' Solids. *Nano Lett.* **2012**, *12* (7), 3518–3525.

(17) Geim, A. K.; Grigorieva, I. V. Van Der Waals Heterostructures. *Nature* **2013**, *499* (7459), 419–425.

(18) Geim, A. K.; Novoselov, K. S. The Rise of Graphene. *Nature* **2007**, *6* (3), 183–191.

(19) Anasori, B.; Xie, Y.; Beidaghi, M.; Lu, J.; Hosler, B. C.; Hultman, L.; Kent, P. R. C.; Gogotsi, Y.; Barsoum, M. W. Two-Dimensional, Ordered, Double Transition Metals Carbides (MXenes). *ACS Nano* **2015**, *9* (10), 9507–9516.

(20) Mak, K. F.; Lee, C.; Hone, J.; Shan, J.; Heinz, T. F. Atomically Thin MoS_2:

A New Direct-Gap Semiconductor. *Phys. Rev. Lett.* **2010**, *105* (13), 136805.

(21) Sasaki, T.; Watanabe, M. Osmotic Swelling to Exfoliation. Exceptionally High Degrees of Hydration of a Layered Titanate. *J. Am. Chem. Soc.* **1998**, *120* (19), 4682–4689.

(22) Coleman, J. N.; Lotya, M.; O'Neill, A.; Bergin, S. D.; King, P. J.; Khan, U.; Young, K.; Gaucher, A.; De, S.; Smith, R. J.; Shvets, I. V.; Arora, S. K.; Stanton, G.; Kim, H.-Y.; Lee, K.; Kim, G. T.; Duesberg, G. S.; Hallam, T.; Boland, J. J.; Wang, J. J.; Donegan, J. F.; Grunlan, J. C.; Moriarty, G.; Shmeliov, A.; Nicholls, R. J.; Perkins, J. M.; Grieveson, E. M.; Theuwissen, K.; McComb, D. W.; Nellist, P. D.; Nicolosi, V. Two-Dimensional Nanosheets Produced by Liquid Exfoliation of Layered Materials. *Science* **2011**, *331* (6017), 568–571.

(23) Tanaka, T.; Ebina, Y.; Takada, K.; Kurashima, K.; Sasaki, T. Oversized Titania Nanosheet Crystallites Derived from Flux-Grown Layered Titanate Single Crystals. *Chem. Mater.* **2003**, *15* (18), 3564–3568.

(24) Mashtalir, O.; Naguib, M.; Mochalin, V. N.; Dall'Agnese, Y.; Heon, M.; Barsoum, M. W.; Gogotsi, Y. Intercalation and Delamination of Layered Carbides and Carbonitrides. *Nat. Commun.* **2013**, *4*, 1716:1-7.

(25) Sofos, M.; Goldberger, J.; Stone, D. a; Allen, J. E.; Ma, Q.; Herman, D. J.; Tsai, W.-W.; Lauhon, L. J.; Stupp, S. I. A Synergistic Assembly of Nanoscale Lamellar Photoconductor Hybrids. *Nat. Mater.* **2009**, *8* (1), 68–75.

(26) Omomo, Y.; Sasaki, T.; Wang, L.; Watanabe, M. Redoxable Nanosheet Crystallites of MnO_2 Derived via Delamination of a Layered Manganese Oxide. *J. Am. Chem. Soc.* **2003**, *125* (12), 3568–3575.

(27) Arima, T. Sliding Electrons Take Charge. *Nat. Mater.* **2008**, *7* (1), 12–13.

(28) Whittaker, L.; Patridge, C. J.; Banerjee, S. Microscopic and Nanoscale Perspective of the Metal-Insulator Phase Transitions of VO_2: Some New Twists to an Old Tale. *J. Phys. Chem. Lett.* **2011**, *2* (7), 745–758.

(29) Patridge, C. J.; Wu, T. L.; Jaye, C.; Ravel, B.; Takeuchi, E. S.; Fischer, D. A.; Sambandamurthy, G.; Banerjee, S. Synthesis, Spectroscopic Characterization, and Observation of Massive Metal-Insulator Transitions in Nanowires of a Nonstoichiometric Vanadium Oxide Bronze. *Nano Lett.* **2010**, *10* (7), 2448–2453.

(30) Yamauchi, T.; Isobe, M.; Ueda, Y. Charge Order and Superconductivity in Vanadium Oxides. *Solid State Sci.* **2005**, *7* (7), 874–881.

(31) Badding, J. V. Cobalt Oxide Layers. *Nature* **2003**, *2*, 208–210.

(32) Ueda, Y. Vanadate Family as Spin-Gap Systems. *Chem. Mater.* **1998**, *10* (10), 2653–2664.

(33) Marley, P. M.; Horrocks, G. A.; Pelcher, K. E.; Banerjee, S. Transformers: The Changing Phases of Low-Dimensional Vanadium Oxide Bronzes. *Chem. Commun.* **2015**, *51* (25), 5181–5198.

(34) Parija, A.; Liang, Y.; Andrews, J. L.; De Jesus, L. R.; Prendergast, D.; Banerjee, S. Topochemically De-Intercalated Phases of V_2O_5 as Cathode

Materials for Multivalent Intercalation Batteries: A First-Principles Evaluation. *Chem. Mater.* **2016**, *28* (16), 5611–5620.

(35) Marley, P. M.; Singh, S.; Abtew, T. A.; Jaye, C.; Fischer, D. A.; Zhang, P.; Sambandamurthy, G.; Banerjee, S. Electronic Phase Transitions of δ-$Ag_xV_2O_5$ Nanowires: Interplay between Geometric and Electronic Structures. *J. Phys. Chem. C* **2014**, *118* (36), 21235–21243.

(36) Wu, T.-L.; Stabile, A. A.; Patridge, C. J.; Banerjee, S.; Sambandamurthy, G. Electrically Driven Metal-Insulator Switching in Δ−KxV2O5 Nanowires. *Appl. Phys. Lett.* **2012**, *101* (16), 163502:1-4.

(37) Chen, Y.; Yang, G.; Zhang, Z.; Yang, X.; Hou, W.; Zhu, J.-J. Polyaniline-Intercalated Layered Vanadium Oxide Nanocomposites - One-Pot Hydrothermal Synthesis and Application in Lithium Battery. *Nanoscale* **2010**, *2* (10), 2131–2138.

(38) Yang, Z.; Ko, C.; Ramanathan, S. Oxide Electronics Utilizing Ultrafast Metal-Insulator Transitions. *Annu. Rev. Mater. Res.* **2011**, *41* (1), 337–367.

(39) Ahn, C. H.; Triscone, J.-M.; Mannhart, J. Electric Field Effect in Correlated Oxide Systems. *Nature* **2003**, *424*, 1015–1018.

(40) Pickett, M. D.; Medeiros-Ribeiro, G.; Williams, R. S. A Scalable Neuristor Built with Mott Memristors. *Nat. Mater.* **2013**, *12* (2), 114–117.

(41) Kato, K.; Kanke, Y.; Oka, Y.; Yao, T. Superstructure of Strontium Vanadium Oxide, $Sr_{0.5}V_2O_5$: Twinning, Group-Symmetry and Interpretation of OD-Structure. *Zeitschrift für Krist.* **1998**, *213* (7), 399–405.

(42) Onoda, M.; Hasegawa, J. The Spin-Singlet States in the Double Trellis-Layer Bronzes $Na_{0.56}V_2O_5$ with a Uniform Valence and $Sr_{0.5}V_2O_5$ with a Valence Order. *J. Phys. Condens. Matter* **2006**, *18*, 2109–2123.

(43) Oka, Y.; Yao, T.; Yamamotoc, N. Layered Structures of Hydrated Vanadium Oxides. Part 5. Single-Crystal Structure of $Rb_{0.5}V_2O_5$ and Phase Changes of Rubidium Intercalate. *J. Mater. Chem.* **1995**, *5* (9), 1423–1426.

(44) Chernova, N. A.; Roppolo, M.; Dillon, A. C.; Whittingham, M. S. Layered Vanadium and Molybdenum Oxides: Batteries and Electrochromics. *J. Mater. Chem.* **2009**, *19* (17), 2526–2552.

(45) Shu, G. J.; Huang, F. T.; Chu, M. W.; Lin, J. Y.; Lee, P. A.; Chou, F. C. Staging Model of the Ordered Stacking of Vacancy Layers and Phase Separation in Layered Na_x CoO_2 (x>0.71) Single Crystals. *Phys. Rev. B* **2009**, *80* (1), 014117.

(46) Gu, L.; Zhu, C.; Li, H.; Yu, Y.; Li, C.; Tsukimoto, S.; Maier, J.; Ikuhara, Y. Direct Observation of Lithium Staging in Partially Delithiated $LiFePO_4$ at Atomic Resolution. *J. Am. Chem. Soc.* **2011**, *133* (13), 4661–4663.

(47) Ma, R.; Liang, J.; Liu, X.; Sasaki, T. General Insights into Structural Evolution of Layered Double Hydroxide: Underlying Aspects in Topochemical Transformation from Brucite to Layered Double Hydroxide. *J. Am. Chem. Soc.* **2012**, *134* (48), 19915–19921.

(48) Baddour-hadjean, R.; Pereira-Ramos, J.-P. Raman Microspectrometry Applied to the Study of Electrode Materials for Lithium Batteries. *Chem.*

Rev. **2008**, *110* (3), 1278–1319.

(49) Velazquez, J. M.; Jaye, C.; Fischer, D. a; Banerjee, S. Near Edge X-Ray Absorption Fine Structure Spectroscopy Studies of Single-Crystalline V_2O_5 Nanowire Arrays. *J. Phys. Chem. C* **2009**, *113* (18), 7639–7645.

(50) Wangoh, L.; Marley, P. M.; Quackenbush, N. F.; Sallis, S.; Fischer, D. A.; Woicik, J. C.; Banerjee, S.; Piper, L. F. J. Electron Lone Pair Distortion Facilitated Metal-Insulator Transition in β-$Pb_{0.33}V_2O_5$ Nanowires. *Appl. Phys. Lett.* **2014**, *104* (18), 182108.

(51) Tolhurst, T. M.; Leedahl, B.; Andrews, J. L.; Marley, P. M.; Banerjee, S.; Moewes, A. Contrasting 1D Tunnel-Structured and 2D Layered Polymorphs of V_2O_5 : Relating Crystal Structure and Bonding to Band Gaps and Electronic Structure. *Phys. Chem. Chem. Phys.* **2016**, *18* (23), 15798–15806.

(52) De Jesus, L. R.; Horrocks, G. A.; Liang, Y.; Parija, A.; Jaye, C.; Wangoh, L.; Wang, J.; Fischer, D. A.; Piper, L. F. J.; Prendergast, D.; Banerjee, S. Mapping Polaronic States and Lithiation Gradients in Individual V_2O_5 Nanowires. *Nat. Commun.* **2016**, *7*, 12022:1-9.

(53) Setyawan, W.; Curtarolo, S. High-Throughput Electronic Band Structure Calculations: Challenges and Tools. *Comput. Mater. Sci.* **2010**, *49* (2), 299–312.

(54) Urquhart, S. G.; Hitchcock, A. P.; Smith, A. P.; Ade, H. W.; Lidy, W.; Rightor, E. G.; Mitchell, G. E. NEXAFS Spectromicroscopy of Polymers: Overview

and Quantitative Analysis of Polyurethane Polymers. *J. Electron Spectros. Relat. Phenomena* **1999**, *100* (1–3), 119–135.

(55) Jacobsen, C.; Wirick, S.; Flynn, G. J.; Zimba, C. Soft X-Ray Spectroscopy from Image Sequences with Sub-100 Nm Spatial Resolution. *J. Microsc.* **2000**, *197* (2), 173–184.

(56) Ade, H.; Hitchcock, A. P. NEXAFS Microscopy and Resonant Scattering: Composition and Orientation Probed in Real and Reciprocal Space. *Polymer (Guildf).* **2008**, *49* (3), 643–675.

(57) Li, Y.; El Gabaly, F.; Ferguson, T. R.; Smith, R. B.; Bartelt, N. C.; Sugar, J. D.; Fenton, K. R.; Cogswell, D. A.; Kilcoyne, A. L. D. D.; Tyliszczak, T.; Bazant, M. Z.; Chueh, W. C. Current-Induced Transition from Particle-by-Particle to Concurrent Intercalation in Phase-Separating Battery Electrodes. *Nat. Mater.* **2014**, *13* (12), 1149–1156.

(58) Orvananos, B.; Ferguson, T. R.; Yu, H.-C.; Bazant, M. Z.; Thornton, K. Particle-Level Modeling of the Charge-Discharge Behavior of Nanoparticulate Phase-Separating Li-Ion Battery Electrodes. *J. Electrochem. Soc.* **2014**, *161* (4), A535–A546.

(59) Maganas, D.; Roemelt, M.; Hävecker, M.; Trunschke, A.; Knop-Gericke, A.; Schlögl, R.; Neese, F. First Principles Calculations of the Structure and V L-Edge X-Ray Absorption Spectra of V_2O_5 Using Local Pair Natural Orbital Coupled Cluster Theory and Spin-Orbit Coupled Configuration Interaction Approaches. *Phys. Chem. Chem. Phys.* **2013**, *15* (19), 7260–7276.

(60) Chen, J. G. NEXAFS Investigations of Transition Metal Oxides, Nitrides, Carbides, Sulfides and Other Interstitial Compounds. *Surf. Sci. Rep.* **1997**, *30* (1–3), 1–152.

(61) Zhao, Y.; Li, F.; Zhang, R.; Evans, D. G.; Duan, X. Preparation of Layered Double-Hydroxide Nanomaterials with a Uniform Crystallite Size Using a New Method Involving Separate Nucleation and Aging Steps. *Chem. Mater.* **2002**, *14* (10), 4286–4291.

(62) Li, F.; Duan, X. Applications of Layered Double Hydroxides. *Struct. Bond.* **2006**, *119*, 193–223.

(63) Toby, B. H. EXPGUI, a Graphical User Interface for GSAS. *J. Appl. Crystallogr.* **2001**, *34* (2), 210–213.

(64) Collins, B. A.; Ade, H. Quantitative Compositional Analysis of Organic Thin Films Using Transmission NEXAFS Spectroscopy in an X-Ray Microscope. *J. Electron Spectros. Relat. Phenomena* **2012**, *185* (5–7), 119–128.

(65) Schwarz, K. DFT Calculations of Solids with LAPW and WIEN2k. *J. Solid State Chem.* **2003**, *176* (2), 319–328.

(66) Perdew, J. P.; Burke, K.; Ernzerhof, M. Generalized Gradient Approximation Made Simple. *Phys. Rev. Lett.* **1996**, *77* (18), 3865–3868.

3. MEMRISTIVE RESPONSE OF A NEW CLASS OF HYDRATED VANADIUM OXIDE INTERCALATION COMPOUNDS*

3.1. Overview

The practical realization of energy-efficient computing vectors is imperative to address the break-down in the scaling of power consumption with transistor dimensions, which has led to substantial underutilized chip space. Memristive elements that encode information in multiple internal states and reflect the dynamical evolution of these states are a promising alternative. Herein we report the observation of pinched loop hysteretic type-II memristive behavior in single-crystalline nanowires of a versatile class of layered vanadium oxide bronzes with the composition δ-$[M(H_2O)_4]_{0.25}V_2O_5$ (M = Co, Ni, Zn), the origin of which is thought to be the diffusion of protons in the interlayer regions.

3.2. Introduction

In recent process generations, the Dennard scaling of power consumption with transistor dimensions has been interrupted, resulting in stagnation of clock frequencies and giving rise to a fundamental utilization wall.[1] As a result, much of the benefits derived from aggressively scaled feature densities are squandered in

* Reprinted (adapted) with permission from Andrews, J. L.; Singh, S.; Kilcoyne, C.; Shamberger, P. J.; Sambandamurthy, G.; Banerjee, S. Memristive Response of a New Class of Hydrated Vanadium Oxide Intercalation Compounds. *MRS Communications*, **2017**, *7* (3), 634-641.

current computing architectures. In practical terms, this break-down in synergy between scaling of transistor density and native transistor speed on the one hand and transistor power consumption on the other hand is mitigated by leaving a substantial fraction of valuable chip real estate underclocked, engendering the term, “dark silicon”.[2] “Dark silicon” is, in fact, a casualty of the metal-oxide-semiconductor field-effect transistor (MOSFET) paradigm, which is fundamentally constrained by the immutable thermodynamics of electric-field-modulated switching of Si devices from OFF to ON states. Circumnavigating these fundamental limits requires either the development of new classes of materials that exploit novel resistance switching mechanisms not subject to the fundamental limitations of conventional FETs,[3] or alternatively the development of a computing architecture that encodes complexity through highly parallelized operations, similar to the human brain.[2]

Memristive systems have received significant interest as potential circuit elements for energy-efficient neuromorphic computing,[4,5] particularly as they relate to mitigating the problems presented by “dark silicon”. A fundamental imperative for such computing vectors is “on-chip learning” wherein specific states are encoded and accessed within circuitry and reflect the evolution of internal state variables as a function of previous voltage, current, or flux exposure.[6,7] Memristive systems are distinctive nonlinear circuit elements that are amenable to this approach since they encode resistance values that capture not just the state of the system at a specific time but also the historical evolution of the

possible states.[5] Notably, the Na^+ and K^+ channels of neurons exhibit fundamentally memristive behavior[4,5] and there are close similarities between memristive circuits and spike-time-dependent plasticity processes thought to underpin learning within neuronal networks. Unlike traditional linear circuit elements, Voltage-controlled memristors:

$$I(t)=G(x, V, t)V(t) \quad \textbf{3.1}$$

$$x=f(x,V,t) \quad \textbf{3.2}$$

where V and I are time-dependent input (voltage) and output (current) of the system, and the conductance, G, varies with an internal state variable, x, which explicitly evolves with voltage and time (Equation 3.1).[4,5] A voltage-controlled memristor can equivalently be described as a current-controlled device by a corresponding pair of relationships in which the state variable evolves as a function of current, rather than voltage. This state variable reflects some internal aspects of device structure that dynamically evolve in response to specific physical phenomena each of which may be described by appropriate equations of motion.[4,5]

Memristive behavior is underpinned by a variety of mechanisms involving electronic or ionic transport mediated by defect migration, formation of hot filaments, electrochemical reactions at interfaces, phase transitions, and Mott—Hubbard modulation of electron correlation.[5,8,9] Perhaps the most studied example of a memristive material is TiO_2, wherein memristivity arises from changes in internal resistance due to the migration of oxygen vacancies between

the two terminals.[10] Alternatively, memristive behavior with a marked hysteresis has also been observed in correlated transition metal oxide systems such as in the case of VO_2,[11–13] rare-earth nickelates,[14] and $M_xV_2O_5$.[15–17] In these systems, the memristive behavior is mediated by electronic phase transitions that bring about a pronounced modulation of conductivity, oftentimes mediated by an underlying structural transformation or disruption of charge ordering.[8]

A versatile class of compounds that has proven to be particularly intriguing for the realization of pronounced nonlinear switching is 2D layered oxide materials with the general formula $M_xV_2O_5$[8,18,19] where M is an intercalated cation and *x* is its stoichiometry. Several structurally-distinct polymorphs are known with infinite 2D bilayered V_4O_{10} sheets (δ-type) or 2D V_2O_5 monolayer sheets (γ- and α-type) separated by intercalated cations. The electronic structure of these compounds can be precisely modulated by choice of the cation M and stoichiometry *x*. The intercalated cations within these structures can furthermore potentially be solvated and such compounds are more rigorously delineated as $[M(X)_n]_xV_2O_5$ where M is a cation, X is a solvating species or coordinating ligand for the cation, *n* is the number of solvent molecules coordinated to the intercalating cation, and *x* is the stoichiometry of the intercalated cation.[18–20] While several of these compounds have been examined for electrochemical energy storage,[21] to the best of our knowledge the transport properties of intercalated vanadium oxide bronzes with solvated cations have not thus far been explored. Herein we demonstrate pronounced nonlinearity, hysteretic loops, and memristive switching in individual

nanowires of a family of isostructural 2D ternary vanadium oxides δ-$[M(H_2O)_4]_{0.25}V_2O_5$ (where M: Co, Ni, Zn). The memristive behavior is of Type II nature with pinched hysteresis loops characterized by an avoided crossing at zero bias and further shows a pronounced thermal dependence. The hysteretic behavior appears to be underpinned by ion diffusion and is suppressed upon desolvation of the intercalated cations. The interlayer separation of 2D layered δ-$[M(H_2O)_4]_{0.25}V_2O_5$ compounds is readily varied by preparing binary mixed-cation solid-solutions.

3.3. Results and Discussion

3.3.1. Synthesis and Structural Characterization of δ-$[M(H_2O)_4]_{0.25}V_2O_5$ Nanowires

The size, charge, and polarizability of the cation M and its stoichiometry *x* provides a means to precisely modulate carrier density and electronic structure of δ-$[M(H_2O)_4]_xV_2O_5$ (similarly for 1D β/β'-$M_xV_2O_5$ systems) and allows for the manifestation of a broad range of electronic instabilities.[8,22] While numerous 2D layered $M_xV_2O_5$ phases with solvated cations have been crystallized, detailed evaluation of their intrinsic transport properties has thus far been absent from the literature. To this point, the aforementioned hydrated bronze was synthesized by the hydrothermal reaction of $Ni(COOCH_3)_2$•$4H_2O$ with V_2O_5, which yielded a dark green paper-like product. Figure 3.1A exhibits a synchrotron powder X-ray diffraction pattern (λ=0.4133410 Å) of the obtained material.

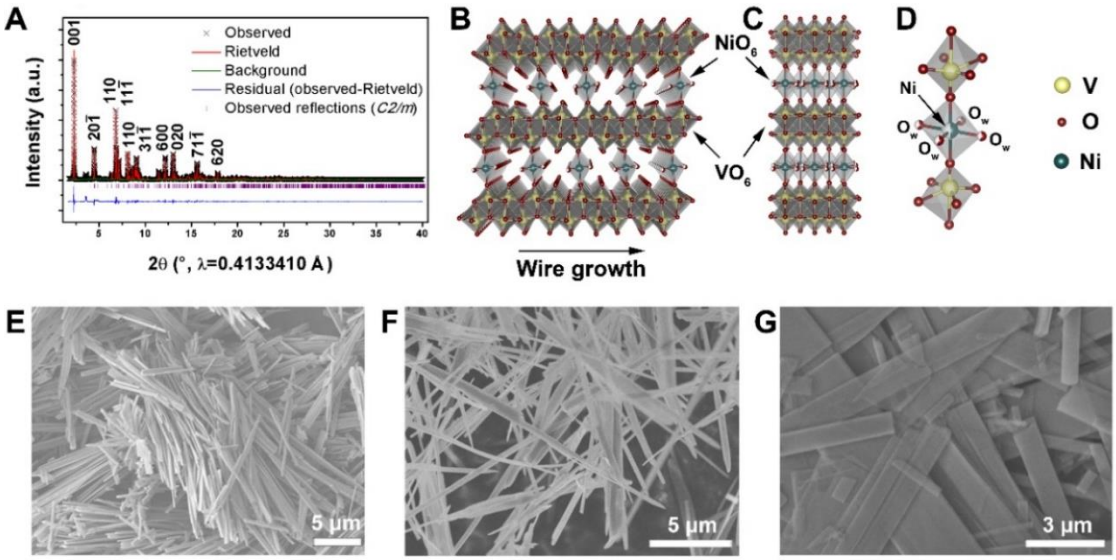

Figure 3.1. (A) High-resolution synchrotron X-ray (λ=0.4133 nm) powder diffraction data collected for the M = Ni compound depicted as black crosses; a Rietveld fit and residuals are depicted in red and blue, respectively. Refined structure as viewed down (B) the *b* axis and (C) down the *a* axis (see Table B.1, Table B.2, Table B.3, and Table B.4). (D) The local coordination geometry of intercalated Ni cations. Scanning electron micrographs of the δ-$[M(H_2O)_4]_xV_2O_5$ nanowires, where (E) M = Ni; (F) M = Co; and (G) M = Zn.

The pattern is characterized by intense (00*l*) reflections suggestive of anisotropic growth of the material along the *a*-*b* plane. A Rietveld refinement to the pattern is depicted in red and the refined average structure is illustrated in Figure 3.1B and Figure 3.1C. The structure comprises alternating condensed double layers of $[V_8O_{20}]$ built from edge- and corner-sharing VO_6 octahedra separated by $[Ni(H_2O)_4]$ layers.[20] Unit cell parameters, atom positions, thermal parameters, and site occupancies have been refined and are listed in Table B.1 and Table B.2. The refinement to the powder pattern yields a final stoichiometry of δ-$[Ni(H_2O)_4]_{0.2475}V_2O_5$•$0.147H_2O$. In comparison to vanadium oxide bronzes[17] with unsolvated cations, every alternate cation site is occupied by the hydrated

Ni-ions, resulting in a maximum site occupancy of x=0.25 *versus* x=0.5 for δ-$M_xV_2O_5$ with unsolvated cations. Figure 3.1D depicts the local coordination geometry of the intercalated Ni-ions, which reside at the centers of subtly distorted octahedral coordination environments; the Ni-ions are located midway between adjacent [V_8O_{20}] double layers and serve to bridge the apical vanadyl groups of these layers; water molecules defining an approximately square planar geometry complete the local coordination environment of the Ni-ions. Table B.3 lists the bond distances and bond angles for the vanadium- and nickel-centered polyhedral building blocks of the structure. The large isotropic thermal parameters of the coordinated water molecules suggest considerable disorder in the 3D orientation of the water ligands at room temperature and is further suggestive of the presence of some interstitial non-coordinated water. The cobalt and zinc analogues of the structure are entirely isostructural and also crystallize in the *C2/m* space group (*vide infra*).

The morphologies of the isostructural δ-$[M(H_2O)_4]_{0.25}V_2O_5$ materials (M = Co, Ni, Zn) have been investigated by SEM and are depicted in Figure 3.1E-G. The micrographs display evidence for highly anisotropic growth, as deduced from the diffraction patterns. The δ-$[M(H_2O)_4]_{0.25}V_2O_5$ nanowires have lateral dimensions of ca. 350 nm and range tens of microns in length. The elemental composition of the isostructural hydrated bronzes has been investigated by energy dispersive X-ray spectroscopy (Figure B.1), which indicates intercalated

cation stoichiometries in reasonable agreement with values derived from refinements to diffraction data.

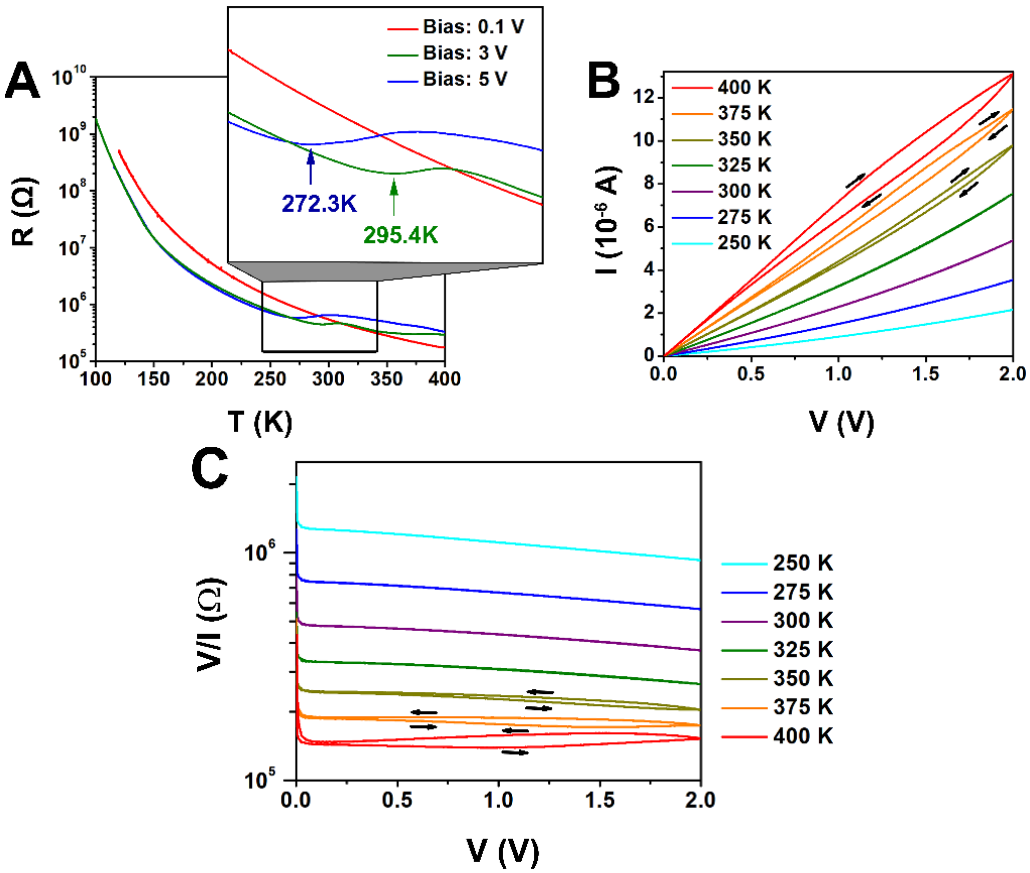

Figure 3.2. (A) Resistance *versus* temperature plots acquired at different DC biases; the inset highlights the varying temperatures at which a second internal resistance state is accessed. (B) current *versus* voltage (*I*—*V*) plots for an individual nanowire of δ-$[Ni(H_2O)_4]_xV_2O_5$ measured at different temperatures. (C) Resistance *versus* voltage curves in the voltage range from 0→2 V showing the existence of two distinct resistance states (low resistance on sweeping from 0→2V, high resistance when sweeping from 2→0 V, as indicated by the black directional arrows.

3.3.2. Observation of Hysteretic Loops, Manifestation of Memristive Behavior, and Mechanistic Underpinnings

Individual nanowires of δ-$[M(H_2O)_4]_{0.25}V_2O_5$ have been integrated within device architectures as depicted in Figure B.2. Figure 3.2, Figure 3.3, and Figure B.3 depict transport data acquired for individual nanowires of δ-$[Ni(H_2O)_4]_xV_2O_5$, δ-$[Co(H_2O)_4]_xV_2O_5$, and δ-$[Zn(H_2O)_4]_xV_2O_5$, respectively.

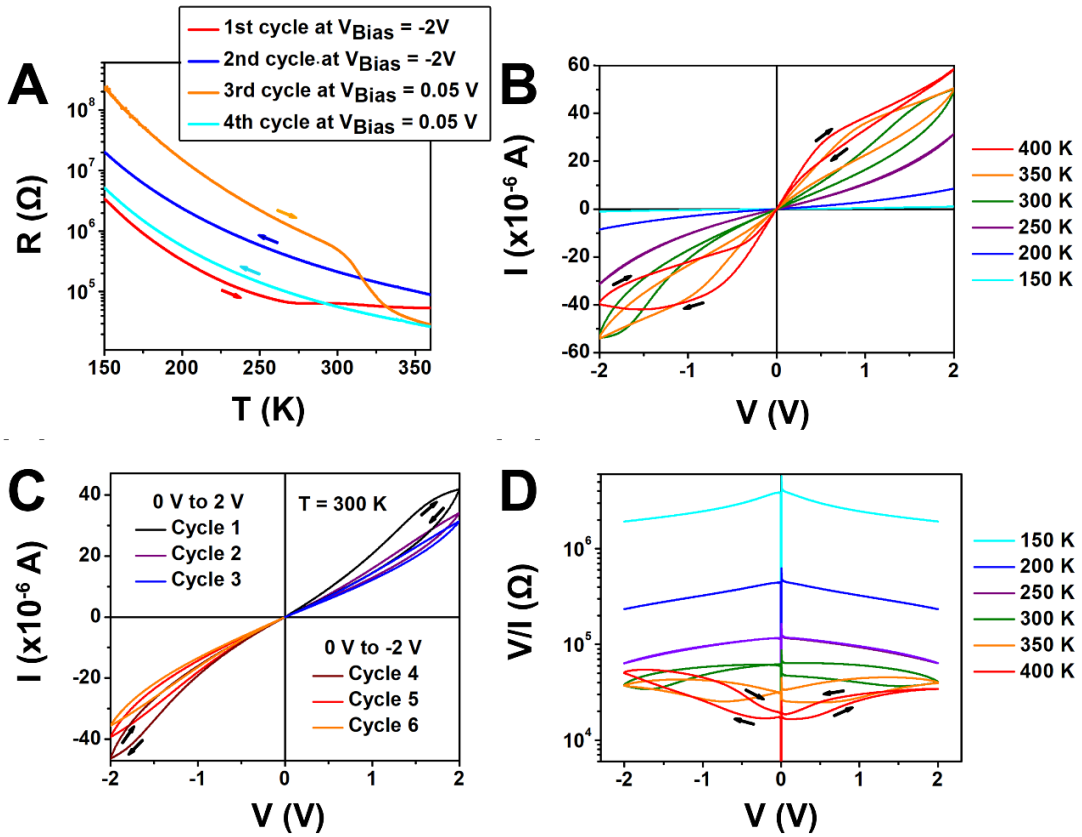

Figure 3.3. (A) Resistance *versus* temperature plots acquired for a single-nanowire of δ-$[Co(H_2O)_4]_xV_2O_5$ when cycling between 0 and -2 V. Current *versus* voltage curves plots acquired (B) as a function of temperature and (C) at a fixed temperature over multiple cycles. (D) Resistance *versus* voltage curves for each of the individual plots depicted in (b) allowing for unambiguous assignment of the observed behavior to a Type-II memristive element.

The resistance *versus* temperature plots acquired for δ-$[Ni(H_2O)_4]_xV_2O_5$ in Figure 3.2A indicate a quasi-exponential decrease of resistance with increasing temperature at low bias (0.1 V) as is typical of a semiconductor; however, at higher bias values, a pronounced discontinuity is discernible, corresponding to stabilization of a second, higher-resistance state. The temperature required to access this higher resistance internal state is a function of voltage and is reduced from 295 K for a bias of 3 V to 272 K at a bias of 5 V. Figure 3.2B depicts current—voltage sweeps measured for this compound as a function of temperature. A pronounced nonlinearity is discernible at all temperatures; however, at temperatures of 350 K and above, a clear hysteretic loop opens and furthermore become wider with increasing temperature. The sweep direction is delineated by black arrows and indicates that with increasing voltage (from 0→2 V), the system transitions to a more highly resistive internal state and then remains in this state as the voltage is decreased from 2→0 V. However, the original, more highly conductive, state is entirely recovered if the device is allowed to relax at zero bias (without need for a change of polarity). This feature is highlighted in Figure 3.2C, where two distinct resistance states are observed at temperatures of 350—400 K. Figure 3.2B and Figure 3.2C indicate that the current through the nanowire is not just a function of the applied voltage and temperature but also reflects its previous thermal and voltage history, which determines the dynamical evolution of the resistance states.

Figure 3.3A depicts the evolution of the resistance of an individual nanowire of δ-$[Co(H_2O)_4]_xV_2O_5$ as a function of temperature at different bias voltages. In this case, as the material is heated at a constant bias of -2 V (red plot), a pronounced discontinuity of the resistance, again with a transition to a higher-resistance state, is observed at *ca*. 275 K. Upon cooling, the dark blue line indicates that the resistance follows the function of the "as written" higher resistance internal state. When the polarity is reversed from negative to positive bias, at a bias of 50 mV, the material remains in the highly resistive state up to a threshold temperature of ca. 302K at which point it is "rewritten" to its initial low-resistance state. As is characteristic of memristive systems,[5] the resistance is a function not just of the temperature and applied bias but also reflects the voltage sweep direction and history of the voltage magnitude. The distinct resistance states can be reversible transformed ("written") or simply "read" depending on the applied bias. Figure 3.3B depicts the relatively more pronounced pinched hysteretic loops observed in current—voltage measurements as a function of temperature; pronounced hysteretic behavior but with a greater degree of asymmetry between the positive and negative voltage regimes is observed at temperatures of 300 K and above. The directions delineated by the arrows in Figure 3.3B suggest that the observed characteristics are typical of a type-II memristor with an avoided crossing at null bias.[4,5] While such behavior cannot uniquely identify the origin of memristive behavior, it can provide a useful test for some proposed physical mechanisms. Figure 3.3C depicts multiple voltage sweep

cycles up to 2V; Figure B.4 shows details of ten cycles along each polarity. The hysteresis width successively decreases with multiple 0 V→2 V→0 V cycles, ultimately collapsing to a finite hysteresis width that is retained through cycles 7—10 (Figure B.4). The collapse to a higher resistance state is thought to reflect depletion of ionic carriers that likely accumulate at the current collector electrodes where they are attracted to image charges. [23] Consistent with this idea, reversing the polarity allows for restoration of the higher conductance state; prolonged cycling at negative bias further results in a diminution of the hysteretic width. The resistance *versus* voltage plots corresponding to Figure 3.3B are depicted in Figure 3.3D and indicates classical double-loop characteristics, which further cements the assignment of the observed transport characteristics to type-II memristive behavior. It is worth noting that for both mentioned systems, application of a high magnitude voltage drives the system to a higher resistance state regardless of polarity; reversing the polarity restores the higher conductance state. The temperature dependence of the hysteresis widths and the dependence of current at a specific applied bias on both voltage and thermal history is reminiscent of memristive thermistors.[5] Figure B.3 exhibits transport data acquired for an individual nanowire of the isostructural *C2/m* Zn analogue. Pinched hysteretic loops, albeit with smaller widths as compared to the Ni and Co bronzes, are discernible at temperatures of 350 K and above and are again characterized by avoided crossings at null bias characteristic of Type-II memristors. From a mechanistic perspective, the observation of memristive

behavior in δ-$[Zn(H_2O)_4]_xV_2O_5$ is intriguing and suggests that phenomena noted in this isostructural family of compounds is not predicated on having a magnetic cation.

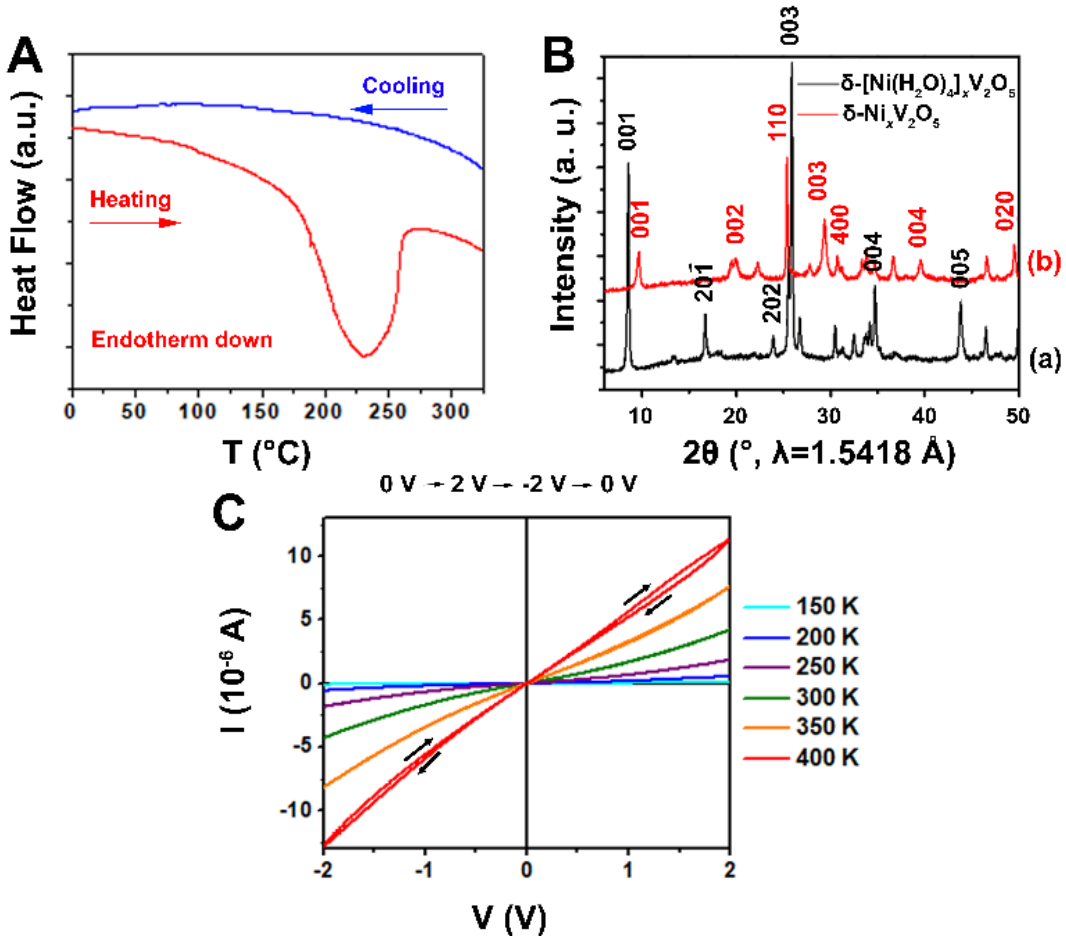

Figure 3.4. (A) Differential scanning calorimetry (DSC) showing gradual dehydration of the bronze from 190-260°C. (B) X-ray diffraction of the pristine δ-$[Ni(H_2O)_4]_{0.25}V_2O_5$ bronze (black) and the same material after being annealed in vacuum at 275°C under vacuum for four hours (red). (C) Current *vs* voltage curve for the dehydrated material showing dramatically reduced hysteresis, belying the crucial role that water plays in the hysteretic behavior. The resistance of the material is also dramatically increased in the dehydrated state relative to the hydrated state (Figure 3.1).

In order to further elucidate the role of the water molecules coordinated to the intercalated cations, a dehydrated δ-$Ni_{0.25}V_2O_5$ phase has been prepared. The annealing temperature is above the irreversible endothermic peak attributable to dehydration of δ-$[Ni(H_2O)_4]_{0.25}V_2O_5$ observed at 230°C in a differential scanning calorimetry measurement shown in Figure 3.4A. The diffraction pattern of the annealed sample is depicted in Figure 3.4B, and exhibits a structure similar to that observed upon annealing δ-$[Ca(H_2O)_4]_{0.25}V_2O_5$.[19] The shift of the (00*l*) reflections to higher 2θ values is consistent with a decrease of the interlayer separation from 10.33 Å to 9.15 Å upon loss of water.[24] Transport properties measured for the dehydrated compound shown in Figure 3.4C are characterized by a pronounced increase of resistance and substantially diminished hysteresis. This result thus suggests that the intercalated water molecules play a pivotal role in mediating charge transport in these systems. Voltage-induced transitions to a higher-resistance state and an increase of hysteresis with temperature observed for δ-$[M(H_2O)_4]_{0.25}V_2O_5$ are markedly different from the transport characteristics measured for β- and δ-phase $M_xV_2O_5$ bronzes with bare (unsolvated) cations.[16,17] The distinctive transport characteristics noted here, specifically, the depletion of charge carriers at high bias (Figure 3.2B and Figure 3.3B), the relaxation to a higher conductance state upon removal of bias (Figure 3.3C and Figure B.4), and the ability to recover the higher conducting state by reversing polarity point to ionic conductivity as the primary underlying mechanism of charge transport.

Next, it is worth considering the specific ions involved in transport. The temperature-dependence of the hysteresis, corresponding to thermistive behavior,[25] is further consistent with a thermodynamically driven increase of ionic carriers with increasing temperature. In analogy with the reactivity of divalent transition metal complexes of nickel, cobalt, and zinc dissolved in aqueous solution[26,27] (pKa values of $[Ni(H_2O)_6]^{2+}$, $[Co(H_2O)_6]^{2+}$, and $[Zn(H_2O)_6]^{2+}$ are 9.9, 9.6, and 9.0).[28] It is reasonable to expect that hydrated transition metal cations intercalated between the V_8O_{20} layers can be readily hydrolyzed as per:

$$[ML_2(H_2O)_4]^{2+} \leftrightarrow [ML_2(OH)(H_2O)_3]^{+}+H^{+} \qquad \textbf{3.3}$$

where in this case L represents the apical vanadyl oxygen ligands to the transition metals. Such a hydrolysis reaction would yield protons as potentially mobile ionic species and would result in each of the cations donating one (instead of two) electrons to the V_8O_{10} layers. In other words, such hydrolysis would be accompanied by oxidation of vanadium sites, utilizing a readily accessible redox couple (note that the oxidation state of the intercalated cation remains unchanged in Equation 3.3),[8] and would result in loss of charge ordering. The idea of proton-mediated conductivity is supported by the loss of hysteresis upon dehydration (Figure 3.4), which would substantially diminish the available number of carriers.

Furthermore, data for hydrolysis of aqueous cobalt(II) complexes suggests a pronounced monotonic increase of pKa and a decrease of pH with increasing temperature.[27] Indeed, this temperature-dependence suggests that the equilibrium for the endothermic reaction depicted in Equation 3.3 is shifted to the

right with increasing temperature, thereby making available a greater concentration of protons, which serve as the mobile ionic species, at higher temperatures. The protons created as per Equation 3.3 likely drift along the interlayer sites upon application of a voltage along a pathway defined by the vanadyl oxygen atoms. The relatively low occupancy of interlayer sites by hydrated cations (as compared to layered bronzes with unsolvated cations) likely further facilities proton diffusion along the 2D layers. Increasing temperature thus increases the carrier concentration within this system as well as facilitates carrier diffusion, bringing about a decrease in resistance spanning orders of magnitude, as observed in Figure 3.2C and Figure 3.3D. However, since the charge carriers are limited by the number of intercalated hydrated cations, beyond a specific voltage, the accumulation of protons at one electrode results in the nanowire being transformed to a higher resistance state. Removal of the voltage allows for protons to drift back along their diffusion gradient across the 2D layers, which incidentally have been found to define very favorable diffusion pathways for monovalent Li- and Na-ions.[29] Indeed, nudged elastic band calculations suggest that the specific diffusion pathway for cations within such structures depends sensitively on the stacking of the 2D layers.[29] The large asymmetry observed in Figure 3.2 and Figure 3.3 likely derive in large measure from accumulation and large concentration gradient of ionic species defined at charged surfaces upon sweeping voltage along one direction and is also increased with increasing temperature as a result of the higher carrier concentration and increased mobility

of carriers. However, unequivocal determination of the underlying mechanism of the memristive behavior will require *in situ* atomic resolution imaging and detailed theoretical evaluation of ion transport mechanisms in these novel intercalation compounds.

3.3.3. Solid-Solution Mixed-Cation Vanadium Oxide Bronzes

Figure 3.5A contrasts the powder XRD patterns of δ-$[Ni(H_2O)_4]_{0.267}V_2O_5$, δ-$[Co(H_2O)_4]_{0.270}V_2O_5$, and δ-$[Zn(H_2O)_4]_{0.168}V_2O_5$; the patterns can all be indexed to the monoclinic *C2/m* space group. The inset to Figure 3.5A depicts a shift of the (001) reflection, corresponding to the separation between the layers of the 2D compound, to lower 2θ values from Ni to Co to Zn. This trend of increasing interplanar separations is well correlated with values of hydrated radii determined for the hexaaqua complexes wherein Ni^{2+}(4.04 Å) < Co^{2+}(4.23 Å) < Zn^{2+}(4.30 Å).[30] Given the close structural similarity of the three compounds, mixed-cation quaternary systems have been prepared. Figure 3.5C-E depict powder XRD patterns of quaternary bronzes with mixed hydrated cations: δ-$[Ni_xCo_{1-x}(H_2O)_4]_{0.25}V_2O_5$ (Figure 3.5C); δ-$[Ni_xZn_{1-x}(H_2O)_4]_{0.25}V_2O_5$ (Figure 3.5D); and δ-$[Co_xZn_{1-x}(H_2O)_4]_{0.25}V_2O_5$ (Figure 3.5E). The monotonic shift of the (001) reflection to lower 2θ values (corresponding to larger interlayer spacing) with increasing incorporation of the larger hydrated metal cation is striking and generally consistent with Vegard's law.

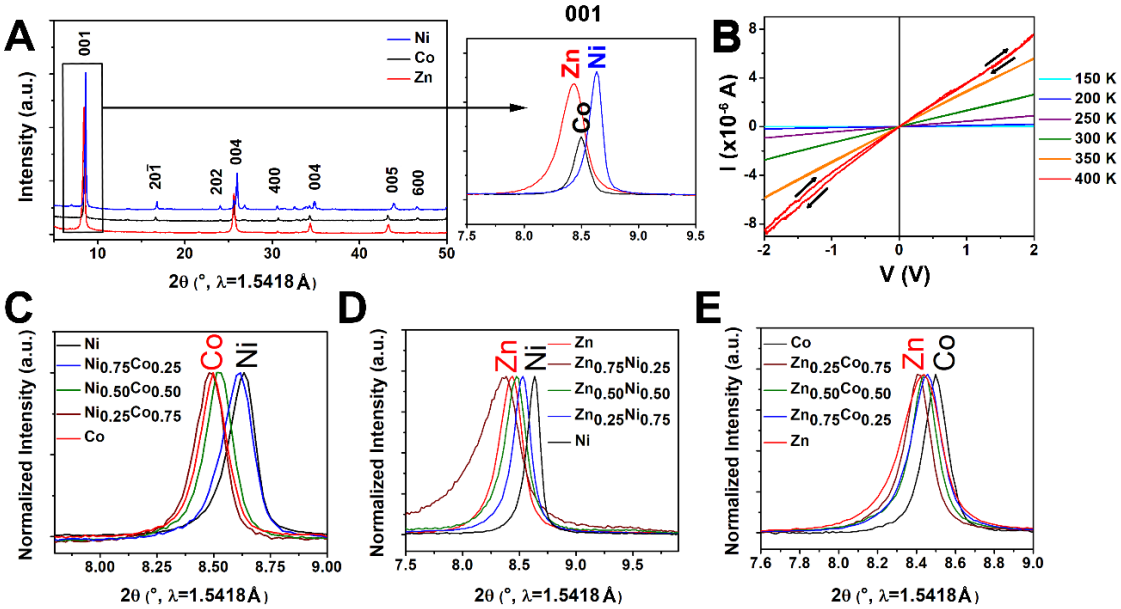

Figure 3.5. Powder diffraction patterns (λ=1.5418 nm) for (A) ternary bronzes (Ni, Co, Zn) verifying the isostructural nature of the bronzes. An expanded view of the (001) reflection clearly shows a monotonic increase in the separation between basal planes mirroring the increase in hydrated ionic radii from Ni^{2+} to Zn^{2+}. (B) transport measurements for a nanowire with mixed Ni^{2+}/Co^{2+} occupancy showing similar Type-II memristive behavior as the end-member nickel and cobalt analogs. Diffraction patterns for mixed-cation quaternary compositions namely (C) δ-$[Ni_xCo_{1-x}(H_2O)_4]_{0.25}V_2O_5$; (D) δ-$[Ni_xZn_{1-x}(H_2O)_4]_{0.25}V_2O_5$; and (E) δ-$[Co_xZn_{1-x}(H_2O)_4]_{0.25}V_2O_5$. Energy dispersive X-ray spectroscopy data for two of the intermediate compositions in depicted in Figure B.5.

However, in each series the sample with intended stoichiometry of δ-$[M_{large(0.75)}M_{small(0.25)}(H_2O)_4]_{0.25}V_2O_5$ exhibits anomalous behavior wherein the interlayer spacing is further expanded with respect to the single-cation δ-$[M_{large}(H_2O)_4]_{0.25}V_2O_5$ material. The anomalous behavior is likely a result of disorder introduced at these stoichiometries that allows for incorporation of additional water molecules. Energy dispersive X-ray spectra obtained for nanowires intermediate in the δ-$[Ni_xZn_{1-x}(H_2O)_4]_{0.25}V_2O_5$ and δ-$[Co_xZn_{1-}$

$_x(H_2O)_4]_{0.25}V_2O_5$ series are presented in Figure B.5. The preparation of mixed-cation bronzes thus allows for modulation of the interlayer separation, which is known to profoundly affect the electronic structure of layered vanadium oxides.[22] Figure 3.5B depicts the transport properties measured for an individual nanowire of δ-$[Co_{0.5}Ni_{0.5}(H_2O)_4]_{0.25}V_2O_5$, which again shows pinched hysteretic Type-II memristive behavior albeit with a narrow hysteresis. The disorder in the intercalated cation layer of mixed-cation bronzes likely serves as an impediment to proton transfer. Nevertheless, the high degree of tunability of structure suggests a versatile family of compounds with tunable coupling between $[V_8O_{20}]$ layers.

3.4. Conclusions

Single-crystalline nanowires of isostructural δ-$[M(H_2O)_4]_{0.25}V_2O_5$ (M = Co, Ni, Zn) compounds have been prepared by a facile hydrothermal route involving the reaction of metal acetate precursors with V_2O_5. The compounds comprise hydrated cation layers separating condensed $[V_8O_{20}]$ double layers with the divalent metal cations coordinated by vanadyl oxygens from the layers above and below. Transport measurements of individual nanowires of all three compounds are characterized by pinched hysteretic loops with avoided crossings at null bias, characteristic of Type-II memristive elements. Higher voltages drive the systems from a high conductance to low conductance state; the high conductance state is recovered upon relaxation of the system at zero bias or upon reversal of polarity. The measured current in these devices is a function of voltage and thermal history. The memristive behavior observed within single domains likely derives from ion

diffusion. The crucial role of both coordinating water as well as free water within the inter-gallery spacing has been established through comparison of water-coordinated and dehydrated samples and suggests the establishment of a proton-mediated conductivity channel, a direct consequence of the two-dimensional structure of the material, which allows for facile diffusion pathways to be defined along the layers.[29] The distinctive layers of hydrated, intercalated transition metal centers within alternating layers of the material are intrinsically related to the observed phenomena. The observation of pronounced memristive behavior at room temperature and above makes these systems particularly intriguing for integration within neuromorphic circuitry wherein specific internal states are encoded based on dynamical evolution of temperature and voltage.

The interlayer separation within these materials is readily tunable through substitution of the intercalated cations to form mixed-cation quaternary intercalation bronzes that appear to retain Type-II memristive behavior. The facile ability to substitute the solvated cations between double-layered V_2O_5 slabs provides a versatile family of compounds that can perhaps further be elaborated to other transition metal cations and ligand molecules other than water.[24] Future work will focused on detailed elucidation of ion conduction pathways in this system as well as an evaluation of the modulation of electronic structure as a function of increasing interlayer separation.

3.5. Experimental Section

3.5.1. Synthesis of δ-$[M(H_2O)_4]_{0.25}V_2O_5$ Nanowires

δ-$[M(H_2O)_4]_xV_2O_5$ nanowires were prepared by a facile single-step hydrothermal reaction. In a typical reaction, 178.1 mg of V_2O_5 (Sigma Aldrich) were ball-milled together in a Spex Certiprep ball-mill with 121.9 mg of $Ni(COOCH_3)_2•4H_2O$ (Sigma-Aldrich) in a 2:1 molar ratio for 1 h using polystyrene beads as the milling media. A 2:1 molar excess (as compared to the final reported stoichiometry of 4:1) was observed to improve the crystallinity of the product. The resulting mixture was added to 15 mL of a 1.17 M aqueous solution of acetic acid and then transferred to a 23 mL polytetrafluoroethylene-lined stainless-steel autoclave. The sealed autoclave was heated at 210°C for 72 h. The cobalt and zinc analogues, as well as the solid-solution mixed-cation compounds were prepared *via* the same method and by replacing appropriate amounts of $Ni(COOCH_3)_2•4H_2O$ with the desired concentrations of cobalt and zinc acetate(s) to obtain the desired 4:1 molar ratio of reactants. Upon completion of the hydrothermal reaction, the resulting light-to-dark-green solids were filtered, washed with copious amounts of water and 2-propanol, and allowed to dry in air overnight. The dehydrated δ-$Ni_{0.25}V_2O_5$ bronze was prepared by annealing the hydrated powder at 300°C within a tube furnace whilst flowing Ar at 100 $mL \cdot min^{-1}$ for 5 h.

3.5.2. Materials Characterization

High-resolution X-ray powder diffraction data for δ-$[Ni(H_2O)_4]_xV_2O_5$ was collected in a poly(4,4'-oxydiphenylene-pyromellitimide) capillary in transmission

geometry at 295 K at beamline 11-BM of the Advanced Photon Source (λ=0.4133410Å). Details of the Rietveld refinement performed on the high-resolution synchrotron diffraction data are provided in Appendix B. Laboratory diffraction data were collected in Bragg-Brentano geometry for the Co and Zn analogues as well as the mixed-cation compounds using a Bruker D8-Focus diffractometer (Cu-Kα: λ=1.5418Å; 40 kV voltage; 25 mA current).

Scanning electron microscopy (SEM) images were obtained using a JEOL JSM-7500F FE-SEM equipped with an Oxford EDS spectrometer for elemental characterization. SEM images were collected at an accelerating voltage of 5 kV; EDS spectra were collected at an accelerating voltage of 20 kV. Differential scanning calorimetry was performed on δ-$[Ni(H_2O)_4]_xV_2O_5$ nanowires using a Q2000 instrument (TA) under a flowing nitrogen atmosphere.

3.5.3. Device Measurements

Individual nanowires were isolated by dilution in 2-propanol followed by ultrasonication. A Si/SiO_2 substrate comprising a Si wafer passivated with a SiO_2 oxide layer with a thickness of 300 nm was cleaned by ultrasonication in acetone, methanol, and deionized water and the dilute dispersion containing the nanowires was drop cast onto the substrate. Individual nanowires were identified by optical microscopy and multi-terminal devices were fabricated using standard photolithographic techniques. Typical devices had a channel length of 5 μm between the source and the drain. Finally, Cr/Au layers (5 nm/70 nm) were deposited using an electron-beam evaporator. Transport measurements were

performed in a two-terminal DC configuration using a Keithley 2400 SourceMeter under high vacuum in a temperature-controlled cryostat cooled using liquid nitrogen. For resistance *versus* temperature measurements, an initial low bias in the linear regime was applied while temperature was swept from 100–400 K. The sweep rate was kept at <3 $K \cdot min^{-1}$ to in order avoid any thermal lag.

3.6. References

(1) Dennard, R. H.; Gaensslen, F. H.; Rideout, V. L.; Bassous, E.; LeBlanc, A. R. Design of Ion-Implanted MOSFET's with Very Small Physical Dimensions. *Proc. IEEE* **1999**, *87* (5), 668–678.

(2) Taylor, M. B. A Landscape of the New Dark Silicon Design Regime. *IEEE Micro* **2013**, *33* (5), 8–19.

(3) Zhou, Y.; Ramanathan, S. Correlated Electron Materials and Field Effect Transistors for Logic: A Review. *Crit. Rev. Solid State Mater. Sci.* **2013**, *38* (4), 286–317.

(4) Chua, L. O.; Sung Mo Kang. Memristive Devices and Systems. *Proc. IEEE* **1976**, *64* (2), 209–223.

(5) Pershin, Y. V.; Di Ventra, M. Memory Effects in Complex Materials and Nanoscale Systems. *Adv. Phys.* **2011**, *60* (2), 145–227.

(6) Pickett, M. D.; Medeiros-Ribeiro, G.; Williams, R. S. A Scalable Neuristor Built with Mott Memristors. *Nat. Mater.* **2013**, *12* (2), 114–117.

(7) Kim, T. H.; Jang, E. Y.; Lee, N. J.; Choi, D. J.; Lee, K. J.; Jang, J. T.; Choi, J. S.; Moon, S. H.; Cheon, J. Nanoparticle Assemblies as Memristors. *Nano*

Lett. **2009**, *9* (6), 2229–2233.

(8) Marley, P. M.; Horrocks, G. A.; Pelcher, K. E.; Banerjee, S. Transformers: The Changing Phases of Low-Dimensional Vanadium Oxide Bronzes. *Chem. Commun.* **2015**, *51* (25), 5181–5198.

(9) Ha, S. D.; Ramanathan, S. Adaptive Oxide Electronics: A Review. *J. Appl. Phys.* **2011**, *110* (7), 071101.

(10) Sun, Z.; Liao, T.; Dou, Y.; Hwang, S. M.; Park, M.-S.; Jiang, L.; Kim, J. H.; Dou, S. X. Generalized Self-Assembly of Scalable Two-Dimensional Transition Metal Oxide Nanosheets. *Nat. Commun.* **2014**, *5* (May), 3813.

(11) Driscoll, T.; Kim, H.-T.; Chae, B.-G.; Kim, B.-J.; Lee, Y.-W.; Jokerst, N. M.; Palit, S.; Smith, D. R.; Di Ventra, M.; Basov, D. N. Memory Metamaterials. *Science (80-.).* **2009**, *325* (5947), 1518–1521.

(12) Whittaker, L.; Patridge, C. J.; Banerjee, S. Microscopic and Nanoscale Perspective of the Metal-Insulator Phase Transitions of VO_2: Some New Twists to an Old Tale. *J. Phys. Chem. Lett.* **2011**, *2* (7), 745–758.

(13) Singh, S.; Abtew, T. A.; Horrocks, G.; Kilcoyne, C.; Marley, P. M.; Stabile, A. A.; Banerjee, S.; Zhang, P.; Sambandamurthy, G. Selective Electrochemical Reactivity of Rutile VO_2 towards the Suppression of Metal-Insulator Transition. *Phys. Rev. B* **2016**, *93* (12), 125132.

(14) Shi, J.; Ha, S. D.; Zhou, Y.; Schoofs, F.; Ramanathan, S. A Correlated Nickelate Synaptic Transistor. *Nat. Commun.* **2013**, *4*, 3676.

(15) Wu, T.-L.; Stabile, A. A.; Patridge, C. J.; Banerjee, S.; Sambandamurthy, G.

Electrically Driven Metal-Insulator Switching in Δ−KxV2O5 Nanowires. *Appl. Phys. Lett.* **2012**, *101* (16), 163502:1-4.

(16) Marley, P. M.; Stabile, A. A.; Kwan, C. P.; Singh, S.; Zhang, P.; Sambandamurthy, G.; Banerjee, S. Charge Disproportionation and Voltage-Induced Metal-Insulator Transitions Evidenced in β-$Pb_xV_2O_5$ Nanowires. *Adv. Funct. Mater.* **2013**, *23* (2), 153–160.

(17) Marley, P. M.; Singh, S.; Abtew, T. A.; Jaye, C.; Fischer, D. A.; Zhang, P.; Sambandamurthy, G.; Banerjee, S. Electronic Phase Transitions of δ-$Ag_xV_2O_5$ Nanowires: Interplay between Geometric and Electronic Structures. *J. Phys. Chem. C* **2014**, *118* (36), 21235–21243.

(18) Yan, B.; Maggard, P. A. M(Bipyridine)V_4O_{10} (M = Cu, Ag): Hybrid Analogues of Low-Dimensional Reduced Vanadates. *Inorg. Chem.* **2007**, *46* (16), 6640–6646.

(19) Marley, P. M.; Banerjee, S. Reversible Interconversion of a Divalent Vanadium Bronze between δ and β Quasi-1D Structures. *Inorg. Chem.* **2012**, *51* (9), 5264–5269.

(20) Oka, Y.; Yao, T.; Yamamoto, N. Crystal Structures of Hydrated Vanadium Oxides with δ-Type V_2O_5 Layers: δ -$M_{0.25}V_2O_5 \cdot H_2O$ M=Ca , Ni. *J. Solid State Chem.* **1997**, *329* (132), 323–329.

(21) Clites, M.; Byles, B. W.; Pomerantseva, E. Effect of Aging and Hydrothermal Treatment on Electrochemical Performance of Chemically Pre-Intercalated Na–V–O Nanowires for Na-Ion Batteries. *J. Mater. Chem. A* **2016**, *4* (20),

7754–7761.

(22) Andrews, J. L.; De Jesus, L. R.; Tolhurst, T. M.; Marley, P. M.; Moewes, A.; Banerjee, S.; Jesus, L. R. De; Tolhurst, T. M.; Marley, P. M.; Moewes, A.; Banerjee, S. Intercalation-Induced Exfoliation and Thickness-Modulated Electronic Structure of a Layered Ternary Vanadium Oxide. *Chem. Mater.* **2017**, *29* (7), 3285–3294.

(23) Savel'ev, S. E.; Alexandrov, A. S.; Bratkovsky, A. M.; Williams, R. S. Molecular Dynamics Simulations of Oxide Memristors: Thermal Effects. *Appl. Phys. A Mater. Sci. Process.* **2011**, *102* (4), 891–895.

(24) Yao, T.; Oka, Y.; Yamamoto, N. Layered Structures of Hydrated Vanadium Oxides. Part 2. Alkali-Metal Intercalates $A_{0.33}V_2O_5 \bullet nH_2O$ (A = Na, K, Rb, Cs and NH_4). *J. Mater. Chem.* **1992**, *2* (3), 331–336.

(25) Yang, J. J.; Pickett, M. D.; Li, X.; Ohlberg, D. a a; Stewart, D. R.; Williams, R. S. Memristive Switching Mechanism for Metal/Oxide/Metal Nanodevices. Supp. *Nat. Nanotechnol.* **2008**, *3* (7), 429–433.

(26) Milic, N. B.; Jelic, R. M. Hydrolysis of Zinc(II) Ion in Sodium Nitrate, Chloride and Perchlorate Medium: The Effect of the Anionic Medium. *J. Chem. Soc. , Dalt. Trans.* **1995**, *3* (ii), 3597–3600.

(27) Giasson, G.; Tewari, P. H. Hydrolysis of Co(II) at Elevated Temperatures. *Can. J. Chem.* **1978**, *56* (4), 435–440.

(28) Baes, C. F.; Mesmer, R. S. The Hydrolysis of Cations. *Berichte der Bunsengesellschaft für Phys. Chemie* **1977**, *81* (2), 245–246.

(29) Parija, A.; Prendergast, D.; Banerjee, S. Evaluation of Multivalent Cation Insertion in Single- and Double- Layered Polymorphs of V_2O_5. *ACS Appl. Mater. Interfaces* **2017**, *9* (28), 23756–23765.

(30) Nightingale, E. R. Phenomenological Theory of Ion Solvation. Effective Radii of Hydrated Ions. *J. Phys. Chem.* **1959**, *63* (9), 1381–1387.

4. MIND OVER MATTER OR MATTER OVER MIND*

4.1. Overview

About a tenth of all energy produced goes towards storing, processing, and transmitting information. The trajectory of data generation has climbed sharply upwards in recent years but computing efficiency has not followed suit. The human brain provides an exemplar of energy-efficient computation. Neuromorphic computing aims to emulate and surpass the energy-efficiency of the human brain but requires an altogether new palette of neuron- and synapse-like materials. Here we discuss how the 'shuttling' of copper-ions in β′-$Cu_xV_2O_5$, drives electron density 'oscillation', triggering a transition from semiconducting to metallic properties, thus providing a means to approximate the spiking behavior of neurons within electrical circuits.

4.2. Societal Issues Addressed: At Moore's End

We live in a data-driven world where, for many, digital communication has emerged as the primary mode of human interaction. Some estimates suggest that by 2020, mankind will have accumulated nearly 50 zettabytes of data (50 billion terrabytes!).[1,2] Amidst the daily flurry of emails, social media uploads, and video

* Adapted from Andrews, J. L.; Handy, J. V.; Banerjee, S. Mind over Matter or Matter over Mind? A Cell Press InSITE Summary of: Parija, A.; Handy, J. V.; Andrews, J. L.; Wu, J.; Wangoh, L.; Singh, S.; Jozwiak, C.; Bostwick, A.; Rotenberg, E.; Yang, W.; Fakra, S. C.; Al-Hashimi, M.; Sambandamurthy, G.; Piper, L. F. J.; Williams, R. S.; Prendergast, D.; Banerjee, S. Metal—Insulator Transitions in β′-$Cu_xV_2O_5$ Mediated by Polaron Oscillation and Cation Shuttling, Matter, *2* (5), 1166-1186. Copyright 2020 Elsevier Inc.

calls, we often forget about what happens to the massive amounts of data that we generate. In 2018, the data centers responsible for processing our data devoured 205 terawatt-hours of energy, equivalent to 1% of global energy consumption.[1] Still larger amounts of data are discarded in the absence of a viable means of storage and processing. About 90% of data collected today is discarded within three hours without any analysis whatsoever.

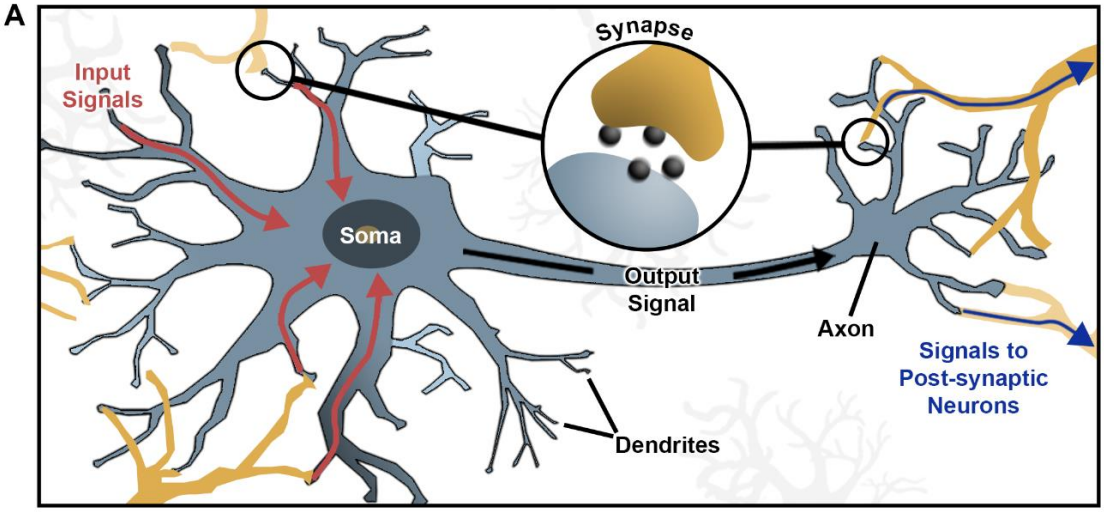

Figure 4.1. (A) Schematic representation of a neuron where input signals (red arrows) are received from 'pre-synaptic' neurons by dendrites, processed by the soma, and transmitted by the axon to 'post-synaptic' neurons (blue arrows) across connections called synapses (labeled inset). (B) Information is primarily encoded in the number of pulses received by the soma, as well as the time intervals between them. This is represented here as five separate input pulses received at five different time intervals, t_1—t_5, from four dendrites, D1—D4. (C) The pulses received across various synapses are integrated (*via* a non-linear summation process) by the soma of the neuron. If the summed pulses do not reach a critical threshold then the soma does not fire. However, if the summed pulses do reach a critical threshold then the neuron 'fires' a pulse. This is known as *thresholding*. The output pulse that is fired has a significantly higher potential than the input pulses, evidencing *amplification*.[4] Panel (D) is adapted in part from[5] and shows one such output pulse.

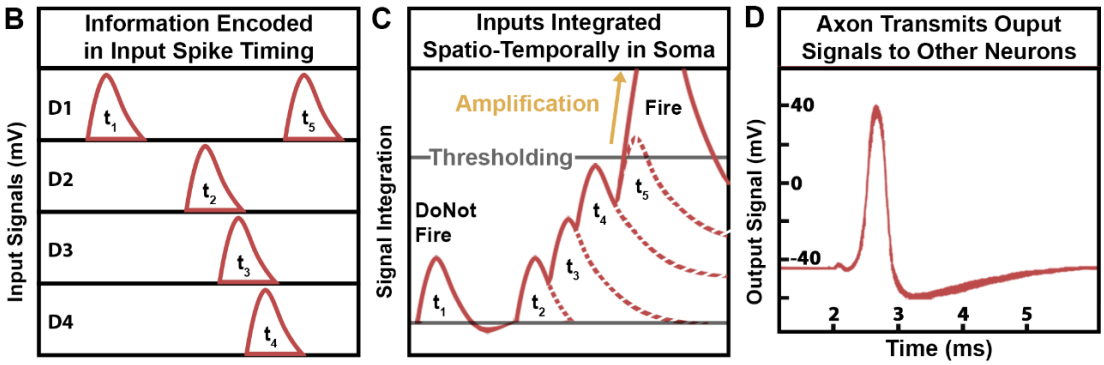

Figure 4.1. Continued.

Alarmingly, the volume of data collected annually (2 zettabytes in 2020) is projected to skyrocket about a millionfold by 2040.[1,2] Data centers are fast running out of tricks as hard-won efficiency improvements eked out over the years are squeezed to the maximum. Moore's law scaling, which described the performance of silicon-based computing for the past 40 years, (derived from shrinking devices to ever-smaller dimensions) has come to an end, thereby setting up a watershed moment in computing, and, by direct extrapolation, global energy consumption and our information-based economies.[3]

Dramatic improvements in computing capabilities and efficiencies are required to realize the promise of transformative visions such as the Internet of Things, autonomous vehicles, and personalized medicine, amongst other societal grand challenges, while staying within the stringent constraints of global energy production.[1,3] Fortunately, nature has provided a powerful exemplar of energy-efficient computing in the human brain, which uses massively interconnected synapses and neurons to perform memory, information processing, and

transmission functions within the same integrated fabric (Figure 4.1).[5] One can thus envision a new paradigm for computing structured around emulating the human brain.

4.3. The Particular Problem: Hacking the Brain

The brain has about 86 billion neurons, each connecting to $>10^4$ other neurons. [4–7] Information is encoded in the number and timing of pulses and stored in the connections between different neurons (Figure 4.1).[4] Collectively, neurons give rise to emergent behavior such as adaptive learning and enable the brain to process information in a dynamically evolving environment. The challenge for neuromorphic computing is to reproduce and surpass the profound complexity, throughput, and speed of the human brain within electronic circuitry.

Simply simulating brain-like computation using conventional silicon circuitry is exorbitantly energy-inefficient and requires many hundreds to thousands of transistors to perform the work of a single neuron.[8] By comparison, the human brain powers billions of neurons on about the same energy of a glazed donut (~300 calories).[4] An alternative approach to achieving brain-like computation is to design materials that mimic neuronal dynamics (Figure 4.1B-D).

Consequently, there is intense interest in designing materials that have in-built ‘instabilities’ so large that arriving pulses trigger abrupt transitions from insulating to metallic states (Figure 4.2B), thereby strongly altering the amplitude and timing of output pulses.

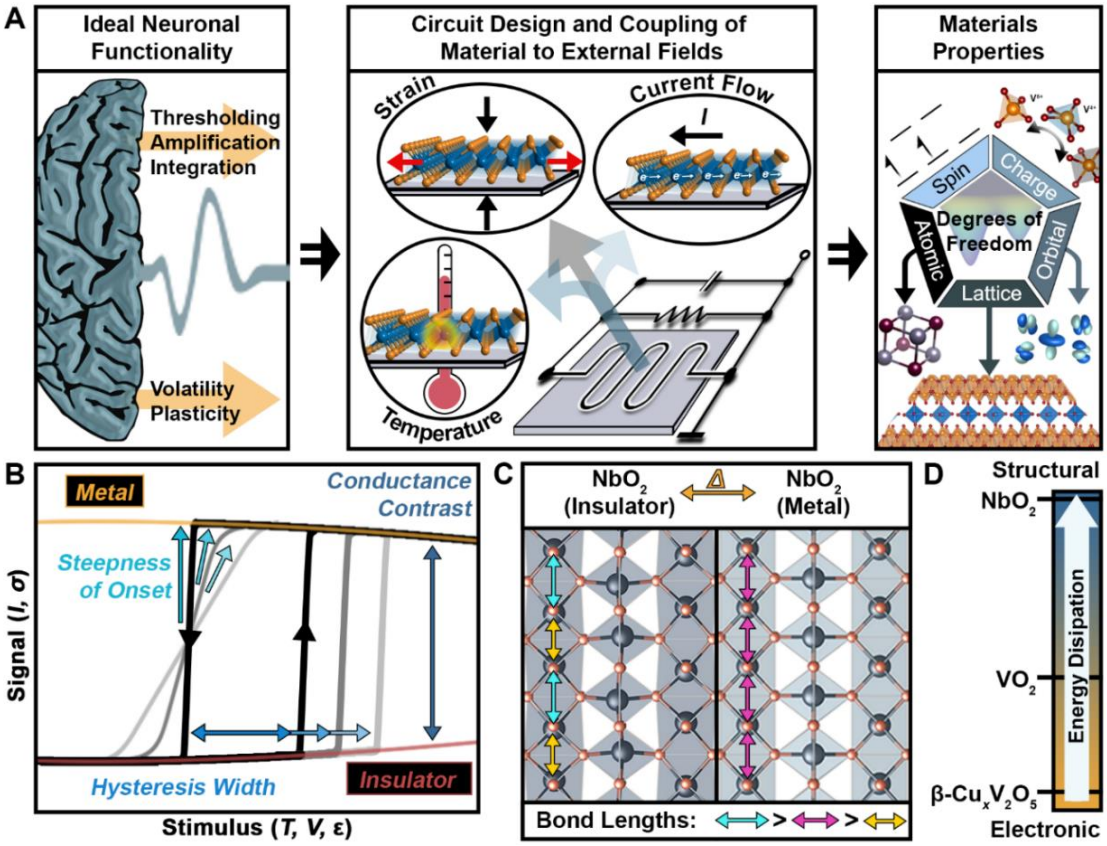

Figure 4.2. (A) The inverse design of materials for brain-like computation hinges on elucidating materials properties critical to emulating neuronal functionality and ultimately on the identification of physical mechanisms –like the one discovered for β′-$Cu_xV_2O_5$ and summarized here – that can be tuned for this purpose. (B) Schematic illustration of a 'metal—insulator' transition (MIT) as viewed on a current *versus* voltage plot (*i.e.*, '*I-V*' curve). *I-V* curves characteristic of materials that are purely metallic (gold trace) and insulating (red trace) are overlaid. Materials that undergo a MIT teeter at the cusp between the two states.[5,12,13] The MIT is reversible, but has a hysteresis (the reverse transition occurs a lower threshold). Tuning the hysteresis width, steepness of transition, and the conductance contrast map to neuronal characteristics of *volatility*, *thresholding*, and *amplification*. (C) An example of an energy-intensive structurally-derived mechanism that gives rise to a MIT in NbO_2. (D) Not all MITs derive from structural transitions. In β′-$Cu_xV_2O_5$, the transition has a substantial contribution from electron delocalization. It is helpful to think of these mechanisms as existing on a spectrum bookended by entirely structural or electronic scenarios.[5,13] Panels C and D adapted from reference [5]**.**

In NbO_2 (Figure 4.2C), a structural transformation causes the unpairing of niobium—niobium pairs and drives the initially insulating material to become a metal.[5,9,10] However, structural transitions requiring large displacements of atoms from their initial positions require a large amount of energy.[5,6,10] Electronic transitions, triggered by electron—electron repulsions and their screening, consume much less energy (Figure 4.2D).

The particular problem concerns the incomplete understanding of physical phenomena used to emulate neuronal function, stemming from insufficient knowledge of how the coupling of atomic connectivity and electronic states evolves in response to external stimuli (Figure 4.2A).[5,11–13] In work summarized here, we detail a new mechanism discovered in β′-$Cu_xV_2O_5$ wherein ionic shuttling and the accompanying dance of electrons drives a metal-to-insulator transition at low energy inputs.[11]

4.4. Understanding the Metal—Insulator Transition in β′-$Cu_xV_2O_5$

4.4.1. What We Looked at: The “Atomic” Texas Two-Step

β′-$Cu_xV_2O_5$ is a member of a broader family of $M_xV_2O_5$ materials (where ‘M’ is an intercalated cation drawn from across the periodic table). β′-$Cu_xV_2O_5$ exhibits a highly tunable MIT that displays a clear dependence on the copper stoichiometry, *x*, where $0.27<x<0.67$. Curiously, the electronic instability in β′-$Cu_xV_2O_5$ is not accompanied by a substantial distortion of the crystal lattice. The bonding and atomic connectivity of the tunnel-structured V_2O_5 framework are preserved up to the edge and across the transition, without notable contraction of

any vanadium—vanadium bonds.[13] Notably, copper in the structure exhibits an unusual “split-site disorder”, where any given copper atom resides in one of two closely positioned, but wholly distinct, sites within the tunnel (Figure 4.3A-C).[11]

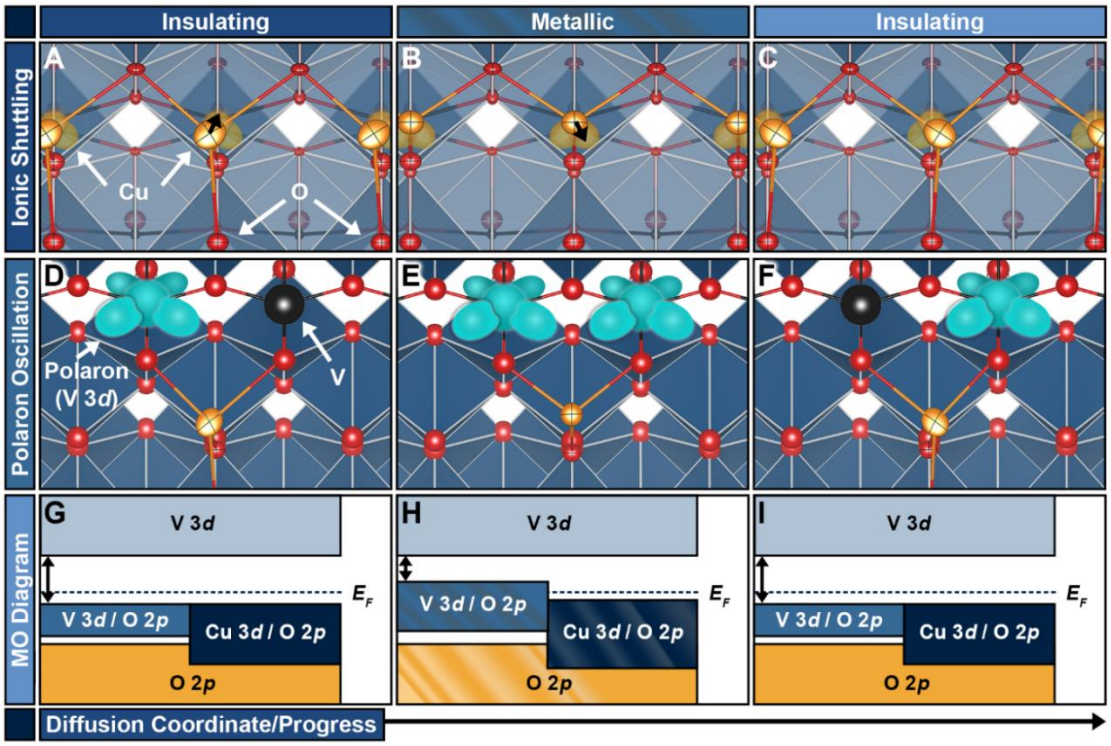

Figure 4.3. The back-and-forth two-stepping of the copper-ions between the two sites is highlighted in the top row (A-C) of the schematic. Electrons localized on vanadium sites also move back-and forth between neighboring vanadium atoms, closely mirroring the dancing of the copper-ions. This orchestrated ‘polaron oscillation’(*i.e.*, back-and-forth electron diffusion) is highlighted in the middle row of the schematic (D-F). The evolution of the electronic states of the material is represented using molecular orbital (MO) diagrams in (G-I).

The unexpected absence of a clear structural transition suggests a predominantly electronic origin of the transition, which is desirable for being less energy guzzling (Figure 4.2D). To definitively understand the underlying

mechanisms and to devise a means of precisely controlling the transition, a closer investigation of both the structural and electronic behavior of β′-$Cu_xV_2O_5$ across the phase transition was needed.

4.4.2. How We Did It: Learning the Texas Two-Step

Obtaining a complete perspective of both structural and electronic contributions to the MIT mechanism in β′-$Cu_xV_2O_5$ required the application of a diverse toolset of characterization techniques individually probing how the connectivity of atoms and the filling of electrons changes up to the edge and across the threshold of the metal-to-insulator transition. Being able to grow large single crystals enabled us to apply single-crystal X-ray diffraction to obtain a 3D atomic view of both the average position of copper atoms within the structure and their thermally driven motion, creating snapshots of the movement of the copper atoms between two adjacent sites inside the tunnels of β′-$Cu_xV_2O_5$. Extended X-ray absorption fine structure spectroscopy (EXAFS) measurements further allowed us to infer the delicate “two-step” of the ions between two adjacent split-sites. Spectroscopic techniques including resonant inelastic X-ray scattering (RIXS), X-ray photoelectron spectroscopy (XPS), and X-ray absorption spectroscopy (XAS) allowed us to probe how electronic states arising from hybridization between vanadium, copper, and oxygen orbitals evolve in response to the increasing motion of the copper-ions in the tunnel triggered by heat or current flow.

RIXS is a particularly powerful tool that uses X-rays to excite core-level electrons into specific unoccupied states. Electrons from other core levels cascade to fill the unstable core-holes resulting in the emission of an X-ray with lower energy than the incident X-ray.[14] We measured the energy of the emitted X-ray against the energy of the original X-rays to obtain a comprehensive view of both valence and conduction states in β′-$Cu_xV_2O_5$, and observed the closing of the bandgap with increasing temperature.[14] Finally, molecular dynamics (MD) simulations provided important insight into how the back-and-forth motion of ionic species pulls electrons into the dance, and closes the bandgap of β′-$Cu_xV_2O_5$. Each technique contributed a critical clue towards elucidating the MIT mechanism in β′-$Cu_xV_2O_5$.

4.4.3. What We Found Out: It Takes Two to Tango

Insights garnered using the above techniques outline a new type of predominantly electronic MIT mechanism (Figure 4.3). Single-crystal diffraction reveals that copper-ions shuttle between two distinct sites with a frequency that increases with temperature, blurring the separation between these sites (Figure 4.3A-C). However, it is not only the copper-ion that moves: the “two-step” of Cu-ions provokes a hullabaloo on the adjacent V_2O_5 framework.

For every copper atom in the tunnel of V_2O_5, one vanadium atom is reduced from V^{5+} to V^{4+}. In other words, a single electron resides on a vanadium atom. The localized electron charge subtly distorts the structure around the vanadium atom. The combination of the localized electron and the distortion constitutes a *small*

polaron. Critically, the negatively charged small polaron is trapped in the vicinity of the positively charged copper-ion. RIXS measurements reveal that below the MIT temperature, the polarons are trapped, but above it, as the copper-ions freely waltz between the two sites, freeing their accompanying polarons in the process.

MD simulations demonstrated that when a copper-ion is situated in the off-center position (Figure 4.3A or Figure 4.3C), the polaron is also trapped, as the electron coalesces into a “puddle” of charge around a singular vanadium atom (Figure 4.3D and Figure 4.3F) thereby exhibiting locally insulating behavior (Figure 4.3G and Figure 4.3I). However, when the copper-ion passes through the central site (Figure 4.3B), the polaron is delocalized across two vanadium atoms (Figure 4.3E), giving rise to a locally metallic phase (Figure 4.3H). Essentially, anytime the copper-ion moves, it drags its accompanying polaron like a hesitant dance partner from one vanadium to the next. When enough delocalized domains are linked together – as governed by the total number of copper-ions in the structure, and the frequency of shuttling (dictated by temperature, voltage, or current flow) — then the entire system is transformed to being metallic.

4.4.4. Why It Is Important: Through the Looking Glass

This work marks the first report of ionic shuttling as the driving force of an electronic instability and demonstrates its potential for realizing neuron-like behavior within an electrical circuit. Although a subtle structural change occurs in the material—the waltzing of copper-ions—the ionic shuttling spans only a fraction of a unit cell and requires minimal energy input since diffusion barriers are known

to be low in β′-$M_xV_2O_5$ materials.[12] The MIT is therefore primarily electronic in nature and is minimally energy dissipative, justifying the positioning of β′-$Cu_xV_2O_5$ on the low-energy end of the structural—electronic spectrum sketched in Figure 4.2D, approaching the ideal of Mott—Hubbard transition as required to achieve multiple orders of magnitude improvements in computing efficiency and speed over digital architectures.

This work also exemplifies an effective means of tackling the challenge of designing neuromorphic materials, illustrated in Figure 4.2. We have used multiple experimental techniques and theoretical simulations to examine dynamical changes in the relative connectivity of atoms and to map the concurrent changes of electronic states. Such an approach allows us to decipher mechanisms for neuronal emulation at the level of atoms and electrons, which is an imperative first step to developing tunable active elements for neuromorphic computing.[5,7]

4.5. Future Directions

4.5.1. Mimicking the Brain Means Jazzing Up the Materials Palette

The palette of materials available for neuromorphic computation is currently sparse in terms of functionality.[5] NbO_2 (Figure 4.2C) has been extensively considered but the structural transition underpinning its MIT is prohibitive in terms of energy consumption (approaching 6 fJ/spike).[5,6,9] An investigation of VO_2 as a neuromorphic computing material suggested that for VO_2 neurons to surpass energy efficiencies of biological neurons, a benchmark of <0.1 pJ/spike is required.[6] However, the transition temperature of VO_2 (67°C) is much

too low since processor temperatures exceed this threshold during routine operation.[6] Materials designed for neuromorphic computation therefore not only need to exhibit low-energy-dissipative MITs but they must also have sufficiently high transition temperatures (ideally ~400 K) to enable operation in dense circuits.

While some evidence suggests that the transition temperature of β′-$Cu_xV_2O_5$ can be optimized, the elucidation of a unique, electronic MIT mechanism has revitalized interest in an expansive, but previously overlooked, class of materials for neuromorphic computing.[5,12,13] $M_xV_2O_5$ materials offer many levers for tuning materials properties: the identity of the intercalated ion, 'M', its stoichiometry, '*x*', and the vanadium—oxygen atomic connectivity can be independently tuned to afford control over spin, charge, orbital, lattice, and atomic degrees of freedom (Figure 4.2A). Ultimately, a more diverse palette of materials exhibiting MITs needs be developed that can be switched at atto-Joule/spike energy and at switching times tunable from sub-ps to μs timescales. The switching properties further need to be mapped to functional neuronal characteristics.[5,12]

In addition to increased energy efficiency, neuromorphic circuits are capable of new types of computing such as adaptive learning, pattern recognition, optimization, and classification. Another next step for β′-$Cu_xV_2O_5$ is to harness the neuron-like behavior of individual circuits to build architectures capable of rapid-update learning in a dynamically evolving environment—crucial, for example, to a self-driving car trapped in Los Angeles traffic.

4.5.2. Ten Years from Now: AI on the Fly

The end of Moore's law scaling has sparked speculation about the future of computing. Neuromorphic computing distinguishes itself from other technologies by its promise of brain-like energy efficiency. The grand challenge articulated in a 2015 report by the Office of Science and Technology Policy is to: "…*create a new type of computer that can proactively interpret and learn from data, solve unfamiliar problems using what it has learned, and operate with the energy efficiency of the human brain*".[15] Developing a palette of **m**aterials **i**nspired by **n**euron **d**ynamics will allow for creation of such a computing paradigm and enable the impending torrents of data to be handled meaningfully without consuming a debilitating proportion of worldwide energy resources.

Neuromorphic computation will further facilitate computing 'at the edge of the internet' where energy supply is scarce. High-fidelity neuronal emulation at the edge will allow for the immediate updating of the system (learning) in response to external events, thereby realizing the full promise of artificial intelligence to learn and respond in real-time. As such, the design of new neuromorphic materials and emulation of the functioning of the human brain will enable physical systems to incorporate the ability to learn and process complex information in a rapid and energy efficient manner.

4.6. References

(1) Masanet, E.; Shehabi, A.; Lei, N.; Smith, S.; Koomey, J. Recalibrating Global Data Center Energy-Use Estimates. *Science* **2020**, *367* (6481), 984–986.

(2) The Data Deluge. *The Economist: Technology* [Online], Feb 27, **2010**. https://www.economist.com/weeklyedition/2010-02-27 (accessed Dec 2, 2020).

(3) Taylor, M. B. A Landscape of the New Dark Silicon Design Regime. *IEEE Micro* **2013**, *33* (5), 8–19.

(4) Gerstner, W.; Kistler, W. M.; Naud, R.; Paninski, L. *Neuronal Dynamics: From Single Neurons to Networks and Models of Cognition*; Cambridge University Press: Cambridge, 2014.

(5) Andrews, J. L.; Santos, D. A.; Meyyappan, M.; Williams, R. S.; Banerjee, S. Building Brain-Inspired Logic Circuits from Dynamically Switchable Transition-Metal Oxides. *Trends Chem.* **2019**, *1* (8), 711–726.

(6) Yi, W.; Tsang, K. K.; Lam, S. K.; Bai, X.; Crowell, J. A.; Flores, E. A. Biological Plausibility and Stochasticity in Scalable VO_2 Active Memristor Neurons. *Nat. Commun.* **2018**, *9* (1), 4661.

(7) Huang, H.-M.; Yang, R.; Tan, Z.-H.; He, H.-K.; Zhou, W.; Xiong, J.; Guo, X. Quasi-Hodgkin-Huxley Neurons with Leaky Integrate-and-Fire Functions Physically Realized with Memristive Devices. *Adv. Mater.* **2018**, 1803849.

(8) Merolla, P. A.; Arthur, J. V.; Alvarez-Icaza, R.; Cassidy, A. S.; Sawada, J.;

Akopyan, F.; Jackson, B. L.; Imam, N.; Guo, C.; Nakamura, Y.; Brezzo, B.; Vo, I.; Esser, S. E.; Appuswamy, R.; Taba, B.; Amir, A.; Flickner, M. D.; Risk, W. P.; Manohar, R.; Modha, D. S. A Million Spiking-Neuron Integrated Circuit with a Scalable Communication Network and Interface. *Science* **2014**, *345* (6197), 668–673.

(9) Pickett, M. D.; Medeiros-Ribeiro, G.; Williams, R. S. A Scalable Neuristor Built with Mott Memristors. *Nat. Mater.* **2013**, *12* (2), 114–117.

(10) Lee, W. C.; Wahila, M. J.; Mukherjee, S.; Singh, C. N.; Eustance, T.; Regoutz, A.; Paik, H.; Boschker, J. E.; Rodolakis, F.; Lee, T. L.; Schom, D. G.; Piper, L. F. J. Cooperative Effects of Strain and Electron Correlation in Epitaxial VO_2 and NbO_2. *J. Appl. Phys.* **2019**, *125* (8), 082539:1-10.

(11) Parija, A.; Handy, J. V.; Andrews, J. L.; Wu, J.; Wangoh, L.; Singh, S.; Jozwiak, C.; Bostwick, A.; Rotenberg, E.; Yang, W.; Fakra, S. C.; Al-Hashimi, M; Sambandamurthy, G.; Piper, L. F. J.; Williams, R. S.; Prendergast, D.; Banerjee, S.Metal-Insulator Transitions in B′-$Cu_xV_2O_5$ Mediated by Polaron Oscillation and Cation Shuttling. *Matter* **2020**, *2* (5), 1166-1186..

(12) Parija, A.; Waetzig, G. R.; Andrews, J. L.; Banerjee, S. Traversing Energy Landscapes Away from Equilibrium: Strategies for Accessing and Utilizing Metastable Phase Space. *J. Phys. Chem. C* **2018**, *122* (45), 25709–25728.

(13) Middey, S.; Chakhalian, J.; Mahadevan, P.; Freeland, J. W.; Millis, A. J.; Sarma, D. D. Physics of Ultrathin Films and Heterostructures of Rare-Earth

Nickelates. *Annu. Rev. Mater. Res.* **2016**, *46* (1), 305–334.

(14) Ament, L. J. P.; Van Veenendaal, M.; Devereaux, T. P.; Hill, J. P.; van den Brink, J. Resonant Inelastic X-Ray Scattering Studies of Elementary Excitations. *Rev. Mod. Phys.* **2011**, *83* (2), 705–767.

(15) Whitman, L.; Bryant, R.; Kalil, T. *A Nanotechnology-Inspired Grand Challenge for Future Computing*. The White House Blog. Oct 20, **2015**. https://obamawhitehouse.archives.gov/blog/2015/10/15/nanotechnology-inspired-grand-challenge-future-computing (accessed Dec 3, 2020).

5. CURVATURE-INDUCED MODIFICATION OF MECHANO-ELECTROCHEMICAL COUPLING AND NUCLEATION KINETICS IN A CATHODE MATERIAL*

5.1. Overview

Intercalation-induced phase transformations in Li-ion battery electrode materials give rise to multi-phase coexistence regimes within individual particles, generating significant lattice coherency strain across dynamically evolving interfaces. We demonstrate here that the lattice coherency strain can be alleviated by leveraging the coupling of electrochemistry, mechanics, and particle geometry to achieve controllable nucleation and deterministic ion transport. Here, we contrast singular kinks and continuous curvature as a means of enabling homogeneous lithiation without developing large stresses within a model cathode material, V_2O_5. The singular kink confirms that local curvature facilitates lithiation but also exacerbates lithiation inhomogeneities and elastic misfit strain. In contrast, the incorporation of continuous curvature enables homogeneous single-phase lithiation, mitigating lattice coherency strain. The studies provide a direct view of the coupling of mechanics and electrochemistry within crystalline

* Reprinted (adapted) with permission from Andrews, J. L.; Stein, P.; Santos, D. A.; Chalker, C. J.; De Jesus, L. R.; Davidson, R. D.; Gross, M. A.; Pharr, M.; Batteas, J. D.; Xu, B.-X.; Banerjee, S. Curvature-Induced Modification of Mechano-Electrochemical Coupling and Nucleation Kinetics in a Cathode Material, *Matter*, **2020**, *3* (5), 1754-1773. Copyright 2020 Elsevier Inc.

electrodes and suggest that mesoscale architectures can help resolve key failure mechanisms limiting the performance of energy-storage systems without sacrificing charge/discharge kinetics.

5.2. Introduction

5.2.1. Coupling Between Electrochemistry and Mechanics in Electrode Materials

Li-ion batteries rely on the coupled shuttling of Li-ions and electrons between anode and cathode materials during battery charge and discharge.[1,2] The insertion and extraction of Li-ions from an intercalation host drives the successive dilation and contraction of its crystal lattice. The intercalation-induced volumetric expansion and contraction of the electrode materials establishes a direct link between the mechanical properties of an intercalation host and its chemical reactivity. In addition to volume expansion, the insertion of Li-ions in a cathode material during discharge of a battery further brings about reduction of the transition metal centers of the intercalation host. As a result of the population of non-bonding and anti-bonding states, the effective bond order is reduced and metal—ligand bond lengths are often observed to increase.[3,4] Local structural distortions derived from Li-ion insertion propagate across the crystal lattice in the form of highly directional lattice stresses. The accumulation of stresses can strongly impact the cycle life of cathode materials, resulting eventually in the fracture and delamination of active electrode materials.[5,6] The coupling of chemistry and mechanics has been widely studied for anodic conversion reactions

such as the alloying of silicon (where a dramatic ~300% volume expansion is observed) [7–10], and in cathode materials, where the intercalation-induced volume changes are comparatively modest (generally <8%) but nonetheless represent significant deformations for brittle ceramics.[9,11–17] While chemo-mechanical coupling has been widely studied, a practical means of designing electrode materials to harness these relationships so as to both improve diffusion kinetics and mitigate volumetric expansion remains elusive. In this work, we use scanning transmission X-ray microscopy (STXM) and the spectroscopic signatures of differently lithiated phases to map the influence of curvature-induced lattice distortions on chemistry—mechanics coupling in a cathode material, orthorhombic V_2O_5, and further delineate the role of curvature in modifying nucleation kinetics in straight and kinked nanoribbons as well as continuously curved architectures.

The precise contours of intercalation-induced strain in cathode materials are governed by a number of intrinsic and extrinsic material properties including stresses developed from lattice mismatch with the substrate, inactive conductive additives, and intraparticle strain arising from phase segregation.[10,18–21] In the case of materials such as $LiFePO_4$ and V_2O_5 that exhibit miscibility gaps between Li-poor and Li-rich phases[14,22–24], the coexistence of several distinct crystallographic phases with disparate unit cell volumes and incommensurate lattices within the same particles gives rise to significant lattice coherency strain.[22,23,25,26] Understanding the evolution of intraparticle strain from singular unit

cell to mesoscale dimensions is critical to the design of mechanically resilient cathode architectures.

Attempts to address failure mechanisms stemming from the coupling of mechanics and electrochemistry[6,8,18,19,27,28] have focused on mitigating the consequences of lattice expansion through compositional modification (e.g., doping),[29,30] modulation of crystal structure and bonding through selection of polymorphs that avoid large displacive transformations,[11,31–34] the implementation of core-shell heterostructures to mitigate crack formation,[28,35] and the design of mesoscale architectures that are resilient to deformation under applied stresses.[17,36,37] Notably, the application of strain can accelerate or inhibit ion diffusion depending on the coupling of the strain fields with the crystal lattice. The relative displacement of atoms alters bond angles and bond lengths and thereby modifies both the electronic structure of strongly correlated systems and the coordination environments along ionic diffusion pathways.[4,32] In cathode materials, easing the coupled diffusion of Li-ions and polarons in the form of self-trapped quasiparticles is critically important,[32,38–41] suggesting that strain represents a promising avenue by which electrode performance can be improved.[16,17,41] Yet only recently have the effects of lattice strain been systematically explored as a potential means of improving the functional performance of Li-ion batteries.[15,42] Pint and coworkers demonstrate that the application of a modest biaxial tensile strain in the *ab*-plane of V_2O_5 (1.66%) can modulate the intercalation potential and improve the diffusion kinetics of Li-ions

by as much as 40 mV and 250%, respectively.[15] However, the promise of strain-induced performance improvements described in these works is limited practically by the need for epitaxial films for which strain is dissipated with increasing film thickness. Developing a means of incorporating elements of strain into powder electrodes, or alternatively for mitigating the evolution of intraparticle strain through the design of scalable mesoscale architectures, represents an important step towards leveraging mechanochemical coupling to improve battery performance.

5.2.2. Phase Inhomogeneities and Strain Evolution in the Orthorhombic V_2O_5 System

V_2O_5 represents a particularly interesting model cathode system as a result of its complex phase evolution upon Li-ion intercalation (Figure 5.1A and Figure A.1A). It is a quasi-layered material (Figure A.1B) with multiple accessible redox states and is in principle capable of accommodating up to 3 Li-ions per formula unit.[4] Despite its promise as a cathode material, orthorhombic V_2O_5 is plagued by sluggish electronic and ionic transport owing to the strong self-trapping of coupled [Li^+-(small polaron)] quasiparticles that contribute to the occurrence of multiple reversible (for $x < 1$ in $Li_xV_2O_5$) and irreversible (for $x > 1$ in $Li_xV_2O_5$) phase transitions (Figure A.1B—E).[18,38,40]

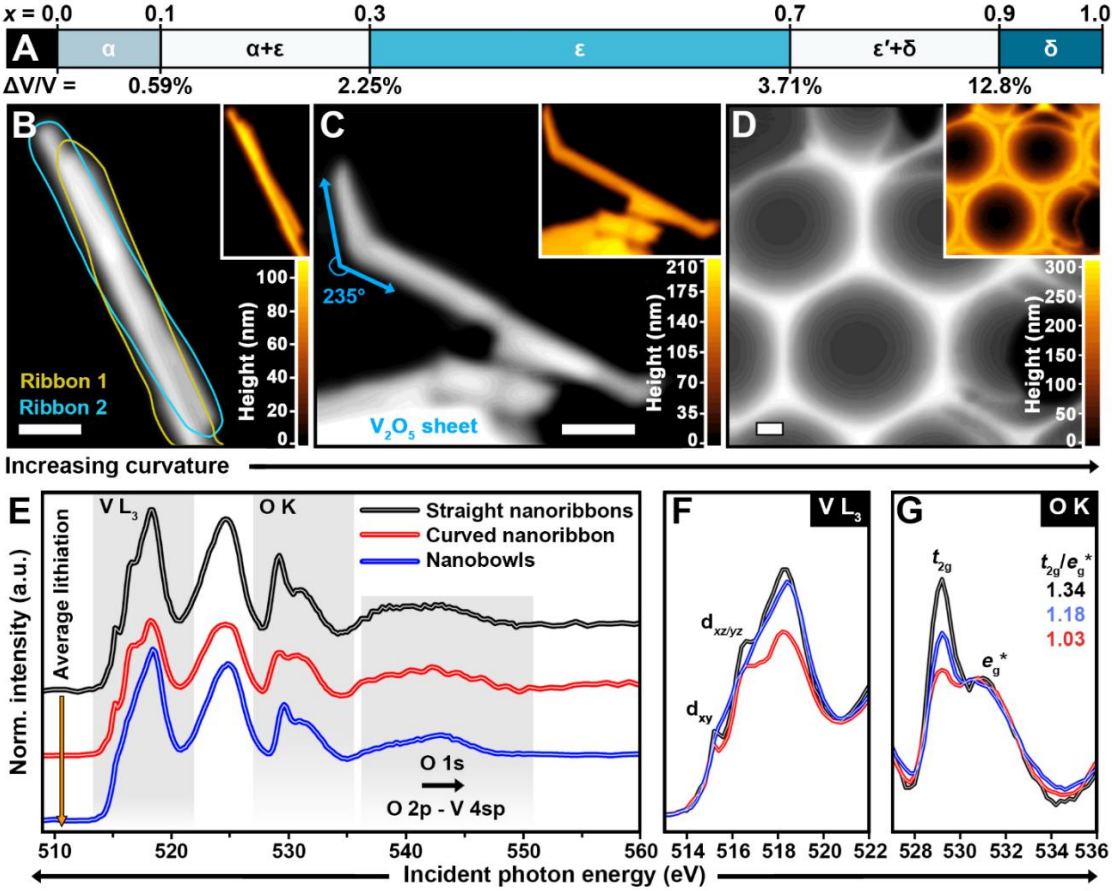

Figure 5.1. (A) Simplified phase diagram showing the evolution of unit cell volume expansion of α-V_2O_5 with increasing lithiation. A more detailed phase diagram compiled from an extensive review of the literature is provided in Figure A.1A. STXM optical-density images collected for (B) two closely-overlapped straight V_2O_5 nanoribbons; (C) a locally curved "kinked" V_2O_5 nanoribbon; and (D) a continuously-curved V_2O_5 nanobowl architecture prepared by colloidal crystal templating. A schematic clearly delineating three-dimensional interconnected nanobowls is provided in Figure C.2. The light blue and gold contours in (A) outline the boundaries of two overlapping nanoribbons. In (B), a V_2O_5 sheet situated near the curved/strained nanoribbon is also labeled. Thickness maps generated by normalization of the STXM image to an elemental profile are shown inset to (B-D). High-resolution thickness maps are provided in Figure C.3 and a direct comparison of thickness profiles for the various geometries is provided in Figure C.3D. (E) Integrated spectra obtained by averaging the spectra embedded at all pixels in the images in (B-D). The integrated spectra are arranged in order of increasing overall or "average" extent of lithiation (top to bottom). Regions of the (F) V L- and (G) O K-edge spectra are shown in greater detail. All scale bars: 500 nm.

Indeed, the intercalation of Li-ions into the layered structure of V_2O_5 induces several structural transformations, each accompanied by volume expansion, as summarized in Figure A.1, with the δ-LiV_2O_5 phase approaching a volumetric expansion of 12.8% with respect to orthorhombic V_2O_5.[43] With increasing Li-ion insertion and localization of electron density, the apical oxygens of the VO_5 square pyramids are canted towards the inserted lithium ions (black arrows, Figure A.1C and Figure A.1D) and the V_2O_5 layers pucker, giving rise to a relatively small decrease in the crystallographic *a* parameter of the unit cell and a relatively large increase in the crystallographic *c* parameter of the unit cell (the crystallographic *b* parameter changes little across the entire phase space). This necessarily gives rise to anisotropic lattice distortions resulting in compressive and tensile strain, respectively, as the material alternately experiences contraction and expansion along different crystallographic directions. As has been noted in the case of Li_xFePO_4, boundaries between these distinct phases of $Li_xV_2O_5$, each having significantly different lattice parameters and thus molar volumes (Figure 5.1 and Figure A.1), exist within the same particle thereby giving rise to substantial elastic misfit/coherency strain across the boundaries.[23,25,26]

STXM serves as a powerful nanoscale probe of electronic structure, enabling spatial domains with distinctive atomistic structure, chemical bonding, and disorder to be distinguished based on their individual spectroscopic signatures.[14,20,23,38,44,45] In this work, we map and contrast phase heterogeneities in V_2O_5 nanoribbons and mesostructured V_2O_5 3D architectures with increasing

extents of curvature, comparing a straight V_2O_5 nanoribbon, a locally curved V_2O_5 nanoribbon, and a continuously-curved interconnected V_2O_5 nanobowl architecture fashioned from colloidal crystal templating, shown schematically in Figure C.2. The studies provide fundamental insight into the role of geometric curvature in altering ion diffusion pathways and further illustrate a means of addressing the coupling of electrochemistry with mechanics to simultaneously accelerate kinetics of Li-ion diffusion while mitigating intercalation-induced stresses.

5.3. Results and Discussion

5.3.1. Scanning Transmission X-Ray Microscopy (STXM) as a Tool for Mapping Electronic Structure Inhomogeneities across Nanostructures

STXM imaging has revealed significant interparticle[20] and intraparticle[14,38] phase inhomogeneities in V_2O_5 cathode materials. The observed inhomogeneities within individual particles derive in part from the barriers to coupled Li-ion-small-polaron diffusion;[4,38,40] the trade-offs between surface-reaction-limited phase nucleation and propagation are further manifested as inhomogeneities across ensembles of particles ascribed to particle-by-particle lithiation (described as a “winner takes all” process) wherein sequential and not simultaneous lithiation is observed across collections of particles.[20,21] In order to map variations in electronic structure upon lithiation with high spectral and spatial resolution, we have used STXM to map chemical domains with increasing extents of curvature.[4,14,20,23,38,44] STXM images collected for a straight/unstrained

nanoribbon, a locally curved nanoribbon, and a continuously-curved V_2O_5 architecture are shown in Figure 5.1B-D.

V_2O_5 nanoribbons were synthesized according to a previously reported method as described in detail in the Experimental Section[46] and were determined to be phase pure by powder X-ray diffraction (Figure C.4A). The nanoribbons exhibit rectangular cross-sections with widths on the order of tens of nanometers and lengths on the order of several micrometers (Figure C.4B-I depict cross-sectional views of the nanoribbons illustrating their flat surfaces). The rectangular crystal habit is consistent with the orthorhombic crystal structure of α-V_2O_5. STXM further enables the visualization of sample thicknesses by normalization of data collected in transmission mode, as detailed in the Experimental Section. Height maps for the straight nanoribbon, locally curved nanoribbon, and the continuously curved V_2O_5 architectures prepared by colloidal crystal templating are shown inset to the STXM images in Figure A.1B—D.

Figure C.5 delineates the process for placing these materials onto silicon nitride grids where they are chemically lithiated using *n*-butyllithium. Each of the materials has been lithiated under the same conditions to facilitate direct comparison of observed lithiated domains (i.e., the materials were subjected to the same concentration of *n*-butyllithium and the same reaction time as described in more detail in Appendix C). The relatively short lithiation time used here ensures that the nanoribbons are not lithiated to completion and enables the viewing of a non-equilibrium ‘snapshot’ of the early stages of lithiation where compositional

inhomogeneity is significant. Statistical image analysis tools, including principal component analysis (PCA), pixel clustering analysis, and singular value decomposition (SVD), are used to obtain rich quantitative chemical maps of lithiated domains that further enable mapping of stress across individual particles as per Figure C.6.

Integrated spectra obtained by averaging across all the pixels in each image are shown in Figure 5.1E. Three regions of the XAS spectra are highlighted corresponding to excitations of core electrons: the V L_3-edge absorption (513—522 eV) arises from transitions from singlet V $2p^6 3d^0$ to V $2p^5 3d^1$ states that are further split by crystal field and multiplet effects; the O K-edge X-ray absorption features (527—536 eV) arise from transitions from O 1s core levels to hybrid V 3d—O 2p states, which are further split by quasi-octahedral (i.e., VO_{5+1}) crystal field splitting into t_{2g} and e_g* manifolds; and a broad feature that arises from transitions from occupied O 1s states to unoccupied hybridized O 2p—V 4sp states (535—550 eV).[47] The lineshapes at the V L_2-edge (521—529 eV) are dominated by a Coster-Kronig Auger decay process from an occupied $2p_{1/2}$ state into the $2p_{3/2}$ hole and are therefore difficult to interpret in terms of electronic structure.[38,47] The relative intensities, line shapes, peak positions, and splitting observed at the V L_3-edge and O K-edge t_{2g}/e_g* manifold provide a rich view of the evolution of lithiated phases in V_2O_5 materials.[4,14,31,38,45] As such, expanded views of these regions are provided in Figure 5.1F and Figure 5.1G and throughout this article. The V L_3-edge comprises two prominent features

corresponding to transitions from occupied V 2p core levels to unoccupied states with V $3d_{xy}$ (split-off conduction band)[38,47] and V $3d_{xz/yz}$ character at the bottom of the conduction band of V_2O_5 (centered at 515.2 and 516.4 eV, respectively). The spectral intensity of these absorption features is directly correlated to the availability of empty states; the features are most intense prior to lithiation as a result of the nominally d^0 character.[34] Upon Li-ion intercalation, electrons have been shown to localize in the narrow V $3d_{xy}$ split-off conduction band, which is separated by a small gap from the bottom of the conduction band.[4,38,40] Indeed, such electron localization within narrow $3d_{xy}$ states is a characteristic signature of small polaron formation. Consequently, with increasing extent of lithiation, previously unoccupied V $3d_{xy}$ states are filled by electrons and the spectral features derived from these empty states 'darken' and diminish in intensity owing to Pauli blocking.[38] The same trend is observed for the $d_{xz/yz}$ feature, highlighted in Figure 5.1F which similarly 'darkens' at still higher levels of lithiation. The sensitivity of the fine structure at the V L_3-edge provides a means to evaluate the pixel-wise extent of lithiation.

The O K-edge region is similarly informative in assessing the extent of lithiation and the evolution of electronic structure but for entirely different reasons.[38] The O K-edge spectra are not convoluted by multiplet effects and exhibit two sets of transitions from O 1s to hybrid V 3d—O 2p states, closely approximating the t_{2g} and e_g* character expected from the crystal field splitting for a quasi-octahedral VO_{5+1} structure. Based on time-dependent density functional

theory (TD-DFT) calculations, the t_{2g} absorption features are attributed primarily to transitions from O 1s core states of the V=O oxygens in VO_5 square pyramids to O $2p_x/2p_y$ states hybridized with V $3d_{xz}$ and $3d_{yz}$ states (with a much more modest contribution derived from transitions from O 1s core levels of bridging oxygen atoms to O $2p_y$ states mixed with V $3d_{xy}$ states). The relative ratio of the t_{2g} to e_g* features serves as a key diagnostic of the extent of lithium intercalation. The diminution of the t_{2g} feature intensity with increasing lithiation results not from Pauli blocking as in the case of the fine structure at the V L-edge, but from the strong distortion and lengthening of the V=O vanadyl bonds illustrated in Figure A.1B and Figure A.1C along with incipient electron correlation as the V $3d_{xy}$ band is partially filled. The emergence of electron correlation results in a lifting of spin degeneracy and the spin-splitting of the V 3d states, which brings about a sharp decrease in the intensity of the primary t_{2g} absorption band. The distortion of the vanadyl moieties also shifts the V $3d_{xz}$ states to higher energies, resulting in the spectral weight diminishing in the t_{2g} manifold and being shifted to higher energies. As such, the ratio of the intensities of the t_{2g} to e_g* manifolds is observed to decrease with increasing extent of lithiation. These ratios are provided throughout this work to facilitate comparison of spectra. The final highlighted region corresponds to transitions from O 1s to hybridized O 2p—V 4sp states.[20] STXM data and spatially-resolved spectra will be interpreted on the basis of these assignments and on the basis of previously reported V L-, O K-edge spectra collected for stoichiometrically-lithiated $Li_xV_2O_5$ materials that allow for

assignment of relative spectral intensities at both the V L-edge and the O K-edge to the extent of lithiation *x* in $Li_xV_2O_5$.[38]

Notably, despite following the same chemical lithiation procedures and conditions (i.e., reagent concentration, lithiation time), substantial differences are observed in the integrated spectrum acquired for each sample, plotted in Figure 5.1E. The spectra compared in Figure 5.1E-G are “average” spectra in the sense that they are obtained by integrating the spectra obtained from every pixel present in the STXM image and thus each $Li_xV_2O_5$ phase present within the imaged material. As such, they are composite spectra comprising spectra from each phase present in the material, weighted by the number of imaging elements containing that phase. This is distinct from the spectra shown in Figure 5.2-4 (*vide infra*) which are obtained by principal component clustering analysis of the spectra and more accurately reveal spatial distribution of differently lithiated phases within individual particles. The spectra are arranged in order of increasing extent of lithiation from top to bottom as evidenced by decreasing intensity of the V $3d_{xy}$ and $3d_{xy/yz}$ features. Although both the V L_3-edge and O K-edge regions (as shown in Figure 5.1F and Figure 5.1G, respectively) are used to assign extent of lithiation throughout the manuscript, since the integrated spectra shown in Figure 5.1 are composite integrated spectra across the entire image, the intensity of the V L_3-edge can most reliably be used to interpret the average extent of lithiation since the darkening of V L_3-pre-edge features can be used as a direct means of evaluating the formal vanadium oxidation state or state of charge. A methodology

for quantitative assignment of the extent lithiation at each pixel (instead of average lithiation of the imaged sample) with reference to standards is delineated below.

Critically, the increase in the extent of lithiation does not track with decreasing diffusion pathlength (Figure C.3D), but rather follows the opposite trend since the much thicker 3D nanobowl architecture is most lithiated. Figure C.3D shows that the width of the straight nanoribbon is smaller than the kinked nanoribbon. Both are far smaller than the width of the continuously curved 3D architecture, even nearing its thinnest point (i.e., the ridge between two bowls). Contrary to what is expected from simple consideration of diffusion pathlengths alone, the thickest material is the most highly lithiated for the same lithiation conditions. The straight/unstrained nanoribbons (Figure 5.1B) exhibit a relatively low extent of lithiation, whereas the locally curved nanoribbon (Figure 5.1C) exhibits an average extent of lithiation intermediate between the two (albeit with substantially greater inhomogeneity as will be discussed below). The continuously curved V_2O_5 architecture exhibits a markedly greater extent of lithiation compared to the nanoribbons, as evidenced by the complete disappearance of all fine structure at the V L_3 edge, characteristic of the formation of a highly lithiated ε-$Li_xV_2O_5$ phase (x = 0.6).[4,14,20,38,47] Given the identical lithiation conditions, it follows that the observed rate of lithiation of the V_2O_5 materials in Figure 5.1B-D instead correlates to increasing curvature. The observed relationship between increasing lithiation rates at higher curvatures parallels the effects of applied strain.[15,42] Mapping of mesoscale domain formation through region-of-interest (ROI)

analysis, PCA, and SVD provide meaningful insight into the spatial distribution of lithiated phases between and within individual particles. The STXM images collected for the three particle morphologies shown in Figure 5.1B-D are evaluated using these techniques in greater detail below. The role of geometric curvature in enhancing lithiation is discussed with regards to anisotropic lattice expansion of the V_2O_5 material and its concomitant directional change of Li-ion diffusivity.

5.3.2. Surface-Limited Inhomogeneous Lithiation in a V_2O_5 Nanoribbon

Figure 5.1B shows the optical density STXM image for two overlapped straight nanoribbons representing the no-curvature condition. Region-of-interest analysis (ROI) for these unstrained nanoribbons is provided in Figure C.7. ROI analysis reveals compositional inhomogeneities, particularly when contrasting the spectra obtained by integrating near the end of the first nanoribbon (labeled as ROI-3 and ROI-5) and the spectra obtained for the interior of the nanoribbon (labeled as ROI-1). In order to develop a more detailed perspective of the local phase distribution, PCA has been performed (Figure C.8)[14,38,48] and has been coupled with pixel clustering analysis (PCA-clustering analysis, Figure 5.1D) to enable the comparison of the spatial distribution of spectrally similar XAS spectra (e.g., in Figure 5.1A).[48] These spectra are distinct from the spectra shown in Figure 5.1 (which are integrated spectra) in that they delineate distinct regions of the material that have spectral features that are clustered based on their similarity. Interpretation of the clustered spectra in Figure 5.2A-C reveals that the regions

corresponding to Cluster 4 are most lithiated whereas the regions corresponding to cluster 3 are least lithiated.

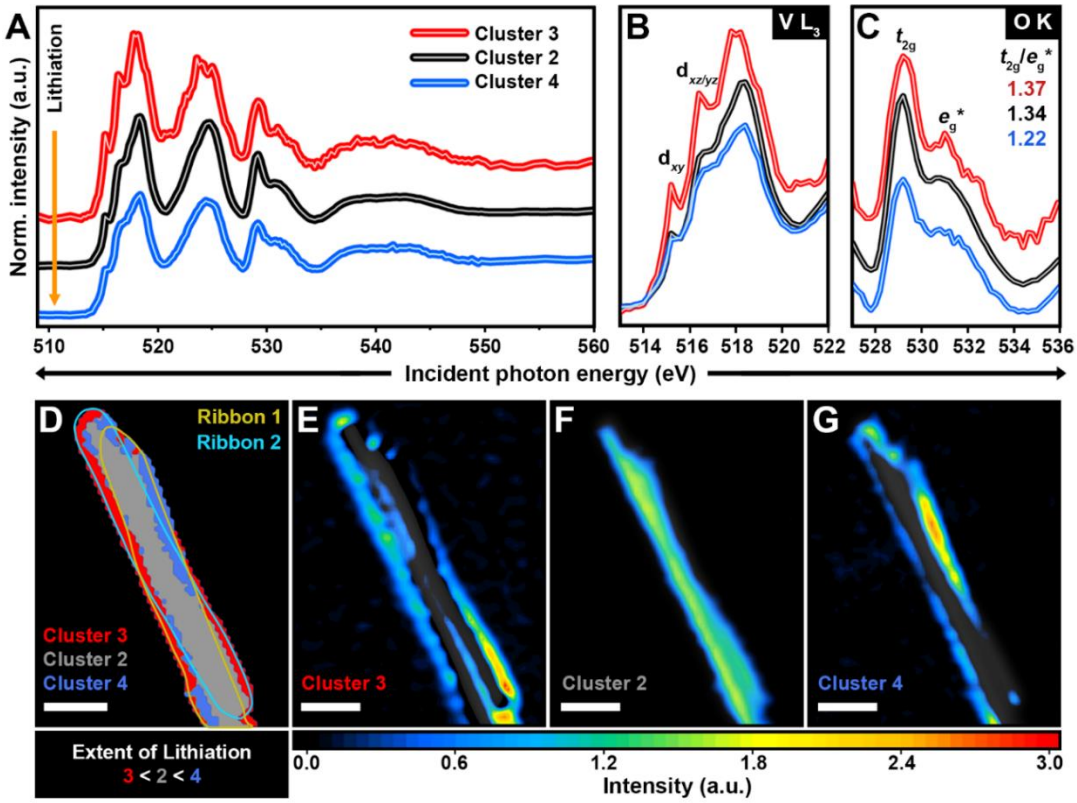

Figure 5.2. (A) Spectra derived from clustering of pixels scored using PCA of the STXM image of an unconstrained pair of straight nanoribbons upon lithiation (Figure C.6 outlines the data processing workflow). The pre- and post-edge normalized spectra are ordered according to increasing lithiation (top to bottom). Panels (B) and (C) highlight the evolution of V L_3- edge features (513—522 eV) and O K-pre-edge features (527—536 eV), respectively. Panel (D) shows the spatial grouping of the spectra in (A) according to PCA where the apparent extent of lithiation increases going from red to grey to blue. (E-G) Intensity maps showing the weighted contribution of the spectra in (A) to each pixel in the STXM image. The Cluster 3 map (E) corresponds to the red spectrum, the Cluster 2 map (F) corresponds to the black spectrum, and the Cluster 4 map (G) corresponds to the blue spectrum. The colored legend quantifies the relative weighting of the cluster spectra at each pixel. The maps in (E-G) are in order of increasing lithiation. Figure C.7 and Figure C.8 depict the ROI and PCA analysis used to identify distinctive lithiated domains and develop the phase maps in (E—G). Scale bars: 500 nm.

The spatial arrangement of the clusters indicates that the smaller nanoribbon (Ribbon 1, ~270 nm in width) is more highly lithiated as indicated by localization of the blue component around the visible edges of the ribbon. In contrast, ribbon 2 (~330 nm in width), which is viewed parallel to the basal planes (down the layer stacking direction, as shown in Figure C.9), shows core—shell lithiation with the edges being sparsely lithiated and the interior showing a relatively higher extent of lithiation. The observation of core—shell behavior derives from the specific orientation of the nanoribbons on the substrate as described in greater detail in the (Figure C.9) and is further consistent with surface-limited lithiation along the crystallographic *c*-direction between the V_2O_5 layers, and limited Li-ion insertion transverse to the layers.[14,20] The PCA-clustered spectra obtained for this sample (Figure 5.2A-C) were used as input spectra for SVD analysis, as shown in Figure 5.2E-F, which further elucidate the contributions of the input spectra to the spectrum at each pixel in real space. Both nanoribbons exhibit core-shell behavior but ribbon 1 is overall more lithiated (ε-$Li_{0.3}V_2O_5$ and α-$Li_{0.1}V_2O_5$), whereas ribbon 2 is less lithiated (α-$Li_{0.1}V_2O_5$ and α-V_2O_5). As shown in Figure A.1, these compositions correspond to nearest-neighbors in the phase diagram. The origins of the different extents of lithiation for the nanoribbons derive in part from geometric irregularities (which drive preferential lithiation fronts)[49] compounded by particle-by-particle lithiation since the wires are in close contact.[20,21,50] In a reaction-limited regime as is typical of lithiation in phase-separating electrodes,[51,52] geometrical features such as sharper edges for the

thinner nanowire can drive heterogeneities altering the local ionic flux that mediates the preferential initiation and propagation of reaction fronts, compounded further by hotspots arising from kinetic, ohmic, and entropic processes.[51,53] Critically, multiphase core-shell behavior within individual particles induces a significant amount of elastic misfit strain at the interface between $Li_xV_2O_5$ phases as a result of lattice incommensurability and the differential in the volumes of the two dilated phases with varying extents of lithiation (Figure 5.1A and Figure A.1).[14,15,43,54] Figure C.10 exhibits additional examples of the core—shell motif observed for straight nanoribbons upon lithiation.[14,38] Core—shell behavior has further been evidenced across ensembles of nanoribbons by using Raman spectroscopy to probe surface lithiation and powder X-ray diffraction to probe nanoribbon interiors.[46] For thin nanoribbons, wherein the scaling factor of the elastic misfit penalty is low, charge striping behavior has been evidenced characterized by the appearance of periodic nanoscopic domains as a result of coherency strain.[26] We have next mapped the effects of curvature on the spatial organization of lithiation patterns both in individual nanoribbons as well as continuously-curved architectures, with a view towards correlating lithiation patterns with accumulated stresses.

5.3.3. Curvature-Assisted Lithiation Induces "Hot Spot" in a Bent V_2O_5 Nanoribbon

Hydrothermal synthesis yields a notable fraction of nanoribbons with curved defects (Figure 5.1C, Figure C.11 and Figure C.12) that have the potential

to induce anisotropic stress fields and thereby modify the kinetics and consequently the spatial distribution of lithiation. Several such kinks have been shown to profoundly modify the spatial distribution of lithiation within individual particles[20] but a quantitative mapping with high spatial resolution has not thus far been performed. Several such nanoribbons incorporate defects that induce one or more (Figure C.12) approximately 45° kinks along the V_2O_5 basal plane. Transmission electron microscopy (TEM) images shown in Figure C.12 clearly evidence stacking faults that induce a change in growth direction and the introduction of accompanying local curvature. Figure C.13 shows a SEM image (also included as an inset to Figure 5.3E) of the curved nanoribbon corresponding to the STXM image shown in Figure 5.1C, which has been lithiated “on-substrate” using conditions exactly paralleling the straight nanoribbons in Figure 5.2 as per the workflow described in Figure C.5. The nanoribbon exhibits a singular ~45° kink near one terminus, likely derived from a stacking fault. As discussed above and as shown in Figure 5.1, the curved nanoribbon exhibits an overall greater extent of lithiation as compared to the unstrained nanoribbon (Figure 5.2); however, the integrated spectrum shown in Figure 5.1E does not accurately represent the vastly different lithiation extents across the curved nanoribbon. The bent nanoribbon was lithiated and analyzed by STXM (Figure 5.3).

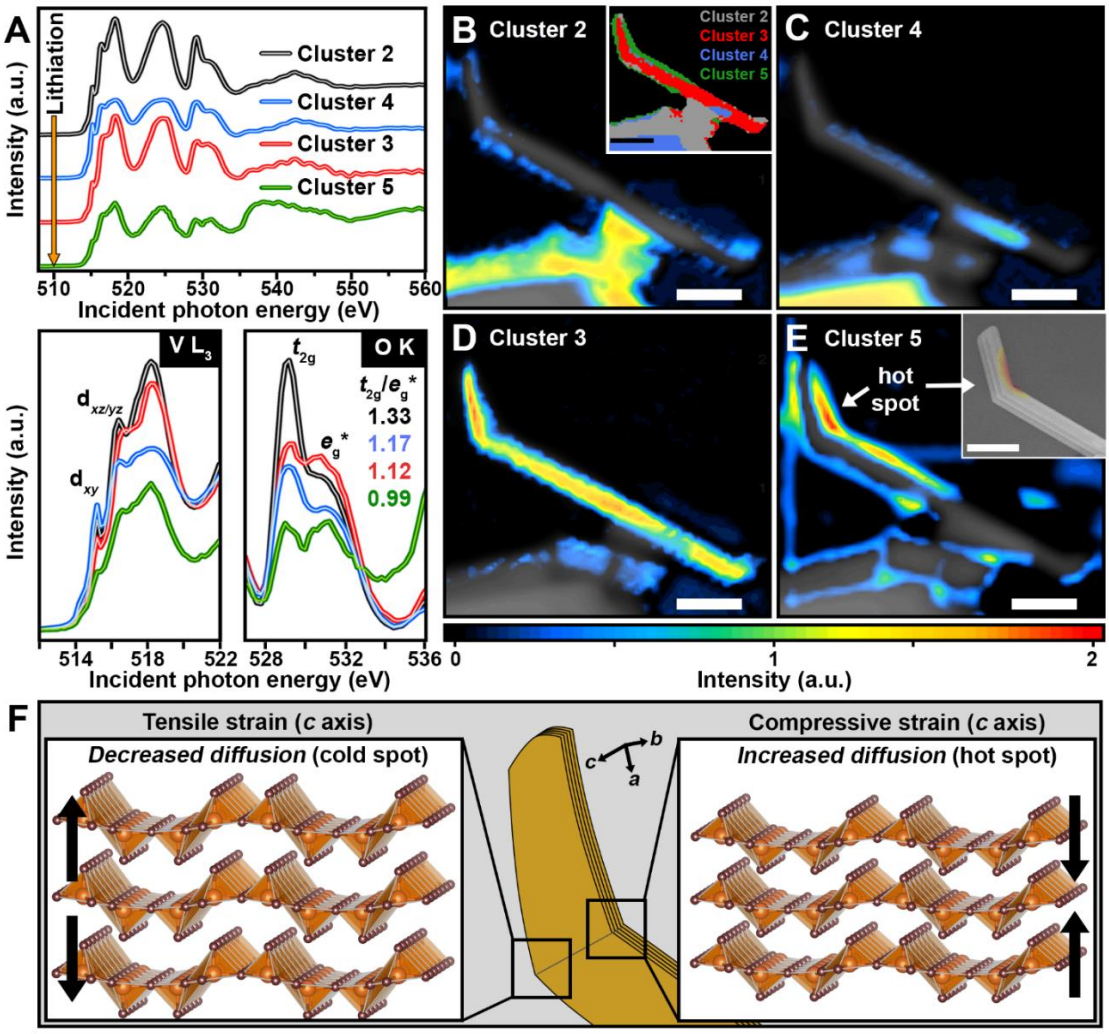

Figure 5.3. (A) Spectra obtained by PCA-clustering of the pixels shown for the locally curved nanoribbon shown in Figure 5.1C. The pre- and post-edge normalized spectra are offset in order of increasing lithiation (top to bottom). The lower panels highlight the V L_3-edge features (513—522 eV) and the O K-pre-edge features (527—536 eV), respectively. (B-E) Intensity maps generated using the PCA-clustering-derived spectra in (A) as input. The maps in (B-E) are in order of increasing lithiation. The PCA clustering image (also shown in Figure C.15) is shown inset to panel D. A scanning electron microscopy (SEM) image of the ~45° kink in the nanoribbon is shown inset to panel G, where the hot spot location formation is overlaid in false color. Scale bars: 500 nm. (F) Schematic detailing the mechanistic origins of “hot spot” and “cold spot” formation in the locally-curved V_2O_5 nanoribbon.

ROI analysis of hyperspectral STXM data is shown in Figure C.14 reveals significant local inhomogeneities within the V_2O_5 nanoribbon, as evidenced by substantial changes in fine structure at the V L_3-edge and large variations of the t_{2g}/e_g* ratios at the O K-edge (Figure 5.3A). PCA-cluster analysis performed for the curved nanoribbon is shown in Figure C.15 and highlights the spatial distribution of distinctive lithiated domains as also shown in the inset to Figure 5.3B. PCA-clustering analysis suggests that the nanoribbon is significantly more lithiated at or around the inside of the kink (i.e., Cluster 5, green, corresponding to an area under residual compressive stress) as compared to the rest of the nanoribbon and adjacent sheet (i.e., regions corresponding to Clusters 3 and 4) There further appears to be a small region of relatively unlithiated V_2O_5 on the outside of the kink of the nanoribbon (i.e., Cluster 2, corresponding to an area under tensile strain). Figure 5.3B-E maps the results of SVD analysis performed using the PCA-clustered spectra shown in Figure 5.3A as input. The nanoribbons, which grow with kink defects, likely have residual strain around the defects; the inner edge of the defect, which is likely to be under compressive strain, is found to be the most lithiated region of the nanoribbon as shown in Figure 5.3E, revealing the formation of a “hot spot”. In contrast, the outer edge of the kink in the nanoribbon (which is likely under residual tensile strain) shows a well-defined band corresponding to low levels of lithiation (Cluster 2), representing a “cold spot”. The adjacent, much thicker, sheet is also sparsely lithiated. In other words, clear “hot” and “cold” spots can be resolved at concave and convex regions of the

curved nanoribbon, respectively. The formation of a hot spot in the vicinity of a region of compressive strain is somewhat counterintuitive since most materials have been shown to exhibit decreased ionic diffusion when subject to compressive strain.[16,17,41] However, the sign (i.e., positive or negative) of the coupling between strain and Li-ion diffusion is dependent on the crystal structure and crystal orientation and is determined by the coupling of these attributes with the directionality of the strain vector. Indeed, compressive strain along the *c* axis in V_2O_5 (corresponding to the interlayer spacing) has been shown to dramatically improve Li-ion diffusivity and, conversely, tensile strain along the *c* axis has been shown to decrease Li-ion diffusivity.[15] TEM images of a kink defect in Figure C.12 suggest that the kink in the nanoribbon is along the *ab*-plane, corresponding to compression of the *c* direction along the interior of the kink. This is shown schematically in Figure 5.3F.[4,31,32] It is furthermore likely that the kink, which alters the strain field in its vicinity, further acts as a nucleation site for the kinetically-limited lithiation phenomenon. The generation of a compositional hot spot in the vicinity of the kink, which is spatially confined, likely contributes to a lithiation "feedback loop". Increased lithiation of the concave side of the nanoribbon as a result of residual compressive strain causes the material to expand into a spatially-constrained area, further generating stress concentrators in response to the reaction front.[55] The increased compressive stress further increases the rate of diffusion in the vicinity of the kink exacerbating the differences in lithiation between the concave and convex regions. Local curvature can thus serve to preferentially

nucleate Li-ion intercalation, generating “hot spots” for Li-ion concentrations and driving phase separation patterns. Notably, SVD analysis (Figure 5.3) indicates that curvature can induce substantially increased lithiation in V_2O_5; however, in the case of local curvature, “hot spot” formation gives rise to local inhomogeneities since the extent of lithiation in the vicinity of the defect is markedly different from the rest of the particle. As such, this observation delineates the need for continuous curvature to homogeneously accelerate lithiation kinetics without accumulating coherency strain across the electrode.

5.3.4. Incorporating Continuous Curvature in Colloidal Crystal Templated Architectures to Improve Phase Homogeneity and Reduce Intercalation-Induced Stress

In order to incorporate continuous curvature such as to obtain rapid kinetics of Li-ion intercalation without forming local hot spots that result in coherency strain, we have examined the lithiation of continuously curved 3D architectures formed by colloidal crystal templating. Thin film electrodes constituted from continuously curved V_2O_5 3D architectures show an order of magnitude improvement in the Li-ion diffusion constants relative to continuous V_2O_5 thin films in half-cell measurements ($D_{Li^+} = 4.7 \times 10^{-13}$ and 4.6×10^{-10} $cm^2 \cdot s^{-1}$ for continuous film and inverse 3D architectures, respectively)[36,56,57] but the specific physical origins of the improved rate performance and the patterns of phase separation remain to be elucidated. To investigate the role of continuous curvature, V_2O_5 3D architectures (monolayer inverse opal structures) have been grown onto silicon

nitride substrates as described in the Experimental Section. Using a modified Blodgett-trough method, a monolayer of the inverse opal structure was grown on a substrate that incorporated 2 μm patterned holes in the silicon nitride substrate (same order of magnitude in size as the 2.5 μm polystyrene spheres). Phase-pure α-V_2O_5 structure was confirmed using Raman spectroscopy (Figure C.16A). Raman modes are labeled using assignments from previously reported work.[46,58] The morphology and texture of the films was evaluated by SEM (Figure C.16B) and TEM (Figure C.17). Figure C.17 illustrates the formation of single-crystalline domains of V_2O_5 following annealing with the basal planes aligned parallel to the silicon nitride substrate.

As shown in Figure 5.1, despite lithiation conditions identical to the straight and locally curved nanoribbons, the continuously curved patterned architecture exhibits a significantly higher average extent of lithiation, indicative of increased diffusion of lithium within the structure. The observed improvement in the kinetics of diffusion derives in part from the porous structure that promotes enhanced electrolyte wetting of the V_2O_5 surface[36,46,57] In remarkable contrast to the unstrained nanoribbon (Figure 5.2) and the curved/strained nanoribbon (Figure 5.3), PCA-clustering analysis of the colloidal crystal templated sample, shown in Figure C.18, indicates almost no inhomogeneity locally within ligaments or globally across the imaged area from one honeycomb region to another. Figure C.20 and Figure C.21 show similar homogeneity for two additional continuously curved 3D architectures prepared by colloidal crystal templating. These additional

3D architectures were lithiated using increased *n*-butyllithium concentrations for extended times (1 h) and thereby exhibit a subtly higher degree of lithiation. In contrast to the straight and bent nanoribbons, where distinctive modulations of the relative intensities and peak positions of the V 3d-derived fine structure and O K-edge spectra are observed, these components exhibit few changes in the relevant regions of the V L-/O K-edge spectra.

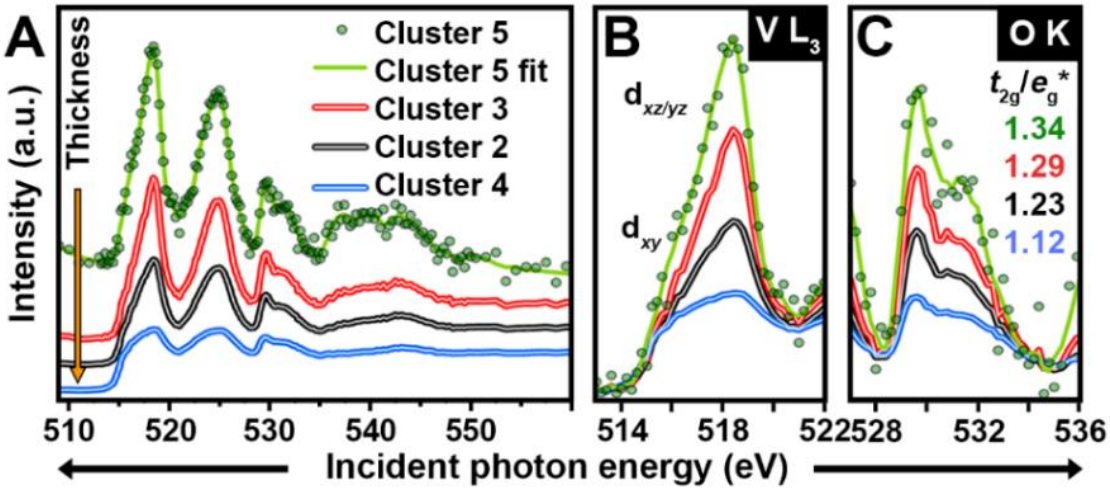

Figure 5.4. (A) Spectra obtained by PCA-clustering of the continuously curved V_2O_5 architecture STXM image shown in Figure 5.1D. The pre- and post-edge normalized spectra are offset in order of increasing thickness (top to bottom). Panels (B) and (C) show expanded regions of the V L_3-edge features and the O K-pre-edge features, respectively. (D-G) Intensity maps obtained using the spectra in (A) as input. The map panels are arranged in order of increasing thickness (left to right, top to bottom).Figure C.17, Figure C.18, and Figure C.19 show the ROI and PCA analysis used to identify distinctive lithiated domains and develop the phase maps in (D)—(G). The spectrum (Cluster 4) corresponding to the thickest parts of the sample shows evidence of detector nonlinearity as a result of thickness effects. Examples of additional nanobowl architectures are provided in Figure C.20 and Figure C.21. Scale bars: 1 μm.

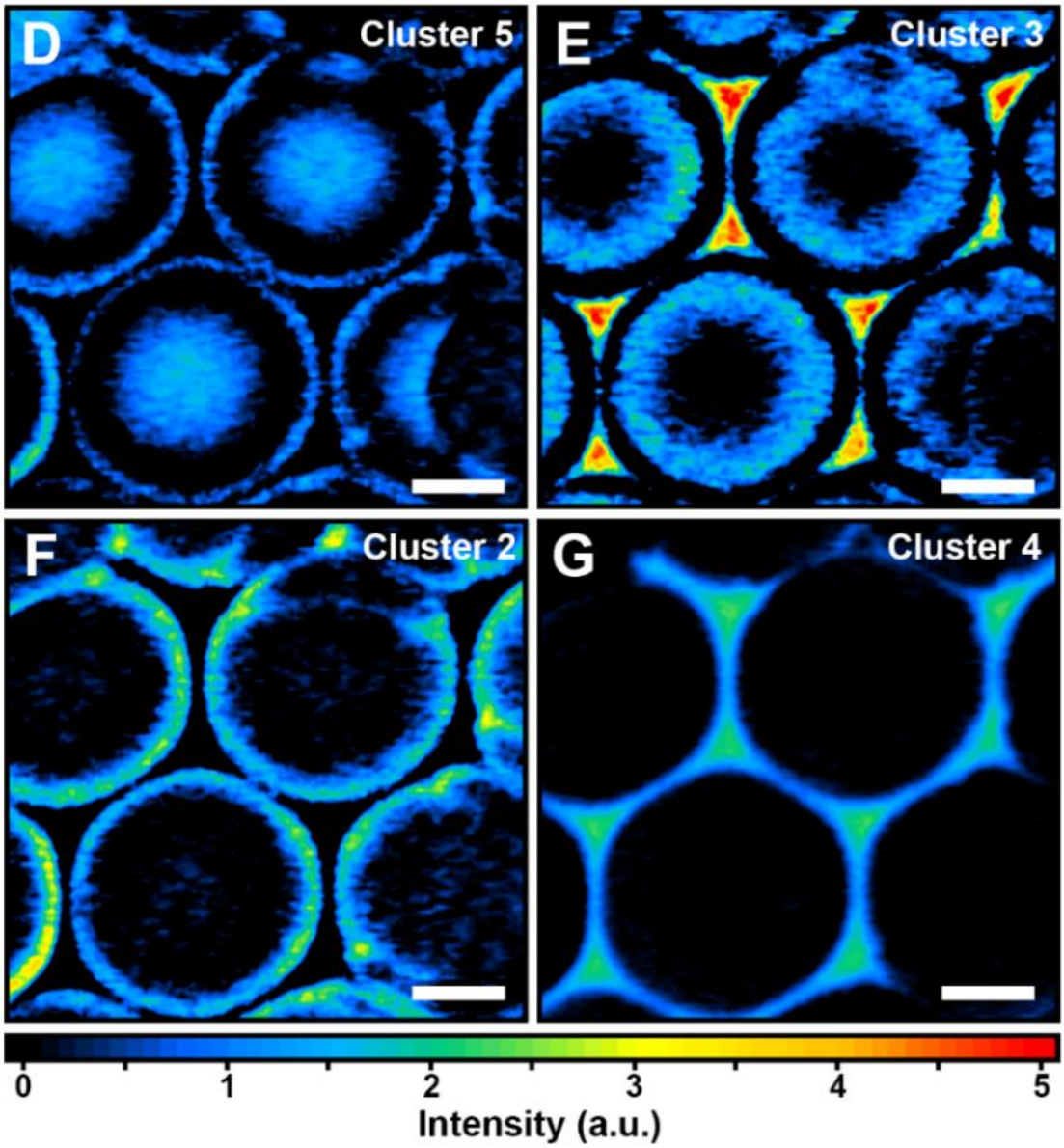

Figure 5.4. Continued.

Indeed, the observed spatial correlations delineated in Figure 5.4 appear to closely approximate the thickness/wall contours of the nanobowl architecture, directly mirroring the thickness maps in Figure 5.1D and in more detail in Figure C.3C. PCA-clustered spectra used as input for SVD mapping are shown in Figure

5.4A. The V L_3-edge is observed to be relatively featureless and does not exhibit any distinctive fine structure, indicative of a high degree of lithiation, corresponding to the stabilization of highly lithiated ε-$Li_xV_2O_5$ (x ~ 0.6) phase.[4,44] Comparison of the spectral features indicates that the spectra differ almost solely in intensity, reflecting differences in film thickness, closely following the contours of the nanobowl architectures as shown in the thickness map in Figure C.3C. The cluster intensity maps shown in Figure 5.4D-G are arranged in order of increasing thickness (left to right, top to bottom).

We have furthermore performed ROI analysis along various nanobowl contours and across different nanobowl contours, as shown in Figure C.19 and Figure C.20. The observed ROI-derived spectra are not only consistent within each nanobowl vacancy but also across different nanobowl vacancies. Given the identical lithiation conditions under which the three V_2O_5 morphologies were subjected, the complete absence of inhomogeneity on such a short lithiation timescale not only shows increased rates of lithiation[36,37,56] but also suggests that continuous curvature provides a means to leverage strain-induced improvements in diffusion kinetics while avoiding the ‘hot spot’ formation induced by local curvature. Compositional homogeneity across nanobowl structures has been observed for additional nanobowl structures lithiated under different conditions, as shown in Figure C.21 and Figure C.22 which further exhibit spectral differences derived from thickness only.

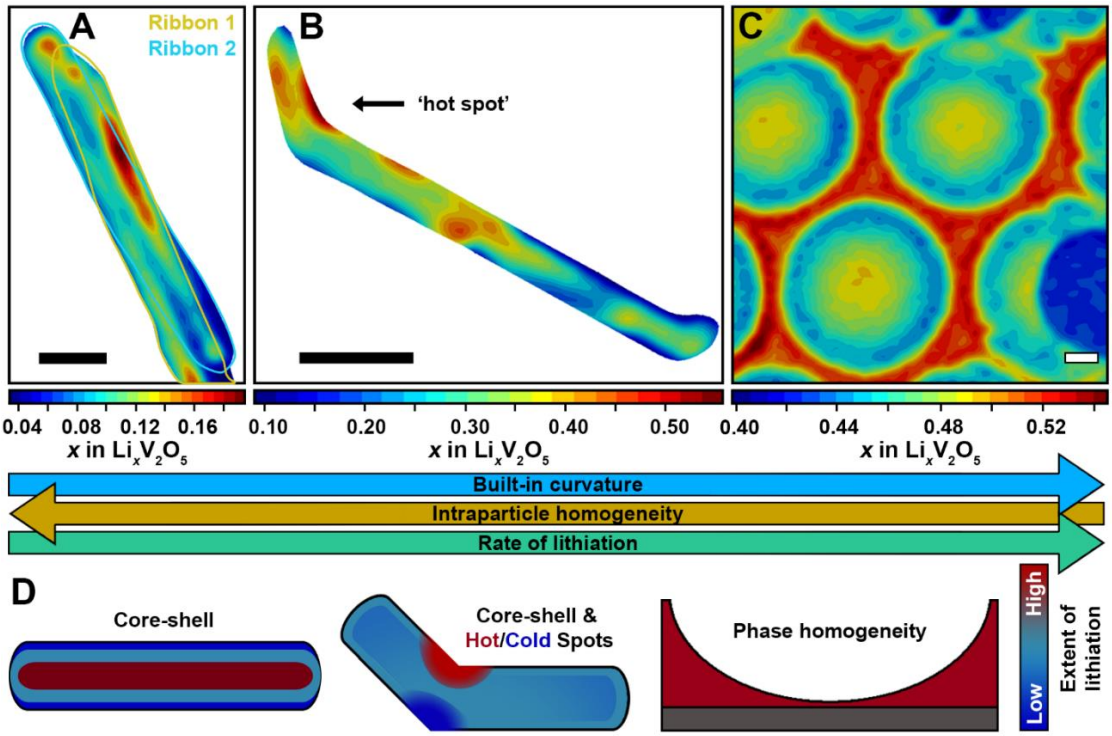

Figure 5.5. Composition maps generated from the SVD maps shown in Figure 5.2D-F, Figure 5.3B-E, and Figure 5.4D-G for (A) the straight nanoribbons (B) the locally curved nanoribbon, and (C) the continuously curved V_2O_5 3D architecture, respectively. All scale bars are 500 nm. The colored bars below the images correspond to composition of the nanoribbons (i.e., *x* in $Li_xV_2O_5$). Composition maps were generated by mapping the local stoichiometric fractions determined by assignment of PCA-clustered spectra to a Gauss filter-smoothed image as described in detail in the Experimental Section and schematically in Figure C.6. (D) Schematic representation summarizing the trends observed across the different geometries.

5.3.5. Quantitative Compositional Mapping and Stress Analysis

Figure C.6illustrates the process by which STXM data (Figure 5.1) is converted into accurate composition maps depicting the distribution of lithiated V_2O_5 domains and subsequently to von Mises stress maps, as shown in Figure 5.5 and Figure 5.6, respectively.[14,20,54] The composition maps exhibit similar trends to the SVD maps shown in Figure 5.2-4 but further take into account

spectral weighting across each pixel and thereby provide a quantitative accounting of the extent of lithiation. Figure 5.5A shows the core—shell lithiation of the underlying straight nanoribbon (ribbon 1) and a higher extent of lithiation for the top nanoribbon (ribbon 2). The composition map for the bent nanoribbon is shown in Figure 5.5B and illustrates a relatively much greater range of inhomogeneity (*x* from 0.088—0.557 in $Li_xV_2O_5$) as compared to the straight nanoribbons (*x* from 0.0333—0.195 in $Li_xV_2O_5$).

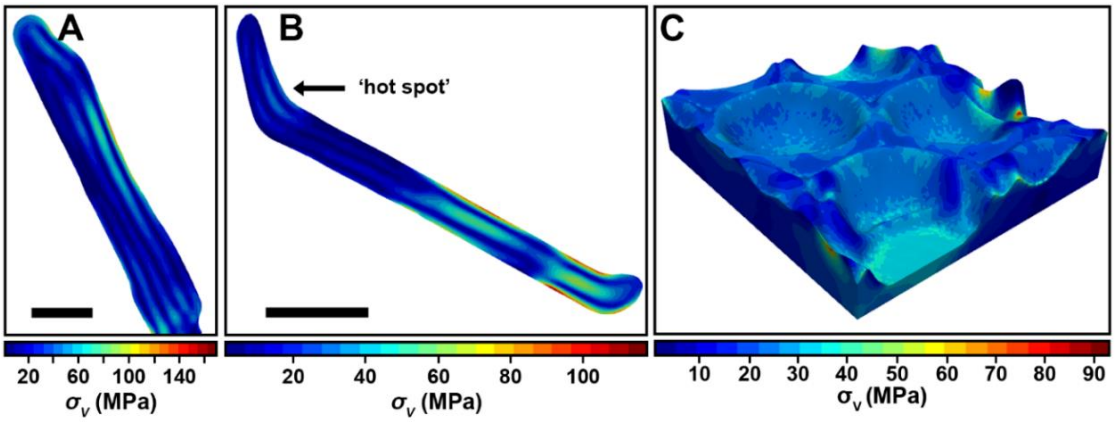

Figure 5.6. von Mises stress maps generated from the composition maps shown in Figure 5.5 for (A) the straight nanoribbons and (B) the locally curved nanoribbon. Scale bars: 500 nm. (C) Stress map derived from a finite element simulation from an optical density-derived thickness map. (D) Normalized equilibrium concentration resulting from the finite element simulation, which shows that under an applied chemical potential (shown here for *t* = 449 s, lithium redistributes across the continuously curved V_2O_5 3D architecture. (E) A two-dimensional top-down view of the three-dimensional mesh shown in (D) capturing the phase composition map observed from STXM in Figure 5.5C. Mesh generation from the thickness data is described in Figure C.23. (F) The displacement of the mesh normal to the substrate during lithiation, which enables relaxation of stresses by dint of the geometric curvature.

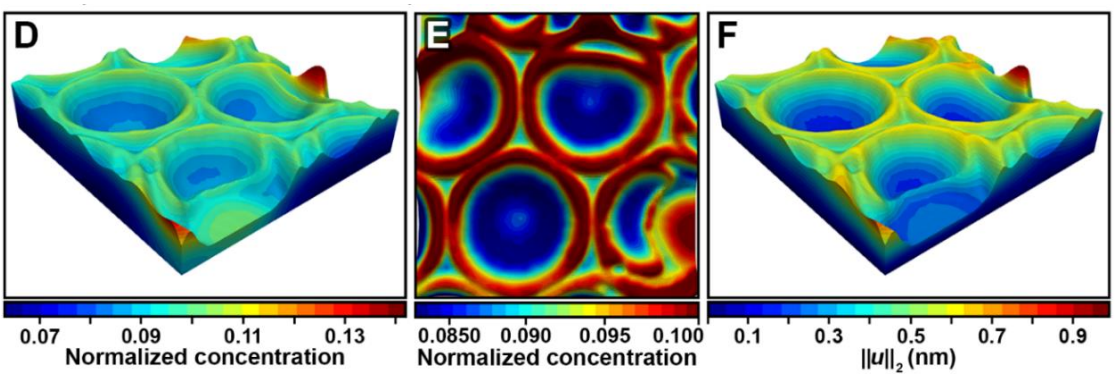

Figure 5.6. Continued.

Consistent with the analysis in preceding sections, the 'hot spot' labeled in the composition map in Figure 5.5B is located at the crease of the curved defect in the V_2O_5 nanoribbon. This hot spot is surrounded by areas of lower lithiation. Indeed, a 'cold spot' is observed on the opposite end, which is under tensile strain. The stark compositional inhomogeneity suggests that the compressive strain resulting at the concave side of the curvature drives more rapid lithiation within about 150 nm of the kink along the surface of the nanoribbon and extending into the nanoribbon about 60 nm. Unlike for the locally curved nanoribbon, no lithiation 'hot spots' are observed to form for the continuously curved architectures prepared by colloidal crystal templating in Figure 5.5C, which depict a much more homogeneous composition profile corresponding to a single lithiated phase (ε-$Li_xV_2O_5$, Figure 5.1A). The observed distribution of $Li_xV_2O_5$ phases present in the straight nanoribbon, bent nanoribbon, and the continuously curved architecture are summarized schematically in Figure 5.5D.

Figure 5.6A and Figure 5.6B show von Mises stress maps obtained for the straight and locally curved nanoribbons through treatment of the STXM data as described in the Experimental Section and in Figure C.6. The most significant stress experienced by the locally curved nanoribbon (Figure 5.6B) following lithiation coincides with the boundary of the hot spot with the rest of the nanoribbon, reflecting the elastic misfit strain at the interface between high and low lithiated domains. In contrast, Figure 5.6A depicts the roughly core—shell contours of stresses in straight nanoribbons.

The compressive strain induced by the defect in the nanoribbon leads to an increased local rate of lithiation. Additionally, the defect, where curvature is highest, promotes surface-limited lithiation, likely serving as a nucleation site for initiation of the phase transformation.[59] The application of strain leads to improved lithium-ion diffusion[15]; however, in the case of single defects where curvature-induced strain is highly localized in and around the “defect” (Figure 5.3 and Figure 5.6B), this engenders the formation of lithiation “hot spots” that further have the effect of inducing elastic misfit strain at the interface between the hot spot and adjacent domains with lower extents of lithiation. These observations thus suggest an important role for particle geometry in mitigating the effects of accumulated stresses. The results further suggest the importance of mesoscale structuring to incorporate curvature and strain more globally across the electrode to accelerate diffusion kinetics. Indeed, a simulated stress map for the continuously curved architecture prepared by colloidal crystal templating is shown in Figure 5.6C.

Whereas stress mapping of straight and curved nanoribbons from STXM-derived composition profiles are enabled by their low and uniform thickness normal to the image plane, for continuously curved architectures such as the 3D nanobowl architectures, STXM yields 2D projections of the compositions. Nevertheless, the composition profiles in Figure 5.5C along with height maps derived from optical density (Figure C.3) enable the construction of three-dimensional finite element meshes. Stress maps derived from such meshes (Figure C.23) for the 3D continuously curved architectures show substantially reduced stresses as compared to the straight and locally-curved geometries, concordant with the substantially greater compositional and phase homogeneity observed in the STXM maps (Figure 5.6D and Figure 5.6E show the 3D simulated composition mesh which accurately captures the experimental concentration distribution in Figure 5.6C). Figure 5.6F illustrates that the unconstrained expansion of the continuously curved architectures allows for facile relaxation of intercalation-induced stresses in this geometry. The deformation is observed to be largest at the centers of the nanobowl ridges since when ascending from the nanobowl centers to the ridge maxima, the structure becomes progressively thinner and thus exerts less resistance to deformation. This further allows for a relaxation of the diffusion-induced stresses within the structure. The ability of the patterned electrode to relax stresses is a strong advantage over planar thin-film electrodes (and even porous high capacity electrodes), where strong directional stresses have been known to cause strong mechanical degradation.[60,61]Incorporating

continuous curvature, as in the case of the continuously curved 3D V_2O_5 architecture thereby yields a much higher extent of lithiation (Figure 5.1) whilst retaining homogeneity across extended domains, thereby mitigating the evolution of lattice coherency strain.

5.4. Conclusions

Inhomogeneous volume expansion in the electrode materials of Li-ion batteries is often implicated in the degradation of cell performance. In cathode materials wherein Li-ion intercalation induces phase transformations, lithiation inhomogeneities within individual particles can give rise to substantial lattice coherency strain. The value of the von Mises stress at a given point reflects the relative compression of the crystal lattice as a result of the lithiation fraction within the matrix and is correlated and interdependent on the local environment, not just the concentration alone. Elastic misfit stresses and strains at the boundaries of phase segregated domains can suppress Li-ion diffusion and the accumulated stresses bring about plastic deformation and fracture of cathode particles. As a corollary, the application of modest directional lattice strain in thin-film cathodes can modify atomistic structure and reduce migration barriers for Li-ion diffusion,[15] enabling improved rate performance. However, these approaches rely on the application of strain through epitaxial interfaces.

Here we illustrate the quantitative mapping of lithium-ion compositions and stress magnitudes within individual particles, ensembles of particles, and across architected electrodes of V_2O_5 using STXM to map the distinctive spectroscopic

signatures of variously lithiated $Li_xV_2O_5$ phases. In V_2O_5 nanoribbons, surface-limited lithiation follows a core—shell pattern. However, in the presence of kinks derived from stacking faults, local curvature serves to preferentially nucleate lithiation along the concave inner surface whilst diminishing lithiation along the convex outer surface. The vastly amplified inhomogeneity of lithiation results is mapped as large von Mises stresses along the interface between low- and high lithiated domains. The introduction of continuous curvature within colloidal crystal templated nanobowl architectures allows for homogeneous and substantially enhanced kinetics of lithiation, mitigating the stress gradients that inevitably arise from local inhomogeneities and elastic misfit strains. Notably, this study has focused on examining the evolution of stress across different geometries during lithiation at the equivalent of low C-rates, wherein kinetic phenomena and surface-reaction-limited processes dominate over diffusion-limited processes.[14,20,52,62,63] For phase-separating materials, such a phenomenon yields morphologies with distinctive intercalation/reaction fronts that reflect nucleation of the lithiated phase at specific sites within the particle (e.g., asperities, defects, and edges have a high potency of nucleation). At high current densities or after nucleation restrictions have been overcome, a diffusion-limited regime is observed.[52] As such, during lithiation the resistance of the electrolyte interface rather than the concentration resistance within the active particle governs the morphology and shape of the reaction front.[49] In contrast, during delithiation, in the absence of nucleation limitations and given the higher degree of compositional inhomogeneity than at

the onset of lithiation, thermodynamic considerations are expected to be dominant, allowing for observation of spinodal decomposition patterns.[62–64] Indeed, recent lithiation/delithiation studies of single crystals of ζ-V_2O_5 even suggests lithium-ions prefer a specific ordering of crystallographic sites upon lithiation (β/β′/C site fill in a specific order) but lithium is removed from all sites at the same time during delithiation.[65] It is expected that the evolution of stress derived from compositional inhomogeneity would be exacerbated during delithiation owing to increased rates of delithiation from hotspots formed during lithiation.[62] Mitigating stress during delithiation (charging) provides further motivation for incorporating geometric curvature into the mesoscale design of cathode materials. The results presented here demonstrate the potential for using mesostructured architectures such as continuously curved nanobowls to incorporate continuous curvature and provides a promising route to leveraging electrochemistry-mechanics coupling to improve the electrochemical performance of cathode materials. The mitigation of failure mechanisms derived from elastic misfit strain is typically achieved by sacrificing the kinetics of lithiation (e.g., charge rate). Here we demonstrate how continuous curvature can be leveraged to simultaneously enable fast Li-ion diffusion kinetics and alleviate mechanical stresses developed during lithiation.

5.5. Experimental Section

5.5.1. Synthesis of V_2O_5 Nanoribbons

Commercially sourced V_2O_5 powder (Sigma Aldrich, 99.5%) was first treated hydrothermally under reducing conditions to obtain $V_3O_7 \cdot H_2O$ nanoribbons. In a typical reaction, 300 mg of V_2O_5 was dispersed in a mixture of deionized water (18.2 MΩ/cm) and 2-propanol (14 and 2 mL, respectively). The reaction mixture was transferred to a 23 mL polytetrafluoroethylene-lined autoclave (Parr), which was sealed and heated in a forced-air convection oven (Shell Labs) to 210°C for 72 h. The oven was calibrated externally using an alcohol thermometer. After the desired reaction duration, the autoclave was removed from heating and allowed to cool to room temperature. A green/blue product ($V_3O_7 \cdot H_2O$ nanoribbons) was separated from the supernatant liquid by centrifugation, washed with water (3×) and 2-propanol (1×), and was lightly ground in an agate mortar and pestle to obtain a free-flowing powder. To obtain V_2O_5 nanoribbons, the $V_3O_7 \cdot H_2O$ powder was calcined in air at 350°C for 12 h, ground lightly in an agate mortar and pestle, and subsequently calcined in air at 350°C for an additional 12 h. The powder was determined to be phase-pure orthorhombic V_2O_5 (*Pmmn*) by powder X-ray diffraction (XRD, Figure C.4A).

5.5.2. Patterning and Growth of Continuously Curved V_2O_5 3D Architectures

In order to enable spatially-resolved STXM characterization of the patterned V_2O_5 architectures, which is performed in transmission mode and thereby requires X-ray transparent substrates and comparatively thin samples

(<300 nm at the V L-edge), the colloidal crystal templating process was modified to enable growth of the 3D patterned V_2O_5 on location-tagged silicon nitride grids. Prior to templated growth of the nanobowl pattern, the silicon nitride substrates were cleaned by UV-ozone treatment (10 min), rinsed with deionized water (18.2 MΩ/cm) and dried under flowing nitrogen gas. A monolayer of polystyrene microspheres (2.4 μm diameter microspheres formed according to a previously reported synthesis)[36] was formed by pipetting ~3 μL a 1:3 v:v polystyrene:ethanol dispersion onto the surface of a deionized water bath. To ensure close-packing of the polystyrene microspheres, 12 μL of a 2 wt.% aqueous solution of sodium dodecyl sulfate was added to the water bath. A silicon nitride X-ray grid (Norcada location-tagged 'holey' TEM grids comprising a 200 nm thick silicon nitride film suspended on a 200 μm thick silicon frame) was placed on a cleaned glass slide, which was then subsequently used to capture the monolayer film via a lift-off process. The successful formation of a monolayer (as opposed to a several or many layer) using this method[36] is critical in order to obtain a structure sufficiently thin for STXM characterization.[37,56,66–68] The silicon nitride substrate was allowed to dry in air before being heated at 110°C for 10 min (ramp rate of 3°C min^{-1}) to promote adhesion of adjacent polystyrene microspheres and to further remove residual water. V_2O_5 deposition within the concave void spaces of the close-packed pattern was achieved through sol-gel chemistry. A fresh precursor sol of vanadium(V)oxyisopropoxide, 2-propanol, and deionized water (18.2 MΩ/cm) was prepared (10:100:1, (v/v/v) in a humidity-controlled tent (10% relative humidity).

Immediately after preparation, 2 μL of the precursor sol was pipetted onto the close-packed polystyrene architecture. The relative humidity of the tent was subsequently increased to atmospheric levels (~45%) over the course of 1 h to initiate formation of a vanadium oxide gel. The grid was removed from the humidity tent and heated at 100°C for 12 h to remove water content prior to crystallization. Including a dehydration step was critical to ensure that the silicon nitride grids did not crack during volume contraction of the 3D architecture. Following dehydration, the material was heated at 200°C for 4 h (ramp rate of 60°C·min^{-1}) to crystalize V_2O_5 within the interstices of the polystyrene template. The polystyrene template was finally removed by calcination in air at 400°C for 4 h (ramp rate of 60°C·min^{-1}) to leave behind only the V_2O_5 framework. Treatment at 400°C was observed to significantly improve the crystallinity of the obtained material (Figure C.17B).

5.5.3. Powder X-Ray Diffraction (XRD)

Powder X-ray diffraction (XRD) patterns were collected in Brag-Brentano geometry on a Bruker D8-focus diffractometer (Cu K-α, λ = 1.5418Å; 40 kV voltage; 25 mA current). All crystal structures depicted in this article were rendered using the Vesta III software suite (JP-minerals).[69] Reflection locations shown in Figure C.4A were generated using the powder diffraction pattern simulation routine as implemented in Vesta III.[69]

5.5.4. Electron Microscopy (SEM, TEM)

Scanning electron microscopy (SEM) images were collected on a JEOL JSM-7500F instrument equipped with a high-brightness conical field-emission gun

and a low-aberration conical objective lens. Prior to imaging, powder samples were pressed onto conductive carbon tape. For samples already cast onto silicon nitride substrates, the substrates were placed onto conductive carbon tape prior to imaging. The carbon tape was configured in a ‘railroad track’ pattern to enable suspension of the delicate (50 nm thick) silicon nitride window above the aluminum substrate (similar to the experimental setup shown schematically in Figure C.5). In order to maintain the pristine nature of the sample and substrate prior to lithiation and subsequent STXM imaging, surface coatings were not employed to improve the conductivity of the samples prior to SEM imaging. Instead, sample charging was mitigated by using a low accelerating voltage (4 kV), low field-emission probe current (6 μA), and by maintaining a short working distance (2-4.5 mm). Transmission electron microscopy (TEM) images were collected on a JEOL 2010 at an accelerating voltage of 200 kV. All TEM images were collected for samples after they were cast (nanoribbons) or grown (3D nanobowl architecture) on a silicon/silicon nitride substrate. All SEM and TEM measurements were performed prior to chemical lithiation or X-ray measurements.

5.5.5. Raman Spectroscopy

Raman spectra (Figure C.16A) were collected using a Jobin-Yvon HORIBA LabRAM HR800 instrument coupled to an Olympus BX41 microscope. The spectrum was collected using the 514.5 nm line of an Ar-ion laser as a source. Raman modes were interpreted and assigned using assignments from previous

studies.[46,58,70] “On-Substrate” Chemical Lithiation of V_2O_5 Nanoribbons and Continuously Curved 3D Architectures

V_2O_5 nanoribbons were dispersed in 2-propanol (5 mg/m) using ultrasonication (2 min) and were subsequently pipetted onto a holey location-tagged silicon nitride substrate. Prior to lithiation and X-ray characterization, SEM was used to identify nanoribbons of interest and record their locations. The silicon nitride substrate was fixed to a thoroughly cleaned stainless steel plate using carbon tape. The steel plate was subsequently fixed to the bottom of a glass beaker using carbon tape. Under an inert atmosphere (Argon, < 0.1 ppm O_2 and <0.1 ppm H_2O), chemical lithiation was achieved using a solution of *n*-butyllithium in heptane (0.0025 M), which was carefully syringed into the beaker to induce lithiation as per:

$$V_2O_5(s)+xC_4H_9Li(l)\rightarrow Li_xV_2O_5(s)+\frac{x}{2}C_8H_{18}(g) \qquad \textbf{5.1}$$

Following this reaction, which was allowed to proceed for 15 min in the case of each sample V_2O_5 geometry, the excess *n*-butyllithium/heptane/octane mixture was carefully removed using a syringe. The beaker and the grid (Figure C.5) were washed with copious amounts of *n*-heptane (3×) to remove any unreacted *n*-butyllithium. Finally, the grid was detached from the steel plate and sealed under an inert argon atmosphere for transport to the Canadian Light Source for characterization by STXM (beamline 10ID-1). Notably, the locations of the nanoribbons on the grids, as recorded using SEM prior to lithiation, were unaltered following this ‘on-substrate’ wet-chemical lithiation process.

5.5.6. Scanning Transmission X-Ray Microscopy (STXM)

STXM data were collected at the spectromicroscopy beamline 10ID-1 of the Canadian Light Source in Saskatoon, SK, CA. This beamline employs an elliptically polarized undulator (EPU) source. An X-ray beam was focused (beam spot is routinely <25 nm) using a Fresnel zone-plate which is equipped with an order-sorting aperture to eliminate undesired diffraction orders. The incident X-ray beam is rastered across the sample region of interest. A 500-line mm^{-1} monochromater was used to select the incident X-ray energy, which was tuned to the V L-, and O K-edges for imaging the V_2O_5 and $Li_xV_2O_5$ sample materials. A dwell time of 1 $ms \cdot pixel^{-1} \cdot energy^{-1}$ was used for signal acquisition. STXM data were analyzed using the aXis2000 software suite (Version updated Oct. 11, 2019, download: http://unicorn.mcmaster.ca/aXis2000.html). The workflow of STXM data processing employed in this work is shown schematically in Figure C.6. Region of interest (ROI) analysis was performed using the 'Stack Analyze' routine within aXis2000. Spectra obtained from ROIs are averaged across user-defined regions (as shown in Figure C.6, Figure C.11, Figure C.16, and Figure C.17). Principal component analysis (PCA) of the obtained spectral stacks was performed using the 'PCA_GUI' routine (version 1.1.1) within aXis2000. Clustering of the individual pixels in the STXM images (Figure 5.2D, Figure C.12, and Figure C.15) by scoring the spectrum at each pixel against the mutually orthogonal principal component eigenspectra was also performed in the 'PCA_GUI' routine. Using previous theoretical and experimental reports, the

average stoichiometry of the materials that give rise to the spectra can be reasonably inferred.[14,38,47,71] As an example, for the spectra in Figure 5.3A, lithium stoichiometries of x = 0.1 (cluster 2 spectrum); 0.3 (cluster 4 spectrum); 0.45 (Cluster 3 spectrum); and 0.6 (cluster 5 spectrum) were assigned as values of x in $Li_xV_2O_5$. These stoichiometric assignments were used as input for generation of compositional and strain maps. Singular value decomposition (SVD) of the spectral stacks was performed using the Singular Value Decomposition (SVD) routine of aXis2000 (Figure 5.2, Figure 5.3, and Figure 5.4). Further experimental details related to the conversion of STXM data (optical density) to thickness maps used for composition and strain map generation is provided in Appendix C.

5.5.7. Generation of Thickness Maps from Optical Density STXM Data

Thickness maps (Figure C.3) were generated using the Stack Fit routine in aXis2000. A spectrum averaged across the entirety of each STXM image (Figure 5.1) was normalized to the pre- and post-edge of an elemental profile generated for a notional 1 nm thick sample. The 1 nm thick elemental profile was generated using the aXis2000 software suite Elemental Profile routine, which calculates the mass absorption for a user-defined composition and density. The thickness maps in Figure C.3corresponding to the unstrained nanoribbon (Figure C.3A), the curved nanoribbon (Figure C.3B), and 3D nanobowl architecture (Figure C.3C) were generated using the following assumptions: uniform compositions of $Li_{0.3}V_2O_5$ (nanoribbon), $Li_{0.45}V_2O_5$ (curved nanoribbon), and $Li_{0.6}V_2O_5$ (continuously curved architecture); and average densities of 3.343 $g \cdot cm^{-3}$

(nanoribbon), 3.357 $g \cdot cm^{-3}$ (curved nanoribbon), and 3.369 $g \cdot cm^{-3}$ (continuously curved 3D architecture).

5.5.8. Composition and Strain Maps Workflow

The generation of composition and strain maps from STXM maps has been adapted from a previously reported procedure.[14] The initial points for the image mesh generation procedure correspond directly to the maps shown in Figure 5.2E-G (straight nanoribbons), Figure 5.3D-G (locally-curved nanoribbon), and Figure 5.4D-G (continuously curved V_2O_5 architecture). These normalized intensities in image space represent the following intensities: x_i; (i) x_1=0.0; (ii) x_2=0.1; and (iii) x_3=0.3 (for the straight nanoribbon), x_i; (i) x_1=0.1; (ii) x_2=0.3; (iii) x_3=0.45; and (iv) x_1=0.6 (for the locally curved nanoribbon), and x_i; (i) x_1=0.45; (ii) x_2=0.5; (iii) x_3=0.55; and (iv) x_1=0.6 (for the continuously curved V_2O_5 architecture) where the values of x_i correspond to various phases of $Li_xV_2O_5$ (i.e., the weights in image space correspond to different assigned values of x in $Li_xV_2O_5$). Prior to mesh generation, these SVD-generated maps were subjected to a Gaussian filter to remove noise. Subsequently, superposition of the pixel intensities, weighted by the corresponding stoichiometric fraction x_i, yields a composition map in image space as shown in Figure 5.5A-C. The composition at each pixel in Figure 5.5A-C is thus derived from a superposition of the various lithiated phases present in each voxel size, as inferred from analysis of the V L- and O K-edge spectra and by SVD. The composition map is therefore a one-to-one image with dimensions defined by the originally-collected STXM image. The as-collected STXM image

exhibits a relatively low resolution of 79×74 pixels (2.51 μm × 2.35 μm image) A continuous representation with retention of data fidelity can be achieved by bilinear interpolation of the pixel data, yielding smooth composition maps as shown in Figure 5.5A-C.

A quantitative composition map was obtained from pixel-wise combination of phase intensities using user-defined stoichiometric values of *x* in $Li_xV_2O_5$. Using the Marching Squares algorithm, the naoribbons' outline curves could be extracted from the image data and served as input for the Finite mesh element generator GMSH.[72] The local stoichiometric fraction was mapped onto the nodes of a planar triangle mesh, and scaled by the ion concentration (i.e., state-of-charge). The resulting finite element model was used to solve for the distribution of stresses and strains using the software package FEAP.[73] To this end, linear elastic isotropic material behavior was assumed together with a chemical eigenstrain model defined by:

$$\sigma_{ij}=C_{ijkl}\varepsilon_{kl}^{el} \quad \textbf{5.2}$$

$$\varepsilon_{kl}^{el}=\varepsilon_{kl}-\frac{\Omega c}{3}\delta_{kl} \quad \textbf{5.3}$$

wherein: σ_{ij} denotes the components of the symmetric second-order Cauchy stress tensor; C_{ijkl} denotes components of the fourth-order elasticity tensor describing the elastic material properties, Ω is the partial molar volume of $Li_xV_2O_5$ upon insertion of Li-ions (linearly interpolated from previously reported unit cell parameters of lithiated orthorhombic V_2O_5.[43,74–79]); and δ_{kl} are the components of the unit tensor. Note that the model can be extended straightforwardly to take into

account the anisotropy of the chemical strain as well as the structural transformation strain by modifying the last term on the right side of Equation 5.3. The components of the symmetric second-order infinitesimal strain tensor (which more broadly describes strain) are described by ε_{kl}, given as:

$$\varepsilon_{ij}=\frac{1}{2}\left(u_{i,j}+u_{j,i}\right) \qquad \textbf{5.4}$$

where u_i denotes the components of the displacement vector and the notation $(\cdot)_{,i}$ indicates a partial derivative with respect to the *i*-th spatial coordinate. The variable ε_{kl}^{el} is the elastic strain, which is correlated directly to the stress. For finite element simulations, the composition (i.e., state-of-charge) as determined by the image conversion process was employed as a constant field causing eigenstrain according to Equation. 5.4. For simplicity, constant concentration-independent elastic parameters and a constant partial molar volume were approximated. In particular, a Young's modulus of E = 43 GPa, a Poisson's ratio of v = 0.3, and a partial molar volume of $\Omega = 2.415\times10^{-6}$ $m^3 \cdot mol^{-1}$ were used as parameter input in the finite element simulations. In order to exclude rigid body displacements, the displacement components were constrained normal to the nanoribbon edges along the image borders. The resulting stresses and strains (Figure 5.5D and Figure 5.5E) were transformed from the Cartesian coordinate frame to a nanoribbon-aligned planar coordinate system using standard techniques.

5.5.9. Three-Dimensional Electrochemical Analysis of Li-Ion Insertion into the Continuously Curved V_2O_5 3D Architectures

The thickness maps (Figure C.3) derived from optical density measurements of the STXM data were converted into a volumetric Finite Element mesh. This process is described schematically in Figure C.23. The basis for the mesh generation was thereby a geometric model of a thin slab in the xy-plane. The vertices on its top surface, situated at z=0, were thereby shifted in vertical direction according to the values of the height map. In order to avoid elements with (nearly) zero thickness (which may have a deleterious effect on the simulation results), we slightly extended the slab thickness in the vertical direction so as to obtain a (chemically active) substrate of 260nm below the sample. Using a chemo-mechanical model described elsewhere[57] we simulated the intercalation process into the active material under prescription of an electrochemical potential difference dφ = -4.88mV between the electrolyte (wetting the sample's top surface) and the active material. We thereby assumed a uniform initial relative concentration c0 equal to the strain-free (normalized) reference concentration cref=c0 = 0.05, a maximum concentration cmax = 1.66e4 mol m-3, Young's modulus E = 43 GPa, Poisson's ratio v = 0.3, partial molar volume Ω=1.85e-6 m3 mol-1, interaction parameter Xχ=1, temperature T = 300 K, and diffusion constant D = 8.1e-15 m2 s-1. Due to the mesh exhibiting a characteristic size of ~5 μm, the model was not made to incorporate surface stresses. Along the lateral edges of the sample, normal displacements were restrained and the chemical flux was set

to zero. Simulations were allowed to proceed until an equilibrium between chemical potential at the surface and the prescribed electrochemical potential drop was achieved.

5.6. References

(1) Whittingham, M. S. Lithium Batteries and Cathode Materials. *Chem. Rev.* **2004**, *104* (10), 4271–4301.

(2) Goodenough, J. B.; Park, K.-S. The Li-Ion Rechargeable Battery: A Perspective. *J. Am. Chem. Soc.* **2013**, *135* (4), 1167–1176.

(3) Marianetti, C. A.; Kotliar, G.; Ceder, G. A First-Order Mott Transition in Li_xCoO_2. *Nat. Mater.* **2004**, *3* (9), 627–631.

(4) De Jesus, L. R.; Andrews, J. L.; Parija, A.; Banerjee, S. Defining Diffusion Pathways in Intercalation Cathode Materials: Some Lessons from V_2O_5 on Directing Cation Traffic. *ACS Energy Lett.* **2018**, *3* (4), 915–931.

(5) Stein, P.; Zhao, Y.; Xu, B. X. Effects of Surface Tension and Electrochemical Reactions in Li-Ion Battery Electrode Nanoparticles. *J. Power Sources* **2016**, *332*, 154–169.

(6) Zhao, Y.; Stein, P.; Bai, Y.; Al-Siraj, M.; Yang, Y.; Xu, B. X. A Review on Modeling of Electro-Chemo-Mechanics in Lithium-Ion Batteries. *J. Power Sources* **2019**, *413* (October 2018), 259–283.

(7) Chan, C. K.; Peng, H.; Liu, G.; Mcilwrath, K.; Zhang, X. F.; Huggins, R. A.; Cui, Y. High-Performance Lithium Battery Anodes Using Silicon Nanowires. *Nat. Nanotechnol.* **2008**, *3*, 31–35.

(8) Hardin, G. R.; Zhang, Y.; Fincher, C. D.; Pharr, M. Interfacial Fracture of Nanowire Electrodes of Lithium-Ion Batteries. *JOM* **2017**, *69* (9), 1519–1523.

(9) Mukhopadhyay, A.; Sheldon, B. W. Deformation and Stress in Electrode Materials for Li-Ion Batteries. *Prog. Mater. Sci.* **2014**, *63* (February), 58–116.

(10) Lewis, J. A.; Tippens, J.; Cortes, F. J. Q.; McDowell, M. T. Chemo-Mechanical Challenges in Solid-State Batteries. *Trends Chem.* **2019**, *1* (9), 845–857.

(11) Thackeray, M. M. Structural Considerations of Layered and Spinel Lithiated Oxides for Lithium Ion Batteries. *J. Electrochem. Soc.* **1995**, *142* (8), 2558–2563.

(12) Reimers, J. N.; Dahn, J. R. Electrochemical and in Situ X-Ray Diffraction Studies of Lithium Intercalation in Li_xCoO_2. *J. Electrochem. Soc.* **1992**, *139* (8), 2091–2097.

(13) Padhi, A. K.; Nanjundaswamy, K. S.; Goodenough, J. B. Phospho-Olivines as Positive-Electrode Materials for Rechargeable Lithium Batteries. *J. Electrochem. Soc.* **1997**, *144* (4), 1188–1194.

(14) De Jesus, L. R.; Stein, P.; Andrews, J. L.; Luo, Y.; Xu, B.; Banerjee, S. Striping Modulations and Strain Gradients within Individual Particles of a Cathode Material upon Lithiation. *Mater. Horizons* **2018**, *5*, 486–498.

(15) Muralidharan, N.; Brock, C. N.; Cohn, A. P.; Schauben, D.; Carter, R. E.;

Oakes, L.; Walker, D. G.; Pint, C. L. Tunable Mechanochemistry of Lithium Battery Electrodes. *ACS Nano* **2017**, *11* (6), 6243–6251.

(16) Ning, F.; Li, S.; Xu, B.; Ouyang, C. Strain Tuned Li Diffusion in $LiCoO_2$ Material for Li Ion Batteries: A First Principles Study. *Solid State Ionics* **2014**, *263*, 46–48.

(17) Tealdi, C.; Heath, J.; Islam, M. S. Feeling the Strain: Enhancing Ionic Transport in Olivine Phosphate Cathodes for Li- and Na-Ion Batteries through Strain Effects. *J. Mater. Chem. A* **2016**, *4* (18), 6998–7004.

(18) Zhang, Y.; Luo, Y.; Fincher, C.; Banerjee, S.; Pharr, M. Chemo-Mechanical Degradation in V_2O_5 Thin Film Cathodes of Li-Ion Batteries during Electrochemical Cycling. *J. Mater. Chem. A* **2019**, *7*, 23922–23930.

(19) Bucci, G.; Swamy, T.; Bishop, S.; Sheldon, B. W.; Chiang, Y.-M.; Carter, W. C. The Effect of Stress on Battery-Electrode Capacity. *J. Electrochem. Soc.* **2017**, *164* (4), A645–A654.

(20) De Jesus, L. R.; Zhao, Y.; Horrocks, G. A.; Andrews, J. L.; Stein, P.; Xu, B.-X. B.; Banerjee, S. Lithiation across Interconnected V_2O_5 Nanoparticle Networks. *J. Mater. Chem. A* **2017**, *5* (38), 20141–20152.

(21) Zhao, Y.; De Jesus, L. R.; Stein, P.; Horrocks, G. A.; Banerjee, S.; Xu, B.-X. Modeling of Phase Separation across Interconnected Electrode Particles in Lithium-Ion Batteries. *RSC Adv.* **2017**, *7* (65), 41254–41264.

(22) Li, D.; Zhou, H. Two-Phase Transition of Li-Intercalation Compounds in Li-Ion Batteries. *Mater. Today* **2014**, *17* (9), 451–463.

(23) Boesenberg, U.; Meirer, F.; Liu, Y.; Shukla, A. K.; Dell'Anna, R.; Tyliszczak, T.; Chen, G.; Andrews, J. C.; Richardson, T. J.; Kostecki, R.; Cabana, J. Mesoscale Phase Distribution in Single Particles of $LiFePO_4$ Following Lithium Deintercalation. *Chem. Mater.* **2013**, *25* (9), 1664–1672.

(24) Zhu, Y.; Wang, C. Strain Accommodation and Potential Hysteresis of $LiFePO_4$ Cathodes during Lithium Ion Insertion/Extraction. *J. Power Sources* **2011**, *196* (3), 1442–1448.

(25) Ulvestad, A.; Singer, A.; Cho, H. M.; Clark, J. N.; Harder, R.; Maser, J.; Meng, Y. S.; Shpyrko, O. G. Single Particle Nanomechanics in Operando Batteries via Lensless Strain Mapping. *Nano Lett.* **2014**, *14* (9), 5123–5127.

(26) Cogswell, D. A.; Bazant, M. Z. Coherency Strain and the Kinetics of Phase Separation in $LiFePO_4$ Nanoparticles. *ACS Nano* **2012**, *6* (3), 2215–2225.

(27) Tippens, J.; Miers, J. C.; Afshar, A.; Lewis, J. A.; Cortes, F. J. Q.; Qiao, H.; Marchese, T. S.; Di Leo, C. V.; Saldana, C.; McDowell, M. T. Visualizing Chemomechanical Degradation of a Solid-State Battery Electrolyte. *ACS Energy Lett.* **2019**, *4* (6), 1475–1483.

(28) Zhao, K.; Pharr, M.; Hartle, L.; Vlassak, J. J.; Suo, Z. Fracture and Debonding in Lithium-Ion Batteries with Electrodes of Hollow Core-Shell Nanostructures. *J. Power Sources* **2012**, *218*, 6–14.

(29) Song, H.; Jeong, T. G.; Yun, S. W.; Lee, E. K.; Park, S. A.; Kim, Y. T. An Upper Limit of Cr-Doping Level to Retain Zero-Strain Characteristics of $Li_4Ti_5O_{12}$ Anode Material for Li-Ion Batteries. *Sci. Rep.* **2017**, *7*, 43335.

(30) Kim, U. H.; Myung, S. T.; Yoon, C. S.; Sun, Y. K. Extending the Battery Life Using an Al-Doped $Li[Ni_{0.7}Co_{0.09}Mn_{0.15}]O_2$ Cathode with Concentration Gradients for Lithium Ion Batteries. *ACS Energy Lett.* **2017**, *2* (8), 1848–1854.

(31) Andrews, J. L.; Mukherjee, A.; Yoo, H. D.; Parija, A.; Marley, P. M.; Fakra, S.; Prendergast, D.; Cabana, J.; Klie, R. F.; Banerjee, S. Reversible Mg-Ion Insertion in a Metastable One-Dimensional Polymorph of V_2O_5. *Chem* **2018**, *4* (3), 564–585.

(32) Parija, A.; Liang, Y.; Andrews, J. L.; De Jesus, L. R.; Prendergast, D.; Banerjee, S. Topochemically De-Intercalated Phases of V_2O_5 as Cathode Materials for Multivalent Intercalation Batteries: A First-Principles Evaluation. *Chem. Mater.* **2016**, *28* (16), 5611–5620.

(33) Tepavcevic, S.; Liu, Y.; Zhou, D.; Lai, B.; Maser, J.; Zuo, X.; Chan, H.; Král, P.; Johnson, C. S.; Stamenkovic, V.; Markovic, N. M.; Rajh, T. Nanostructured Layered Cathode for Rechargeable Mg-Ion Batteries. *ACS Nano* **2015**, *9* (8), 8194–8205.

(34) Tolhurst, T. M.; Leedahl, B.; Andrews, J. L.; Marley, P. M.; Banerjee, S.; Moewes, A. Contrasting 1D Tunnel-Structured and 2D Layered Polymorphs of V_2O_5 : Relating Crystal Structure and Bonding to Band Gaps and Electronic Structure. *Phys. Chem. Chem. Phys.* **2016**, *18* (23), 15798–15806.

(35) Su, L.; Jing, Y.; Zhou, Z. Li Ion Battery Materials with Core-Shell

Nanostructures. *Nanoscale* **2011**, *3* (10), 3967–3983.

(36) Chalker, C. J.; An, H.; Zavala, J.; Parija, A.; Banerjee, S.; Lutkenhaus, J. L.; Batteas, J. D. Fabrication and Electrochemical Performance of Structured Mesoscale Open Shell V_2O_5 Networks. *Langmuir* **2017**, *33* (24), 5975–5981.

(37) Li, L.; Steiner, U.; Mahajan, S. Improved Electrochromic Performance in Inverse Opal Vanadium Oxide Films. *J. Mater. Chem.* **2010**, *20* (34), 7131–7134.

(38) De Jesus, L. R.; Horrocks, G. A.; Liang, Y.; Parija, A.; Jaye, C.; Wangoh, L.; Wang, J.; Fischer, D. A.; Piper, L. F. J.; Prendergast, D.; Banerjee, S. Mapping Polaronic States and Lithiation Gradients in Individual V_2O_5 Nanowires. *Nat. Commun.* **2016**, *7*, 12022.

(39) Ellis, B.; Perry, L. K.; Ryan, D. H.; Nazar, L. F. Small Polaron Hopping in $Li_x FePO_4$ Solid Solutions: Coupled Lithium-Ion and Electron Mobility. *J. Am. Chem. Soc.* **2006**, *128* (35), 11416–11422.

(40) Watthaisong, P.; Jungthawan, S.; Hirunsit, P.; Suthirakun, S. Transport Properties of Electron Small Polarons in a V_2O_5 Cathode of Li-Ion Batteries: A Computational Study. *RSC Adv.* **2019**, *9* (34), 19483–19494.

(41) Lee, J.; Pennycook, S. J.; Pantelides, S. T. Simultaneous Enhancement of Electronic and Li^+ Ion Conductivity in $LiFePO_4$. *Appl. Phys. Lett.* **2012**, *101* (3), 1–5.

(42) Muralidharan, N.; Carter, R.; Oakes, L.; Cohn, A. P.; Pint, C. L. Strain

Engineering to Modify the Electrochemistry of Energy Storage Electrodes. *Sci. Rep.* **2016**, *6* (June), 27542.

(43) Satto, C.; Sciau, P.; Dooryhee, E.; Galy, J.; Millet, P. The Δ→ε→γ LiV_2O_5 '"High Temperature"' Phase Transitions Evidenced by Synchrotron X-Ray Powder Diffraction Analysis. *J. Solid State Chem.* **1999**, *109* (1), 103–109.

(44) Horrocks, G. A.; De Jesus, L. R.; Andrews, J. L.; Banerjee, S. X-Ray Spectroscopy and Imaging as Multiscale Probes of Intercalation Phenomena in Cathode Materials. *JOM* **2017**, *69* (9), 1469–1477.

(45) Luo, Y.; De Jesus, L. R.; Andrews, J. L.; Parija, A.; Fleer, N.; Robles, D. J.; Mukherjee, P. P.; Banerjee, S. Roadblocks in Cation Diffusion Pathways: Implications of Phase Boundaries for Li-Ion Diffusivity in an Intercalation Cathode Material. *ACS Appl. Mater. Interfaces* **2018**, *10* (36), 30901–30911.

(46) Horrocks, G. A.; Likely, M. F.; Velazquez, J. M.; Banerjee, S. Finite Size Effects on the Structural Progression Induced by Lithiation of V_2O_5: A Combined Diffraction and Raman Spectroscopy Study. *J. Mater. Chem. A* **2013**, *1*, 15265–15277.

(47) Maganas, D.; Roemelt, M.; Hävecker, M.; Trunschke, A.; Knop-Gericke, A.; Schlögl, R.; Neese, F. First Principles Calculations of the Structure and V L-Edge X-Ray Absorption Spectra of V_2O_5 Using Local Pair Natural Orbital Coupled Cluster Theory and Spin-Orbit Coupled Configuration Interaction Approaches. *Phys. Chem. Chem. Phys.* **2013**, *15* (19), 7260–7276.

(48) Lerotic, M.; Jacobsen, C.; Gillow, J. B.; Francis, A. J.; Wirick, S.; Vogt, S.; Maser, J. Cluster Analysis in Soft X-Ray Spectromicroscopy: Finding the Patterns in Complex Specimens. *J. Electron Spectros. Relat. Phenomena* **2005**, *144–147*, 1137–1143.

(49) Mistry, A. N.; Smith, K.; Mukherjee, P. P. Secondary-Phase Stochastics in Lithium-Ion Battery Electrodes. *ACS Appl. Mater. Interfaces* **2018**, *10* (7), 6317–6326.

(50) Li, Y.; El Gabaly, F.; Ferguson, T. R.; Smith, R. B.; Bartelt, N. C.; Sugar, J. D.; Fenton, K. R.; Cogswell, D. A.; Kilcoyne, A. L. D.; Tyliszczak, T.; Bazant, M. Z.; Chueh, W. C. Current-Induced Transition from Particle-by-Particle to Concurrent Intercalation in Phase-Separating Battery Electrodes. *Nat. Mater.* **2014**, *13* (12), 1149–1156.

(51) Mistry, A.; Usseglio-Viretta, F. L. E.; Colclasure, A.; Smith, K.; Mukherjee, P. P. Fingerprinting Redox Heterogeneity in Electrodes during Extreme Fast Charging. *J. Electrochem. Soc.* **2020**, *167* (9), 090542.

(52) Fraggedakis, D.; Nadkarni, N.; Gao, T.; Zhou, T.; Zhang, Y.; Han, Y.; Stephens, R. M.; Shao-Horn, Y.; Bazant, M. Z. A Scaling Law to Determine Phase Morphologies during Ion Intercalation. *Energy Environ. Sci.* **2020**, *13*, 2142–2152.

(53) Mistry, A.; Smith, K.; Mukherjee, P. P. Stochasticity at Scales Leads to Lithium Intercalation Cascade. *ACS Appl. Mater. Interfaces* **2020**, *12* (14), 16359–16366.

(54) Zhao, Y.; Xu, B. X.; Stein, P.; Gross, D. Phase-Field Study of Electrochemical Reactions at Exterior and Interior Interfaces in Li-Ion Battery Electrode Particles. *Comput. Methods Appl. Mech. Eng.* **2016**, *312*, 428–446.

(55) Boebinger, M. G.; Yeh, D.; Xu, M.; Miles, B. C.; Wang, B.; Papakyriakou, M.; Lewis, J. A.; Kondekar, N. P.; Cortes, F. J. Q.; Hwang, S.; Sang, X.; Su, D.; Unocic, R. R.; Xia, S.; Zhu, T.; McDowell, M. T. Avoiding Fracture in a Conversion Battery Material through Reaction with Larger Ions. *Joule* **2018**, *2* (9), 1783–1799.

(56) Armstrong, E.; McNulty, D.; Geaney, H.; ODwyer, C. Electrodeposited Structurally Stable V_2O_5 Inverse Opal Networks as High Performance Thin Film Lithium Batteries. *ACS Appl. Mater. Interfaces* **2015**, *7* (48), 27006–27015.

(57) Stein, P.; Wissel, S.; Xu, B.-X. The Influence of Surface Stress on the Chemo-Mechanical Behavior of Inverse-Opal Structured Electrodes for Lithium-Ion Batteries. *J. Electrochem. Soc.* **2020**, *167* (1), 013529.

(58) Baddour-hadjean, R.; Pereira-Ramos, J.-P. Raman Microspectrometry Applied to the Study of Electrode Materials for Lithium Batteries. *Chem. Rev.* **2008**, *110* (3), 1278–1319.

(59) Hudak, B. M.; Depner, S. W.; Waetzig, G. R.; Talapatra, A.; Arroyave, R.; Banerjee, S.; Guiton, B. S. Real-Time Atomistic Observation of Structural Phase Transformations in Individual Hafnia Nanorods. *Nat. Commun.* **2017**,

8 (May), 15316.

(60) Beaulieu, L. Y.; Eberman, K. W.; Turner, R. L.; Krause, L. J.; Dahna, J. R. Colossal Reversible Volume Changes in Lithium Alloys. *Electrochem. Solid-State Lett.* **2001**, *4* (9), 7–10.

(61) Barai, P.; Mukherjee, P. P. Mechano-Electrochemical Stochastics in High-Capacity Electrodes for Energy Storage. *J. Electrochem. Soc.* **2016**, *163* (6), A1120–A1137.

(62) Lim, J.; Li, Y.; Alsem, D. H.; So, H.; Lee, S. C.; Bai, P.; Cogswell, D. A.; Liu, X.; Jin, N.; Yu, Y.-S.;Salmon, N. J.; Shapiro, D. A.; Bazant, M. Z.; Tylizzczak, T.; Chueh, W. C. Origin and Hysteresis of Lithium Compositional Spatiodynamics within Battery Primary Particles. *Science* **2016**, *353* (6299), 566–571.

(63) Bazant, M. Z. Thermodynamic Stability of Driven Open Systems and Control of Phase Separation by Electro-Autocatalysis. *Faraday Discuss.* **2017**, *199*, 423–463.

(64) Nadkarni, N.; Rejovitsky, E.; Fraggedakis, D.; Di Leo, C. V.; Smith, R. B.; Bai, P.; Bazant, M. Z. Interplay of Phase Boundary Anisotropy and Electro-Auto-Catalytic Surface Reactions on the Lithium Intercalation Dynamics in Li_xFePO_4 Plateletlike Nanoparticles. *Phys. Rev. Mater.* **2018**, *2* (8), 085406.

(65) Handy, J. V; Luo, Y.; Andrews, J.; Bhuvanesh, N.; Banerjee, S. An Atomic View of Cation Diffusion Pathways from Single-Crystal Topochemical Transformations. *Angew. Chemie - Int. Ed.* **2020**, *59* (38), 16385–16392.

(66) Armstrong, E.; O'Dwyer, C. Artificial Opal Photonic Crystals and Inverse Opal Structures-Fundamentals and Applications from Optics to Energy Storage. *J. Mater. Chem. C* **2015**, *3* (24), 6109–6143.

(67) Sakamoto, J. S.; Dunn, B. Hierarchical Battery Electrodes Based on Inverted Opal Structures. *J. Mater. Chem.* **2002**, *12* (10), 2859–2861.

(68) Tong, Z.; Hao, J.; Zhang, K.; Zhao, J.; Su, B. L.; Li, Y. Improved Electrochromic Performance and Lithium Diffusion Coefficient in Three-Dimensionally Ordered Macroporous V_2O_5 Films. *J. Mater. Chem. C* **2014**, *2* (18), 3651–3658.

(69) Momma, K.; Izumi, F. VESTA: A Three-Dimensional Visualization System for Electronic and Structural Analysis. *J. Appl. Crystallogr.* **2008**, *41* (3), 653–658.

(70) Baddour-Hadjean, R.; Marzouk, A.; Pereira-Ramos, J. P. Structural Modification of $Li_xV_2O_5$ in a Composite Cathode ($0 \leq x < 2$) Investigated by Raman Spectroscopy. *J. Raman Spectrosc.* **2012**, *43* (1), 153–160.

(71) Scanlon, D. O.; Walsh, A.; Morgan, B. J.; Watson, G. W. An Ab Initio Study of Reduction of V_2O_5 through the Formation of Oxygen Vacancies and Li Intercalation. *J. Phys. Chem. C* **2008**, *112* (26), 9903–9911.

(72) Geuzaine, C.; Remacle, J.-F. Gmsh: A 3-D Finite Element Mesh Generator with Built-in Pre- and Post-Processing Facilities. *Int. J. Numer. Methods Eng.* **2009**, *79* (11), 1309–1331.

(73) Taylor, R. L.; Govindjee, S. FEAP-A Finite Element Analysis Program

Version 8.5. 2017, pp 1–663.

(74) Murphy, D. W.; Christian, P. A.; DiSalvo, F. J.; Waszczak, J. V. Lithium Incorporation by Vanadium Pentoxide. *Inorg. Chem.* **1979**, *18* (10), 2800–2803.

(75) Cava, R. J.; Santoro, A.; Murphy, D. W.; Zahurak, S. M.; Fleming, R. M.; Marsh, P.; Roth, R. S. The Structure of the Lithium-Inserted Metal Oxide δ-LiV_2O_5. *J. Solid State Chem.* **1986**, *65* (1), 63–71.

(76) Enjalbert, R.; Galy, J. A Refinement of the Structure of V_2O_5. *Acta Crystallogr.* **1986**, *C42*, 1467–1469.

(77) Cocciantelli, J. M.; Doumerc, J. P.; Pouchard, M.; Broussely, M.; Labat, J. Crystal Chemistry of Electrochemically Inserted $Li_xV_2O_5$. *J. Power Sources* **1991**, *34* (2), 103–111.

(78) Dickens, P. G.; French, s. J.; Hight, A. T.; Pye, M. F. Phase Relationships in the Ambient Temperature $Li_xV_2O_5$ System. *Mater. Res. Bull.* **1979**, *14* (10), 1295–1299.

(79) Meulenkamp, E. A.; Van Klinken, W.; Schlatmann, A. R. In-Situ X-Ray Diffraction of Li Intercalation in Sol-Gel V_2O_5 Films. *Solid State Ionics* **1999**, *126* (3), 235–244.

6. REVERSIBLE Mg-ION INSERTION IN A METASTABLE ONE-DIMENSIONAL POLYMORPH OF V_2O_5*

6.1. Overview

The Li-ion paradigm of battery technology is fundamentally constrained by the monovalency of the Li-ion. A straightforward solution is to transition to multivalent ion chemistries, with Mg^{2+} the most obvious candidate due to considerations of size and mass. Despite early interest, the realization of Mg batteries has faced myriad obstacles, including a sparse selection of cathode materials demonstrating the ability to reversibly insert divalent ions. Here, we show evidence of reversible topochemical and electrochemical insertion of Mg^{2+} into a metastable one-dimensional polymorph of V_2O_5, up to a capacity of 0.33 Mg^{2+} per formula unit. An electrochemical capacity of 90 $mAhg^{-1}$ is retained after 50 cycles with an average operating potential of 1.65 V *versus* Mg^{2+}/Mg^0. Not only does ζ-V_2O_5 represent a rare addition to the pantheon of functional Mg battery cathode materials, but is also distinctive in exhibiting a combination of high stability, high specific capacity due to ion insertion, and moderately high operating voltage.

* Reprinted (adapted) from Andrews, J. L.; Mukherjee, A.; Yoo, H. D.; Parija, A.; Marley, P. M.; Fakra, S.; Prendergast, D. G.; Cabana, J.; Klie, R. F.; Banerjee, S. Reversible Mg-Ion Insertion in a One-Dimensional Polymorph of V_2O_5. *Chem*, **2018**, *4* (3), 564-585. Copyright 2018 Elsevier Inc.

6.2. Introduction

Electrochemical energy storage is at a crossroads where numerous fundamental impediments must be addressed for large-volume production to meet technology needs in transportation and grid storage.[1] The shortcomings of the current paradigm, the Li-ion battery, are well known.[2] Significant effort has been devoted both to maximizing the energy density of the cell *via* the discovery of new solid electrode materials that can intercalate high concentrations of Li-ions at either highly reducing or oxidizing potentials,[3] and to improving kinetics and reversibility by nanostructuring existing candidates.[4,5] However, Li-ion batteries continue to encounter issues of safety and sustainability and are ultimately limited by the most fundamental of limitations: the monovalency of the Li-ion.

Several alternatives have been proposed as direct replacements for Li-ion technology, including Na-ion and multivalent ion (Mg^{2+}, Ca^{2+}, and Al^{3+}) technologies. Na-ion is viewed as a direct and more sustainable replacement to Li-ion owing to its monovalency and greater crustal abundance. However, the much larger radius of Na^{+} creates bottlenecks to reversible insertion and Na^{+} technologies do not overcome limitations of Li-ion in terms of the amount of charge that can be stored. In contrast multivalent-ion technologies are viewed as competitive successors to Li-ion batteries in part due to the prospect of storing more charge per ion at the cathode. These cations have the added benefit of being much more earth abundant than Li, and much less reactive in metallic form, adding to the safety of the technology. In particular, batteries based on the

shuttling of Mg^{2+} represent the most attractive alternatives because the small size and mass of these ions can be extrapolated to high theoretical energy storage metrics.[2,6] Indeed, the use of metallic Mg as the anode would bring about a transformative leap in volumetric energy density (theoretically predicted values are 3832 mAh cm^{-3} for metallic Mg *versus* ca. 800 mAh cm^{-3} for the graphite anode of Li-ion cells).[6,7] The shift to Mg also promises to allay long-term concerns regarding the sustainability of Li-ion battery technologies stemming from the low crustal abundance of Li (0.006%),[8] which will eventually necessitate the mining of Li from brine and deep-sea vents, leading to potential environmental impacts of unknown severity.[9,10] In contrast, magnesium has a much higher abundance than lithium (1.94%),[8] and is more desirable from a safety perspective because magnesium is non-dendrite forming, effectively eliminating the risk of thermal runaway.[11,12]

Despite the straightforward conceptual notion of substituting a monovalent cation for a divalent cation, attempts at developing Mg battery technologies have been thwarted by a plethora of materials limitations, including a lack of suitable electrolytes[8,13–15] and cathode materials. Arguably the greatest of these obstacles is the lack of cathode materials amenable to the reversible insertion of Mg-ions, primarily due to their slow solid state diffusion kinetics, which have been attributed to the significant polarization of anionic frameworks and stronger cation—cation repulsions induced by the much more “hard” (high charge-to-radius ratio) Mg-ion.[6] This same problem has plagued the search for Al-ion batteries, making suitable

cathode materials even rarer, since the highly localized trivalent charge is even more polarizing.[16] One proposed approach to solving this problem is to move beyond Mg-ion to Ca-ion chemistries, thereby retaining the benefits of the divalent charge but increasing the radius and thus decreasing the polarizing strength of the intercalating cation; however, as in the case of the larger Na^+, the increased ionic radius of Ca^{2+} makes the identification of suitable cathode materials rather difficult.[17,18]

Currently, Al-[19] and Ca-ion[17,18] cathode architectures are very scarce and will not be discussed further herein. However, it is worth noting that several modifications of the V_2O_5 framework have found use as cathode materials for Li-, Na-, and Mg-ion insertion. In particular, the thermodynamically stable (orthorhombic) phase of V_2O_5, a naturally occurring mineral ore, has been extensively studied as a cathode material for electrochemical insertion of various cations. In fact, this material was one of the first proposed by Whittingham[20] when evaluating materials for Li-ion intercalation. Indeed, α-V_2O_5 presents many desirable characteristics; it is a layered material, with ample interlayer spacing within which to accommodate intercalating ions. The 'single-layered' V_2O_5 structure comprises up-up-down-down-facing VO_5 square pyramids, which are edge and corner-sharing. Lithium, which is small, can diffuse through this framework although small polarons are stabilized, coupling the intercalated Li-ions with an electron and a localized lattice distortion.

While Na-[21] and Mg-ion[22–24] intercalation in the orthorhombic single-layer V_2O_5 has been observed, capacities are much lower than expected based on spatial or redox considerations (~0.17 Mg per V_2O_5).[22] Relatively higher capacities have been observed for the xerogel phase of V_2O_5.[25,26] This xerogel phase is a bilayered V_2O_5 polymorph, which incorporates interlayer and structural water molecules[27] and can more accurately be described as having a composition of $V_2O_5 \cdot 1.8H_2O$. There are two structural features of the xerogel phase which contribute to the increased intercalation capacities observed for Na^+ and Mg^{2+}. First, the water present within the structure greatly expands the interlayer spacing from 4.37 Å for α-V_2O_5 to 11.53 Å for the bilayered structure.[27] As mentioned previously, the primary difficulty in intercalating Na-ions is accounting for the increased ionic radius. In this way, the expanded interlayer spacing of this xerogel or 'bilyared' phase increases the capacity of Na-ions. The water present in the interlayer spacing serves a second role when intercalating Na- and Mg-ions. The water molecules likely coordinate to the diffusing species and help to screen the cation charge, thereby facilitating ionic diffusion. Li-ion intercalation has further been explored within a metastable puckered γ-$Li_xV_2O_5$ phase;[28] the puckered framework is retained upon reversible lithiation.[29] However, the intercalation of Na- or Mg-ions within this phase remains to be examined although recent calculations[30] indicate the feasibility of Na- and Ca-ion intercalation within this framework. A second example of the use of metastable V_2O_5 phases as cathode materials is for lithium insertion into the quenched high-pressure β-V_2O_5 phase,

which comprises double-layered V_2O_5 units incorporating corner-sharing motifs.[31] However, the 'saw-tooth' structure of this polymorph represents a particularly tortuous pathway for Li-ion diffusion; let-alone for Mg^{2+} diffusion. To date, there have been no reports of metastable V_2O_5 polymorphs being used as cathode materials for multivalent-ion batteries. This study thus provides a first example of using a metastable phase as a multivalent ion cathode material.

The importance of evaluating metastable phases as cathode materials derives from recent reports which demonstrate that the crystal structure motifs of potential cathode materials are only one aspect of designing cathode materials to accommodate ions beyond Li;[16,30,32] specifically, the electronic structure of such candidates is of equal importance in facilitating ionic diffusion.[16,30,32] Consequently, for reasons of both crystallographic and electronic structure, many proposed cathode materials are not able to accommodate Na^+ and multivalent cations such as Ca^{2+}, Mg^{2+}, and Al^{3+}, because structural or electronic structure impediments that may be minor for the monovalent Li^+ are exacerbated for di- and trivalent ions. Metastable phases hold promise for a allowing a broader range of structural motifs and connectivity but remain to be examined as viable cathode materials. Specifically, in the case of Mg^{2+}, the few suitable materials that are able to undergo Mg^{2+} insertion[6,21,33–40] are often limited by poor reversibility and massive phase inhomogeneity due to charge trapping and small polaron formation.[41,42] Mitigating this problem often requires heavy chalcogenide anionic frameworks, such as the Mo_6S_8 Chevrel phases, to screen Mg^{2+} as it diffuses,

leading to fundamentally lower operating potentials (ca. 1 V *vs.* Mg^{2+}/Mg^{0})[43–47] and gravimetric capacities.[33,43] Utilizing an oxide cathode promises fundamentally greater operating potentials[48] and improved gravimetric capacities; however, an oxide that combines the attributes necessary for reversible Mg^{2+} insertion from non-aqueous electrolytes with a high potential of operation remains elusive. Among the oxides studied so far, Mg^{2+} insertion with a reasonable voltage has been achieved in α-V_2O_5[23,49] and in related xerogels containing water[21,40]; however, despite calculations which predict that the high-temperature *δ*-$Mg_{0.5}V_2O_5$ phase (isostructural with *δ*-LiV_2O_5[50]) might be accessible upon magnesiation[36] as well as claims of capacities as large as $Mg_{0.66}V_2O_5$,[13,51] it has been demonstrated by direct evidence that Mg^{2+} insertion levels are much smaller, around $Mg_{0.17}V_2O_5$,[22,23] where the excess capacity observed in several studies has been attributed to proton intercalation.[24]

In past theoretical work, we have proposed the use of metastable V-O frameworks stabilized by the topochemical extraction of cations from ternary vanadium oxides as electrode materials,[16,30] thereby greatly expanding the available range of potential cathode materials and suggesting entirely different vanadium—oxygen connectivity not accessible within thermodynamic minima. We have posited that several of these compounds will enforce 'frustrated coordination environments' on the Mg-ions and should thus facilitate the facile diffusion of highly polarizing inserted ionic species.[16,36,52] Furthermore, the elimination of split-off conduction bands characteristic of 2D materials and the resulting improved d-

band overlap can potentially mitigate charge localization and the resulting stabilization of small polarons[41,53] that impede ion diffusion. We demonstrate here that a metastable ζ-phase of V_2O_5, stabilized by topochemical leaching of cations from β-phase ternary vanadium oxide bronzes,[54] is capable of reversibly inserting Mg-ions up to 0.33 Mg-ions per V_2O_5 unit within its 1D tunnel framework. Various methods of magnesiation including aqueous and non-aqueous chemical insertion of Mg^{2+} and high-voltage electrochemical magnesiation are demonstrated for this framework, clearly illustrating its ability to function as a reversible Mg-ion insertion host. Herein, we provide a refined crystal structure of the chemically magnesiated material, detail the electronic structure of the relevant phases to elucidate the mechanistic basis for the observed facile and reversible magnesiation, and evaluate the electrochemical performance of the material in a coin cell demonstrating a moderately high average operating potential of 1.65 V vs. Mg^{2+}/Mg^0 and a capacity retention of 90 $mAhg^{-1}$ after 50 cycles.

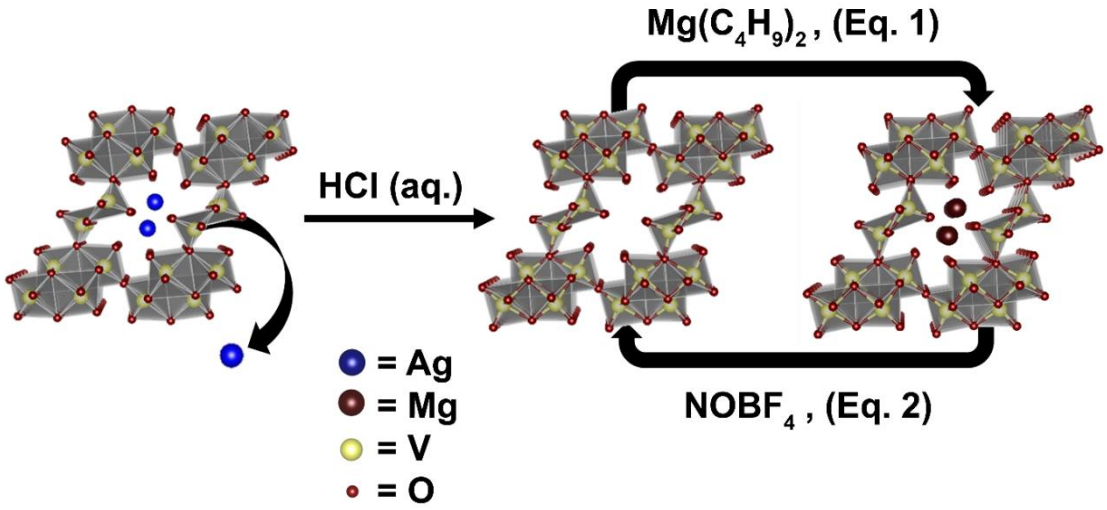

Figure 6.1. A ternary vanadium oxide bronze with a tunnel structure, β-$Ag_{0.33}V_2O_5$, is topochemically leached with HCl to stabilize an empty polymorph, ζ-V_2O_5, under hydrothermal conditions with complete retention of the tunnel structure (Equation 6.1). The empty ζ-V_2O_5 polymorph is evaluated for both chemical and electrochemical Mg-ion insertion. In the topochemical approach, shown here, di-*n*-butylmagnesium is used as the magnesiating agent (Equation 6.1) and $NOBF_4$ is used as the demagnesiating agent (Equation 6.2).

6.3. Results

6.3.1. Topochemical Mg^{2+} Insertion in ζ-V_2O_5

It has been well-established that topochemical reactions can serve as a useful analogue to related electrochemical processes.[55,56] Figure 6.1 illustrates the approach utilized in this work to synthesize the ζ-V_2O_5 phase, as well as an approach to 'topochemical cycling' of the materials by first magnesiating the structure *via* reaction with di-*n*-butylmagnesium in heptane followed by demagnesiation *via* reaction with $NOBF_4$ in acetonitrile, each with retention of the original oxide framework. The quasi-one-dimensional ζ-V_2O_5 phase is a metastable open framework that is obtained by topochemical leaching of Ag-ions

from nanowires of a tunnel-structured β-$Ag_{0.33}V_2O_5$ phase[54] and has thus far not been stabilized in the bulk. Leaching of Ag-ions with HCl yields a AgCl precipitate along with ζ-V_2O_5 with the remnant Ag content greatly reduced to about 0.04 per formula unit of V_2O_5, as described in our previous work.[54] To obtain a phase-pure material for topochemical and electrochemical intercalation studies, the mixture is washed with an aqueous solution of $Na_2S_2O_3$ as evidenced by powder diffraction in Figure D.1.

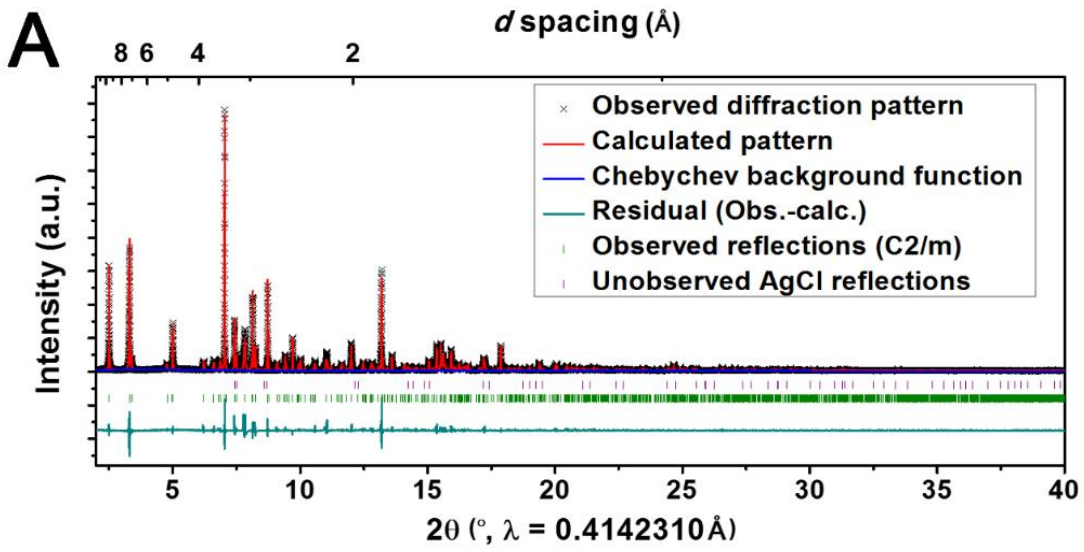

Figure 6.2. High-resolution synchrotron powder X-ray diffraction data (λ=0.4136 Å) collected for (A) empty ζ-V_2O_5, and for (B) the chemically magnesiated structure β-$Mg_xV_2O_5$, synthesized using the same sample shown in (A). The raw collected data is represented as black crosses, the Rietveld fit is shown as a red line, the background function is depicted as a dark blue line, and the residual (observed-calculated) is depicted as a light blue line. A magnified view of the 2θ = 8.5—8.9° range of (A) showing that the refined structure maps well to the peak profiles and confirms the phase purity and successful elimination of residual AgCl. (C) A refined structure of the chemically magnesiated ζ-V_2O_5 phase where Mg sits in a pseudo square-pyramidal β-site. A fractional occupancy of x=0.331 is obtained for magnesium on this site.

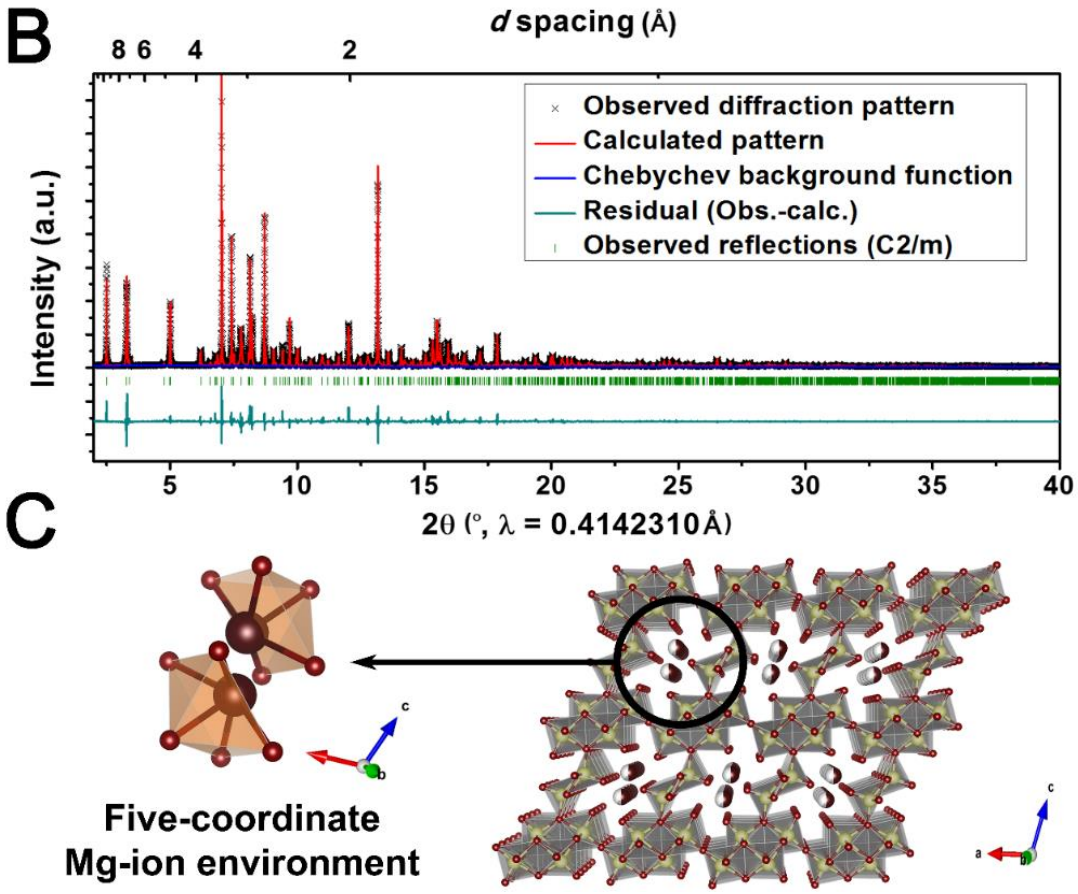

Figure 6.2. Continued.

The geometric structure of the materials has been investigated by X-ray diffraction (Figure 6.2**)**. Figure 6.2A depicts a high-resolution synchrotron powder diffraction pattern (λ=0.4136Å) for the pristine ζ-V_2O_5 material, including a refinement of the crystal structure. The sample used in this study has a residual Ag content of x≈0.06. The distinctive tunnel structure of ζ-V_2O_5 has also been investigated by transmission electron microscopy, electron diffraction, and aberration-corrected scanning transmission electron microscopy (STEM), presented in Figure 6.3. Figure 6.3A shows a low-magnification TEM image of ζ-

V_2O_5, which elucidates the nanowire morphology; the electron diffraction pattern shown as an inset to Figure 6.3A verifies the single-crystalline nature of the pristine nanowires. It is important to note that in this system, as shown in Figure 6.3A, the growth direction of the nanowires is perpendicular to the one-dimensional tunnels. Hence, ion insertion is expected to occur radially within these ζ-V_2O_5 nanowires.

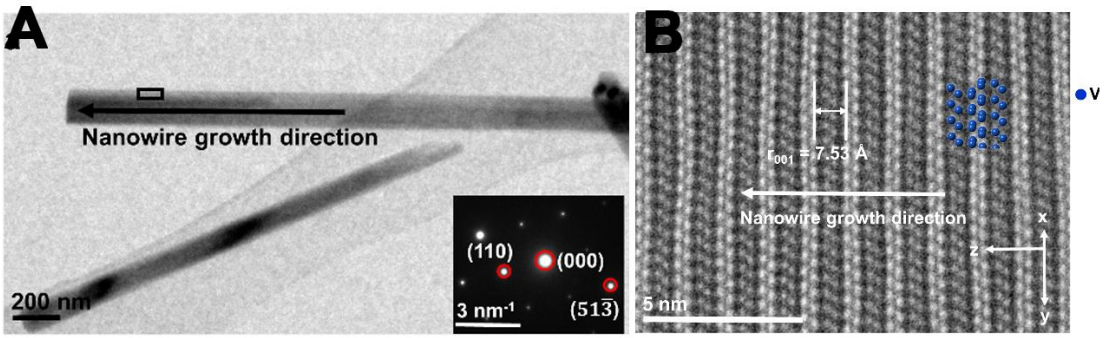

Figure 6.3. (A) Low magnification TEM image of ζ-V_2O_5 nanowires, thin area used for atomic-resolution imaging marked with a rectangle, inset shows electron diffraction. (B) Atomic-resolution high angle annular dark field (HAADF) image (filtered) showing tunnels perpendicular to nanowire growth. Structural model for ζ-V_2O_5 along the [110] zone axis showing V atoms (light blue) overlaid on the experimental image. Scale bars for the images are (A) 200 nm, inset (A) 3 nm^{-1} and (B) 5 nm.

The atomic-resolution high angle annular dark field (HAADF) image (Figure 6.3B) confirms the structure solution of this metastable polymorph,[54] which is depicted in greater detail in Figure D.2. In this HAADF image, which is sensitive to *Z*-contrast, the vanadium atoms can be clearly imaged and the observed motif is reproduced well by the structural model of pristine ζ-V_2O_5 along the [110] zone

which is overlaid on the experimentally acquired image. This provides a direct view of the empty tunnels and verifies the structural assignment noted above. The nanowire growth direction as well as the spacing between V atomic columns is clearly marked on the atomic-resolution HAADF image presented in Figure 6.3B.

The empty ζ-V_2O_5 structure can subsequently be chemically magnesiated by aqueous and non-aqueous routes.[54] In the former method, which was used to synthesize the sample generating the pattern depicted in Figure 6.2B, the chemically magnesiated phase is obtained by reaction with metallic Mg nanoplatelets in water.[54,57] It is crucial to note that the same pristine sample used to generate the pattern in Figure 6.2A was chemically magnesiated and used to obtain the diffraction pattern in Figure 6.2B. Thus, changes in the diffraction pattern from 2A to 2B can be directly attributed to the magnesiation reaction. The most significant difference between the diffraction patterns is a slight expansion in lattice parameters, indicative of insertion of the small Mg-ions into the 1D tunnels of ζ-V_2O_5, resulting in a change in volume from 522.96 to 525.63 $Å^3$ (Table D.1). The small change in volume is along the lines of predictions from DFT calculations, which suggest that the 3D rigid framework is not extensively deformed by topochemical insertion of Mg-ions.[16] A significant diminution in peak intensity for reflections from the {200} family of planes is observed upon Mg-ion intercalation; these planes slice the two β- sites where the inserted cations reside; the significant decrease in peak intensity of the (200) reflection can be attributed to increased electron density within the tunnels upon insertion of Mg-ions nearing

the stoichiometric limit of x=1/3 for this material, as enforced by the space constraints of the empty β-site.[58] A similar diminution in the intensity of {111} reflections, which intersect the 1D tunnels is also observed.

These changes to the diffraction profile suggest a topochemical expansion of the lattice to accommodate the intercalated Mg-ions, which reside within square-pyramidal sites as illustrated by the orange polyhedra in Figure 6.2C, which are quite distinct from the seven-coordinated local geometries of Na- and Ag-ions in isostructural Wadsley-type β-$M_xV_2O_5$ bronzes.[54,59,60] Notably, a five-coordinate local geometry is not preferred by Mg-ions and this structure thus enforces a somewhat "frustrated" local coordination sphere. The refined structure of β-$Mg_{0.331}V_2O_5$ is shown in Figure 6.2C and in further detail in Figure D.2. The details of the refinement including atom positions (Table D.1) and bond distances and angles (Table D.2) are provided in Appendix D. Careful analysis of X-ray diffraction data obtained for ζ-V_2O_5 nanowires magnesiated chemically in a non-aqueous medium as per Equation 6.1 (Figure 6.4) and those magnesiated electrochemically (Figure D.4) yield the same crystal structure as the one obtained by the refinement of those magnesiated chemically by the aqueous method, discussed above (Figure 6.2).

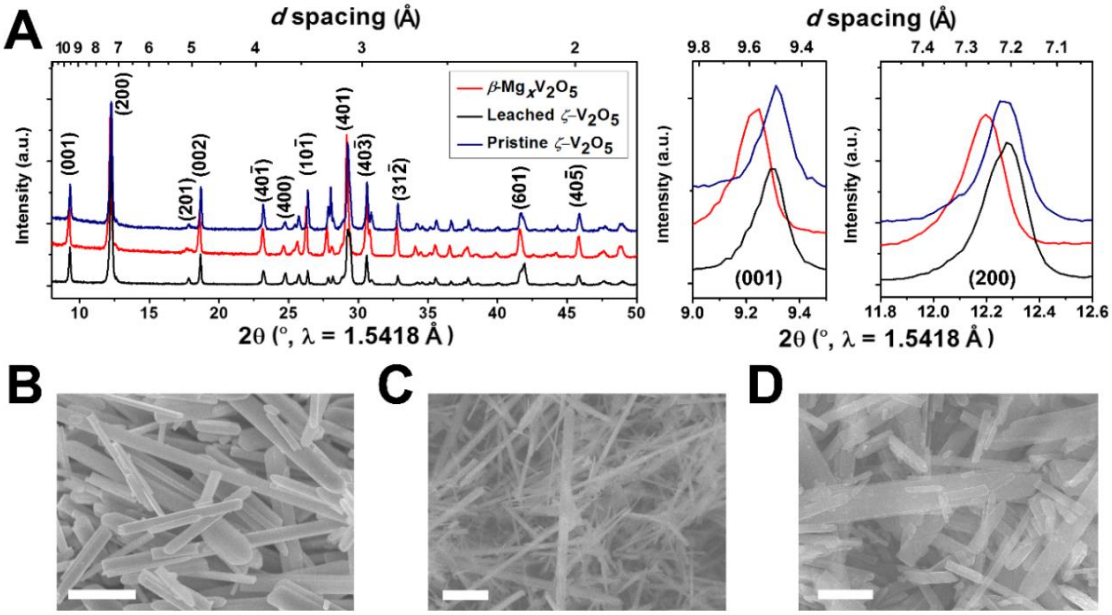

Figure 6.4. (A) Powder XRD patterns showing reversible topochemical intercalation and extraction of Mg^{2+} as per Equation 6.1 and Equation 6.2. The slight expansion of the lattice upon incorporation of Mg-ions is reflected in a shift of the (001) and (002) reflections to lower 2θ values, as depicted in the magnified regions of (A). The intensities of the reflections shown in the magnified regions are normalized such that the intensity of the (200) reflection is unity. SEM images of (B) pristine ζ-V_2O_5 nanowires, (C) chemically magnesiated β-$Mg_xV_2O_5$ nanowires, and (D) $NOBF_4$-leached ζ-V_2O_5 nanowires. The scale bars on the SEM images are 1 µm, 3 µm, and 1µm respectively. The retention of morphology after each reaction corroborates the topochemical nature of the reaction.

6.3.2. Reversibility of Mg^{2+} Insertion in ζ-V_2O_5

Pristine ζ-V_2O_5 can also be topochemcially magnesiated by direct reaction with di-*n*-butylmagnesium[56] in heptane solution under reflux as per:

$$\zeta\text{-}V_2O_5(s) + 0.33Mg(C_4H_9)_2\ (\text{heptane}) \xrightarrow{\Delta}$$

$$\beta\text{-}Mg_{0.33}V_2O_5(s) + 0.33C_8H_{18}(g) \qquad \textbf{6.1}$$

Subsequently, the inserted Mg-ions can be extracted from the β-$Mg_{0.33}V_2O_5$ structure (as well as from β-$Mg_{0.33}V_2O_5$ prepared under aqueous conditions) by

treatment with a strong oxidizing agent, $NOBF_4$, in dry acetonitrile solution as per:[61]

$$\beta\text{-}Mg_{0.33}V_2O_5(s)+0.66NOBF_4(MeCN) \rightarrow$$

$$\zeta\text{-}V_2O_5(s)+0.33Mg(BF_4)_2(s)+0.66NO(g) \qquad \textbf{6.2}$$

Characterization of the structure and morphology of the samples magnesiated as per Equation 6.1 and demagnesiated as per Equation 6.2 is depicted in Figure 6.4. The structural change upon magnesiation/demagnesiation as observed in powder diffraction is manifest in a change in the 2θ position of the {00*l*} and {*l*00} reflections, as shown in expanded views of these reflections in Figure 6.4A. The shift of both reflections to lower 2θ values upon magnesiation is consistent with expansion of the tunnels on Mg^{2+} insertion. The return of the reflections to values near those of the pristine material indicates recovery of the pristine ζ-V_2O_5 structure upon $NOBF_4$ treatment and attests to the reversibility of the magnesiation process. A pronounced change in color from orange-yellow (characteristic of V^{5+}) to dark green is observed upon magnesiation (Figure D.3). Importantly, the removal of the Mg-ions is necessarily coupled to a re-oxidation of the V_2O_5 lattice, which brings about a reversion to an orange/yellow color. Energy dispersive X-ray spectroscopy analysis (EDX) is shown in Figure D.3 and corroborates that Mg-ions are indeed incorporated in and removed from the sample, respectively, necessitating that their introduction into the structure should lead to changes in structure of ζ-V_2O_5 revealed by diffraction. Reaction as per Equation 6.1 allows for nearly complete occupancy of the β-sites along the 1D

tunnels. In contrast, the Mg-ions are almost entirely removed upon leaching with $NOBF_4$. It is important to note that, in contrast to other vanadium oxide materials wherein co-intercalation of water with Mg^{2+} has been observed to increase the observed capacity of the material due to proton insertion,[24] we have observed no evidence of co-intercalation of water or hydrogen into the relatively spatially constrained quasi-one-dimensional tunnels of ζ-V_2O_5 as evidenced by a lack of spectroscopic signatures of water in X-ray absorption spectroscopy, as will be discussed later.

The ζ-V_2O_5 materials prepared here have lateral dimensions of 149±5 nm and range several microns in length, consistent with previously reported dimensions for the precursor, β-$Ag_xV_2O_5$,[54] although their lengths are somewhat reduced due to grinding of the powders prior to topochemical magnesiation/demagnesiation. Figure 6.4D—F indicate retention of morphology upon magnesiation/demagnesiation, attesting to the topochemical nature of this process and further suggesting a high degree of structural stability and the ability to mitigate strain induced by volume expansion (which is <1% based on the refinements above). It is important to note that because the one-dimensional tunnels are perpendicular to the direction of wire growth, Mg^{2+} diffusion occurs along the shortest dimension of the wires which is likely conducive to facilitating homogeneous magnesiation and demagnesiation by providing short diffusion path-lengths for the cations and thereby helps to improve slow diffusion kinetics like those observed with orthorhombic V_2O_5.[21,23,62,63] Critically, despite the ~150

nm one-dimensional diffusion path lengths, finite size effects in other V_2O_5 phases have not been considered significant until dimensions are scaled to ~50 nm.[5] It is therefore likely that the behavior exhibited here more closely approximates 'bulk' behavior for this material, making nanostructuring of great importance for future studies aiming to improve diffusion kinetics.

6.3.3. Electrochemical Mg^{2+} Insertion in ζ-V_2O_5

The ζ-V_2O_5 nanowires were also electrochemically cycled in a Mg^{2+} electrolyte using coin-type cells in a hybrid configuration at 50°C (Figure 6.5). As a comparison, the topochemical synthesis were performed at room temperature for the aqueous method and 98°C for the non-aqueous method.

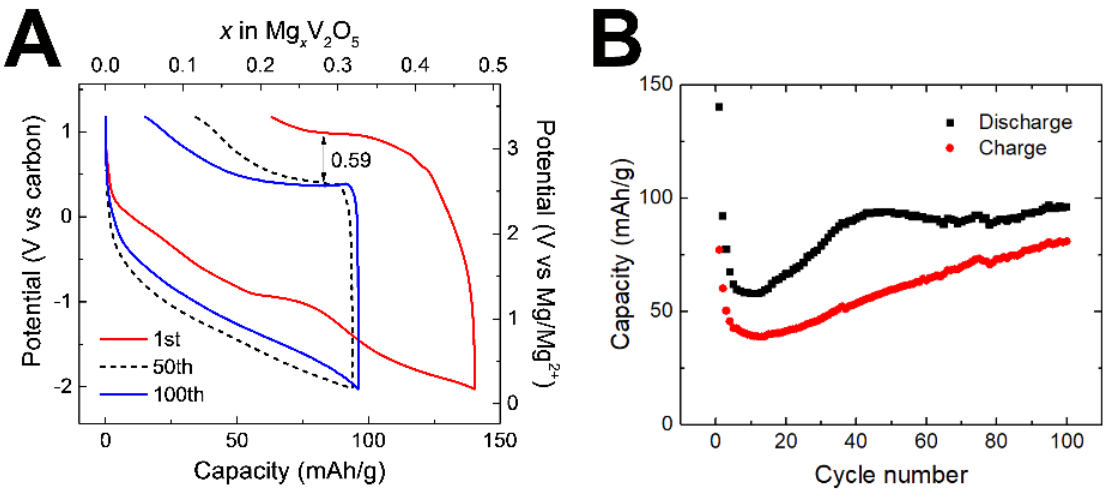

Figure 6.5. (A) Voltage *versus* capacity profiles acquired at different cycle numbers for the electrochemical cycling of ζ-V_2O_5. After 50 cycles, the material exhibits a stable discharging capacity of 90 mAh/g with an exceptional average operating voltage of 1.65 V *versus* Mg/Mg^{2+}. (B) Capacity *versus* cycle number plot (for cycles 1-85) which illustrates the exceptional stability and reversibility of the material during cycling (C) XRD patterns of pristine, discharged, and subsequently charged ζ-V_2O_5.

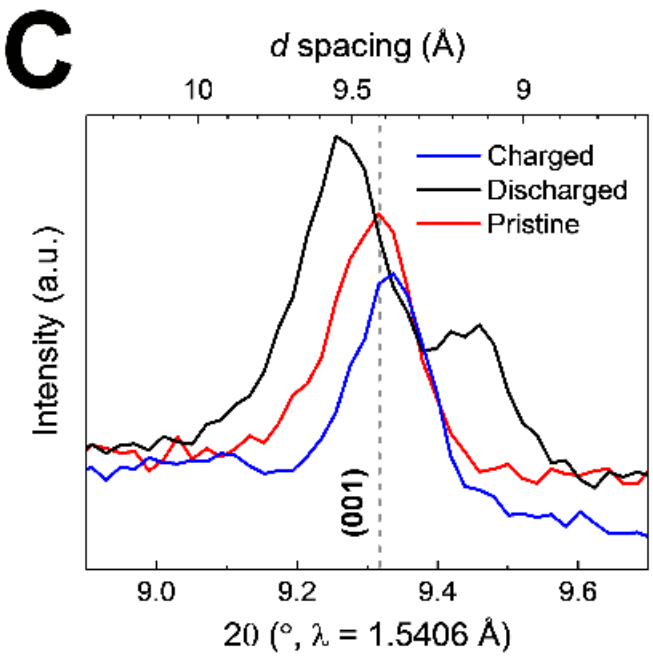

Figure 6.5. Continued.

The first discharge cycle (Figure 6.5A) shows a capacity of 140 mAh g^{-1}, which corresponds to the intercalation of 0.48 Mg^{2+} per V_2O_5 unit, as opposed to 0.331 Mg^{2+} observed for chemically discharged samples. This increased capacity observed for the first cycle is likely due to the decomposition of electrolyte at the cathode surface to form a solid electrolyte interphase (SEI) region and is evidenced by the poor Coulombic efficiency observed for the first cycle (55%). Despite the poor initial Coulombic efficiency, the discharge capacity is stabilized at 90 mAh/g (i.e., 0.31 Mg^{2+}) after 50 cycles. The observed capacity suggests magnesium intercalation very close to the expected maximum capacity of the crystallographic β-site (Figure D.10), which represents the most favorable intercalation site for the inserted cations.[16,28] Although the Coulombic efficiency

was limited to 55% during the first cycle, likely due to the observed sluggish intercalation kinetics, especially during demagnesiation (charging). Continued cycling reduces the polarization of charging by 0.59 V and enhances Coulombic efficiency up to 84.2% for 100th cycle, suggesting improved intercalation kinetics with increased cycling, likely due to a combination of interfacial stabilization and improved wetting of the composite electrode by the electrolyte. Such an abrupt increase in coulombic efficiency over the first several cycles is often observed as the solid-electrolyte interphase (SEI) layer is formed and then reconstituted, marking a pronounced decrease in the amount of parasitic, irreversible side reactions, which limit capacity in early cycling.[64] As the number of parastitic reactions decreases and SEI is stabilized, the accessible capacity stabilizes at 90 mAh/g. This exceptional cycling stability is depicted strikingly in Figure 6.5B, which depicts cycling performance and a stabilization of the capacity at 90 mA h g^{-1} after 85 cycles. A magnified view of powder XRD patterns in Figure 6.5C (Figure D.4) further evidences the reversibility of the structural changes during electrochemical cycling (collected following the initial discharge cycle). The similarities between the diffraction patterns of the topochemically and electrochemically prepared samples (Figure 6.4A, Figure 6.5C, and Figure D.4, respectively) are striking and suggest that the two processes occur via the same mechanism, allowing structural insight deduced from the chemically prepared phase to be applied to that of the electrochemically prepared phase. Upon magnesiation (discharge), the (001) reflection shifts to a lower angle ζ-V_2O_5, reflecting an expansion of the lattice due

to Mg^{2+} insertion and V reduction. An additional reflection is observed at a higher angle of 9.5° and likely corresponds to stage-ordering phenomena wherein upon electrochemical insertion, specific tunnels are filled. Regardless, the insertion is entirely reversible as the reflection disappears on demagnesiation.

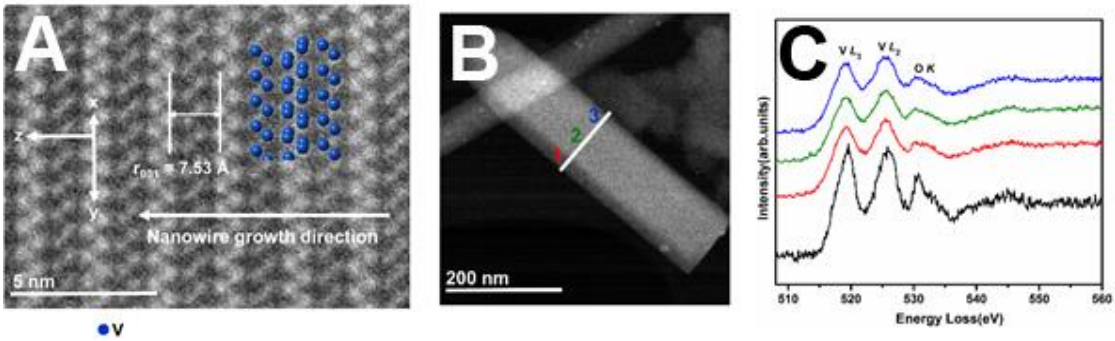

Figure 6.6. (A) Atomic-resolution HAADF image of the electrochemically magnesiated ζ-V_2O_5 nanowires (collected following the initial discharge cycle), corresponding structural model for ζ-V_2O_5 along the [110] zone axis overlaid. (B) HAADF image showing nanowire for EELS linescan with the probed area clearly marked. (C) Comparison of EEL spectra between pristine and electrochemically magnesiated ζ-V_2O_5 nanowire showing a reduction of the V valence state in the magnesiated sample. An integrated EDX spectrum showing ca. 4 ± 4 at.% of Mg, corresponding to a stoichiometry in the range of ca. $Mg_{0.26}V_2O_5$ – $Mg_{0.32}V_2O_5$ as shown in Figure D.5 (C). Scale bars for the images are: (A) 5 nm and (B) 200 nm.

Interestingly, upon charging, the (001) reflection returns to an angle higher than that of even pristine ζ-V_2O_5, likely due to the removal of a very small amount of residual silver within the empty tunnels of the pristine material under high potential (ca. 0.04 Ag per V_2O_5). The electrochemically magnesiated ζ-V_2O_5 nanowires have also been investigated by transmission electron microscopy techniques, which is depicted in Figure 6.6 (collected following the initial discharge

cycle). The atomic-resolution HAADF image (Fig 6a) for the electrochemically magnesiated ζ-V_2O_5 nanowires clearly identifies the V atomic framework. This image can be compared directly with the structural model of pristine ζ-V_2O_5 overlaid on the experimental image, which similarly shows only V atoms along the [110] zone axis. This verifies that these ζ-V_2O_5 nanowires retained their tunnel structure upon Mg-ion insertion, consistent with the high structural reversibility seen in the XRD data presented in Figure 6.4A and Figure D.4. Evidence of Mg-ion intercalation is provided by EDX analysis. The atomic-resolution HAADF image used for EDX line scan is presented in Figure D.5A which has also been acquired along the [110] zone axis. The EDX line scan presented in Figure D.5B, performed perpendicular to the tunnels, along the *z* direction, shows clear evidence for Mg, indicating presence of Mg within the tunnel sites. The integrated EDX spectra collected along the same line scan is presented in Figure D.5C. It shows a clear Mg signal (along with V and O, as expected), corresponding to a ca. 4 ± 4 at% value for Mg, corresponding to a stoichiometry in the range $Mg_{0.26}V_2O_5$ –$Mg_{0.32}V_2O_5$ upon electrochemical Mg- ion insertion. This value is also consistent with the extent of Mg-ion insertion levels deduced from the stabilized discharge capacity of 90 mAh/g after 50 cycles (Figure 6.5A). The close agreement between the EDX-quantified Mg content within the tunnels, the capacity deduced electrochemically, and occupancy values obtained from Rietveld refinement for chemically magnesiated samples is remarkable and indeed provides strong corroboration for topochemical Mg-ion intercalation and

suggests that reversible Mg-ion insertion, rather than proton insertion as has been observed for layered vanadium oxides, is the origin of the observed capacity.[24] This is indeed further supported by the absence of distinctive water signature in the X-ray absorption spectra collected for the magnesiated samples (Figure 6.7A).

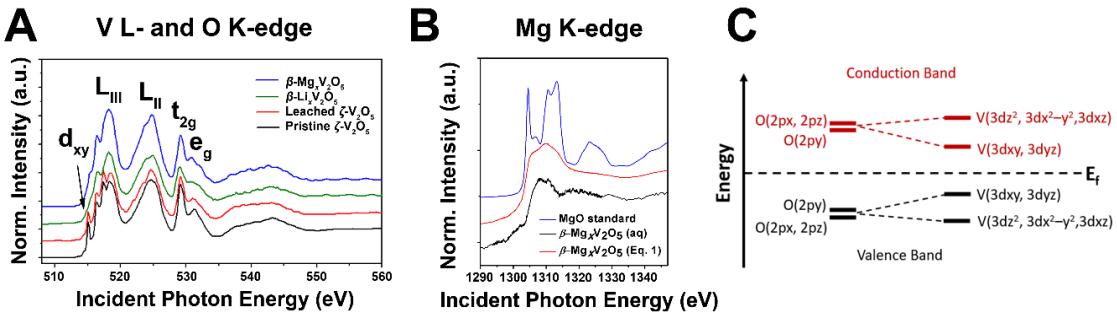

Figure 6.7. (A) Integrated X-ray absorption spectra collected for individual nanowires of empty ζ-V_2O_5 precursor (black), magnesiated β-$Mg_xV_2O_5$ (blue), $NOBF_4$-leached ζ-V_2O_5 (red), and β'-$Li_{0.66}V_2O_5$ (green). The spectra are superimposed to highlight changes in electronic structure upon insertion and extraction of Mg-ions. (B) Ensemble Mg K-edge X-ray absorption spectra were collected for magnesiated samples and are superimposed with spectra acquired for a MgO standard. Spectra for samples magnesiated as in aqueous media using Mg nanoplatelets and as per Equation 6.1 in heptane solution using di-*n*-butylmagnesium are contrasted. (C) A simplified schematic representation of the hybridization of V 3d orbitals and O 2p orbitals in the valence and the conduction bands. Three crystallographically inequivalent vanadium atoms each have somewhat different splitting of 3d states owing to differences in their local coordination environment. GGA DFT+U calculated atom-projected density of states (DOS) for V (red), O (green), and Mg (blue) for ζ-V_2O_5 magnesiated to a limit of (D) x=0.083 and (E) x = 0.33. Upper and lower halves of the DOS correspond to up and down spins, respectively, where the V-O 'midgap state' at the edge of the conduction band (ca. 0.5 eV) is not present in the lower half. The gray regions correspond to the total density of states. Local density of states (LDOS) for ζ-V_2O_5 magnesiated to (F) x=0.083 and (G) x = 0.33.

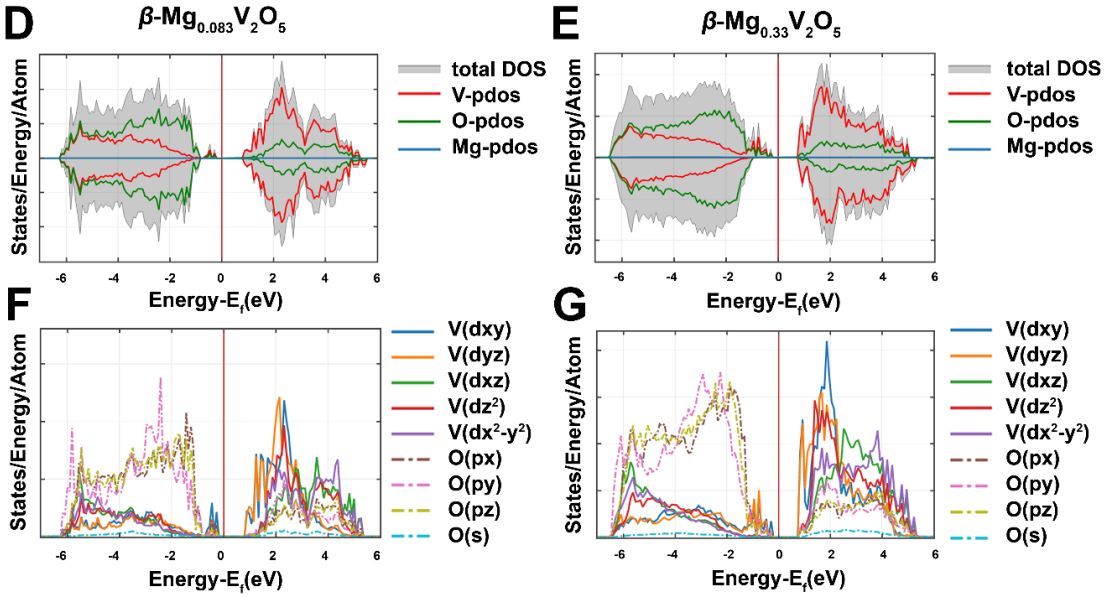

Figure 6.7. Continued.

The large hysteresis in the electrochemical curves (Figure 6.5) complicates the definition of a value of equilibrium potential. We report an average voltage of 1.65 V *vs* Mg^{2+}/Mg^{0} by simply taking the average of the values at which Mg insertion and deinsertion were observed in Figure 6.5A, as measured in plots of the corresponding first derivative (dQ/dV, Figure D.6).This average value (1.65 V), which we have reported here is not the equilibrium voltage, which, nonetheless, should be located between the experimental values measured on discharge (~1.2 V *versus* Mg^{2+}/Mg^{0}) and charge (~3.1 V), respectively. Deviations from the equilibrium value are typically ascribed to overpotential ascribed to kinetic limitations, for instance, in interfacial charge transfer or bulk diffusion.[23,42] The equilibrium voltage can be computed *ab initio* using DFT, as demonstrated for α-V_2O_5, where reasonable agreement with experiments was found,[16,65] albeit in

most of these studies the voltage observed is not due to exclusively Mg^{2+} insertion but rather mixed Mg^{2+} and H^{+} insertion. The voltages calculated in this work and in our previous work were computed using an onsite Coulombic and exchange interaction parameter. But, since first-principles-computed voltages are strongly dependent on the degree of electron localization in these strongly correlated systems, computations were carried out for $Mg_xV_2O_5$ with different values of the on-site Coulomb and exchange interaction parameter, *U*. The calculated voltage increases with increasing value of *U* (i.e., increasing electron localization) when $x>0.2$, with calculated voltages ranging from ~2.9 V for $U=4.0$ to ~1.6 V for $U=0$ (Figure 8E). All these values are between the experimental values observed for discharge and charge, making them consistent with the experiments. Asymmetric deviations from the equilibrium value indicate that the kinetics of charge and discharge are different, which is not uncommon in electrochemical reactions. In this work, we have accessed Mg^{2+} capacities of $x = 0.33$ in $Mg_xV_2O_5$, but previous work suggests that stoichiometries of $x = 0.66$ may be accessible based on the availability of intercalation sites.[16,66,67] Figure D.7 therefore shows the variation of voltage with *U* at higher capacities. The results indicate that above $x = 0.25$, the voltage decreases with decreasing *U* as the degree of electron correlation decreases. Nevertheless, for the purposes of this discussion, $U = 4$ was used to calculate all potentials and diffusion barriers when using DFT+*U.* For further comparison, Figure D.7F compares the difference in chemical potential for *ζ* and α polymorphs of V_2O_5. Despite the greater stability of the magnesiated *ζ*-V_2O_5

phase relative to magnesiated α-V_2O_5, the metastability of empty *ζ*-V_2O_5 results in a larger potential difference between empty and magnesiated phases for *ζ*-V_2O_5 (0.52 eV for α- *vs.* 0.61 eV for ζ-V_2O_5).

6.3.4. Electronic Structure Considerations

Cation insertion into a cathode framework necessitates concomitant reduction of the transition metal center to maintain charge balance. In the case of ζ-V_2O_5, the oxidation state is expected to change from exclusively V^{5+} to mixed valence V^{5+}/V^{4+}, making a detailed study of its electronic structure necessary both for confirming Mg-ion insertion and for explaining electronic contributions to facile diffusion. As such, the electronic structure of this material has been studied as a function of topochemical insertion and extraction and electrochemical cycling. Scanning transmission X-ray microscopy (STXM) has been used as a spectrally and spatially resolved probe of the unoccupied density of states of the empty ζ-V_2O_5 precursor nanowires, chemically magnesiated β-$Mg_{0.331}V_2O_5$ nanowires (Equation 6.1), and the chemically de-intercalated nanowires (Equation 6.2). Figure 6.7 depicts integrated V $L_{2,3}$-edges and O K-edge X-ray absorption spectra acquired for individual nanowires of each sample; a spectrum acquired for a lithiated β'-$Li_{0.66}V_2O_5$ nanowire is also depicted alongside for comparison. The absorption features correspond to transitions of core electrons from V 2p to partially occupied and unoccupied V 3d states at the V $L_{2,3}$-edges and from O 1s to partially unoccupied or unoccupied O 2p states at the O K-edge.[53,68–70] Life-time broadening, due to a Coster-Kronig Auger decay process, which fills the X-ray

excited $2p_{1/2}$ hole with a $2p_{3/2}$ electron, renders the V L_{II} edge less informative; however, the V L_{III} edge (immune to this process) displays fine-structure, which can be assigned based on previous electronic structure calculations as well as with analogy to measurements for orthorhombic α-V_2O_5.[41,53,68–70] These features comprise transitions from the singlet V $2p^6 3d^0$ into V $2p^5 3d^1$ states split predominantly by crystal field (and also potentially by multiplet) effects. Figure 6.7 depicts calculated atom- and orbital-projected density of states for low and high concentrations of magnesium occupancy, *x,* in β-$Mg_xV_2O_5$. The electronic structure can be understood with reference to Figure 6.7C, which provides a schematic depiction of the hybridization of the V 3d orbitals and O 2p orbitals in the valence and conduction bands. Figure 6.7D and E suggest that the valence band is derived primarily from O 2p states, whereas the conduction band is primarily V 3d in origin. ζ-V_2O_5 has three separate crystallographically inequivalent vanadium atoms; however, the conduction band edge primarily comprises V $3d_{xy}$ states derived from one of the vanadium atoms (the V $3d_{xy}$ states for the other two vanadium atoms are slightly higher in energy) although these states are not split-off from the rest of the conduction band as in α-V_2O_5. Transitions to V $3d_{xy}$ and the next higher energy V $3d_{yz}$ states are clearly resolved as absorption features at the V L_{III}-edge in the spectrum acquired for ζ-V_2O_5 nanowires, shown in Figure 6.7A. Upon insertion of Mg-ions (as well as for Li-ions), Figure 6.7A indicates a greatly diminished intensity of the first two absorption features at 515 and 516.4 eV at the VL_{III}-edge arising from Pauli state blocking as the lowest-lying

conduction band states are filled by electrons from the ionized cations. As also observed for lithiation of α-V_2O_5,[16,71] the filling of these states provides direct evidence for local reduction of pentavalent vanadium sites. Remarkably, upon de-intercalation using $NOBF_4$, these states are recovered and indeed the ζ-V_2O_5 precursor and the chemically demagnesiated sample show strikingly similar spectroscopic signatures. This recovery of electronic structure (as also evidenced by recovery of the orange—yellow coloration, Figure D.3 following de-insertion is indicative of near complete extraction of the Mg-ions and corroborates the overall reversibility of the process. The similarities between β-$Mg_xV_2O_5$ and β'-$Li_{0.66}V_2O_5$ are also compelling at the V L- and O K-edge, and are explicable given that both materials have the same nominal vanadium oxidation state (V^{5+}:V^{4+} of ca. 2:1), and are nearly isostructural, save for the crystallographic positions of the diffusing ions (β sites in $Mg_xV_2O_5$ as compared to β' sites shifted down the 1D tunnel by half a unit cell length in $Li_{0.66}V_2O_5$).[54,58,72] The localized reduction of vanadium sites is further corroborated by vanadium K-edge XANES spectroscopy. The spectra displayed in Figure D.8 were collected between 5355—5765 eV for pristine ζ-V_2O_5, and β-$Mg_xV_2O_5$ magnesiated to two different extents (low extent of magnesiation, where $x_{intended}$=0.2 and high extent of magnesiation, where x=0.33). V K-edge measurements are particularly sensitive to vanadium oxidation state. In particular, the peak centroid position and peak intensity of the pre-edge feature centered at ~5470 eV is critically sensitive to vanadium oxidation state and local V coordination environment.[71] The observed shift of the peak centroid to

lower energies is monotonic with increasing magnesiation and is direct evidence of decreasing local oxidation state of the vanadium within the lattice (the peak position of this feature in VO, which is exclusively V^{4+} is centered ~2 eV below that of V_2O_5).[25] The monotonic decrease in vanadium valence state with increasing concentration of magnesium source (di-*n*-butylmagnesium), where solvent water levels are held constant at <20 ppm, strongly suggests that vanadium reduction is due to further Mg^{2+} insertion into the lattice rather than proton insertion within the tunnels as has been observed in α-V_2O_5.[24]

The O K-edge XAS spectra reflect transitions of O 1s core electrons to O 2p states, which, in turn, are hybridized with V 3d states and, thus, reflect their crystal field splitting. Figure 6.7 also suggests that there is no substantial Mg—O hybridization, as we have observed for other $M_xV_2O_5$ bronzes.[73] Upon magnesiation, the changes in the O K-edge can be understood with respect to the orbital projected density of states plotted in Figure 6.7F and Figure 6.7G. The O K-edge XANES for ζ-V_2O_5 is split into two separate manifolds centered at ca. 529.2 and 531.2 eV, which can be attributed to transitions to V3d—O2p hybrid states of t_{2g} and e_g symmetry corresponding to π and end-on σ-interactions, respectively. Upon insertion of Mg-ions, Figure 6.7 suggests a diminished spectral weight for the t_{2g} peaks and a broader energy dispersion. These spectral changes can be directly correlated to Mg-ion intercalation. Figure 6.7F and Figure 6.7G indicate that upon magnesiation, the low-lying V3d_{xy} and 3d_{yz} states are filled and give rise to ‘mid-gap’ states, resulting in loss of spectral intensity from the t_{2g}

manifold. Furthermore, the structural distortion induced by magnesiation yields a distinctive crystal field splitting pattern wherein the V $3d_{xz}$ states appear at energies intermediate between the t_{2g} (V$3d_{xy}$ and $3d_{yz}$) and e_g (V$3d_{z2}$ and $3d_{x2-y2}$) levels. This splitting pattern is reflected in a broader spread of energies and decreased separation between the t_{2g} and e_g peaks. It is worth noting that the well-resolved two-peak lineshape for ζ-V_2O_5 is again completely recovered at the O K-edge upon extraction of the Mg-ions by treatment with $NOBF_4$ (Figure 6.7A). Moreover, spectroscopic signatures of intercalated water observed for V_2O_5 xerogels or hydrated Sr-ions intercalated between double-layered V_2O_5 slabs are not observed[73] further indicating that desolvated and bare Mg^{2+}, not hydrated Mg^{2+}, are the intercalating species. Additionally, Mg K-edge XANES spectra (Figure 6.7B), calibrated with respect to a MgO standard, show resonances characteristic of divalent magnesium as observed in prior Mg K-edge XAS studies.[74,75] The relative broadness of the resonances stems from the facile diffusivity of Mg-ions in these compounds, which thereby yield a broad range of local environments. First-principles calculations of Mg K-edge spectra are thus far not available for these compounds but it appears that the samples intercalated by reaction with di-*n*-butylmagnesium show greater structure and are better ordered, which might be a result of the higher temperature of the latter process.

The electrochemically magnesiated samples were also analyzed by electron energy loss spectroscopy (EELS), presented in Figure 6.6B and Figure 6.6C (data collected after X cycles). A comparison of EEL spectra between

pristine and electrochemically magnesiated ζ-V_2O_5 is provided. The EELS data for the electrochemically magnesiated ζ-V_2O_5 was extracted from three areas probed during a linescan, as indicated in the HAADF image in Figure 6.6B. The O *K*- pre-edge showed a sharp feature in the case of the pristine EEL spectrum, which lost intensity in case of the electrochemically magnesiated sample. Furthermore, the ratio of the two peaks at 531 and 533 eV corresponding to t_{2g} and e_g, respectively, inverts upon magnesiation, which is consistent with studies on the electronic structure of V_2O_5 on lithiation.[41,67] It has previously been reported[76] that the relative intensity of O K- pre-edge compared to V L_{III}- edge increases linearly with the valence of vanadium. Hence, the decreased intensity when moving from the pristine to the electrochemically magnesiated sample indicates a reduction of the compound, consistent with a true Mg^{2+} insertion reaction. It is also consistent with the XAS data presented in Figure 6.7, wherein loss of spectral intensity from the t_{2g} manifold of O K- edge can be seen going from the pristine to the chemically magnesiated ζ-V_2O_5 sample, further confirming the similarities between the chemical and electrochemical processes reported here. An interesting aspect of the magnesiation of ζ-V_2O_5 is the appearance of hybrid V-O 'mid-gap' states that evolve 0.5 eV below the Fermi level, and are completely absent in empty ζ-V_2O_5. At low Mg-ion concentrations, the midgap state primarily has V $3d_{xy}$ and O $p_{x/y/z}$ hybrid character. With increasing magnesiation, the midgap state takes on significant V d_{yz} character and overlaps with the valence band. With increasing magnesiation, the band-gap is thus strongly reduced. The eventual degeneracy

of the V $3d_{xy}$ and $3d_{yz}$ states is in marked contrast to α-V_2O_5, where lithiation or magnesiation yields distinct polaronic states within the bandgap[16,41] that are derived exclusively from the non-degenerate V $3d_{xy}$ states. In other words, electron localization and formation of small polarons is partially mitigated in ζ-V_2O_5 by the increased overlap of the V $3d_{xy}$ and $3d_{yz}$ states in this material as compared to α-V_2O_5.

Several of our previous studies in V_2O_5 systems have highlighted the role of polaron formation in hindering ion diffusion, particularly in the thermodynamically stable α-V_2O_5 phase.[41] The roles of electronic structure, band gap, electron localization, and self-trapping of ions in polaronic wells have not been emphasized within the literature. Rather, much attention has been paid to rationalizing the sluggish solid state diffusion kinetics of Mg^{2+} relative to Li^+ solely in terms of the increased polarization of the cathode lattice owing to the increased charge to radius ratio (“hardness”) of the divalent Mg-ion.[13] Surely, this increase in polarizing ability represents a serious fundamental impediment and contributes a great deal to the reported slow diffusion kinetics; however, given the role of polaron formation deduced in limiting lithiation of α-V_2O_5, a similar evaluation is warranted here for the ζ-V_2O_5 polymorph. Considered fundamentally, the diffusion of an inserted charged species can be separated into two components: the diffusion of the cationic species through the lattice and the diffusion of the electron through specific hybrid states of the cathode lattice (which in transition metal oxides is closely coupled to specific phonon modes i.e., a polaron).[41,77,78] Indeed,

theoretical calculations which we have performed in this work and in previous work (the methods used for the calculations have been explicitly detailed in Appendix D)[16,41] have been aimed at isolating and independently calculating the diffusion barriers to the polaron within the V_2O_5 lattice (in the absence of Li^+ or Mg^{2+}) and to the Li- or Mg-ion diffusion in the lattice absent the polaron(s) (results tabulated in Table D.4). The results of these calculations, which show a reduction in both the ionic diffusion barrier (600-900 meV) and a reduction in the polaronic diffusion barrier (100 meV per polaron) when moving from α-V_2O_5 to ζ-V_2O_5 indicate that the reduction in ionic diffusion barrier due to the frustrated coordination environments of ζ-V_2O_5 represent the larger contribution to the overall reduction in diffusion barrier; however, the reduction of 100 meV per polaron (two polarons) represents between 25-40% of the overall calculated reduction in diffusion barrier between the two polymorphs and thus appears to contribute to the improved Mg^{2+} diffusion observed within the ζ-V_2O_5 polymorph. It should be mentioned, however, that isolating the diffusion of Mg^{2+} from the resulting bipolaron that localizes on the adjacent V 3d orbitals does not explicitly account for the fact that the diffusion of the cation and the polaron are electrostatically coupled due to self-trapping of the Mg^{2+} ions in stabilized polaronic wells. Consequently, while the approach delineated here for parsing ionic and polaronic barriers is valuable, it does not entirely capture the complexity of this system. Due to the increased overlap of the V $3d_{xy}$ and $3d_{yz}$ states in the metastable material ζ-V_2O_5 (as compared to in α-V_2O_5) the strength of self-trapping of the cation by the polaron is substantially

mitigated. This is evidenced quantitatively by the decreased diffusion barriers for the polaron formed upon lithiation of metastable ζ-V_2O_5 (240 meV, Figure D.9B and Table D.3) as compared to the thermodynamically stable α-V_2O_5 (340 meV)[41] when a single polaron is stabilized in close proximity to the inserted Li^+ (100 meV reduction in polaron diffusion barrier for a single polaron). It is important to note that this is the energy barrier for diffusion of one half of the bipolaron. The ability of ζ-V_2O_5 to mitigate the depth of the polaronic well becomes more important when moving from the monovalent case where the diffusion of one polaron is coupled to the diffusion of one Li^+, to the divalent case at hand, where the diffusion of Mg^{2+} is coupled to the diffusion of two polarons, whereby the diffusion barrier reduction is doubled in the divalent case (equating to a 200 meV reduction in polaronic diffusion barrier). Therefore, despite the apparent dominance of the ionic diffusion barrier, mitigating polaron diffusion barriers is nonetheless of importance as a means of mitigating self-trapping.

As such, there are two distinct origins for the improved Mg^{2+} diffusion (relative to α-V_2O_5) observed here: the frustrated Mg-ion coordination environments (discussed in detail below) serve to mitigate the ionic diffusion barrier. Secondly, the improved d orbital overlap and smaller band gap of ζ-V_2O_5 diminish the barrier to polaron diffusion. Although the barrier to polaron diffusion is smaller than the barrier to ionic diffusion, both aspects contribute to facilitating Mg^{2+} diffusion by reducing the tendency towards self-trapping.

6.4. Discussion

6.4.1. Elucidation of the Chemical and Structural Origins of Mg^{2+} Diffusion in ζ-V_2O_5

The rather sparse selection of frameworks that allow for reversible insertion of Mg^{2+} represents a major stumbling block in the development of Mg batteries. The predictive discovery of such materials has not been intuitive, and many materials initially considered to have been good Mg-ion intercalation hosts have now been abandoned. The sum of the evidence presented in this work indicates that ζ-V_2O_5 is able to reversibly accommodate Mg-ions within its 1D tunnels. Remarkably, the insertion and extraction of Mg^{2+} is accompanied by a complete retention of crystal structure and symmetry with a minimal volume change of <1% on insertion with complete retention of nanowire morphology, suggesting a truly topochemical intercalative mechanism. A general lack of rigorous characterization of discharge products and the natural of capacity in previous literature reports renders a direct comparison of the performance of various cathode materials challenging. In many of the reported Mg^{2+} cathode materials, Mg-ion insertion has not been proven rigorously by local chemical analysis methods (e.g. STEM, EDX, XANES or refinement of Mg occupancies) and there remain considerable questions in several cases as to the role of water as a co-intercalant. Nevertheless, a stark contrast is evidenced between the tunnel-structured metastable ζ-V_2O_5 and the thermodynamically stable single-layered α-V_2O_5, which has so far been identified as a poor candidate for Mg-ion intercalation.[13,36]

Specifically, ζ-V_2O_5 exhibits a very high capacity 90 mAh/g after 100 cycles, which can be compared with a value of 75 mAh/g reported for α-V_2O_5 in dry electrolyte after just 10 cycles[24] or a value of 47 mAh/g in a wet electrolyte for the xerogel phase of V_2O_5 after 10 cycles.[26] Despite the difficulty in directly comparing electrochemical measurements, the results here mark a significant improvement over the other phases. The reported capacity and cycle stability are furthermore comparable with capacities reported for MnO_2 (100 mAh/g @ 20 cycles)[79] and $Mg_xMo_6O_8$ (60 mAh/g @2000 cycles).[63] For reference in qualitatively comparing various proposed Mg-ion cathode materials, previously reported performance values for several phases are included in Table D.5.

The markedly improved Mg-ion capacity observed in the metastable ζ-V_2O_5 polymorph can be attributed to a combination of several factors. First, Figure 6.2C confirms a square-pyramidal MgO_5 local coordination sphere as predicted by DFT calculations, as depicted in Figure D.10.[16] Because of the open tunnel-structured framework of the ζ-V_2O_5 structure, there are several possible sites that inserted cations can occupy.[28] For smaller cations, two of these sites are relevant at low values of x in $M_xV_2O_5$: the β and β' sites, which correspond to coordination environments defined by five and four oxygen atoms, respectively. Nudged elastic band calculations indicate that the diffusing Mg^{2+} traverse a pathway between these two sites through a trigonal planar transition state. These coordination sites and their specific location within the ζ-V_2O_5 structure are depicted in Figure D.10B. This pathway represents the lowest-energy diffusion pathway within this structure

and, most importantly, requires only a minimal change in formal coordination number along the pathway from the 5-coordinate β-site through a 3-coordinate transition state, and finally to the 4-coordinate β' site. In the next half of the pathway, the Mg^{2+} diffuses from the 4-coordinate β' site to an adjacent β site again passing through a 3-coordinated transition state. Figure D.10 thus depicts the following sequence: β (5-coordinate) → (3-coordinate transition state) → β' (4-coordinate) → (3-coordinate transition state) → β (5-coordinate). As cations diffuse, they must overcome multiple activation energy barriers across the energy landscape. As such, minimizing the change in coordination environment is critical for improving diffusion kinetics and limiting self-trapping of the diffusing cations. The benefit of this small change in coordination number is particularly stark when viewed in contrast to the change in coordination number for diffusing Mg^{2+} in α-V_2O_5. In α-V_2O_5, the Mg^{2+} diffuses along a pathway between an 8-coordinate environment through a 3-coordinate transition state before settling back into the same 8-coordinate environment, as depicted in Figure D.10A. The diffusion pathway for α-V_2O_5 can be summarized as: 8-coordinate → 3-coordinate transition state → 8-coordinate. Furthermore, the trigonal planar transition state in ζ-V_2O_5 is much broader than the transition state in α-V_2O_5.[16] Notably, none of the coordination environments depicted in Figure D.10B for ζ-V_2O_5 are particularly desirable for Mg^{2+}, illustrating the idea of frustrated coordination.[16] The ability of this structure to enforce frustrated coordination promotes facile diffusion of Mg-ions through the tunnels. In contrast, considering Mg^{2+} within α-V_2O_5 (8→3→8),

the ions can be readily ensconced in stable eight-coordinated environments,[36] from which they are difficult to dislodge. Restated, the 1D ζ-phase structure, which does not crystallize with Mg-ions within the tunnel under thermodynamic conditions, forces diffusing Mg^{2+} ions into typically unfavorable sites, thereby raising the site energy of the "frustrated" sites and improving diffusion. We posit that this is a direct result of the metastable character of this compound and indeed the modified conduction pathways available in this material are the primary origin of the relatively facile Mg^{2+} diffusion. Figure 6.7 points to a secondary electronic origin of the facile diffusivity of Mg-ions in ζ-V_2O_5. The increased energetic degeneracy and energy dispersion of V3d states (Figure 6.7F and Figure 6.7G) and the elimination of split-off conduction bands characteristic of α-V_2O_5[41,53] results in increased charge delocalization and substantially mitigates polaron formation. The ζ-V_2O_5 polymorph has consequently been shown to be more covalent relative to α-V_2O_5, which exhibits relatively more ionic character as evidenced by the relative t_{2g}/e_g ratios of the two polymorphs.[53] This is important, because greater degree of covalency for molybdenum-sulfur bonds relative to the typically more ionic nature of the metal-oxide bonds has been cited as an effective way to screen the charge of diffusing $Mg^{2+}$and as the primary origin of faster Mg-ion diffusion kinetics observed in the molybdenum sulfide cluster-based Chevrel phases[6,43,44] From a thermodynamic perspective, the metastability of the ζ-V_2O_5 polymorph contributes to an *ab initio* calculated voltage larger than that calculated for the thermodynamically stable α-V_2O_5 and leads to an average operating

voltage above 1.65 V vs. Mg^{2+}/Mg^{0} (Figure 6.5), which represents a gain with respect to the low operating voltages which have been a drawback of the Chevrel phases. While the electrode reaction is viable and remarkably reversible, the insertion kinetics are somewhat sluggish, as hinted by the large hysteresis in potential between charge and discharge. It is likely that much smaller particle sizes are required to mitigate this issue, which will be a focus of subsequent research. Indeed, further reducing the diffusion path length of Mg^{2+} in this material will be imperative for realizing the full potential of *ζ*-V_2O_5 as a Mg-ion cathode material. Future work will also involve detailed electrochemical evaluation of the *ζ*-V_2O_5 polymorph in full cells with Mg metal, as well as elaboration of the idea of metastable compounds as Mg electrodes to other V_2O_5 frameworks accessible by topochemical leaching.

6.5. Experimental Section

6.5.1. Synthesis of Pristine ζ-V_2O_5

Pristine ζ-V_2O_5 nanowires were synthesized by an adaptation of our previously reported approach involving the topochemical leaching of Ag from within the tunnels of β-$Ag_{0.33}V_2O_5$.[54] [40] The β-$Ag_{0.33}V_2O_5$ nanowires were first synthesized *via* a hydrothermal reaction between V_2O_5 and $AgCOOCH_3$ in a 3:1 molar ratio (69.6% water volume loading, 14.36 mg/mL solid V_2O_5 loading) in a polytetrafluoroethylene-lined sealed stainless steel autoclave for 72 h at 210 °C. These nanowires (300 mg) were treated hydrothermally at a temperature of 210°C with stoichiometric amounts of HCl (69.6% volume loading with 0.5825 M HCl) in

water (ρ = 18 μΩ cm^{-1}) for 24 h, resulting in the formation of the topochemically leached ζ-V_2O_5 polymorph and insoluble AgCl impurity in a 3:1 ratio. The powder X-ray diffraction (XRD) pattern of the products obtained from the topochemical leaching process are depicted in Figure D.1. To eliminate AgCl, the ζ-V_2O_5 nanowires were washed with a 5 wt.% aqueous solution of $Na_2S_2O_3$, which forms a water-soluble complex with AgCl(s). Care was taken to wash with copious amounts of water to remove residual acid prior to washing with $Na_2S_2O_3$ to avoid the formation of SO_2 (g) and the precipitation of a colloidal sulfur impurity (S_8).[80] The resulting orange-brown powder was finally washed with copious amounts of water and was recovered by filtration.

6.5.2. Topochemical Mg-Ion Insertion and Extraction in ζ-V_2O_5

Subsequent topochemical insertion of Mg into pristine ζ-V_2O_5 was achieved by two separate routes. First, aqueous magnesiation (Equation 6.2) was performed by reacting ζ-V_2O_5 with stoichiometric amounts of Mg nanoparticles[57] in water at ambient temperature and pressure for 24 h with constant stirring. The Mg nanoparticles used in this reaction were obtained from the electroless reduction of CH_3MgCl by lithium naphthalide in an anhydrous tetrahydrofuran solution.[57,81] The resulting solid product was obtained as a dark-green powder, washed with copious amounts of water and 2-propanol, allowed to dry, and finally stored in a glovebox to minimize the formation of a hydrated phase prior to subsequent characterization. A non-aqueous magnesiation route was also developed wherein the ζ-V_2O_5 nanowires (typically 200 mg) were mixed with a

stoichiometric excess of di-*n*-butylmagnesium (1:2 molar ratio) in 50 mL heptane. The reaction mixture was allowed to reflux with gentle stirring at 100°C for 48 h under an Ar atmosphere in order to avoid the formation of MgO. The resulting green powder was washed with copious amounts of hexanes, 2-propanol, and ethanol, and allowed to dry overnight. The magnesiated product is oxidized within about a week under ambient conditions and must be sealed under Ar for long-term storage.

Finally, topochemical leaching of Mg-ions from the magnesiated phases was accomplished by reacting the β-$Mg_xV_2O_5$ nanowires with an excess of $NOBF_4$ (Equation 6.4) in dry acetonitrile at a concentration of 0.035 M for 12 h, accompanied by gentle stirring.[61] The resulting powder was washed with acetonitrile, ethanol, acetone, and water. stoichiometric ratios, reaction conditions, and product handling for the reactions mentioned above and in Equation 6.1 and Equation 6.2 are described in detail in Appendix D.

6.5.3. High-Resolution Synchrotron Diffraction

High-resolution powder XRD for the topochemically leached ζ-V_2O_5 and for β-$Mg_xV_2O_5$ were obtained by packing the powders into a poly-oxydiphenylene-pyromellitimide capillary and measured in transmission geometry at 295 K at beamline 11-BM of the Advanced Photon Source at Argonne National Laboratory (λ = 0.4136860). Rietveld refinement of the collected data was performed using the GSAS/EXPGUI software suite.[82] Unit cell parameters, atom positions, thermal parameters, and site occupancies were refined and are listed in Table D.1. All

structural images depicted were generated using the VESTA software suite.[83] Powder XRD data for ζ-V_2O_5 before magnesiation, after magnesiation with di-*n*-butylmagnesium, and after topchemical leaching with $NOBF_4$ were collected in Bragg-Brentano geometry on a short-arm Bruker D8-Focus diffractometer (Cu Kα: λ = 1.5418Å source, 40 kV voltage, 25 mA current) equipped with a Lynxeye detector.

6.5.4. Scanning Electron Microscopy

SEM was performed on a JEOL JSM-7500F FE-SEM equipped with an Oxford EDS spectrometer for elemental characterization at an accelerating voltage of 20 kV. Powders were spread onto carbon tape prior to imaging.

6.5.5. Transmission Electron Microscopy

TEM images and electron diffraction patterns were acquired using a JEOL JEM 3010 operated at 300 keV. The STEM images, EELS and EDX data were acquired with a probe-side aberration-corrected JEOL JEM ARM200CF with a cold field emission gun operated at 200 keV. For both imaging and EELS, probe convergence semi angle of 28 mrad was used with a probe current of 19 pA and probe size of 0.78 Å. The EELS spectrometer collection angle was 45 mrad and the dispersion was set to 0.1 eV/channel. Due to the beam sensitive nature of this ζ-V_2O_5 sample, the emission current (I_E) was lowered to 7 μA (usual acquisition conditions I_E = 15 μA) during imaging, EELS and EDX analysis.

6.5.6. Scanning Transmission X-Ray Microscopy

STXM measurements were performed at the SM (10-ID1) beamline of the Canadian Light Source (CLS), a 2.9 GeV third-generation synchrotron facility. Right circularly polarized X-rays, generated by an elliptically polarized undulator (EPU), were used in the experiments. A 25 nm outermost-zone zone plate was used to obtain a diffraction-limited spatial resolution better than 30 nm. A 500 line mm^{-1} plane grating monochromator (PGM) was used to acquire the V L-edge and O K-edge spectral stacks. The incident photon flux (I_o) count rate was optimized to ca. 17 MHz as read by the STXM detector within a hole located in proximity of the sample of interest and measured at 560 eV by adjusting the exit slits to 20/20 µm (dispersive/non-dispersive). The V L- and the O K-edge stacks were acquired in the energy range from 508—560 eV with energy steps of 0.2 eV in the region of interest and with energy steps 1 eV in the continuum region beyond the specific elemental edges with a uniform dwell time of 1 ms for each spectral section. All STXM data were analyzed and processed using aXis2000 (http://unicorn.mcmaster.ca/aXis2000.html). The spectra obtained in Figure 6.4 were obtained by integrating the individual spectra obtained for each pixel across the entire nanowire.

6.5.7. Mg K-Edge Measurements

Ensemble Mg K-edge X-ray absorption near-edge structure (XANES) spectra were collected in the energy range between 1290-1350 eV at the resonant elastic and inelastic X-ray scattering (REIXS) beamline (10lD-2) using the X-ray

emission spectroscopy end-station at the Canadian Light Source (CLS). Monochromatic soft X-rays were sourced from an undulator and grating monochromator. XAS measurements were acquired in total electron yield (TEY) mode. The absolute energy of the collected XAS spectra were calibrated using reference spectra acquired for MgO, which has a pronounced resonance at 1303 eV.[84]

6.5.8. Vanadium K-Edge Measurements

Vanadium K-edge X-ray absorption near-edge structure (XANES) spectra were collected at the Advanced Light Source (ALS) bending magnet beamline 10.3.2 (2.1- 17 keV) with the storage ring operating at 500 mA and 1.9 GeV.[85] V K-edge extended XANES spectra were recorded in transmission mode, by continuously scanning the Si (111) monochromator (Quick XAS mode) from 5355 to 5765 eV, using a beam spot size of 12 µm x 3 µm. Spectra were calibrated using a V foil (1st derivative peak set at 5463.76 eV). LabVIEW custom software available at the beamline was used to perform deadtime correction, energy calibration, and glitch removal. The Athena software[86,87] (IFEFFIT Demeter package) was used to pre-edge background subtract and post-edge normalize the XANES spectra.[88]

6.5.9. Preparation of Electrodes and Electrolyte

The ζ-V_2O_5 powder was first thoroughly mixed with acetylene black as a conductive agent using a mortar and pestle. Next, a solution of polymeric binder was added to the mortar and further mixed to obtain a slurry. The binder solution

was 6 wt.% polyvinylidene fluoride (PVDF, Solvay) dissolved in 1-methyl-2-pyrrolidinone (NMP, Sigma Aldrich, >99%) solvent. The mass ratio of active material, conductive agent, and polymeric binder was adjusted to 6:2:2. The slurry was coated on aluminum foil substrates, followed by drying under an IR-lamp for 30 min and in a vacuum oven at 80 °C overnight. The surface area of the cathodes was 1.27 cm^2 with a mass loading of ca. 1.6 mg. The electrolyte was prepared by mixing 0.2 M Magnesium *bis*(trifluoromethylsulfonyl)imide or $Mg(TFSI)_2$ (Solvionic, 99.5% dried at 150 °C in a vacuum oven) salt and propylene carbonate (PC, Sigma-Aldrich, 99.7%, <20 ppm H_2O) as the solvent under stirring to form a homogeneous solution. All the processes were performed within argon-filled gloveboxes (held at <0.1 ppm H_2O). PC was chosen as the solvent due to compatibility with oxide cathodes. Since the incompatibility of PC with Mg metal is well documented, activated carbon was used as the counterelectrode in the current experimental setup.

6.5.10. Fabrication and Test of Electrochemical Cells

Activated carbon cloth (ACC-5092-20, Kynol Co.) with mass of 29.3 mg and area of 2 cm^2 was used as the anode for the electrochemical cells. The activated carbon cloth (ACC) was dried under vacuum at 80°C overnight. The high specific surface area of ACC (ca. 2000 $m^2\ g^{-1}$) gives rise to sufficient double-layer charging within the electrolyte's voltage stability window to match the charge for the cycling of the cathodes. Coin-type cells were fabricated by stacking the cathode and anode separated by glass fiber (VWR, grade 691, 210 μm thick)

soaked with the electrolyte. A multi-channel potentiostat (VMP3, Bio-Logic) was used for the electrochemical tests. The potential of the cathode was calibrated by considering the AC anode's potential, which is originally 2.2 V vs Mg/Mg^{2+} and linearly proportional to the state-of-charge. An oven with forced-convection (BINDER) was used to fix the temperature of the cells to 50°C.

6.5.11. Electronic Structure Calculations

Density functional theory (DFT) method[89,90] as implemented in Vienna ab initio simulation package (VASP)[91] was used to perform ground-state electronic calculations. Perdew−Burke−Ernzerhof (PBE)[92] formulation of the generalized gradient approximation (GGA) was implemented to incorporate the electronic exchange and correlation effects. The open circuit voltage was calculated using the DFT+*U* formalism as described by Anisimov et al.,[93] wherein the strong onsite Coulomb interactions of the vanadium 3d-electrons are approximated using the Hubbard model. The open circuit voltage reported in our previous work and herein was calculated using a reasonable value of U=4.0,[94] given the high degree of electron correlation in vanadium oxides. Because the degree of electron localization changes with increasing magnesiation as empty d orbitals are populated, we have subsequently implemented onsite potentials of U=0 and 3.1[95] to compare expected voltage values with increasing magnesiation. A plane wave basis set with kinetic energy cutoff of 600 eV was used for electronic structure calculations. The projector augmented wave (PAW) formalism was used to describe the electron-ion interactions. To calculate the total energies, the

numerical sampling of the first Brillouin zone was done using a Monkhorst-Pack reciprocal-space grid of 2 × 2 × 2 *k*-points for the supercells of size 1 × 2 × 1. A threshold value of 10^{-6} eV was used for the convergence of electronic self-consistency cycles.

The ionic and the polaronic diffusion barriers were calculated using the nudged elastic band (NEB) method as implemented in VASP.[96,97] A total of seven linearly interpolated images were included between the initial and the final relaxed structures. In order to decouple the ionic migration barrier from the polaronic migration barrier the following steps were used: (1) DFT was used instead of DFT+U for the calculation of ionic diffusion barrier in order to preclude the effect of polarons (as noted by Maxisch *et al.*)[98], (2) DFT+U (U= 4.0 eV) was used in the calculation of polaronic barrier keeping the ions constant and only moving the polaron from one vanadium atom to another in order to eliminate the effect of ionic diffusion (as performed in other work[99]). In order to localize a polaron on a specific vanadium site, we introduced a local lattice deformation around a chosen site and then relaxed the atomic positions in the supercell. The Cartesian components of the forces were relaxed below ±0.05 eV $Å^{-1}$ for the initial and the final images, whereas for the forces along the NEB path, the relaxation criterion was 0.1 eV $Å^{-1}$. The supercells were larger than 7.3 Å in order to avoid spurious interactions.

6.6. References

(1) van Noorden, R. The Rechargeable Revolution: A Better Battery. *Nature* **2014**, *507*, 26–28.

(2) Nitta, N.; Wu, F.; Lee, J. T.; Yushin, G. Li-Ion Battery Materials: Present and Future. *Mater. Today* **2015**, *18* (5), 252–264.

(3) Park, Y.-U.; Seo, D.-H.; Kim, B.; Hong, K.-P.; Kim, H.; Lee, S.; Shakoor, R. a; Miyasaka, K.; Tarascon, J.-M.; Kang, K. Tailoring a Fluorophosphate as a Novel 4 V Cathode for Lithium-Ion Batteries. *Sci. Rep.* **2012**, *2*, 704.

(4) Tarascon, J.; Poizot, P.; Laruelle, S.; Grugeon, S.; Dupont, L. Nano-Sized Transition-Metal Oxides as Negative-Electrode Materials for Lithium-Ion Batteries. *Nature* **2000**, *407* (6803), 496–499.

(5) Horrocks, G. A.; Likely, M. F.; Velazquez, J. M.; Banerjee, S. Finite Size Effects on the Structural Progression Induced by Lithiation of V_2O_5: A Combined Diffraction and Raman Spectroscopy Study. *J. Mater. Chem. A* **2013**, *1*, 15265–15277.

(6) Yoo, H. D.; Shterenberg, I.; Gofer, Y.; Gershinsky, G.; Pour, N.; Aurbach, D. Mg Rechargeable Batteries: An on-Going Challenge. *Energy Environ. Sci.* **2013**, *6* (8), 2265–2279.

(7) Liu, M.; Rong, Z.; Malik, R.; Canepa, P.; Jain, A.; Ceder, G.; Persson, K. A. Spinel Compounds as Multivalent Battery Cathodes: A Systematic Evaluation Based on Ab Initio Calculations. *Energy Environ. Sci* **2015**, *8* (3), 964–974.

(8) Besenhard, J. O.; Winter, M. Advances in Battery Technology: Rechargeable Magnesium Batteries and Novel Negative-Electrode Materials for Lithium Ion Batteries. *ChemPhysChem* **2002**, *3* (2), 155–159.

(9) Kesler, S. E.; Gruber, P. W.; Medina, P. A.; Keoleian, G. A.; Everson, M. P.; Wallington, T. J. Global Lithium Resources: Relative Importance of Pegmatite, Brine and Other Deposits. *Ore Geol. Rev.* **2012**, *48*, 55–69.

(10) Barbier, E. B. Protect the Deep Sea. *Nature* **2014**, *505*, 475–477.

(11) DeWitt, S.; Hahn, N.; Zavadil, K.; Thornton, K. Computational Examination of Orientation-Dependent Morphological Evolution during the Electrodeposition and Electrodissolution of Magnesium. *J. Electrochem. Soc.* **2016**, *163* (3), A513–A521.

(12) Jäckle, M.; Groß, A. Microscopic Properties of Lithium, Sodium, and Magnesium Battery Anode Materials Related to Possible Dendrite Growth. *J. Chem. Phys.* **2014**, *141* (17), 174710.

(13) Novak, P.; Imhof, R.; Haas, O. Magnesium Isertion Electrodes for Rechargeable Nonaqueous Batteries — a Competitive Alternative to Lithium? *Electrochim. Acta* **1999**, *45*, 351–367.

(14) Lu, Z.; Schechter, A.; Moshkovich, M.; Aurbach, D. On the Electrochemical Behavior of Magnesium Electrodes in Polar Aprotic Electrolyte Solutions. *J. Electroanal. Chem.* **1999**, *466* (2), 203–217.

(15) Aurbach, D.; Suresh, G. S.; Levi, E.; Mitelman, A.; Mizrahi, O.; Chusid, O.; Brunelli, M. Progress in Rechargeable Magnesium Battery Technology. *Adv. Mater.* **2007**, *19* (23), 4260–4267.

(16) Parija, A.; Liang, Y.; Andrews, J. L.; De Jesus, L. R.; Prendergast, D.; Banerjee, S. Topochemically De-Intercalated Phases of V_2O_5 as Cathode

Materials for Multivalent Intercalation Batteries: A First-Principles Evaluation. *Chem. Mater.* **2016**, *28* (16), 5611–5620.

(17) Cabello, M.; Nacimiento, F.; González, J. R.; Ortiz, G.; Alcántara, R.; Lavela, P.; Pérez-Vicente, C.; Tirado, J. L. Advancing towards a Veritable Calcium-Ion Battery: $CaCo_2O_4$ Positive Electrode Material. *Electrochem. commun.* **2016**, *67*, 59–64.

(18) Lipson, A. L.; Pan, B.; Lapidus, S. H.; Liao, C.; Vaughey, J. T.; Ingram, B. J. Rechargeable Ca-Ion Batteries: A New Energy Storage System. *Chem. Mater.* **2015**, *27* (24), 8442–8447.

(19) Wang, W.; Jiang, B.; Xiong, W.; Sun, H.; Lin, Z.; Hu, L.; Tu, J.; Hou, J.; Zhu, H.; Jiao, S. A New Cathode Material for Super-Valent Battery Based on Aluminium Ion Intercalation and Deintercalation. *Sci. Rep.* **2013**, *3* (1), 3383.

(20) Whittingham, M. S. The Role of Ternary Phases in Cathode Reactions. *J. Electrochem. Soc.* **1976**, *123* (3), 315–320.

(21) Tepavcevic, S.; Liu, Y.; Zhou, D.; Lai, B.; Maser, J.; Zuo, X.; Chan, H.; Král, P.; Johnson, C. S.; Stamenkovic, V.; Markovic, N. M.; Rajh, T.. Nanostructured Layered Cathode for Rechargeable Mg-Ion Batteries. *ACS Nano* **2015**, *9* (8), 8194–8205.

(22) Mukherjee, A.; Sa, N.; Phillips, P. J.; Burrell, A.; Vaughey, J.; Klie, R. F. Direct Investigation of Mg Intercalation into Orthorhombic V_2O_5 Cathode Using Atomic Resolution Transmission Electron Microscopy. *Chem. Mater.*

2017, *29* (5), 2218–2226.

(23) Gershinsky, G.; Yoo, H. D.; Gofer, Y.; Aurbach, D. Electrochemical and Spectroscopic Analysis of Mg^{2+} Intercalation into Thin Film Electrodes of Layered Oxides: V_2O_5 and MoO_3. *Langmuir* **2013**, *29* (34), 10964–10972.

(24) Sa, N.; Wang, H.; Proffit, D. L.; Lipson, A. L.; Key, B.; Liu, M.; Feng, Z.; Fister, T. T.; Ren, Y.; Sun, C. J.; Vaughey, J. T.; Fenter, P. A.; Persson, K. A.; Burrell, A. K. Is Alpha-V_2O_5 a Cathode Material for Mg Insertion Batteries? *J. Power Sources* **2016**, *323*, 44–50.

(25) Tepavcevic, S.; Xiong, H.; Stamenkovic, V. R.; Zuo, X.; Balasubramanian, M.; Prakapenka, V. B.; Johnson, C. S.; Rajh, T. Nanostructured Bilayered Vanadium Oxide Electrodes for Rechargeable Sodium-Ion Batteries. *ACS Nano* **2012**, *6* (1), 530–538.

(26) Sa, N.; Kinnibrugh, T. L.; Wang, H.; Sai Gautam, G.; Chapman, K. W.; Vaughey, J. T.; Key, B.; Fister, T. T.; Freeland, J. W.; Proffit, D. L.; Chupas, P. J.; Ceder, G.; Bareno, J. G.; Bloom, I. D.; Burrell, A. K. Structural Evolution of Reversible Mg Insertion into a Bilayer Structure of $V_2O_5 \cdot MH_2O$ Xerogel Material. *Chem. Mater.* **2016**, *28* (9), 2962–2969.

(27) Petkov, V.; Trikalitis, P. N.; Bozin, E. S.; Billinge, S. J. L. L.; Vogt, T.; Kanatzidis, M. G. Structure of V_2O_5 NH_2O Xerogel Solved by the Atomic Pair Distribution Function Technique. *J. Am. Chem. Soc.* **2002**, *124* (8), 10157–10162.

(28) Galy, J.; Darriet, J.; Hagenmuller, P. The $Li_xV_2O_5$ Bronzes: Structure of the

B′ and Refinement of the γ Phase. *Rev. Chim. Miner.* **1971**, *8* (January), 509–522.

(29) Cocciantelli, J. M.; Gravereau, P.; Doumerc, J. P.; Pouchard, M.; Hagenmuller, P. On the Preparation and Characterization of a New Polymorph of V_2O_5. *J. Solid State Chem.* **1991**, *93* (2), 497–502.

(30) Parija, A.; Prendergast, D.; Banerjee, S. Evaluation of Multivalent Cation Insertion in Single- and Double- Layered Polymorphs of V_2O_5. *ACS Appl. Mater. Interfaces* **2017**, *9* (28), 23756–23765.

(31) Arroyo y de Dompablo, M. E.; Gallardo-Amores, J. M.; Amador, U.; Morán, E. Are High Pressure Materials Suitable for Electrochemical Applications? HP-V_2O_5 as a Novel Electrode Material for Li Batteries. *Electrochem. commun.* **2007**, *9* (6), 1305–1310.

(32) Kulish, V. V.; Manzhos, S. Comparison of Li, Na, Mg and Al-Ion Insertion in Vanadium Pentoxides and Vanadium Dioxides. *RSC Adv.* **2017**, *7*, 18643–18649.

(33) Sun, X.; Duffort, V.; Mehdi, B. L.; Browning, N. D.; Nazar, L. F. Investigation of the Mechanism of Mg Insertion in Birnessite in Nonaqueous and Aqueous Rechargeable Mg-Ion Batteries. *Chem. Mater.* **2016**, *28* (2), 534–542.

(34) Kim, C.; Phillips, P. J.; Key, B.; Yi, T.; Nordlund, D.; Yu, Y. S.; Bayliss, R. D.; Han, S. D.; He, M.; Zhang, Z.; Burrell, A. K.; Klie, R. F.; Cabana, J. Direct Observation of Reversible Magnesium Ion Intercalation into a Spinel Oxide Host. *Adv. Mater.* **2015**, *27* (22), 3377–3384.

(35) Incorvati, J. T.; Wan, L. F.; Key, B.; Zhou, D.; Liao, C.; Fuoco, L.; Holland, M.; Wang, H.; Prendergast, D.; Poeppelmeier, K. R.; Vaughey, J. T. Reversible Magnesium Intercalation into a Layered Oxyfluoride Cathode. *Chem. Mater.* **2016**, *28* (1), 17–20.

(36) Gautam, G. S.; Canepa, P.; Abdellahi, A.; Urban, A.; Malik, R.; Ceder, G. The Intercalation Phase Diagram of Mg in V_2O_5 from First-Principles`. *Chem. Mater.* **2015**, *27* (10), 3733–3742.

(37) Orikasa, Y.; Masese, T.; Koyama, Y.; Mori, T.; Hattori, M.; Yamamoto, K.; Okado, T.; Huang, Z.-D.; Minato, T.; Tassel, C.; Kim, J.; Kobayashi, Y.; Abe, T.; Kageyama, H.;; Uchimoto, Y. High Energy Density Rechargeable Magnesium Battery Using Earth-Abundant and Non-Toxic Elements. *Sci. Rep.* **2014**, *4*, 5622.

(38) Liang, Y.; Feng, R.; Yang, S.; Ma, H.; Liang, J.; Chen, J. Rechargeable Mg Batteries with Graphene-like MoS_2 Cathode and Ultrasmall Mg Nanoparticle Anode. *Adv. Mater.* **2011**, *23* (5), 640–643.

(39) Tao, Z.-L.; Xu, L.-N.; Gou, X.-L.; Chen, J.; Yuan, H.-T. TiS_2 Nanotubes as the Cathode Materials of Mg-Ion Batteries. *Chem. Commun.* **2004**, No. 18, 2080–2081.

(40) Imamura, D.; Miyayama, M.; Hibino, M.; Kudo, T. Mg Intercalation Properties into V_2O_5 Gel/Carbon Composites under High-Rate Condition. *J. Electrochem. Soc.* **2003**, *150* (6), A753.

(41) De Jesus, L. R.; Horrocks, G. A.; Liang, Y.; Parija, A.; Jaye, C.; Wangoh, L.;

Wang, J.; Fischer, D. A.; Piper, L. F. J.; Prendergast, D.; Banerjee, S. Mapping Polaronic States and Lithiation Gradients in Individual V_2O_5 Nanowires. *Nat. Commun.* **2016**, *7*, 12022:1-9.

(42) De Jesus, L. R.; Zhao, Y.; Horrocks, G. A.; Andrews, J.; Stein, P.; Xu, B.; Banerjee, S. Lithiation across Interconnected V2O5 Nanoparticle Networks. *J. Mater. Chem. A* **2017**, *5* (38), 20141–20152.

(43) Thöle, F.; Wan, L. F.; Prendergast, D. Re-Examining the Chevrel Phase Mo_6S_8 Cathode for Mg Intercalation from an Electronic Structure Perspective. *Phys. Chem. Chem. Phys.* **2015**, *17* (35), 22548–22551.

(44) Wan, L. F.; Perdue, B. R.; Apblett, C. A.; Prendergast, D. Mg Desolvation and Intercalation Mechanism at the Mo_6S_8 Chevrel Phase Surface. *Chem. Mater.* **2015**, *27* (17), 5932–5940.

(45) Levi, E.; Gershinsky, G.; Aurbach, D.; Isnard, O. Crystallography of Chevrel Phases, MMo_6T_8 (M = Cd, Na, Mn, and Zn, T = S, Se) and Their Cation Mobility. *Inorg. Chem.* **2009**, *48* (18), 8751–8758.

(46) Liang, Y.; Yoo, H. D.; Li, Y.; Shuai, J.; Calderon, H. A.; Robles Hernandez, F. C.; Grabow, L. C.; Yao, Y. Interlayer-Expanded Molybdenum Disulfide Nanocomposites for Electrochemical Magnesium Storage. *Nano Lett.* **2015**, *15* (3), 2194–2202.

(47) Levi, E.; Gofer, Y.; Aurbach, D. On the Way to Rechargeable Mg Batteries: The Challenge of New Cathode Materials. *Chem. Mater.* **2010**, *22* (3), 860–868.

(48) Liu, C.; Neale, Z. G.; Cao, G. Understanding Electrochemical Potentials of Cathode Materials in Rechargeable Batteries. *Mater. Today* **2016**, *19* (2), 109–123.

(49) Pereira-Ramos, J. P.; Messina, R.; Perichon, J. Electrochemical Formation of a Magnesium Vanadium Bronze $Mg_xV_2O_5$ in Sulfone-Based Electrolytes at 150°C. *J. Electroanal. Chem.* **1987**, *218* (1–2), 241–249.

(50) Millet, P.; Satto, C.; Sciau, P.; Galy, J. MgV_2O_5 and δ-$Li_xV_2O_5$: A Comparative Structural Investigation. *J. Solid State Chem.* **1998**, *136* (1), 56–62.

(51) Gregory, T. D.; Hoffman, Ronald, J.; Winterton, R. C. Nonaqueous Electrochemistry of Magnesium. *J. Electrochem. Soc.* **1990**, *137* (3), 775–780.

(52) Gautam, G. S.; Canepa, P.; Malik, R.; Liu, M.; Persson, K.; Ceder, G. First-Principles Evaluation of Multi-Valent Cation Insertion into Orthorhombic V_2O_5. *Chem. Commun.* **2015**, *51* (71), 13619–13622.

(53) Tolhurst, T. M.; Leedahl, B.; Andrews, J. L.; Marley, P. M.; Banerjee, S.; Moewes, A. Contrasting 1D Tunnel-Structured and 2D Layered Polymorphs of V_2O_5 : Relating Crystal Structure and Bonding to Band Gaps and Electronic Structure. *Phys. Chem. Chem. Phys.* **2016**, *18* (23), 15798–15806.

(54) Marley, P. M.; Abtew, T. A.; Farley, K. E.; Horrocks, G. A.; Dennis, R. V.; Zhang, P.; Banerjee, S. Emptying and Filling a Tunnel Bronze. *Chem. Sci.*

2015, *6* (3), 1712–1718.

(55) Whittingham, M. S.; Dines, M. B. *N*-Butyllithium—An Effective, General Cathode Screening Agent. *J. Electrochem. Soc.* **1977**, *124* (9), 1387–1388.

(56) Bruce, P. G.; Krok, F.; Nowinski, J.; Gibson, V. C.; Tavakkoli, K. Chemical Intercalation of Magnesium into Solid Hosts. *J. Mater. Chem.* **1991**, *1* (4), 705–706.

(57) Viyannalage, L.; Lee, V.; Dennis, R. V; Kapoor, D.; Haines, C. D.; Banerjee, S. From Grignard's Reagents to Well-Defined Mg Nanostructures: Distinctive Electrochemical and Solution Reduction Routes. *Chem. Commun.* **2012**, *48* (42), 5169–5171.

(58) Galy, J.; Darriet, J.; Casalot, A.; Goodenough, J. B. Structure of the $M_xV_2O_5$,-β and $M_xV_{2-y}T_{<i>Y</i?}O_5$-β Phases. *J. Solid State Chem.* **1970**, *1*, 339–348.

(59) Wadsley, A. D. The Crystal Structure of $Na_{2-x}V_6O_{15}$. *Acta Crystallogr.* **1955**, *8* (11), 695–701.

(60) Déramond, E.; Savariault, J. M.; Galy, J. Silver Insertion Mode in β-$Ag_xV_2O_5$ Tunnel Structure. *Acta Crystallogr.* **1994**, *C50* (2), 164–166.

(61) Lee, K. T.; Ramesh, T. N.; Nan, F.; Botton, G.; Nazar, L. F. Topochemical Synthesis of Sodium Metal Phosphate Olivines for Sodium-Ion Batteries. *Chem. Mater.* **2011**, *23* (16), 3593–3600.

(62) Parent, L. R.; Cheng, Y.; Sushko, P. V.; Shao, Y.; Liu, J.; Wang, C. M.; Browning, N. D. Realizing the Full Potential of Insertion Anodes for Mg-Ion

Batteries through the Nanostructuring of Sn. *Nano Lett.* **2015**, *15* (2), 1177–1182.

(63) Aurbach, D.; Lu, Z.; Schechter, A.; Gofer, Y.; Gizbar, H.; Turgeman, R.; Cohen, Y.; Moshkovich, M.; Levi, E. Prototype Systems for Rechargeable Magnesium Batteries. *Nature* **2000**, *407* (6805), 724–727.

(64) Gyenes, B.; Stevens, D. a.; Chevrier, V. L.; Dahn, J. R. Understanding Anomalous Behavior in Coulombic Efficiency Measurements on Li-Ion Batteries. *J. Electrochem. Soc.* **2015**, *162* (3), A278–A283.

(65) Canepa, P.; Sai Gautam, G.; Hannah, D. C.; Malik, R.; Liu, M.; Gallagher, K. G.; Persson, K. A.; Ceder, G. Odyssey of Multivalent Cathode Materials: Open Questions and Future Challenges. *Chem. Rev.* **2017**, *117* (5), 4287–4341.

(66) Galy, J.; Lavaud, D.; Casalot, A.; Hangenmuller, P. The Vanadium-Oxygen Bronzes of the Formula $Cu_xV_2O_5$: Crystal Structure of the Phases $Cu_xV_2O_5$-β and ε. *Journal of Solid State Chemistry*. 1970, pp 531–543.

(67) Horrocks, G. A.; Parija, A.; De Jesus, L. R.; Wangoh, L.; Sallis, S.; Luo, Y.; Andrews, J. L.; Jude, J.; Fischer, D. A.; Prendergast, D.; Piper, L. F. J.; Banerjee, S. Mitigating Cation Diffusion Limitations and Intercalation-Induced Framework Transitions in a 1D Tunnel-Structured Polymorph of V_2O_5. *Chem. Mater.* **2017**, *November 1*, 10.1021/acs.chemmater.7b03800.

(68) Goering, E.; Müller, O.; Klemm, M.; DenBoer, M. L.; Horn, S. Angle Dependent Soft-X-Ray Absorption Spectroscopy of V_2O_5. *Philos. Mag. Part*

B **1997**, *75* (2), 229–236.

(69) Velazquez, J. M.; Jaye, C.; Fischer, D. a; Banerjee, S. Near Edge X-Ray Absorption Fine Structure Spectroscopy Studies of Single-Crystalline V_2O_5 Nanowire Arrays. *J. Phys. Chem. C* **2009**, *113* (18), 7639–7645.

(70) Maganas, D.; Roemelt, M.; Hävecker, M.; Trunschke, A.; Knop-Gericke, A.; Schlögl, R.; Neese, F. First Principles Calculations of the Structure and V L-Edge X-Ray Absorption Spectra of V_2O_5 Using Local Pair Natural Orbital Coupled Cluster Theory and Spin-Orbit Coupled Configuration Interaction Approaches. *Phys. Chem. Chem. Phys.* **2013**, *15* (19), 7260–7276.

(71) Horrocks, G. A.; Braham, E. J.; Liang, Y.; De Jesus, L. R.; Jude, J.; Velázquez, J. M.; Prendergast, D.; Banerjee, S.; Velazquez, J. M.; Prendergast, D.; Banerjee, S. Vanadium K-Edge X-Ray Absorption Spectroscopy as a Probe of the Heterogeneous Lithiation of V_2O_5: First-Principles Modeling and Principal Component Analysis. *J. Phys. Chem. C* **2016**, *120* (42), 23922–23932.

(72) Marley, P. M.; Horrocks, G. A.; Pelcher, K. E.; Banerjee, S. Transformers: The Changing Phases of Low-Dimensional Vanadium Oxide Bronzes. *Chem. Commun.* **2015**, *51* (25), 5181–5198.

(73) Andrews, J. L.; De Jesus, L. R.; Tolhurst, T. M.; Marley, P. M.; Moewes, A.; Banerjee, S. Intercalation-Induced Exfoliation and Thickness-Modulated Electronic Structure of a Layered Ternary Vanadium Oxide. *Chem. Mater.* **2017**, *29* (7), 3285–3294.

(74) Wan, L. F.; Prendergast, D. The Solvation Structure of Mg Ions in Dichloro Complex Solutions from First-Principles Molecular Dynamics and Simulated X-Ray Absorption Spectra. *J. Am. Chem. Soc.* **2014**, *136* (41), 14456–14464.

(75) Benmayza, A.; Ramanathan, M.; Arthur, T. S.; Matsui, M.; Mizuno, F.; Guo, J.; Glans, P. A.; Prakash, J. Effect of Electrolytic Properties of a Magnesium Organohaloaluminate Electrolyte on Magnesium Deposition. *J. Phys. Chem. C* **2013**, *117* (51), 26881–26888.

(76) Lin, X. W.; Wang, Y. Y.; Dravid, V. P.; Michalakos, P. M.; Kung, M. C. Valence States and Hybridization in Vanadium Oxide Systems Investigated by Transmission Electron-Energy-Loss Spectroscopy. *Phys. Rev. B* **1993**, *47* (7), 3477–3481.

(77) Ellis, B.; Perry, L. K.; Ryan, D. H.; Nazar, L. F. Small Polaron Hopping in $Li_x FePO_4$ Solid Solutions: Coupled Lithium-Ion and Electron Mobility. *J. Am. Chem. Soc.* **2006**, *128* (35), 11416–11422.

(78) Yu, J.; Sushko, M. L.; Kerisit, S.; Rosso, K. M.; Liu, J. Kinetic Monte Carlo Study of Ambipolar Lithium Ion and Electron − Polaron Diffusion into Nanostructured TiO_2. *J. Phys. Chem. Lett.* **2012**, *3*, 2076–2081.

(79) Zhang, R.; Yu, X.; Nam, K. W.; Ling, C.; Arthur, T. S.; Song, W.; Knapp, A. M.; Ehrlich, S. N.; Yang, X. Q.; Matsui, M. α-MnO_2 as a Cathode Material for Rechargeable Mg Batteries. *Electrochem. Commun.* **2012**, *23* (1), 110–113.

(80) Davis, R. E. Displacement Reaction at the Sulfur Atom. I. An Interpretation of the Decomposition of Acidified Thiosulfate. *J. Am. Chem. Soc.* **1958**, *80* (21), 3565–3569.

(81) Norberg, N. S.; Arthur, T. S.; Fredrick, S. J.; Prieto, A. L. Size-Dependent Hydrogen Storage Properties of Mg Nanocrystals Prepared from Solution. *J. Am. Chem. Soc.* **2011**, *133* (28), 10679–10681.

(82) Toby, B. H. EXPGUI, a Graphical User Interface for GSAS. *J. Appl. Crystallogr.* **2001**, *34* (2), 210–213.

(83) Momma, K.; Izumi, F. VESTA 3 for Three-Dimensional Visualization of Crystal, Volumetric and Morphology Data. *J. Appl. Crystallogr.* **2011**, *44* (6), 1272–1276.

(84) Ley, L.; McFeely, F. R.; Kowalczyk, S. P.; Jenkin, J. G.; Shirley, D. A. Many-Body Effects in X-Ray Photoemission from Magnesium. *Phys. Rev. B* **1975**, *11* (2), 600–612.

(85) Marcus, M. A.; MacDowell, A. A.; Celestre, R.; Manceau, A.; Miller, T.; Padmore, H. A.; Sublett, R. E. Beamline 10.3.2 at ALS: A Hard X-Ray Microprobe for Environmental and Materials Sciences. *J. Synchrotron Radiat.* **2004**, *11* (3), 239–247.

(86) Newville, M. IFEFFIT: Interactive XAFS Analysis and FEFF Fitting. *J. Synchrotron Radiat.* **2001**, *8* (2), 322–324.

(87) Ravel, B.; Newville, M. ATHENA, ARTEMIS, HEPHAESTUS: Data Analysis for X-Ray Absorption Spectroscopy Using IFEFFIT. *J. Synchrotron Radiat.*

2005, *12* (4), 537–541.

(88) Ravel, B.; Newville, M. ATHENA and ARTEMIS: Interactive Graphical Data Analysis Using IFEFFIT. *Phys. Scripta.* **2005**, *T115*, 1007–1010.

(89) Hohenberg, P.; Kohn, W. Inhomogeneous Electron Gas. *Phys. Rev. B* **1964**, *136* (3), 864–871.

(90) Kohn, W.; Sham, L. J. Self-Consistent Equations Including Exchange and Correlation Effects. *Phys. Rev. A* **1965**, *140* (4), 1133–1138.

(91) Kresse, G.; Furthmüller, J. Efficiency of *Ab-Initio* Total Energy Calculations for Metals and Semiconductors Using a Plane-Wave Basis Set. *Comput. Mater. Sci.* **1996**, *6* (1), 15–50.

(92) Perdew, J. P.; Burke, K.; Ernzerhof, M. Generalized Gradient Approximation Made Simple. *Phys. Rev. Lett.* **1996**, *77* (18), 3865–3868.

(93) Anisimov, V. I.; Aryasetiawan, F.; Lichtenstein, A. I. First-Principles Calculations of the Electronic Structure and Spectra of Strongly Correlated Systems: The LDA + *U* Method. *J. Phys. Condens. Matter* **1997**, *9*, 767–808.

(94) Zhou, B.; Shi, H.; Cao, R.; Zhang, X.; Jiang, Z. Theoretical Study on the Initial Stage of a Magnesium Battery Based on a V_2O_5 Cathode. *Phys. Chem. Chem. Phys.* **2014**, *16* (34), 18578–18585.

(95) Wang, L.; Maxisch, T.; Ceder, G. Oxidation Energies of Transition Metal Oxides within the GGA+*U* Framework. *Phys. Rev. B* **2006**, *73*, 195107.

(96) Sheppard, D.; Terrell, R.; Henkelman, G. Optimization Methods for Finding

Minimum Energy Paths. *J. Chem. Phys.* **2008**, *128* (13), 134106.

(97) Sheppard, D.; Xiao, P.; Chemelewski, W.; Johnson, D. D.; Henkelman, G. A Generalized Solid-State Nudged Elastic Band Method. *J. Chem. Phys.* **2012**, *136* (7), 074103.

(98) Maxisch, T.; Zhou, F.; Ceder, G. Ab Initio Study of the Migration of Small Polarons in Olivine Li_xFePO_4 and Their Association with Lithium Ions and Vacancies. *Phys. Rev. B* **2006**, *73* (10), 104301.

(99) Ong, S. P.; Chevrier, V. L.; Hautier, G.; Jain, A.; Moore, C.; Kim, S.; Ma, X.; Ceder, G. Voltage, Stability and Diffusion Barrier Differences between Sodium-Ion and Lithium-Ion Intercalation Materials. *Energy Environ. Sci.* **2011**, *4* (9), 3680–3688.

7. HOLE EXTRACTION BY DESIGN IN PHOTOCATALYTIC ARCHITECTURES INTERFACING CdSe QUANTUM DOTS WITH TOPOCHEMICALLY STABILIZED TIN VANADIUM OXIDE*

7.1. Overview

Tackling the complex challenge of harvesting solar energy to generate energy-dense fuels such as hydrogen requires the design of photocatalytic nanoarchitectures interfacing components that synergistically mediate a closely interlinked sequence of light-harvesting, charge separation, charge/mass transport, and catalytic processes. The design of such architectures requires careful consideration of both thermodynamic offsets and interfacial charge-transfer kinetics to ensure long-lived charge carriers that can be delivered at low overpotentials to the appropriate catalytic sites while mitigating parasitic reactions such as photocorrosion. Here we detail the theory-guided design and synthesis of nanowire/quantum dot heterostructures with interfacial electronic structure specifically tailored to promote light-induced charge separation and photocatalytic proton reduction. Topochemical synthesis yields a metastable β-$Sn_{0.23}V_2O_5$ compound exhibiting Sn 5s-derived midgap states ideally positioned to extract

* Reprinted (adapted) with permission from Andrews, J. L.; Cho, J.; Wangoh, L.; Suwandaratne, N.; Sheng, A.; Chauhan, S.; Nieto, K.; Mohr, A.; Kadassery, K. J.; Popeil, M. R.; Thakur, P. K.; Sfeir, M.; Lacy, D. C.; Lee, T.-L.; Zhang, P.; Watson, D. F.; Piper, L. F. J.; Banerjee, S. Hole Extraction by Design in Photocatalytic architectures interfacing CdSe Quantum Dots with Topochemically Stabilized Tin Vanadium Oxide. *Journal of the American Chemical Society*, **2018**, *140* (49), 17163-17174.

photogenerated holes from interfaced CdSe quantum dots. The existence of these midgap states near the upper edge of the valence band (VB) has been confirmed and β-$Sn_{0.23}V_2O_5$/CdSe heterostructures have been shown to exhibit a 0 eV midgap state-VB offset, which underpins ultrafast sub-picosecond hole transfer. The β-$Sn_{0.23}V_2O_5$/CdSe heterostructures are further shown to be viable photocatalytic architectures capable of efficacious hydrogen evolution. The results of this study underscore the criticality of precisely tailoring the electronic structure of semiconductor components to effect rapid charge separation necessary for photocatalysis

7.2. Introduction

Achieving efficient conversion of solar energy incident on the planet to energy-dense, combustible fuels as required to generate power is arguably one of the defining challenges of our time.[1–4] Accomplishing this objective using photocatalytic architectures constituted from earth-abundant elements would represent a transformative step in the journey towards a low-carbon, environmentally sound, and sustainable economy. Solar photocatalysis requires absorption of photons, separation of excitons to mobile charge carriers, diffusion of such carriers to catalytic sites, diffusion of reactive species to active sites, and ultimately catalysis of redox processes at the active sites. Given the myriad challenges and their individual difficulties, it is unlikely that a single material can be designed to simultaneously fulfill each requisite role. Consequently, an alternative approach to solar energy conversion has focused on the design of

heterostructures comprising a light harvesting semiconductor acting as a charge donor and a wide-bandgap semiconducting material functioning as a charge acceptor.[5–8] In such a configuration, wherein the two components are closely interfaced, charge carriers are generated in the charge donor upon photoexcitation, and charge separation occurs across one or more interfaces, necessarily outcompeting various possible recombination channels. The mobile carriers are then supplied to redox catalysts at the appropriate potentials to catalyze oxidation and reduction half-reactions.[4,9]

The design of architectures for solar water splitting is subject to several constraints. First, as a result of the high overpotential of the water oxidation reaction, wide-bandgap semiconductors have been typically used, such as TiO_2 in the seminal work by Honda—Fujishima;[10] however, these materials have low absorption cross-sections in the visible region and much of the harvested free energy is squandered in overcoming the large activation energy that is reflected in the high overpotential of the reaction. The discovery of water-oxidation catalysts that operate at much lower overpotentials[11,12] implies that wide bandgap semiconductors are no longer necessary, allowing for better utilization of the solar spectrum. The design of charge acceptors that can supply holes to water-oxidation catalysts at potentials only slightly positive of the water-oxidation potential is thus a first imperative. Chalcogenide quantum dots (QDs) are promising light-harvesting elements given their high absorption coefficients as well as considerable compositional and dimensional tunability.[13,14] However, their

utilization in photocatalytic architectures has been limited by the vexing challenge of anodic photocorrosion, which is mediated by photogenerated holes localized at surface traps, resulting in the rapid oxidation of nanoparticle surfaces.[14,15] While several strategies for mitigating photocorrosion have been developed, including the growth of core-shell structures, substitutional doping, and the addition of sulfide-based hole-scavenging electrolytes,[14,16–18] a fundamental imperative for viable QD-based photocatalysis is to extract holes from the photoexcited QDs on ultrafast timescales before they are able to participate in surficial oxidation reactions. In the research reported here, we have addressed both imperatives – namely extracting holes from QDs and transferring them into states at potentials appropriate for water oxidation – through the design of a novel metastable β-$Sn_{0.23}V_2O_5$ compound, which has midgap states derived from the stereoactive lone pairs of Sn^{2+} ions that are strategically positioned to extract holes from photoexcited CdSe QDs. Rapid sub-picosecond hole extraction is evidenced in CdSe/β-$Sn_{0.23}V_2O_5$ heterostructures, which are furthermore demonstrated to function as viable architectures for photocatalytic water splitting.

Efficient hole extraction from a light-harvesting semiconductor requires both suitable energetic offsets of the valence and conduction band edges of the donor and acceptor as well as optimal dynamics of charge transfer as dictated by interfacial structure and thermodynamic driving forces.

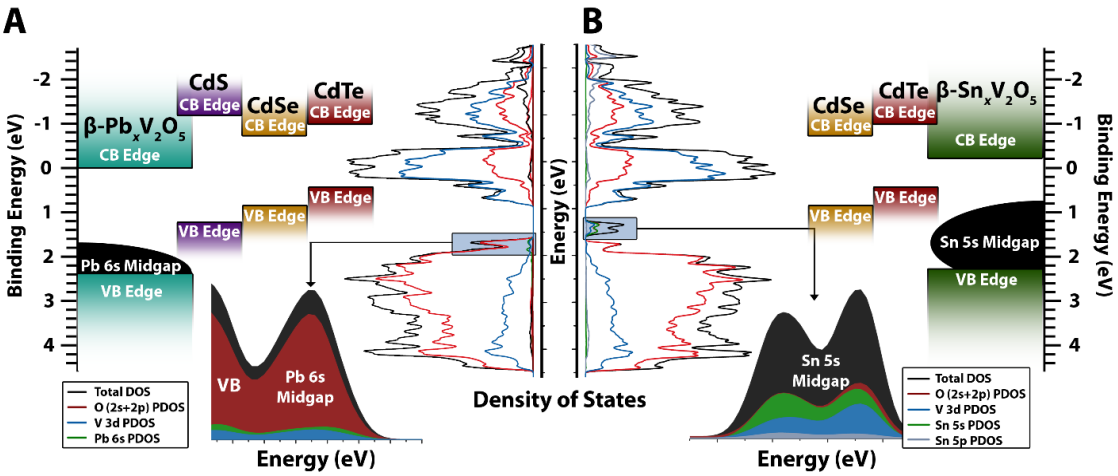

Figure 7.1. The schematic illustrates the importance of precisely modulating the electronic structure of both semiconducting components to achieve the desired outcome of extraction of photogenerated holes from QDs to the mid-gap states of the $M_xV_2O_5$ nanowires. (A) Energy positioning of mid-gap states of β-$Pb_xV_2O_5$ with respect to the valence band (VB) and conduction band edges (CB) of chalcogenide QDs, CdX (X = S, Se, Te), as determined from HAXPES and optical spectroscopy measurements, and calculated total and projected density of states.[10–12] The mid-gap states are derived from anti-bonding Pb $6s^2$—O 2p interactions. (B) Total and projected density of states calculated for β-$Sn_{0.23}V_2O_5$ and energy positioning with respect to the VB and CB edges of CdSe QDs. The relatively greater thermodynamic driving force for hole transfer from the top of the CdSe valence band to the mid-gap states of β-$Sn_{0.23}V_2O_5$ (as compared to β-$Pb_xV_2O_5$) is clearly discernible. Relative band alignments used to construct the figure are delineated in Table E.1 and are depicted in more detail in Figure E.9. DFT calculations are depicted in greater detail in Figure 7.3 and Figure E.7.

The valence and conduction band edges of semiconductors are primarily reflective of the chemical bonding and the extent of covalency/ionicity within the structures and are thus largely immutable. One strategy to address this constraint and develop reconfigurable materials involves open framework structures into which cations can be incorporated through intercalation chemistry to introduce electronic states at specific energies. We hypothesize that in the case of specific cations, such electronic states can be positioned to enable desired overlap with

the valence band edges of photoexcited semiconductor QDs, thereby providing a means of tuning energetic offsets and thermodynamic driving forces for charge transfer within heterostructures.[19–21] In recent work, we have demonstrated that β-$Pb_{0.31}V_2O_5$ can serve as a charge acceptor in β-$Pb_{0.31}V_2O_5$/CdX (X = S, Se, Te) QD heterostructures. Midgap states derived from the $6s^2$ stereoactive lone-pairs of intercalated Pb^{2+} cations[22,23] overlap the valence bands of the QDs, which enables the extraction of photogenerated holes.[19–21] Figure 7.1A sketches the band alignments of β-$Pb_{0.31}V_2O_5$ with CdX (X = S, Se, Te) QDs as determined from hard X-ray photoelectron spectroscopy (HAXPES) and density functional theory (DFT) calculations.[19–21] However, Figure 7.1A illustrates that the energetic positioning of the Pb^{2+}-derived midgap states is at much too positive of a potential to permit hole extraction from the valence band edges of QDs.[19,20,24] In order to obtain the desired thermodynamic alignment of energy levels, the acceptor component of the heterostructure needs to be designed with midgap states positioned at less positive potentials such as to facilitate hole extraction from the top of the QD valence band. The vast structural and compositional diversity of $M_xV_2O_5$ bronzes,[24,25] where M is a cation drawn from across the periodic table, holds promise for identifying compositions tailored to have the desired overlap with the valence band edges of QDs. The ability to intercalate different cations within V—O frameworks of varying connectivity[26,27] provides considerable design space for installing an electronic state formulated to have optimal energetic offsets. In this article, we report on the design of a metastable $M_xV_2O_5$ compound

with optimally-positioned midgap states and demonstrate charge separation within corresponding $M_xV_2O_5$/QD heterostructures, which can in turn be exploited in photocatalysis. Importantly, the midgap states described here are intrinsic to the composition of the material and are derived from periodically inserted ions, specifically main group ns^2np^0 cations, residing within well-defined crystallographic sites. As such, these states differ fundamentally from midgap states derived from stochastic surface traps and defect states localized within certain regions of the material.[28,29]

The inclusion of a metal cation, M, into the V_2O_5 framework necessitates a concomitant reduction of the d^0 (V^{5+}) framework to a partially reduced d^1/d^0 (V^{4+}/V^{5+}) framework. Depending on the electronic structure specific to the inserted cations, new states can overlap with valence or conduction band edges of the V_2O_5 framework or give rise to primarily non-bonding states between these bands.[30,31] Extensive studies of p-block ns^2np^0 cations across a variety of compounds indicate that in the solid state, such cations reside on a continuum between truly inert pairs and stereoactive lone pairs.[31,32] Indeed, based on elucidation of the atomistic and electronic structure of β-$Pb_xV_2O_5$,[22,23] the latter lone pair scenario seems to most accurately capture the nature of the Pb^{2+} ions in this compound.[19–21] Replacing Pb^{2+} cations with other post-transition metal cations to improve the energetic offsets depicted in Figure 7.1A is clearly of utmost importance. However, despite unparalleled compositional diversity,[33–38] the only

thermodynamically stable $M_xV_2O_5$ structures bearing main-group lone pairs accessible from direct synthesis are β-$Pb_{0.31}V_2O_5$ and δ-$Tl_{0.48}V_2O_5$.[22,23,38]

Consequently, the development of synthetic methods to prepare metastable β-$M_xV_2O_5$ phases with varying p-block cations is an urgent imperative.[27] The recent stabilization of the empty tunnel-structured ζ-V_2O_5 phase based on topochemical extraction of Ag-ions from β-$Ag_{0.33}V_2O_5$[27,39] yields an important synthetic building block, although intercalation chemistry approaches for filling the tunnels have thus far been confined to electropositive s-block cations.[27,35]

In this work, we demonstrate the design and topochemical stabilization of a metastable β-$Sn_{0.23}V_2O_5$ compound that is predicted from first-principles calculations to have $5s^2$ midgap states situated at a higher energy (more negative potential) than the midgap states of β-$Pb_xV_2O_5$, thereby enabling the directional charge transfer of photoexcited holes from the valence band edges of CdSe QDs to the midgap states. The compound has been prepared through a novel and versatile intercalation method that allows for intercalation of late-transition-metal and post-transition-metal cations within the tunnels of quasi-1D ζ-V_2O_5, and has been further verified using HAXPES to have a diffuse midgap state located close to the Fermi level, as predicted by DFT calculations. Ultrafast transient absorption (TA) spectroscopy measurements demonstrate sub-picosecond hole-transfer kinetics in β-$Sn_{0.23}V_2O_5$/CdSe heterostructures prepared by the successive ionic layer adsorption and reaction (SILAR) process. These heterostructures

furthermore demonstrate photocatalytic hydrogen evolution (0.20 μmol H_2 h^{-1} with the passage of 50 mC) with excellent Faradaic efficiency (82±5%). These results illustrate a new approach to catalyst design inspired by the application of chemical intuition to the prediction and elucidation of electronic structure and capitalize on the installation of intercalative states through topochemical modification of a metastable structure. The synthetic methods detailed herein render $M_xV_2O_5$/QD heterostructures a versatile and compositionally reconfigurable platform for energy-relevant light harvesting, charge separation, and redox photocatalysis.

7.3. Results and Discussion

7.3.1. Computationally Guided Design of Target p-Block $M_xV_2O_5$ Compounds

In order to address the limitations of $Pb_xV_2O_5$ noted above, we have used DFT calculations to design novel $M_xV_2O_5$ compounds with lone-pair-derived midgap states situated closer to the Fermi level than previously observed in β-$Pb_xV_2O_5$. Figure 7.1A shows DFT-calculated projected density of states (DOS) for β-$Pb_xV_2O_5$ illustrating that the relatively weak Pb 6s—O 2p hybridization yields filled midgap states (antibonding Pb 6s—O 2p in origin)[23] just slightly higher in energy than the O 2p valence band edge, which is still somewhat lower in energy than desired for hole extraction from QDs. Anion mixing is expected to be substantially increased for fifth-period post-transition metals in the absence of relativistic effects, improved shielding of nuclear charge by 4d states, and higher bond energies facilitated by lower cation—anion bond distances. A more

pronounced lone pair distortion is expected to furthermore allow for mixing of Sn 5p character resulting in more diffuse non-bonding states shifted up towards the Fermi level, as observed in the case of $SnWO_4$ and SnO.[31,32] Such a shift in the energy positioning of midgap states would indeed be welcome for the design of heterostructures, as it would render hole transfer thermodynamically more favorable from the valence band edges of CdSe QDs. One practical impetus for selecting Sn $5s^2$-derived states for hole extraction derives from the difficulties of stabilizing oxidation states that preserve filled ns^2 states in the solid state (which follows Pb^{2+}>Sn^{2+}>Ge^{2+}). Depending on the energy positioning of the midgap state, such a material could perhaps facilitate hole transfer from smaller-bandgap CdTe QDs, thereby allowing for more effective utilization of the solar spectrum.[14] DFT calculations performed for the hypothetical β-$Sn_xV_2O_5$ structure are shown in Figure 7.1B. Indeed, the atom-projected density of states suggest filled antibonding Sn 5s—O 2p midgap states energetically positioned at more negative potentials, closer to the Fermi level as compared to the 6s midgap states of β-$Pb_xV_2O_5$, and thus should exhibit considerably improved band alignment with the QD components of the heterostructures (Figure 7.1B). Table E.1 delineates the energies used to construct the band alignment diagrams based on HAXPES measurements of midgap states, X-ray photoemission spectroscopy (XPS) measurements of valence band edges, diffuse reflectance spectroscopy (DRS) measurements of the band gaps of the $M_xV_2O_5$ materials, and literature values for the bandgaps of bulk chalcogenide QDs. The implications of the electronic

structure of β-$Sn_xV_2O_5$ for hole extraction within heterostructures is discussed in greater detail below.

7.3.2. Topochemical Synthesis and Structural Characterization of Metastable Late-Transition-Metal and p-Block β-$M_xV_2O_5$

The hypothetical compound β-$Sn_xV_2O_5$ has not thus far been reported and is inaccessible from solid-state and hydrothermal reactions between conventional metal salt, metallic, and V_2O_5 precursors (indeed no $Sn_xV_2O_5$ phases are known even for alternative V—O connectivities[24,25] entirely different from the tunnel-structured phase predicted above). Given the tantalizing prospect of improved energetic overlap, we have instead designed a topochemical means of preparing this compound by inserting divalent Sn ions within a 1D metastable ζ-V_2O_5 phase. While chemical methods for inserting Li-, Mg-, and similar electropositive metal cations are well established,[27,40,41] the palette of synthetic methods for incorporating late transition metal and post-transition-metal cations in interstitial sites remains almost entirely unexplored. In this article, metastable β-$Sn_xV_2O_5$ has been prepared by a modified oxalate decomposition reaction (where M = Sn) as per the following equation:

$$\zeta\text{-}V_2O_5(s) + xMC_2O_4(s) \xrightarrow{\Delta} \beta\text{-}M_xV_2O_5(s) 2xCO_2(g) \qquad \textbf{7.1}$$

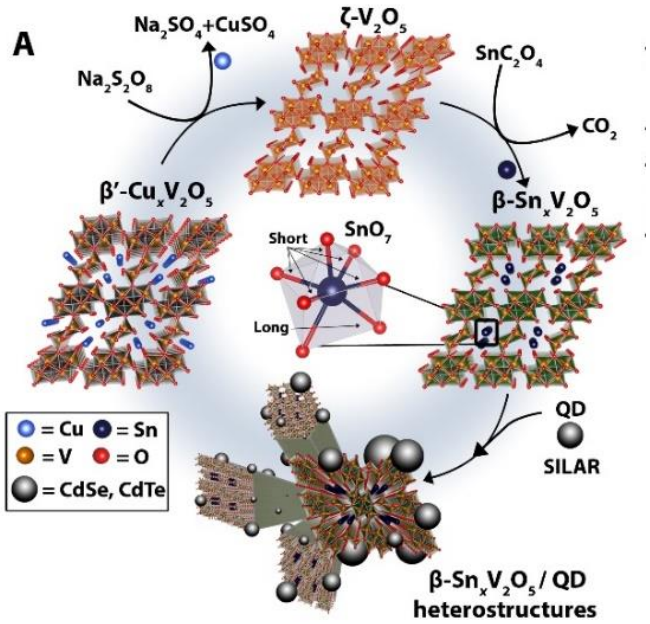

Figure 7.2. Synthetic approach and structural characterization of β-$Sn_{0.23}V_2O_5$ nanowires and β-$Sn_{0.23}V_2O_5$/QD heterostructures. (A) Illustration of topochemical synthetic approach for the stabilization of metastable β-$Sn_{0.23}V_2O_5$ nanowires and their surface functionalization with CdTe and CdSe QDs using the SILAR process. Metastable ζ-V_2O_5 nanowires have been stabilized by topochemical deintercalation of Cu ions from β'-$Cu_xV_2O_5$ (Figure E.1). The reaction of ζ-V_2O_5 nanowires with metal oxalates yields intercalated β-$M_xV_2O_5$ (M: Pb, Sn, Ni, Co, Figure E.2—Figure E.4). The refined β-$Sn_{0.23}V_2O_5$ structure is shown with the pentagonal bipyramidal local coordination environment of the inserted Sn cations depicted at the center of the graphic. β-$Sn_{0.23}V_2O_5$/QD heterostructures have been prepared by the SILAR deposition of CdSe and CdTe QDs onto the surfaces of β-$Sn_{0.23}V_2O_5$ nanowires. (B) Powder XRD pattern measured for β-$Sn_{0.23}V_2O_5$ nanowires. The collected data are plotted as black crosses, the calculated diffraction pattern is plotted in red, residuals are shown in light blue, and the reflections from the Rietveld refinement are delineated as pink ticks. Further refinement details, lattice parameters, and atom positions are provided in Table E.2 and Table E.3. (C) Lattice-resolved HRTEM image acquired for a β-$Sn_{0.23}V_2O_5$ nanowire indicating the separation between (002) planes. (D) Indexed SAED pattern acquired for the nanowire depicted in (C). (E) Low-magnification HRTEM image of CdSe-coated β-$Sn_{0.23}V_2O_5$ nanowires. (F) HRTEM image of β-$Sn_{0.23}V_2O_5$/CdSe heterostructures; the observed lattice spacing of 0.37 nm corresponds to the separation between the (002) planes of CdSe (PDF# 77-2307).[41] The inset shows false-color maps derived from diffraction imaging that illustrate the spatial localization of β-$Sn_{0.23}V_2O_5$ and CdSe phases. Red corresponds to regions of greater QD coverage and green corresponds to regions with relatively lower QD coverage. (G) Indexed SAED pattern acquired for heterostructures with individual diffraction spots indexed to β-$Sn_{0.23}V_2O_5$ and broad rings indexed to CdSe QDs.

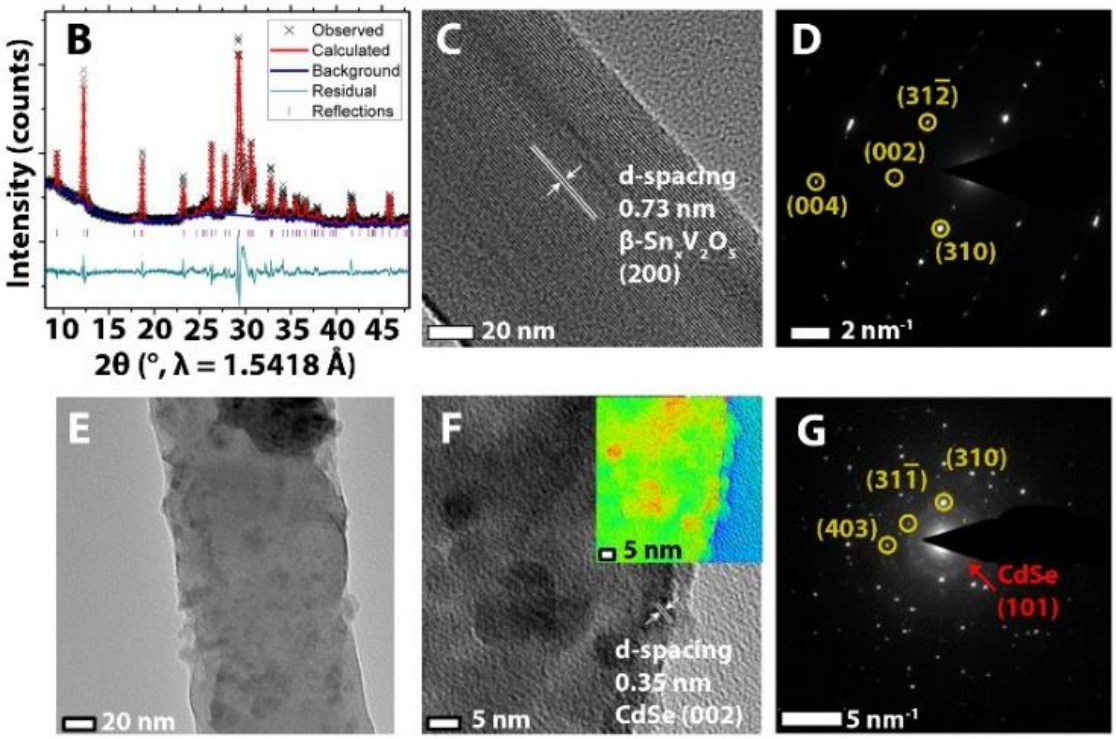

Figure 7.2. Continued.

The synthetic approach to prepare the desired β-$Sn_{0.23}V_2O_5$ compound, which involves the hydrothermal preparation of β'-$Cu_xV_2O_5$ nanowires, topochemical persulfate leaching of Cu-ions to stabilize the quasi-1D metastable ζ-V_2O_5 phase, and finally reaction with a tin oxalate precursors as per Equation 7.1, is schematically depicted in Figure 7.2A. The reaction is entropically driven by the formation of gaseous CO_2 and is thought to result in the formation of oxide/reactive metallic intermediates (for less electropositive metals, e.g., Sn, Ni, Co, Pb), which subsequently diffuse into V_2O_5 to form ternary vanadium oxide bronzes.[42] Since oxalate decomposition occurs at relatively low temperatures in the range between ca. 170 to 390°C (depending on the metal oxalate), the V—O

metastable phase can be preserved without reversion to the thermodynamically stable α-V_2O_5 polymorph (which is initiated above approximately 490°C).[39] Consequently, this versatile oxalate decomposition method can be further generalized to insert late-transition-metal cations within the tunnels of quasi-1D ζ-V_2O_5 (*vide infra*).

Figure E.1 contrasts the powder X-ray diffraction (XRD) patterns of the ζ-V_2O_5 precursor and the β-$Sn_xV_2O_5$ compound prepared using the oxalate decomposition reaction. A pronounced modulation in the intensity of several reflections is noted; in addition, a clear expansion of the tunnels upon Sn-insertion is observed, as indicated by shifts of the 200 and 002 Bragg reflections to lower 2θ values. Figure 7.2B shows powder XRD data for β-$Sn_xV_2O_5$ (x ~ 0.23) as well as a Rietveld refinement performed to solve the structure and determine the atomic positions.

Table E.2 lists refinement statistics as well as obtained lattice parameters and atom positions. Figure 7.2A depicts the refined structure of the prepared metastable β-$Sn_{0.23}V_2O_5$ compound and further illustrates the seven-coordinated sites occupied by the inserted Sn^{2+} ions. Select bond angles and bond lengths of the vanadium-centered polyhedra and SnO_7 pentagonal bipyramid are listed in Table E.3. The insertion of Sn^{2+} ions proceeds with complete retention of the nanowire morphology of the ζ-V_2O_5 precursor. Figure E.1B shows that the latter are ca. 100—150 nm in width with lengths spanning tens of microns. The SEM and TEM images in Figure E.2A and Figure E.2B, respectively, show that the β-

$Sn_{0.23}V_2O_5$ nanowires are similarly ca. 100—150 nm in width, consistent with an entirely topochemical insertion process. Figure 7.2C and Figure 7.2D show a high-resolution transmission electron microscopy (HRTEM) image and indexed selected area electron diffraction (SAED) pattern, respectively, acquired for the β-$Sn_{0.23}V_2O_5$ nanowires.

The HRTEM image and SAED pattern confirm the single-crystalline nature of the β-$Sn_{0.23}V_2O_5$ nanowires; well-defined lattice fringes with a lattice spacing of 0.73 nm are observed, and can be assigned to the interplanar separations between (200) planes of β-$Sn_{0.23}V_2O_5$, as determined from the Rietveld refinement to the powder XRD pattern depicted in Figure 7.2B. The nanowires are observed to grow along the (200) crystallographic plane with the quasi-1D tunnel direction oriented parallel to the growth direction of nanowires, consistent with previous observations for the hydrothermal growth of β-$Cu_xV_2O_5$.[43] High-resolution XPS spectra in the Sn $3d_{5/2}$ region could only be fit with one peak, as shown in Figure E.2C; this peak is centered around 486.3 eV, as expected for a Sn^{2+} charge state.[44,45] The single peak profile shape fitting furthermore supports the conclusion that formation of the tetravalent tin species is avoided. Furthermore, the Sn^{2+} assignment is corroborated by the measured valence band spectrum (Figure 7.3C and *vide infra*), as predicted by DFT (Figure 7.1B).

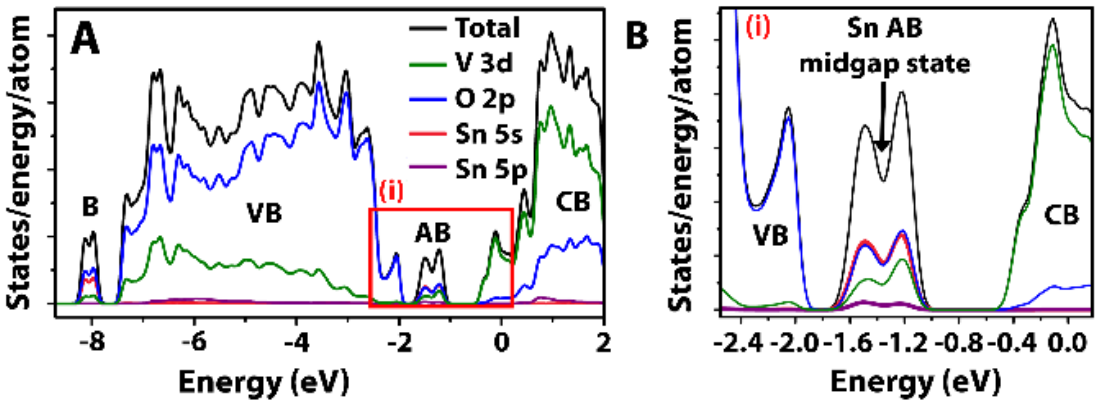

Figure 7.3. (A) DFT calculated density of states and atom-projected density of states for β-$Sn_{0.23}V_2O_5$ showing contributions from: Sn 5s and 5p orbitals; O 2s and 2p orbitals; and V 3d orbitals. Core states (<-9 eV) comprise primarily O 2s and Sn 4d states and are not depicted. The valence band (VB) primarily comprises O 2p states with some V 3d character, whereas the conduction band (CB) primarily comprises hybridized O 2p—V 3d states. The bonding (labeled 'B') and antibonding (labeled 'AB') bands below and above the VB, respectively are primarily Pb 6s and O 2p in character. (B) An expanded region of the DOS in (A) more clearly elucidates the nature of the Sn-derived antibonding states, or 'midgap' state predicted for β-$Sn_{0.23}V_2O_5$. (C) HAXPES data collected for β-$Sn_{0.23}V_2O_5$ provide a detailed picture of the valence band and confirm the existence of the Sn 5s midgap-derived states predicted by DFT. Bonding (B) and antibonding (AB) states are assigned in the spectra. The bonding states have strong Sn 5s character, whereas anionic O 2p states mediate mixing of Sn 5s and 5p character in the antibonding states. (D) X-ray absorption spectra collected for ζ-V_2O_5 (black), β-$Sn_{0.23}V_2O_5$ (red), and β-$Sn_{0.23}V_2O_5$/CdSe heterostructures (blue) provide a detailed picture of the conduction band and provide further evidence of the intercalation of tin within the nanowires by illustrating filling of the lowest-lying unoccupied V $3d_{xy}$ states. Corresponding HAXPES measurements were collected for (E) bare and CdSe/CdTe-coated ζ-V_2O_5 (F) and bare and CdSe/CdTe-coated β-$Sn_{0.23}V_2O_5$. Vertical dashed lines in (C), (E), and (F) indicate the Fermi energy. HAXPES-determined band alignments for (G) ζ-V_2O_5/CdSe and (H) β-$Sn_{0.23}V_2O_5$/CdSe. The band alignments are oriented with respect to the positioning of the H_2/H_2O (hydrogen evolution) and O_2/H_2O (oxygen evolution) couples as indicated by the blue dashed lines. The positioning of the Sn-derived midgap state 1.5 eV above the V-O derived valence band edge onset of the pristine material is indicated by a shaded blue box.

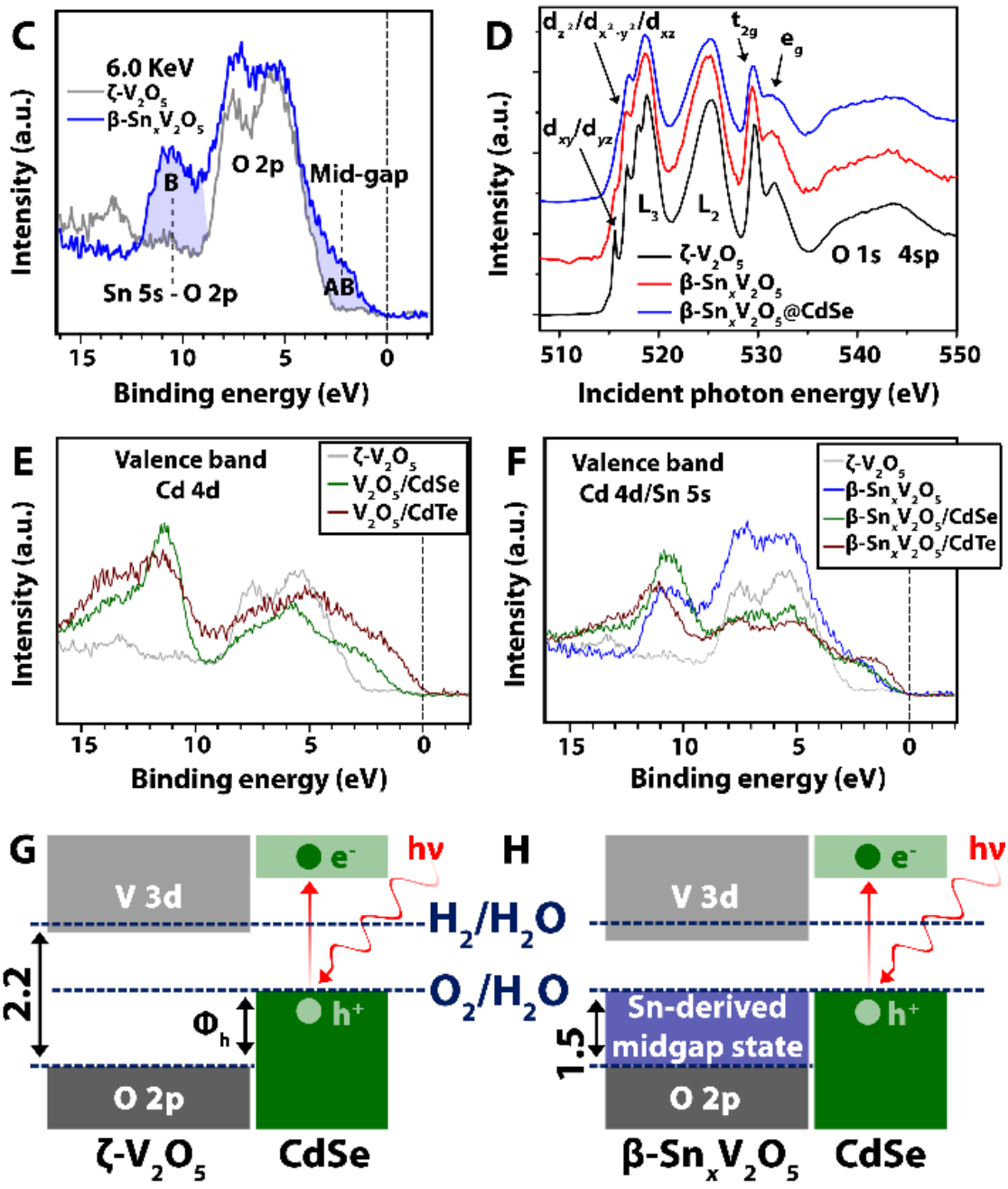

Figure 7.3. Continued.

In the case of Sn^{4+}, only occupied V 3d states at the top of the valence band would be expected. In the Sn^{2+} oxidation state, the Sn 5s orbital is occupied

and therefore contributes to states at the top of the valence band. This confirms that the top of the valence band for $Sn_xV_2O_5$ comprises hybridized states of Sn 5s, Sn 5p, and O 2p contribution, which is in accordance with the lone pair formation mechanism.[31,46] The retention of the Sn $5s^25p^0$ configuration is, of course, critical to the utilization of this compound for hole extraction. XPS data in Figure E.2D further attest to the mixed V^{4+}/V^{5+} valence, owing to the reduction of vanadium V^{5+} sites of ζ-V_2O_5 to compensate for the insertion of Sn^{2+} ions. Comparison of the V^{4+}/V^{5+} XPS peak areas (Figure E.2D) suggest a material stoichiometry consistent with the fractional tin occupancy obtained by Rietveld refinement. Procedures for peak fitting of the Sn 3d and V 2p XPS data are shown in Figure E.2. The mixed vanadium valence is further confirmed by X-ray absorption spectroscopy data shown in Figure 7.3 (*vide infra*).

As noted above, soft chemical approaches for inserting late-transition-metal and p-block cations are relatively unexplored. In addition to the synthesis of β-$Sn_{0.23}V_2O_5$, the oxalate reaction method (more generally described by Equation 7.2) has been used to prepare β-$Pb_xV_2O_5$ nanowires with control over the Pb stoichiometry (x) by reacting the appropriate amount of lead oxalate with ζ-V_2O_5 nanowires at a temperature of 400°C, above the decomposition temperature of PbC_2O_4.[47] Unlike β-$Sn_{0.23}V_2O_5$, β-$Pb_xV_2O_5$ is indeed accessible from direct hydrothermal synthesis[22] but varying the Pb content (below x = 0.31) inserted within the tunnels by hydrothermal synthesis is difficult. Figure E.3 indicates that the Pb content in β-$Pb_xV_2O_5$ can be varied from x = 0.11—0.33 by the oxalate

method reported here. The versatile oxalate decomposition approach has furthermore been used to prepare vanadium oxide bronzes of the late transition metals, specifically β-$Ni_xV_2O_5$ and β-$Co_xV_2O_5$ (Figure E.4). Figure E.4A shows the Rietveld refinement of the powder XRD pattern for a topochemically stabilized β-$Ni_{0.331}V_2O_5$ phase. Table E.4 lists refinement statistics as well as the refined lattice parameters and atom positions. Select bond angles and bond lengths of the vanadium-centered octahedra and NiO_5 pentagonal bipyramid are listed in Table E.5. Comparing powder XRD data for the different intercalated compounds, the tunnel framework is found to increase monotonically with increasing radius of the inserted cations (Figure E.4 and Table E.6).

7.3.3. Synthesis and Characterization of β-$Sn_xV_2O_5$/QD Heterostructures

The topochemically stabilized β-$Sn_{0.23}V_2O_5$ nanowires have been interfaced with CdX (X = Se, Te) QDs through the SILAR process,[19–21] a modified chemical bath deposition method comprising sequential dispersion in anionic and cationic solutions of II-VI chalcogenide precursors[48,49] (Figure 7.2A). In contrast to the smooth facets of the β-$Sn_{0.23}V_2O_5$ nanowires (Figure 7.2C and Figure E.2B), TEM images acquired for the β-$Sn_{0.23}V_2O_5$/CdSe heterostructures (Figure 7.2E and Figure 7.2F) show a distinctly speckled appearance; agglomerated particles observed on the nanowire surfaces correspond to surface-grown CdSe QDs. Lattice fringes indexed to the separation between the (002) crystallographic planes of wurtzite CdSe are observed by HRTEM in Figure 7.2F, corroborating the growth of crystalline CdSe QDs on the surfaces of β-$Sn_{0.23}V_2O_5$ nanowires.[50]

The inset of Figure 7.2F shows a false-color phase domain TEM image of β-$Sn_{0.23}V_2O_5$/CdSe heterostructures, allowing for visualization of the spatial localization of QDs across the surfaces of β-$Sn_{0.23}V_2O_5$ nanowires. Higher QD coverage is reflected as red/yellow coloration in the intensity map. A SAED pattern acquired for the heterostructures shows a combination of diffraction spots indexed to β-$Sn_{0.23}V_2O_5$ (Figure 7.2D) and diffuse ring patterns derived from wurtzite CdSe QDs (Figure 7.2G). A similar approach has furthermore been used to interface β-$Sn_{0.23}V_2O_5$ nanowires with CdTe QDs. Figure E.5 shows HRTEM images, colorized diffraction maps, and SAED patterns acquired for similarly prepared β-$Sn_{0.23}V_2O_5$/CdTe heterostructures. Figure E.6 shows EDX spectra and maps acquired for the β-$Sn_{0.23}V_2O_5$/CdSe and β-$Sn_{0.23}V_2O_5$/CdTe heterostructures further verifying the integration of QDs onto the nanowire surfaces. The maps indicate the homogeneous distribution of CdSe and CdTe quantum dots across the nanowire surfaces.

7.3.4. Deciphering the Electronic Structure of β-$Sn_xV_2O_5$ and Emergent Midgap States

A key motivation for stabilizing metastable β-$Sn_{0.23}V_2O_5$ and its heterostructures is that the Sn $5s^2$-derived midgap state is expected to be energetically favorably positioned for the extraction of photogenerated holes from QDs (as suggested by the DFT calculations shown in Figure 7.1B). Figure 7.3A plots the orbital-projected density of states of β-$Sn_{0.23}V_2O_5$ calculated using DFT. Consistent with the electronic structure of ternary vanadium oxides, the valence

band (VB) is primarily O 2p in character, whereas the conduction band (CB) comprises V 3d—O 2p hybrid states.[27,33,34,51,52] Sn 5s-derived bonding (B) and antibonding (AB) states appear below and above the VB, respectively.[19] An expanded view of the midgap state and band gap region (red box labeled (i) in Figure 7.3A) is provided in Figure 7.3B, and more clearly delineates the nature of the Sn-derived midgap state. Based on the lower binding energy of the Sn 5s states relative to Pb 6s states,[19,23] the Sn 5s midgap state is positioned closer to the Fermi level. The midgap state comprises contributions from V 3d, O 2p, O 2s, Sn 5s, and Sn 5p states (O 2s not depicted for clarity). The Sn 5p as well as V 3d states are observed to contribute to the hybridization of the filled Sn $5s^2$ and oxygen 2p states as a result of the reduced symmetry of the Sn^{2+} site, which is distinctly different from previous findings for Pb $6s^2$-derived states in β-$Pb_xV_2O_5$ (orbital-projected density of states of β-$Pb_xV_2O_5$ are shown in Figure E.7 for direct comparison), and gives rise to a more diffuse state with classical stereoactive lone pair character near the Fermi level.[31,32]

The electronic structure of β-$Sn_{0.23}V_2O_5$ has also been examined by XPS, HAXPES, and scanning transmission X-ray microscopy (STXM) in order to probe the existence of the midgap state, examine its energy positioning with respect to the valence and conduction band edges of this material, and further understand the influence of Sn^{2+} insertion on the electronic structure of ζ-V_2O_5. Figure 7.3C exhibits HAXPES (6 keV) measurements, which probe the upper edge of the VB near the Fermi level, that were collected for β-$Sn_{0.23}V_2O_5$ and ζ-V_2O_5. As indicated

in the DFT calculations, the VB is primarily O 2p in character and indeed this is the most prominent feature in spectra measured for both compounds. Figure 7.3C illustrates the appearance of two distinct states centered at 2.20 eV (spanning ca. 0.8—3.0 eV) and 10.52 eV (spanning ca. 8.4-12.4 eV) in HAXPES spectra acquired for β-$Sn_{0.23}V_2O_5$ which are not observed for ζ-V_2O_5 (light grey). Based on their relative energy positioning, the features are assigned to the antibonding (AB) and bonding (B) Sn-hybridized states predicted by DFT (Figure 7.3A). HAXPES measurements thus confirm that a broad state reaching much closer to the Fermi level (as compared to previous measurements of the midgap states in β-$Pb_xV_2O_5$),[23] which is desirable for improving alignment with the valence band edges of QDs, is thereby obtained upon insertion of Sn^{2+} within ζ-V_2O_5.

STXM measurements at the V L- and O K-edges have been used to probe the unoccupied density of states of ζ-V_2O_5 and β-$Sn_{0.23}V_2O_5$ (Figure 7.3D). The spectra show characteristic absorption features corresponding to transitions from V 2p→V 3d (V L_{III}- and V L_{II}-edges separated by spin—orbit coupling of ca. 7 eV in ζ-V_2O_5) and O 1s→O 2p states concordant with a change in angular momentum quantum number, $\Delta l = \pm 1$. The fine structure at the V L_{III}-edge arises from transitions to V3d states of the three crystallographically inequivalent vanadium atoms of ζ-V_2O_5 that are split by crystal field and multiplet effects. The assignments to final V 3d states delineated in Figure 7.3D are based on DFT calculations of the orbital-projected density of states with V $3d_{xy/yz}$ states situated at the bottom of the conduction band.[52–55] Similarly, at the O K-edge, two distinct

sets of absorption features can be distinguished, reflecting the hybridization of O 2p states with V 3d states that are split in energy as a result of crystal field effects. Considering the quasi-octahedral VO_6 polyhedra of ζ-V_2O_5, states with t_{2g} symmetry corresponding to V—O π* anti-bonding and e_g symmetry corresponding to end-on V—O σ* anti-bonding states can be distinguished.[53–55] A pronounced modification of the electronic structure is observed upon Sn-intercalation and concomitant reduction of the V_2O_5 lattice (Figure 7.3D and Figure E.8). Specifically, the relative intensity of the lowest-lying V d_{xy}/d_{yz} states is greatly diminished at the V L_{III}-edge as a result of Pauli blocking owing to these states at the bottom of the conduction band being filled upon partial reduction of the vanadium sublattice (as corroborated by XPS measurements plotted in Figure E.2D). This darkening signifies a repositioning of these states to below the Fermi level as they are filled, and such states likely further contribute to the hybrid midgap state. Similarly, the relative ratio of t_{2g} to e_g states is strongly decreased, again suggesting the filling of hybrid V 3d—O 2p states at the CB edge. Notably, STXM measurements acquired across topochemically stabilized β-$Sn_{0.23}V_2O_5$ nanowires show essentially homogeneous V L_{III}-edge and O K-edge spectra within the limits of resolution, suggesting that the topochemical intercalation of Sn^{2+} ions proceeds homogeneously across the wires (Figure E.8).

7.3.5. Achieving "Downhill" Hole Transfer by Improved Band Alignment of β-$Sn_xV_2O_5$ with QD VB Edges

Figure 7.3E and Figure 7.3F contrast HAXPES measurements collected for β-$Sn_{0.23}V_2O_5$/CdX (X = Se, Te) heterostructures, empty ζ-V_2O_5 and bare β-$Sn_{0.23}V_2O_5$ nanowires. Comparing the VB onsets for β-$Sn_{0.23}V_2O_5$ and β-$Sn_{0.23}V_2O_5$/CdX heterostructures confirms the excellent alignment of the CdSe VB edge and Sn-derived midgap states, indicating that excited-state hole transfer is thermodynamically favorable from the valence band edge, as well as from deeper and more energetic holes within the valence band, of CdSe QDs. Indeed, the HAXPES measurements indicate an offset of 0 eV between the valence bands of β-$Sn_{0.23}V_2O_5$ and CdSe QDs. Despite a considerably improved overlap of the Sn-derived midgap states of β-$Sn_{0.23}V_2O_5$ with the VB of CdTe, as compared to the Pb-derived midgap states in the β-$Pb_xV_2O_5$ case shown in Figure 7.1A, a thermodynamic barrier to hole transfer from the VB edge still exists in heterostructures of the heavier chalcogenide. Energetic offsets and band alignments calculated from HAXPES data are listed in Table E.1 and have been used to sketch the band alignments shown in Figure 7.3G and Figure 7.3H (for CdSe alignment) and in Figure E.9 (for CdTe alignment). Bulk CdX (X = S, Se, and Te) bandgaps have been used to calculate the relative band alignments;[56] notably, quantum confinement is known to most substantially alter the energy positioning of the CB edges of QDs but has much less of an effect on the VB edges, which instead are determined by the electronegativity of the anion as per

Fajan's formalism.[57,58] Figure E.10 shows HAXPES data which provide further evidence of the retention of the mixed valence vanadium oxidation state upon SILAR deposition of the chalcogenide QDs, consistent with XANES spectra collected for β-$Sn_{0.23}V_2O_5$/CdSe (Figure 7.3D). In summary, using HAXPES measurements, the existence of these midgap states near the upper edge of the VB has been confirmed and the anticipated overlap of the Sn-derived midgap states with the VB of CdSe QDs within β-$Sn_{0.23}V_2O_5$/CdSe heterostructures has been experimentally verified, achieving remarkable band alignment with an energetic offset of 0 eV.

7.3.6. Dynamics of Hole Transfer between Photoexcited CdX (X = Se, Te) and β-$Sn_xV_2O_5$

The central advance of this work is the rationally predicted and experimentally realized improvement of the alignment of the Sn-derived midgap state with the VB of the CdSe QDs relative to the alignment of Pb-derived midgap states with CdSe QDs. We next turn our attention to determining whether the observed optimal interfacial energetics indeed promote efficacious or rapid hole extraction from the VB of photoexcited QDs using transient absorbance (TA) spectroscopy measurements, as would be expected from energy offset diagrams (Figure 7.3G, Figure 7.3H, and Figure E.9).[20,21] The 3D TA color maps clearly elucidate the presence of transient induced absorption features (indicated in red) and the recovery of the transient bleaches (indicated in blue) as a function of delay time. The bare β-$Sn_{0.23}V_2O_5$ nanowires (Figure 7.4A and Figure 7.4C) are

characterized by two broad induced absorption bands at 500—600 nm and 650—750 nm as well as a bleach centered at ca. 465 nm. We have previously conducted TA spectroscopy studies of charge transfer processes in the structurally related β-$Pb_xV_2O_5$ and employed spectroelectrochemical measurements to assist in the interpretation of the nature of the observed induced absorption features;[20,21] accordingly, the short-wavelength induced absorption feature observed here for β-$Sn_{0.23}V_2O_5$ can be ascribed to transitions from deep VB states into the midgap states following initial photoexcitation of electrons from the midgap states (and thus is indicative of oxidation of the nanowires).

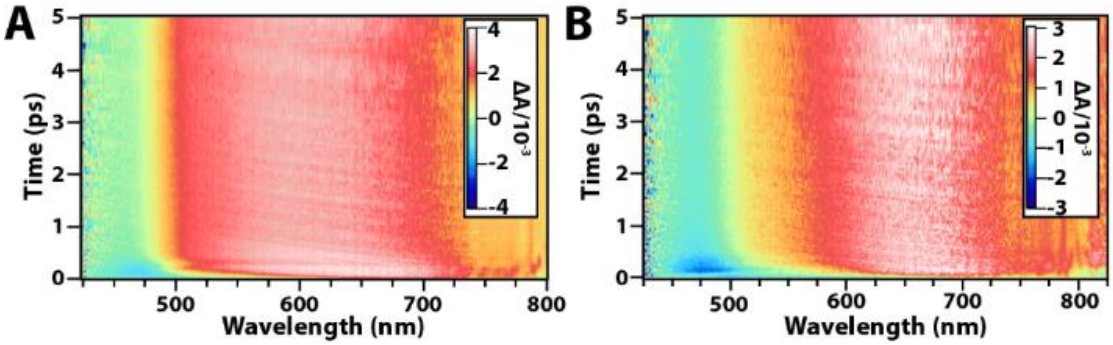

Figure 7.4. Transient absorption (TA) intensity maps acquired for (A) β-$Sn_{0.23}V_2O_5$ nanowires and (B) β-$Sn_{0.23}V_2O_5$/CdSe heterostructures at delay times from 0—5 ps across a probe wavelength range of 425—825 nm at an excitation wavelength of 360 nm. TA spectra collected within the same time range for (C) β-$Sn_{0.23}V_2O_5$ nanowires and D) β-$Sn_{0.23}V_2O_5$/CdSe heterostructures. Each individual spectrum in (C) and (D) is taken as a horizontal 'slice' of the 3D maps in (A) and (B) at specific delay times (integrated across: a ±0.1 ps time window for the 0.5 ps decay; a ±0.5 ps time window for 1, 2.5, and 5 ps decay traces; and a ±2.5 ps time window for 10, 20 ps decay traces). TA decay and recovery traces as well as multiexponential fits are shown in Figure E.11.

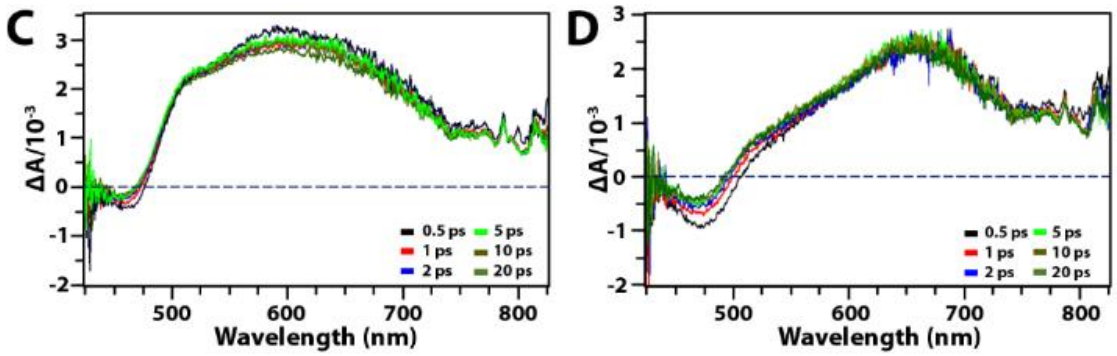

Figure 7.4. Continued.

The induced absorption band observed at longer-wavelengths can in turn be assigned to excitation of electrons in the conduction band of β-$Sn_{0.23}V_2O_5$ to higher energy states (corresponding to the reduction of the nanowires).[19,20] In other words, the shorter wavelength (500—600 nm) and longer wavelength (650—750 nm) induced absorption features can be assigned to excited-state holes in the midgap gap state and electrons situated in the conduction bands of β-$Sn_{0.23}V_2O_5$ nanowires, respectively. Upon direct photoexcitation at 360 nm, both bands are present in TA spectra within the instrument response time, corresponding to the creation of holes in the midgap states and excited electrons in the conduction band. The TA spectra of β-$Sn_{0.23}V_2O_5$/CdSe heterostructures (Figure 7.4B and Figure 7.4D) show some stark differences from spectra acquired for the bare β-$Sn_{0.23}V_2O_5$ nanowires. A significant reduction in the induced absorption band at 500—600 nm is clearly discernible, which is a result of overlap with the characteristic excitonic bleach of CdSe QDs.[20] The bleach of the ground-state absorption of CdSe QDs, combining both first and second excitonic

transitions, gives rise to an initial broad bleach feature in the Δ*A* spectra.[20,59] A pronounced rise of the β-$Sn_{0.23}V_2O_5$ induced absorption bands and the recovery of the CdSe bleach (to the blue-shifted bleach of β-$Sn_{0.23}V_2O_5$) is clearly distinguishable in the differential absorption spectra (Δ*A*) acquired within 5 ps. The recovery of the CdSe excitonic bleach at picosecond timescales is attributed to electron transfer from the conduction band of the QDs to the CB of β-$Sn_{0.23}V_2O_5$ nanowires (bleaches observed in excited QDs primarily reflect electron dynamics).[60,61] Note that this process occurs in binary heterostructures in the absence of protons or an electron-accepting reduction catalyst that would facilitate spatial separation of the hole and electron in photocatalysis. Given that the only time-resolvable event is electron transfer, hole-transfer from photoexcited CdSe QDs to the midgap states of β-$Sn_{0.23}V_2O_5$ occurs within the instrument response time on ultrafast sub-picosecond timescales,[20,21] whereas the electron transfer process can be resolved within the first few picoseconds. The excellent transfer kinetics observed for β-$Sn_{0.23}V_2O_5$/CdSe are consistent with those expected based on the quantitative band alignments shown in Figure 7.1B. The photocatalysis measurements described below provide further evidence of improved charge separation and ultrafast hole transfer kinetics.

TA recovery traces have been extracted and fitted for the exciton bleach feature attributed solely to QDs (centered at 485 nm); similarly, TA decay traces have been analyzed for an induced absorption band coupled to the QD bleach centered at 525 nm (Figure E.11). The TA recovery and decay traces have been

fitted using multiexponential functions since multiple relaxation pathways are operational, including multiple trap-state-mediated recombination processes.[19,21] The fitting parameters used to describe the decay and recovery kinetics are listed in Table E.7. Decay traces obtained for the β-$Sn_{0.23}V_2O_5$/CdSe heterostructures are well described using biexponential decay functions. As noted above, the hole transfer kinetics cannot be resolved within the instrument response time; however, the multiexponential fits suggest that complete recovery of the CdSe excitonic bleach and growth of the corresponding induced absorption band at 525 nm (both corresponding to electron transfer processes) occur within 1—2 ps. The deduced average lifetimes $\langle\tau\rangle$ at probe wavelengths of 485 and 525 nm are calculated to be 0.4±0.1 ps and 0.3±0.1 ps, respectively (Table E.7).

Analogous TA data acquired for β-$Sn_{0.23}V_2O_5$/CdTe heterostructures is shown in Figure E.12A and Figure E.12B. The stabilization of β-$Sn_{0.23}V_2O_5$ and the optimal placement of the Sn midgap state enable the use of CdTe QDs as the light-harvesting component, since the energetic offset (Figure 7.1B andFigure E.9) is similar to the offset between β-$Pb_{0.31}V_2O_5$ and CdSe, which we have previously demonstrated to have sub-picosecond hole transfer.[20,21] Hole transfer kinetics are expected to be slower owing to the larger CB offset with β-$Sn_{0.23}V_2O_5$ as compared to CdSe (Figure 7.1B and Figure E.9). The 3D TA intensity maps and time-resolved TA spectra are again consistent with ultrafast sub-picosecond hole transfer (which cannot be resolved within the instrument response time), whereas electron transfer (observed as recovery of the excitonic bleach of CdTe

QDs)[62] is demonstrably slower as compared to the CdSe heterostructures. The pronounced rise of Δ*A* over time arises from the diminution of the excitonic bleach of CdTe, which is attributable to the injection of electrons from the CB of CdTe QDs to the CB of β-$Sn_{0.23}V_2O_5$. Figure E.12C illustrates the TA decay and recovery traces and their corresponding multiexponential fits measured for β-$Sn_{0.23}V_2O_5$/CdTe heterostructures at 485 nm and 675 nm. The former corresponds to excitonic bleach CdTe QDs, whereas the latter has contributions from both the first excitonic feature of CdTe QDs and the induced absorption feature of β-$Sn_{0.23}V_2O_5$. The average lifetimes <τ> at 485 and 675 nm are 4.3±0.3 and 3.5±0.8 ps, respectively, which suggest a considerably slower electron transfer process as compared to the β-$Sn_{0.23}V_2O_5$/CdSe heterostructures. The slower electron transfer dynamics can be attributed to the decreased thermodynamic driving force for charge transfer relative to β-$Sn_{0.23}V_2O_5$/CdSe (Figure 7.4).[63–66] In summary, the TA results attest to the ultra-fast hole extraction mediated by Sn-derived midgap states within β-$Sn_{0.23}V_2O_5$/CdX heterostructures with notably improved offsets for charge transfer for CdSe as compared to CdTe.

7.3.7. Catalytic Hydrogen-Evolution Activity of β-$Sn_{0.23}V_2O_5$/CdSe Heterostructures

Finally, we have performed photoelectrochemical measurements to evaluate whether ultrafast charge separation could be exploited in the photocatalytic reduction of protons to hydrogen. Linear sweep voltammograms were acquired for bare fluorine-doped tin oxide (FTO) electrodes modified with β-

$Sn_{0.23}V_2O_5$/CdS heterostructures within a single-compartment three-electrode cell under chopped visible-light (400—720 nm) illumination. The electrolyte contained lactic acid as the source of protons and a sacrificial reductant. Reductive photocurrents were measured at applied potentials more negative than 0.05 V *versus* SCE. The onset of photocurrent is more than 600 mV positive relative to the onset of dark reduction (Figure 7.5), consistent with the reduction of photogenerated holes rather than ground-state holes situated in the conduction band of QDs or NWs.

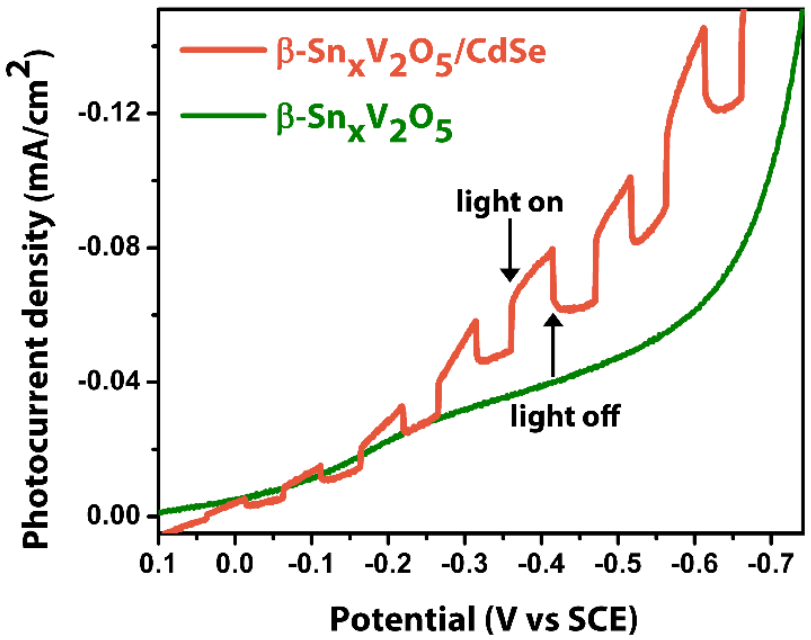

Figure 7.5. Catalytic hydrogen evolution from β-$Sn_{0.23}V_2O_5$/CdSe heterostructures. Linear sweep voltammograms of three-electrode cells with β-$Sn_{0.23}V_2O_5$/CdSe-modified (orange) and the bare β-$Sn_{0.23}V_2O_5$-modified (green) working electrodes, under chopped white-light illumination (60 mW cm^{-2}). Only the β-$Sn_{0.23}V_2O_5$/CdSe-modified electrode (orange) exhibits reductive photocurrent, indicative of improved hole transfer.

The observed photocurrent saturates at approximately -0.6 V *versus* SCE. It is crucial to note that, despite its semiconducting nature, no photocurrents were measurable for bare β-$Sn_{0.23}V_2O_5$ electrodes (Figure 7.5, green trace). Taken together, these data are consistent with the measured TA data, suggesting that the transfer of photoinduced holes from CdSe to β-$Sn_{0.23}V_2O_5$ increases the lifetimes of electrons and holes and promotes subsequent reduction processes, giving rise to the measured photocurrents.

To further investigate the mechanism of reductive photocatalysis, chronocoulometry data were acquired for heterostructure-modified electrodes (Figure E.13), and, following prolonged white-light illumination, the headspace above the electrolyte was sampled by gas chromatography (Figure E.14). Hydrogen was the sole photoproduct with no other detectable products in the headspace. In a typical measurement, 0.20 μmol of H_2 was evolved with the passage of 50 mC of cathodic charge upon 1 h of illumination; the average Faradaic efficiency was 82±5%. In control experiments, no H_2 was detectable as a product in the absence of illumination or photocatalyst, or for electrodes modified with bare, unfunctionalized β-$Sn_{0.23}V_2O_5$ nanowires. These results provide compelling evidence that photoinduced transfer of holes from CdSe QDs to midgap states of β-$Sn_{0.23}V_2O_5$ nanowires and the corresponding increase in charge-carrier lifetimes both enable the photocatalytic reduction of protons to hydrogen.

7.4. Conclusions

Rapid and efficient extraction of holes from the valence band of photoexcited QDs represents a formidable challenge that requires consideration of both thermodynamic offsets and interfacial charge transfer kinetics. The theory-guided design and topochemical synthesis of metastable β-$Sn_{0.23}V_2O_5$ paves the way to β-$Sn_{0.23}V_2O_5$/CdSe heterostructures wherein Sn 5s-derived midgap states are ideally positioned to extract photogenerated holes from CdSe QDs. The energetic offsets have been verified by photoemission spectroscopy measurements and <0.5 ps hole transfer kinetics have been observed within these heterostructures. The reconfiguration of ζ-V_2O_5 to precisely position states derived from stereoactive lone pairs of p-block cations, achieved through development of a novel and highly versatile topochemical synthesis route, represents a significant advance in materials design and suggest a versatile strategy for optimizing energetic offsets. The β-$Sn_{0.23}V_2O_5$/CdSe heterostructures evidence rapid excited-state charge-transfer kinetics and are shown to be viable light-harvesting and charge-separating photocatalytic architectures capable of efficacious hydrogen evolution. Future work will focus on the preparation of ternary heterostructures with the inclusion of an electron acceptor to enhance charge separation, as well as a detailed evaluation of photocathode stability to investigate the impact of the improved hole transfer kinetics on the stability of CdSe quantum dots.

7.5. Experimental Section

7.5.1. DFT Calculations

DFT-based[67,68] electronic structure calculations of β-$Sn_{0.23}V_2O_5$ and β-$Pb_{0.33}V_2O_5$ were carried out using the QUANTUM ESPRESSO package.[69] The Perdew-Burke-Ernzerhof functional[70] was used to describe the exchange and correlation terms along with ultrasoft pseudopotentials to accurately describe the electron-ion interactions.[70,71] Vanadium 3s and 3p, tin 4d, and lead 5d semicore electrons were included in the calculations. A relatively high cutoff energy of 60 Ry was used for the plane wave expansion of the wave functions. All structures were optimized until the residual forces were smaller than 10^{-4} Ry/a.u. The Brillouin zone integration was carried out using a 5×5×5 uniform k-grid for structural models containing 88 atoms. For the density of states (DOS) calculations, a higher k-grid density of 10×10×10 was used.

7.5.2. Synthesis of Metastable ζ-V_2O_5 Precursor

ζ-V_2O_5, a tunnel-structured metastable polymorph of V_2O_5, has previously been stabilized based on topochemical extraction of Ag-ions from β-$Ag_{0.33}V_2O_5$;[27,39] however, this method leaves residual Ag-ions within the structure ranging between x = 0.04—0.06, which obscure the upper edge of the valence band in X-ray emission spectroscopy measurements owing to the large absorption cross-section of Ag 4d states. Consequently, an alternate method has been developed here based on extraction of Cu-ions from β′-$Cu_xV_2O_5$, which reduces the copper content down to x= 0.0004 based on refinement of the powder XRD

pattern.[27,39] In a typical reaction, β′-$Cu_{0.5}V_2O_5$ nanowires were synthesized hydrothermally, adapting a previously reported synthesis.[72] In a typical reaction, V_2O_5 (Beantown Chemical, 99.5%), $VO(C_5H_7O_2)_2$ (Beantown Chemical), and $Cu(NO_3)_2$ hemipentahydrate (Sigma Aldrich, 98%) (total mass loading of 300 mg, in a 3:5:3 stoichiometric ratio) were dispersed in 16 mL of deionized water (ρ = 18 MΩ·cm^{-1}) and subsequently added to a 23 ml polytetrafluorethylene-lined autoclave (Parr) and subsequently allowed to react at 210°C for 24 h.[72] The resulting nanowires were washed with copious amounts for water and 2-propanol and dried in air overnight. Subsequently, Cu-ions were leached out of the material by reacting the nanowires with a 0.5 M aqueous solution of $Na_2S_2O_8$ at 80°C for 48 h using a 8:1 $Na_2S_2O_8$:$Cu_{0.5}V_2O_5$ molar ratio. The resulting nanowires were washed several times with deionized water (ρ = 18 MΩ·cm^{-1}) to facilitate complete removal of surface-adsorbed Na-ions.

7.5.3. Design Strategies for the Oxalate Decomposition Route and Synthesis of Additional β-$M_xV_2O_5$ bronzes (M = Ni, Co, Pb)

Divalent oxalate salts decompose at various temperatures,[47] as per:

$$(x+y+z)MC_2O_4(s) \xrightarrow{\Delta}$$

$$xM(s)+yMO(s)+zMCO_3(s)+(y+z)CO(g)+(2x+y)CO_2(g) \qquad \textbf{7.2}$$

where the specific decomposition product (metal, metal oxide, metal carbonate) or ratio of products is contingent on both synthetic conditions and on the electronegativity of the cation, M. When decomposed under ambient atmosphere, oxide and carbonate (y, z > 0) are predominantly observed, as would be expected

with oxidation of any metal products, M.[47] But under inert conditions (N_2, Ar, vacuum), the decomposition route is dependent primarily on the electronegativity of the element, M.[47] For more electronegative metal cations, *x* approaches unit and metallic products predominate. Thus, notably, the approach developed here cannot be used for insertion of electropositive metals (e.g., Na, K); the oxalate salts of these cations are instead rapidly decomposed to their respective carbonates and reactions proceed according to a different mechanism or not at all.[42,47] For reactions where M = Ni, Co (in MC_2O_4), materials were prepared in a similar fashion to that described in the methods section of the main manuscript (as described for the synthesis of β-$Sn_xV_2O_5$), except a 1:3 ratio of ζ-V_2O_5:MC_2O_4 was used given the higher observed occupancies achieved for these cations within the tunnels. In these instances, reaction temperatures were also varied between 300—400°C to ensure temperatures exceeded the corresponding oxalate decomposition temperature.[47]

7.5.4. Topochemical Synthesis of Metastable β-$M_xV_2O_5$ Nanowires

Metastable β-$Sn_{0.23}V_2O_5$ nanowires were synthesized by reacting ζ-V_2O_5 nanowires with metal oxalate precursors. In a typical reaction, stoichiometric amounts of ζ-V_2O_5 and SnC_2O_4 (oxalate salt) were mixed in a 4:1 molar ratio and lightly ground together using a mortar and pestle in a slurry of dry hexanes for 30 min. The dried mixture was then transferred to a ceramic crucible and placed inside a tube furnace (Thermo Scientific). The materials were heated at 350°C for 12 h under a combination of vacuum and flowing Ar atmosphere (100 $mL \cdot min^{-1}$),

to help facilitate removal of evolved CO_2 and avoid metal oxide/carbonate byproduct formation. The green powders obtained after the first thermal treatment were again manually ground together using a mortar and pestle and annealed for second time at the same temperature and pressure detailed above for 4 h to obtain phase-pure samples. β-$Sn_{0.23}V_2O_5$ nanowires were subsequently interfaced with CdX QDs using the SILAR method.[19–21] During this process, the nanowires were dispersed sequentially in cationic and anionic precursor solutions to grow CdX (X = Se, Te) QDs on the surface of the nanowires.

7.5.5. Synthesis of β-$Sn_xV_2O_5$/CdX (X = Se, Te) QD Heterostructures

β-$Sn_xV_2O_5$ nanowires were interfaced with CdX QDs using the SILAR method in a glovebag under an argon atmosphere.[19–21] In a typical SILAR process, as-prepared β-$Sn_xV_2O_5$ nanowires were first dispersed in an ethanol solution of the cadmium precursor ($Cd(NO_3)_2 \cdot H_2O$, Alfa Aesar, 98.5%) for 45 seconds under manual stirring, washed with ethanol, and recovered by centrifugation at 6000 rpm for 2 minutes. In a second step, the material was then immersed in an ethanol solution of the sodium chalcogenide precursor (Na_2X, Alfa Aesar, 99.8% in ethanol, X = Se, Te) for 45 seconds under manual stirring, washed with ethanol, and finally recovered by centrifugation at 6000 rpm for 2 minutes. One SILAR cycle thus comprises immersion in the cadmium precursor solution and an ethanol washing step, followed immediately by immersion in the chalcogenide precursor and an ethanol washing step. Three complete SILAR cycles were performed to prepare the β-$Sn_xV_2O_5$/CdX heterostructures examined

in this study. After three SILAR cycles, the heterostructures were washed with a large excess of ethanol to remove excess QDs not adhered to the nanowire surfaces and were finally allowed to dry at room temperature under ambient conditions.

7.5.6. Hydrothermal Synthesis of β-$Pb_{0.31}V_2O_5$ Nanowires

Nanowires of β-$Pb_{0.31}V_2O_5$ were also synthesized according to a previously reported method.[22] In a typical reaction, 0.1230 g of $Pb(COOCH_3)_2 \cdot 3H_2O$ (Alfa Aesar, 99%) were dissolved in 16 mL of deionized water (18 MΩ cm^{-1}). 0.1770 g of V_2O_5 (Beantown Chemical, 99.99%) was suspended in this solution (1:3 Pb:V_2O_5 molar ratio) and the reaction mixture was added to a 23 mL polytetrafluoroethylene-lined stainless-steel autoclave (Parr). The autoclave was heated at 250°C for 72 h and subsequently allowed to cool to room temperature. The resulting green powder was separated from the supernatant and washed with copious amounts of deionized water and 2-propanol.

7.5.7. Structural characterization of β-$M_{0.23}V_2O_5$ nanowires and β-$M_xV_2O_5$/CdX heterostructures

X-ray diffraction (XRD) patterns were collected in Bragg-Brentano geometry on a D8-focus diffractometer (Cu Kα radiation; λ = 1.5418 Å; 40 kV voltage; 25 mA current). All Rietveld refinements and Pawley fitting of lattice parameters were performed using the EXPGUI user interface of GSAS I.[73] Atomic positions, profile terms, lattice parameters, and inserted metal occupancies (M = Sn, Ni, Co, Pb) were refined from laboratory XRD data using isotropic thermal

parameters. All crystal structure renditions were prepared using the Vesta III software suite (JP-Minerals).[74]

Low-magnification transmission electron microscopy (TEM) images were collected using a JEOL JEM-2010 electron microscope at an operating voltage of 200 kV. High-resolution transmission electron microscopy (HRTEM) images and selected area electron diffraction (SAED) patterns were acquired using a FEI Tecnai G2 F20 FE-TEM operated at 200 kV. Prior to imaging, powder samples were dispersed in ethanol and drop-cast onto formvar-coated 400 mesh grids. Scanning electron microscopy (SEM) images, energy dispersive X-ray (EDX) spectra, and elemental maps were collected using a FEI Quanta 600 FE-SEM operated at 10 kV equipped with an Oxford EDX elemental characterization system as well as on a JEOL JSM-7500F FE-instrument equipped with a high-brightness conical field-emission gun, a low aberration conical objective lens, and an Oxford EDS spectrometer (Oxford). Prior to imaging, powdered heterostructure materials were affixed to conductive carbon tape or drop-cast from a dispersion of nanowires in 2-propanol onto SiO_2/Si wafer substrates.

7.5.8. Scanning Transmission X-Ray Microscopy (STXM) Measurements

STXM measurements were performed at the SM beamline (10ID-1) of the Canadian Light Source. A 25-nm outermost-zone zone plate was used to obtain spatial resolution better than 20 nm. V L- and O K-edge energy stacks were acquired using a 500-lines/mm plane grating monochromator. The incident photon flux (I_0) was adjusted to 18 MHz during focusing, as read by the STXM detector

through a hole within the substrate. Right circularly polarized X-rays, generated by an elliptically polarized undulator (EPU gap optimized to -0.9), were used for the measurements. All STXM data were analyzed and processed using aXis2000 software (http://unicorn.mcmaster.ca/aXis2000.html).

7.5.9. HAXPES and XPS Measurements

Hard X-ray photoelectron spectroscopy (HAXPES) measurements were conducted at the Surface and Interface Structural Analysis beamline (beamline I09) of the Diamond Light Source, Ltd. (DLS), UK. The beamline has two canted undulators that enable access to photon energies spanning the range from 100 eV to 20 keV. The photon beam was monochromated using a channel-cut Si (004) crystal following a Si(111) double-crystal monochromator. Photoelectron spectra were energy resolved and measured using a VG Scienta EW40000 high-energy analyzer with a 60° acceptance angle. Measurements were performed at hv ≈6 keV with an overall energy resolution of better than 250 meV.[75] XPS measurements were performed using a Phi VersaProbe 5000 laboratory instrument outfitted with a monochromated Al Kα source and a hemispherical analyzer with an overall resolution of 450 meV. A flood-gun was employed to achieve charge neutralization. All samples were measured with both XPS and HAXPES. For HAXPES, the samples were rastered to avoid possible beam damage. The (HA)XPS spectra were energy calibrated to O 1s and V 2p core-levels of reference ζ-V_2O_5 (energy aligned to the Fermi level of a gold foil) in order

to account for any shifts due to charging. Further details of the instrumental set up have been described by Lee and Duncan.[75]

7.5.10. Fitting of XPS Peak Areas and Determination of Sn Oxidation States

XPS peak areas were determined by fitting with Voight profile peaks having a Gaussian width of 0.5 eV to match the experimental resolution. Figure E.2D displays curve-fitting results of the XPS O 1s and V 2p spectra of β-$Sn_{0.23}V_2O_5$. The inelastic background has been subtracted using Shirley-like profile. The charge state was assigned based on the relative energy difference between the O 1s and V $2p_{3/2}$ peaks, using the method described by Silversmit *et al*.[76] Peak centroid values obtained by fitting the XPS data in Figure E.2D (12.9 eV and 14.2 eV) are in good agreement with expected values for V^{5+} and V^{4+}, respectively. The amount of vanadium reduction, based on the peak V^{5+} and V^{4+} areas (i.e. $V^{4+}/(V^{4+} + V^{5+})$), was determined to be 0.20. This value further confirms the expected ratio of 0.23 fractional occupancy obtained for tin (β-$Sn_{0.23}V_2O_5$) by Rietveld refinement of the PXRD data. Given that XPS is surface-sensitive, we expect a small contribution of the V^{4+} is surface, which would account for the small discrepancy between 0.20 and 0.23.

7.5.11. Transient Absorption Measurements

Ultrafast TA spectra were collected using a Ti:sapphire amplified laser (Spectra-Physics Spitfire Pro, 800 nm, 1 kHz repetition rate, 100 fs pulse) with detection using Helios spectrometers (Ultrafast Systems). The majority (90%) of the laser pulse from the amplifier was passed through an optical parametric

amplifier (OPA; Light Conversion Ltd.) to produce pump pulses of tunable wavelengths. The remaining 10% of the amplifier output was used to generate a white light continuum from 425—900 nm by focusing a fraction of the 800 nm laser pulse into a sapphire disc. The resulting broadband white light continuum was split into probe and reference beams. Both probe and reference beams were directed into a fiber-coupled silicon (visible) or InGaAs (infrared) diode array on a shot-by-shot basis. The delay time between pump and probe was mechanically controlled by a motorized delay stage (Newport). TA decay traces were compiled by averaging Δ*A* values over a given range of probe wavelengths at each delay time. Thin films prepared by spray-coating a dispersion of β-$Sn_{0.23}V_2O_5$/CdX (X = Se, Te) powders in ethanol onto glass microscope slides at a concentration of 1 mg/mL were used for all TA measurements.

7.5.12. Fitting of Transient Absorption Decay Traces with Multiexponential Functions

The TA decay traces were fitted with multiexponential functions of the form:

$$\Delta A = \Delta A_0 + \sum_i A_i e^{\left(\frac{t}{\tau_i}\right)} \qquad \textbf{7.3}$$

where ΔA_0 is the differential absorbance, ΔA_0 is the differential absorbance that the data approaches at long timescales, A_i is a pre-exponential weighting factor for the *i*th exponential term, t is the delay time, and τ_i is the lifetime of each term. The best fits were achieved using the smallest number of individual decay lifetimes (τ_i) while minimizing χ^2.[20] The average carrier lifetime was obtained using

Equation 7.4, which normalizes the amplitude-weighted lifetime using a pre-exponential weight factor, A_i:

$$\langle \tau \rangle = \frac{\sum_i A_i \tau_i}{\sum_i A_i} \qquad \textbf{7.4}$$

7.5.13. Photoelectrochemical Measurements

Photoelectrochemical measurements, including linear sweep voltammetry and chronocoulometry, were acquired with a Princeton Applied Research (PAR) VersaSTAT 3 potentiostat. Data were acquired at room temperature using a custom-built, air-tight three-compartment electrochemical cell (Figure E.13) with β-$Sn_{0.23}V_2O_5$/CdSe-modified FTO or β-$Sn_{0.23}V_2O_5$-modified FTO as the working electrode, a coiled Pt wire as the auxiliary electrode, and saturated calomel electrode (SCE) as the reference electrode. The electrolyte consisted of KNO_3 (0.2 M), lactic acid (0.1 M), and a Ni(3-MPA) co-catalyst (formed *in situ* from Ni^{2+} (10 mM) and 3-MPA (20 mM)) dissolved in a 1:4 (*v*:*v*) water:acetonitrile (pH=3) solution. Linear sweep voltammograms were measured at a scan rate of 10 $mV \cdot s^{-1}$ under manually chopped illumination (5 s on/off). A Luxeon Rebel Star cool white 700 mA LED was used as the light source with an intensity of 60 mW/cm^2. For H_2 generation measurements, the electrochemical cell was first purged with Ar for 30 min. The light source was a 100 W Xe arc lamp (Oriel 133 Photomax) equipped with a filter transmitting light from 400 to 720 nm (120 mW/cm^2).

7.5.14. Quantitative Analysis of H_2 Generation

For gas quantification, a sample of gas (3 mL) was obtained with a 10 mL gastight syringe from the headspace above the electrolyte (in the cell depicted in

Figure E.13) and was analysed with a Perkin Elmer Clarus 580 GC (thermal conductivity detector, Ar carrier gas). The Faradaic efficiency was calculated using the following equation:

$$\text{Faradaic efficiency } (\%) = \frac{[H_2 \text{ produced (mol) x 2 x 96485 (C/mol)}]}{\text{Charge passed during electrolysis (C)}} \times 100\ \% \qquad \textbf{7.5}$$

7.6. References

(1) Fukuzumi, S.; Ohkubo, K.; Suenobu, T. Long-Lived Charge Separation and Applications in Artificial Photosynthesis. *Acc. Chem. Res.* **2014**, *47* (5), 1455–1464.

(2) Nocera, D. G. The Artificial Leaf. *Acc. Chem. Res.* **2012**, *45* (5), 767–776.

(3) Su, J.; Vayssieres, L. A Place in the Sun for Artificial Photosynthesis? *ACS Energy Lett.* **2016**, *1* (1), 121–135.

(4) Takanabe, K. Photocatalytic Water Splitting: Quantitative Approaches toward Photocatalyst by Design. *ACS Catal.* **2017**, *7* (11), 8006–8022.

(5) Sun, J.; Zhong, D. K.; Gamelin, D. R. Composite Photoanodes for Photoelectrochemical Solar Water Splitting. *Energy Environ. Sci.* **2010**, *3* (9), 1252–1261.

(6) Nanayakkara, S. U.; van de Lagemaat, J.; Luther, J. M. Scanning Probe Characterization of Heterostructured Colloidal Nanomaterials. *Chem. Rev.* **2015**, *115* (16), 8157–8181.

(7) Selinsky, R. S.; Ding, Q.; Faber, M. S.; Wright, J. C.; Jin, S. Quantum Dot Nanoscale Heterostructures for Solar Energy Conversion. *Chem. Soc. Rev.* **2013**, *42* (7), 2963–2985.

(8) Bonaccorso, F.; Colombo, L.; Yu, G.; Stoller, M.; Tozzini, V.; Ferrari, A. C.; Ruoff, R. S.; Pellegrini, V. Graphene, Related Two-Dimensional Crystals, and Hybrid Systems for Energy Conversion and Storage. *Science (80-.).* **2015**, *347* (6217), 1246501–1246501.

(9) Semonin, O. E.; Luther, J. M.; Beard, M. C. Quantum Dots for Next-Generation Photovoltaics. *Mater. Today* **2012**, *15* (11), 508–515.

(10) Fujishima, A.; Honda, K. Electrochemical Photolysis of Water at a Semiconductor Electrode. *Nature* **1972**, *238* (5358), 37–38.

(11) Kanan, M. W.; Surendranath, Y.; Nocera, D. G. Cobalt-Phosphate Oxygen-Evolving Compound. *Chem. Soc. Rev.* **2009**, *38* (1), 109–114.

(12) Kanan, M.; Yano, J.; Surendranath, Y.; Dincă, M.; Yachandra, V. K.; Nocera, D. G. Structure and Valency of a Cobalt−phosphate Water Oxidation Catalyst Determined by in Situ X-Ray Spectroscopy. *J. Am. Chem. Soc.* **2010**, *132* (25), 13692–13701.

(13) Kamat, P. V. Quantum Dot Solar Cells. The next Big Thing in Photovoltaics. *J. Phys. Chem. Lett.* **2013**, *4* (6), 908–918.

(14) Bang, J. H.; Kamat, P. V. Quantum Dot Sensitized Solar Cells . A Tale of Two Semiconductor Nanocrystals: CdSe and CdTe. *ACS Nano* **2009**, *3* (6), 1467–1476.

(15) Kim, W. D.; Baum, F.; Kim, D.; Lee, K.; Moon, J. H.; Lee, D. C. Photocorrosion-Assisted Transformation of Metal Selenide Nanocrystals into Crystalline Selenium Nanowires. *Cryst. Growth Des.* **2014**, *14* (3),

1258–1263.

(16) Lee, Y.-L.; Lo, Y.-S. Highly Efficient Quantum-Dot-Sensitized Solar Cell Based on Co-Sensitization of CdS/CdSe. *Adv. Funct. Mater.* **2009**, *19* (4), 604–609.

(17) Sheng, P.; Li, W.; Cai, J.; Wang, X.; Tong, X.; Cai, Q.; Grimes, C. A. A Novel Method for the Preparation of a Photocorrosion Stable Core/Shell CdTe/CdS Quantum Dot TiO_2 Nanotube Array Photoelectrode Demonstrating an AM 1.5G Photoconversion Efficiency of 6.12%. *J. Mater. Chem. A* **2013**, *1* (26), 7806–7815.

(18) Park, J. P.; Heo, J. Hy.; Im, S. H.; Kim, S.-W. Exceptional Stability of Mg Implemented PbS Quantum Dot Solar Cells by Galvanic Corrosion Protection. *J. Mater. Chem. A* **2015**, *3* (16), 8433–8437.

(19) Pelcher, K. E.; Milleville, C. C.; Wangoh, L.; Chauhan, S.; Crawley, M. R.; Marley, P. M.; Piper, L. F. J.; Watson, D. F.; Banerjee, S. Integrating β-$Pb_{0.33}V_2O_5$ Nanowires with Cdse Quantum Dots: Toward Nanoscale Heterostructures with Tunable Interfacial Energetic Offsets for Charge Transfer. *Chem. Mater.* **2015**, *27* (7), 2468–2479.

(20) Milleville, C. C.; Pelcher, K. E.; Sfeir, M. Y.; Banerjee, S.; Watson, D. F. Directional Charge Transfer Mediated by Mid-Gap States: A Transient Absorption Spectroscopy Study of CdSe Quantum Dot/β-$Pb_{0.33}V_2O_5$ Heterostructures. *J. Phys. Chem. C* **2016**, *120* (9), 5221–5232.

(21) Pelcher, K. E.; Milleville, C. C.; Wangoh, L.; Cho, J.; Sheng, A.; Chauhan,

S.; Sfeir, M. Y.; Piper, L. F. J.; Watson, D. F.; Banerjee, S. Programming Interfacial Energetic Offsets and Charge Transfer in β-$Pb_{0.33}V_2O_5$/Quantum-Dot Heterostructures: Tuning Valence-Band Edges to Overlap with Midgap States. *J. Phys. Chem. C* **2016**, *120* (51), 28992–29001.

(22) Marley, P. M.; Stabile, A. A.; Kwan, C. P.; Singh, S.; Zhang, P.; Sambandamurthy, G.; Banerjee, S. Charge Disproportionation and Voltage-Induced Metal-Insulator Transitions Evidenced in β-$Pb_xV_2O_5$ Nanowires. *Adv. Funct. Mater.* **2013**, *23* (2), 153–160.

(23) Wangoh, L.; Marley, P. M.; Quackenbush, N. F.; Sallis, S.; Fischer, D. A.; Woicik, J. C.; Banerjee, S.; Piper, L. F. J. Electron Lone Pair Distortion Facilitated Metal-Insulator Transition in β-$Pb_{0.33}V_2O_5$ Nanowires. *Appl. Phys. Lett.* **2014**, *104* (18), 182108.

(24) Marley, P. M.; Horrocks, G. A.; Pelcher, K. E.; Banerjee, S. Transformers: The Changing Phases of Low-Dimensional Vanadium Oxide Bronzes. *Chem. Commun.* **2015**, *51* (25), 5181–5198.

(25) Zavalij, P. Y.; Whittingham, M. S. Structural Chemistry of Vanadium Oxides with Open Frameworks. *Acta Crystallogr. B* **1999**, *55* (5), 627–663.

(26) De Jesus, L. R.; Andrews, J. L.; Parija, A.; Banerjee, S. Defining Diffusion Pathways in Intercalation Cathode Materials: Some Lessons from V_2O_5 on Directing Cation Traffic. *ACS Energy Lett.* **2018**, *3* (4), 915–931.

(27) Andrews, J. L.; Mukherjee, A.; Yoo, H. D.; Parija, A.; Marley, P. M.; Fakra, S.; Prendergast, D.; Cabana, J.; Klie, R. F.; Banerjee, S. Reversible Mg-Ion

Insertion in a Metastable One-Dimensional Polymorph of V_2O_5. *Chem* **2018**, *4* (3), 564–585.

(28) Ip, A. H.; Thon, S. M.; Hoogland, S.; Voznyy, O.; Zhitomirsky, D.; Debnath, R.; Levina, L.; Rollny, L. R.; Carey, G. H.; Fischer, A.; Kemp, K. W.; Kramer, I. J.; Ning, Z.; Labelle, A. J.; Chou, K. W.; Amassian, A.; Sargent, E. H. Hybrid Passivated Colloidal Quantum Dot Solids. *Nat. Nanotechnol.* **2012**, *7* (9), 577–582.

(29) Kim, D.; Kim, D. H.; Lee, J. H.; Grossman, J. C. Impact of Stoichiometry on the Electronic Structure of PbS Quantum Dots. *Phys. Rev. Lett.* **2013**, *110* (19), 196802:1-5.

(30) Yamauchi, T.; Isobe, M.; Ueda, Y. Charge Order and Superconductivity in Vanadium Oxides. *Solid State Sci.* **2005**, *7* (7), 874–881.

(31) Walsh, A.; Payne, D. J.; Egdell, R. G.; Watson, G. W. Stereochemistry of Post-Transition Metal Oxides: Revision of the Classical Lone Pair Model. *Chem. Soc. Rev.* **2011**, *40* (9), 4455–4463.

(32) Stoltzfus, M. W.; Woodward, P. M.; Seshadri, R.; Klepeis, J. H.; Bursten, B. Structure and Bonding in $SnWO_4$, $PbWO_4$, and $BiVO_4$: Lone Pairs vs Inert Pairs. *Inorg. Chem.* **2007**, *46* (10), 3839–3850.

(33) De Jesus, L. R.; Zhao, Y.; Horrocks, G. A.; Andrews, J.; Stein, P.; Xu, B.; Banerjee, S. Lithiation across Interconnected V2O5 Nanoparticle Networks. *J. Mater. Chem. A* **2017**, *5* (38), 20141–20152.

(34) Andrews, J. L.; De Jesus, L. R.; Tolhurst, T. M.; Marley, P. M.; Moewes, A.;

Banerjee, S. Intercalation-Induced Exfoliation and Thickness-Modulated Electronic Structure of a Layered Ternary Vanadium Oxide. *Chem. Mater.* **2017**, *29* (7), 3285–3294.

(35) Horrocks, G. A.; Parija, A.; De Jesus, L. R.; Wangoh, L.; Sallis, S.; Luo, Y.; Andrews, J. L.; Jude, J.; Fischer, D. A.; Prendergast, D.; Piper, L. F. J.; Banerjee, S. Mitigating Cation Diffusion Limitations and Intercalation-Induced Framework Transitions in a 1D Tunnel-Structured Polymorph of V2O5. *Chem. Mater.* **2017**, *29* (24), 10386–10397.

(36) Marley, P. M.; Banerjee, S. Reversible Interconversion of a Divalent Vanadium Bronze between δ and β Quasi-1D Structures. *Inorg. Chem.* **2012**, *51* (9), 5264–5269.

(37) Marley, P. M.; Singh, S.; Abtew, T. A.; Jaye, C.; Fischer, D. A.; Zhang, P.; Sambandamurthy, G.; Banerjee, S. Electronic Phase Transitions of δ-$Ag_xV_2O_5$ Nanowires: Interplay between Geometric and Electronic Structures. *J. Phys. Chem. C* **2014**, *118* (36), 21235–21243.

(38) Ganne, M.; Jouanneaux, A.; Tournoux, M.; Le Bail, A. Structure and Phase Transitions of Low-Dimensional Thallium Vanadium Bronze $Tl_xV_2O_5$ ($0.44 < x < 0.48$). *J. Solid State Chem.* **1992**, *97* (1), 186–198.

(39) Marley, P. M.; Abtew, T. A.; Farley, K. E.; Horrocks, G. A.; Dennis, R. V.; Zhang, P.; Banerjee, S. Emptying and Filling a Tunnel Bronze. *Chem. Sci.* **2015**, *6* (3), 1712–1718.

(40) Whittingham, M. S.; Dines, M. B. *N*-Butyllithium—An Effective, General

Cathode Screening Agent. *J. Electrochem. Soc.* **1977**, *124* (9), 1387–1388.

(41) Lee, K. T.; Ramesh, T. N.; Nan, F.; Botton, G.; Nazar, L. F. Topochemical Synthesis of Sodium Metal Phosphate Olivines for Sodium-Ion Batteries. *Chem. Mater.* **2011**, *23* (16), 3593–3600.

(42) Parize, J.-L.; Medouar, A.; Savariault, J.-M.; Ballivet-Tkatchenko, D.; Galy, J. Formation of Sodium and Copper Vanadium Oxibronzes via Oxalate Decomposition: Thermal and X-Ray Studies. *Mater. Res. Bull.* **1989**, *24* (9), 1147–1153.

(43) Patridge, C. J.; Wu, T.-L.; Sambandamurthy, G.; Banerjee, S. Colossal Above-Room-Temperature Metal-Insulator Switching of a Wadsley-Type Tunnel Bronze. *Chem. Commun.* **2011**, *47* (15), 4484–4486.

(44) Wahila, M. J.; Butler, K. T.; Lebens-higgins, Z. W.; Hendon, C. H.; Nandur, A. S.; Treharne, R. E.; Quackenbush, N. F.; Sallis, S.; Mason, K.; Paik, H.; Schlom, D. G.; Woicik, J. C.; Guo, J.; Arena, D. A.; White, B. E.; Watson, G. W.; Walsh, A.; Piper, L. F. J. Lone-Pair Stabilization in Transparent Amorphous Tin Oxides: A Potential Route to p-Type Conduction Pathways. *Chem. Mater.* **2016**, *28*, 4706–4713.

(45) Hanyš, P.; Janeček, P.; Matolín, V.; Korotcenkov, G.; Nehasil, V. XPS and TPD Study of Rh/SnO_2 System – Reversible Process of Substrate Oxidation and Reduction. *Surf. Sci.* **2006**, *600*, 4233–4238.

(46) Walsh, A.; Watson, G. W. Influence of the Anion on Lone Pair Formation in Sn(II) Monochalcogenides: A DFT Study. *J. Phys. Chem. B* **2005**, *109* (40),

18868–18875.

(47) Dollimore, D.; Nicholson, D.; Griffiths, D. L.; Nicholson, D. The Thermal Decomposition of Oxalates. Part II. Thermogravimetric Analysis of Various Oxalates in Air and in Nitrogen. *J. Chem. Soc.* **1963**, 2617–2623.

(48) Vogel, R.; Hoyer, P.; Weller, H. Quantum-Sized PbS, CdS, Ag_2S, Sb_2S_3, and Bi_2S_3 Particles as Sensitizers for Various Nanoporous Wide-Bandgap Semiconductors. *J. Phys. Chem.* **1994**, *98* (12), 3183–3188.

(49) Lee, H. J.; Chen, P.; Moon, S. J.; Sauvage, F.; Sivula, K.; Bessho, T.; Gamelin, D. R.; Comte, P.; Zakeeruddin, S. M.; Seok, S. I.; Gratzel, M.; Nazeeruddin, Md. K. Regenerative PbS and CdS Quantum Dot Sensitized Solar Cells with a Cobalt Complex as Hole Mediator. *Langmuir* **2009**, *25* (13), 7602–7608.

(50) Soni, U.; Arora, V.; Sapra, S. Wurtzite or Zinc Blende? Surface Decides the Crystal Structure of Nanocrystals. *CrystEngComm* **2013**, *15* (27), 5458–5463.

(51) Eyert, V.; Höck, K.-H. Electronic Structure of V_2O_5: Role of Octahedral Deformations. *Phys. Rev. B* **1998**, *57* (20), 12727–12737.

(52) Maganas, D.; Roemelt, M.; Hävecker, M.; Trunschke, A.; Knop-Gericke, A.; Schlögl, R.; Neese, F. First Principles Calculations of the Structure and V L-Edge X-Ray Absorption Spectra of V_2O_5 Using Local Pair Natural Orbital Coupled Cluster Theory and Spin-Orbit Coupled Configuration Interaction Approaches. *Phys. Chem. Chem. Phys.* **2013**, *15* (19), 7260–7276.

(53) Velazquez, J. M.; Jaye, C.; Fischer, D. a; Banerjee, S. Near Edge X-Ray Absorption Fine Structure Spectroscopy Studies of Single-Crystalline V_2O_5 Nanowire Arrays. *J. Phys. Chem. C* **2009**, *113* (18), 7639–7645.

(54) Tolhurst, T. M.; Leedahl, B.; Andrews, J. L.; Marley, P. M.; Banerjee, S.; Moewes, A. Contrasting 1D Tunnel-Structured and 2D Layered Polymorphs of V_2O_5 : Relating Crystal Structure and Bonding to Band Gaps and Electronic Structure. *Phys. Chem. Chem. Phys.* **2016**, *18* (23), 15798–15806.

(55) De Jesus, L. R.; Horrocks, G. A.; Liang, Y.; Parija, A.; Jaye, C.; Wangoh, L.; Wang, J.; Fischer, D. A.; Piper, L. F. J.; Prendergast, D.; Banerjee, S.Mapping Polaronic States and Lithiation Gradients in Individual V_2O_5 Nanowires. *Nat. Commun.* **2016**, *7*, 12022:1-9.

(56) Hinuma, Y.; Grüneis, A.; Kresse, G.; Oba, F. Band Alignment of Semiconductors from Density-Functional Theory and Many-Body Perturbation Theory. *Phys. Rev. B* **2014**, *90* (15), 155405.

(57) Jasieniak, J.; Califano, M.; Watkins, S. E. Size-Dependent Valence and Conduction Band-Edge Energies of Semiconductor Nanocrystals. *ACS Nano* **2011**, *5* (7), 5888–5902.

(58) Lee, J. R. I.; Meulenberg, R. W.; Hanif, K. M.; Mattoussi, H.; Klepeis, J. E.; Terminello, L. J.; Van Buuren, T. Experimental Observation of Quantum Confinement in the Conduction Band of CdSe Quantum Dots. *Phys. Rev. Lett.* **2007**, *98* (14), 146803:1-4.

(59) Bawendi, M. G.; Wilson, W. L.; Rothberg, L.; Carroll, P. J.; Jedju, T. M.; Steigerwald, M. L.; Brus, L. E. Electronic Structure and Photoexcited-Carrier Dynamics in Nanometer-Size CdSe Clusters. *Phys. Rev. Lett.* **1990**, *65* (13), 1623–1626.

(60) Klimov, V. I. Optical Nonlinearities and Ultrafast Carrier Dynamics in Semiconductor Nanocrystals. *J. Phys. Chem. B* **2000**, *104* (26), 6112–6123.

(61) Klimov, V. I. Spectral and Dynamical Properties of Multiexcitons in Semiconductor Nanocrystals. *Annu. Rev. Phys. Chem.* **2007**, 635–673.

(62) Smith, A. M.; Lane, L. A.; Nie, S. Mapping the Spatial Distribution of Charge Carriers in Quantum-Confined Heterostructure. *Nat. Commun.* **2014**, *5*, 4506.

(63) Marcus, R. A. On the Theory of Oxidation-Reduction Reactions Involving Electron Transfer. I. *J. Chem. Phys.* **1956**, *24* (5), 966–978.

(64) Marcus, R. A. Electron Transfer Reactions in Chemistry: Theory and Experiment. *Rev. Mod. Phys.* **1993**, *65* (3), 599–610.

(65) Dibbell, R. S.; Watson, D. F. Distance-Dependent Electron Transfer in Tethered Assemblies of CdS Quantum Dots and TiO_2 Nanoparticles. *J. Phys. Chem. C* **2009**, *113* (22), 3139–3149.

(66) Guijarro, N.; Shen, Q.; Giménez, S.; Mora-Seró, I.; Bisquert, J.; Lana-Villarreal, T.; Toyoda, T.; Gómez, R. Direct Correlation between Ultrafast Injection and Photoanode Performance in Quantum Dot Sensitized Solar Cells. *J. Phys. Chem. C* **2010**, *114* (50), 22352–22360.

(67) Hohenberg, P.; Kohn, W. Inhomogeneous Electron Gas. *Phys. Rev. B* **1964**, *136* (3), 864–871.

(68) Kohn, W.; Sham, L. J. Self-Consistent Equations Including Exchange and Correlation Effects. *Phys. Rev. A* **1965**, *140* (4), 1133–1138.

(69) Giannozzi, P.; Baroni, S.; Bonini, N.; Calandra, M.; Car, R.; Cavazzoni, C.; Ceresoli, D.; Chiarotti, G. L.; Cococcioni, M.; Dabo, I.; Corso, A. D.; de Gironcoli, S.; Fabris, S.; Fatesi, G.; Gebauer, R.; Gerstmann, U.; Gougoussis, C.; Kokalj, A.; Lazzeri, M.; Martin-Samos, L.; Marzari, N.; Mauri, F.; Mazzarello, R.; Paolini, S.; Pasquarello, A.; Paulatto, L.; Sbraccia, C.; Scandolo, S.; Sclauzero, G.; Seitsonen, A. P.; Smogunov, A.; Umari, P.; Wentzcovitch, R. M. QUANTUM ESPRESSO: A Modular and Open-Source Software Project for Quantum Simulations of Materials. *J. Phys. Condens. Matter* **2009**, *21* (39), 395502.

(70) Perdew, J. P.; Burke, K.; Ernzerhof, M. Generalized Gradient Approximation Made Simple. *Phys. Rev. Lett.* **1996**, *77* (18), 3865–3868.

(71) Vanderbilt, D. Soft Self-Consistent Pseudopotentials in a Generalized Eigenvalue Formalism. *Phys. Rev. B* **1990**, *41* (11), 7892–7895.

(72) Hu, W.; Du, X.; Wu, Y.; Wang, L. Novel ε-$Cu_{0.95}V_2O_5$ Hollow Microspheres and α-CuV_2O_5 Nanograins: Facile Synthesis and Application in Lithium-Ion Batteries. *J. Power Sources* **2013**, *237*, 112–118.

(73) Toby, B. H. EXPGUI, a Graphical User Interface for GSAS. *J. Appl. Crystallogr.* **2001**, *34* (2), 210–213.

(74) Momma, K.; Izumi, F. VESTA 3 for Three-Dimensional Visualization of Crystal, Volumetric and Morphology Data. *J. Appl. Crystallogr.* **2011**, *44* (6), 1272–1276.

(75) Lee, T.; Duncan, D. A. A Two-Color Beamline for Electron Spectroscopies at Diamond Light Source. *Synchrtron Radiat. News* **2018**, *31* (4), 16–22.

(76) Silversmit, G.; Depla, D.; Poelman, H.; Marin, G. B.; De Gryse, R. Determination of the V2p XPS Binding Energies for Different Vanadium Oxidation States (V5+ to V0+). *J. Electron Spectros. Relat. Phenomena* **2004**, *135* (2–3), 167–175.

8. CONCLUSIONS

8.1. Summary of Dissertation Research

In this dissertation, several approaches to tuning the electron correlation of binary and ternary vanadium oxides have been presented. Efforts to tune the electronic structure of $M_xV_2O_5$ materials for the design of materials for neuromorphic computing were detailed in Chapters 2-4. Chapters 5 and 6 explored the use of techniques spanning atomistic to mesoscale to mitigate electron localization in binary V_2O_5 materials. Insight gained from Chapters 2-6 were leveraged to develop an approach to independently tuning composition and structure in the metastable $M_xV_2O_5$ system. A detailed chapter-by-chapter summary of the findings detailed in this dissertation are listed below.

Chapter 2 describes a method for modulating the bandgap of a layered δ-$Sr_{0.5}V_2O_5$ compound. Dimensional reduction and exfoliation were used to (i) modulate the bandgap with an increased bandgap observed with decreasing layer thickness and (ii) reduce the extent of electron correlation as evidenced by the decreasing weight of the lower Hubbard band at the upper edge of the valence band. In Chapter 3, the consequences of hydration of the M site cation (in this instance Ni, Co, Zn) within the same δ-type layered class of materials was explored. Notably, the dehydrated $M_{0.25}V_2O_5$ compounds exhibit transport properties characteristic of insulators; however, when hydrated, $[M(H_2O)_4]_{0.25}V_2O_5$ materials exhibit memristive properties characteristic of a thermistor. Chapter 4

summarizes the role of coupled ionic and polaronic diffusion in driving the metal—insulator transition of β-$Cu_xV_2O_5$. Importantly, the extent of correlation in this compound and consequently the threshold of the metal—insulator transition can be tuned by modulation of copper stoichiometry, *x*.

Chapters 5 and 6 examine the role of metastability to examine structure function relationships in binary vanadium oxides with an eye towards mitigating charge localization and polaron formation in intercalation cathode mterials. Chapter 5 describes a method of mitigating polaron localization in α-V_2O_5 using mesoscale design templates. The results indicate that incorporating mesoscale curvature can be used to leverage chemo-electrochemical coupling to improve ionic diffusion. In Chapter 6, atomistic considerations are employed to mitigate electron localization and polaron formation in V_2O_5. A metastable polymorph (ζ-V_2O_5) is stabilized and exhibits dramatically altered ionic diffusion pathways and decreased polaron localization.

Finally, in Chapter 7, ζ-V_2O_5 is used as a solid-state “synthon” in the topochemical stabilization of β-$Sn_xV_2O_5$. This approach has been expanded to stabilize a number of metastable β-$M_xV_2O_5$ materials wherein the composition (identity of M, its stoichiometry, *x*) can be selected and tuned without engendering a structural transformation of the V_2O_5 lattice. This approach necessarily enables the installation of specific electronic states arising from the hybridization between states centered on the inserted cation, M, and hybrid states centered on the V—O lattice.

When considered individually, the insight gained from the fundamental studies described in this dissertation have led to discovery of: (i) the first high voltage, high capacity, and high cyclability insertion host for Mg ions, ζ-V_2O_5; (ii) a metastable β-$Sn_xV_2O_5$ compound that resolves the longstanding challenge of photocorrosion of light-harvesting quantum dots; (iii) and layered materials that afford control over electron correlation as a function of layer thickness and degree of hydration. When taken as a whole, the topochemical transformations and synthetic techniques described in this dissertation represent a significant advance towards decoupling composition and "structural destiny". Indeed, the ability to independently tailor composition and structure/bonding in these systems represents a tremendous opportunity to make "designer" materials for a number of practical applications.

8.2. Future Directions for Exploring Metastable Phase Space in Binary and Ternary Vanadium Oxide Phase Space

Despite the great progress that has been made towards the initial goal of decoupling structure and composition in V_2O_5 and $M_xV_2O_5$ systems, there remains a great number of avenues left to be explored. By very definition, the vast majority of phase space is metastable (after all, under a given set of conditions—such as a specific temperature and pressure—only one phase can be thermodynamically-stable) and remains untapped and under-explored. While this dissertation has focused primarily on tuning electron correlation in the layered δ-$M_xV_2O_5$ phases and the one-dimensional tunnel-structured β-$M_xV_2O_5$ phases, the approaches

detailed in this dissertation have led to the discovery of several additional polymorphs of V_2O_5 with dramatically altered structure and V—O bonding. One of these phases, λ-V_2O_5, is shown in Figure 8.1.

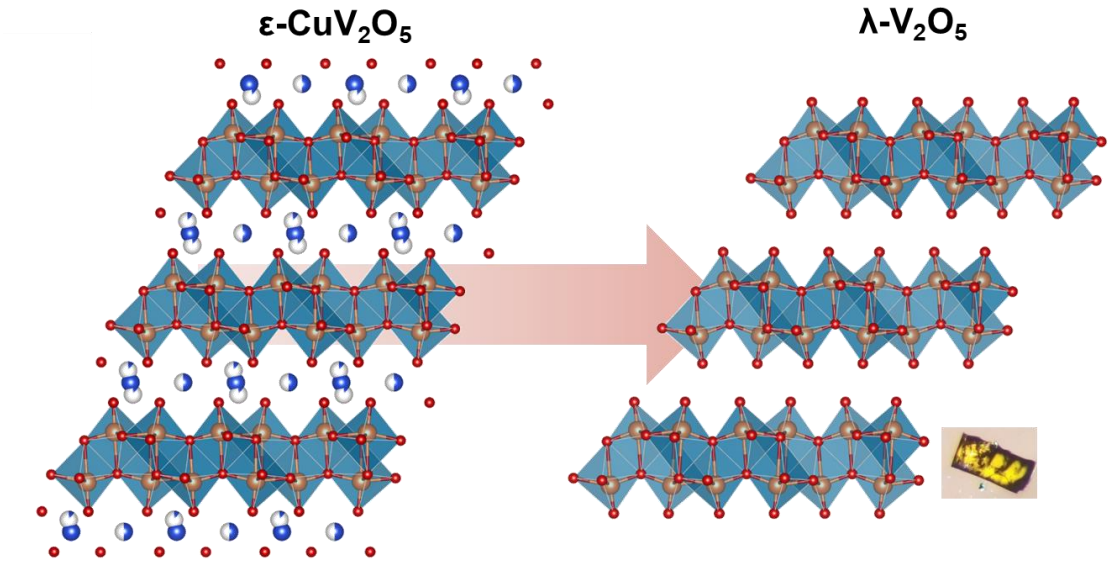

Figure 8.1. Topochemical stabilization of λ-V_2O_5 from ε-$Cu_xV_2O_5$.

This metastable polymorph of V_2O_5 can be topochemically accessed by deintercalation of Cu from the double-layered ε-$Cu_xV_2O_5$ phase. Notably, this material can be prepared in powder form or as a single crystal. The structures shown in Figure 8.1 were solved from single crystal diffraction. Like ζ-V_2O_5, the material is capable of reversibly inserting Mg ions but up to a much larger capacity of 0.5 Mg per V_2O_5. Initial results also suggest that the material can also be topochemically intercalated with Sn^{2+} and Pb^{2+} to form metastable layered $M_xV_2O_5$ materials much as described in Chapter 7 (Figure 8.2). The demonstration of the

use of an additional polymorph as an intercalation cathode material evidences two critical points: (i) stabilization of metastable polymorphs represents a generalizable strategy with much promise beyond ζ-V_2O_5 that is the focus of this work and (ii) the intercalation of Sn^{2+} and other cations into λ-V_2O_5 further highlights the potential of these systems and the ability to independently tune both compositions (i.e., M and *x*) and the vanadium oxide structure.

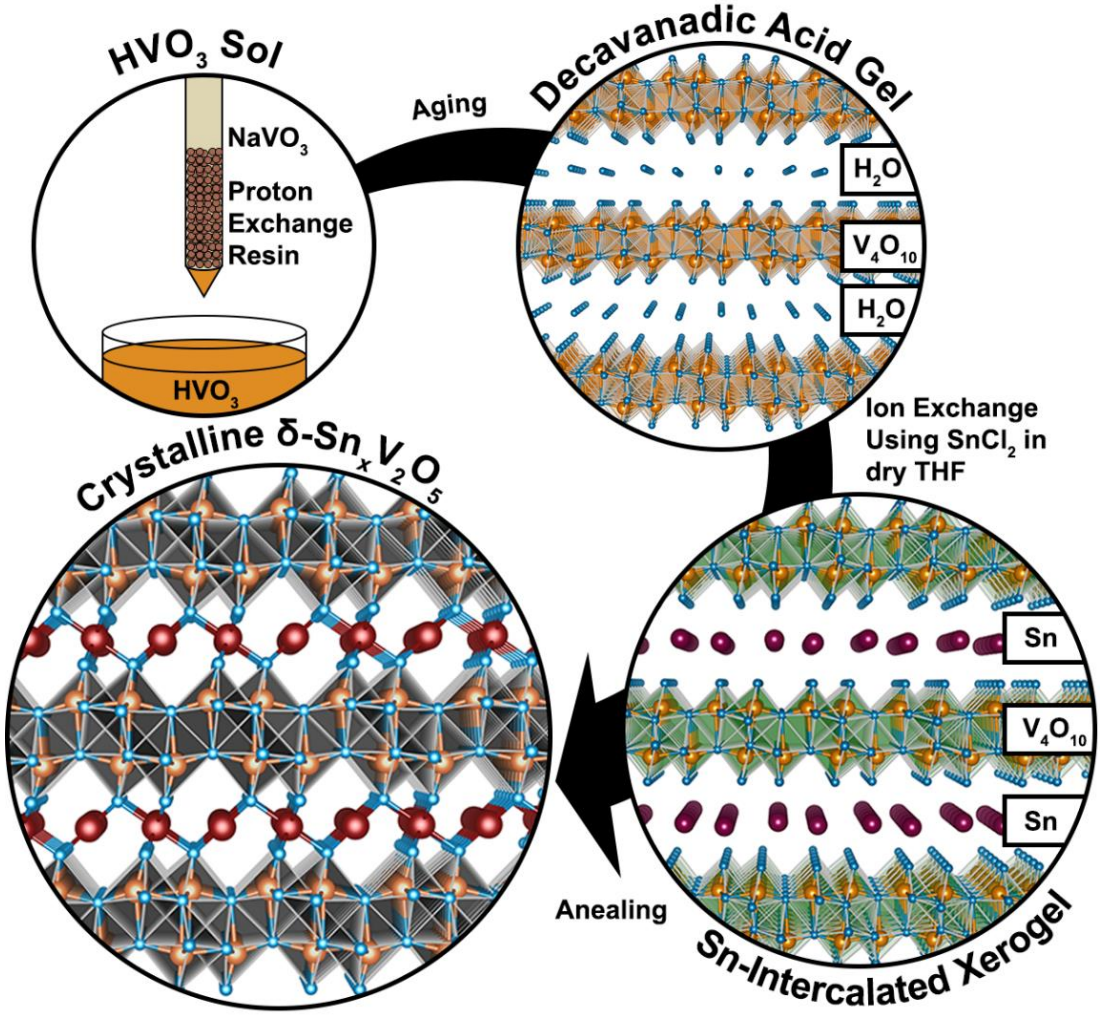

Figure 8.2. Topochemical stabilization of the metastable δ-$Sn_xV_2O_5$ material.

APPENDIX A

SUPPLEMENTARY FIGURES AND TABLES

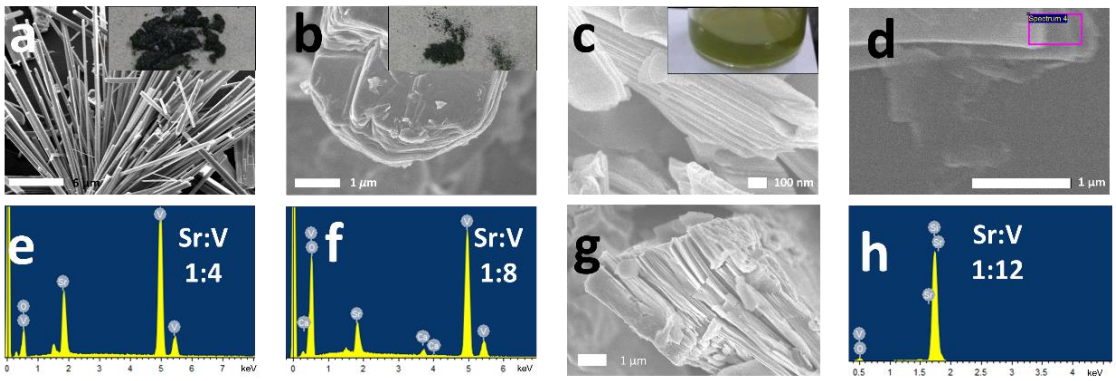

Figure A.1. (a) Low-magnification SEM image illustrating the microbeam morphology of the hydrothermally prepared δ-$Sr_{0.50}V_2O_5$ crystals. The inset indicates the lustrous black color of the powders. The corresponding EDX spectrum in (e) shows a Sr:V ratio of ca. 1:4. (b) SEM images of acid-treated powders with an expanded interlayer spacing. The inset shows a dark green coloration. The corresponding EDX spectrum is depicted in (f) and suggests that approximately half of the Sr cations have been substituted for protons. (c) SEM image of exfoliated nanosheets after TBAOH intercalation and flocculation indicating a lamellar structure. The inset depicts the green coloration of a suspension of exfoliated nanosheets. (g) depicts a higher magnification SEM image. In (d), a single nanosheet is imaged at a low accelerating voltage and the corresponding EDX spectrum for the single nanosheet is indicated in (h).

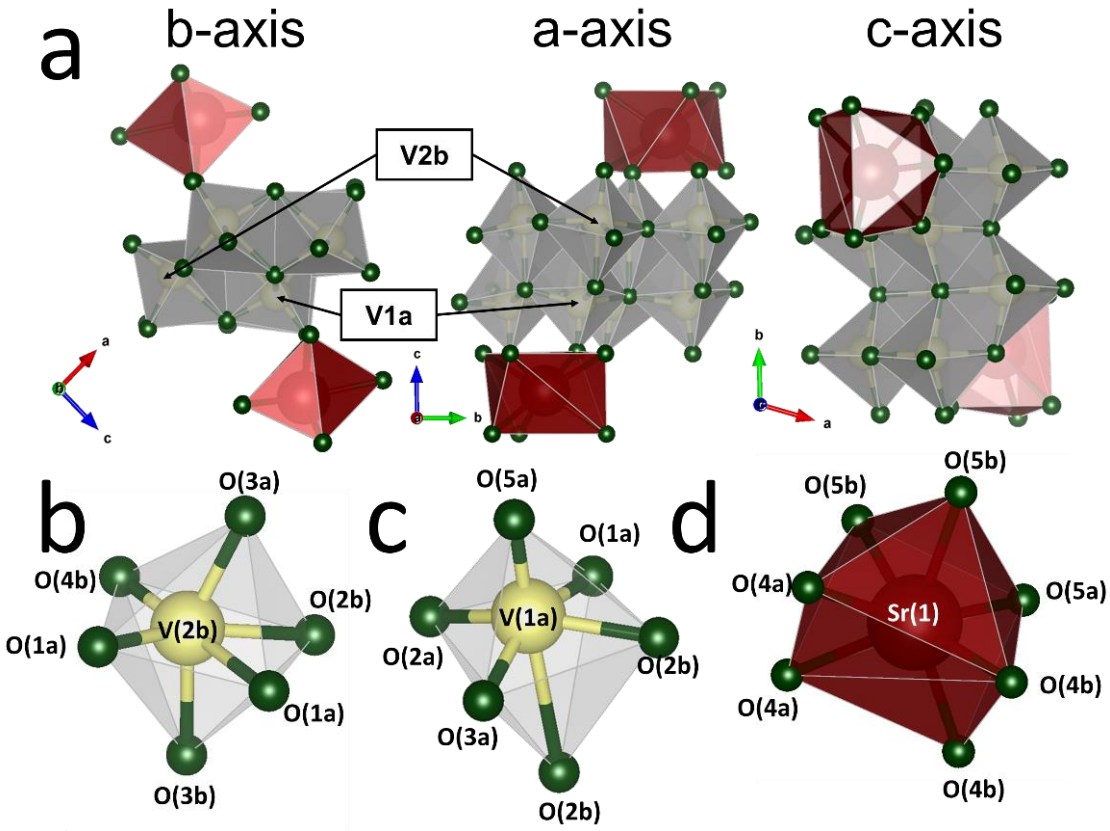

Figure A.2. (a) Single unit cell of δ-$Sr_{0.50}V_2O_5$ obtained from Rietveld refinement of high-resolution synchrotron diffraction data shown along the *b*, *a*, and *c* axes from left to right, respectively. Local coordination environment for two unique vanadium atoms, labeled V(2b) and V(1a) in panel a (b, c), both in a distorted octahedral configuration. There are four crystallographically unique vanadium sites, each of which is in an octahedral coordination with the vanadium atom closer to the apical vanadyl oxygen (O(3a), O(5a) above); however, all four octahedra can be adequately represented by the depicted two types of octahedra due to pseudo symmetry relationships within the unit cell, albeit with small differences in bond angles and distances between different VO_6 octahedra. In panel (d), the seven-coordinate SrO_7 polyhedron is depicted. Bond angles and distances for the reported octahedra are given in Table A.1 and Table A.2.

Table A.1. Tabulated atom positions, thermal parameters, and occupancies as obtained from a Rietveld refinement of the structure. Refinement statistics, including goodness of fit ($\chi 2$ = 1.998), weighted goodness of fit (wRp = 8.53%) and the individual point residuals (Rp = 6.60%) show good agreement between the observed and calculated patterns and are included in the header of the table. Strontium occupancies, strontium thermal parameters, and oxygen thermal parameters were refined together and constrained to singular values. Refined lattice parameters were *a* = 6.16969(1) Å, *b* = 7.39947(1) Å, *c* = 8.79509(1) Å, α = 89.9701°, β = 88.2845°, γ = 107.4916° giving rise to a unit cell volume = 382.782(1) Å^3.

Atom Label	x	y	z	Uiso*100	Occupancy
Sr1	0.81951(7)	0.20661(7)	0.01128(5)	0.92(1)	1.006(1)
V1a	0.54231(11)	0.38123(14)	0.34243(8)	0.34(2)	1.000(0)
V1b	0.47538(11)	0.11441(14)	0.66286(8)	0.39(2)	1.000(0)
V2a	0.12211(11)	0.03752(13)	0.33896(7)	0.27(2)	1.000(0)
V2b	0.13657(12)	0.52977(14)	0.33814(8)	0.31(2)	1.000(0)
O1a	0.1714(4)	0.5454(5)	0.59253(26)	0.46(6)	1.000(0)
O1b	0.1565(4)	0.0335(5)	0.60620(27)	0.39(6)	1.000(0)
O2a	0.4694(4)	0.1196(5)	0.39714(27)	0.61(6)	1.000(0)
O2b	0.4713(4)	0.6145(5)	0.37220(26)	0.29(6)	1.000(0)
O3a	0.2051(4)	0.2964(4)	0.37374(25)	0.10(4)	1.000(0)
O3b	0.1966(4)	0.8052(5)	0.34780(26)	0.10(4)	1.000(0)
O4a	0.0882(4)	0.0450(4)	0.15264(26)	0.38(7)	1.000(0)
O4b	0.0833(4)	0.4990(5)	0.15280(28)	1.07(7)	1.000(0)
O5a	0.5658(4)	0.3645(4)	0.16127(30)	1.28(8)	1.000(0)
O5b	0.4423(4)	0.0834(4)	0.84767(28)	0.68(7)	1.000(0)

Table A.2. Tabulated bond distances as obtained from a Rietveld refinement of the δ-$Sr_{0.5}V_2O_5$ structure.

	Vector	Bond Length
SrO7 Trigonal Bipyramid	Sr1_O4a	2.6069(26)
	Sr1_O4a	2.5606(29)
	Sr1_O4b	2.5783(28)
	Sr1_O4b	2.5396(30)
	Sr1_O5a	2.6031(28)
	Sr1_O5b	2.6175(23)
	Sr1_O5b	2.6041(26)
V1a Octahedron	V1a_O1a	1.7629(21)
	V1a_O2a	1.9155(33)
	V1a_O2b	1.9238(33)
	V1a_O2b	2.5142(23)
	V1a_O3a	2.0115(22)
	V1a_O5a	1.6121(27)
V1b Octahedron	V1b_O1b	1.9273(22)
	V1b_O2a	2.3368(24)
	V1b_O2a	1.9390(33)
	V1b_O2b	1.9586(33)
	V1b_O3b	1.9351(22)
	V1b_O5b	1.6513(25)
V2a Octahedron	V2a_O1b	2.3548(24)
	V2a_O1b	1.7225(23)
	V2a_O2a	2.0919(22)
	V2a_O3a	1.8512(31)
	V2a_O3b	1.9096(33)
	V2a_O4a	1.6490(23)
V2b Oct.	V2b_O1a	2.2412(24)
	V2b_O1a	1.9294(22)

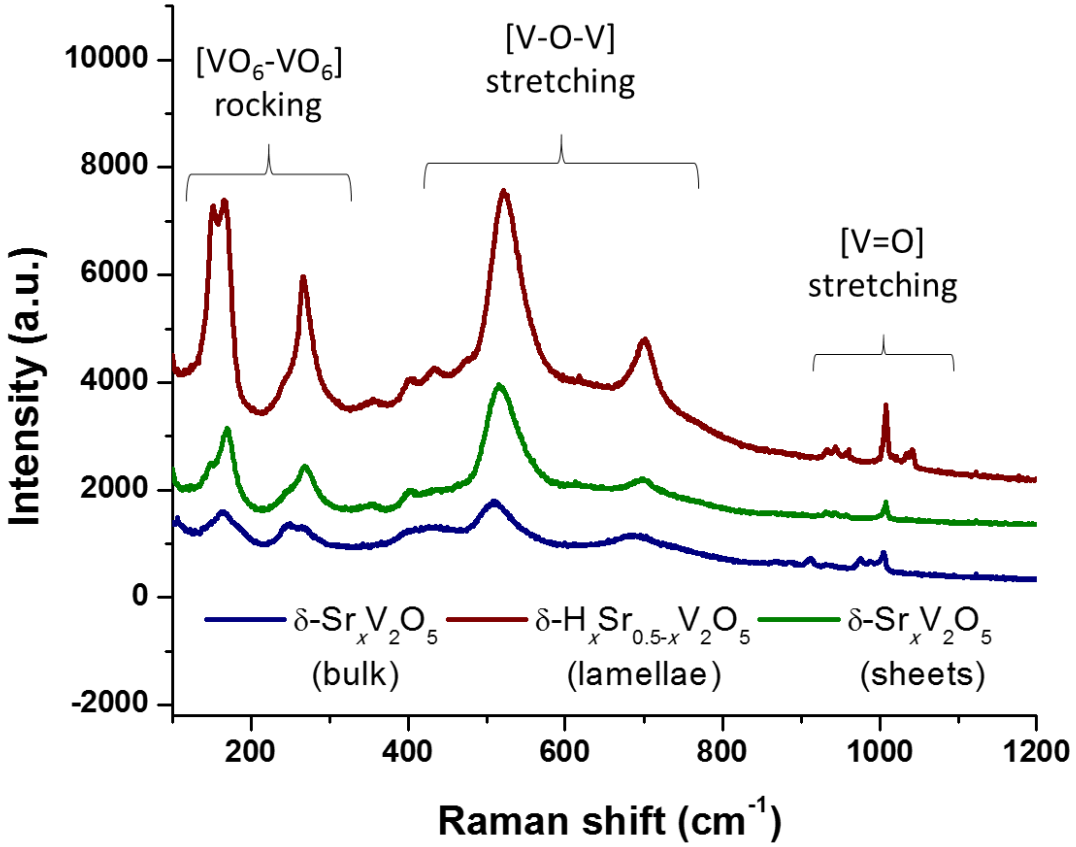

Figure A.3. Raman spectra (λ_{ex}=514.5 nm) acquired for as-prepared δ-$Sr_{0.50}V_2O_5$ (blue), acid-treated δ-$H_ySr_{0.50-y}V_2O_5$ (red), and exfoliated δ-$Sr_xV_2O_5$ (green) illustrate that the primary Raman modes are retained throughout the exfoliation process suggesting preservation of the local structure (short-range order). The modes at high energy (c.a. 1000 cm^{-1}) are characteristic of vanadyl bond stretching at the edges of the V_2O_5 double layers (by analogy to the vanadyl stretches of orthorhombic V_2O_5)[1,2] and remain unchanged. The ca. 400-800 cm^{-1} bands relate to the stretching of specific V-O-V bonds within the structure. The low energy bands (<400 cm^{-1}) correspond to the lower-frequency concerted rocking of [VO_6] units relative to each other. Perturbations to the local bonding (V-O-V) and average in-plane structure ([VO_6]-[VO_6]) appear minimal, indicating exfoliation with retention of the parent structural motifs. It is also important to note the absence of the characteristic bands of orthorhombic V_2O_5 or monoclinic VO_2, indicating the preservation of the original structural motifs without degradation to orthorhombic V_2O_5. Si background signal was subtracted from the spectra during processing.

Table A.3. Separations between valence and conduction band states contrasting the second derivative and leading-edge methods. The use of the second-derivative instead of the leading-edge method is justified when examining the DOS, depicted in Figure 2.4, which shows that the material is not a metal, rendering the values obtained for the leading-edge method unreliable in this instance.

Material	Second-Derivative	Leading-Edge
Exfoliated δ-$Sr_xV_2O_5$	2.32	0.858 eV
Expanded δ-$Sr_xV_2O_5$	1.96	0.147 eV
δ-$Sr_xV_2O_5$	1.07	-0.179 eV

APPENDIX B

SUPPLEMENTARY FIGURES AND TABLES

Table B.1. Refinement parameters derived from Rietveld refinement of powder X-ray diffraction data acquired for δ-$[Ni(H_2O)_4]_{0.2475}V_2O_5$•$0.147H_2O$. The diffraction data, refined pattern, and residuals are depicted in Figure 3.1. Rietveld refinement of the collected pattern was performed using the GSAS/EXPGUI software suite [Toby, B. H.; EXPGUI, a Graphical User Interface for GSAS. *J. Appl. Crystallogr*. **2001**, *34* (2), 210-213.]. The refined structures were rendered using the VESTA software suite.

Parameter	Refined Value
Space Group	*C2/m*
a	11.75306(6) Å
b	3.64801(2) Å
c	10.37164(9) Å
β	95.087(1) Å
V	442.935(5) $Å^3$
χ^2	4.241
R_{wp}	12.52%
R_w	0.0920

Table B.2. Values of atom positions, thermal parameters, and occupancies, as determined from Rietveld refinement of powder X-ray diffraction data acquired for δ-$[Ni(H_2O)_4]_xV_2O_5$ depicted in Figure 3.1.

Atom Label	x	y	z	U_{iso}*10^2	Occupancy
Ni	0.00(0)	0.00(0)	0.50(0)	0.50(7)	0.495(2)
V(1)	0.94692(7)	0.00(0)	0.14244(11)	0.58(3)	1.000(0)
V(2)	0.24086(8)	0.00(0)	0.13860(11)	0.39(3)	1.000(0)
O(1)	0.90946(23)	0.50(0)	0.11983(35)	0.07(9)	1.000(0)
O(2)	0.09015(26)	0.00(0)	0.0940(4)	0.03(8)	1.000(0)
O(3)	0.26481(24)	0.50(0)	0.1042(4)	0.08(9)	1.000(0)
O(4)	0.97053(27)	0.00(0)	0.2965(4)	1.6(1)	1.000(0)
O(5)	0.24031(25)	0.00(0)	0.2980(4)	1.0(1)	1.000(0)
O_w	0.38417(34)	1.104(1)	0.5177(5)	5.3(3)	0.569(4)
*O_w = oxygen from water ligand					

Table B.3. Bond distances for the three unique polyhedra within the δ-$[Ni(H_2O)_4]_xV_2O_5$ depicted in Figure 3.1.

Polyhedron	Bond Vector	Bond length (Å)
NiO_6	Ni_O(4)	2.108(4)
	Ni_O(4)	2.108(4)
	Ni_O(w)	2.006(4)
	Ni_O(w)	2.006(4)
	Ni_O(w)	2.006(4)
	Ni_O(w)	2.006(4)
$V(1)O_6$	V(1)_O(1)	1.8861(8)
	V(1)_O(1)	1.8861(8)
	V(1)_O(2)	1.7989(31)
	V(1)_O(2)	2.452(4)
	V(1)_O(3)	2.1420(30)
	V(1)_O(4)	1.597(4)
$V(2)O_6$	V(2)_O(1)	2.0081(28)
	V(2)_O(2)	1.7905(3)
	V(2)_O(3)	1.8845(9)
	V(2)_O(3)	1.8845(9)
	V(2)_O(3)	2.513(4)
	V(2)_O(5)	1.654(4)
V-V distances	V(1)_V(2)	3.0293(10)
	V(2)_V(2)	3.4276(19)
	V(1)_V(2)	3.4584(12)
	V(1)_V(2)	3.4966(16)
	V(1)_V(1)	3.64801(2)
	V(2)_V(2)	3.64801(2)

Table B.4. Bond angles for the three unique polyhedra within the δ-$[Ni(H_2O)_4]_xV_2O_5$ depicted in Figure 3.1.

Polyhedron	Bonds	Angles (°)
NiO_6	O(4)_Ni_O(4)	180.000(0)
	O(4)_Ni_O(w)	92.25(15)
	O(4)_Ni_O(w)	87.75(15)
$V(1)O_6$	O(1)_V(1)_O(1)	150.50(18)
	O(1)_V(1)_O(2)	100.33(9)
	O(1)_V(1)_O(3)	76.03(8)
	O(1)_V(1)_O(4)	98.18(12)
	O(1)_V(1)_O(2)	100.33(9)
	O(1)_V(1)_O(3)	76.03(8)
	O(1)_V(1)_O(4)	98.18*12)
	O(2)_V(1)_O(3)	153.22(16)
	O(2)_V(1)_O(4)	101.27(18)
	O(3)_V(1)_O(4)	105.51(16)
$V(2)O_6$	O(1)_V(2)_O(2)	159.55(16)
	O(1)_V(2)_O(3)	79.42(9)
	O(1)_V(2)_O(3)	79.42(9)
	O(1)_V(2)_O(5)	100.85(17)
	O(2)_V(2)_O(3)	96.43(9)
	O(2)_V(2)_O(3)	96.43(9)
	O(2)_V(2)_O(5)	99.60(17)
	O(3)_V(2)_O(3)	150.88(12)
	O(3)_V(2)_O(5)	101.73(12)
	O(3)_V(2)_O(5)	101.73(12)

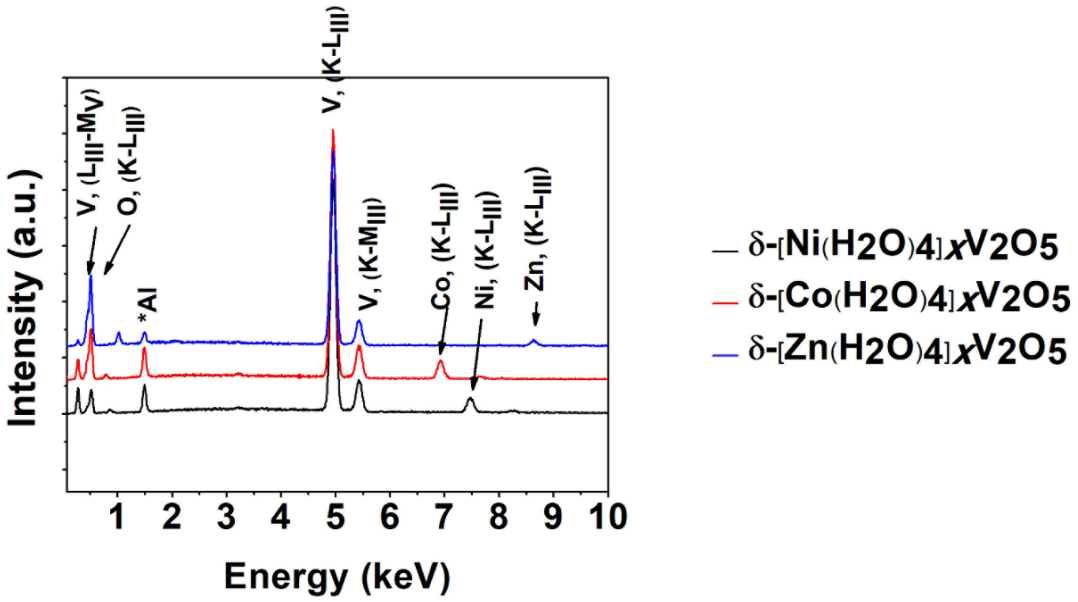

Figure B.1. Energy-dispersive X-ray spectra suggesting stoichiometries of δ-$[Ni(H_2O)_4]_{0.267}V_2O_5$(black), δ-$[Co(H_2O)_4]_{0.270}V_2O_5$(red), and δ-$[Zn(H_2O)_4]_{0.168}V_2O_5$ (blue).

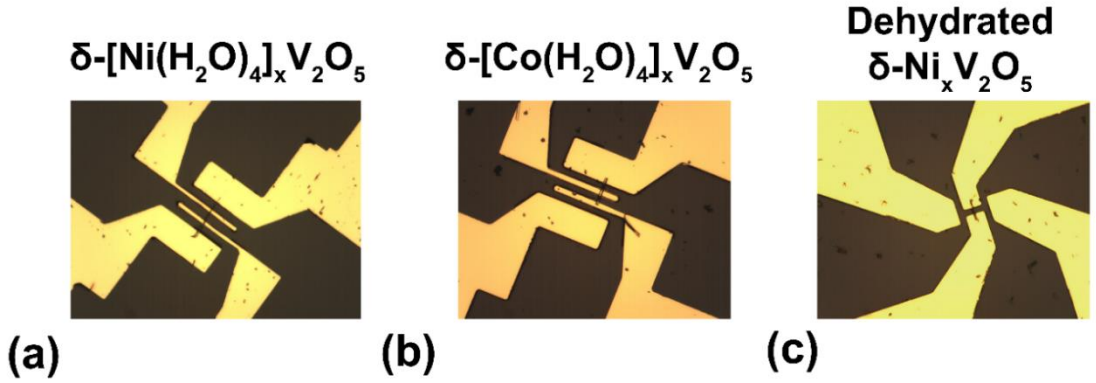

Figure B.2. Optical microscopy images of individual-nanowire devices fabricated for (a) δ-$[Ni(H_2O)_4]_{0.25}V_2O_5$; (b) δ-$[Co(H_2O)_4]_{0.25}V_2O_5$; and (c) dehydrated δ-$Ni_{0.25}V_2O_5$.

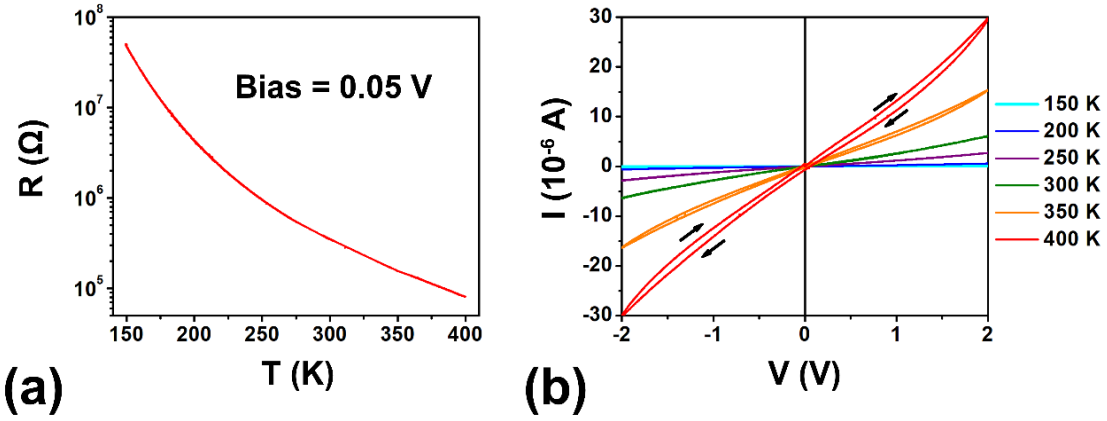

Figure B.3. (a) Resistance *versus* temperature curves and (b) current *versus* voltage curves as a function of temperature. The Zn analog that has a somewhat reduced occupancy as a result of larger cation size and further shows relatively diminished hysteretic behavior, which can be attributed to a lower concentration of protons created by hydrolysis.

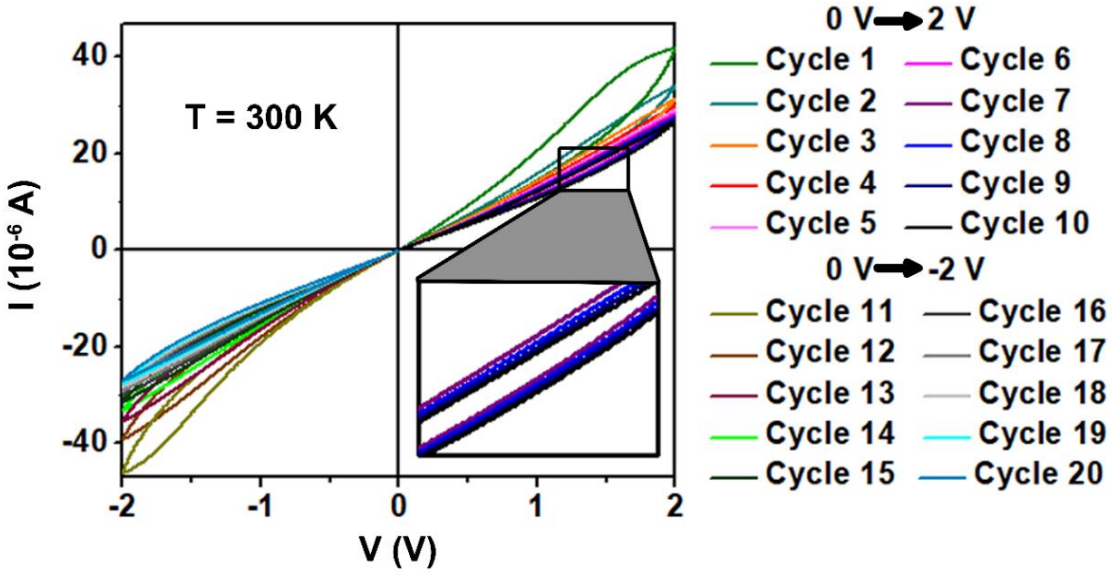

Figure B.4. IV curves demonstrate relaxation of the hysteresis loop to a minimum width after 10 sweeps along the same voltage range (0 → 2V). Similar behavior is observed when cycling in a negative voltage window (0 → -2V). Despite relaxation of the hysteresis loop, the pristine (uncycled) resistance states (as observed in cycles 1 and 11) can be recovered by changing the polarity of the applied bias. The inset to the figure shows the excellent reproducibility of the hysteresis across cycles 7—10.

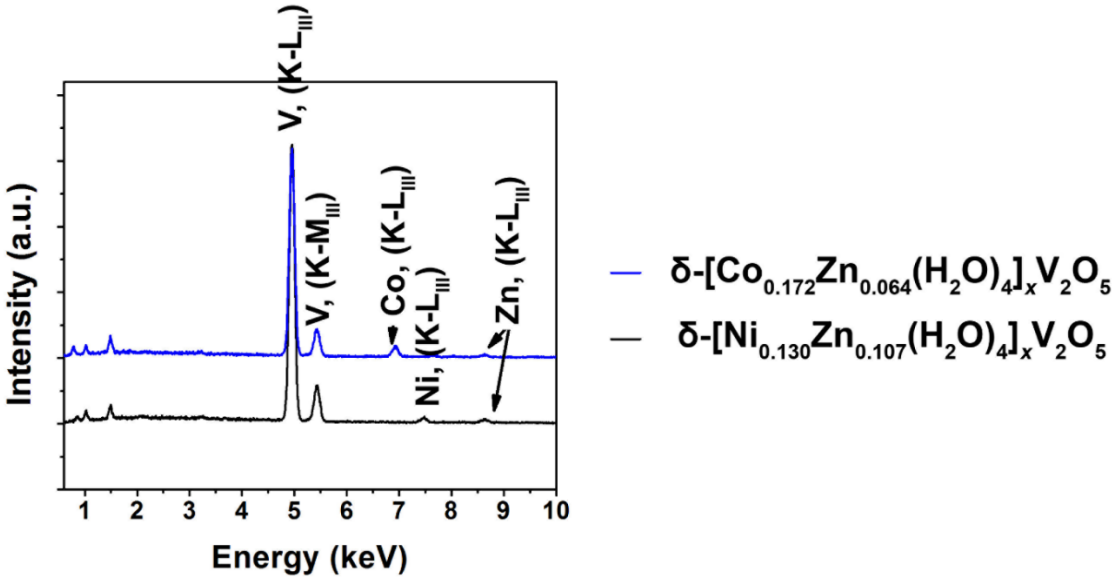

Figure B.5. Energy-dispersive X-ray spectra collected for intermediate compositions: δ-[$Co_{1-y}Zn_y(H_2O)_4]_xV_2O_5$ (blue) and δ-[$Ni_{1-y}Zn_y(H_2O)_4]_xV_2O_5$ (black).

APPENDIX C

SUPPLEMENTARY FIGURES AND TABLES

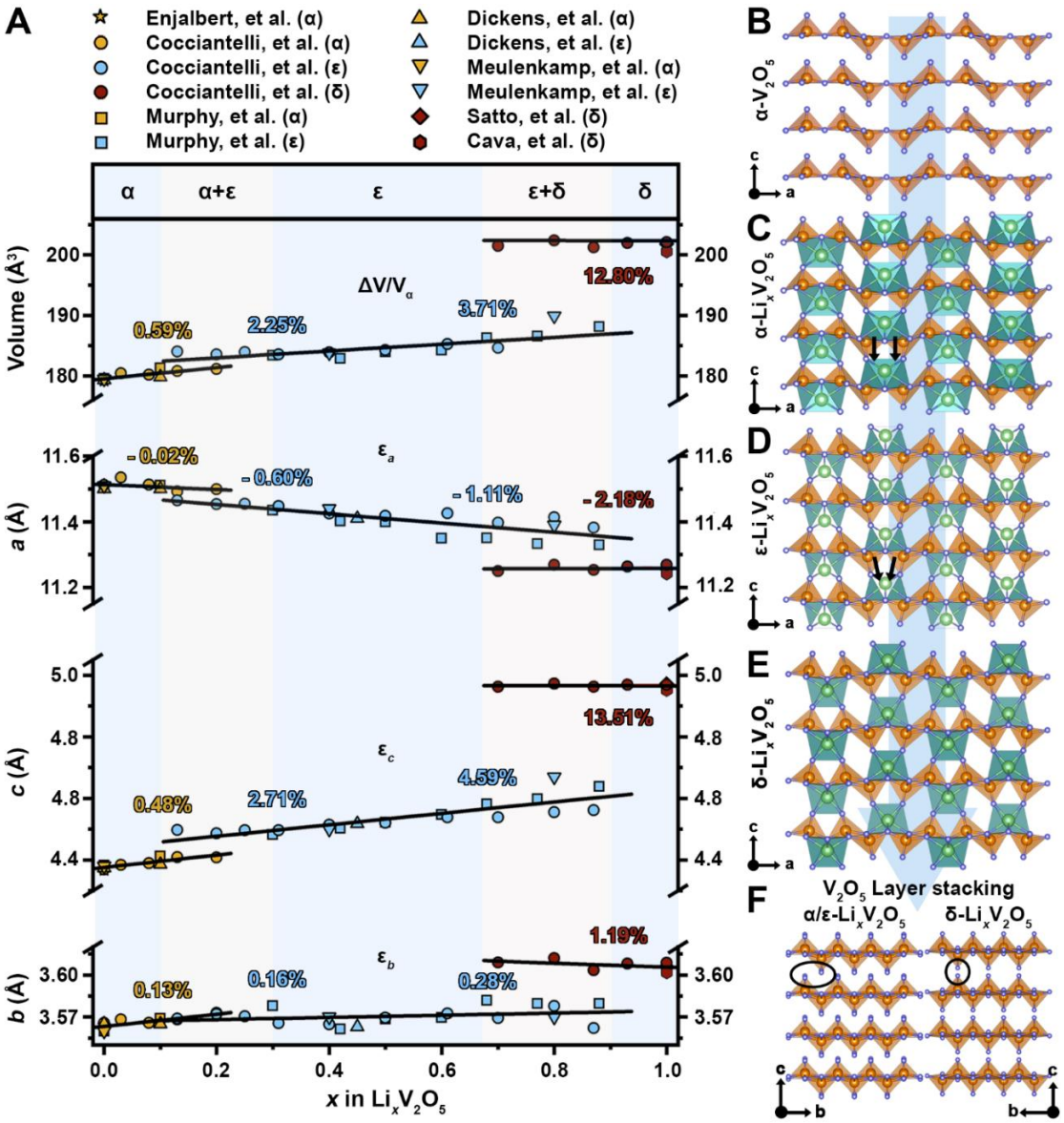

Figure C.1. (A) $Li_xV_2O_5$ (V_2O_5–LiV_2O_5) phase diagram constructed by digitizing and replotting powder X-ray diffraction data found in the literature [Enjalbert, R.; Galy, J. A Refinement of the Structure of V_2O_5. *Acta Crystallogr.* **1986**, *C42*, 1467–1469.; Cocciantelli, J. M.; et al. Crystal Chemistry of Electrochemically Inserted $Li_xV_2O_5$. *J. Power Sources* **1991**, *34* (2), 103–111.; Murphy, D. W.; et al. Lithium Incorporation by Vanadium Pentoxide. *Inorg. Chem.* **1979**, *18* (10), 2800–2803.;

Dickens, P. G.; et al.Phase Relationships in the Ambient Temperature $Li_xV_2O_5$ System. *Mater. Res. Bull.* **1979**, *14* (10), 1295–1299.; Meulenkamp, E. A.; et al. In-Situ X-Ray Diffraction of Li Intercalation in Sol-Gel V_2O_5 Films. *Solid State Ionics* **1999**, *126* (3), 235–244.; Satto, C.; et al. The Δ→ε→γ LiV_2O_5 '"High Temperature"' Phase Transitions Evidenced by Synchrotron X-Ray Powder Diffraction Analysis. *J. Solid State Chem.* **1999**, *109* (1), 103–109.; Cava, R. J.; et al. The Structure of the Lithium-Inserted Metal Oxide δ-LiV_2O_5. *J. Solid State Chem.* **1986**, *65* (1), 63–71.]. Solid solution regions of the phase diagram are highlighted in light blue. Regions where two phases are metastable are set against a white background. Individual lattice parameters (i.e., *a*, *b*, *c*) and the unit cell volume are plotted independently. Linear best fit lines, calculated using diffraction data collected for both chemically and electrochemically lithiated samples, are provided as a guide to the eye. Values calculated for anisotropic lattice strain relative to pristine α-V_2O_5 (*e.g.*, $\varepsilon_a = \Delta a/a_\alpha$) and volumetric expansion (*e.g.*, $\Delta V/V_\alpha$) are provided at the phase boundaries of the α-phase (gold text), the ε-phase (blue text), and the δ-phase (red text). The crystal structures for each phase (α, ε, δ) shown in (A) are provided in (B-E) The observed lithiation-induced crystal structure rearrangement in these phases primarily comprises increasing puckering of the V_2O_5 layers, wherein the apical vanadyl oxygen atoms are canted towards the intercalated Li atoms, as illustrated by the black angled arrows in panels (C) and (D). To facilitate direct comparison, unit cell boundaries have been omitted and each phase has been transformed to the same coordinate system (*e.g.*, the α- and ε-phase are *Pmmn* but the δ-phases is *Amma,* but all are represented here using the same coordinate system). Furthermore, the δ-phase exhibits a doubling of the unit cell along the *b* axis. As such, the values shown for *b* in the δ-phase are in fact *b*/2 and the unit cell volume for the δ-phase has been halved to enable direct comparison. Lattice expansion in this system is strongly anisotropic, characterized by a substantial increase of the *b* lattice parameter, modest decrease of the *a* lattice parameter, and very little change of the *c* lattice parameter. The volumetric expansion observed across the transition from the ε- to δ-phase is notably an order of magnitude larger than across the entire ε-phase solid-solution owing to significant rearrangement of the layer stacking configuration, as shown in panel (F).

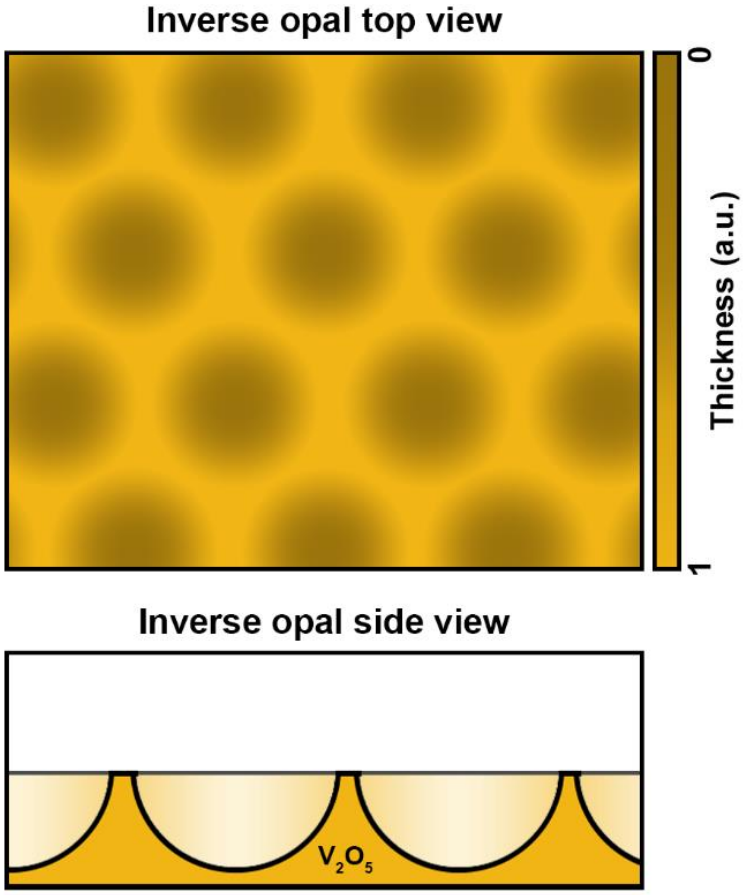

Figure C.2. From the top, the continuously curved structures used in this work resemble a sheet with spherical wells spaced according to a hexagonally close-packed geometry. From the side, the wells resemble half-sphere cutouts (i.e., semi-spherical wells into the V_2O_5 thin film). In this sense, the network of the continuously curved 3D architecture obtained from colloidal crystal templating structure closely resembles a “nanobowl” structure.

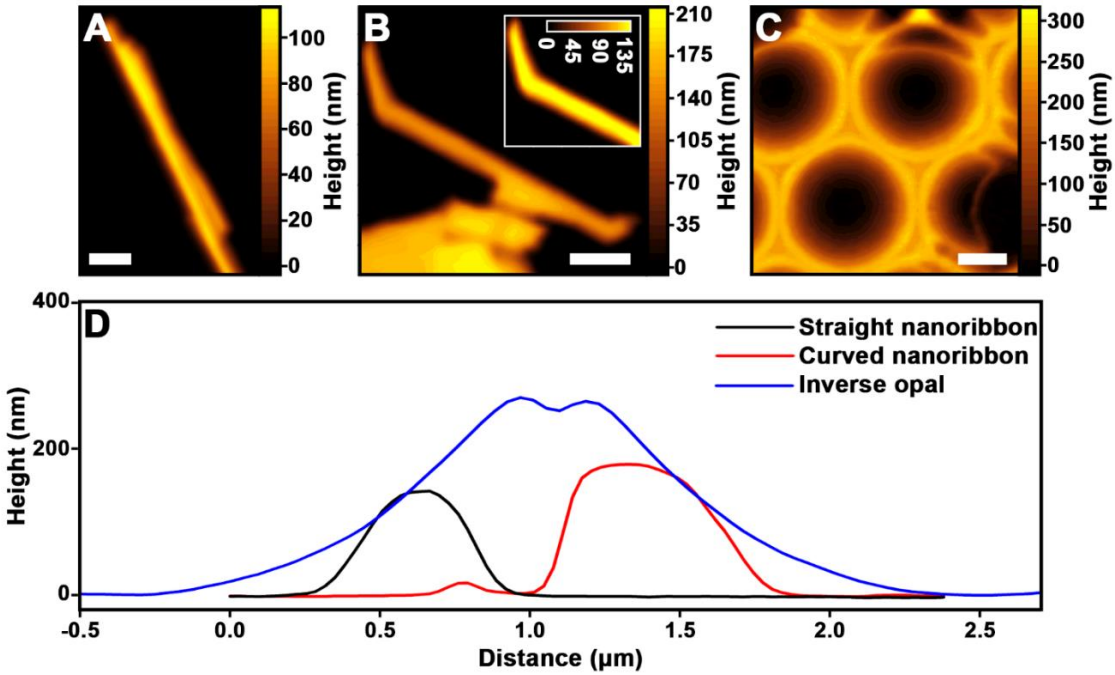

Figure C.3. Thickness maps derived by normalizing the optical density of the STXM stacks (Figure 5.1B-D) to the calculated optical density of a 1 nm thick sample of $Li_xV_2O_5$. Thickness maps for (A) the straight nanoribbon cluster shown in Figure 5.2 (B) the locally-curved nanoribbon and adjacent V_2O_5 nanosheet in Figure 5.3, and (C) the continuously curved V_2O_5 architecture shown in Figure 5.4. The thickness maps were used in generating the compositional and strain maps shown in Figure 5.5. The inset to (B) shows an expanded view near the kinked region of the locally-curved nanoribbon. Scale bars: 500 nm. (D) Line profiles taken from the images in (A-C) are compared. The continuously curved architecture is far thicker than the curved and straight nanoribbons; dimensions of the materials shown in (A-C) are opposite the trend in lithiation (i.e., the continuously curved architecture is most lithiated).

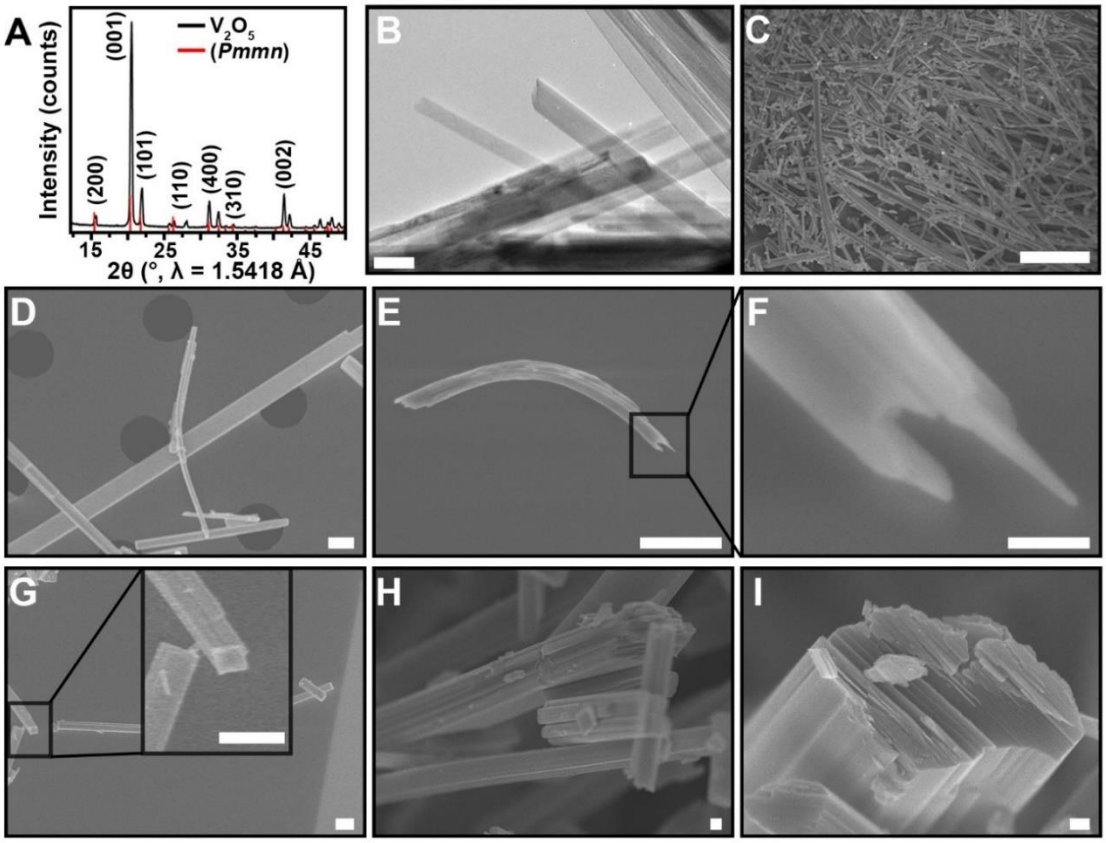

Figure C.4. Powder X-ray diffraction (XRD) pattern of as-synthesized V_2O_5 nanoribbons. The reflections and their relative intensities are marked by red vertical ticks and are indexed to an orthorhombic unit cell (*Pmmn*) with lattice parameters of *a* = 11.503Å, *b* = 3.557Å, and *c* = 4.369Å. (B) Transmission electron microscopy (TEM) image collected for as-synthesized V_2O_5 nanoribbons exhibiting a roughly rectangular cross-section. (C-I) Scanning electron microscopy (SEM) images of the V_2O_5 nanoribbons. Scale bars: (B) 50 nm (C) 10 μm; (D, E) 1 μm; (F) 100 nm; (G) 1 μm; and (H, I) 100 nm.

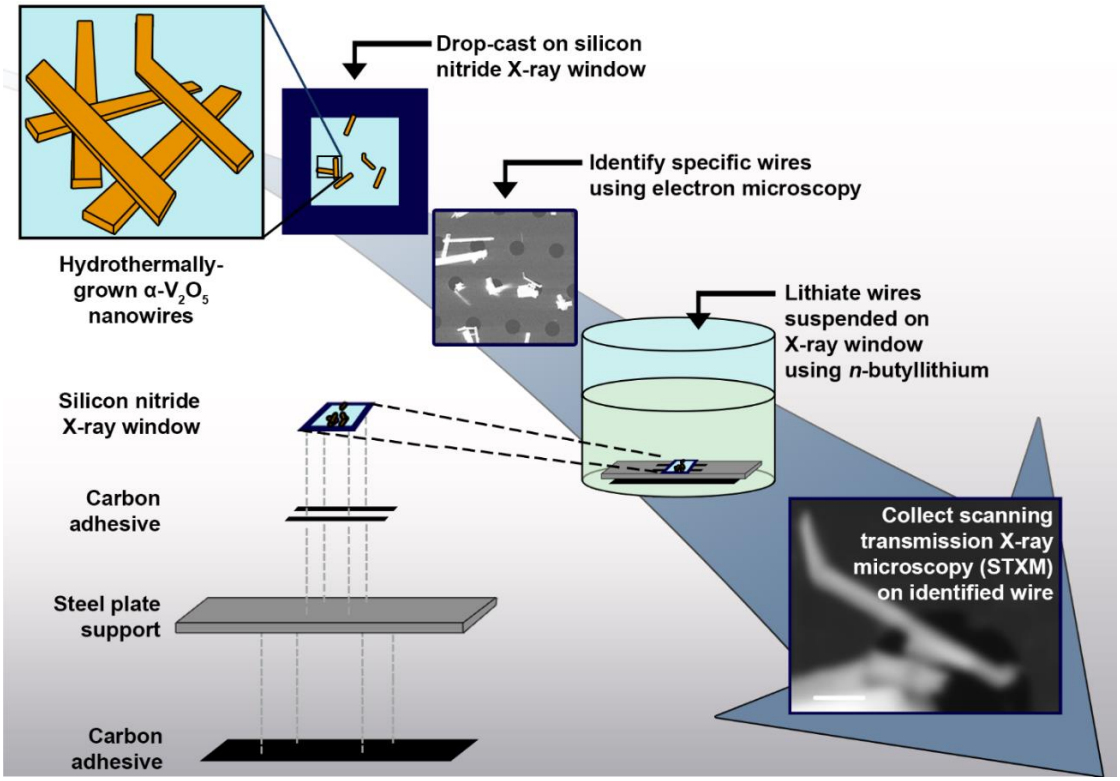

Figure C.5. As-synthesized V_2O_5 nanoribbons are dispersed in 2-propanol (5 mg/mL) and drop-cast onto a holey location-tagged silicon nitride grid. Prior to lithiation and X-ray characterization, SEM is employed to identify nanoribbons of interest and record their locations. Next, the nanoribbons are lithiated by chemical reaction with *n*-butyllithium. The silicon nitride grid is fixed to a steel plate using carbon tape. The steel plate is subsequently fixed to the bottom of a glass beaker (assembly shown in bottom left of schematic). The chemical lithiation reagent is added carefully into the beaker using a syringe. Upon completion of the reaction, the supernatant *n*-butyllithium/heptane solution is carefully removed using a syringe. The beaker and X-ray grid assembly is carefully washed with heptane three times to remove unreacted *n*-butyllithium. Finally, the grid is detached from the steel plate and sealed under vacuum for transport to the synchrotron facility where it is subsequently characterized by scanning transmission X-ray microscopy (STXM).

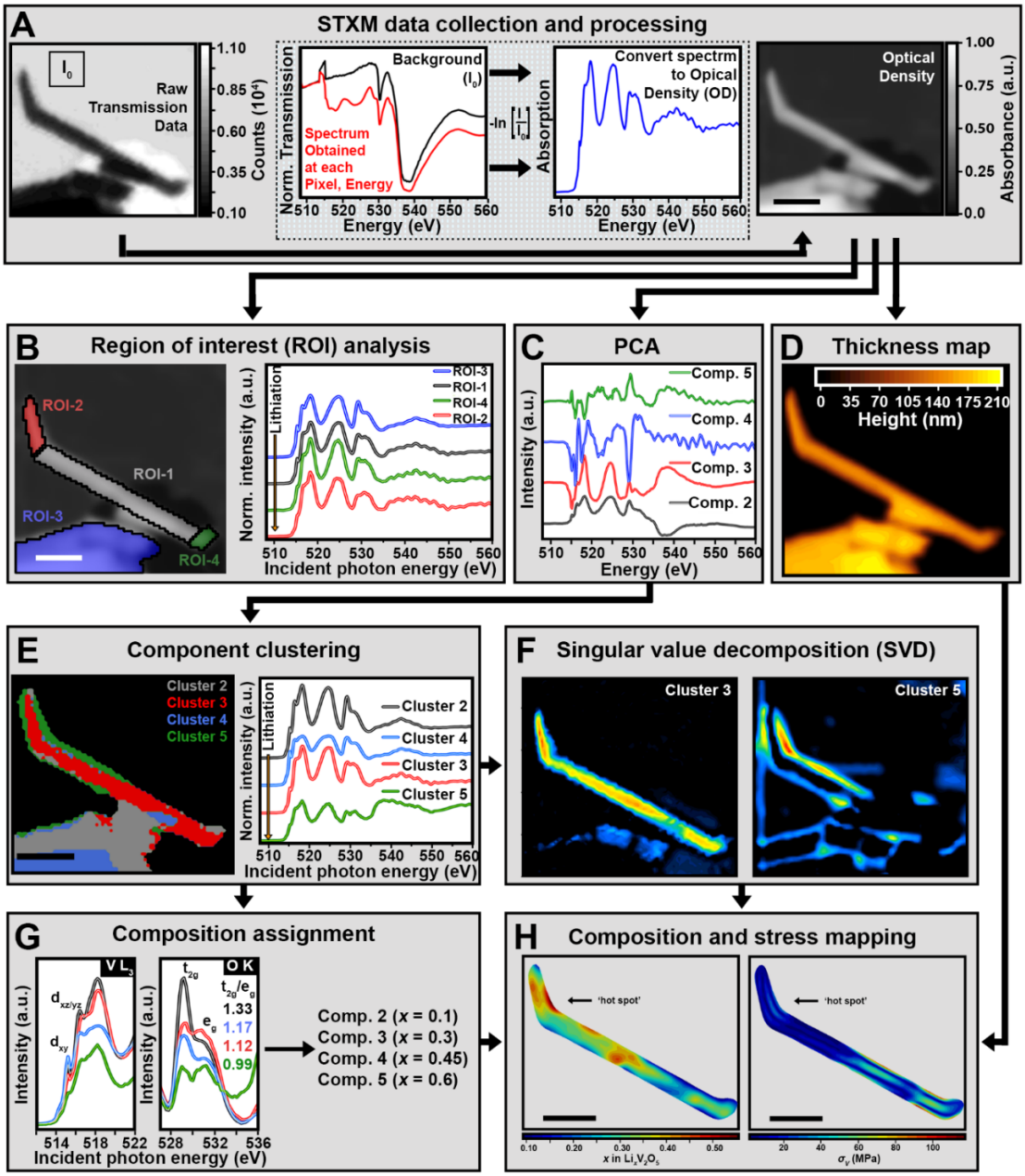

Figure C.6. After samples are dispersed on a silicon nitride substrate and chemically lithiated (as per the schematic in Figure C.5), they are imaged by STXM. (A) The acquired STXM data are a hyperspectral stack of images collected across a range of X-ray energies (each pixel of the combined 2D image 'stack' contains an entire X-ray absorption spectrum). After the image stack is aligned to account for detector and sample stage drift, a region of the image is defined as the background spectrum (I_0, labeled with a square region) and used to convert the obtained transmission data to absorption data. (B) Region-of-interest (ROI) analysis is performed by selecting specific regions of the sample and averaging

the spectrum across the user-defined pixels. (C) In order to better understand the spatial distribution of spectrally similar regions of the sample, principal component analysis (PCA) coupled to cluster analysis is employed. PCA defines mutually-orthogonal eigenspectra (see Figure C.7, Figure C.12D, and Figure C.15D) that provide the best separation of the spectra obtained at each pixel in the STXM image by maximizing variance and covariance within the hyperspectral data. (D) Thickness maps can be generated from the raw STXM data as required for generating composition maps. (E) The pixels (i.e., spectrum at each pixel) are scored along each eigenspectrum and then clustered together based on the similarity of their scores. The maps in Figure 5.2D, Figure C.14, and Figure C.18 thus reveal the spatial distribution of spectrally similar pixels. Each pixel is assigned a single color despite receiving contribution from multiple eigenspectra and for this reason PCA-clustering is referred to as a "winner-takes-all" approach to image processing. The resulting PCA-clustering spectra are obtained by integrating the spectra across all clustered pixels (i.e., the "Cluster 3" spectrum in Figure 5.2A is obtained by integrating the spectra at each red pixel in Figure 5.2D). (F) Singular value decomposition (SVD) can be performed to map each of these eigenspectra and their weights across each pixel of the image, which provides a means of developing a composition map. (G) Compositional values are assigned to each of the spectra obtained by PCA-clustering by comparison to previously published theoretical and experimental studies of lithiated V_2O_5 materials [Maganas, D.; et al. First Principles Calculations of the Structure and V L-Edge X-Ray Absorption Spectra of V_2O_5 Using Local Pair Natural Orbital Coupled Cluster Theory and Spin-Orbit Coupled Configuration Interaction Approaches. *Phys. Chem. Chem. Phys.* 2013, *15* (19), 7260–7276.; Scanlon, D. O.; et al. An Ab Initio Study of Reduction of V_2O_5 through the Formation of Oxygen Vacancies and Li Intercalation. *J. Phys. Chem. C* **2008**, *112* (26), 9903–9911.; De Jesus, L. R.; et al. Striping Modulations and Strain Gradients within Individual Particles of a Cathode Material upon Lithiation. *Mater. Horizons* **2018**, *5*, 486–498.].(H) The SVD maps in (F) and the spectra/composition values assigned in (G) can be used to generate compositional and stress maps for individual nanoparticles [De Jesus, L. R.; et al. Striping Modulations and Strain Gradients within Individual Particles of a Cathode Material upon Lithiation. *Mater. Horizons* **2018**, *5*, 486–498.].

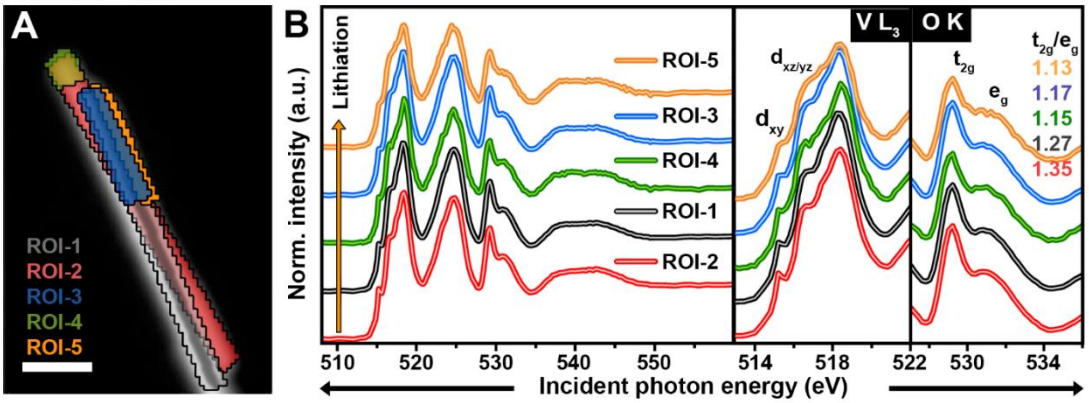

Figure C.7. (A) Stack-averaged SXTM image collected for two closely-overlapping V_2O_5 nanoribbons (as shown in Figure 5.1B). The area of the first ribbon is closely approximated by the grey and blue polygons, whereas the cross-section of the larger nanoribbon is closely approximated by the red and green polygons. (B) Spectra obtained by averaging across the corresponding colored regions in (A). The selected polygons and the spectra are color-coordinated. The individual spectra display subtle but notable differences in spectral features, as highlighted by expanded views of the V L_3- and O K-edges. First, the fine structured low-energy features at the V L_3-edge are observed to diminish slightly in intensity upon reduction of the V_2O_5 material. The increased apparent extent of lithiation in both ROI-2 and ROI-5 is further confirmed at the O K-edge, where the ratio of the intensity of the t_{2g} to e_g* manifolds is diminished (as a result of lifting of spin-degeneracy resulting from the emergence of electron correlation and the distortion of vanadyl moieties towards Li-ions). Scale bar: 500 nm.

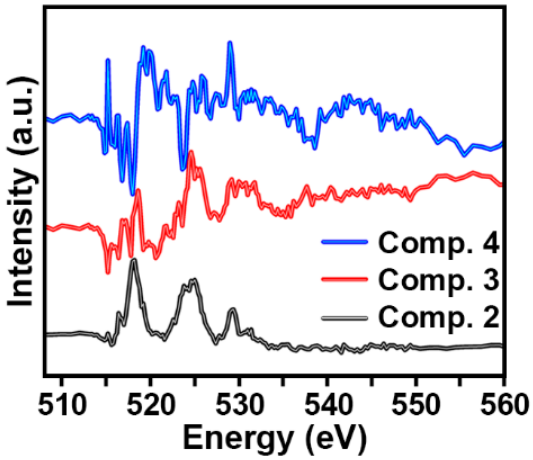

Figure C.8. Mutually-orthogonal principal components generated using the PCA routine as implemented in aXis2000 for the STXM map shown in Figure 5.1B. Each pixel was scored along these three eigenspectra and grouped (i.e., clustered) according to score to reproduce the PCA-cluster map in Figure 5.2D.

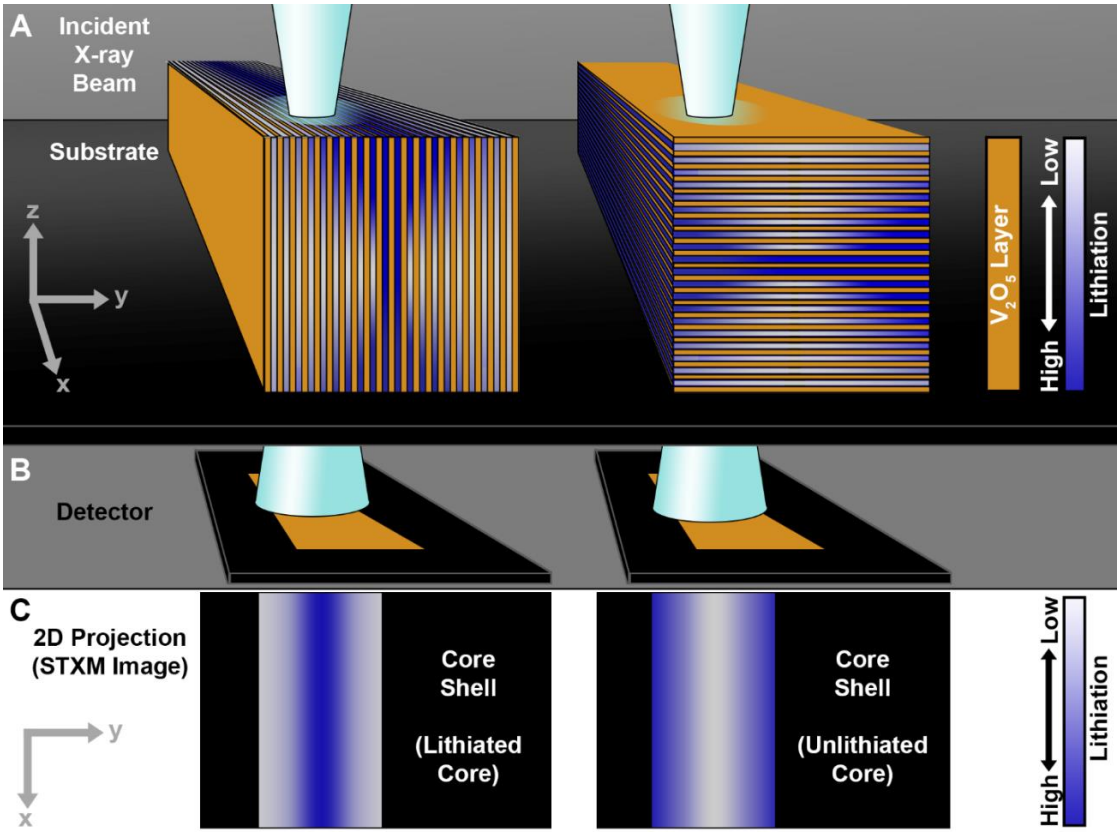

Figure C.9. V_2O_5 has an inherently layered crystal structure motif (represented schematically by orange stripes, shown in **Figure C.1**B-E). (A) V_2O_5 nanoribbons with an approximately square cross-section can be situated on the substrate in two different configurations – with basal planes normal (left) or parallel (right) to the substrate plane. The lithiation of V_2O_5 has been observed to proceed via a staging-type process extending from the middle layers of the nanoribbon outwards. The extent of lithiation between the V_2O_5 layers is represented here on a scale from high lithiation (blue) to low lithiation (white). (B) STXM images for the 3D nanoribbons are collected in transmission mode yielding a 2D projection. The specific orientation of the ribbons shown in (A) alters the spatial distribution of lithiation images in 2D, as shown in (C). When viewing the ribbon down the 'book pages' the ribbons often show apparent core-shell behavior with a more lithiated core, whereas when viewed down the 'book cover' the 2D projection indicates core-shell behavior with a less lithiated core.

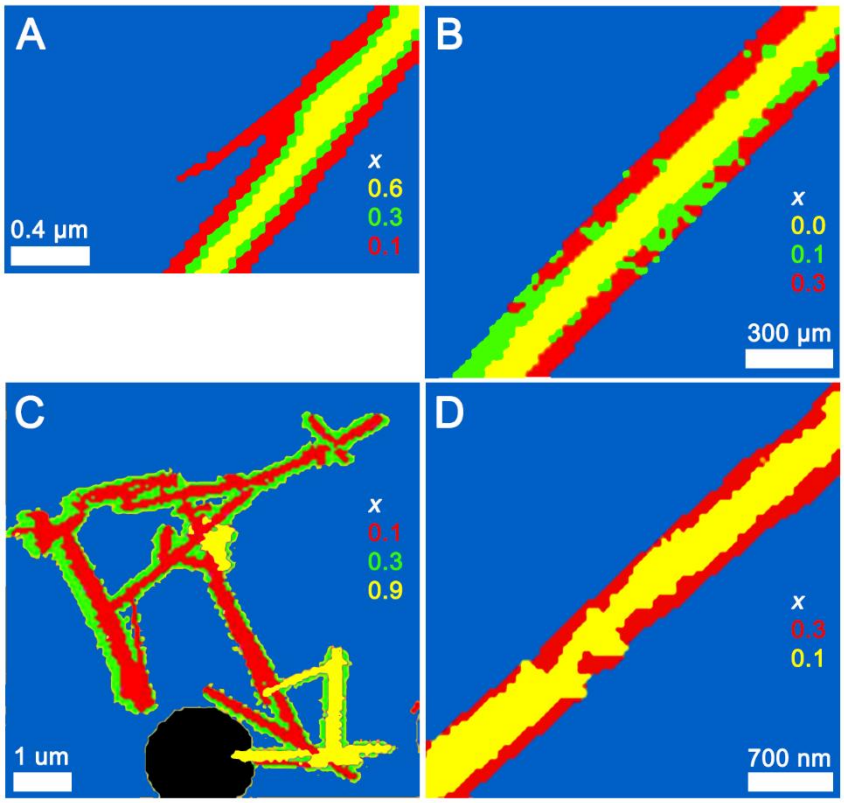

Figure C.10. Core-shell lithiation of a V_2O_5 using *n*-butyllithium. (B) Core-shell lithiation of a single V_2O_5 nanoribbon using a 4x molar excess of *n*-butyllithium chemical reagent. (C) Core-shell lithiation of a grouping of interconnected V_2O_5 nanoribbons using a 4x molar excess of *n*-butyllithium chemical reagent. (D) Example of core-shell formation during delithiation of a V_2O_5 material. The material exhibits a more highly lithiated shell and almost fully delithiated core. $NOBF_4$ is a highly oxidizing chemical deintercalation agent. Data adapted from [A: De Jesus, L. R.; et al. Mapping Polaronic States and Lithiation Gradients in Individual V_2O_5 Nanowires. *Nat. Commun.* **2016**, *7*, 12022.] and [De Jesus, L. R.; et al. Striping Modulations and Strain Gradients within Individual Particles of a Cathode Material upon Lithiation. *Mater. Horizons* **2018**, *5*, 486–498.]. Lithium stoichiometries are assigned with respect to standard STXM datasets.

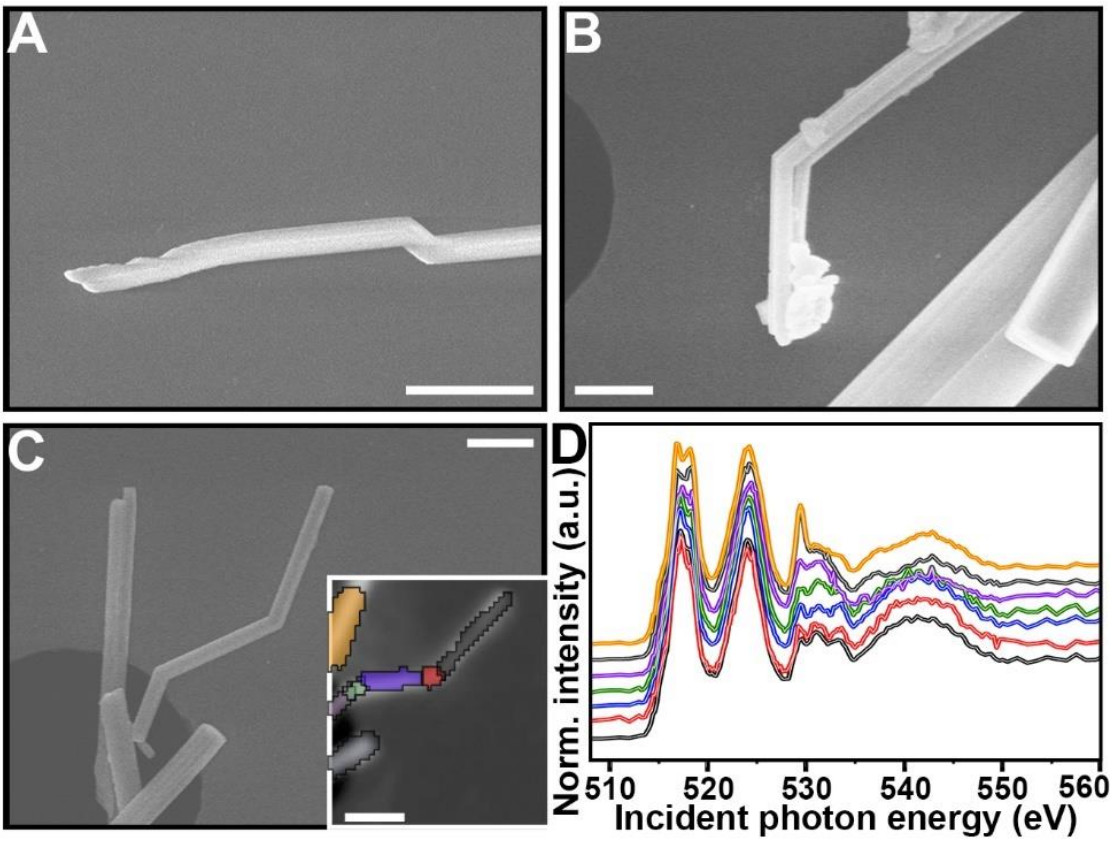

Figure C.11. (A) Locally-curved α-V_2O_5 nanoribbons are commonly obtained from the hydrothermal synthesis. SEM images of three examples of locally-curved nanoribbons are shown (A-C). A STXM image of one of these nanoribbons, which contains two ~45° bends, is shown inset. ROI analysis of the nanoribbon (which was chemically lithiated with 0.025 M *n*-butyllithium for 1 h) is overlaid. (D) Color-coded spectra collected over the regions in (C) are shown. Spectra indicate significant extents of lithiation across the entire nanoribbon at longer lithiation times (1 h). Scale bars: 500 nm.

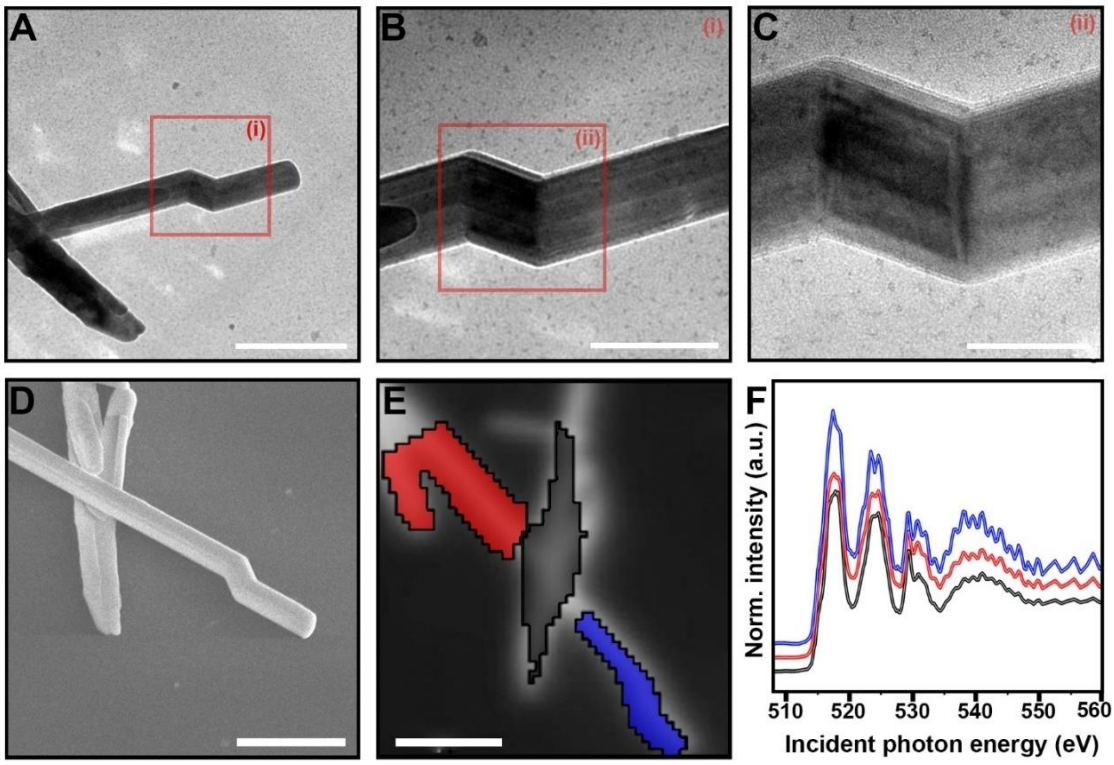

Figure C.12. Locally-curved α-V_2O_5 nanoribbons are commonly obtained from the hydrothermal synthesis. TEM images of one nanoribbon exhibiting two 45° kinks in close proximity are shown in (A-C). (D) SEM image of the same nanoribbon. (E) STXM image of the same nanoribbon with colored regions corresponding to ROI spectra in (F). Spectra indicate significant extents of lithiation due to longer lithiation times (1 h) and higher concentrations (0.025 M). Scale bars: (A) 500 nm; (B) 200 nm; (C) 100 nm; (D) 500 nm; and (E) 500 nm.

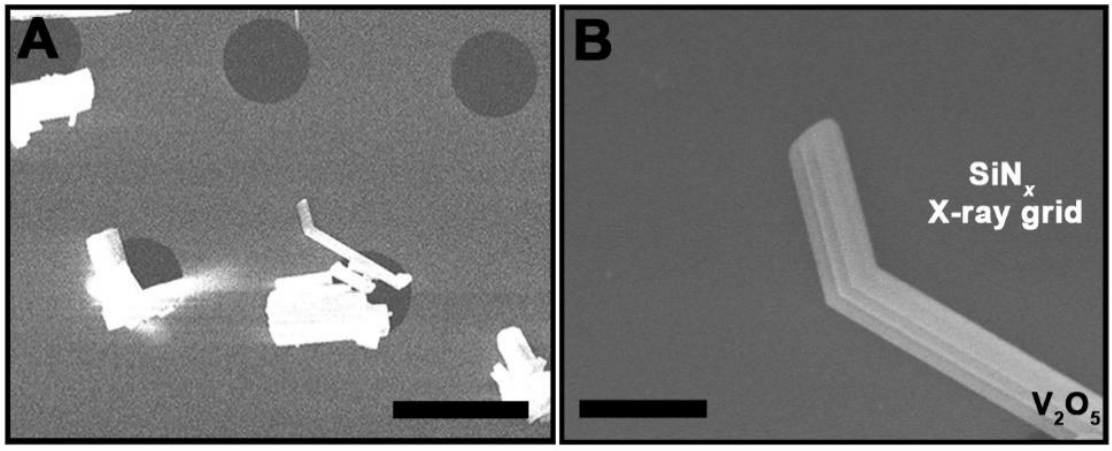

Figure C.13. (A) SEM image showing locally-curved nanoribbon adjacent to the large V_2O_5 sheet. (B) SEM image highlighting an expanded view of the kink near the terminus of the nanoribbon. This SEM image is also shown as an inset to Figure 5.2G. Scale bars: (A) 3 μm; (B) 500 nm.

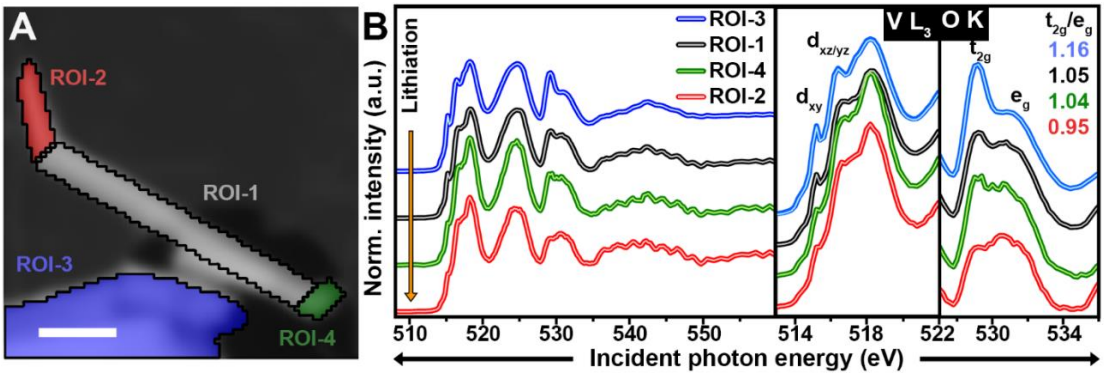

Figure C.14. Stack-averaged STXM image collected for the locally-curved nanoribbon shown in Figure 5.3. Areas selected for region of interest (ROI) analysis are indicated by colored polygons. (B) Spectra obtained by integrating over the regions defined by the colored polygons in (A). The starkest differences revealed by ROI analysis are observed when contrasting the spectra obtained near the kink (ROI-2), away from the defect (ROI-4), and then across the region corresponding to the thick V_2O_5 sheet adjacent to the curved nanoribbon (ROI-3). The nanoribbon appears to be more significantly lithiated in proximity of the kink (ROI-2) and relatively unlithiated in the region below the defect in the nanoribbon (ROI-1). The spectra shown in (B) are also shown in Figure 5.3A-C and are reproduced here for reference. Scale bar: 500 nm.

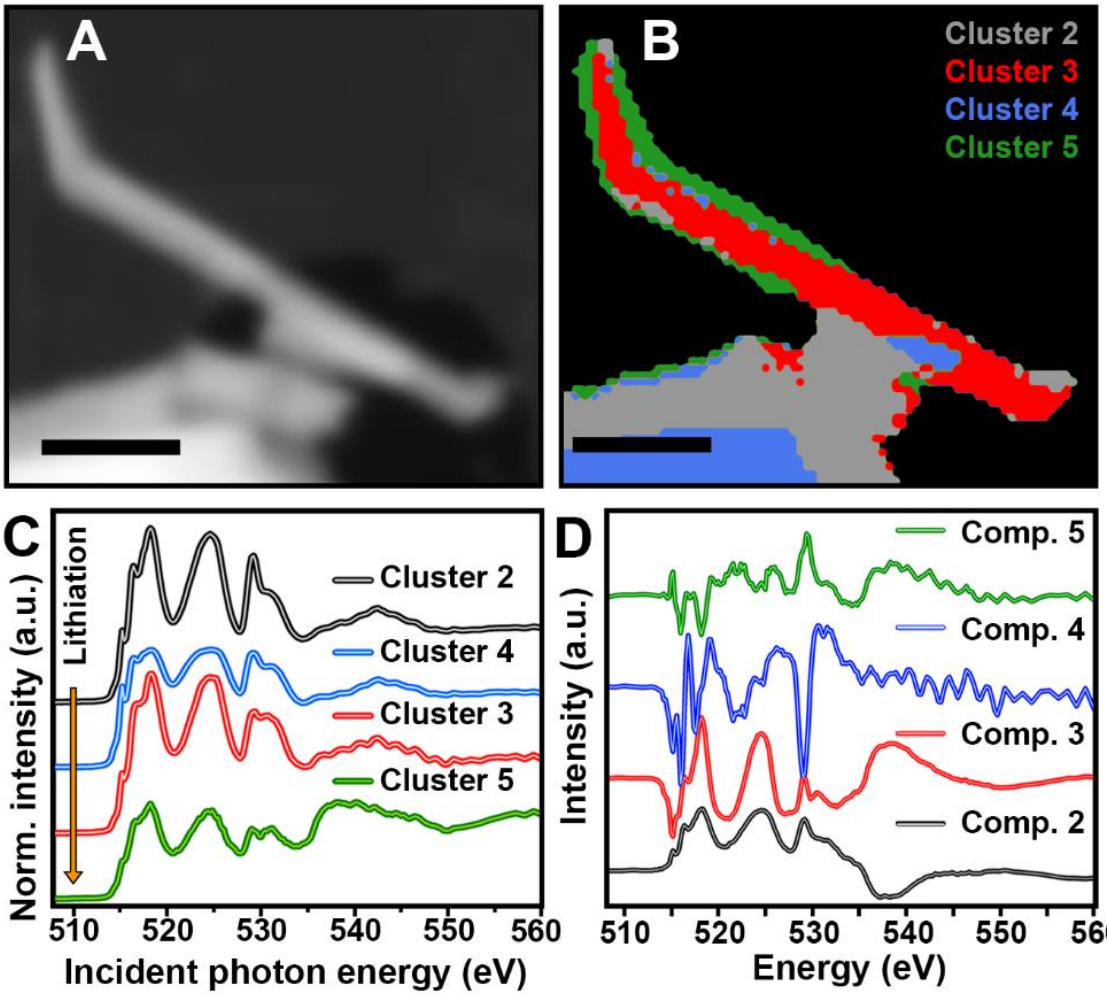

Figure C.15. (A) STXM image of a bent nanoribbon following lithiation. This image is also shown in Figure 5.1B and is reproduced here for easy comparison to the PCA-clustering map. (B) PCA-clustering map corresponding to the optical density image in (A). This panel is also displayed inset to Figure 5.3D and is provided here at higher resolution for reference (C) Spectra averaged over the color-coordinated polygons in (B). These spectra are also shown in Figure 5.3A and are reproduced here for comparison These spectra were used as input for singular value decomposition (SVD) as shown in Figure 5.3. It should be noted that evidence of some oxide formation (*e.g.*, Li_2O Li_2O_2, or LiOH) is apparent in the cluster 5 spectrum. Notably, both PCA and SVD analysis (Figure 5.3G) indicate that the LiO_x layer is localized, can be clearly resolved, and can be distinguished from the spectral signatures of different $Li_xV_2O_5$ phases. (D) Raw eigenspectra obtained from principal component analysis of the locally-curved nanoribbon. Scale bars: 500 nm.

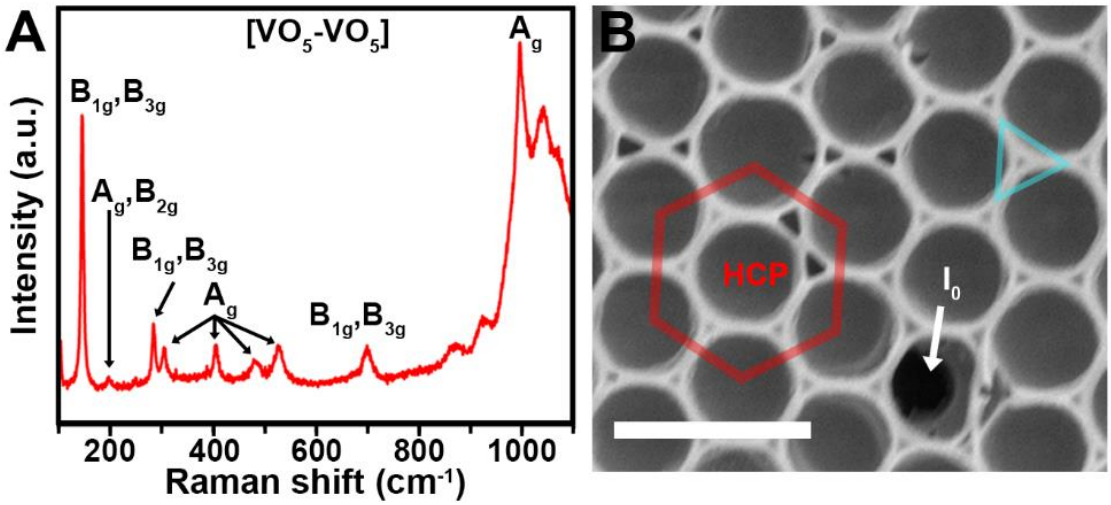

Figure C.16. (A) Raman spectrum collected for the pristine inverse opal structure. Raman modes have been assigned based on recent density functional theory calculations and experiments [Baddour-hadjean, R.; Pereira-Ramos, J.-P. Raman Microspectrometry Applied to the Study of Electrode Materials for Lithium Batteries. *Chem. Rev.* **2008**, *110* (3), 1278–1319.; Horrocks, G. A.; et al. Finite Size Effects on the Structural Progression Induced by Lithiation of V_2O_5: A Combined Diffraction and Raman Spectroscopy Study. *J. Mater. Chem. A* **2013**, *1*, 15265–15277.; Baddour-Hadjean, R.; et al. Structural Modification of $Li_xV_2O_5$ in a Composite Cathode ($0 \leq x < 2$) Investigated by Raman Spectroscopy. *J. Raman Spectrosc.* **2012**, *43* (1), 153–160.] and match well to phase-pure α-V_2O_5. (B) SEM image collected for a continuously curved V_2O_5 architecture grown on a silicon nitride substrate. The roughly hexagonally close-packed ordering of the nanobowl architecture is evident and highlighted with a transparent red hexagon. One of the location-tagged holes patterned onto the silicon nitride substrate is labeled as 'I_0' in the bottom right of the SEM image and enables sampling of I_0 for processing of STXM data (as demonstrated in Figure C.6A). One of the triangular regions at the intersection of three close-packed spheres is highlighted in light blue. Scale bar: 1 μm.

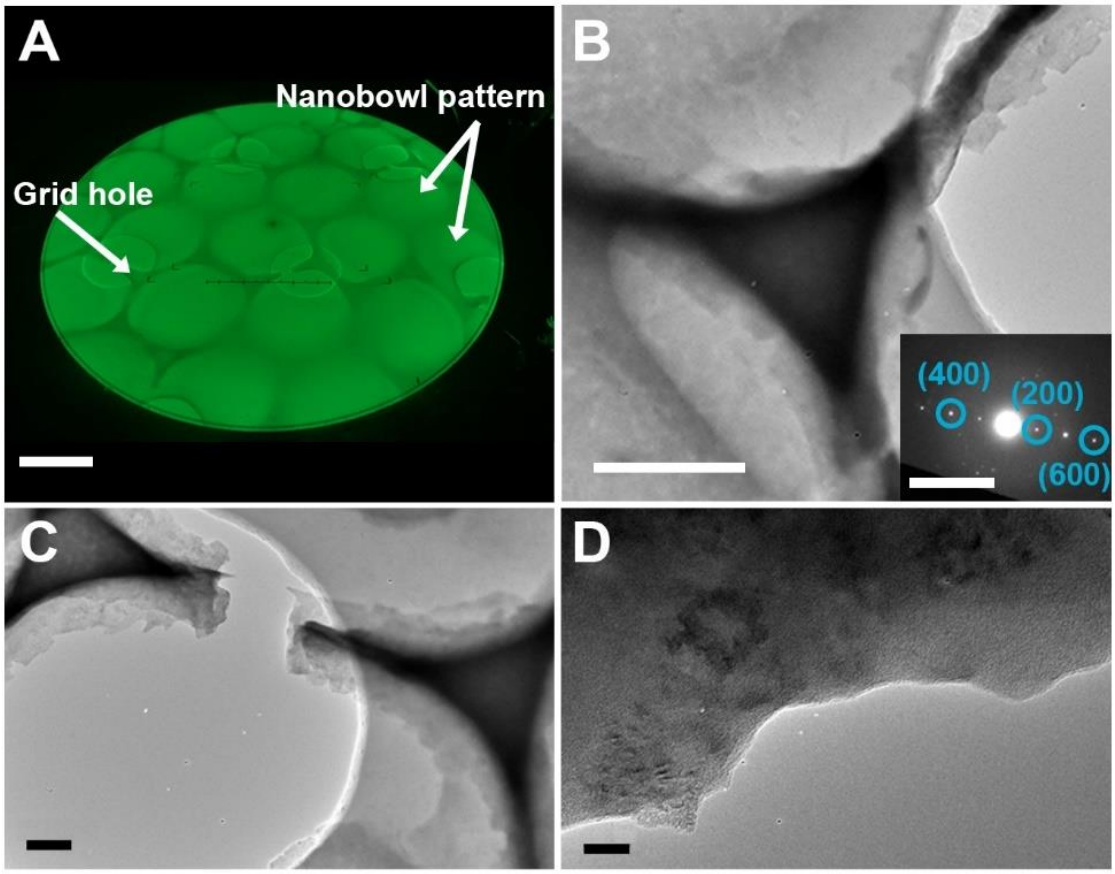

Figure C.17. (A) Optical image of a transmission electron microscopy (TEM) image as viewed through a TEM viewport. Patterned 2 μm holes in the X-ray grid (labeled as “grid hole”) are clearly discernible below the 3D architecture (labeled as “nanobowl pattern”). (B) TEM image collected for the roughly triangular region at the intersection of three closely-packed nanobowls. Interestingly the architecture exhibits small regions of decreased thickness (possibly hollow regions) near the tetrahedral holes of the hexagonally-close-packed structure, as indicated in **Figure C.17**B. Notably, selected area electron diffraction (SAED, inset) pattern collected at the region shown in (B) evidences single crystalline orthorhombic V_2O_5 oriented with basal planes parallel to the silicon nitride substrate. (C and D) TEM images showing various features observed in the continuously curved 3D architecture, including (C) locations where the template is fractured due to lattice mismatch between the V_2O_5 and the silicon nitride grid during annealing and (D) template edges showing a contiguous microstructure. Scale bars: (A) 2 μm; (B) 0.5 μm; (B, inset) 5 nm^{-1}; (C) 0.2 μm; and (D) 20 nm.

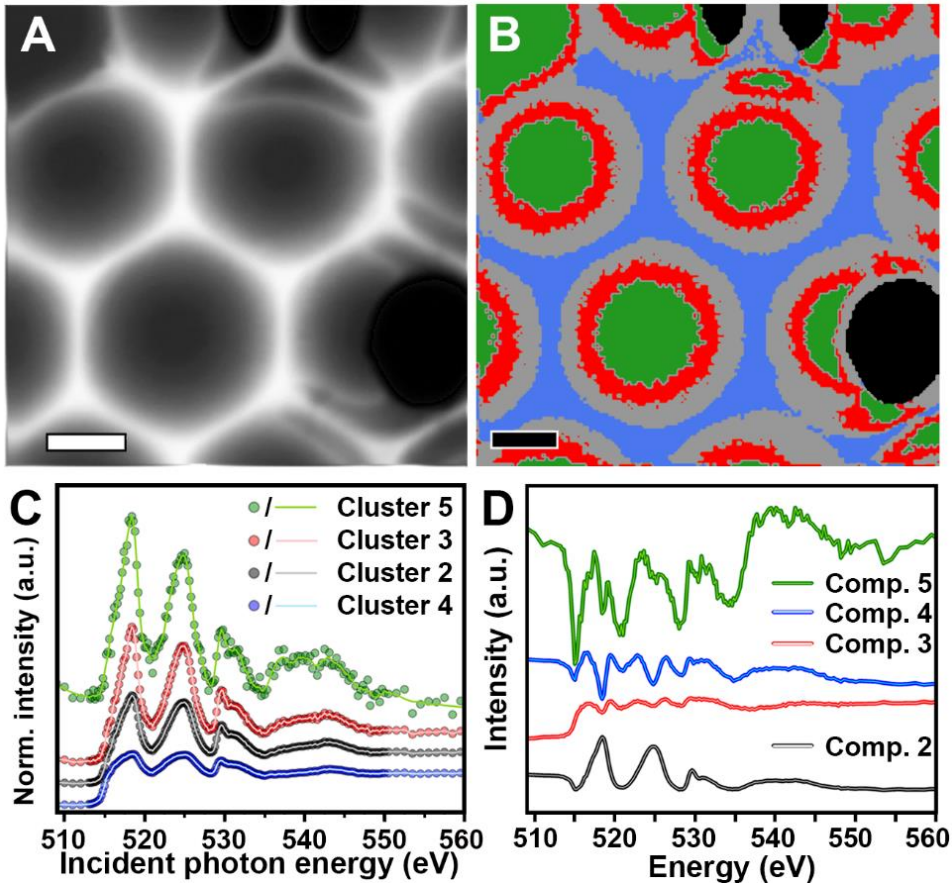

Figure C.18. (A) Optical density image obtained by averaging across a stack of STXM images, also shown in Figure 5.1D. White regions indicate greater X-ray absorption across the entire scanned energy range (508—560 eV) and thus correlate with thickness (assuming compositional homogeneity. (B) PCA-clustering map reveals five distinct pixel clusters. (C) The spectra corresponding to these pixel clusters are color-coordinated with the delineated regions in (B) and are also plotted in Figure 5.4A, main manuscript. It is evident that the observed spectra correlate to thickness and not inhomogeneity (which would have been reflected in alteration of line shapes and peak positions as observed in Figure 5.2A-C and Figure 5.3A-C for straight and curved nanoribbons, respectively). This is further reflected in the correlation between the pixel clusters in (B) and in the observed thickness map inset to Figure 5.1D and Figure C.3C. The thinnest cluster spectrum (green, Cluster 5) is noisy, and exhibits characteristics of a very thin sample. As such, the spectrum is plotted both as a scatter plot to reflect the actual data and as a line using a 3-point boxcar average to reduce noise. Cluster 5 is highly localized in the center of the templated voids and cluster 4 is located in the nanobowl walls, which are expected to be quite thick. Cluster 2 and cluster 3 are located as rings around the contour of the templated void spaces. The raw eigenspectra obtained by PCA of the STXM image are provided in (D). Scale bars:1 μm.

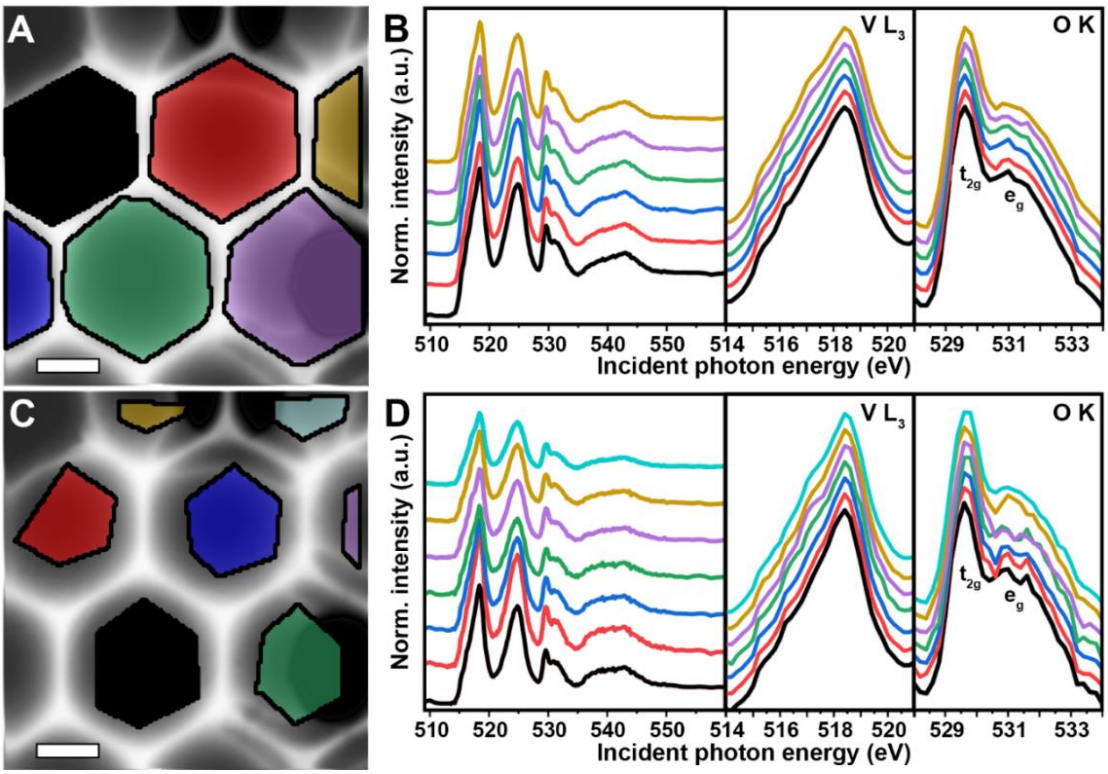

Figure C.19. Region of interest analysis (ROI) was performed across the 3D architecture in Figure 5.4. Regions were selected based on the results of PCA clustering and correlated to expected variations in template thickness, as supported by TEM data in Figure C.17 and the thickness maps in Figure C.3. The colored polygons in (A, C, and E) indicate the regions over which the spectra in (B, D, and F) are averaged. Multiple areas are selected and the corresponding ROI-averaged spectra are compared, reflecting homogeneous lithiation across the structure. Specifically, ROI analysis was performed for: (A) the entire “sphere vacancy”; (C) the center of the “sphere vacancy”; and (E) the rims of the “sphere vacancies”. For each selected area type (A, C, E), the corresponding averaged spectra show no discernable variance. The striking homogeneity is consistent with PCA clustering (Figure C.18) and SVD analysis of the 3D architecture (Figure 5.4). Variation between the center of the sphere vacancies and the rims of the vacancies is evident, but this variation derives entirely from differences in sample thickness, as indicated by the STXM thickness maps (Figure C.3), SEM images (Figure C.16B), and TEM images (Figure C.17). The observed spectral variation due to thickness indicates a non-linear detector response, as expected for very thick samples (>300 nm @ V L-edge). Scale bars: 1 μm.

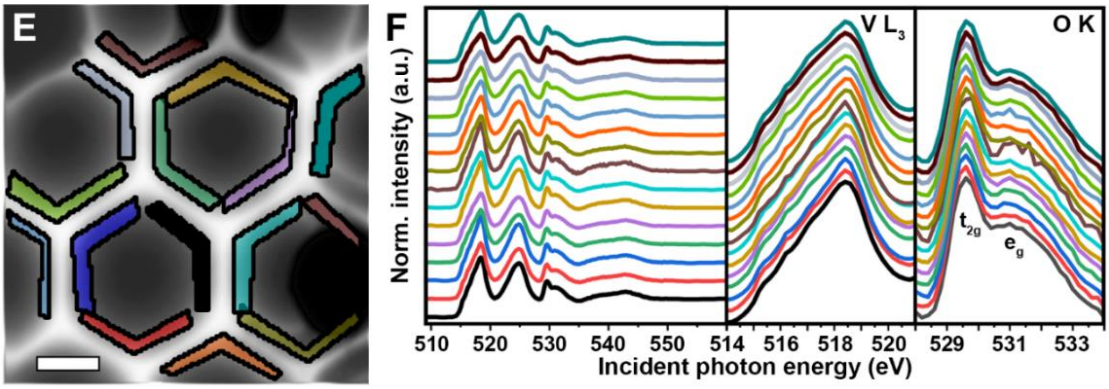

Figure C.19. Continued.

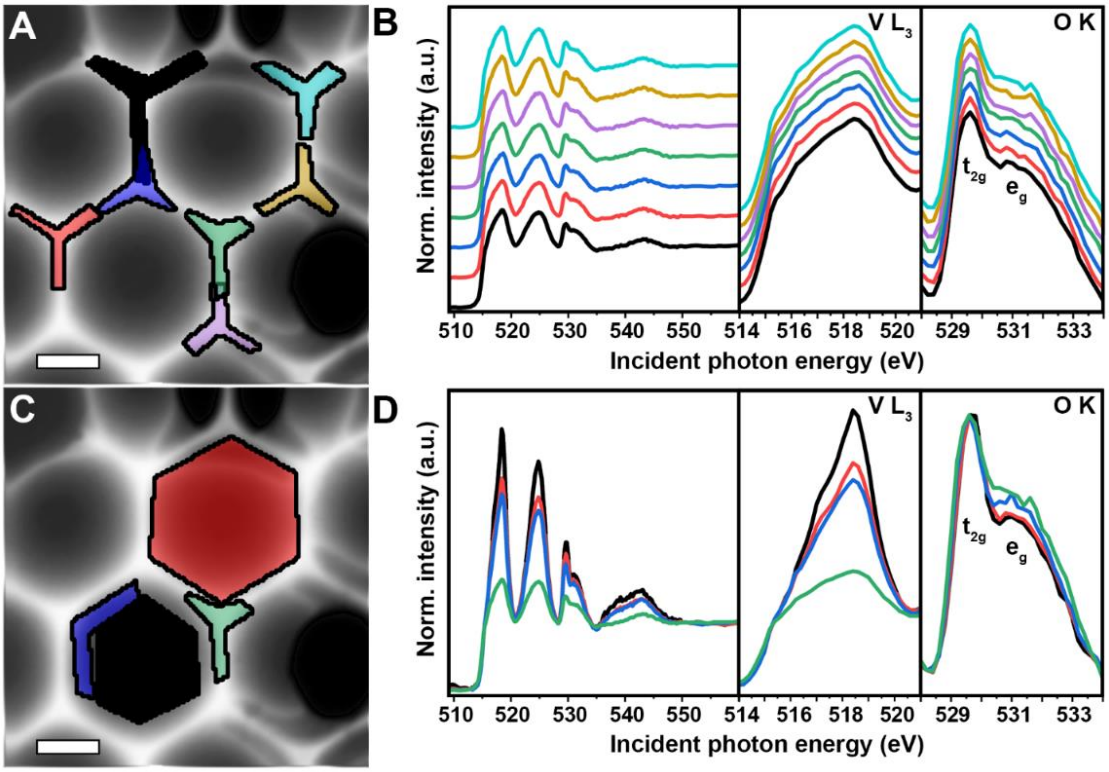

Figure C.20. Region of interest analysis (ROI) was performed across the 3D architecture in Figure 5.4. The colored polygons in (A) indicate the regions over which the spectra in (B) are averaged. The corresponding averaged spectra are self-consistent and show no discernable variance. (C) Multiple ROI area types (as shown in Figure C.19A, Figure C.19C, Figure C.19D and Figure C.20A) are compared in (D) and show variance derived from sample thickness. The striking homogeneity is consistent with PCA clustering and SVD analysis of the 3D architecture (Figure C.18 and Figure 5.4, respectively). Scale bars: 1 μm.

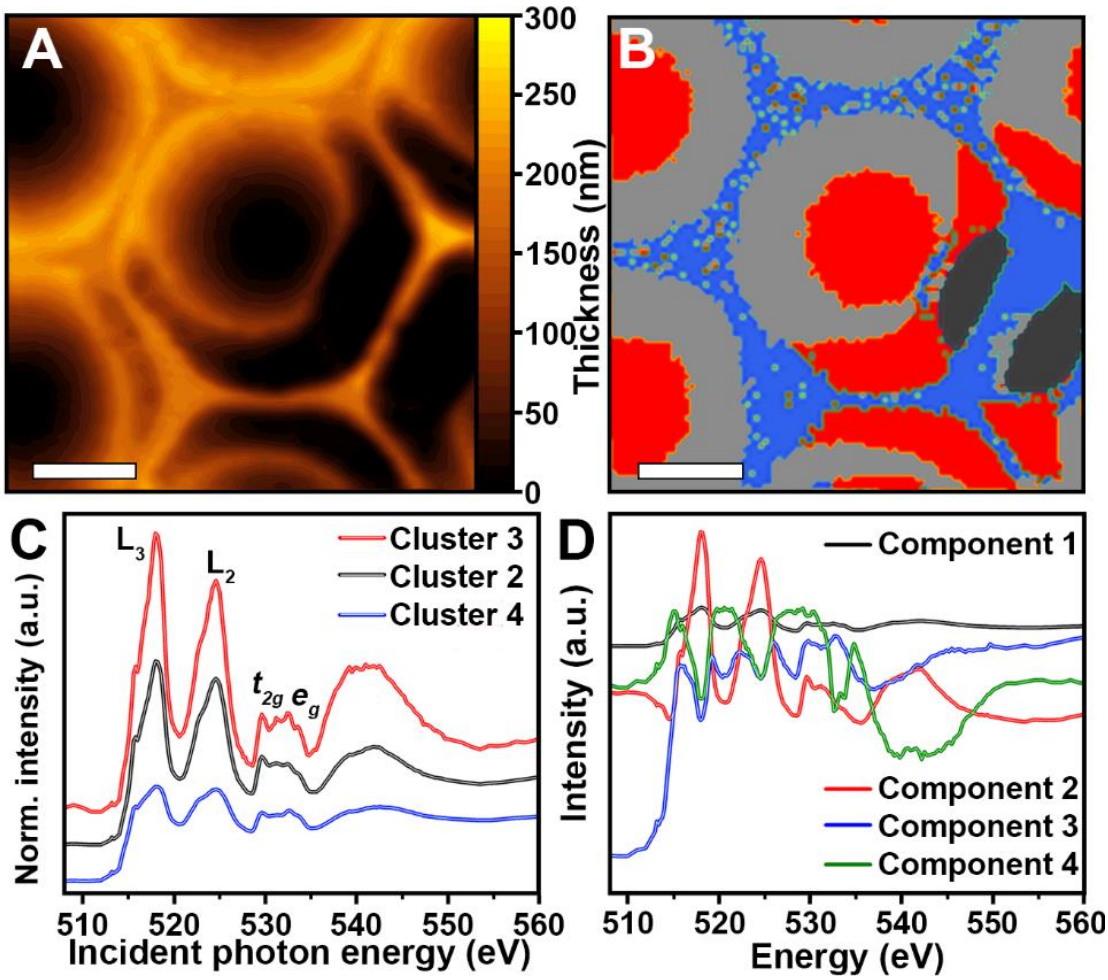

Figure C.21. (A) Thickness map derived from optical density STXM image of a 3D architecture prepared on a second silicon nitride grid. (B) Principal component clustering analysis of the sample shown in (A). Evidence of some oxide formation is shown in the Cluster 3 spectrum. Clusters are arranged in order of increasing thickness (top to bottom). (C) Spectra color-coordinated to the clustered regions in (B). (D) Raw principal components along which the spectra in (C) were scored during clustering analysis. Scale bars: 1 μm.

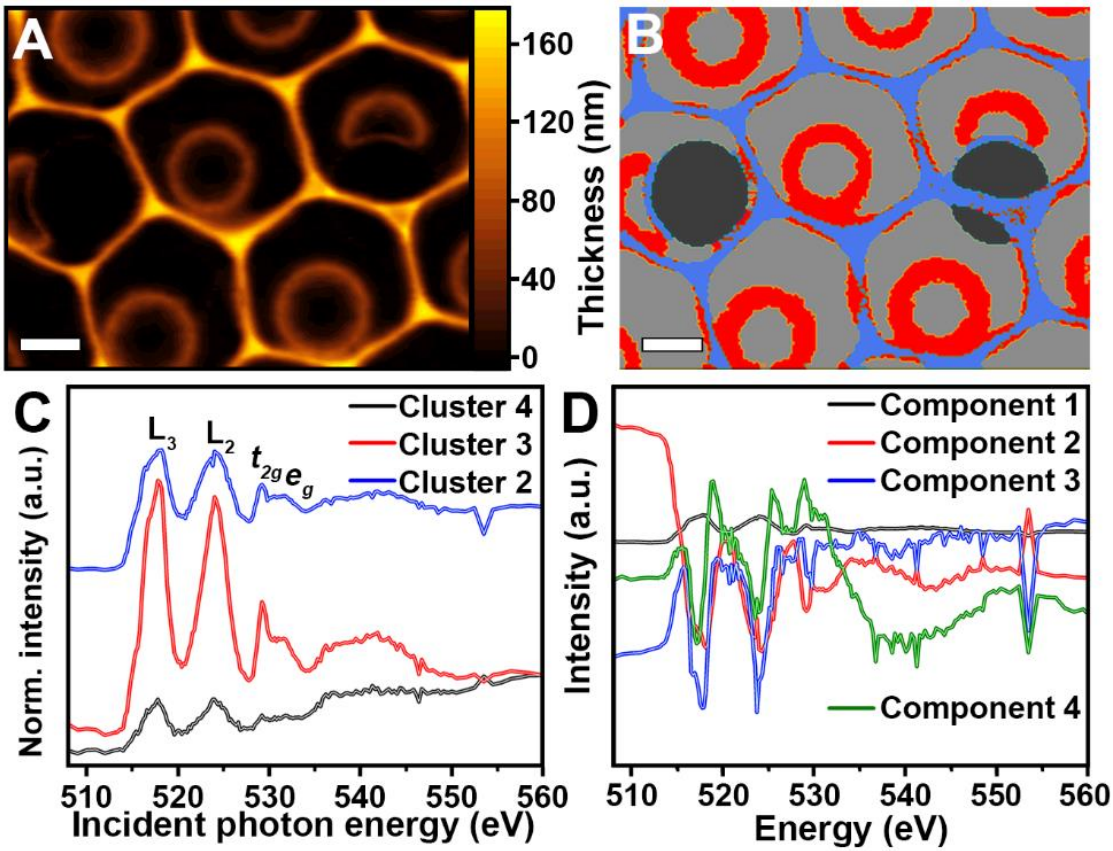

Figure C.22. (A) Thickness map derived from optical density STXM image of the 3D architecture prepared on a second silicon nitride grid. (B) Principal component clustering analysis of the sample shown in (A). (C) Spectra color-coordinated to the clustered regions in (B). Spectra are arranged in order of decreasing thickness. (D) Raw principal components along which the spectra in (C) were scored during clustering analysis. Scale bars: 1 μm.

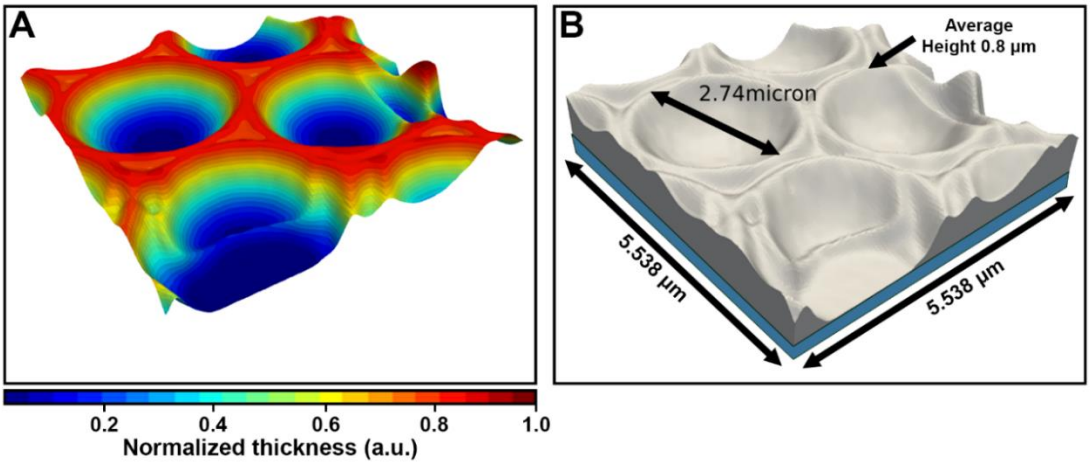

Figure C.23. (A) 3D height map generated from the optical density STXM images using the Beer-Lambert Law. The thickness obtained from analysis of the 3D architecture was normalized to known dimensions for the nanobowl architecture (i.e., an architecture prepared by the same method as we have reported previously [Chalker, C. J.; et al. Fabrication and Electrochemical Performance of Structured Mesoscale Open Shell V_2O_5 Networks. *Langmuir* **2017**, *33* (24), 5975–5981.]). These thicknesses are known to be between 0.8-1.3 µm (roughly half the height of the polystyrene templating beads used to form the nanobowl architecture. (B) This height information was filled to create a finite element mesh which was used for subsequent Finite Element Simulations [Stein, P.; et al. The Influence of Surface Stress on the Chemo-Mechanical Behavior of Inverse-Opal Structured Electrodes for Lithium-Ion Batteries. *J. Electrochem. Soc.* **2020**, *167* (1), 013529.].

APPENDIX D

SUPPLEMENTARY FIGURES AND TABLES

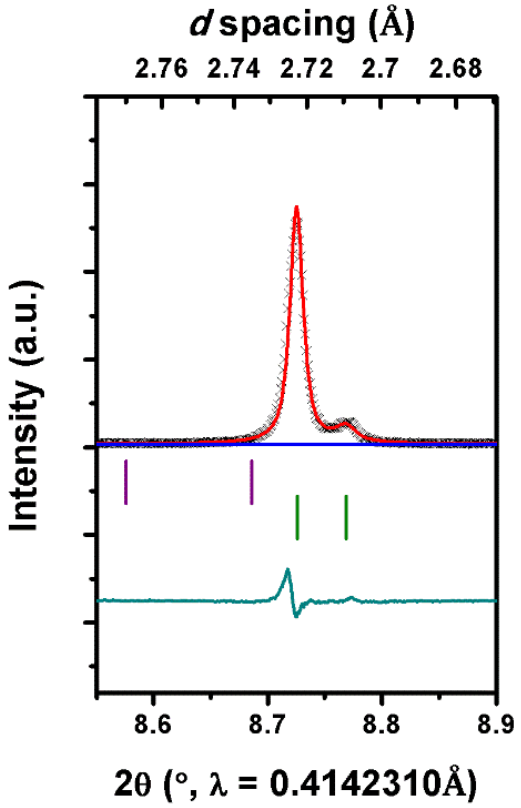

Figure D.1. Two major reflections characteristic of AgCl (*Fm$\bar{3}$m*, 5.45 Å and 5.54 Å unit cells), which should appear at 2*θ* values of ~8.55 2θ and ~8.65 (purple tick marks) are not observed in the displayed 2*θ* range (8.5-8.9°). Furthermore, no AgCl reflections are observed in the entire range. The absence of AgCl reflections indicates the successful removal of the AgCl impurity [Marley, P. M.; et al. Emptying and Filling a Tunnel Bronze. *Chem. Sci.* **2015**, *6* (3), 1712–1718.].

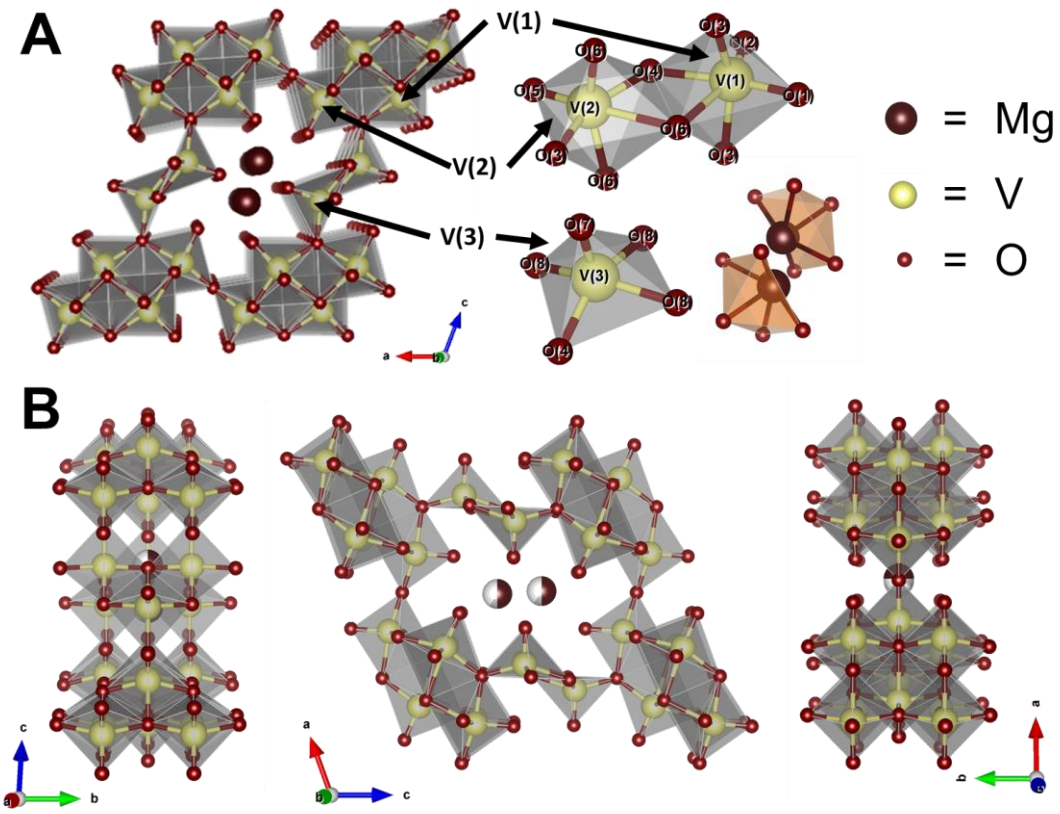

Figure D.2. Individual vanadium and magnesium polyhedra are depicted in (A), where the vanadium octahedra and square pyramid are depicted in grey. The frustrated five-coordinated MgO_5 coordination environment is depicted in orange. A single unit cell is depicted in (B) where the structure can be viewed along the *a*, *b*, and *c* axes, respectively.

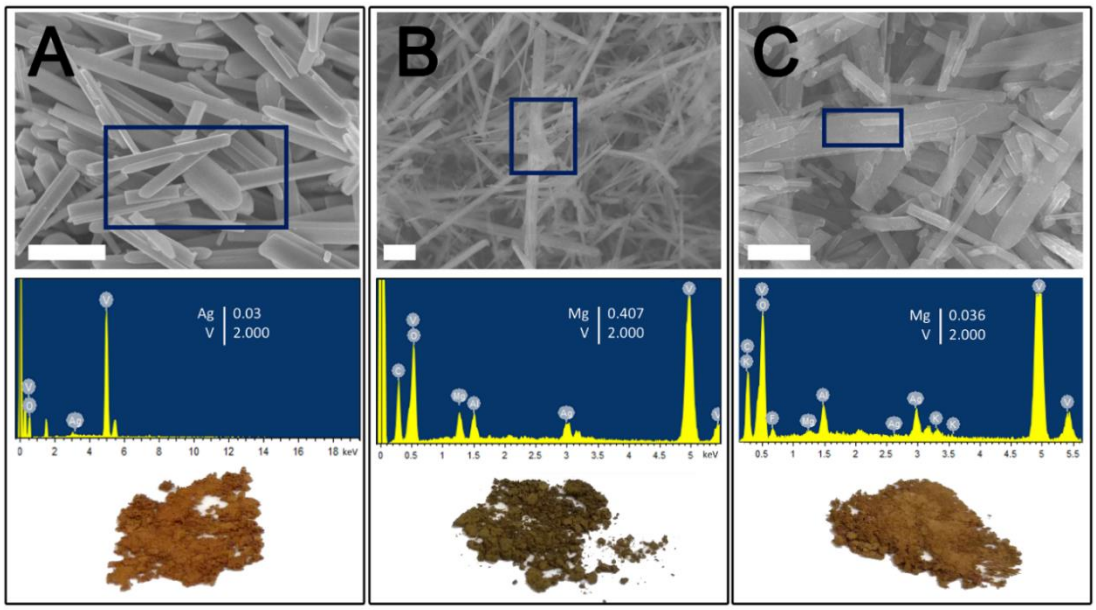

Figure D.3. Scanning electron micrograph, energy dispersive X-ray spectrum, and optical image for (A) pristine, as-prepared ζ-V_2O_5, (B) magnesiated β-$Mg_xV_2O_5$, and (C) $NOBF_4$ – leached ζ-V_2O_5. The SEM images indicate retention of nanowire morphology, confirming the topochemical nature of the chemical magnesiation/demagnesiation process. The blue boxes in the SEM images indicated the region from which the semi-quantitative EDS was acquired, which shows qualitatively the insertion/deinsertion of the magnesium. The optical images illustrate that the reduction of the V_2O_5 lattice on Mg^{2+} insertion is accompanied by a change in color from orange/brown characteristic of V^{5+} to a dark green, indicative of a mixed $V^{4+/5+}$ vanadium valence. Upon topochemical leaching of the magnesium from within the tunnels, restoration of the orange/brown coloration is observed, suggesting a concomitant reduction/oxidation of the lattice with Mg^{2+} insertion.

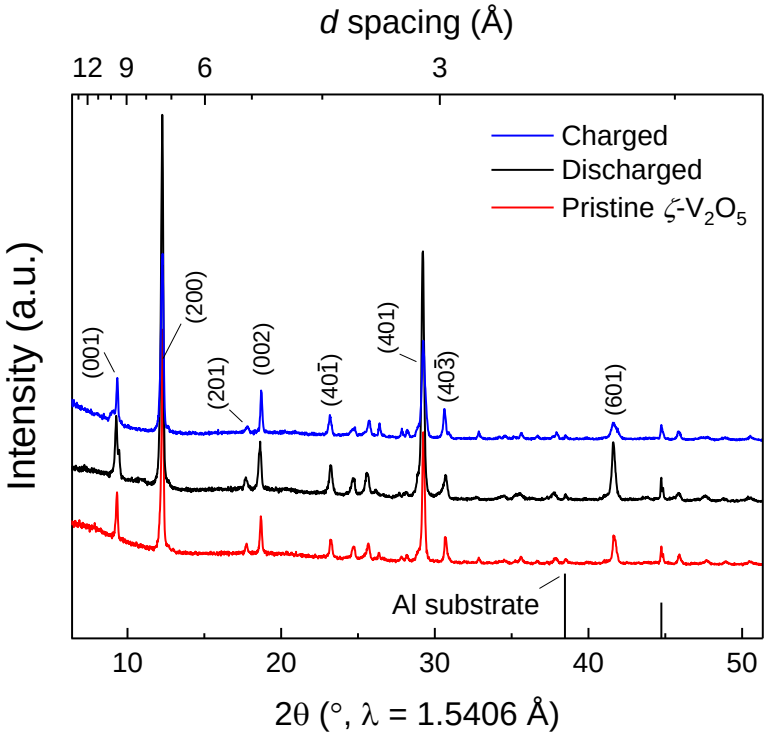

Figure D.4. All reflections revert to their original position upon demagnesiation, indicating the topotactic nature of the insertion, as well as the reversibility of the reaction. The similarities between the diffraction patterns collected for electrochemical (shown here) and chemical (Figure 5.3) cycling are striking.

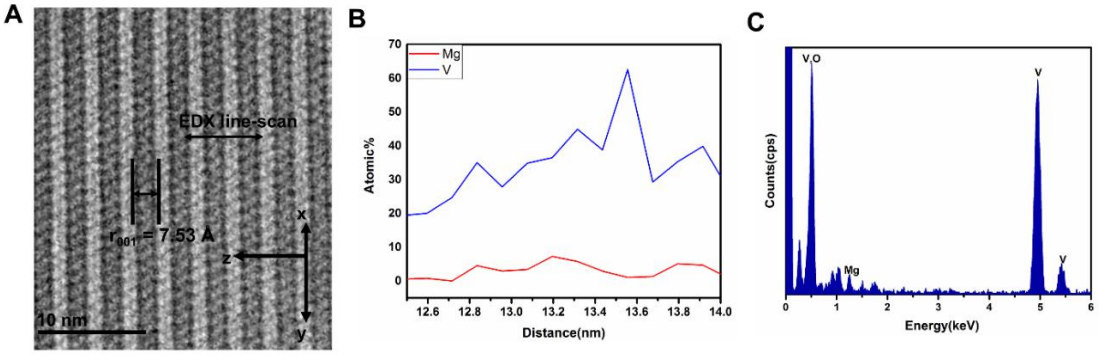

Figure D.5. (A) Atomic-resolution HAADF image in the [110] zone axis, showing the direction of the EDX line scan perpendicular to the tunnel growth direction. Scale bar is 10 nm (B) the results of the EDX line scan showing V (blue) and Mg (red) signals in units of atomic percent. (C) Integrated EDX scan showing relative intensities of the V, O, and Mg. The integrated values yield a ca. 4 ± 0.4 at% value for Mg, corresponding to a stoichiometry in the range $Mg_{0.26}V_2O_5$- $Mg_{0.32}V_2O_5$.

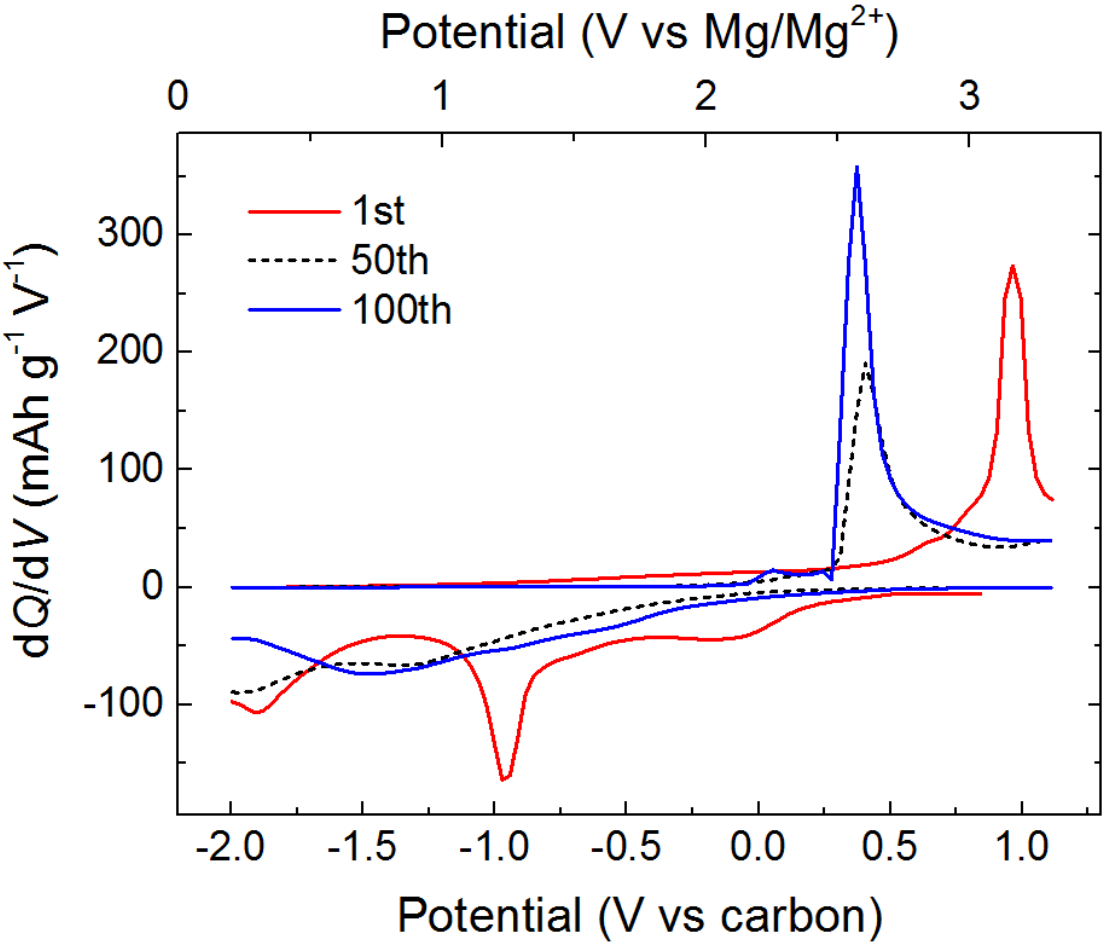

Figure D.6. The dQ/dV plot was used to determine the reported average operating voltage (1.65 V vs Mg^{2+}/Mg^{0}). Curves for the 1^{st}, 50^{th}, and 100^{th} cycles are depicted in solid-red, dashed-black, and solid-blue respectively.

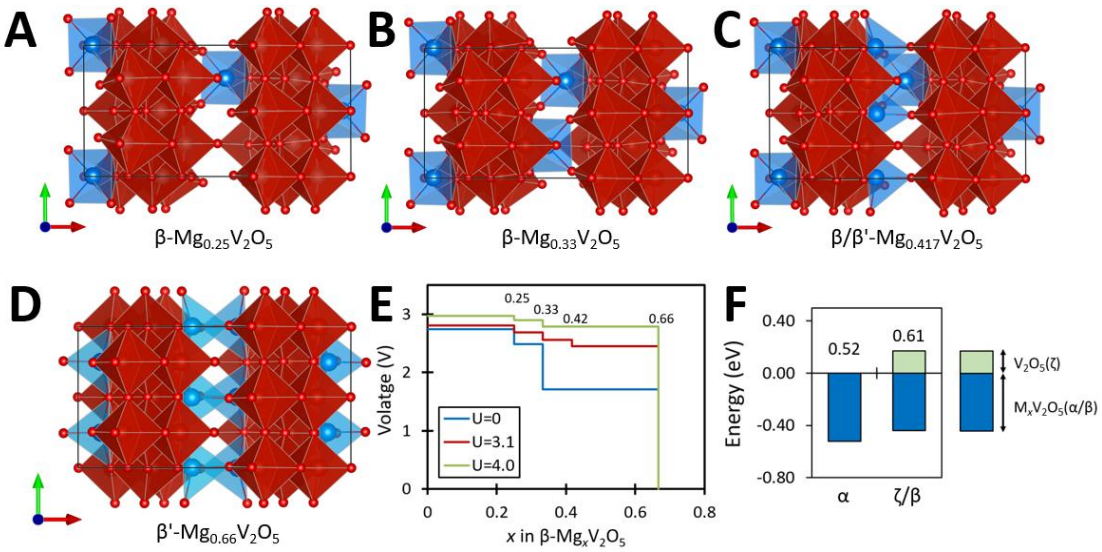

Figure D.7. Selected optimized structures of $Mg_xV_2O_5$ for (A) x = 0.25, (B) x = 0.33, (C) x = 0.417, and (D) x = 0.66. The O and Mg atoms are shown in red and blue, respectively. It is important to note that in (A) and (B), the magnesium occupies the β sites of the tunnels, which are in close proximity. As such, they can only be occupied to half capacity (0.33 per V_2O_5). There are several other sites within the tunnel which allow for double capacity (β'). Panels (C) and (D) depict occupation of these sites, which remains to be experimentally achieved. (E) Calculated voltage profile for Mg insertion into ζ-V_2O_5 for various values of *U*; (F) A comparison of the relative energies of the metastable polymorphs ζ-V_2O_5 (in eV) with α-V_2O_5 for both the charged and discharged states. The relative instability of the metastable phase ζ-V_2O_5 with respect to α-V_2O_5 is plotted using light green bar. The numerical sum of these two values (shown on top of the bars) provides a measure of the open circuit voltage.

.

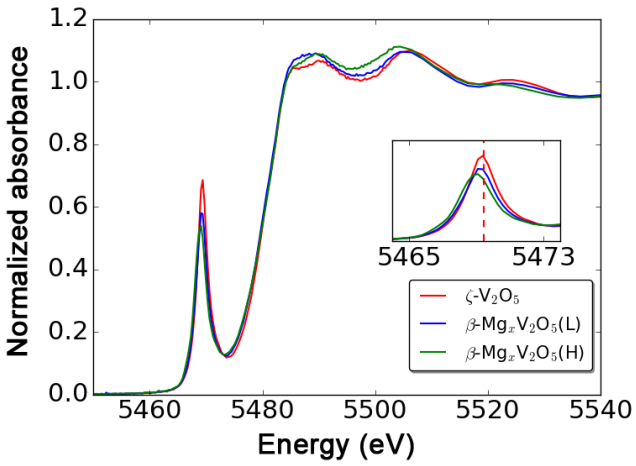

Figure D.8. Vanadium K-edge normalized spectra collected for pristine ζ-V_2O_5 (in red), magnesiated β-$Mg_xV_2O_5$ (with intended *x* value of ca. 0.2, in blue), and magnesiated β-$Mg_xV_2O_5$ (in green, with intended *x* value of 0.48 magnesiation was performed using di-*n*-butylmagnesium). The inset plot shows an expanded view of the pre-edge peak centered at ~569 eV and depicts a red-shift of the peak indicating local reduction of the vanadium.

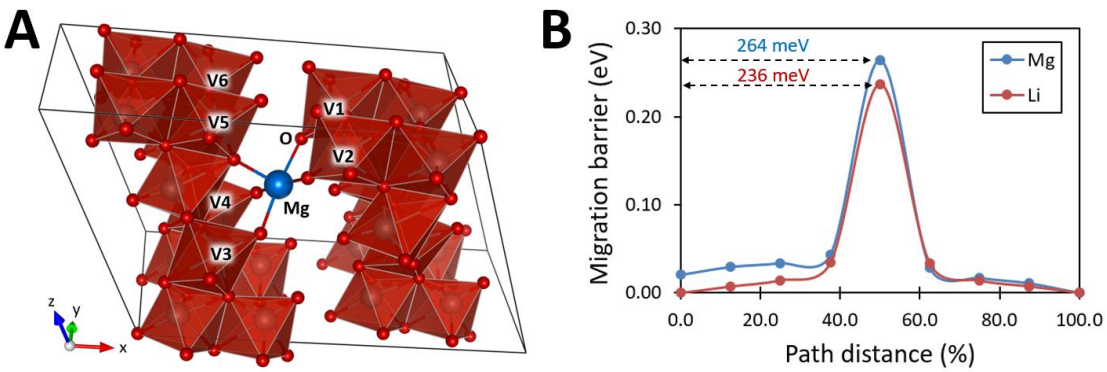

Figure D.9. (A) The possible sites for polaron formation on vanadium atoms marked as V1-5 after insertion of Mg ion in β-$Mg_{0.083}V_2O_5$; (B) the energy barrier for the migration of the bi-polaron on V2 and V3 to V1 and V3 in β-$Mg_{0.083}V_2O_5$, and the migration of a polaron on V5 to V6 in β'-$Li_{0.083}V_2O_5$. Migration barriers for the polaron between various sites in panel A are tabulated in Table D.3.

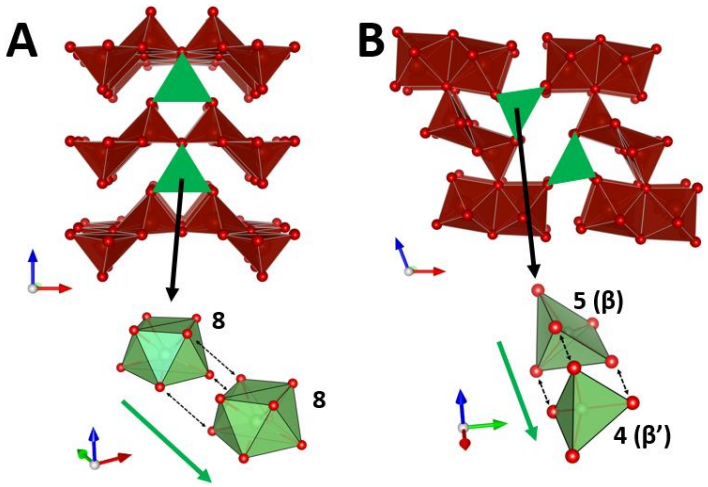

Figure D.10. Depiction of local coordination environments and diffusion pathways accessible for Mg^{2+} in (A) α-$Mg_xV_2O_5$; and (B) β-$Mg_xV_2O_5$. A magnified view of the coordination environments is shown in the lower panel. The green arrow shows the lowest energy diffusion pathways as determined by nudged elastic band calculations; the number labels represent the change in coordination number along this pathway.

Table D.1. Atom positions, fractional occupancies and thermal parameters obtained from refinement of the chemically magnesiated β-$Mg_{0.33}V_2O_5$. structure. Refined lattice parameters are *a* = 15.33627(17) Å, *b* = 3.61187(14) Å, *c* = 10.083053(59) Å, *α* = 90°, *β* = 109.762(1)°, and *γ* = 90° giving a volume = 525.633(7) Å^3. Refinement statistics are included in the table header.

χ2 = 6.408; Rwp = 0.1443; Rw = 11.18%					
Atom Label	*x*	*y*	*z*	*Uiso*100*	*Occupancy*
Mg(1)	0.9955(5)	0.0000000(0)	0.4033(5)	- -	0.497(0)
V(1)	0.11528(9)	0.0000000(0)	0.11528(12)	0.148	1.000(0)
V(2)	0.33885(9)	0.0000000(0)	0.10256(12)	0.455	1.000(0)
V(3)	0.28903(10)	0.0000000(0)	0.41222(13)	0.465	1.000(0)
O(1)	0.0000000(0)	0.0000000(0)	0.0000000(0)	0.231	1.000(0)
O(2)	0.10791(29)	0.0000000(0)	0.2741(4)	0.034	1.000(0)
O(3)	0.12977(32)	0.5000000(0)	0.0768(4)	0.034	1.000(0)
O(4)	0.25492(30)	0.0000000(0)	0.2161(4)	0.03	1.000(0)
O(5)	0.43889(31)	0.0000000(0)	0.2161(4)	0.0357	1.000(0)
O(6)	0.31581(28)	0.5000000(0)	0.0545(4)	0.034	1.000(0)
O(7)	0.39528(32)	0.0000000(0)	0.4712(4)	1.085	1.000(0)
O(8)	0.25594(30)	0.5000000(0)	0.4223(4)	0.064	1.000(0)
Ag1	0.9958160(0)	0.0000000(0)	0.4035260(0)	- -	0.091(0)

Table D.2. Bond lengths for the refined chemically magnesiated β-$Mg_{0.33}V_2O_5$ structure.

	Vector	Bond Length		Vector	Bond Length
[MgO_5] square pyramid	Mg(1)-O(2)	2.487(5)	V(2) octahedron	V(2)-O(3)	2.023(4)
	Mg(1)-O(5)	2.543(5)		V(2)-O(4)	1.991(4)
	Mg(1)-O(5)	2.543(5)		V(2)-O(5)	1.574(4)
	Mg(1)-O(7)	2.497(6)		V(2)-O(6)	1.8723(10)
	Mg(1)-O(7)	2.497(6)		V(2)-O(6)	1.8723(10)
V(1) octahedron	V(1)-O(1)	1.7570(13)		V(2)-O(6)	2.365(4)
	V(1)-O(2)	1.643(4)	V(3) square pyramid	V(3)-O(4)	1.867(4)
	V(1)-O(3)	1.8760(11)		V(3)-O(7)	1.534(4)
	V(1)-O(3)	1.8760(11)		V(3)-O(8)	1.8879(13)
	V(1)-O(4)	2.037(5)		V(3)-O(8)	1.8879(13)
	V(1)-O(6)	2.296(4)		V(3)-O(8)	2.010(4)

Table D.3. The relative formation energies of bi-polarons centered on various vanadium atoms with respect to the bi-polaron centered on V1 and V3. The position of the polarons is with reference to Figure D.9 above.

Polaron's position	Formation energy (eV)
V13	0.00
V23	0.02
V12	0.39
V25	0.12
V34	0.42
V35	0.14

Table D.4. Summary of calculated diffusion barriers for α-V_2O_5 and ζ-V_2O_5.

	α-V_2O_5	ζ-V_2O_5
Mg^{2+} ionic diffusion barrier	1.2 eV* (GGA)	0.6-0.9 eV (GGA)
Single polaron diffusion barrier	0.34 eV* (U = 4.0)	0.24 eV* (U = 4.0)
Polaron formation energy	0.41 eV*	0.36 eV*
*Parija et. al. *Chemistry of Materials*, 2016, *28*, 5611-5620		

Table D.5. Tabulated metrics for Mg-ion cathode materials reported within the literature. Tabulated values were obtained from references: (1) Aurbach et. al. *Nature*, **2000**, *407* (6805) 724-727.; (2) Sa et. al. *Journal of Power Sources*. **2016**, *323*, 44-50.; (3) Mukherjee et. al. *Chemistry of Materials*. **2017**, *29*, 2218-2226.; (4) Sa et. al. *Chemistry of Materials*, **2016**, *28* (9), 2962-2969.

Material	Capacity (1^{st} cycle) (mAh/g)	Cycle Stability (# cycles)	Capacity (n^{th} cycle) (mAh/g)	Voltage (V)	Voltage Hysteresis (V)	Coulombic Efficiency	Temp. (°C)	Morphology.	Ref.
$Mg_xMo_6S_8$	70	>2000	~60	1.1 (Disch.)	~0.3	N/A	-20 to 80	Bulk	(1)
α-V_2O_5 (dry)	~80	>10	~75	~2.4	N/A	N/A	r.t.	Bulk	(2)
α-V_2O_5 (wet)	~260	>10	N/A	~2.4	N/A	N/A	r.t.	Bulk	(2)
α-V_2O_5 (dry)	10	10	40	~2.2 (avg.)	2.5	N/A	N/A	Bulk	(3)
Xerogel V_2O_5	23	10	47	1.9 (avg.)	~2.2	N/A	r.t.	Not specified	(4)
ζ-V_2O_5 (this work)	148	>100	90	1.65 (avg.)	~2.0	84.2% @ 100^{th} cycle	50	Nanowires (150 nm width)	This work

APPENDIX E

SUPPLEMENTARY FIGURES AND TABLES

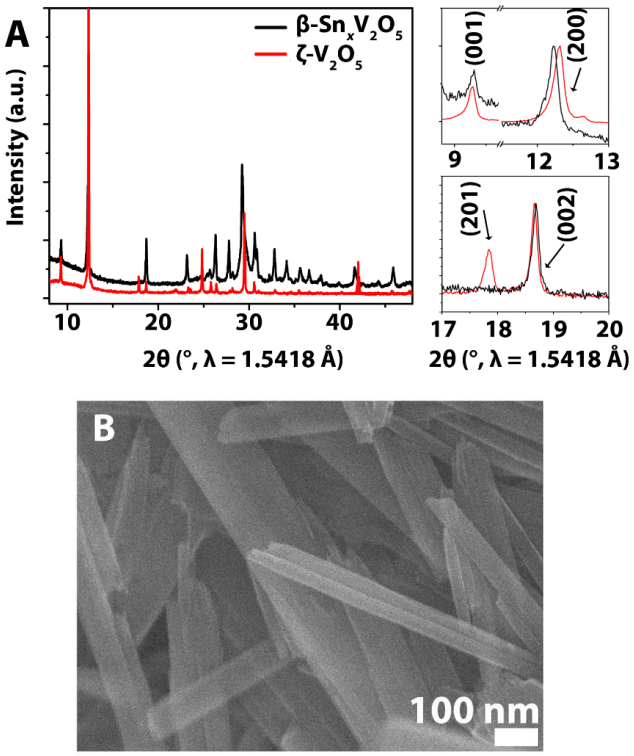

Figure E.1. (A) Powder XRD pattern of the metastable ζ-V_2O_5 precursor material contrasted with the diffraction pattern for β-$Sn_xV_2O_5$ illustrating the changes in several key reflections as a result of the insertion of Sn^{2+} ions. An expanded view of the (001) and (200) Bragg reflections are shown as insets to (A) to better illustrate expansion of the unit cell, primarily along the crystallographic *a*-axis. The expanded views have been independently normalized to the (200) reflection (top) and (002) reflection (bottom). (B) SEM image of ζ-V_2O_5 nanowires prepared by topochemical extraction of Cu-ions from β'-$Cu_xV_2O_5$ indicating an average width of ca. 100—150 nm.

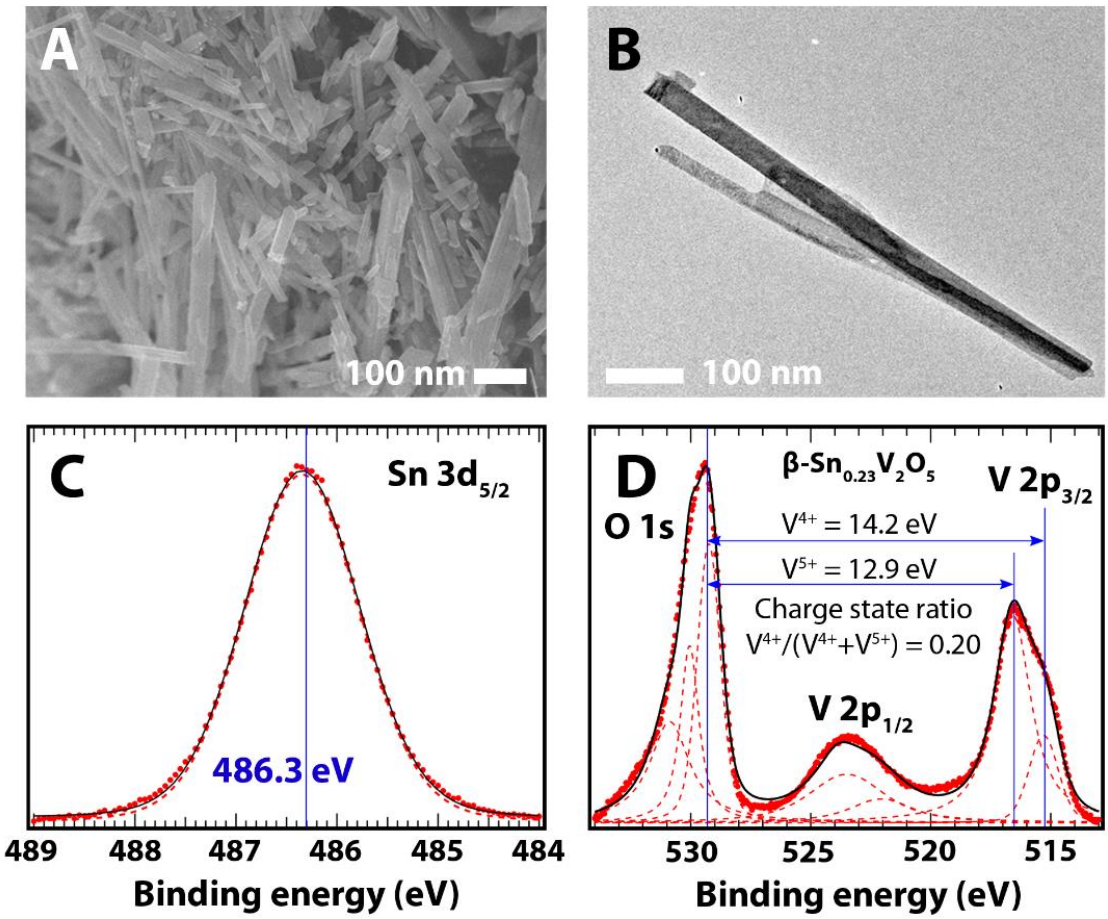

Figure E.2. (A) A SEM image and (B) a low-magnification TEM image of β-$Sn_{0.23}V_2O_5$ nanowires indicating retention of the nanowire morphology of the ζ-V_2O_5 precursor following Sn^{2+} insertion. (C) XPS peak fitting of β-$Sn_xV_2O_5$, which indicates a single oxidation state (Sn^{2+}) for tin within the ζ-V_2O_5 structure. (D) Fitting of O 1s and V 2p core level spectra of β-$Sn_{0.23}V_2O_5$, consistent with reduction of the vanadium host lattice upon Sn^{2+} intercalation.

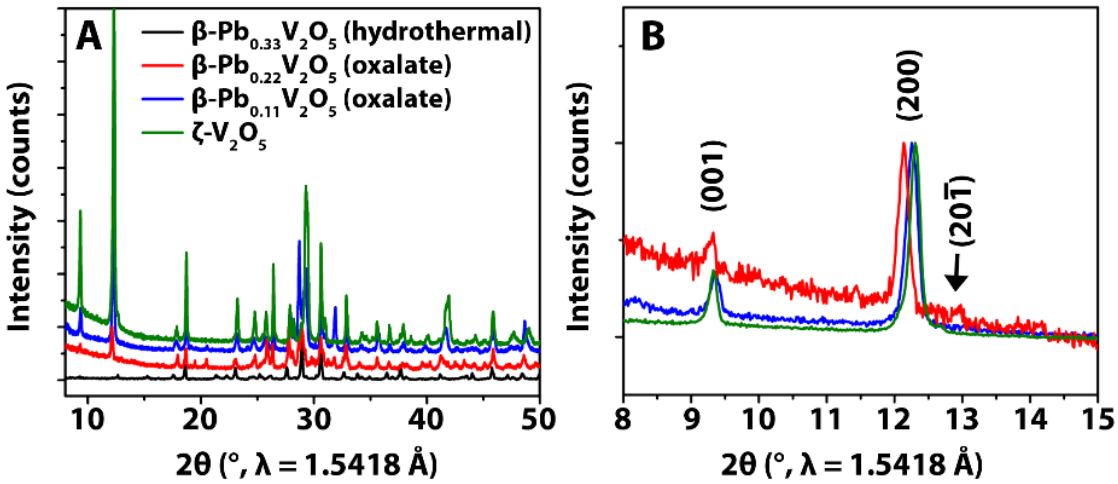

Figure E.3. (A) Powder XRD patterns for β-$Pb_xV_2O_5$ synthesized with intended occupancies of x = 0.11 (blue), x = 0.22 (red), and x = 0.33 (black) contrasted with the XRD pattern of ζ-V_2O_5. The $x_{intended}$ = 0.11 and 0.22 materials have been synthesized by topochemical insertion using the oxalate decomposition approach, whereas the $x_{intended}$ = 0.33 material was synthesized according to a previously reported hydrothermal route [Marley, P. M.; et al. Charge Disproportionation and Voltage-Induced Metal-Insulator Transitions Evidenced in β-$Pb_xV_2O_5$ Nanowires. *Adv. Funct. Mater*. **2013**, *23* (2), 153–160.]. (B) An expanded view of the 2θ region between 8.5—13.0° showing monotonic expansion of the lattice with increasing Pb insertion. The expanded region is independently normalized to the intensity of the (200) reflection to better allow for visualization of the peak shifts.

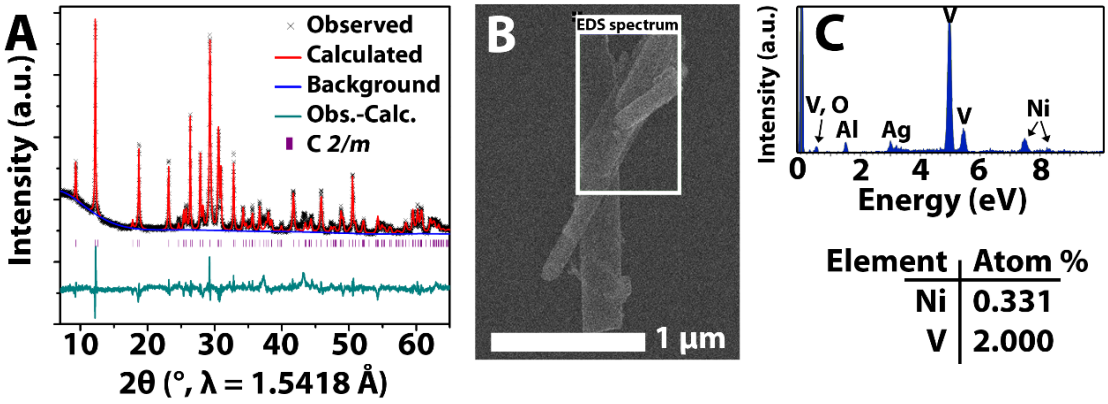

Figure E.4. (A) Rietveld refinement of powder XRD data collected for β-$Ni_xV_2O_5$ (*x* of ca. 0.331). Black crosses correspond to collected data, the red line is the calculated pattern, the blue line is the background function, and the teal line plots the residual of the refinement. Calculated reflections are marked below the observed data with vertical purple tick marks. Rietveld refinement statistics, lattice parameters, atom positions, and bond angles are listed in Table E.4 and Table E.5 (B) SEM image of β-$Ni_{0.331}V_2O_5$ on a Si/SiO_2 substrate. (C) Energy dispersive X-ray spectrum collected across the region of the wire indicated by the purple box in (B). The integrated peak areas of the spectrum indicate a stoichiometry of β-$Ni_{0.331}V_2O_5$. (D) Powder X-ray diffraction patterns collected for various transition (Ni, Co) and post-transition metal (Sn, Pb)-intercalated materials. The powder diffraction patterns are normalized to the intensity of the (11-1) reflection positioned at ca. 2Θ = 26.27° to better facilitated comparison of changes in peak location and intensity. All the powder diffraction patterns shown in (D) have been collected with the inclusion of an internal standard (α-Al_2O_3, 25 wt.%) to verify shifts in the reflections. The (310) and (410) reflections of α-Al_2O_3 are shown in (E). (F) Expanded view of the 2Θ region between 8.8—12.8° shown for XRD patterns of ζ-V_2O_5, β-$Ni_{0.331}V_2O_5$, β-$Co_{0.270}V_2O_5$, β-$Sn_{0.225}V_2O_5$, and β-$Pb_{0.22}V_2O_5$.The solid tick marks denote the maxima of the (200) reflection for each pattern and illustrate that the expansion of the tunnels is proportional to the ionic radii of the inserted cations [Shannon, R. D.; Revised Effective Ionic Radii and Systematic Studies of Interatomic Distances in Halides and Chalcogenides. *Acta Crystallog. Sect A* 1976, *32* (5), 751-767.].

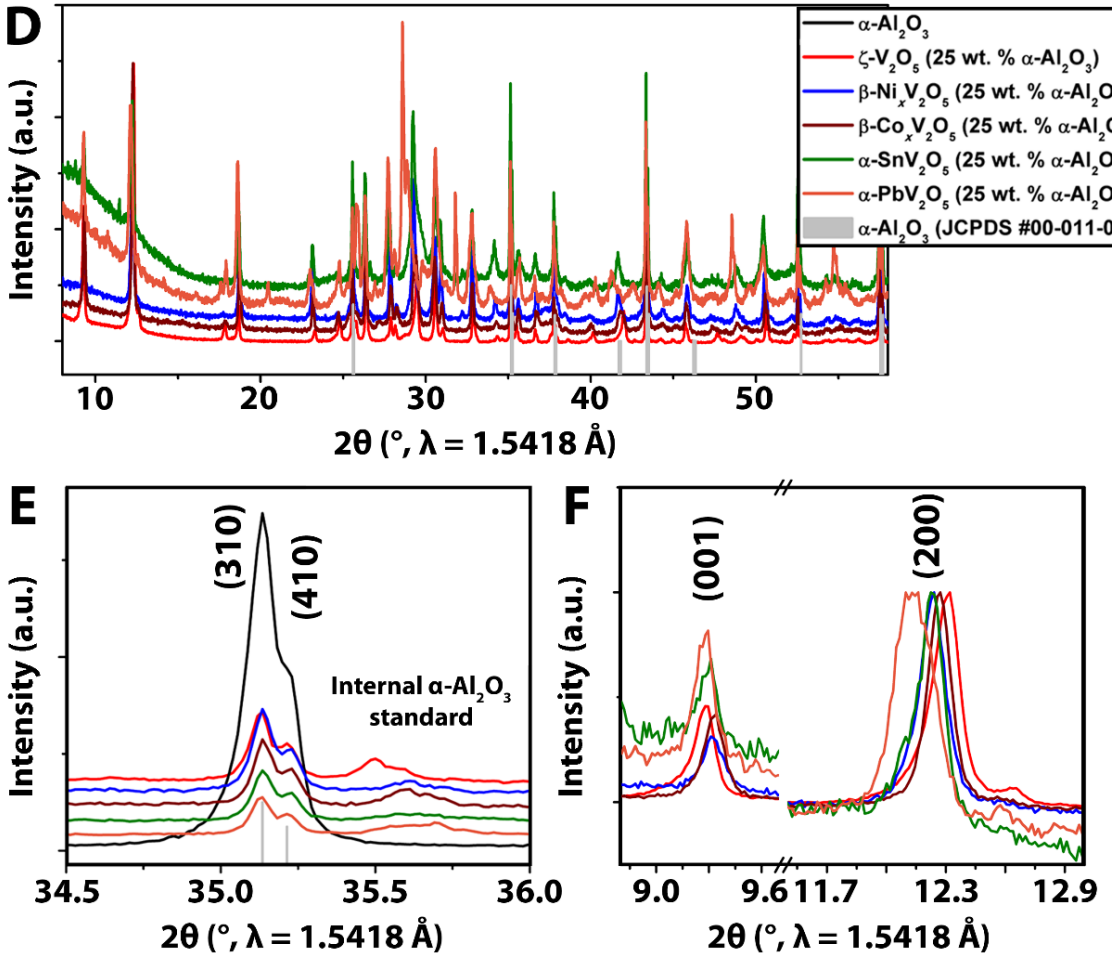

Figure E4. Continued.

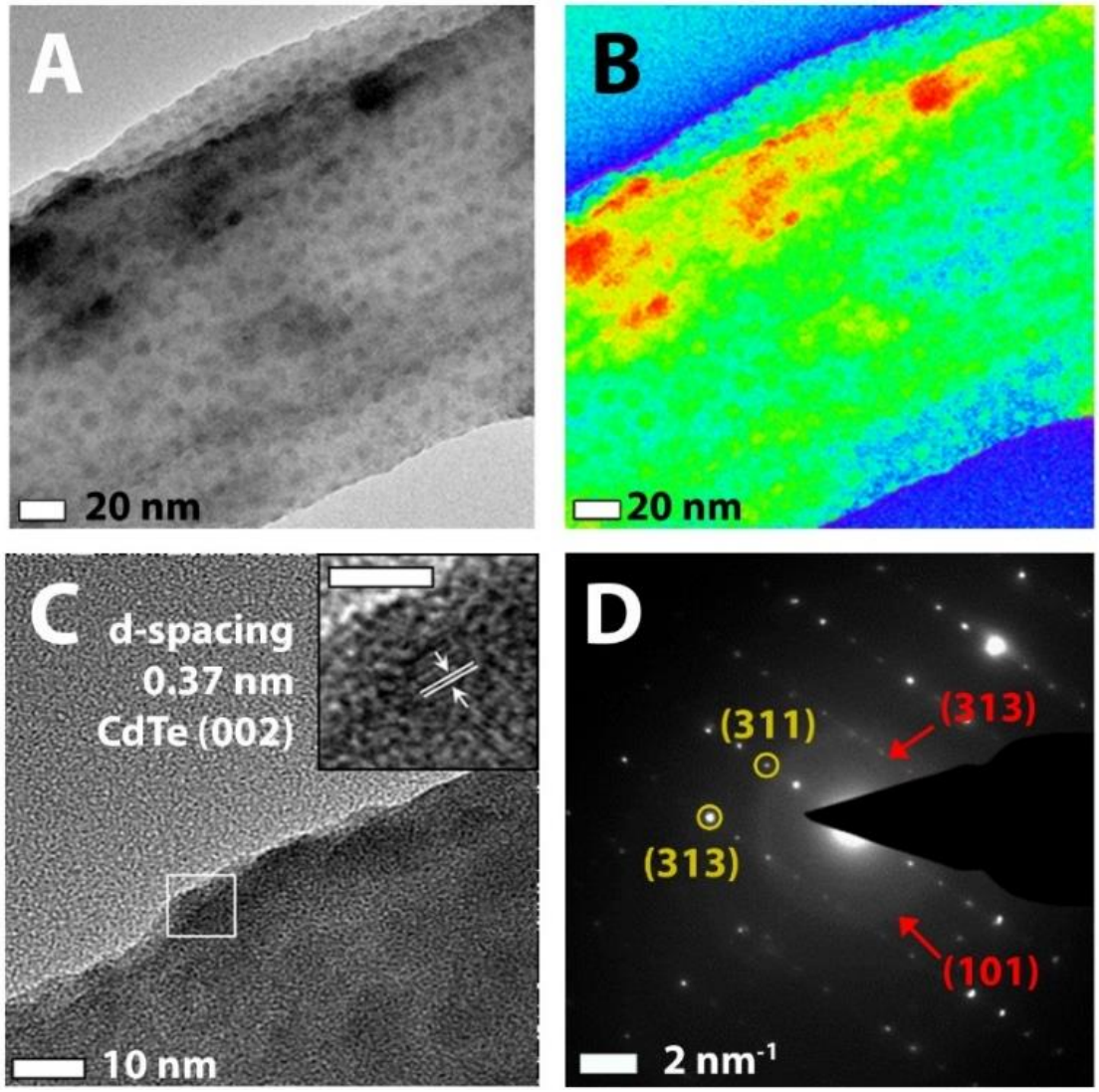

Figure E.5. (A) TEM image of β-$Sn_xV_2O_5$/CdTe heterostructures. (B) Colorized phase domain map indicating the relative surface coverage of β-$Sn_xV_2O_5$ nanowires with CdTe QDs. (C) HRTEM image and (D) corresponding SAED pattern of the β-$Sn_xV_2O_5$/CdTe heterostructure. The inset to (C) shows lattice fringes corresponding to the separation between the (002) planes of wurtzite CdTe lattice (JCPDS # 19-013). The SAED pattern in (D) comprises diffraction spots from β-$Sn_xV_2O_5$ and diffuse rings derived from CdTe QDs [Kumar, S.; Nann, T. Hexagonal CdTe Nanoparticles of Various Morphologies. *Chem. Commun.* **2003**, *19*, 2478-2479].

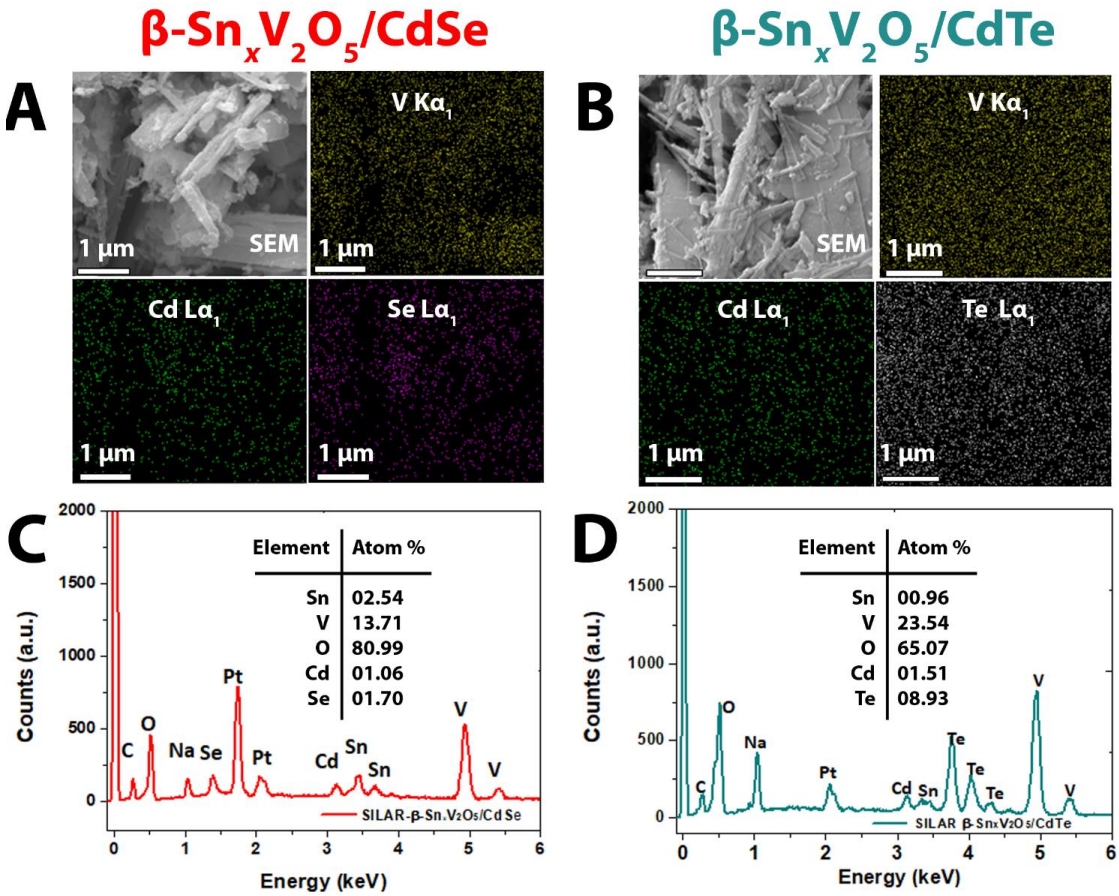

Figure E.6. (A) SEM image of β-$Sn_xV_2O_5$/CdSe heterostructures and corresponding EDX maps showing the distribution of V (yellow), Cd (green), and Se (purple). (B) SEM image of β-$Sn_xV_2O_5$/CdTe heterostructures and corresponding maps showing the spatial distribution of V (yellow), Cd (green) and Te (white). (C, D) The integrated EDX spectra corresponding to the elemental maps in (A) and (B), respectively.

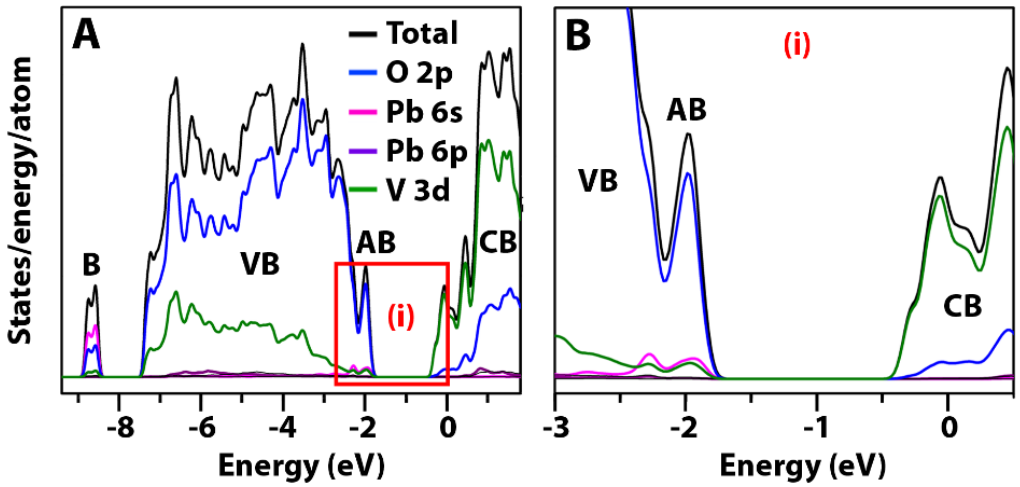

Figure E.7. (A) DFT-calculated density of states for β-$Pb_xV_2O_5$. Similar to β-$Sn_xV_2O_5$, the valence band comprises V-O hybridized state of primarily O 2p character, whereas the conduction band comprises V-O hybridized states. The Pb 6s—O2p hybrid bonding states are situated below the valence band, whereas the antibonding states are situated adjacent to the upper edge of the valence band. An expanded view of this region, labeled (i) is given in (B), where the Pb 6s contribution is discernible.

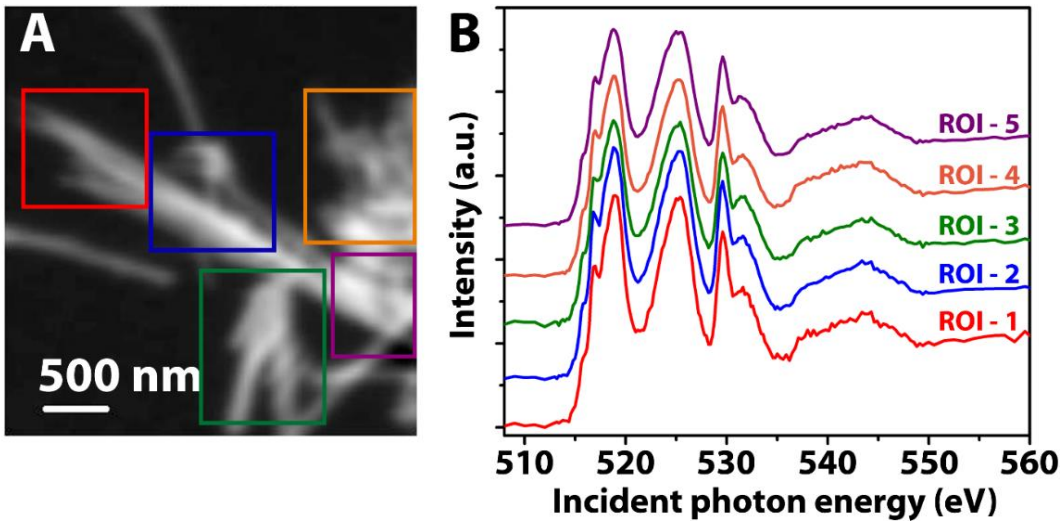

Figure E.8. (A) Stack-averaged optical density STXM image of β-$Sn_xV_2O_5$ nanowires illustrating retention of nanowire morphology after insertion of Sn ions into ζ-V_2O_5, consistent with SEM and TEM results (Figure E.2). (B) Spectra integrated across different regions of the nanowires, with colors corresponding to the indicated rectangular regions in (A) are strikingly similar and suggest that Sn-intercalation across the length of the nanowires and across different nanowires proceeds homogeneously.

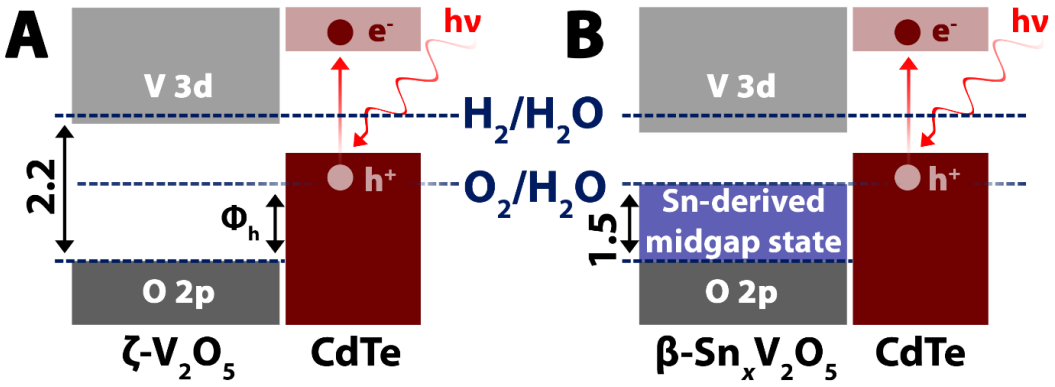

Figure E.9. Band alignments for (A) ζ-V_2O_5/CdTe and (B) β-$Sn_xV_2O_5$/CdTe heterostructures. The band alignments are oriented with respect to the positioning of the H_2/H_2O (hydrogen evolution) and O_2/H_2O (oxygen evolution) redox couples as indicated by the blue dashed lines. The positioning of the Sn-derived midgap state 1.5 eV above the V-O derived valence band edge onset of the pristine material is indicated by a shaded blue box in (B). A major advance here is illustrated by the improved alignment of the Sn-derived midgap state (blue) with the valence band of the CdTe quantum dots (green), leading to a diminished thermodynamic barrier (Φ_h) for hole transfer from the photoexcited quantum dot to the semiconducting nanowire, potentially enabling the use of CdTe QDs in heterostructures.

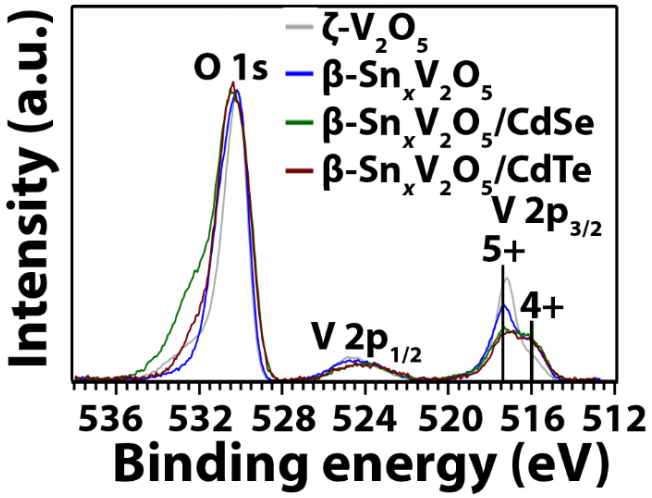

Figure E.10. HAXPES measurements for β-$Sn_xV_2O_5$ and β-$Sn_xV_2O_5$/CdX heterostructures (X = Se, Te).

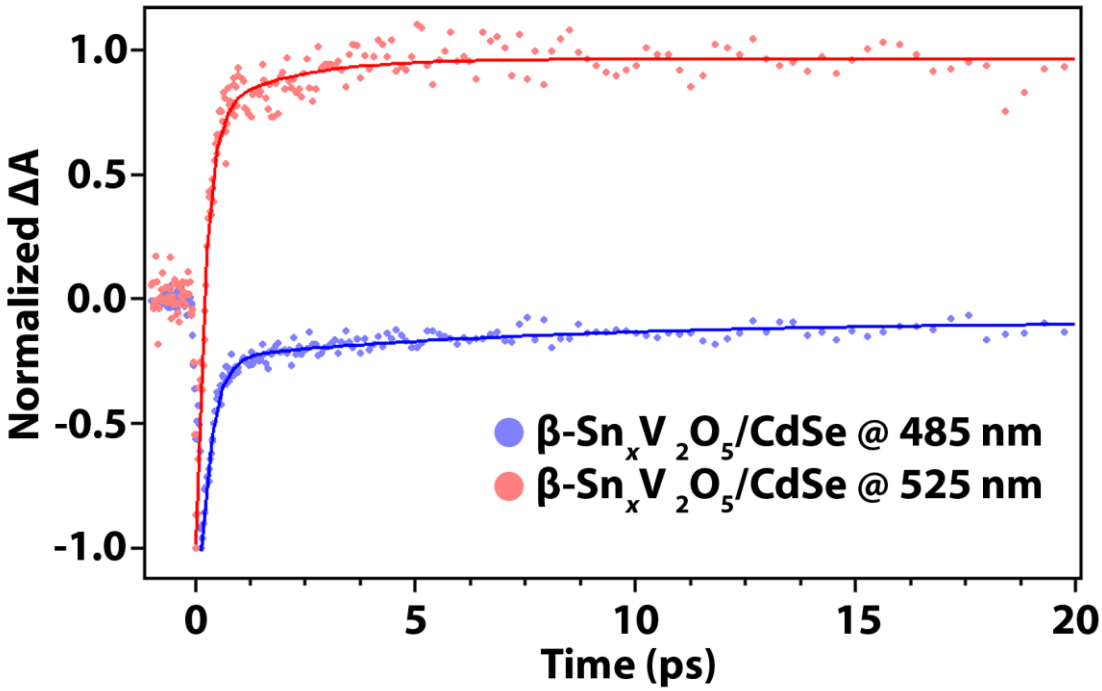

Figure E.11. A kinetic trace of collected TA data and multiexponential kinetic fitting for β-$Sn_xV_2O_5$/CdSe heterostructures at a probe wavelength of 485 nm (which effectively isolates the contribution from bleach feature of CdSe QDs) and 525 nm (which is a convolution of the contribution from the bleach feature of CdSe QDs and the induced absorption feature of the β-$Sn_xV_2O_5$ nanowires). The experimentally-observed absorbance difference values at each probe wavelength are displayed as red (525 nm) and blue (485 nm) dots, while the multiexponential kinetic fit to the data at each wavelength is displayed as a solid line of the same color. Kinetic fitting parameters and calculated average lifetimes are listed in Table E.7.

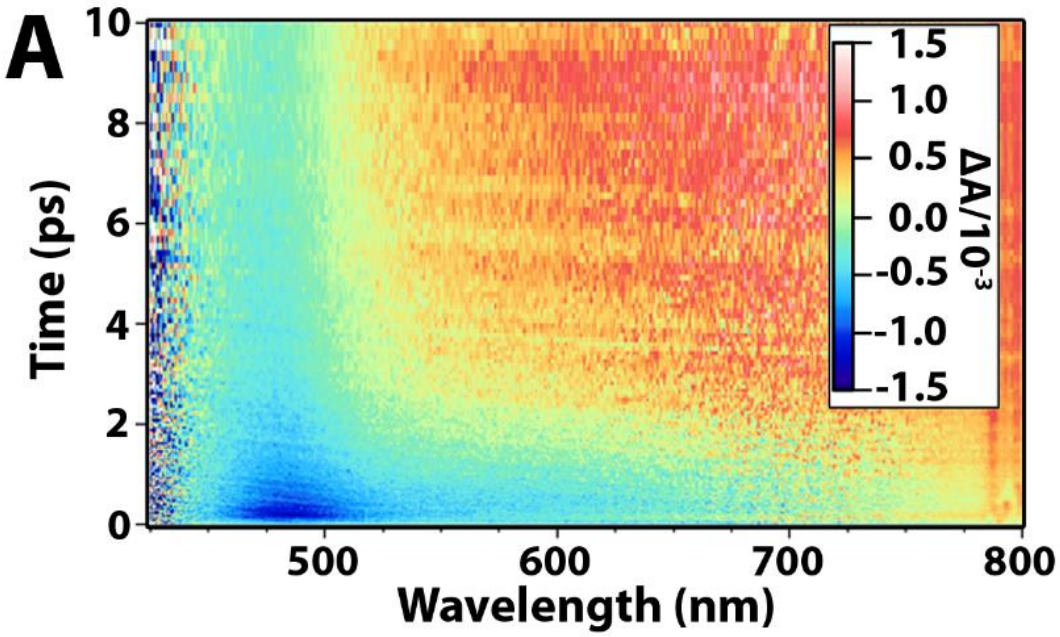

Figure E.12. (A) TA intensity map acquired for β-$Sn_xV_2O_5$/CdTe heterostructures in the delay time range of 0—10 ps across probe wavelength range of 425—800 nm at an excitation wavelength of 360 nm. TA spectra collected within a greater range of 0—20 ps for the same material. Each individual spectrum in (B) is taken as a horizontal 'slice' of the 3D intensity map in (A) at specific delay times (integrated across: a ±0.1 ps time window for the 0.5 ps decay; a ±0.5 ps time window for 1, 2.5, and 5 ps decay traces; and a ±2.5 ps time window for 10, 20 ps decay traces). (C) TA kinetic trace of the TA spectra and multiexponential kinetic fit for β-$Sn_xV_2O_5$/CdTe heterostructures at a probe wavelength of 485 nm (which effectively isolates the contribution from the bleach feature of CdTe QDs) and 675 nm (which is a convolution of the contribution from the bleach feature of CdTe QDs and the induced absorption of β-$Sn_xV_2O_5$ nanowires). The experimentally-observed absorbance difference values at each probe wavelength are displayed as red (675 nm) and blue (485 nm) dots, while the multiexponential kinetic fit to the data at each wavelength is displayed as a solid line of the same color. Kinetic fitting parameters and calculated average lifetimes are listed in Table E.7.

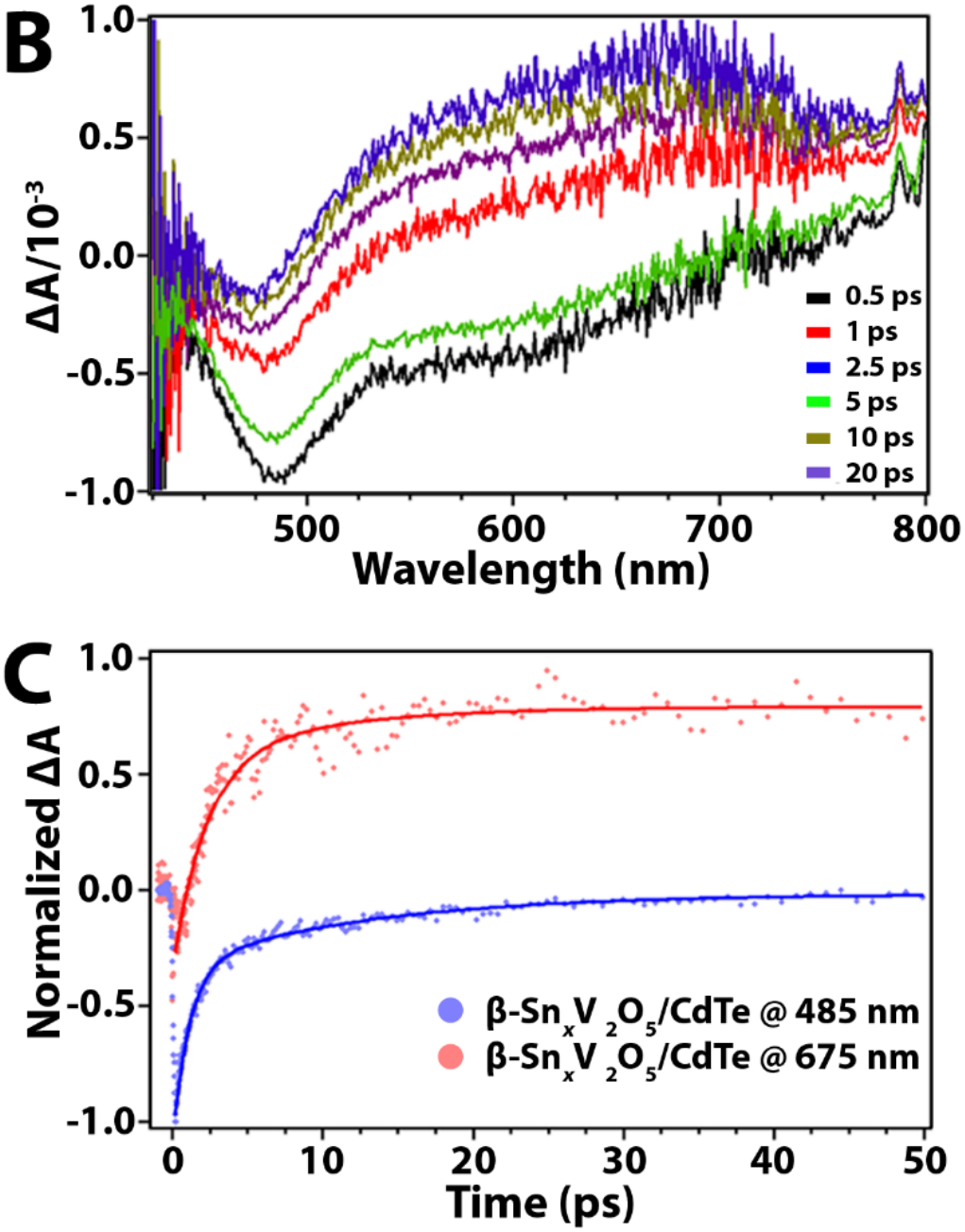

Figure E12. Continued.

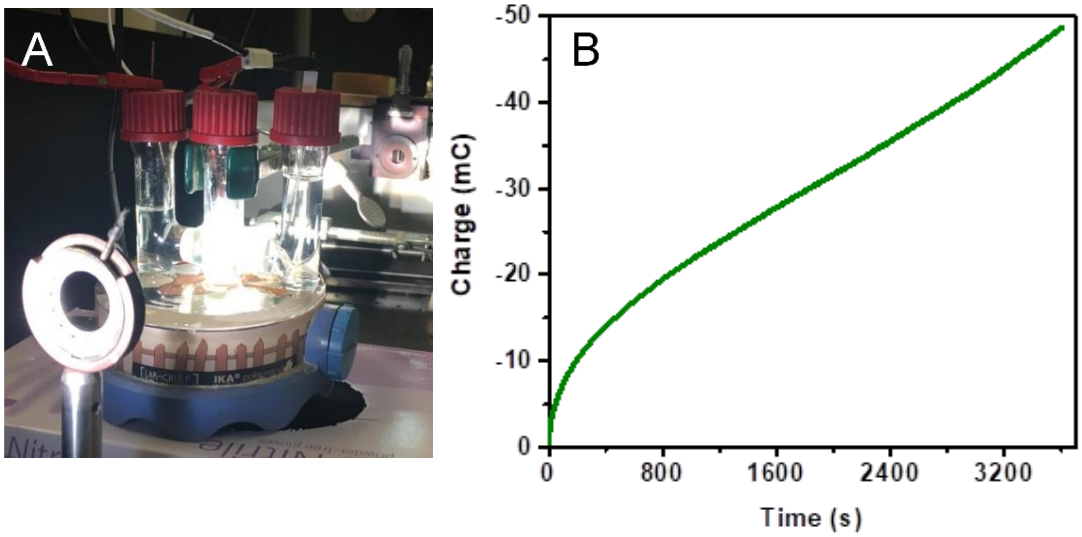

Figure E.13. (A) Three-electrode photoelectrochemical cell with β-$Sn_xV_2O_5$/CdSe photocathode, Pt mesh counter electrode, and SCE reference electrode. (B) Chronocoulometry (charge *versus* time) data collected under visible-light illumination at 120 mW/cm^2 at an applied potential of 0 V *versus* NHE. The electrolyte was a solution of Ni^{2+} (10 mM), 3-MPA (20 mM), 0.2 M KNO_3, and 0.1 M lactic acid in a 1:4 (*v*:*v*) water:acetonitrile (pH = 3) mixture and was degassed with Ar prior to the measurements.

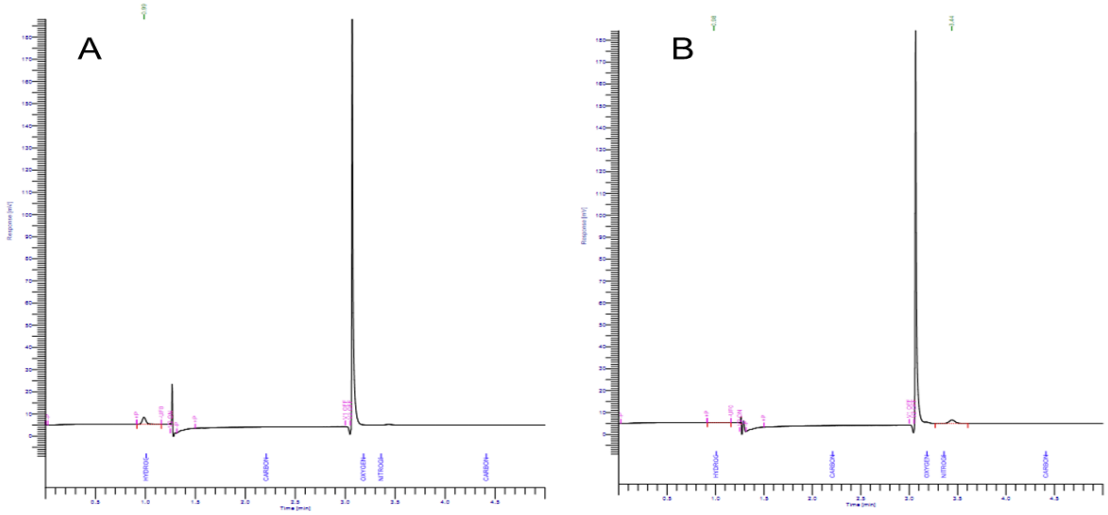

Figure E.14. A gas chromatogram of the headspace above the electrolyte following chronocoulometry measurements under visible-light illumination at 120 mW/cm^2 (A) and in the dark (B). Peaks attributable to H_2 are observed in the data for the illuminated sample, at a retention time of approximately 1 min. The peaks at longer retention times correspond to column switches.

Table E.1. Energetic positioning of the valence band edges (VBE, determined from XPS measurements), band gaps (determined from diffuse reflectance spectroscopy (DRS) measurements), and maxima of midgap states (determined from HAXPES) used to construct the relative band alignment diagram sketched in Figure 5.1 and Figure E.9.

Sample	VBE (eV)	Band gap (eV)	Midgap state max. (eV)
β-$Sn_{0.23}V_2O_5$	2.3 (XPS)	2.4 (DRS)	0.85 (XPS)
β-$Pb_{0.31}V_2O_5$	2.4 (XPS)	2.4 (DRS)	1.6 (HAXPES)
CdS	1.25 (XPS)	2.42	N/A
CdSe	0.85 (XPS)	2.73	N/A
CdTe	0.3 (XPS)	1.45	N/A

Table E.2. Refinement statistics, lattice parameters, and atom positions as obtained from Rietveld refinement of pattern for β-$Sn_{0.225}V_2O_5$ depicted in Figure 5.2B. Lattice parameters obtained from Rietveld refinement are *a* = 15.339(2) Å, *b* = 3.6217(3) Å, *c* = 10.0781(8) Å, *β* = 109.829(7) Å, with a volume = 526.67(6) Å^3. Refinement statistics are provided in the table header.

χ^2 = 6.147, Rw = 6.52%, wRp = 8.96%					
Atom	x	y	z	Occupancy	Uiso
Sn(1)	1.0095(12)	0.00	0.412(2)	0.225(6)	0.006
V(1)	0.1189(8)	0.00	0.1209(11)	1.0	0.008
V(2)	0.3511(9)	0.00	0.1032(14)	1.0	0.008
V(3)	0.2965(8)	0.00	0.4175(13)	1.0	0.008
O(1)	0.00(0)	0.00(0)	0.00(0)	1.0	0.015
O(2)	0.0958(25)	0.00	0.285(4)	1.0	0.015
O(3)	0.1529(24)	0.50	0.095(4)	1.0	0.015
O(4)	0.2533(24)	0.00	0.214(4)	1.0	0.015
O(5)	0.4482(23)	0.00	0.254(4)	1.0	0.015
O(6)	0.3258(23)	0.50	0.0228(33)	1.0	0.015
O(7)	0.4129(27)	0.00	0.518(4)	1.0	0.015
O(8)	0.2748	0.50	0.3861	1.0	0.015

Table E.3. Bond angles and lengths for MO_x polyhedral as obtained from Rietveld refinement of pattern for β-$Sn_xV_2O_5$ depicted in Figure 5.2B.

V-O Polyhedra	V-O	Distance (Å)	O-V-O	Angle (°)
$V(1)O_6$ Octahedra	V(1)—O(1)	1.818(10)	O(1)—V(1)—O(3)	99.5(11)
			O(1)—V(1)—O(4)	167.9(14)
	V(1)—O(2)	1.81(4)	O(1)—V(1)—O(6)	95.4(10)
			O(2)—V(1)—O(3)	105.8(11)
	V(1)—O(3)	1.927(13)	O(2)—V(1)—O(3)	105.8(11)
			O(2)—V(1)—O(4)	93.5(15)
	V(1)—O(3)	1.927(13)	O(2)—V(1)—O(6)	166.0(16)
			O(3)—V(1)—O(3)	140.0(22)
	V(1)—O(4)	1.954(35)	O(3)—V(1)—O(4)	77.1(12)
			O(3)—V(1)—O(6)	71.7(12)
	V(1)—O(6)	1.91(4)	O(3)—V(1)—O(4)	77.1(11)
			O(3)—V(1)—O(3)	71.7(11)
			O(4)—V(1)—O(6)	72.5(15)
$V(2)O_6$ Octahedra	V(2)—O(3)	1.98(4)	O(3)—V(2)—O(4)	137.4(13)
			O(3)—V(2)—O(5)	127.5(21)
	V(2)—O(4)	2.15(4)	O(3)—V(2)—O(6)	69.5(10)
			O(3)—V(2)—O(6)	69.5(10)
	V(2)—O(5)	1.730(28)	O(4)—V(2)—O(5)	95.0(18)
			O(4)—V(2)—O(6)	98.0(14)
	V(2)—O(6)	1.968(13)	O(4)—V(2)—O(6)	98.0(14)
			O(5)—V(2)—O(6)	110.6(10)
	V(2)—O(6)	1.968(13)	O(5)—V(2)—O(6)	110.6(10)
	V(2)—O(6)	2.576(26)	O(5)—V(2)—O(6)	133.9(17)
$V(3)O_5$ Square Pyramid	V(3)—O(4)	1.926(35)	O(4)—V(3)—O(7)	122.5(16)
	V(3)—O(7)	1.728(30)	O(4)—V(3)—O(7)	80.8(4)
	V(3)—O(8)	1.8490(24)	O(4)—V(3)—O(8)	80.8(4)
	V(3)—O(8)	1.8490(24)	O(7)—V(3)—O(8)	100.98(34)
	V(3)—O(8)	2.565(12)	O(7)—V(3)—O(8)	100.98(34)
			O(8)—V(3)—O(8)	156.7(7)
$Sn(1)O_7$ Distorted pentagonal bipyramid	Sn(1)—O(2)	2.13(5)	O(2)—Sn(1)—O(5)	77.4(12)
			O(2)—Sn(1)—O(5)	77.4(12)
	Sn(1)—O(5)	2.385(24)	O(2)—Sn(1)—O(7)	79.0(12)
			O(2)—Sn(1)—O(7)	79.0(12)
	Sn(1)—O(5)	2.385(24)	O(5)—Sn(1)—O(5)	98.8(13)
	Sn(1)—O(7)	2.771(31)	O(5)—Sn(1)—O(7)	68.2(9)
	Sn(1)—O(7)	2.771(31)	O(5)—Sn(1)—O(7)	155.1(17)
	Sn(1)—O(7)	2.150(19)	O(5)—Sn(1)—O(7)	68.2(9)
	Sn(1)—O(7)	2.150(19)	O(7)—Sn(1)—O(7)	114.7(16)

Table E.4. Refinement statistics, lattice parameters, and atom positions as obtained from Rietveld refinement of pattern for β-$Ni_{0.333}V_2O_5$ depicted in Figure E.4. Lattice parameters obtained from the refinement are *a* = 15.3711(7) Å, *b* = 3.6100(1) Å, *c* = 10.0726(5) Å, *β* = 109.968(4) Å, with a volume of V = 525.34(3) $Å^3$.

χ^2 = 6.379, Rw = 4.85%, wRp = 6.81%					
Atom	x	y	z	Occupancy	Uiso
Ni(1)	1.0042	0.000(0)	0.3926(11)	0.507(5)	0.008
V(1)	0.1240(5)	0.000(0)	0.1138(7)	1.0	0.008
V(2)	0.3392(4)	0.000(0)	0.1067(6)	1.0	0.008
V(3)	0.2881(5)	0.000(0)	0.4234(6)	1.0	0.008
O(1)	0.0000(0)	0.000(0)	0.0000(0)	1.0	0.0126
O(2)	0.1083(15)	0.000(0)	0.2653(19)	1.0	0.0126
O(3)	0.1321(16)	0.500(0)	0.0555(19)	1.0	0.0126
O(4)	0.2860(15)	0.000(0)	0.2501(21)	1.0	0.0126
O(5)	0.4400(13)	0.000(0)	0.2324(21)	1.0	0.0126
O(6)	0.3129(14)	0.500(0)	0.1005(21)	1.0	0.0126
O(7)	0.4083(14)	0.000(0)	0.4670(18)	1.0	0.0126
O(8)	0.2496(19)	0.500(0)	0.4100(0)	1.0	0.0126

Table E.5. Bond angles and lengths for MO*x* (M = V, Ni) polyhedral as obtained from Rietveld refinement of pattern for β-$Ni_{0.331}V_2O_5$ depicted in Figure E.4.

V-O Polyhedra	V-O	Distance (Å)	O-V-O	Angle (°)
$V(1)O_6$ Octahedra	V(1)—O(1)	1.859(7)	O(1)—V(1)—O(2)	97.4(9)
	V(1)—O(2)	1.624(18)	O(1)—V(1)—O(3)	88.3(7)
	V(1)—O(3)	1.915(7)		88.3(7)
	V(1)—O(3)	1.915(7)	O(2)—V(1)—O(3)	109.5(6)
	V(1)—O(4)	2.267(18)		109.5(6)
	V(1)—O(6)	2.65127(12)	O(3)—V(1)—O(3)	140.9(12)
$V(2)O_6$ Octahedra	V(2)—O(3)	1.832(20)	O(3)—V(2)—O(4)	169.0(11)
			O(3)—V(2)—O(5)	103.7(11)
	V(2)—O(4)	1.888(20)	O(3)—V(2)—O(6)	95.0(8)
				95.0(8)
	V(2)—O(5)	1.632(18)	O(4)—V(2)—O(5)	87.2(9)
	V(2)—O(6)	1.846(5)	O(4)—V(2)—O(6)	83.0(7)
				83.0(7)
			O(5)—V(2)—O(6)	99.5(7)
	V(2)—O(6)	1.846(5)		99.5(7)
	V(2)—O(6)	2.548(17)		155.8(14)
$V(3)O_5$ Square pyramid	V(3)—O(4)	2.872(11)	O(4)—V(3)—O(7)	84.7(9)
	V(3)—O(7)	2.872(11)	O(4)—V(3)—O(8)	91.75(27)
				91.75(27)
	V(3)—O(8)	1.8903(20)		162.8(8)
	V(3)—O(8)	1.8903(20)	O(7)—V(3)—O(8)	107.27(20)
				107.27(20)
	V(3)—O(8)	1.953(7)		112.5(7)
			O(8)—V(3)—O(8)	145.4(4)
				83.31(21)
				83.31(21)
$Ni(1)O_7$ Pentagonal bipyramid	Ni(1)—O(2)	2.368(24)	O(2)—Ni(1)—O(7)	135.33(34)
	Ni(1)—O(5)	2.397(14)		88.5(6)
	Ni(1)—O(5)	2.397(14)	O(5)—Ni(1)—O(5)	97.7(8)
	Ni(1)—O(7)	2.402(13)	O(5)—Ni(1)—O(7)	61.8(5)
				125.0(6)
				168.9(9)
	Ni(1)—O(7)	2.402(13)		81.3(4)
	Ni(1)—O(7)	2.597(15)	O(2)—Ni(1)—O(5)	80.4(7)
			O(7)—Ni(1)—O(7)	97.5(7)
	Ni(1)—O(7)	2.597(15)		127.7(6)
				64.3(8)

Table E.6. Tabulated lattice parameters for β-$M_xV_2O_5$ materials (M = Ni, Co, Sn, and Pb) as depicted in Figure E.4. Ionic radii were adapted from [Shannon, R. *Acta Crystallographica A*, **1976**, *32* (5), 751-767.]

Sample	*x*	*a* (Å)	*b* (Å)	*c* (Å)	β (Å)	V (Å)	Radius (Å)
ζ-V_2O_5	NA	15.25253(3)	3.602132(4)	10.104167(13)	110.088(0)	521.369(1)	N/A
$Ni_xV_2O_5$	0.331	15.3711(7)	3.6101(1)	10.0726(5)	109.968(4)	525.335(27)	0.63
$Co_xV_2O_5$	0.270	15.384	3.6185	10.0893	110.130	527.36	0.67
$Sn_xV_2O_5$	0.225	15.339(2)	3.6217(3)	10.0781(8)	109.829(7)	526.67(6)	1.22
$Pb_xV_2O_5$	0.220	15.470(2)	3.6153(4)	10.083(1)	109.396(10)	531.947	1.23

Table E.7. Kinetic fitting parameters and calculated average lifetimes for picosecond TA decay traces of β-$Sn_{0.225}V_2O_5$/CdSe and β-$Sn_{0.225}V_2O_5$/CdTe heterostructures.

Sample	λ_{pump} (nm)	λ_{probe} (nm)	ΔA_0	A_1	τ_1 (ps)	A_2	τ_2 (ps)	$<\tau>$ (ps)	χ^2
β-$Sn_xV_2O_5$/CdSe	360	485	-0.124 (±0.007)	-3.228 (±0.242)	0.248 (±0.012)	-0.156 (±0.016)	3.671 (±0.770)	0.406 (±0.053)	0.132
β-$Sn_xV_2O_5$/CdSe	360	525	0.968 (±0.009)	-5.110 (±0.433)	0.221 (±0.017)	-0.252 (±0.074)	1.925 (±0.655)	0.301 (±0.052)	1.082
β-$Sn_xV_2O_5$/CdTe	360	485	-0.023 (±0.004)	-0.734 (±0.013)	1.113 (±0.043)	-0.318 (±0.013)	11.77 (±0.835)	4.33 (±0.301)	0.123
β-$Sn_xV_2O_5$/CdTe	360	675	0.786 (±0.011)	-0.878 (±0.196)	2.222 (±0.443)	-0.248 (±0.203)	8.389 (±5.29)	3.578 (±0.811)	1.379